

**Final Report**

0.2 1.84

P 336

**SRM Internal Flow Tests  
and  
Computational Fluid Dynamic Analysis**

**Volume II  
RSRM Full Scale Motor Analyses**

**November, 1995**

**Prepared for:  
George C. Marshall Space Flight Center  
National Aeronautics and Space Administration  
Marshall Space Flight Center, AL 35812**

**Contract NAS8-39095**

**Prepared by:  
ERC, Incorporated  
555 Sparkman Drive, Suite 1622  
Huntsville, AL 35816**



## **Table of Contents**

### **Volume II**

#### **3.1 Full Scale Motor Analyses**

##### **3.1.1 RSRM Motor Analyses**

- 3.1.1.1 Pressure Perturbation Investigation**
- 3.1.1.2 NBR Stiffness Investigation**
- 3.1.1.3 Nozzle O-Ring Investigation**
- 3.1.1.4 Analysis Drawings**
- 3.1.1.5 Internal Aerodynamic Torque**
- 3.1.1.6 External Aerodynamic Torque**

### **Volume III**

#### **3.1.2 Titan Motor Failure Analysis**

##### **3.1.3 ASRM Motor Design Verification Analyses**

- 3.1.3.1 Motor Port Environment Analyses**
- 3.1.3.2 Structural/Fluid Dynamic Stress Analysis**
- 3.1.3.3 Igniter Analysis**
- 3.1.3.4 Internal and External Nozzle Torque Analysis**
- 3.1.3.5 Analysis Drawings**

#### **3.2 Subscale Motor Analyses**

- 3.2.1 NITM Two-Inch Motor Analysis**
- 3.2.2 Five-Inch Spin Motor Design and Test Analysis**
- 3.2.3 ASRM Subscale Plume Test**





## **Volume IV**

### **3.3 Cold Flow Analyses**

- 3.3.1 Checkout Model Analysis**
- 3.3.2 ASRM/Technology Model**
- 3.3.3 ASRM Aft Section/Nozzle Model**
- 3.3.4 ASRM Aft Segment/Nozzle Water Flow Model**
- 3.3.5 SAF Loss of Storage Tank Investigation**
- 3.3.6 SAF Model Test Plan**
- 3.3.7 ASRM Igniter Exhaust Port Model**
- 3.3.8 RSRM Nozzle Slag Ejection Precursor Tests**
- 3.3.9 RSRM Scaled Nozzle Slag Ejection Model**
- 3.3.10 RSRM Inhibitor Dynamics Model**
- 3.3.11 RSRM 10% Scale Cold Flow Model**

### **3.4 CFD Analysis Capability Development**

- 3.4.1  $\kappa$ - $\epsilon$  Equation Coefficients Adjustment**



# **PRECURSOR COLD FLOW MODEL**

## **Introduction**

The purpose of the RSRM Nozzle Slag Ejection Precursor Test is to investigate the effect that slag ejection from the RSRM nozzle has on the chamber pressure and thrust of the SRBs.

It should be noted that this is a precursor test. These tests will obtain data ASAP to generate information on this phenomenon to verify and calibrate the analytical slag ejection model. These tests will utilize the Solid Rocket Motor Air Flow Facility (SAF) which is capable of testing various solid rocket motor model configurations over a range of chamber pressures and flowrates and is capable of full scale RSRM Reynolds Number simulation of a 10% scale model. This precursor test will use Checkout Model 538 which is a 10% scale RSRM model (Figure 1). However, the model nozzle is not of the submerged nose type, rather it is a converging diverging nozzle scaled to 10% RSRM throat and exit diameters. The chamber diameter results in a port Mach Number of 0.24 which represents an earlier burn time than desired. However, later tests will make use of a submerged nose nozzle and a chamber diameter scaled to a burn time of approximately 70 seconds.

## **Objectives**

The primary objective of the RSRM Nozzle Slag Ejection Precursor Tests is to establish the feasibility of using cold flow test techniques to investigate the effects of slag ejection from the nozzle of the full scale motor on motor chamber pressure. This will be accomplished by measuring the pressure response in the model chamber to a liquid being injected into the model chamber and passing through the model nozzle throat.

### **Objective 1: Evaluate the effect of varying model chamber pressure and flowrate**

Varying the model chamber pressure will allow one to see the effect of the model nozzle blockage over a range of Reynolds Numbers and Weber Numbers. This will increase confidence in the analytical model and allow the results of the testing to be applied over a greater motor pressure range with more confidence.

**Objective 2: Evaluate the effect of varying the fluid injection rate and velocity**

Varying the rate at which the fluid is injected into the system will allow one to determine how the system reacts to blockage in the nozzle model throat as registered by the magnitude of the observed pressure spike.

The injection speed of the water at a given flowrate will also be varied. This will be accomplished by varying the diameter of the water injector nozzle.

**Objective 3: Evaluate the effect of varying the location where the fluid is injected into the system.**

Instrumentation ports are available at the upstream end of spool piece #1 and at the downstream end of spool piece #3. In the slag ejection tests the injected fluid will be introduced through the instrumentation ports of the spool pieces. Because spool pieces #1 and #3 are interchangeable it allows four possible axial locations for fluid introduction. These locations are the upstream end of spool piece #1 and downstream end of spool piece #3 with each spool piece in two locations, respectively.

The radial position of water injection may also be varied. The two primary radial locations will be the model centerline and near the model wall.

**Objective 4: Experiment with a variety of different fluids to be injected into the system**

The initial slag ejection tests are to be carried out using water as the injected fluid. However, other fluids may be tried at a later date, such as ethylene glycol, water based gels, or light oils. The different fluids would be tried in order that a Weber number match might be obtained between the RSRM full-scale motor and the RSRM Nozzle Slag Ejection Model while at the same time matching Reynolds Number or another simulation parameter.

**Objective 5: Develop a means to measure the injected fluid velocity at the nozzle exit plane.**

The purpose of measuring the injected fluid velocity at the nozzle exit plane is to enable the thrust increase due to slag ejection to be calculated. The injected fluid velocity could be measured by the use of a high speed camera in the model nozzle diffuser to record the trajectory of the fluid through the nozzle exit plane. Analysis of a fluid droplet position versus time will enable the velocity of the fluid to be found.

**RSRM Pressure Perturbation Cold Flow Tests  
and  
Computational Fluid Dynamic Analyses**

**24 February 1994**

**Prepared for:  
George C. Marshall Space Flight Center  
National Aeronautics and Space Administration  
Marshall Space Flight Center, AL 35812**

**Contract NAS8-39095**

**Prepared by:  
ERC, Incorporated  
555 Sparkman Drive, Suite 1622  
Huntsville, AL 35816**

# **COLD FLOW MODEL**

**24 February 1994**

## **Test Requirements**

The test requirements for the RSRM Nozzle Slag Ejection Precursor Tests were developed using various similarity parameters. The test requirements are summarized in Table 1 and Table 2 gives a detailed test matrix. The first test conditions were drawn up by matching the Reynolds number of the full scale RSRM motor and the Checkout Model 538. In order to obtain the same percentage throat blockage it is necessary to calculate a water injection flowrate. The water flowrate is dependent on the chamber pressure of the model. Once this dependency was calculated, it was possible to arrive at test conditions that would match the full scale RSRM motor. In order to apply the results to a wider range of cases, tests were run at 25%, 50%, and 75% of the full scale RSRM motor Reynolds Number.

The next test case in Table 1 was developed using a dynamic similarity parameter. In this case, the ratio of the air momentum to water momentum is set equal to the ratio of combustion gas momentum to slag momentum. By doing this it is possible to calculate the chamber pressure required in the model.

Thirdly, a Weber number simulation was calculated. As was the case for the Reynolds Number, test conditions were calculated to obtain a Weber Number match. Because the test condition required to match the Weber Number are above the facility performance capabilities, the Weber Number would match approximately 90% of full scale.

**Table 1. RSRM Nozzle Slag Ejection Tests**

<b>Simulation Parameter</b>	<b>Manifold Pressure (psia)</b>	<b>Chamber Pressure (psia)</b>	<b>Flowrate (lbm/sec)</b>	<b>Water Flowrate<sup>1</sup> (lbm/sec)</b>
Reynolds No.	797	405	212.5	19.3
75% Reynolds No.	598	304	159.5	16.7
50% Reynolds No.	398	202.5	106	14.9
25% Reynolds No.	199	101 <sup>2</sup>	53	10.8
Dynamic Ratio	715	363.5	191	18.2
Weber No.	1381	701.7 <sup>3</sup>	187	27.0
Modified Weber No.	138	70.2	18.7	9.0

The primary test matrix consisted of three model chamber pressure, three water flow rates, and have two injector nozzle diameters as listed in Table 2.

**Table 2. Primary Test Matrix**

**Water Injection Nozzle Diameters**

0.532 in.

0.712 in.

**Model Chamber Pressures**

405 psi

304 psi

203 psi

**Water Flow Rates**

18.4 lbm/sec

12.8 lbm/sec

7.2 lbm/sec

**Precursor Test Summary**

Approximately 140 total runs were completed including the investigation of secondary variables and test repeatability. The magnitude of model pressure perturbation during water injection ranged from 4.0 psi to 16.5 psi depending on test conditions. The tests were successful in generating data on the relationship between pressure spike amplitude and water flow rate. A typical raw data test result plot is shown in Figure 2. The bottom trace is from a pressure transducer on the water injector supply line and shows when water flow is initiated. The middle trace is from a transducer near the aft end of the model chamber and shows that the model chamber pressure is elevated 6 psi for the entire 1.04 records of water flow duration. The attempts to visually record and measure fluid ejection velocity at the exit plane using high spaced movie and video were unsatisfactory. This information was to be used to calculate the simulated slag thrust needed to ultimately determine an experimental total thrust to pressure ratio. A dual beam laser will be used in a plexiglass exhaust duct downstream of the model nozzle to solve this problem in the following test series with a scaled submerged nose RSRM nozzle.

A summary of the data correlation achieved with the test results is shown in Figures 3 and 4. The parameters plotted are the amplitude of the pressure increase normalized by the model chamber pressure versus the water flowrate. The open symbols connected by solid lines represent the predictions by the Slag Ballistics Model and the solid symbols represent the measured data. Two inputs to the Slag Ballistics Model are the drag coefficient of the slag cloud and the density multiplier for the slag cloud. A parametric study was performed by running the analytical model over a range of values for these variables and comparing to the experimental data. A set of values was arrived at which



produced the best fit between the experimental data and the analytical model prediction. The final value for the drag coefficient was chosen as 0.5 and the slag density multiplier was selected to be 0.3.

It may be seen that the calibrated Slag Ballistic Model does an excellent job of matching the test data over a wide range of model chamber pressures and water flow rates. Properties of air and water are used along with the model geometry in the model for the experimental data correlation but when the model is applied to RSRM, combustion gas and alumina properties are used along with the full scale motor nozzle geometry. The model matches the data better at the highest pressure which is of more interest since the motor Reynolds number is matched at this condition.

Thus, it may be concluded that the Precursor Tests definitely support and validate the ability of the Slag Ballistics Model to correctly relate the amplitude of the pressure spike to the slag flow rate.

## **RSRM 6.5% SCALED NOZZLE SLAG MODEL**

### **Introduction**

In past firings of the Space Shuttle Solid Rocket Motor, both static test motors and flight motors have shown pressure perturbations primarily between 65 and 80 second burn times. These pressure perturbations result in a thrust imbalance between the solid rocket boosters (SRB) and an increase in the external tank loads. Films of the motor firings, Real Time Radiography, and Plume Radiometers have evidenced the ejection of slag debris from the motor nozzle coinciding with the pressure perturbations. Increases in the thrust to pressure ratio have also been measured in static tests which confirms the presence of nozzle ejecta. The purpose of the RSRM 6.5% Scaled Slag Ejection Tests is to demonstrate and quantify the effect that slag ejection from the Redesigned Solid Rocket Motor (RSRM) nozzle has on the chamber pressure and thrust of the SRBs.

These tests will utilize the Solid Rocket Motor Air Flow Facility (SAF) with additional hardware developed specifically for these tests. This facility is capable of testing various solid rocket motor model configurations over a wide range of chamber pressures and flowrates and is capable of full scale RSRM Reynolds Number simulation. This test will use Checkout Model 538 spool pieces to model the motor chamber but will make use of a newly designed submerged nose nozzle scaled to the RSRM nozzle geometry including the exit expansion section (see Figure 5). This model will be a 6.5% scale RSRM model scaled to a burn time of approximately 67 seconds. The model will have provisions to inject water into the model through ports underneath the submerged nose to simulate slag accumulation in the aft cavity underneath the nozzle nose. This model is a follow-on model to the preceding Precursor Model which used a ten percent scale converging/diverging nozzle and axial water injectors in the port ahead of the nozzle. The Precursor Model was successful in demonstrating the feasibility of using a cold flow model with water injection to simulate slag ejection out the full scale motor nozzle.

### **Objectives**

The primary objective of the RSRM 6.5% Scaled Slag Ejection Tests is to demonstrate and quantify the effects of slag ejection from the nozzle on the performance of the full scale motor. This will be accomplished with a cold flow model using injected water and at least one other fluid to simulate the slag accumulation in the full scale motor. The cold flow model will best simulate the slag expulsion phenomena present in the horizontal static firing motors. A

secondary objective is to investigate potential internal motor triggering mechanisms for the ejection of slag. A follow-on test program will include modeling of aft joint inhibitor dynamics and possibly the releasing of sections of inhibitor to travel down the model port to interact with the simulated slag pool underneath the nozzle nose. An addendum to this pretest report will be prepared to describe the inhibitor dynamics testing. Specific test objectives are as listed below:

**Objective 1: Demonstrate that slag can be entrained in the complex separated flow field around the nozzle nose and ejected through the nozzle to produce a pressure perturbation.**

The RSRM Nozzle Slag Ejection Precursor Tests have shown that by ejecting a fluid through the nozzle of a cold flow model, it is possible to obtain a pressure perturbation similar to those seen in the RSRM. In these initial tests, the water was injected into the model chamber through an injector located on the model centerline upstream of the nozzle. This model will further investigate the potential for slag induced pressure perturbations by demonstrating the entrainment of slag into the flow from a pool of simulated slag underneath the submerged nozzle nose. The slag entrainment phenomena will be studied at fixed gimbal angles of 0, 2, and 4 degrees. By comparing transient test results during the initial period of water flow for the three fixed gimbal angles, the effect of nozzle gimbal angle as a triggering mechanism for slag ejection in the full scale motor can be determined.

**Objective 2: Obtain quantitative measurements of the effect of slag ejection on motor pressure and thrust.**

The model will be tested over a range of fluid flow rates and chamber pressures to investigate the effect of slag nozzle blockage over a range of Reynolds Numbers and Weber Numbers simulating flow and slag conditions in the full scale motor. The fluid flow rates will be selected to provide approximately the same percent throat blockage experienced in the full scale motor. Model thrust will be determined indirectly by measuring the fluid velocity at the exit plane and calculating the thrust contribution from the momentum equation. This will enable confirmation of the enhancement of the total thrust to pressure ratio expected from the simulated slag ejection which is important since it is ultimately the thrust loads transmitted to the external tank of the Space Shuttle that is of concern.

**Objective 3: Determine the effect of fluid properties on the relationship between fluid flow rate and pressure perturbation magnitude.**

The effect of fluid properties such as surface tension and viscosity are not directly accounted for in the analytical slag ballistics model although fluid density is included. The effect of surface tension as it relates to slag droplet breakup is

simulated in the cold flow testing by conducting the tests at near the full scale motor Weber number. However there may be viscosity effects that are not simulated and therefore it is desirable to determine if using another test fluid significantly affects the relationship between fluid flow rate and pressure spike amplitude. If so, the analytical model may have to be expanded.

**Objective 4: Validate the analytical slag ballistics model for use in predicting the relationship between slag flow rates and pressure perturbation magnitudes for the RSRM.**

The analytical slag ballistics model will be used with air and test fluid properties to correlate the cold flow data taken over a range of fluid flow rates and model pressures. The test results will be used to implement suggested improvements to the model and calibration of the constants in the model to best represent or correlate the data over the entire range of testing. Thus the cold flow data will be used to calibrate the analytical model which will significantly increase the confidence of the predictions performed for the full scale motor.

**Objective 5: Investigate the role of inhibitor dynamics as a possible internal triggering mechanism for slag ejection from the motor.**

The aft field joint of the motor is simulated in the cold flow model including the use of a flexible inhibitor protruding into the bore approximating the geometry at 67 seconds burn time. Resonance between the mechanical vibration mode of the inhibitor and the first longitudinal mode of the motor has been proposed as a possible influence on slag ejection through effects on the aft motor nozzle nose cavity flow field. Also, this resonance significantly increases the amplitude of the first and second longitudinal modes and may contribute to the breakup of the charred castable inhibitor remnant at the forward field joint. This latter effect may be modeled by releasing segments of the simulated aft field joint inhibitor such that the pieces are free to travel down the bore and interact with the simulated slag pool underneath the nozzle nose. These follow-on tests and required special instrumentation will be described in an addendum to this report at a later date. The inhibitor will not be installed in the initial test series.

**Test Requirements**

The test requirements for the RSRM 6.5% Scaled Slag Ejection Tests were developed using various similarity parameters. The criteria used to develop the test requirements are summarized in Table 3. The first test conditions were drawn up by matching the Reynolds number of the full scale RSRM motor (40.78E06) and the RSRM 6.5% Scaled Slag Ejection Model. In addition, the port Mach number and dynamic pressure of the model will match the RSRM at the 67 seconds burn time. Water injection flowrates were calculated for this

model to obtain the same percentage throat blockage as observed in the full scale motors (approximately 2%). The water flowrate is dependent on the chamber pressure of the model. Once this dependency was calculated, it was possible to arrive at test conditions that would match the full scale RSRM motor. In order to apply the results to a wider range of cases, tests will also be run at 50% and 75% of the full scale RSRM motor Reynolds Number. It should also be noted that the minimum test duration is set at 20 seconds.

**Table 3. Simulation Criteria for Test Conditions**

<b>Simulation Parameter</b>	<b>Manifold Pressure (psia)</b>	<b>Chamber Pressure (psia)</b>	<b>Air Flowrate (lbm/sec)</b>	<b>Water Flowrate (lbm/sec)</b>
Reynolds No.	1035	623	138	7
75% Reynolds No.	776	467	104	6.1
50% Reynolds No.	518	312	69	5.4
Dynamic Ratio	1226	738	164	6.6
Weber No.	1793	1080	239	9.8

The next test case in Table 3 was developed using a dynamic similarity parameter. In this case, the ratio of the air momentum to water momentum is set equal to the ratio of combustion gas momentum to slag momentum. By doing this it is possible to calculate the chamber pressure required in the model. The location at which the dynamic similarity was calculated was the throat plane. Thus, the conditions are for Mach 1 flow.

Thirdly, a Weber number simulation was calculated. As was the case for the Reynolds Number, test conditions were calculated to obtain a Weber Number match. The Weber Number was also calculated using test conditions at the throat plane. The model chamber pressure required to produce a Weber Number match is not possible with this model but by matching the Reynolds Number a 58% Weber Number match will be made. Again, the conditions used to calculate the Weber Number match were nozzle throat conditions.

### **Facility Description**

The Solid Rocket Motor Air Flow Facility (SAF) Phase II configuration is shown in Figure 6. The air storage for the SAF consists of eight storage tanks having 9100 cubic feet of storage capacity. This air supply is a pressure blowdown system which is discharged through the test model to the atmosphere. The inlet air is filtered through a bonded fiberglass cylindrical canisters filter that is designed for a maximum pressure of 1960 psig and a maximum flowrate of 320 lbm/sec. The ROV isolation valve is downstream of the filter and is rated for a

maximum pressure of 1960 psig. This valve can be shut down at maximum speed in case of emergency. The actual test model inlet pressure is controlled by a quiet trim control valve. The valve uses a hydraulic operator for actuation and will hold the test model stagnation pressure constant for each test run. Downstream of the quiet valve, a pilot operated relief valve is located to discharge 100% of the flow operating at 1320 psia. The flowrate will be metered by a venturi, which is stationed downstream of the quiet valve.

Next, the flow is split into the two facility supply legs, as shown in Figure 6. These facility supply legs each feed two manifold arms, for a total of four arms. The pressure sensing location for the quiet valve feedback control is located in these facility supply legs upstream of the choked metering nozzles in the manifold arms. Each one of these manifold arms includes a metering nozzle. With the metering nozzles installed the facility operates in Mode "A". The facility has the capability to operate in a Mode "B" where the four metering nozzles are removed. The installation of the metering nozzles ensures a constant flowrate through the system which is independent of any nozzle blockage. The manifold arms feed into an adapter chamber at the head end of the model. From the adapter chamber the flow is passed through the model port and exits the model through the submerged nose nozzle.

The mass flow through the system is ducted to atmosphere through the test model diffuser. The diffuser enables the test model to operate at full scale booster nozzle expansion ratio without flow separation. Before the air reaches the atmosphere, it is ducted through an 85 dB Silencer which is located outside of building 4777.

Testing will be conducted in Mode "A" with a minor modification. Instead of having all four choked metering nozzles installed in each of the four header pipes, two opposing header pipes will employ the choked metering nozzles while the other two header pipes will be blanked off. This is necessary in order to be able to correctly model the motor Reynolds Number at the burn time chosen. The metering nozzles were designed to choke with a 10% scale model. It is necessary to blank off two of the manifold arms in order to keep the metering nozzles choked with the 6.5% model at the operating pressure and flowrates for these tests. The manifold arms designated B (Bottom South) and D (Top North) will be operational while arms A (Top South) and C (Bottom North) will be blanked off. Again, by operating in test Mode "A", the checkout model flowrate will be independent of any fluid induced blockage phenomena occurring during the test.

## **Model Description**

The RSRM 6.5% Scaled Slag Ejection Model consists of three model chamber spool pieces from Checkout Model 538 with a submerged nose nozzle. The spool pieces will be arranged in the order of 3-2-1 in the direction of the airflow. This will be done to move the model chamber injector further upstream of the nozzle entrance. The submerged nozzle nose and contoured expansion section are scaled to 6.5% RSRM size as shown in Figure 5. Wedge shaped gimbal flanges between the nozzle and the chamber will enable the model to be tested at three fixed gimbal angles of 0, 2, and 4 degrees. Figure 5 also describes the names of specific model components. All Test Requirements will use this model terminology to describe various calculations performed at different axial stations along the flow of the RSRM 6.5% Scaled Slag Ejection Model.

In addition, the RSRM 6.5% Scaled Slag Ejection Model will be fitted with an injector system. This system will allow a fluid to be injected into the model from ports underneath the nozzle nose. The system will make it possible to flood the volume underneath the nozzle nose quickly but with a low injection velocity. The water to be injected into the model is held in a large capacity water tank. The tank is pressurized with air and the water exits the tank via a two inch line. The two inch line leads to a ball valve and a metering orifice which will be used to ensure the correct water flowrate to the model. The water is then passed through a high pressure manifold which will distribute the water to the different injection ports under the nozzle nose. The manifold is connected to the model by one inch flex hose. Just before each of the twelve injection ports is another ball valve for control of the flow to the model.

This injection system could be run in either one of two modes. In the first option all the lines are filled with water up to the ball valves in the one inch flex hoses with the two inch ball valve remaining open. The test is begun and when the water is to be injected all twelve of the one inch ball valves would open at once. The second option would again fill all the lines with water up to the model but would use the two inch ball valve to control the flow to the model with the twelve one inch ball valves, or any combination of the twelve, remaining open throughout the test.

In addition, the model will retain the capability of the RSRM Nozzle Slag Ejection Precursor Model to inject fluid into the motor port upstream of the nozzle nose tip. The injector will be connected to its own high pressure reservoir to enable it to operate in the high pressure environment of the model chamber.

The RSRM 6.5% Scaled Slag Ejection Model will have the ability to model the aft field joint of the RSRM motor. This modeling can include a flexible inhibitor to simulate the inhibitor in the actual RSRM motor. For these immediate tests the flexible inhibitor will not be used and will be replaced instead by a metal spacer.

## **Instrumentation**

The RSRM 6.5% Scaled Slag Ejection Tests will have approximately 47 model measurements, which are located axially and circumferentially throughout the model at key locations (or stations) in the model. These measurements include total, static and dynamic pressures as well as bulk temperatures.

A total of 47 test measurements will be taken for each test and are broken down into individual measurements in the following list. This listing provides the number of measurements required to complete the test objectives.

- 24 Static Pressure Taps
- 1 Total Pressure Probe
- 16 Dynamic Pressure Gauges
- 6 Temperature Probes
- 47 Total**

Pressure data will be measured using differential pressure transducers with appropriate ranges connected to an electronic scanning system. This system is a 256 channel unit which has modules that can record ranges of differential and absolute pressures. These measurements will be recorded as digital test data on a Hewlett Packard recorder and will be translated into engineering units. The recording method will use frames of averaged data per test, at steady state, which is in turn read into the Aero Fluids Analysis System (AFAS) VAX. The AFAS database measurement label standard indicates specific formats to which an instrumentation label can be determined. Dynamic pressures will be recorded on an FM tape recorder.

In addition to the above instrumentation, a dual beam laser/photo diode set-up will be employed to record the velocity of the ejected fluid just downstream of the model nozzle exit plane. This system will make use of a Plexiglas diffuser section which will be installed at the nozzle exit. The two laser beams will pass through this diffuser section approximately 4-5 inches apart. The time of passage of the slag between the two beams will be measured and used along with the distance separating the beams to determine the exit velocity of the slag from the nozzle exit.

In addition, a miniature video system in the model chamber may be used to observe the fluid underneath the nozzle nose before and during the ejection event. This camera will be used to observe the accumulation of the water underneath the submerged nose, and the shape and size of the slag pool. In addition, it is hoped that the way in which the water becomes entrained in the air flow underneath the nozzle nose and is carried into the nozzle entrance will be observed.



## **Performance Reduction Program**

A performance program will be developed specifically for the RSRM 6.5% Scaled Slag Ejection testing. The input data will be in terms of averaged frames of data over a period of time at steady state conditions. Ten to twenty frames of data per measurement, per test, is expected. Sometimes the framed data has a value that is inconsistent with the other values in a particular steady state frame. This anomaly could be caused by a number of reasons, however, in order to have an averaged frame that represents steady state, all anomalies or "outliers" will have to be deleted before an averaged value can be determined from one set of values in a frame. Therefore, the performance program will include a statistical algorithm to delete any extreme points from the steady state data. The algorithm compares each observation with the nearest point in a small sample of data. If one observation is not statistically close to the rest of the sample data, the point is removed. This method is a valid method for a small population of data. The data will then be averaged and used in one-dimensional equations to describe characteristics of the flow through the required pressure ranges.

It is recognized that the model may not operate in a steady state mode with respect to the pressure perturbation amplitude. In other words, the discharge of simulated slag around the nozzle may be a periodic or random event with corresponding pressure spikes even though the water will be injected into the model at a steady flowrate. In this case, the dynamic pressure gauge data will be evaluated outside the steady state averaging scheme.

The program will use one-dimensional equations to make calculations including local Mach numbers, total pressures, static pressures, total temperatures, local velocities and flowrates. In addition, for the RSRM 6.5% Scaled Slag Ejection Tests, Reynolds Number, Weber Number, Dynamic fluid/air ratios and nozzle fluid blockage ratios will be calculated. Predicted pressure spike amplitudes will be compared with measured pressure amplitudes.

The program will also contain equations that will be used to calculate the additional thrust due to the ejection of fluid through the nozzle. This additional thrust from the fluid ejection is due to the momentum that the fluid acquires as it passes through the nozzle. This fluid thrust is equal to the mass flowrate of the fluid multiplied by the velocity of the fluid at the nozzle exit plane. This fluid thrust is added to the motor thrust to obtain a total thrust value. This total thrust is then divided by the chamber pressure to obtain an F/P, thrust divided by pressure, time history.

Computational Fluid Dynamic (CFD) calculations will also accompany the one-dimensional performance calculations, since two-dimensional as well as three-dimensional effects will exist in several places in the RSRM 6.5% Scaled Slag Ejection Model, especially with the gimbaled nozzle positions.

## **APPLICATION OF COLD FLOW DATA TO RSRM**

This section will explain how the cold flow test data was used in the Slag Ballistics Model to make predictions for the full scale RSRM motor. However, there is a good answer to the concern expressed.

The primary result of the cold flow tests was to measure the relationship between the simulated slag (water) flow rate and the amount of model throat area blockage achieved. This is the primary achievement of the Slag Ballistics Model. That is, the trajectory analysis of the slag in the nozzle is for the purpose of translating a certain amount of throat blockage into an instantaneous slag flow rate which can be integrated over time to calculate the total amount of slag ejected over a given time period. The amount of chamber pressure increase in the full scale motor is related to the throat blockage through a transient ballistics model for RSRM including the chamber mass storage terms.

For the cold flow model data analysis, the simulated slag (water) flow rate was measured directly and the amount of throat area reduction was directly proportional to the amount of model chamber pressure increase. This was true only because the model mass flow rate was a constant during the water ejection through the nozzle because of the upstream choked metering nozzles. Without a constant model flow rate it would have been impossible to determine the amount of throat blockage achieved with a given water flow rate. The Trajectory Module from the Slag Ballistics Model was used with the cold flow data to calculate the amount of throat blockage expected with a given water flow rate. The cold flow model chamber pressure increase for a calculated throat blockage was then calculated knowing that the increase was directly proportional to the percent throat area reduction. The uncertain constants of the slag (water) drag coefficient and the effective slag (water) density multiplier, which accounts for the entrained gases, were then adjusted to obtain the best match of predicted model pressure increase with measured pressure increase for a given water flow rate. The final value of the slag drag coefficient was 0.5 and the slag cloud density multiplier was 0.3.

These same empirical constants were then transferred back to the RSRM Slag Ballistics Model where combustion gas properties and aluminum oxide slag properties are used. In the RSRM Model, the chamber pressure increase from a certain amount of throat blockage is calculated with the transient continuity equation which, of course, accounts for the mass generation effect which includes the burn rate law with the pressure exponent effect. Thus the cold flow model data was only used to calibrate the Trajectory Module of the Slag Ballistics Model by measuring the amount of throat blockage achieved for a given fluid flow rate; not to relate fluid flow rate to pressure increase. It is not necessary for the chamber pressure to be related to throat blockage in the same

way for the model as it is for the full scale motor. We can not be sure that the slag cloud will be accurately represented by the fluid cloud in the cold flow model in terms of droplet size distribution, shape and breakup but we have demonstrated that the Slag Ballistics Model is capable of correctly calculating throat blockage over a range of fluid flow rates and pressures.

# RSRM Pressure Perturbation Briefing

## Preliminary Test Results

### Dynamic Pressure Measurements

RUN 7/1

MODEL PRESSURE = 100 PSI

WATER PRESSURE = 300 PSI

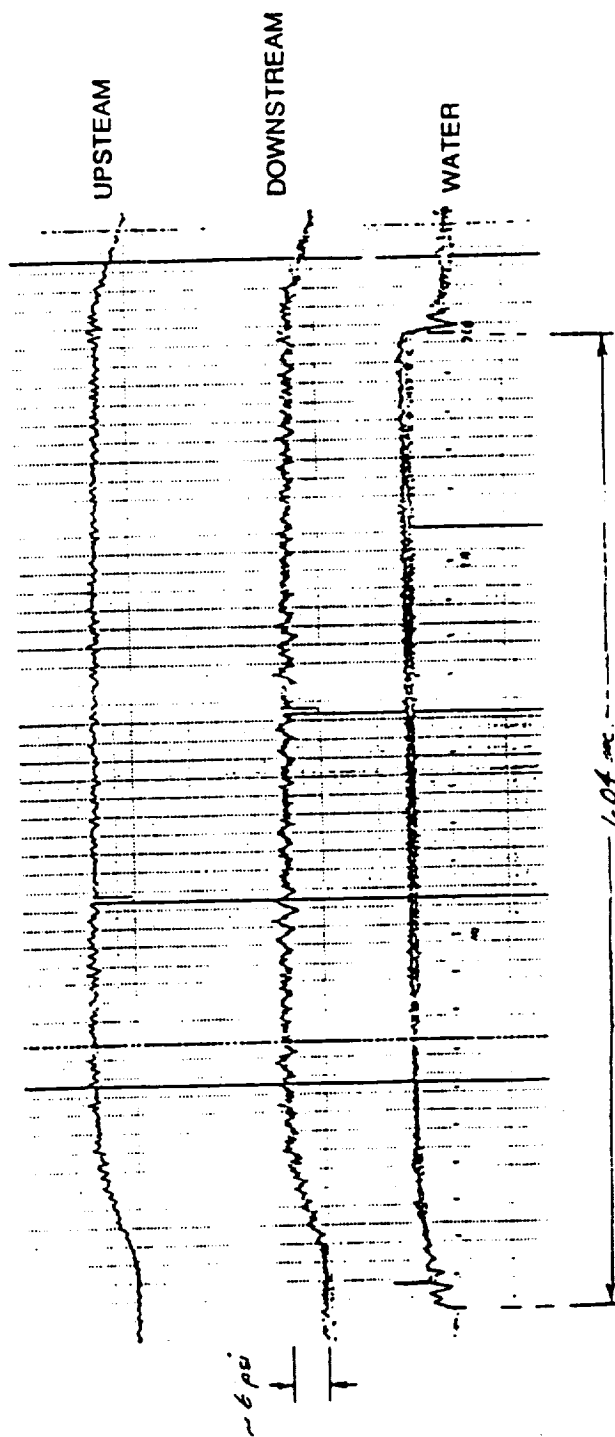


Figure 2

# RSRM Nozzle Slag Precursor Tests

## Injector Type 1 Dia. = 0.532 Aft Location

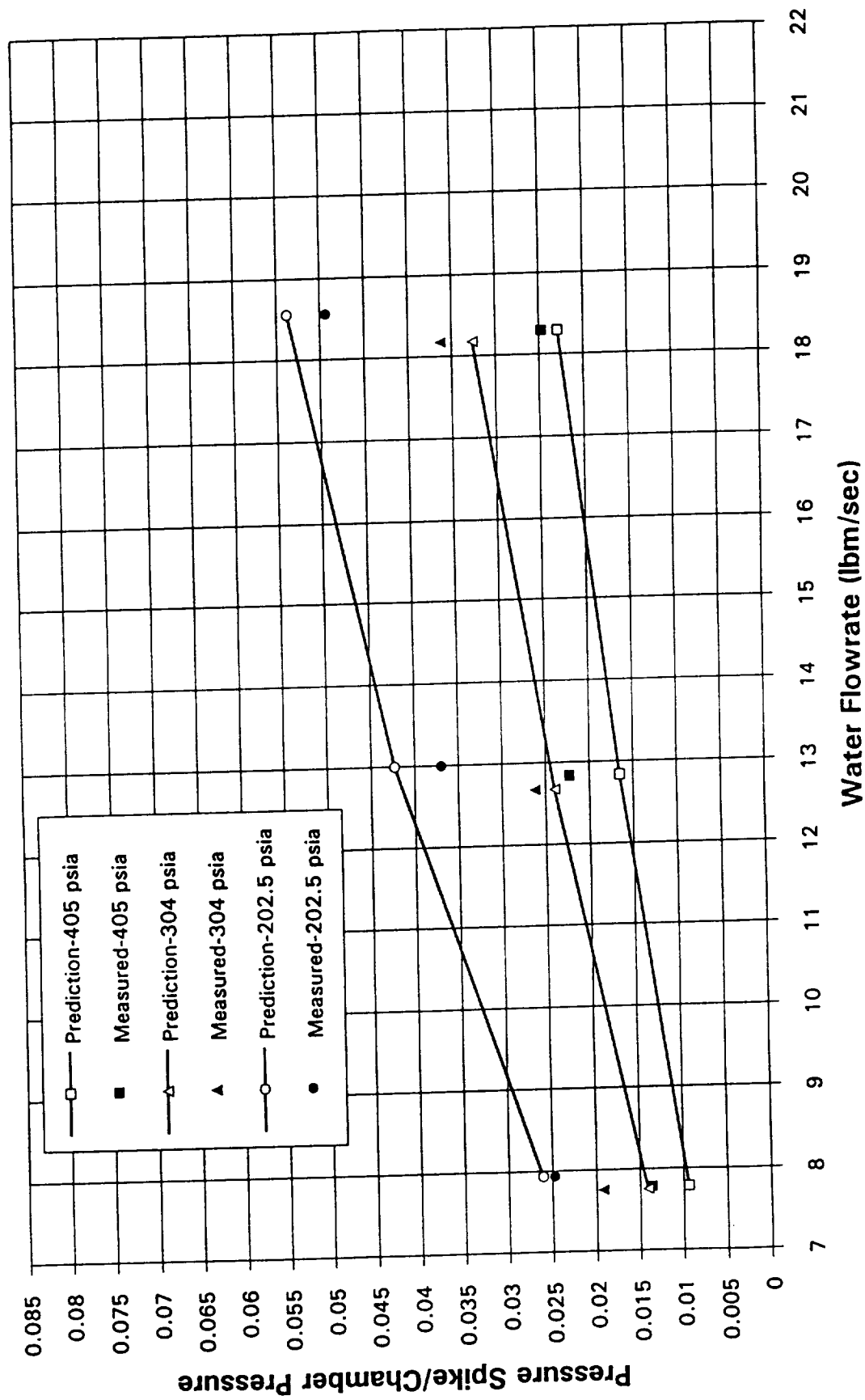


Figure 3

# RSRM Nozzle Slag Precursor Tests

## Injector Type 2 Dia. = 0.712 Aft Location

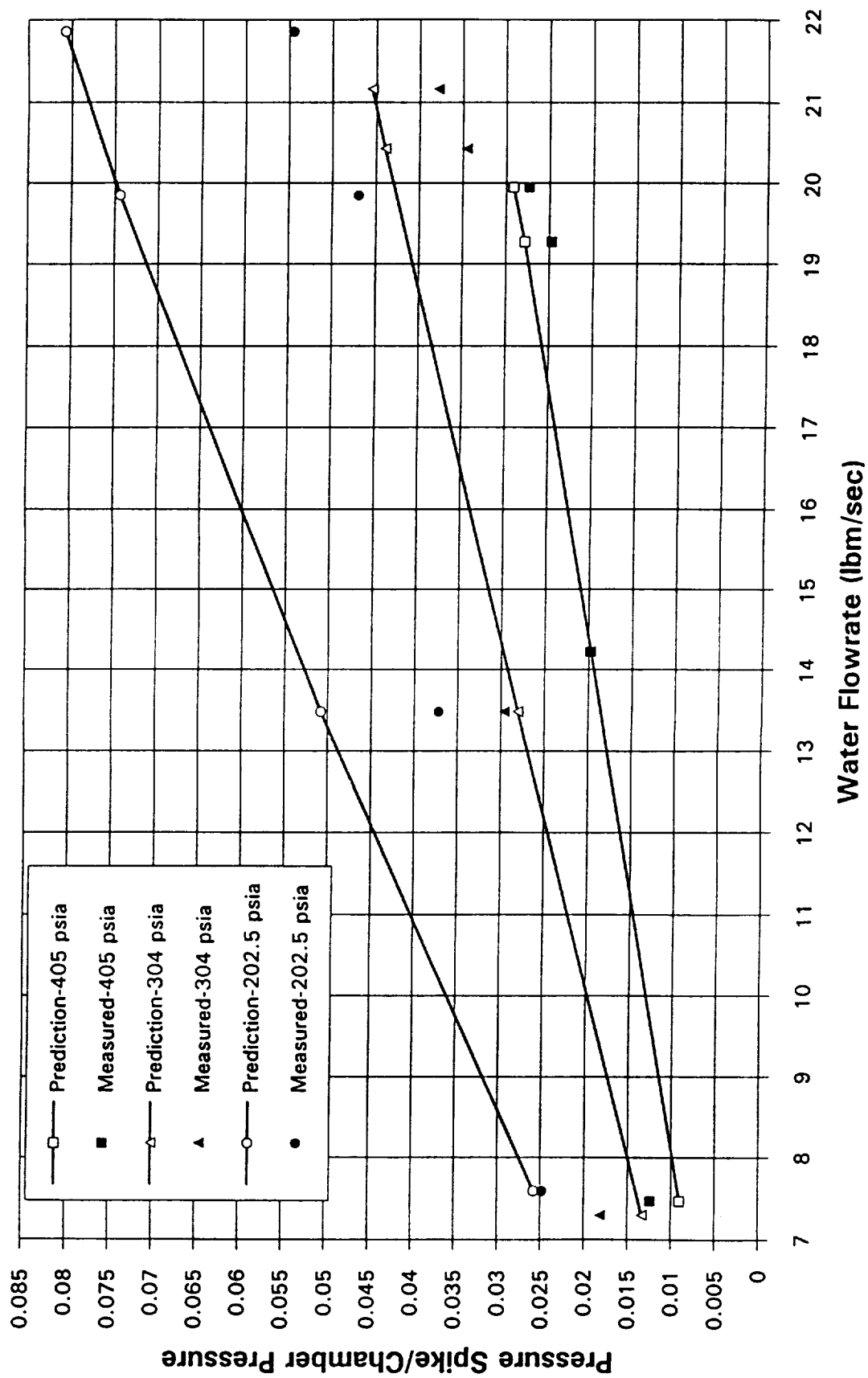


Figure 4

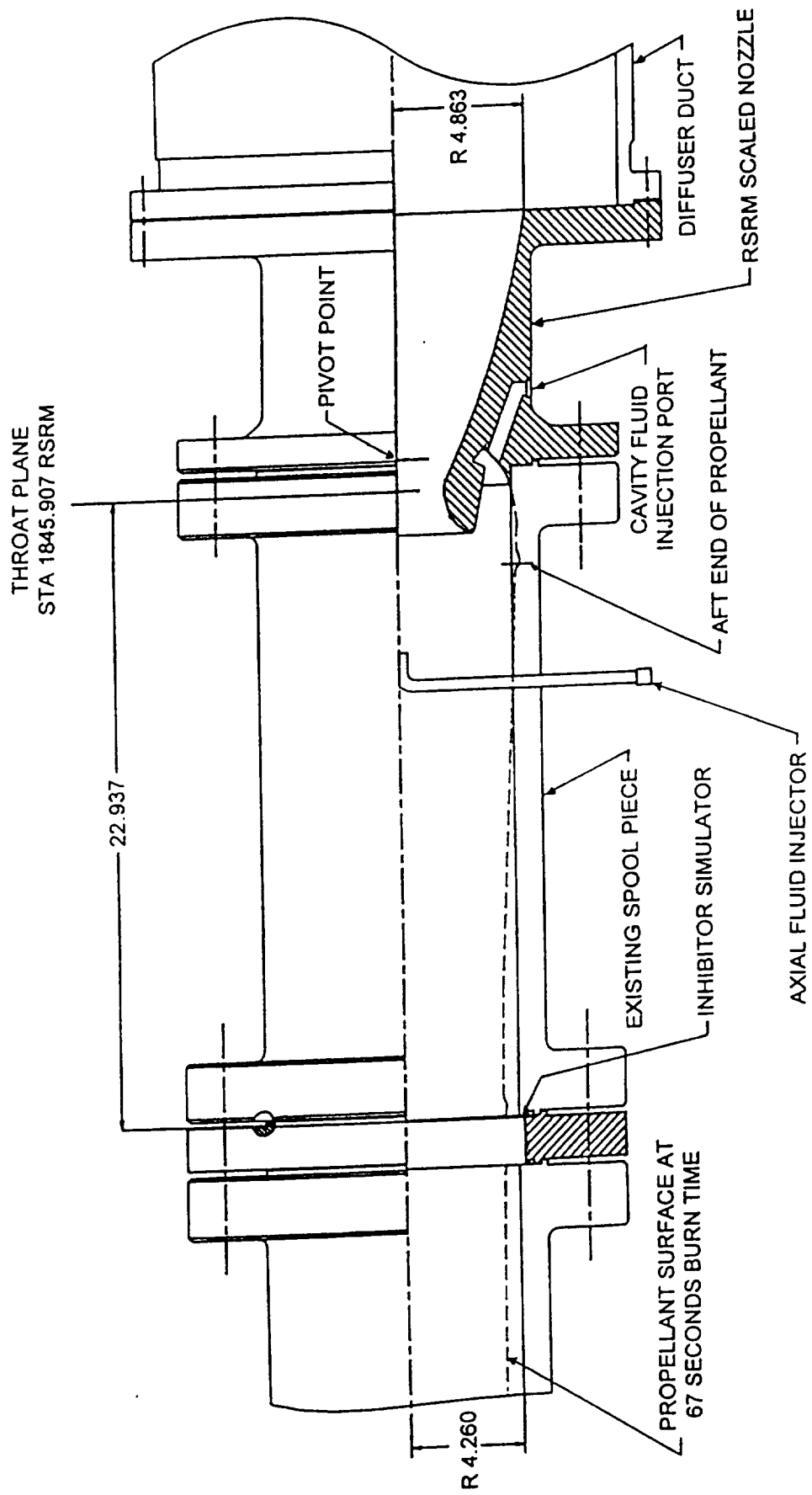
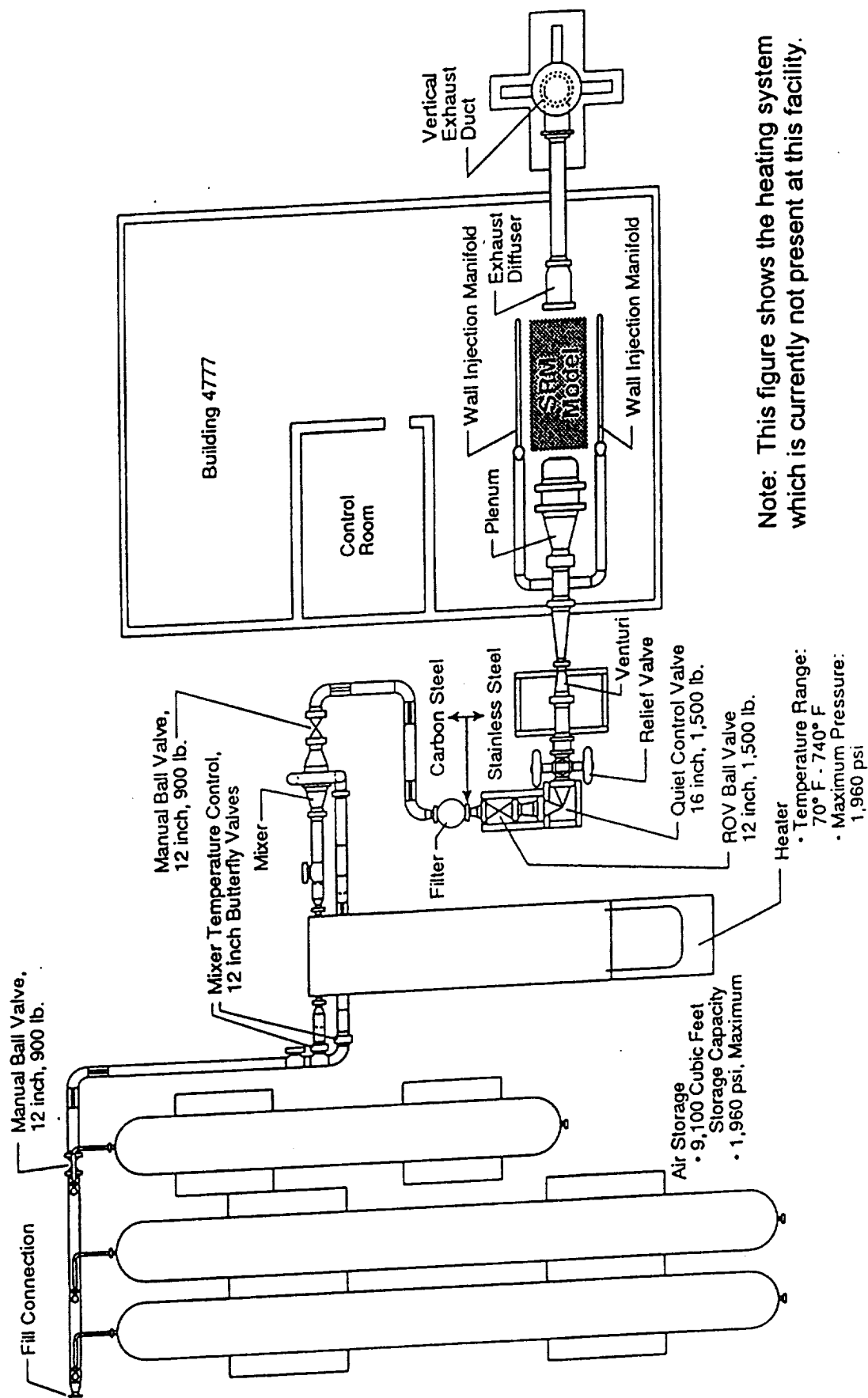


Figure 5. RSRM 6.5% Scaled nozzle Slag Ejection Test Names of Model Components



Note: This figure shows the heating system which is currently not present at this facility.

Figure 6. Solid Rocket Motor Air Flow Test Equipment



# **SLAG BALLISTICS MODEL**

**24 February 1994**

## **SLAG BALLISTICS MODEL**

### **Slag Ballistics Computer Model**

The entrainment of slag into the gas flow and subsequent ejection of the slag through the nozzle is viewed as a very complex event involving transient, three-dimensional, three-phase flow phenomena. A significant body of evidence is available to indicate slag as the primary source of the pressure perturbations. However, it is necessary to try to quantify the effect of slag debris on motor performance. Due to the size of this motor and the time duration of the slag ejection event, it is believed that the motor performance effects can be evaluated using a global model that deals with the instantaneous average slag flow rate of all the discrete globules or separate streams flowing at any one time. This instantaneous mass rate can be integrated to determine the total slag ejected for a given pressure perturbation to compare with the amount of slag available.

The current slag ballistic models attempt to do just this. It does not appear feasible or necessary to model on a micro-scale basis the detailed and discretely separate slag agglomerate globules. The cold flow model does not currently yield any quantitative information on the effects of slag ejection on motor thrust in order to verify the slag ballistics model but efforts are underway to include model thrust measurements on the next set of model tests. Static motor firing data does quantitatively support the Slag Ballistics Model on its prediction of the enhanced thrust augmentation due to the additional momentum contribution from the slag ejection. Continual improvements and variations of the Slag Ballistic Model are currently being pursued.

The Slag Ballistics Models do not deal with the triggering mechanism which leads to the entrainment of the slag in the flow and subsequent ejection from the nozzle. The SLOSH Model attempts to explain this phenomena based on vehicle accelerations and the dynamics of the liquid slag motion in the nozzle cavity. Other motor internal excitation sources may contribute such as debris released from up forward in the motor port, shifts in the structure of the nozzle nose flow attachment or changing vortex patterns in the nozzle cavity associated with the natural turbulence in the high Reynolds Number flow.

The following is a description of the Slag Ballistics Model which calculates the effect of slag ejection through the nozzle on motor performance. The analysis takes an input pressure versus time history and calculates the slag which is required to be ejected through the nozzle in order to produce the input pressure profile. The analysis has also been adapted for other uses including the prediction of test conditions used in cold flow work performed at NASA/Marshall Space Flight Center. In addition, the program has been used to correlate the cold flow data from the experiments performed at NASA/Marshall Space Flight Center.

The analysis is actually two separate programs. The first program is a FORTRAN program which takes the pressure versus time history and predicts the throat area versus time needed to produce the given pressure history. This program solves the continuity equation for the solid rocket motor including the chamber mass storage terms. Thus, the mass produced in the motor is equal to the mass ejected from the motor in addition to the mass stored in the motor to produce the pressure perturbation and fill up the free volume produced as the propellant burns. The equation solved is actually the differential equation form of the continuity equation. Along with the pressure versus time data, inputs to this program include the motor conditions at the time of the pressure perturbation. These conditions include the propellant density, burn rate, initial volume, Cstar, gas temperature, and a surface area versus web thickness table.

$$\text{Mass Generated} = \text{Mass Ejected} + \text{Mass Stored}$$

$$dm_g/dt = dm_D/dt + \{P_c(dV/dt) + V (dP/dt)\}/RT$$

$$dm_g/dt = \text{Rate of mass generation}$$

$$dm_D/dt = \text{Rate of mass discharge}$$

$$\{P_c(dV/dt) + V (dP/dt)\}/RT = \text{Rate of mass storage}$$

$$P_c = \text{Motor chamber pressure}$$

$$(dV/dt) = \text{Rate of change of motor free volume}$$

$$V = \text{Motor chamber volume}$$

$$(dP/dt) = \text{Rate of change of motor chamber pressure}$$

$$R = \text{Ideal Gas Constant}$$

$$T = \text{Gas temperature}$$

$$dm_D/dt = A_{t\text{effect}} P_c / C^*$$

$$A_{t\text{effect}} = \text{Effective throat area accounting for blockage effect}$$

$$C^* = \text{Cstar}$$

Next, the output from the FORTRAN program is input into an Excel 4.0 spreadsheet which has been set up to perform the remainder of the necessary calculations and plot

any information needed in a graphical form. The information passed to the Excel spreadsheet includes the chamber pressure versus time and the throat area versus time. A nozzle blockage area is computed from the effective throat area versus time by subtracting it from the nominal throat area without blockage for the motor at the appropriate times.

$$A_b = A_{t_{\text{nominal}}} - A_{t_{\text{effect}}}$$

$$A_b = \text{Blockage area}$$

$$A_{t_{\text{nominal}}} = \text{Nominal throat area}$$

The maximum throat blockage is now input into a trajectory calculation to determine the speed of the slag being ejected from the motor nozzle. A sphere of frontal area equal to the maximum throat blockage is flown down the nozzle from the nose tip plane to the exit plane. In order to make these calculations it is necessary to know the conditions through the nozzle. These conditions are found by using compressible, isentropic, one-dimensional flow equations. The area ratios at a number of nozzle locations are used to calculate the gas velocity, Mach number, density, temperature and pressure at these same locations.

In order to calculate the weight of the sphere it is treated as a cloud of slag. The density of this slag cloud (33 lbm/cu. ft.) is set equal to 0.3 times the density of molten Aluminum Oxide (110 lbm/cu. ft.). This value was chosen after work with the cold flow model was performed and this value was found to produce the best pressure perturbation predictions for that work. A drag coefficient was also needed for the sphere. A value of 0.5 was used, again this value being finalized after predictions were compared with cold flow testing data. This value is also representative of a sphere at high Reynolds number. The values 0.3 and 0.5 for the slag cloud density multiplier and the drag coefficient were arrived at by correlating the prediction made by this program with actual results obtained during the cold flow testing at NASA/Marshall Space Flight Center.

The flight of the slag cloud through the nozzle is dependent upon its speed in relation to the gas flow in the nozzle. In order to calculate the slag cloud velocity the drag on the sphere is needed. However, the drag force is dependent on this velocity differential. The iterative solving capability of Excel is used to solve this circular dependence. An initial guess is made for the slag cloud speed in relation to the gas velocity and then the iterative solving of Excel computes new values until convergence is met. The initial velocity of the slag cloud at the nozzle nose tip plane can be input to any value, although zero initial velocity is predominantly used to simulate slag being spilled from underneath the nozzle nose.

$$D = 0.5 \rho_{\text{gas}} V_{\text{slag}}^2 A_{b_{\text{max}}} C_D$$

**D = Drag force**

**$\rho_{\text{gas}}$  = Density of gas in motor**

**$V_{\text{slag}}$  = Velocity of slag relative to gas velocity**

**$A_{b_{\text{max}}}$  = Maximum blockage area**

**$C_D$  = Drag coefficient (0.5)**

**$V_{\text{slag}|_{t+\Delta t}} = \text{SQRT}\{(G_F + D/m_{\text{sphere}})2\Delta L + V_{\text{slag}|_t}^2\}$**

**$G_F$  = G-force motor is subjected to during flight**

**$m_{\text{sphere}}$  = Mass of sphere being flown through nozzle**

**$\Delta L$  = Distance between computation locations in the nozzle**

**$T_{t+\Delta t} = \Delta L/V_{\text{slag}} + T_t$**

**$T_t$  = Time of flight of sphere in nozzle**

Once the velocity of the slag cloud is determined, the flow rate of the slag through the nozzle is calculated. The velocity of the slag cloud at the nozzle throat plane is used to make this calculation. The mass flow is calculated at small time intervals so that it may be summed to determine the total mass of slag discharged through the nozzle during a given time period.

**$m_s = \rho_{\text{slag cloud}} A_b V_{\text{slag}|_{\text{throat}}}$**

**Total Mass of Slag =  $\Sigma m_s \Delta t$**

**$m_s$  = Instantaneous slag flow rate**

**$\rho_{\text{slag cloud}}$  = Density of slag cloud (33 lbm/cu. ft.)**

**$A_b$  = Blockage area**

**$V_{\text{slag}|_{\text{throat}}}$  = Slag cloud velocity at nozzle throat plane**

**$\Delta t$  = Time interval between calculation steps**

Finally, the slag thrust is calculated. This thrust component is a result of the momentum that the slag has as it is ejected from the nozzle exit. The slag cloud velocity at the nozzle exit plane is used in order to make this calculation. The thrust due to the combustion products is also calculated and added to the slag thrust to obtain a value for the total motor thrust. The program uses a constant value for the overall thrust coefficient in the computation of the gas thrust. A thrust over pressure time history can be calculated by dividing the total motor thrust by the motor chamber pressure.

$$F_{\text{slag}} = m_s V_{\text{slag|exit}}$$

$$F_{\text{gas}} = P_c A_{\text{effect}} C_{FM}$$

$$F_{\text{total}} = F_{\text{slag}} + F_{\text{gas}}$$

$$F_{\text{slag}} = \text{Thrust due to slag ejection}$$

$$V_{\text{slag|exit}} = \text{Velocity of slag cloud at nozzle exit plane}$$

$$F_{\text{gas}} = \text{Thrust due to exhaust of combustion gases}$$

$$P_c = \text{Motor chamber pressure}$$

$$C_{FM} = \text{Overall thrust coefficient (1.68)}$$

$$F_{\text{total}} = \text{Total motor thrust}$$

$$F/P = F_{\text{total}}/P_c$$

$$F/P = \text{Ratio of motor thrust to motor chamber pressure}$$

## **STS-54 Analysis Results**

The Slag Ballistic Model was used to analyze the pressure perturbation spike of 13 psi which occurred at 67 seconds for STS-54. The pressure spike was modeled with a linear decrease in throat area over a 0.8 second time span. The maximum calculated throat reduction or blockage is 47.52 in<sup>2</sup>. The throat area blockage was calculated as a function of time from the measured pressure trace using a lumped volume ballistic code module. The input parameter of surface area, free volume, throat area, burn rate and gas properties were taken from the actual Thiokol RSRM ballistic performance analysis.

The second analysis set is accomplished with a one-dimensional trajectory code designed to fly a sphere of slag through the nozzle to determine the average velocity of the slag stream at the throat and exit planes. The slag sphere is assumed to have a cross sectional area of 47.52 in<sup>2</sup>, the maximum blockage area. A drag coefficient of 0.5 is used for the hypothetical sphere.

The slag flow rate is then calculated at the nozzle throat plane versus time knowing the time-dependent blockage area, slag velocity and the average density. The average density is calculated by multiplying the liquid aluminum oxide density at flame temperature, 110 lbm/ft<sup>3</sup>, by a factor, 0.3, to account for the slag froth due to entrainment and mixing of gases with the liquid aluminum oxide. This factor was derived from the cold flow experiment and supported by density measurements of porous slag clods recovered from flight motors.

The back calculated nozzle blockage area versus time and the comparison of the model prediction with the data is shown in the accompanying Figure 1. The nozzle is assumed to be clear of slag blockage at the peak of the spike and the natural predicted blow-down process of the motor is seen to match the measured data well. The calculated pressure falls back to the initial pressure at 67 seconds since in the model prediction for their run the throat area and burning surface area are held at 67 second values.

The predicted slag flow rate is plotted versus time in Figure 2. The slag discharge lasts 0.8 seconds and the total integrated weight is 1791 lbm. Thus the 13 psi pressure spike for STS-54 required about 1800 total pounds of slag. This is well within available slag quantities predicted by the two-phase CFD analyses to accumulate by 67 seconds burn time.

## **Thrust to Pressure Ratio Augmentation**

The Slag Ballistics Model which relates the pressure spike to slag flow rate and total motor thrust predicts an increase in the thrust to pressure ratio during a slag expulsion event. This is contrary to conventional experience for expulsion of single objects. However, the expulsion of a stream of slag may last for approximately one second and then a quasi-steady analysis approach may be used since the time duration is large

compared to the acoustic response time. The total motor thrust is calculated by adding the slag momentum thrust to the normal motor thrust, which is reduced due to the throat blockage. The slag momentum thrust is calculated from the slag flow rate and slag nozzle exit plane velocity from the Slag Ballistics Model. When the total motor thrust is divided by the pressure, an increase in thrust to pressure ratio is predicted during slag expulsion.

The calculated ratio of F/P with slag to F/P without slag is approximately 1.033 for static test motor QM1. The calculated ratio of  $\Delta F_s$ , the total thrust increase with slag, to  $\Delta F$ , the total thrust increase without slag is 1.32. The relationship between these ratios is shown in Figure 3. Thus, the percentage change in the F/P ratio is small but that results in a large increase in the percent change of  $\Delta F$ , the thrust differential.

The accompanying Figure 4 shows the results of a parametric study using the Slag Ballistics Mode. The ratio of  $\Delta F$  with slag to  $\Delta F$  without slag is plotted against the pressure spike amplitude. The excellent agreement between the model results and the QM1 data point at 1.34 for a pressure spike of 9 psi supports the validity of the Slag Ballistics Mode.

### **Depressions In Pressure Traces**

Apparent depressions in the pressure trace where the measured pressure drops below the "nominal" occasionally occur just before a "spill" (STS-52B, STS-56B) and sometimes occur just after a "spill" (STS-54B, STS-53A). Various explanations have been offered for this phenomena including propellant temperature gradients and local burn rate gradients related to propellant rheology effects near the wall. A recent explanation related to a slag effect will be quantified in this answer. If a significant amount of large aluminum agglomerates began to accumulate underneath the nozzle nose such as to create a significant mass sink effect, then a decrease in chamber pressure compared to the nominal prediction might be expected. The reasonableness of this explanation was evaluated by making the calculations shown in the attached three charts.

The equilibrium form of the continuity equation is used to calculate the effect of a mass flow sink on the equilibrium chamber pressure level. Also, the rate of pressure change associated with this phenomena is small. The equation relating the various ballistic parameters for a situation where the nozzle mass flow rate is reduced by the flow into a mass sink is shown at the bottom of Figure 5. The ratio of the chamber pressure without the mass sink to the chamber pressure with the sink effect is shown in the equation at the top of the second page. The fraction of aluminum oxide captured was estimated at the time by multiplying the percent of particles above 100 microns by the percentage of the total motor port cross sectional flow area that exists between the nozzle nose and the case wall. This yields a captured fraction of 4.51%. When this result is multiplied by the weight fraction of aluminum oxide in the combustion products



and the total mass flow rate, the result is a captured flow rate of 124 lbm/sec of particulates. This result has since been supported by two-phase flow analysis results at Thiokol and MSFC.

The first case calculated (Figure 6) represents a case where the Cstar is not affected by the mass sink. This would represent the situation of a leak in the motor case where the combustion products going out the leak representing the mass sink are the same as the products going out the nozzle. Thus a leak rate of 124 lbm/sec would cause a drop in motor pressure of 12.0 psi for the stated initial conditions. The second case calculations shown in Figure 7 represent the situation where the sink flow is particles only and thus the Cstar for the products exhausting through the nozzle is altered by the reduction in the fraction of aluminum oxide. However, the total temperature of the combustion products exhausting through the nozzle is unaffected. The calculations show the necessary corrections to the nozzle flow Cstar. The result is a reduction in chamber pressure of 9.9 psi due to the capture rate of 124 lbm/sec of particulates.

This calculated reduction of 9.9 psi exceeds the magnitude of the observed decreases in chamber pressure and thus is considered a plausible explanation for any smaller decreases. It might be reasonable to expect that just before a large slag discharge the slag capture rate underneath the nozzle would be large and likewise, just after a large slag discharge, the slag capture rate might increase due to the recent depletion making room for more slag. Significant slag capture rates can not occur before approximately 50 seconds due to the propellant configuration and no pressure depressions are observed before this time. Slag capture rates might not be expected to be continuous and changing smoothly with time due to the highly turbulent nature of the flow field and associated vortex phenomena around the separated flow field underneath the nozzle nose.

### **TEM-10 Dynamic Data Analysis**

The dynamic data analysis for static test TEM-10 revealed the presence of oscillation around the 500 Hz frequency which were not explained by hardware resonance or acoustic phenomena. It was hypothesized that pressure pulses created by slag debris expulsion might be the explanation. Calculations in Figure 8 support the contention that debris would require about .002 seconds to pass through the throat zone thus generating a 500 Hz frequency for a parade of debris objects.

### **Limit Value For Pressure Spike Amplitude**

The issue of establishing a limit value for the magnitude of the pressure perturbation spike has been our goal for some time, but the calculation of an absolute limit based on physical limitations of geometry, slag quantity or expulsion mechanism limit has been elusive since we cannot mathematically model all of the simultaneous flow dynamics, slag pool dynamics, and interactions which may be involved in generating a slag

discharge at a particular time. Nevertheless, we did formulate a logic path to calculate a maximum pressure spike amplitude based on certain assumptions and the best current two-phase CFD solutions. This approach uses two-phase CFD solutions to determine the maximum amount of slag that is accumulated underneath the nozzle nose by a burn time of 67 seconds. The predicted amount of slag accumulated underneath the nozzle by the time period of maximum pressure perturbations is 2700 lbs. Furthermore, it is assumed that the slag is entrained and dispersed in the gases under the nozzle nose and that only the slag entrained in the vortex can be transported forward out from under the nose and be expelled. The slag in the extreme rear zone, which is a "dead" flow region cannot be transported forward and be expelled, see Figure 9. These assumptions enable a total available slag expulsion weight of 2400 lbs. ( $.87 * 2700$  lbs.) to be calculated. The existing slag ballistics model, which relates slag discharge quantity to motor pressure, was next used to calculate the pressure amplitude by making an additional assumption of a discharge time of 0.8 seconds which comes from STS-54. The resulting "limit" amplitude is 20 psi which appears to be a reasonable value and is also consistent with the statistical analysis. This value was given as an interim value subject to further "maturing" of the analyses involved and with all the limits of the necessary assumptions.

# Nozzle Blockage Analysis RSRM-29B, STS-54

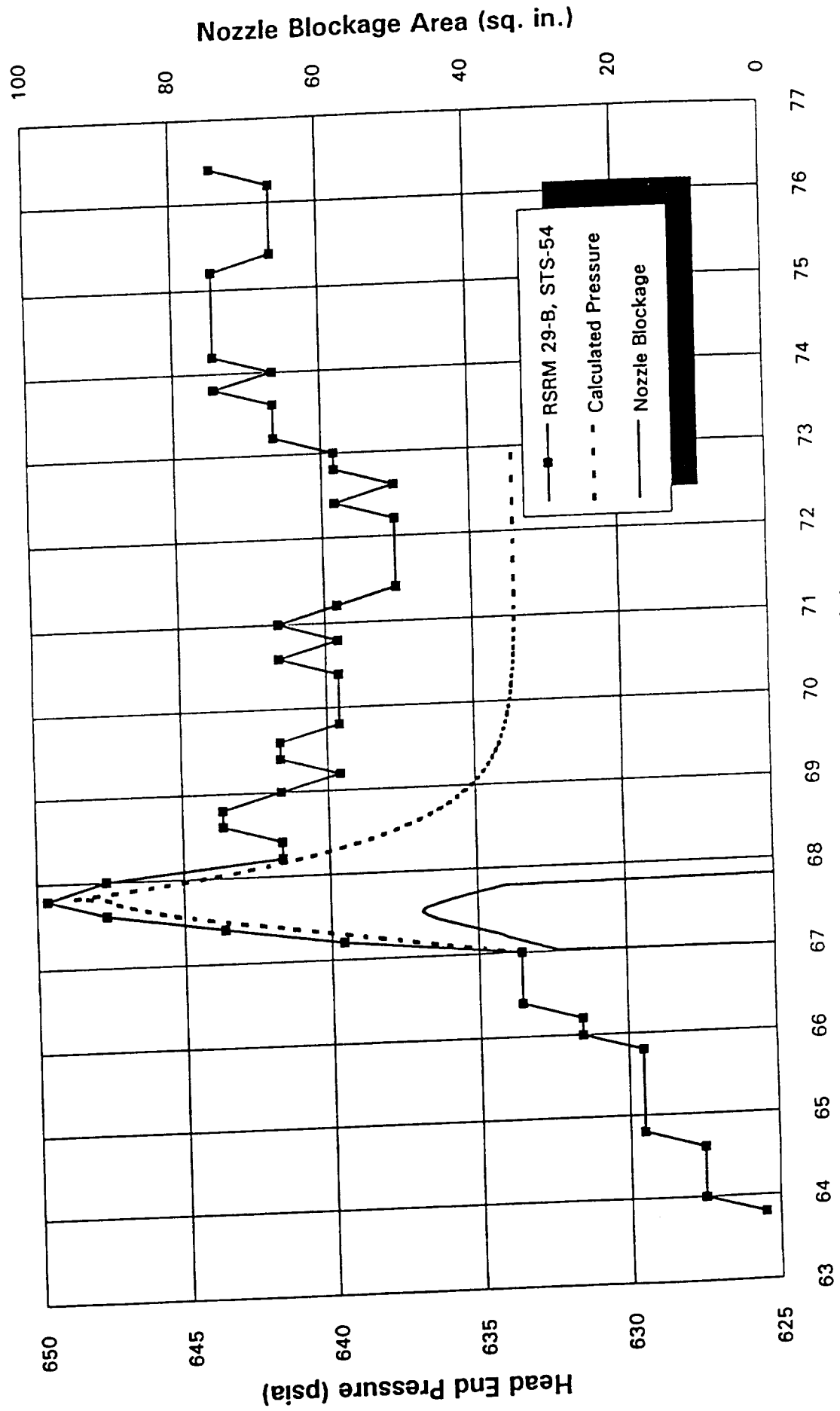
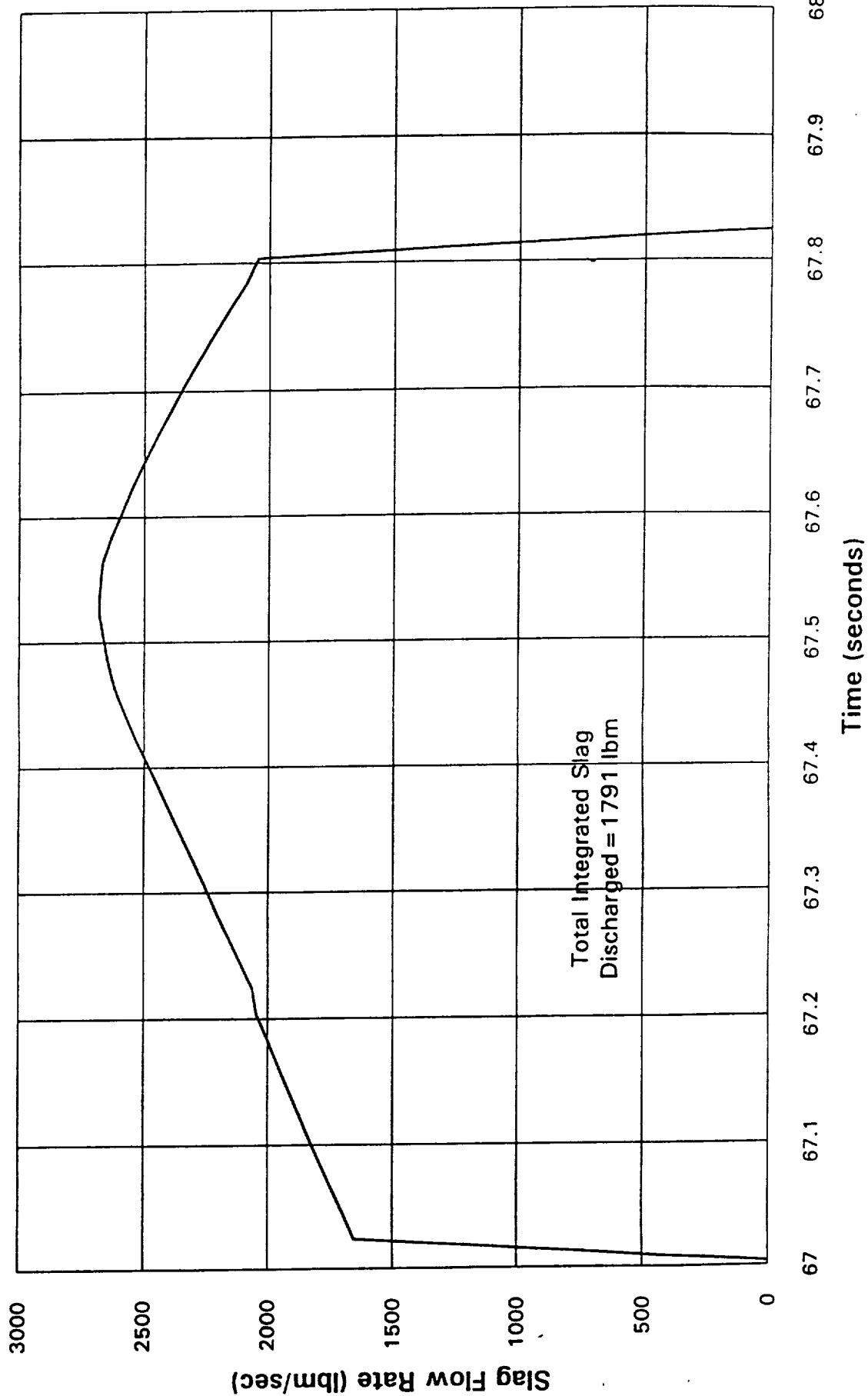


Figure 1

# Nozzle Blockage Analysis RSRM-29B, STS-54



## EFFECT OF THRUST/PRESSURE RATIO INCREASE ON THRUST IMBALANCE

$$\Delta F)_r = \frac{\Delta F)_{\text{slag}}}{\Delta F)_{\text{norm}}} = \frac{F/P)_s P_2 - F/P)_n P_1}{F/P)_n P_2 - F/P)_n P_1}$$

$$\Delta F)_r = \frac{F/P)_r P_2 - P_1}{\Delta P}$$

where	$\Delta F)_r$	=	Ratio of thrust imbalance with slag to thrust imbalance without slag
	$F/P$	=	Thrust to pressure ratio
	$P$	=	Chamber pressure
Subscript 2		=	At pressure spike peak
1		=	Before pressure spike
s		=	Slag Flow Condition
n		=	Normal Condition
r		=	Ratio Slag Condition/Normal Condition

ERC, Inc.

10/12/93

Figure 3

## RSRM Nozzle Slag Blockage Analysis

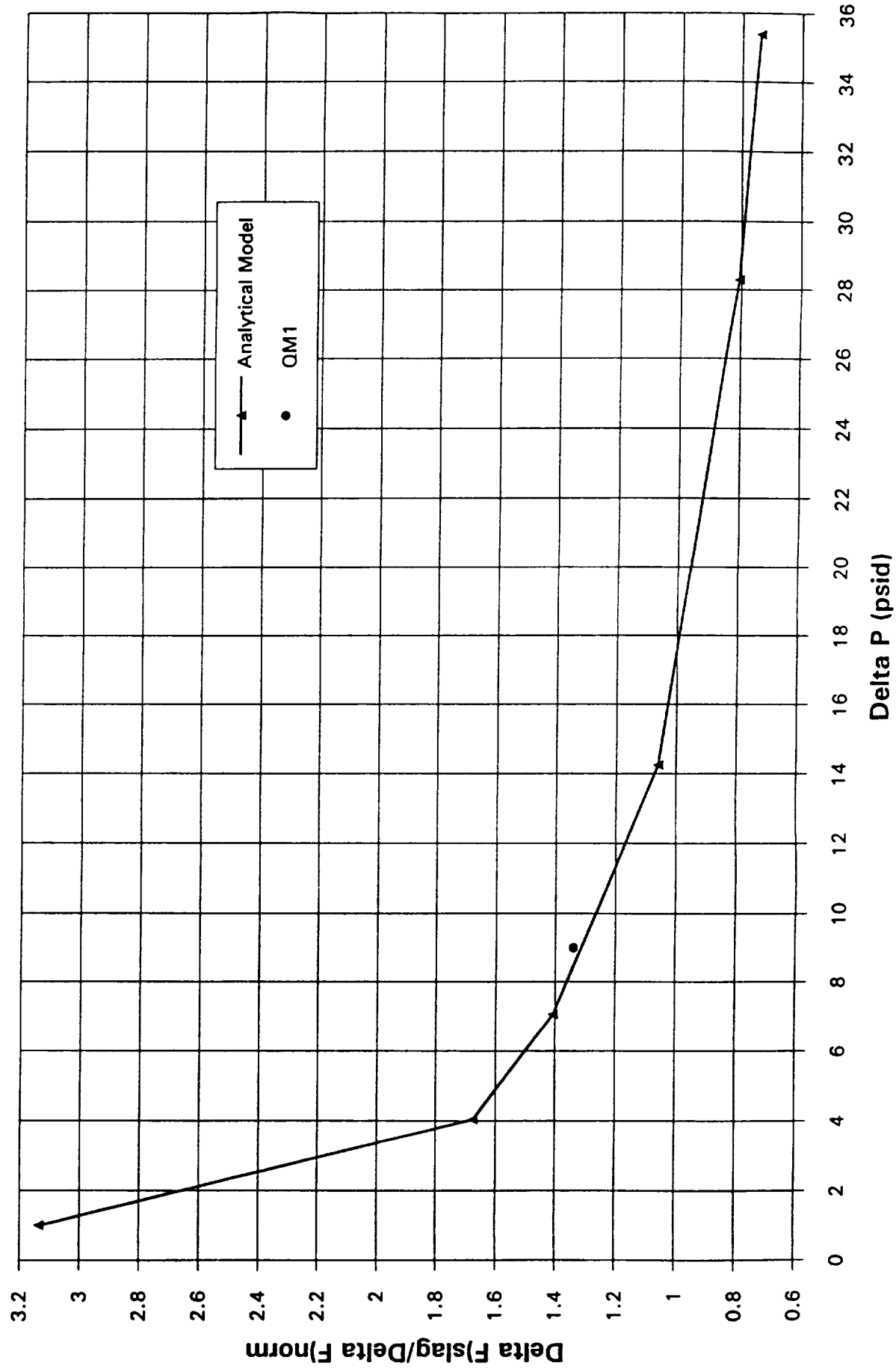


Figure 4

# EFFECT OF PARTICLE CAPTURE ON RSRM CHAMBER PRESSURE

## Continuity (Equilibrium Form with Particle Sink)

$$\dot{w}_{\text{gen}} - \dot{w}_{\text{cap}} = \dot{w}_{\text{dis}}$$

where

$$\dot{w}_{\text{gen}} = r_b A_s \rho_p \quad (\dot{w} \text{ generated})$$

$$\dot{w}_{\text{dis}} = g_o A_t P_d / C^* \quad (\dot{w} \text{ discharged})$$

$$\dot{w}_{\text{cap}} = f_{\text{cond}} \dot{w}_{\text{gen}} f_{\text{cap}} \quad (\dot{w} \text{ captured})$$

where

$f_{\text{cond}}$  = weight fraction condensed species

$f_{\text{cap}}$  = fraction of  $\text{Al}_2\text{O}_3$  captured

$$\frac{P_c}{r_b} = \frac{P_c^{1-n}}{\alpha} = C^* \rho_p \frac{A_s}{g_o A_t} (1 - f_{\text{cond}} \bullet f_{\text{cap}})$$

ERC, Inc.  
10/15/93

Figure 5

## EFFECT OF PARTICLE CAPTURE ON RSRM CHAMBER PRESSURE

### Pressure Ratio for Particle Capture

Condition 1: Normal Flow, No Particle Sink

Condition 2: Flow With Particle Sink

$$\frac{P_c}{P_1} = \left[ \frac{C^* 2}{C^*_1} (1 - f_{\text{cond}} \bullet f_{\text{cap}}) \right]^{1/1-n}$$

For RSRM @ 67 sec,  $P_1 = 628.9$ ,  $f_{\text{cond}} = .2877$ ,

$C^*_2 = C^*_1$  (No Effect Of Particle Depletion)

$$f_{\text{cap}} = .08 \times .564 = .04512$$

$$\dot{w}_{\text{cap}} = .04512 \times .2877 \times 9572.5 = 124 \text{ lbm/sec}$$

$$P_2 = 616.9$$

$$\Delta P = 12.0 \text{ (Pressure Decrease With No } C^* \text{ Effect)}$$



## EFFECT OF PARTICLE CAPTURE ON RSRM CHAMBER PRESSURE

### Effect of Particle Depletion on C\*

Condensed Specie Weight Fraction, TP-H1148 = .2877

Fraction Of  $\text{Al}_2\text{O}_3$  Above Critical  $100\mu\text{m}$  Capture Size = .08

Fraction Of Flow Outboard Of Nozzle Nose = .564

Fraction Of  $\text{Al}_2\text{O}_3$  Captured = .04512

Adjusted  $\text{Al}_2\text{O}_3$  Weight Fraction After Capture = .2783; Adjusted AL Ingredient Fraction = 15.408

C\* And Chamber Temperature, TP-H1148 = 5152 ft/sec And 6063.9 °R

C\* And Chamber Temperature, Adjusted AL Propellant = 5150 ft/sec and 6031.5 °R

Correct C\* To TP-H1148 Flame Temp

$$C^*_{\text{corr}} = 5150 \left( \frac{6063.9}{6031.5} \right)^{\frac{1}{2}} = 5163.8 \text{ ft/sec}$$

$$P_2/P_1 = .98427, P_1 = 628.9, P_2 = 619.0$$

$$\Delta P_{\text{decrease}} = 9.9 \text{ psi}$$

ERC, Inc.  
10/15/93

Figure 7

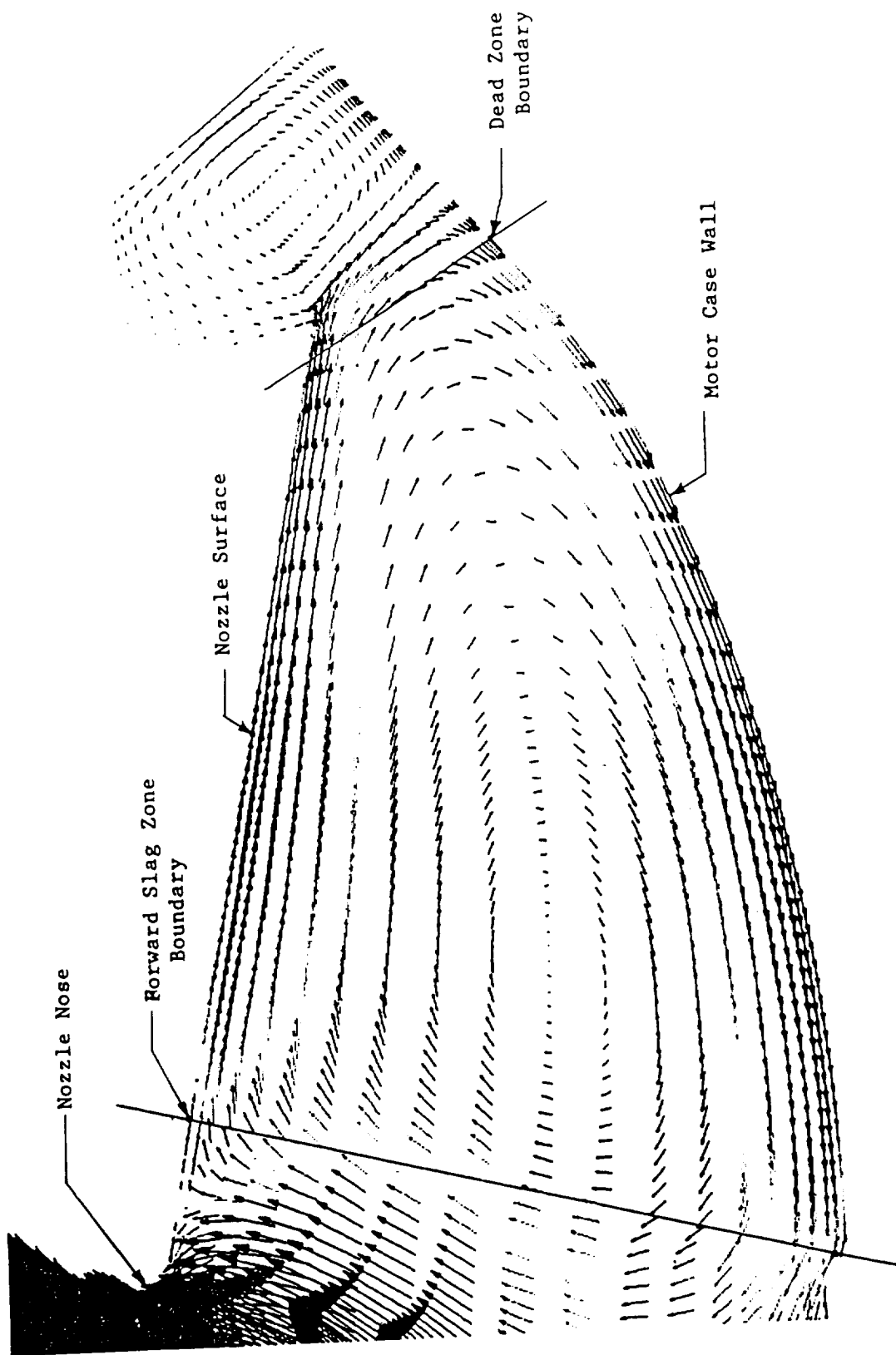
## TEM-10 DYNAMIC DATA ANALYSIS

### Motor Frequency Calculation

Premise: The frequency of chamber pressure oscillations that occur during debris expulsion are related to the time duration of pressure pulses directly caused by throat blockage

Throat Area Blockage	
• Pressure Spike Magnitude	5 psi
• Throat Area Blockage (Transient Analysis)	28 in
• Throat Area	2392
• Blockage Ratio	.9883
• Blockage Diameter Ratio	.9941
• Upstream Distance, in.	-3
• Downstream Distance, in.	+2
TOTAL Distance	5

Frequency of Pressure Pulses	
• Velocity of Slag / Debris, ft. /s (Trajectory)	234
• Choked Distance Traveled, ft.	.417
• Duration of Pressure Pulse	.00178
• Pulse Frequency	560



CFD Velocity Vector Plot  
Nozzle Cavity Recirculation Zone

Figure 9

# **TU-168 SPIN MOTOR TESTS ANALYSES**

**24 February 1994**

## **TU-168 SPIN MOTOR TESTS ANALYSES**

### **TU-168 Spin Motor Test Support**

Thiokol is planning a series of subscale motor tests to evaluate the propensity for slag production of RSRM TP-H1148 propellant. Propellant grains for the motor will be made from various lots of ammonium perchlorate with varying particle size distributions. The effect of other ingredient variations will also be evaluated. ERC, Incorporated is doing conceptual configuration design for a submerged nose nozzle to replace the existing motor converging/diverging nozzle. The motor is a five inch cylindrical port spin motor originally designed to measure spin induced propellant burn rate enhancement. ERC, Incorporated will also perform two-phase CFD analyses to help determine the desired test spin rate to capture the desired particle fractions. The spin motor tests objectives and the approach to testing are summarized in Figure 1.

Several different nozzle configurations were analyzed to determine a good capture design for the TU-168 replacement nozzle. The chosen design referred to as TU-168 nozzle mod C design was presented to Thiokol in February of 1994. Figure 2 shows a schematic of the mod C nozzle design.

The thermochemical properties used in this analysis are shown in Table 1. An equilibrium thermochemistry model was used in the analysis and the model was derived using the nominal RSRM propellant mixture of 16 % aluminum.

**Table 23. TU-168 Spin Test Motor Thermochemical Properties**

Chamber Pressure, psia	600
Viscosity, lbm/ft-s	$6.189 \times 10^{-5}$
Thermal Conductivity, BTU/sec-ft-R	$6.222 \times 10^{-5}$
Stagnation Temperature, R	6064

The target mass injection rate used in the analysis was obtained from the burn rate of the RSRM propellant, 2.6318 lbm/sec. This mass flux is injected uniformly over the propellant surface.

The nominal converging/diverging nozzle configuration of the TU-168 motor was analyzed first. The computational grid for this configuration of the motor is shown in Figure 3. The grid resolution for this case is 93 axial grid lines by 30 radial grid lines. The flow field, as expected, does not provide a good capture zone for particulate but depends totally on the particles solidifying on the cooler nozzle wall.

The mod C nozzle design flow field was also analyzed. The computational grid for this configuration is shown in Figure 4. The flow field velocity vectors in the submerged nozzle region are shown in Figure 5. It was desired to have a flow field with a recirculation region in the submerged cavity of the nozzle. This was desired to permit additional particle capture capability by dividing the main port flow from that in the submerged region. The mod C design clearly provides this kind of flow and the dividing streamline is clearly visible on the underside of the submerged nozzle.

This analysis will continue with the next step being to perform a two-phase analysis on the flow field to determine the appropriate spin rate to be used during the motor tests.

## TU-168 SPIN TESTS WITH RSRM PROPELLANT

### **OBJECTIVE:**

Evaluate Effect of AP Particle Size Distributions and Other Propellant Ingredient Characteristics on the Propensity for Slag Generation in a Subscale Motor Environment

### **APPROACH:**

- Use Existing TU-168 Spin Motor and Stand to Measure Slag Accumulation and Burn Rate Augmentation for each Propellant Sample
- Modify Nozzle Entrance geometry to Enhance Slag Accumulation which is the Primary Emphasis for this Experiment
- Select AP Sample and Define Propellant Variations to be Tested - Generate Test Matrix
- Design Submerged Nose Geometry within Geometric Constraints of Existing Nozzle Body
- Use CFD to Ensure that Modified Nozzle has an Apparent Defined Slag Capture Rate
- Use Two-Phase CFD to Analyze Test Data and Link Results to Quench Bomb Data and to Apply Subscale Results to Full Scale RSRM

Figure 1. TU-168 Spin Test Motor Objectives and Test Approach

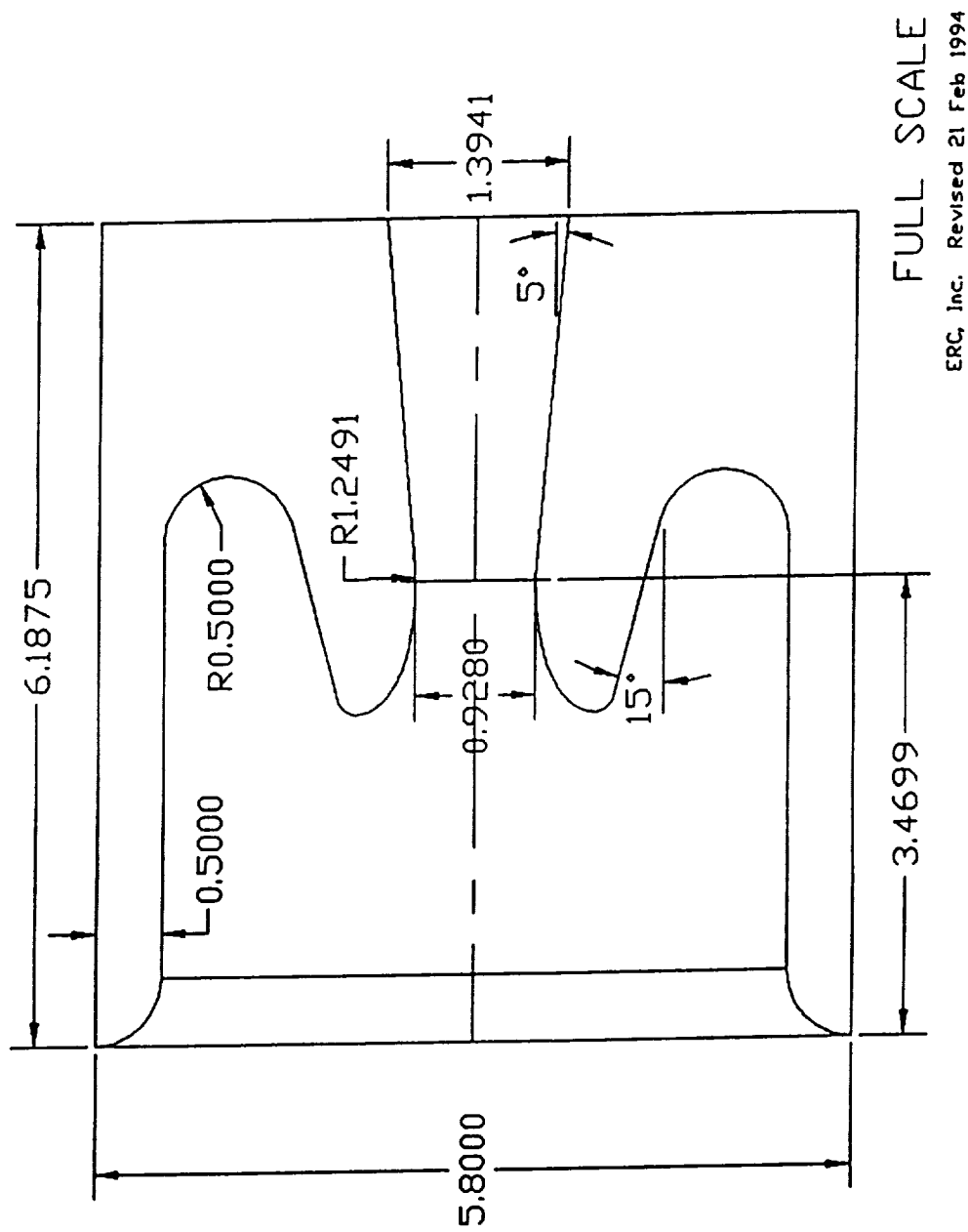
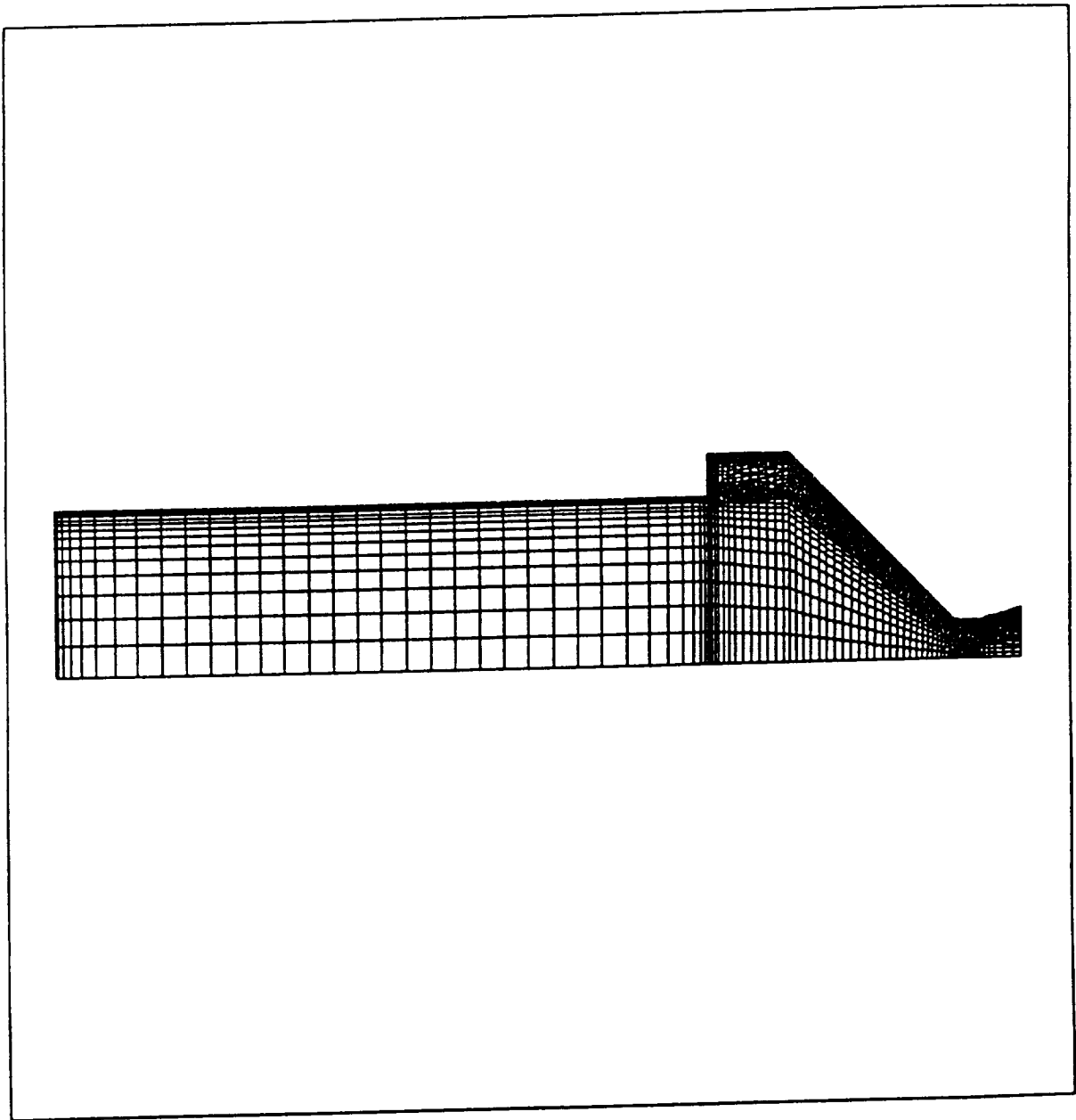
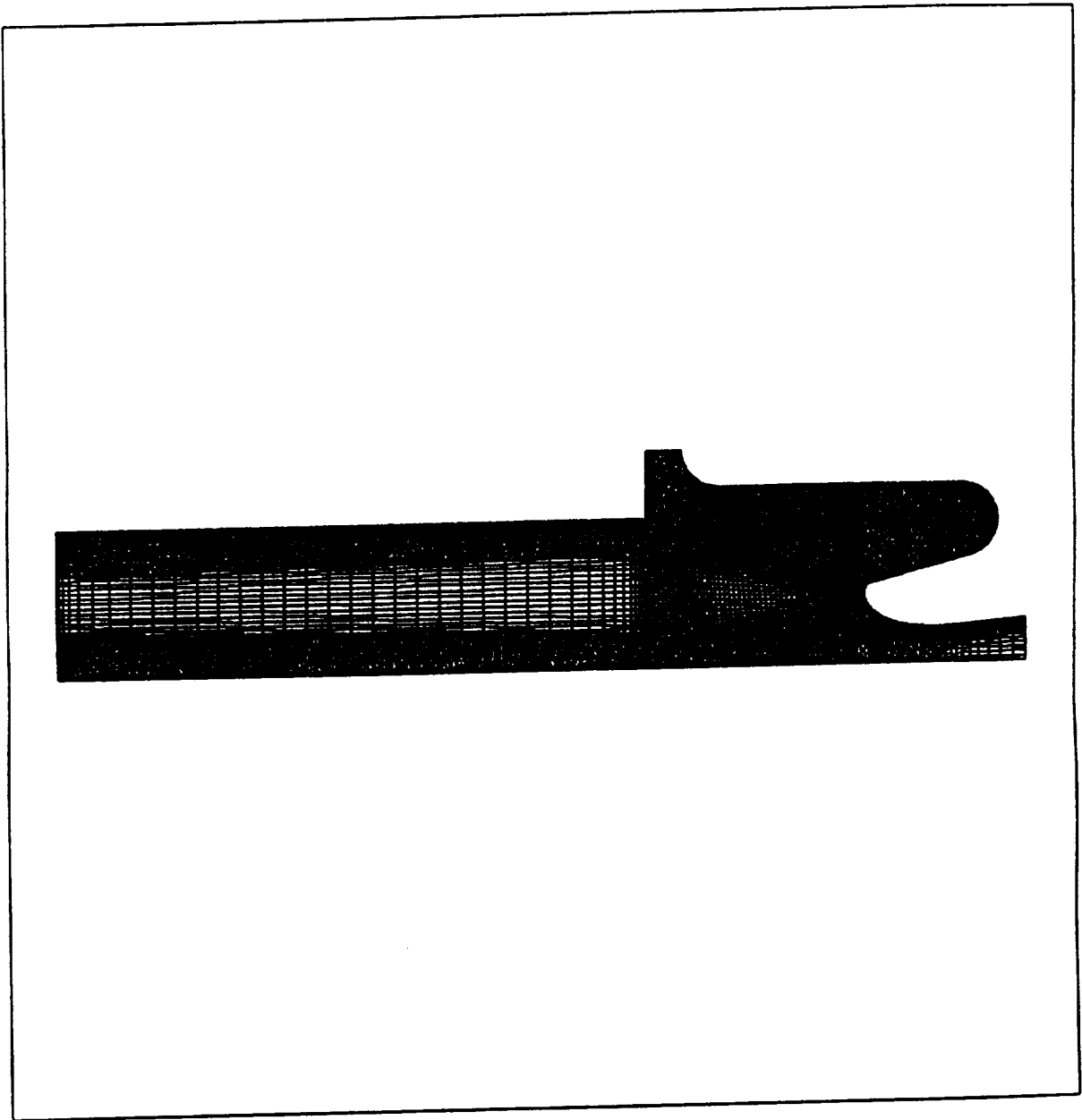


Figure 2. TU-168 Mod C Motor Drawing





**Figure 3. Converging/Diverging Nozzle Grid**



**Figure 4. TU-168 Mod C Nozzle Grid**

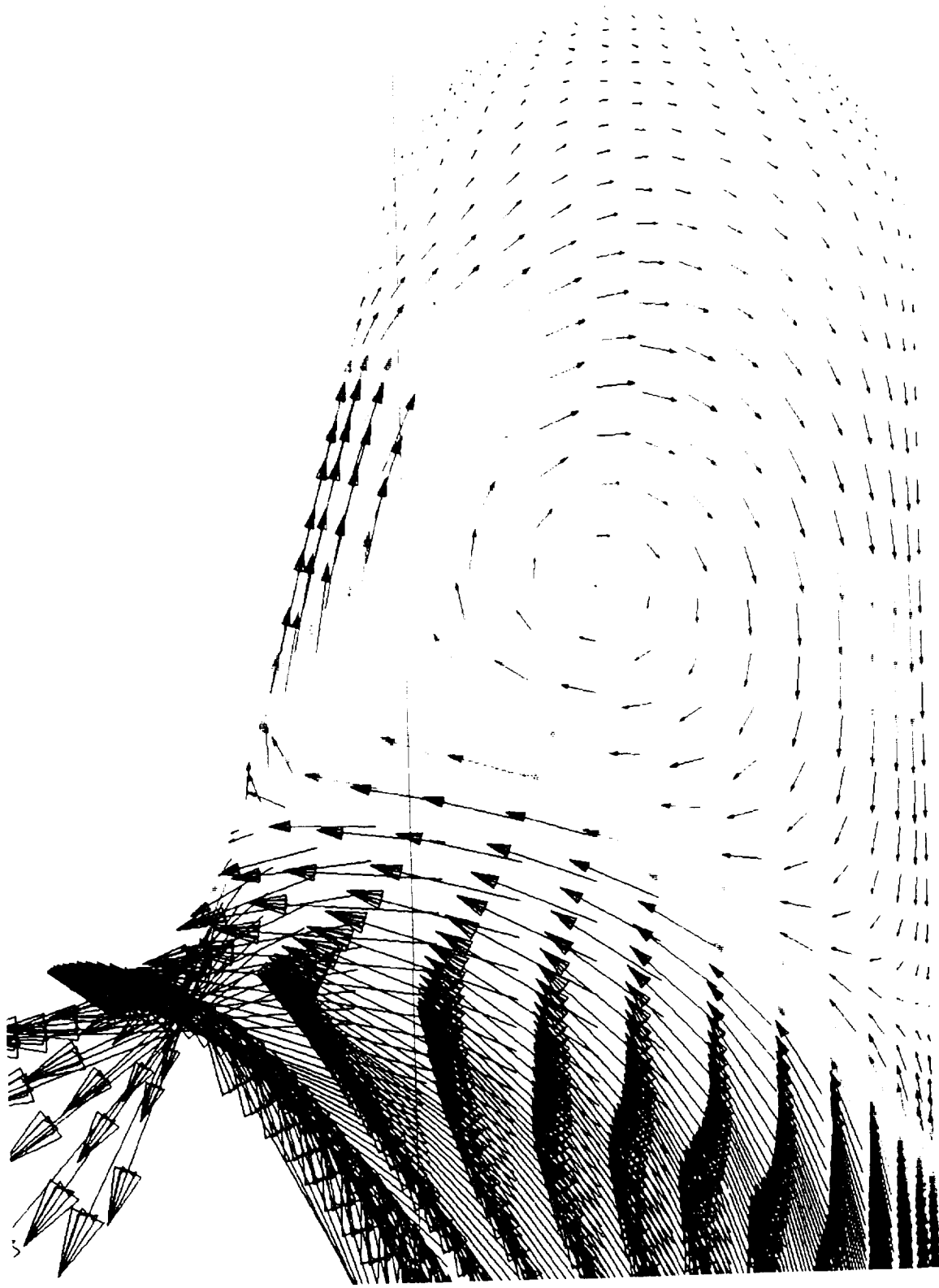


Figure 5. Velocity Field for the TU-168 Mod C Nozzle

# **RSRM CFD ANALYSES**

**24 February 1994**

# **RSRM CFD ANALYSES**

## **Introduction of the CFD Analyses Associated with the STS-54 Pressure Perturbation Investigation**

CFD support analysis for the RSRM motor was initiated beginning 19 January 1993 to help determine the cause of the 13 psi pressure spike in RSRM-29B and the associated thrust imbalance. Since that time many computational fluid dynamic analyses have been performed to assess the overall flow field of the RSRM motor near the burn time of interest. Many factors associated with the flow field were of interest including the flow field induced environment, mechanical loads on the inhibitor stubs and propellant grain, load changes due to port blockage, slag spillage fluid dynamic induced mechanisms, and slag accumulation in field joints and the nozzle bucket. Many analyses have also been performed to assess various possible causes for the pressure spike and possible failure scenarios. The results of the various analyses are presented in separate sections which are separated by general topic. The objectives of each of the analyses to be presented are given in this introduction.

### **1) Full-Length Motor Chamber Analysis of the RSRM 67 Second Burn Time Motor**

This analysis was performed using the Fluent/BFC code. This analysis was the first performed under this effort and at the time of performance was very time critical. The flow field induced environment from the motor head end to a point just upstream of the submerged nozzle was assessed. The purpose of this was to obtain general flow field characteristics for the motor at the 67 second burn time, such as flow field induced pressure loading on the inhibitors and propellant grain, characteristics of the pressure drop across the field joints, investigate the existence of unusual flow characteristics around the field joint inhibitors, and assess the development of the flow down the motor port and how the inhibitors affect the velocity field at the aft end of the motor. A two-phase flow field analysis was not performed as part of this work but the flight of  $\text{Al}_2\text{O}_3$  particles from various locations in the motor was observed. This was done to determine what size particles would be trapped in the field joints. This analysis was performed as a first step at looking at the accumulation of slag in the field joints and submerged nozzle region until a fully coupled two-phase flow field analysis could be performed.

This analysis also included an assessment of how a piece of broken inhibitor would affect the motor pressure characteristics as the piece of inhibitor passed to the aft end of the motor and blocked the motor port.

### **2) Aft Segment Analysis of Effects of Slag Filling in the Submerged Nozzle Bucket**

This analysis included many computational fluid dynamic solutions for both two-dimensional and three-dimensional configurations of the RSRM 67 burn time motor aft

segment. The objective of this analysis was to determine how the motor flow field in the aft end of the motor was affected by the slag filling in the submerged nozzle bucket. This was to done to investigate possible flow field induced mechanisms which might either trigger or contribute to the spilling of slag from the submerged nozzle bucket. The three-dimensional solutions investigated the effects of circumferentially generated velocities behind the nozzle nose due to the slag pool in the submerged nozzle bucket being tilted due to motor flight orientation. The two-dimensional analyses discussed in this section were performed using the Fluent/BFC code and the three-dimensional analyses were performed using the Fluent v4.22 code.

### **3) Fully Couple Two-Phase Full-Length Motor Analysis of the RSRM 67 Second Burn Time Motor**

The previous motor flow field analyses have been performed using effective gas analysis techniques where the effects of both motor chemistry and discrete particulate were ignored. The purpose of this analysis was two-fold: To determine how much the flow field changes due to considering equilibrium motor chemistry, aluminum combustion and discrete particles and also to determine the amount of slag that is collected in various regions of the motor. If large amounts of slag are accumulated at any location in the motor a trigger mechanism for dumping the slag might cause the observed pressure spike behavior. This made it very important to determine the regions of the motor which might generate potential problems associated with slag accumulation. The major objective of the analysis was to determine the rate at which slag was collected in the motor head end, all motor field joints and the submerged nozzle bucket. Parametrics for nominal motor particulate conditions were investigated to determine the effects of uncertainties in the characteristics of the propellant. These parametrics included investigation of the effects of propellant aluminum particle mass mean diameter uncertainty, vertical and axial launch acceleration effects, and effects of smoke agglomeration and particle breakup.

### **4) CFD Methodology**

A brief summary of the operational capabilities and the numerical algorithm will be given for each of the three CFD codes utilized in the analyses discussed in this report. The three codes discussed are Fluent/BFC, Fluent 4.22, and CELMINT.

## **Presentation of the Problem Results**

### **Full-Length Motor Chamber Analysis of the RSRM 67 Second Burn Time Motor**

A CFD analysis of the RSRM-29B, STS-54 motor was performed during late January of 1993 as the first step in the process of determining the source of a motor problem which triggered the pressure blimp observed during the flight of this motor. The motor

configuration definition geometry for this analysis was obtained from Thiokol and is for the 67 second motor burn time. Figure 1 shows a cutaway illustration of the RSRM motor with both the 0 and 67 second burn time propellant configurations. This figure can be used as a reference figure for all the CFD analyses presented in this CFD section. The bent over inhibitors were added to this nominal configuration geometry as prescribed by Thiokol in a fax sent to ERCI on January 27th. Grid geometry models were constructed for these bent over inhibitors which were very close to the Thiokol prescribed geometry.

A computational grid was constructed for the section of the RSRM motor shown in Figure 2. Figure 2 shows only the 67 second propellant burn back but the features in this figure can be compared with figure 1 to get a better understanding of the what parts of the RSRM motor are being modeled. This geometry corresponds to the geometry description obtained from Thiokol. The configuration geometry includes the prediction of the RSRM motor geometry from the motor head end to the aft end at a 67 second propellant burn back. The submerged nozzle was not included in the geometry description and was not needed for this analysis. In order to conserve grid as well as increase solution stability, the upstream boundary of the motor was chosen at the front end of the forward propellant segment. The flow velocity was very low here and the inlet was several motor diameters upstream of the forward slot so the choice of not modeling the propellant deplete head end region of the motor was insignificant for this analysis. Since this task was of a time critical nature, a very fine resolution grid was not used to model the flow field at this time. The grid spacing was chosen as to provide adequate resolution of all the flow field features of interest, yet provide a solution in a relatively short period of time. A total of 300 grid lines in the axial direction and 35 grid lines in the radial direction were used to resolve the flow. Figure 3 shows an overview of the complete computational grid used for this analysis.

There were three slots modeled in the analysis. The nominal inhibitor stub lengths associated with the three slots as specified by Thiokol are listed in Table 1. The inhibitors were bent over in the motor flow field downstream direction due to flow field induced forces. The amount of bending of each inhibitor was prescribed by Thiokol documentation. The shape of the inhibitors provided by Thiokol were curve fit to obtain a shape that could be formed into a computational grid.

**Table 1. Thiokol Prescribed Bent-Over Inhibitor Stub Heights**

	<b>Inhibitor Stub Height</b>	<b>Maximum Axial Displacement of Inhibitor Stub Tip</b>
Forward Inhibitor	12.7"	7.514"
Center Inhibitor	8.5"	5.669"
Aft Inhibitor	6.9"	3.623"

The forward slot was simplified to the geometry shown in Figure 4. This simplification assumes that the castable inhibitor on the aft end of the forward propellant grain lays flush on the surface of the inhibitor bonded to the forward center propellant segment as shown in the diagram of Figure 5. The computational grid in the forward slot region contained 20 grid lines in the axial direction and 20 grid lines in the radial direction from the propellant surface to the tip of the bent over inhibitor. The motor port core flow region from the motor centerline to the tip of the inhibitor stub protruding from the slot was resolved by an additional 15 radial grid lines. The center slot was the interface between the first and second center propellant segments and the grid in this region of the motor is shown in Figure 6. The grid spacing in the slot region was the same as the forward slot. However, an additional 20 x 20 grid was used to resolve the slot void between the two propellant segments. The same grid resolution was used to model the region of the aft slot shown in Figure 7. This slot was the interface between the second center propellant segment and the aft propellant segment. The grid was finer near the propellant surface in this aft slot region because the bent over aft inhibitor stub prescribed by Thiokol was significantly shorter at this slot.

The analyses performed in this section were performed using an effective gas analysis technique where the molecular weight of the analyzed gas was a combined molecular weight of the propellant chemical system. The RSRM thermochemical properties were obtained from the NASA Lewis TRAN72 equilibrium thermochemistry computer code. The assumed thermochemical properties for a chamber pressure of 635 psia are given in Table 2.

**Table 2. RSRM Motor Thermochemical Properties**

Chamber Pressure, psia	635
Specific Heat Ratio	1.138
Viscosity, lbf/ft-s	$6.189 \times 10^{-5}$
Thermal Conductivity, BTU/sec-ft-R	$6.222 \times 10^{-5}$
Molecular Weight	28.04
Gas Constant, ft-lbf/lbm-R	55.112
Stagnation Temperature, R	6064

The boundary conditions for the CFD solution were obtained from a Thiokol RSRM ballistic run. In this analysis the RSRM motor was modeled as axisymmetric. The motor centerline was modeled as a symmetry boundary. Refer to Figure 8 for clarification of this discussion on boundary conditions. A velocity inlet boundary condition was used at the motor upstream boundary condition at the forward end of the forward propellant segment. A uniform radial velocity profile was used along this boundary because of its simplicity. Since this boundary is a low velocity boundary and is located far upstream of the forward slot, the effects of this choice were negligible. The ballistic run was used to determine the mass flow rates and estimated



temperatures and pressures associated with the various propellant segments. The injection mass flux was then assumed equally distributed over the area of the propellant segment in question. This process was performed to determine separate specified injection velocities for four propellant segments as shown in Figure 6. The exit boundary was located at the corner of the propellant grain just upstream of the submerged nozzle nose. A fixed static pressure boundary condition was used at the exit. The pressure used was obtained from the ballistic run at this motor station. Table 3 contains a summary of the boundary conditions discussed in this paragraph. The injection velocities shown in Table 3 were applied as normal to the propellant surfaces.

**Table 3. RSRM 67 Second Burn Time Boundary Conditions**

Upstream Boundary, Inlet Velocity	14.35 ft/sec
Propellant Segment 1, Injection Velocity	12.48 ft/sec
Propellant Segment 2, Injection Velocity	12.36 ft/sec
Propellant Segment 3, Injection Velocity	12.67 ft/sec
Propellant Segment 4, Injection Velocity	13.39 ft/sec
Exit Static Pressure Boundary	635 psia

The mass flow rate distribution corresponding to these velocity boundary conditions for the forward, forward center and aft center segments, and aft propellant segments is shown in Table 4.

**Table 4. Mass Flow Rate Distribution for the 67 Second Burn Time RSRM Motor**

	<b>Mass Flow Rate</b>
Forward Segment	1555.9 lbm/sec
Forward Center Segment	2587.5 lbm/sec
Aft Center Segment	2672.7 lbm/sec
Aft Segment	2756.4 lbm/sec
Total Mass Flow Rate	9572.5 lbm/sec

A general overview of the flow field for the converged CFD solution is shown in Figure 9. This figure shows a color raster plot of the Mach number in the motor. The velocity and pressure differences being observed in the slot regions were very small for this problem. The mass flux error between the inlet and exit surfaces was less than 0.03%. The velocity steadily increases from the head end to the aft end of the motor. The developed motor velocity profile can be seen in the aft end of the motor where the red along the centerline illustrates the high velocity flow and the blue along the wall illustrates the low velocity flow. The flow field in the vicinity of the forward, center and aft slots is of particular interest in this analysis. Figures 10, 11, 12 show the velocity vector field (m/sec) in the vicinity of the forward, center and aft slots respectively. The only observed recirculation was noted as a very small flow separation at the tips of the

bent over inhibitors. Also, the center and aft slots showed a recirculation region in the downstream corners of the voids between the propellant segments.

Figures 13, 14, and 15 show color raster plots of the pressure field in the immediate vicinity of the three field joints. The pressure is shown in pascals and the pressure difference around the inhibitor is very small. The pressures plotted along the propellant grain and at the motor centerline for the forward, center and aft slots are shown respectively in Figures 16, 17 and 18. There is an expected pressure drop as flow is accelerated around the bent over inhibitor. Since the inherent port velocity is greater as flow progresses downstream, the pressure drop increases from the forward slot to the center slot. The pressure drop at the forward slot is less than 1 psi. The pressure drop at the center slot is almost 2.5 psi and the pressure drop observed at the aft slot is 1.5 psi. The pressure drop at the aft slot is less than the pressure drop at the center slot for this configuration because the aft inhibitor stub height is significantly less than the height of the center slot inhibitor stub. This creates a smaller flow obstruction at the aft slot even though the port flow velocity is higher. The centerline and propellant surface pressure values converge downstream of each slot obstruction so that there is no significant radial pressure gradient except in the immediate vicinity of the slots.

Due to the uncertainty of the actual length of the inhibitors due to thermal erosion and the amount of bending in the inhibitors, analyses were performed for two geometric perturbations of the nominal Thiokol propellant/inhibitor configuration. In the first configuration, referred to as excursion 1, the same length inhibitors were used but the inhibitors were not bent over. The CFD computed fluid dynamic loads for this straight inhibitor geometry were used by Rockwell to perform a mechanical load analysis on the inhibitors. This analysis was used to determine if the bending in the inhibitors due to the loads predicted by this flow field solution agreed with the bending predicted by Thiokol. The second solution, referred to as excursion 2, also used an unbent inhibitor configuration. The inhibitors in this configuration were 25% longer than for the nominal Thiokol configuration. This configuration had inhibitor stub lengths as shown in Table 5.

**Table 5. Extended Inhibitor Stub Heights**

	<b>Inhibitor Stub Heights</b>
<b>Forward Inhibitor</b>	<b>15.875"</b>
<b>Center Inhibitor</b>	<b>10.625"</b>
<b>Aft Inhibitor</b>	<b>8.625"</b>

The full RSRM motor propellant and inhibitor geometry for excursion 1 is the same as for the nominal bent-over inhibitor configuration except at the field joints where, for excursion 1, the inhibitors are unbent. The full computational grid for excursion 1 is shown in Figure 19. There were three slots modeled in the analysis. The forward slot was simplified to the geometry shown in Figure 20. The computational grid in the forward slot region contained 20 grid lines in the axial direction and 20 grid lines in the

radial direction from the propellant surface to the tip of the bent over inhibitor. The motor port core flow region from the motor centerline to the tip of the inhibitor stub protruding from the slot was resolved by an additional 15 radial grid lines. The center slot was the interface between the first and second center propellant segments and the grid in this region of the motor is shown in Figure 21. The grid spacing in the slot region was the same as the forward slot. However, an additional 20 x 20 grid was used to resolve the slot void between the two propellant segments. The same grid resolution was used to model the region of the aft slot shown in Figure 22. This slot was the interface between the second center propellant segment and the aft propellant segment. The grid was finer near the propellant surface in this aft slot region because the bent over aft inhibitor stub prescribed by Thiokol was significantly shorter at this slot.

The converged CFD solution mass flux error between the inlet and exit surfaces was less than 0.2%. The general flow field solution is illustrated by the Mach number color raster plot shown in Figure 23. The velocity steadily increases from the head end to the aft end of the motor. The developed motor velocity profile can be seen in the aft end of the motor where the red along the centerline illustrates the high velocity flow and the blue along the wall illustrates the low velocity flow. The maximum Mach number is slightly larger for the unbent inhibitor case than for the bent-over inhibitor case since the extension of the inhibitors into the flow causes a greater restriction of the port flow area locally at the aft slot. The flow field in the vicinity of the forward, center and aft slots is of particular interest in this analysis. Figures 24, 25, and 26 show the velocity vector field in the vicinity of the forward, center and aft slots, respectively. There is more vortex shedding observed for this geometric configuration than for the Thiokol nominal bent-over inhibitor configuration. There is recirculation present downstream of the forward and center inhibitor stub tips. The lack of a noticeable vortex at the aft inhibitor stub is probably due to the higher port velocity and the fact that the aft inhibitor is comparatively much shorter than the forward and center inhibitors. The center and aft slots also show a recirculation region in the downstream corners of the voids between the propellant segments.

The pressure along the propellant grain and at the motor centerline is shown in Figure 27 for the excursion 1 geometry. As expected, the pressure drop for the unbent inhibitors is greater than was observed for the bent-over inhibitors of the nominal configuration. The pressure drops reported here are measured from the bottom of the inhibitor nearest the motor case to the tip of the inhibitor which protrudes into the port flow. The pressure drop at the forward inhibitor for the bent-over inhibitor case was 1 psi. This has increased to 2 psi for the unbent inhibitor. The pressure drop at the center slot was 2.5 psi for the bent-over inhibitor case and has increased to 6.4 psi for the unbent inhibitor. The behavior of the flow in the vicinity of the aft inhibitor stub is similar to that of the nominal bent-over inhibitor case. The pressure drop is less than for the center slot because the inhibitor stub is much shorter. The pressure drop at the aft slot was about 1 psi for the bent-over inhibitor case and has remained about 1 psi for the unbent inhibitor. These pressure drops are of small magnitude from a

mechanical load standpoint. The centerline and propellant surface pressure values converge downstream of each slot obstruction so that there is no significant radial pressure gradient except in the immediate vicinity of the slots. Radial pressure gradients in the vicinity of the nozzle are not considered. Shearing forces are also small for both the bent-over and unbent inhibitor stub configurations.

The excursion 2 propellant and inhibitor geometry was the same as that for excursion 1 except that the length of the inhibitors were extended 25% farther into the port flow. This excursion configuration was run in order to observe the flow field effects if erosion of the inhibitors is 25% less than predicted by Thiokol. The grid for excursion 2 was similar to the grid for excursion 1 except that an additional 5 grid lines were used to resolve the flow between the propellant surface and the tips of the inhibitors. This was done to account for the additional length of the inhibitors for this case. The converged solution had a mass flux error between the inlet and exit surfaces of 0.2%.

The Mach number plot for excursion 2 is similar in appearance to that of excursion 1 except that the maximum Mach number for excursion 2 was 2.63. The maximum Mach number for excursion 1 was 2.19. The flow field velocity vectors in the vicinity of the forward, center and aft slots are shown in Figures 28, 29 and 30 respectively. There was recirculation evident downstream of the inhibitor tips for all three slots for this case.

The extended length of the inhibitors also increases the pressure drop at the slots as would be expected. Figure 31 shows a plot of the pressure along the centerline and at the propellant surface for this configuration. The pressure drop at the forward slot is 3.6 psi. The pressure drop at the center slot is 10.2 psi and the pressure drop at the aft slot has increased significantly over excursion 1 to 8.4 psi.

A particle tracking analysis was performed for the nominal bent-over inhibitor stub geometry and for the excursion 1 and excursion 2 solutions. This was done to investigate the tendency of aluminum oxide particles of various sizes to be trapped in the slots and form slag deposits on the inhibitors. This analysis considered particle sizes ranging from 50  $\mu\text{m}$  to 200  $\mu\text{m}$  in diameter for the nominal inhibitor stub configuration. For the trajectory locations considered only particles of the 200  $\mu\text{m}$  size were trapped in the field joints. Figure 32 and Figure 33 show the particle traces for 200  $\mu\text{m}$  diameter particles released from five location for the center and aft field joints. Only the particle nearest to the bottom of the field joint remained trapped. The particle density used was 110  $\text{lbm/ft}^3$  and the initial velocity given to the particles was the same as the fluid velocity associated with the grid cell from which they originated. This particle density corresponds to the density of aluminum oxide at the elevated motor temperature. No particles were trapped in the forward slot location.

As stated, a particle tracking analysis for excursion 1 was also performed. This analysis considered particle sizes ranging from 50  $\mu\text{m}$  to 150  $\mu\text{m}$  in diameter. Figure 34 shows the trajectories for the 150  $\mu\text{m}$  particles in the forward slot. None of the particles

of this size were trapped in the forward slot. Figures 35, 36 and 37 show the trajectories for the particle sizes investigated in the center slot. And figure 38 shows the trajectories for the 150  $\mu\text{m}$  particles in the aft slot. Table 6 shows the specific particles which were trapped in the center slot. Table 7 shows the specific particles which were trapped in the aft slot. At the aft slot, only particles emanating from the propellant grain near the bottom of the slot were trapped.

**Table 6. Locations at Which Aluminum Oxide Particles Escape from the Center Slot**

Particle location	150 $\mu\text{m}$ particles	100 $\mu\text{m}$ particles	50 $\mu\text{m}$ particles
1	o	o	o
2	o	o	o
3	o	o	o
4	o	o	o
5	#	#	o
6	#	#	#

The key to explain Table 3 is as follows.

o - particle escapes from the slot

# - particle trapped in the slot

**Table 7. Locations At Which Aluminum Oxide Particles Escape From The Aft Slot**

Particle location	150 $\mu\text{m}$ particles	100 $\mu\text{m}$ particles	50 $\mu\text{m}$ particles
1	o	o	o
2	o	o	o
3	o	o	o
4	o	o	o
5	o	o	o
6	#	#	#

The particle tracking analysis summary performed for the excursion 2 solution is shown in Table 8 and Table 9. This analysis considered particle sizes ranging from 50  $\mu\text{m}$  to 150  $\mu\text{m}$  in diameter. The particle density used was 110  $\text{lbm/ft}^3$  and the initial velocity given to the particles was the same as the fluid velocity associated with the grid cell from which they originated. No particles were trapped in the forward slot location. Table 8 shows the specific particles which were trapped in the center slot. Table 9 shows the specific particles which were trapped in the aft slot. These results show that the increased inhibitor heights have a significant effect on the number of particles trapped in the slot as compared to the excursion 1 solution.

**Table 8. Locations At Which Aluminum Oxide Particles Escape From The Center Slot**

Particle location	150 $\mu\text{m}$ particles	100 $\mu\text{m}$ particles	50 $\mu\text{m}$ particles
1	o	o	o
2	o	o	o
3	#	o	o
4	#	o	o
5	#	#	#
6	#	#	#

The key to explain Table 3 is as follows.

o - particle escapes from the slot

# - particle trapped in the slot

**Table 9. Locations At Which Aluminum Oxide Particles Escape From The Aft Slot**

Particle location	150 $\mu\text{m}$ particles	100 $\mu\text{m}$ particles	50 $\mu\text{m}$ particles
1	o	o	o
2	o	o	o
3	#	o	o
4	o	o	o
5	#	o	o
6	#	#	#

The pressure distribution on the front and back sides of the forward and aft inhibitors was computed and given to NASA/MSFC in mid June. Plots and numerical tables of the pressure loads on the forward and aft inhibitors were provided to NASA/MSFC in order to assess the stress on the inhibitors and analyze failure scenarios. These plots were provided for both the upstream and downstream faces of the inhibitor stubs in both the nominal length bent-over and unbent configurations. In this discussion the upstream face of the inhibitor is the face closest to the head end of the motor and the downstream face is the face closest to the motor nozzle. Figure 39 shows the pressure distribution on the upstream face of the forward slot inhibitor. The pressure is plotted as a differential pressure between the surface pressure and the pressure in the bottom of the slot (referred to as the reference pressure in the plots). This differential pressure is plotted as a function of radial distance from the motor centerline along the surface of the inhibitor. The three inhibitor configurations are plotted along with an interpolated curve. The interpolated curve is an average between the bent-over inhibitor and the extended straight inhibitor extrapolated out to the length of the extended straight inhibitor. This curve was constructed to account for an inhibitor which was bent-over midway between the straight configuration and the Thiokol bent over configuration. As shown in the plot, there is an increase in the pressure load as the inhibitor stub height increases. Figure 40 shows the pressure distribution on the downstream side of the forward inhibitor. Figure 41 shows the pressure load on the upstream side of the aft

inhibitor. Figure 42 shows the differential pressure on the downstream side of the aft inhibitor. The same observations are true for the aft inhibitor as were stated for the forward inhibitor. The differential pressure loads which exist on the forward and aft slot inhibitors are not significantly different. Even though the port Mach number is higher at the aft inhibitor than at the forward inhibitor, the aft inhibitor height is much less. Since there is a significant velocity profile across the port and the aft inhibitor does not protrude into the higher speed portion of the velocity profile, the pressure loads remain approximately the same relative to the forward slot inhibitor.

Another RSRM scenario was also investigated relating to the motor chamber and inhibitors. This was a port blockage scenario created by the failure of one of the inhibitors. In this scenario one of the inhibitors fails and passes down the motor port. This analysis was to determine the effect of the inhibitor on the motor flow field in the aft segment region of the motor. Again refer to Figure 1 to see the overall RSRM motor configuration. Only the aft end of the motor was analyzed since this was where the obstruction was modeled. The obstruction was located approximately 60 inches downstream of the aft slot. The Thiokol bent over aft inhibitor was used in this analysis. The obstruction was modeled as a simple disc located on the motor port centerline. The total frontal area of the obstruction was 20 square feet. The L/D thickness ratio of the obstruction was 0.255. Figure 43 shows the computational grid for this configuration. The computational grid contains 185 axial grid lines and 40 radial grid lines in the port region. There are 25 axial grid lines used upstream of the aft slot, 45 axial grid lines used between the aft inhibitor and the obstruction and 65 axial grid lines used to resolve the flow downstream of the obstruction. The void in the aft slot was modeled using a 20x20 grid. The axial length of the obstruction was resolved by 20 grid lines. The radial extent of the obstruction was resolved using 15 grid lines. A total of 15 grid lines were used to resolve the port flow existing between the top of the obstruction and the tip of the inhibitor stub. Also, 15 radial grid lines are used to resolve the flow from the propellant surface to the tip of the inhibitor.

The thermochemical properties used in for this case are the same as those specified in Table 2. Figure 44 shows the various boundaries defining the problem. The mass flow rate through the upstream inlet boundary was determined from the Thiokol ballistic run at the specified motor station corresponding to the inlet. A velocity boundary condition was applied at the inlet. The propellant inflow boundary condition was specified as a normal velocity boundary condition. The mass flow rates at the propellant surfaces were determined from the ballistic run. A summary of the boundary conditions used in this analysis are shown in Table 10. A specified exit pressure boundary condition was used at the downstream exit. This pressure was obtained from the Thiokol ballistic run.

**Table 10. Boundary Conditions For The Motor Aft Region Obstruction Run**

Upstream Boundary, Average Inlet Velocity	326.37 ft/sec
Propellant Segment 1, Injection Velocity	12.68 ft/sec
Propellant Segment 2, Injection Velocity	12.68 ft/sec
Propellant Segment 3, Injection Velocity	14.08 ft/sec
Exit Static Pressure Boundary	625.2 psia

Figure 36 shows a color raster plot of the Mach number in the region of the port obstruction. It is apparent in the plot that a uniform velocity profile was used at the inlet for this run. This was done in order to save convergence time over a Culick profile and because only the bulk pressure changes due to the port obstruction are of interest in this case. The stagnation flow in front and behind the port obstruction are very noticeable. The flow is rapidly accelerated over the obstruction due to the restriction in port area. The velocity field in the vicinity of the obstruction is shown in Figure 46. The flow is affected well upstream of the obstruction. There is also a large, strong recirculation region downstream of the obstruction. The flow separation at the top of the obstruction also causes a further effective decrease in the port flow area and corresponding further acceleration of the flow around the obstruction.

A 1-D ballistic analysis was also run for this obstruction problem. The pressure response due to the obstruction calculated for the 1-D analysis and the CFD flow field analysis are compared in Figure 47.

#### **Aft Segment Analysis of Effects of Slag Filling in the Submerged Nozzle Bucket**

This section contains analysis information relating to the flow field environment at the aft segment/nozzle of the 67 second burn time RSRM motor configuration. The configuration geometry analyzed is shown in Figure 48. This RSRM aft segment/nozzle configuration analyzes the complete submerged nozzle bucket with no slag accumulated in the bucket.

The inlet plane for this problem was chosen at the axial motor port location coincident with the downstream edge of the aft slot inhibitor in the unbent configuration. The length of the inhibitor stub was taken to be 9.6 inches which was the nominal inhibitor height prescribed by Thiokol. The physical grid used to model this configuration is shown in Figure 49. Figure 50 shows an enlargement of the grid in the submerged nozzle region. Fifty-five radial grid lines were used to resolve the flow field inlet. An additional fifteen radial grid lines were used to resolve the region from the propellant surface to the tip of the inhibitor protruding into the port. Eighty-five grid lines were used to resolve the axial extent between the aft grain corner point and the case behind the nozzle. One-hundred and fifteen grid lines were used to resolve the radial coordinate direction in the submerged nose region. The port was resolved by seventy radial grid lines and twenty-five radial grid lines were used to resolve the nozzle. The



large number of radial grid lines in the port region were necessary in order to adequately map the complex eroded geometry behind the submerged nozzle.

A velocity boundary condition was specified at the problem inlet plane. The velocity boundary condition was implemented as a Culick velocity profile across the inlet. The average port velocity at the inlet was 392.7 ft/sec. A velocity boundary condition was also used at the propellant surfaces. The normal velocity specified at the propellant surfaces was 12.01 ft/sec. All the solid wall non-propellant surfaces were modeled as no-slip wall boundaries. The motor centerline was modeled as a symmetry boundary and a supersonic extrapolated boundary condition was used at the exit plane in the nozzle expansion section just downstream of the throat. The thermochemical properties used in this analysis are given in Table 11. The analyses in this section were performed assuming an effective gas with molecular weight equal to the molecular weight of the propellant gas mixture.

**Table 11. RSRM Motor Aft Segment/Nozzle Problem Thermochemical Properties**

Inlet Static Pressure, psia	627.5
Specific Heat Ratio	1.138
Viscosity, lbm/ft-s	$6.189 \times 10^{-5}$
Thermal Conductivity, BTU/sec-ft-°R	$6.222 \times 10^{-5}$
Molecular Weight	28.04
Gas Constant, ft-lbf/lbm-°R	55.112
Stagnation Temperature, °R	6064

Figure 51 shows a color raster plot of the velocity magnitude (m/sec) in the problem domain. The Culick velocity profile at the inlet is clearly illustrated by the stratified color change from the centerline to the wall. The velocity is low along the propellant surface and in the submerged nozzle region. The port velocity decreases just downstream of the inhibitor due to the immediate port area increase downstream of the inlet. After the initial decrease in velocity aft of the inlet, the velocity steadily increases due to the additional mass flux from the propellant surface. Figure 52 shows a view of the flow field velocity vectors in the submerged nozzle region of the motor. The velocity vectors are colored from blue (lowest velocity) to red (highest velocity) with a maximum velocity of 100 m/sec or 328 ft/sec. The velocity vectors are scaled in length by a factor of 50 since the velocities in the submerged region are small compared to velocities in the nozzle. There are large recirculation regions present in the flow field and the dividing streamline between the flow moving out the nozzle and flow moving behind the nozzle is clearly visible. Figure 53 shows the flow field in the immediate vicinity of the aft stiffener joint. The maximum velocity shown as red in the figure is 50 m/sec or 164 ft/sec. The velocity vectors are scaled by a factor of 100. The recirculation velocities, although small, move in the general upstream motor direction across the aft dome-stiffener joint. This motion tends to deter slag flow from the depression upstream of the aft dome-stiffener joint into the submerged nozzle region. Figure 54 shows a color

raster plot of the pressure field in the submerged nozzle region. The pressure in the propellant depleted submerged region is slightly higher than the pressure in the immediate vicinity of the nozzle nose. The effects of the nozzle nose on the port pressure is evident well upstream of the nozzle nose.

The next part of the aft segment/nozzle analysis was to determine the flow field if the bucket behind the submerged nozzle was assumed to be partially filled with slag. Figure 48 shows the aft segment/nozzle configuration without slag and Figure 55 shows the aft segment/nozzle configuration with slag partially filling the cavity behind the submerged nozzle. This analysis was performed to determine how the flow field in the vicinity of the nozzle nose is affected by slag collection in the cavity behind the submerged nozzle. As for the previous analysis, the aft dome-stiffener joint located behind the nozzle nose was of interest because of observed local heavy erosion in this region of the motor.

The aft segment/nozzle motor geometry used in this analysis was the same as already described in this section except for the decrease in flow volume behind the nozzle nose. Figure 56 and Figure 57 show a comparison of the computational grid in the submerged nozzle region for the two problems discussed above (no slag in the submerged nozzle cavity and slag filling the submerged nozzle cavity). Fifty-five radial grid lines were used to resolve the flow field inlet. An additional fifteen radial grid lines were used to resolve the region from the propellant surface to the tip of the inhibitor protruding into the port. Eighty-five grid lines were used to resolve the axial extent between the aft grain corner point and the case behind the nozzle. The grid used to resolve the region behind the submerged nozzle was 80 x 30. The port was resolved by seventy radial grid lines and twenty-five radial grid lines were used to resolve the nozzle. The large number of radial grid lines in the port region were necessary in order to adequately map the complex eroded geometry associated with the submerged nozzle.

The same velocity boundary conditions used in the aft segment/nozzle analysis without slag were used in this analysis. A velocity boundary condition was specified at the problem inlet plane. The velocity boundary condition was implemented as a Culick velocity profile across the inlet. The average port velocity at the inlet was 392.7 ft/sec. A velocity boundary condition was also used at the propellant surfaces. The normal velocity specified at the propellant surfaces was 12.01 ft/sec. The thermochemical properties used in this analysis are given in Table 11.

The boundary conditions and thermochemical properties for the two aft segment/nozzle runs were identical and therefore the overall port flow characteristics for the two problems were very similar. Figure 58 shows a color raster plot of the velocity magnitude in the problem domain. The bulk flow is identical to that of the aft segment/nozzle problem without slag. The velocity is low along the propellant surface and in the submerged nozzle region. The port velocity decreases just downstream of the inhibitor due to the immediate port area increase downstream of the inlet. After the

initial decrease in velocity aft of the inlet, the velocity steadily increases due to the additional mass flux from the propellant surface. Since slag fills the submerged nozzle cavity, the upstream effects of the submerged nozzle region propagate farther upstream of the nozzle nose than for the case without slag behind the nozzle. Figures 59 and 60 show a view of the flow field velocity vectors in the submerged nozzle region of the motor for the submerged cavity with and without slag respectively. The velocity vectors are colored from blue (lowest velocity) to red (highest velocity). The magnitudes shown are in units of meters/second. There are large recirculation regions present in the flow field and the dividing streamline between the flow moving out the nozzle and flow moving behind the nozzle is clearly visible. As expected, the flow fields for the two problems are quite different in the region of the nozzle nose. Figures 61 and 62 show enlarged views of flow around the aft dome-stiffener joint for the case with no slag and with slag, respectively. The recirculation velocities in the upstream direction are smaller at the aft dome-stiffener joint for the slag filled cavity but the character of the flow in the immediate vicinity of the aft stiffener joint is similar for the two cases. The major difference in the flow fields of the two cases is that flow into the empty cavity is such that solid particles would tend to be entrained into the cavity. In the slag filled cavity case the flow is such that slag churned up at the slag surface would tend to be carried through the nozzle.

A more detailed three-dimensional solution for the RSRM 67 second motor problem was also worked. A three-dimensional aft segment/nozzle problem was analyzed to determine the flow field and in particular the circumferential velocities in the bucket behind the submerged nozzle. This problem was not axisymmetric-symmetric although the nozzle considered has a zero degree cant angle. The asymmetry comes from the slanted slag surface being modeled in the cavity behind the submerged nozzle. The slag surface is slanted due to the fact that the motor is flying at angle of attack. The nominal slant angle was  $12^\circ$  so that the slag is close to the nose on one side and recessed on the other side of the nozzle. A solution for a  $6^\circ$  slant angle was also run. The problem was modeled as having a  $180^\circ$  symmetry condition.

The computational grid for the  $12^\circ$  solution is shown first. Figure 63 shows a view of the  $180^\circ$  of the aft segment/nozzle modeled in this problem. The other  $180^\circ$  of the motor is a mirror image of the  $180^\circ$  modeled. The slanted surface of the slag causes the volume behind the nozzle at the lower side of the plot to be greater than the volume behind the nozzle on the upper side. This becomes clearer by observing Figure 64 which shows a view of the problem domain from above, looking down onto the nozzle. The recessed slag side of the nozzle is the left side of the figure and the filled slag side is the right side of the figure. Figure 65 shows a plot of several grid planes used to resolve the flow field. The grid shown in Figure 65 is a 50, 30, 31 grid (where this corresponds to the grid size in the axial, radial and circumferential directions).

The computational grid for the  $6^\circ$  slag inclination angle configuration is shown in Figures 66 and 67. Figure 66 and Figure 67 show a view of the axial/radial grid and the

radial/circumferential grid, respectively, which was constructed for this problem. The grid is the same size as used for the 12° degree slag inclination solution and the grid resolutions for the two problems are very similar. The grid size is 51x32x31 where the three dimensions are the axial, circumferential and radial coordinate sizes. The boundary conditions and thermochemical properties for both slag inclination angles are the same as shown in Table 2.

The boundary conditions for this analysis were taken from the Thiokol ballistic analysis at the 67 second motor burn time. A Culick velocity profile was used at the port inlet with the average velocity corresponding to an inlet mass flux of 8555.5 lbm/sec. The inlet turbulence intensity level was taken as 5% and the characteristic length scale as the hydraulic diameter at the inlet. The axial inlet location was taken as motor station 1696.68 inches. The mass flow rate from the remaining propellant surface was taken as 1017.0 lbm/sec.

Color plots describing the flow field are shown for the 12° slanted slag surface solution. No plots are shown for the 6° solution since the flow field was very similar to the 12° flow field. The main difference between the two flow fields was a reduced circumferential velocity in the bucket region for the 6° slanted slag configuration. Since the 12° slanted slag configuration is the most stressing configuration, it is discussed. Figure 68 shows a Mach number color raster plot of the flow field domain at the symmetry plane. The flow field axial velocity near the wall and behind the nozzle in the submerged region is observed to be small. There is a rapid acceleration of the axial velocity around the nozzle nose and the effects of the nozzle are observed near the centerline upstream of the nozzle. The region of nozzle influence extends to approximately the axial location of the propellant. Figure 69 shows the pressure field in the aft end of the motor. There is very little pressure change in the aft end of the motor from the problem inlet to the submerged nozzle region and the changes in pressure behind the nozzle are small. Figures 70 and 71 show the pressure field in the bucket at the symmetry plane on the recessed slag side and the filled slag side of the nozzle. Figure 72 and 73 show the corresponding velocity vector plots. The flow moves from the higher pressure region in Figure 71, which is toward the nozzle nose and this is confirmed by observing the velocity vector plot for this configuration, Figure 73. On the filled side of the slag pool, Figure 70, the flow again moves from the higher pressure region to the lower pressure region which is toward the nose except for a recirculation near the motor case insulation as shown in Figure 72. Small circumferential pressure gradients do exist in the submerged bucket region and the flow field behind the nozzle is very complex. The magnitude of the pressure gradient existing in the axial direction behind the nozzle from a point just behind the nozzle nose to the slag pool surface was 2 psid. The circumferential pressure gradient ranged from approximately 0.2 psid near the slag pool surface to just over 2 psid just behind the nozzle nose. Figure 74 shows the circumferential pressure field in the bucket and Figure 75 shows the corresponding velocity field. Flow is not symmetric and moves strongly from the bucket around the nozzle nose toward the nozzle exit.

## **Fully Couple Two-Phase Full-Length Motor Analysis of the RSRM 67 Second Burn Time Motor**

As a direct result of the October 19th and 20th meeting at Thiokol, a series of fully coupled two phase flow field analyses was initiated to determine the instantaneous particulate mass flow rate and total integrated slag accumulation in the RSRM motor. Since geometry definition was available for the 67 second motor burn time, this was the first analysis performed. An effective gas analysis was originally performed on this configuration using Fluent/BFC but the propellant depleted head end region and the submerged nozzle region were not analyzed. In the current analysis both the head end region and the submerged nozzle are included in the analysis. Also, the bent over inhibitor stubs are included in this model at the various motor joints. Figure 76 shows the overall geometric outline of this motor configuration. Several motor regions discussed are labeled in the figure including the head end region, the forward slot region, the center slot region, the aft slot region and the aft dome/nozzle region. Figure 77 shows a plot of the head end region of the motor while Figure 78 shows the computational grid used to model the head end region. The solid line in the Figure 77 is the exposed motor insulation. The exposed insulation in the head end region is cooler than the combustion gases and discrete particles are expected to condense on contact so that any discrete phase particles that impinge on the head end exposed insulation are captured and counted as slag accumulating in the head end of the motor. The forward face of the forward propellant grain and the port surface of the forward propellant grain are also shown in Figure 77. The forward propellant grain continues downstream to the forward slot as shown in Figure 79. The bent inhibitor is shown in the figure but the gap between the forward and forward center propellant grains is not modeled. The aft face of the forward propellant segment and the forward face of the forward center propellant segment are inhibited. Since the castable inhibitor is bent until it lays flush on the forward center propellant segment NBR inhibitor, there is no gap between the inhibitors and the slot gap is not modeled. Discrete phase particles which strike the upstream side of the inhibitor surface are accumulated as slag in the slot. The propellant segment downstream of the inhibitor is the forward center segment and this segment continues to the center slot shown in Figure 80. Figure 81 shows the computational grid in the region of the center slot. This grid resolution is typical of all the motor slots. The port surface of the forward center segment is shown in Figure 80. The aft face of the forward center segment is the upstream side of the center slot. The insulation exposed in the bottom of the slot is shown along with the inhibited forward face of the aft center propellant segment. The inhibited forward face of the aft center segment also has a bent piece of the inhibitor which protrudes into the port. The aft center propellant segment downstream of the inhibitor continues to the aft slot shown in Figure 82. The port side of the aft center segment and the aft face of the segment are shown and both have the normal propellant boundary conditions. The propellant grain downstream of the aft slot is the aft propellant segment and this segment ends near the nozzle nose as shown in Figure 83. Also, Figure 84 shows the computational grid used in the motor nozzle region. Referring to Figure 83, the end of the dashed line where the

arrow is pointing is the end of the aft segment. The bump downstream of the propellant segment is the aft dome stiffener insulation. Any discrete particles which impinge on the upper or lower walls in the submerged nozzle region between the arrows are accumulated as slag trapped in the submerged nozzle region. Also, any particle which becomes trapped in the vortex in the submerged nozzle region is accumulated as slag trapped in the submerged nozzle.

The total mass flow rate from all propellant surfaces is 9572.3 lbm/sec. Table 12 shows the mass flow rate information for the various propellant segments which was given to NASA/MSFC on November 19th. These conditions were obtained from a Thiokol motor ballistics run at the 67 second motor burn time.

**Table 12. Mass Flow Rate Boundary Conditions For The 67 Second Configuration**

<b>Propellant Segment</b>	<b>Mass Flow Rate (lbm/sec) Per Segment</b>	<b>Mass Flow Rate (lbm/sec) Cumulative</b>
Forward	1555.9	1555.9
Forward Center	2587.5	4143.4
Aft Center	2579.3	6722.7
Aft	2849.6	9572.3

The motor ballistics run which produced these mass flow rate boundary conditions had a head end pressure of 635.4 psia and a nozzle end static pressure of 625.2 psia. The nozzle end stagnation pressure was 628.9 psia. The throat area of the ballistic configuration was 2391.68 in<sup>2</sup>. The throat area for the CFD run configured from the above geometry description has a smaller throat area since no nozzle erosion was considered in the definition of the geometry. The throat area for the CFD geometry is 2278.36 in<sup>2</sup>. Table 13 shows the summary of thermochemical boundary conditions given to NASA/MSFC for this 67 second CFD solution. These general boundary conditions and thermochemical properties were used by ERC, Incorporated in the CFD two phase analysis performed for the 67 second propellant burn back. These boundary conditions and thermochemistry were used along with a computational grid which contained 465 axial grid cells and 60 radial grid cells to solve for the RSRM motor flow field.

**Table 13. Thermochemical Properties For The 67 Second Motor Configuration**

Ratio of Specific Heats, $\gamma$	1.138
Molecular Weight, $M_{wt}$	28.04
Flame Temperature, $T_f$	6064 °R
Specific Heat (frozen), $C_p$	0.4735 Btu/lbm-°R
Viscosity, $\mu$	6.189x10-5 lbm/sec-ft
Prandtl Number, Pr	0.4777
Thermal Conductivity, k	6.222x10-5 Btu/sec-ft-°F

The continuous phase chemistry used in the solutions presented was treated using a chemical equilibrium model since the kinetic time scales associated with the reactions in the continuous phase are small compared to the fluid dynamic time scales in the chamber. Two different types of combustion processes were considered in this analysis. The first kind of combustion process modeled is referred to as a surface combustion model. In this model it is assumed that all of the aluminum in the motor is burned at the propellant surface and the particles released from the surface are aluminum oxide. There is no combustion in the chamber and the particle size remains constant in the motor. The second type of combustion involves what is referred to as a distributed combustion model. In this type of model there is no combustion at the surface of the propellant and all aluminum combustion occurs from the motor surface to the nozzle exit. A Hermesen combustion rate model is used to control the rate of burning and the particle size changes as a complex function of the particle burning, temperature, density, and elemental composition. Aluminum oxide agglomerates on the particles as they pass through the motor.

The initial particle distribution for all cases was obtained from particle collection bomb data obtained from Thiokol. Studies performed by Salita, et. al., show that the distribution of particles in the discrete phase can be successfully represented by a bimodal log-normal size distribution. There is a size distribution peak centered at approximately the 1 $\mu$ m particle diameter and another size distribution peak centered above the 100  $\mu$ m particle diameter. This representative bimodal distribution is shown in Figure 85. In these analyses the small particles which closely follow the path of the flow field stream lines are considered to be part of the continuous phase, so that the larger size particles are the discrete phase represented by a log-normal size distribution.

Data from Thiokol was used to obtain the fraction of Al which is in the larger size distribution. Figures 86 and 87 show the particle bomb data for the burning of RSRM-29A, RSRM-29B and WECCO propellants at 500 psia and 1000 psia, respectively. The figures show the percent of particles collected which were smaller than a given particle diameter. The first flat portion of the curve represents the end of the particles associated with the 1 $\mu$ m size particles. These particles are considered as part of the continuous phase. Comparing the various curves in the figures and considering the

chamber pressure for the 67 second motor run, an approximate value of about 70% of the particles are in the smaller size distribution. This means that 30% of the Al is available to form  $\text{Al}_2\text{O}_3$  for the discrete phase. Considering this amount of Al and the weight fraction difference of  $\text{Al}_2\text{O}_3$  compared to Al (which was obtained from the equilibrium chemistry model for consistency), the mass flow rate of  $\text{Al}_2\text{O}_3$  was 826.1 lbm/sec (if all the aluminum burns). The injected mean and standard deviation of the particle diameter for these particles was obtained from the paper by Salita. A particle diameter of 150  $\mu\text{m}$  was used as the nominal mean particle diameter with a standard deviation of 0.2. Parametrics were performed for the particle size and these results are shown. Also, the injected particles were given a velocity which was specified as 80% of the continuous phase injection velocity.

Figure 88 shows a color raster plot of the mach number in the motor to give an overview of the flow field relative velocity magnitudes. Figure 89 shows the pressure field for the same view of the motor. A typical view of the flow field in the submerged region of the 67 second burn time RSRM motor is shown in Figure 90. The dividing streamline on the underside of the nozzle is clearly evident and separates the flow into the nozzle bucket.

Results for two surface combustion cases are shown in Table 14 and 15. The two cases reported have different particle mass mean diameters. The case shown in Table 14 has a particle mass mean diameter of 150  $\mu\text{m}$  with a standard deviation of 0.2 while the case shown in Table 15 has a particle mass mean diameter of 200  $\mu\text{m}$  with a standard deviation of 0.2. Since in the surface combustion model there is no further burning of the released particles, the particle size distribution remains the same throughout the motor. This will not be true for the distributed combustion model which considers aluminum combustion down the port of the motor.

Several parameters are presented for the surface combustion cases shown in Tables 14 and 15. The particulate mass flow rates at 67 seconds burn time for particles accumulating at several locations in the motor are also presented. These regions include the submerged nozzle region, the head end region, the forward slot region, the center slot region, the aft slot region and the nozzle outlet. The arithmetic mean diameter and the mass mean diameter of the particles collected in these regions are part of the information presented. Statistics for the properties of all slag accumulated in the motor and passing out the nozzle exit are also given for the 200  $\mu\text{m}$  particle diameter case but were not computed for the 150  $\mu\text{m}$  particle diameter case. The 150  $\mu\text{m}$  particle diameter case results show that 71.8 lbms/sec are being collected in the submerged nozzle region at the 67 second burn time. Insignificant amounts of slag are accumulating in all the other regions of the motor except the center slot. The center slot is accumulating slag at a rate of 12.9 lbms/sec at this point in the motor burn.



**Table 14. Surface Combustion Case 1 Solution Results**

<b>Motor Location</b>	<b>Particulate Mass flow rate (lbm/sec)</b>	<b>Particulate Arithmetic Mean Diameter (microns)</b>	<b>Particulate Mass Mean Diameter (microns)</b>
Nozzle Exit	742.4	79.6	144.3
Submerged Nozzle Region	71.8	107.9	185.7
Head End Region	0.0008	307.9	307.9
Forward Slot	0.07	73.6	117.5
Center Slot	12.9	90.4	155.7
Aft Slot	0.2	240.1	308.4
Total Motor	827.5	Not Available	Not Available

\* Particulate Initial Mass Mean Diameter is 150  $\mu\text{m}$ .

**Table 15. Surface Combustion Case 2 Solution Results**

<b>Motor Location</b>	<b>Particulate Mass flow rate (lbm/sec)</b>	<b>Particulate Arithmetic Mean Diameter (microns)</b>	<b>Particulate Mass Mean Diameter (microns)</b>
Nozzle Exit	716.3	105.9	192.9
Submerged Nozzle Region	96.4	140.5	233.7
Head End Region	2.0	107.9	223.2
Forward Slot	0.06	88.2	137.6
Center Slot	13.4	116.2	200.6
Aft Slot	0.8	246.9	358.6
Total Motor	828.9	108.0	198.0

\* Particulate Initial Mass Mean Diameter is 200  $\mu\text{m}$ .

The center slot accumulates more slag than the aft slot because of the length of the center slot inhibitor stub. The center slot inhibitor stub is much longer and protrudes further into the port flow than the aft slot inhibitor stub. Only the larger particles are trapped in the aft slot as evidenced from observing the much larger arithmetic mean of the particles.

The results for the 200  $\mu\text{m}$  particle diameter case show that if the particle diameter is increased by 50  $\mu\text{m}$ , there is a significant increase in the mass flow rate accumulating in the submerged nozzle region. The rate at which slag accumulates increases by 24.6 lbms/sec. The head end region also shows a significant increase in the mass flow rate of the accumulating slag. There was essentially no mass accumulating in the head end of the motor for the 150  $\mu\text{m}$  particle diameter case. The mass flow rate accumulating for the 200  $\mu\text{m}$  particle diameter case is 2 lbms/sec. It should also be said here that the calculated mass accumulation in the motor is only due to the large particle collisions with the motor case insulation. The accumulation of smoke particles of the size range of 1  $\mu\text{m}$  diameter are not included in the calculations. Condensation of smoke particles on the motor insulation due to collisions is probably insignificant in most of the motor. This is because the small particles follow the flow field streamlines very closely. However, the condensation of smoke particles in the head end region may be significant since the flow field velocities are very low, the insulation is cooler than the particles and the flow field is very complex with many recirculation regions.

Many cases using the distributed combustion model were also run. The first distributed combustion case, referred to as Case 3, uses an injected particle mass mean diameter of 150  $\mu\text{m}$  with a standard deviation of 0.2. The second case, referred to as Case 4, uses an injected particle mass mean diameter of 180  $\mu\text{m}$  with the same standard deviation. The results for Case 3 are shown in Table 16. The results for Case 4 are shown in Table 17. The results show that for Case 3 the computed mass mean diameter for all the particles released in the motor after burning was approximately 120  $\mu\text{m}$ . This relates to a particle shrinkage of approximately 30  $\mu\text{m}$  from the injected size distribution. Preliminary results for Case 4, which may not be fully converged at this point, show that the shrinkage for the particles in this case was approximately 39  $\mu\text{m}$  or a mass mean diameter of approximately 141  $\mu\text{m}$ . This final mass mean diameter of the collected particles is near the injected mass mean diameter used in the surface combustion case. The results for Case 3 show a significantly lower mass accumulation rate in the submerged nozzle region due to the reduced size of the particles in the motor.

Where possible, the results presented show a ( $\pm$ ) value associated with the particular motor parameter in the table. This shows the average value of the parameter over the last specified number of iterations. The case runs are made in increments of 500 iterations and averaged over some number of runs. For example, three runs of 500 iterations each were used to obtain the average results shown in Table 16. The mass flow rate and mean diameters for each of the runs was averaged and the  $\pm$  value of 3.0 for the nozzle exit mass flow rate means that the maximum variation for the 3 runs was no greater than this value from the average.

**Table 16. Distributed Combustion, Case 3 Solution Results**

<b>Motor Location</b>	<b>Particulate Mass flow rate (lbm/sec)</b>	<b>Particulate Arithmetic Mean Diameter (microns)</b>	<b>Particulate Mass Mean Diameter (microns)</b>
Nozzle Exit	796.2±3.0	64.7±0.2	117.1±0.3
Submerged Nozzle Region	59.0±0.4	85.6±0.4	155.1±0.4
Head End Region	1.9±0.5	67.0±3.2	117.1±7.4
Forward Slot	0.12±0.001	60.3±1.5	117.6±3.3
Center Slot	14.1±0.4	73.6±1.4	128.9±2.4
Aft Slot	0.04±0.01	206.1±60.4	258.8±39.9
Total Motor	871.3±2.2	64.4±2.1	119.8±0.3

\* Particulate Initial Mass Mean Diameter is 150  $\mu\text{m}$ .

\*\* Averaged over 1500 steps

**Table 17. Distributed Combustion, Case 4 Solution Results**

<b>Motor Location</b>	<b>Particulate Mass flow rate (lbm/sec)</b>	<b>Particulate Arithmetic Mean Diameter (microns)</b>	<b>Particulate Mass Mean Diameter (microns)</b>
Nozzle Exit	778.0	75.8	137.1
Submerged Nozzle Region	77.1	103.9	179.3
Head End Region	3.8	71.5	125.9
Forward Slot	0.13	72.0	139.4
Center Slot	14.5	87.3	153.6
Aft Slot	0.06	269.6	321.5
Total Motor	873.5	77.0	141.0

\* Particulate Initial Mass Mean Diameter is 180  $\mu\text{m}$ .

Solution results for the 150  $\mu\text{m}$  particle diameter case with the smoke agglomeration model active are given in Table 18. Most of the smoke has been swept up by the large particles near the nozzle exit due to the large velocities in the nozzle. This is not important for this problem but what is important is that a significant amount of the smoke size particles have been swept up in the motor chamber. The results for case 5 show that the mass flow rate of slag into the submerged nozzle cavity has more than

doubled. As would be expected, the particle diameters have increased due to the agglomeration of the large particles with the smoke which subsequently causes more particles to be trapped in the submerged nozzle cavity. Also, the amount of slag accumulating in the center slot has almost doubled. The smoke size particle diameter for this case is 1.5  $\mu\text{m}$ .

**Table 18. Distributed Combustion, Case 5 Solution Results**

<b>Motor Location</b>	<b>Particulate Mass flow rate (lbm/sec)</b>	<b>Particulate Arithmetic Mean Diameter (microns)</b>	<b>Particulate Mass Mean Diameter (microns)</b>
Nozzle Exit	2487.8 $\pm$ 4.3	99.6 $\pm$ 0.3	154.7 $\pm$ 0.1
Submerged Nozzle Region	107.1 $\pm$ 1.3	96.2 $\pm$ 0.5	176.2 $\pm$ 0.5
Head End Region	0.3 $\pm$ 0.15	71.8 $\pm$ 4.1	143.4 $\pm$ 0.6
Forward Slot	0.12 $\pm$ 0.001	60.9 $\pm$ 0.8	116.8 $\pm$ 3.2
Center Slot	25.8 $\pm$ 0.5	89.8 $\pm$ 0.6	129.1 $\pm$ 0.3
Aft Slot	0.045 $\pm$ 0.005	266.3 $\pm$ 20.8	300.0 $\pm$ 19.3
Total Motor	2621.1 $\pm$ 3.4	99.3 $\pm$ 0.3	155.3 $\pm$ 0.01

\* Particulate Initial Mass Mean Diameter is 150  $\mu\text{m}$ .

\*\* Smoke agglomeration model active, smoke particle mass mean diameter, 1.5  $\mu\text{m}$ .

\*\*\* Averaged over 1500 steps

Solution results for the 150  $\mu\text{m}$  mass mean diameter case with the smoke agglomeration model and the particle break-up model active are shown in Table 19. This run uses the  $4/C_D$  breakup criterion in the code. If the Weber number exceeds this value the particle breaks up. The results are preliminary because they only show 500 particle injection steps but the results show that the break-up model does affect the results in the submerged nozzle cavity, although the results for the center slot are not affected. Some parametrics must be run on the critical break-up Weber number before a real understanding of these results can be gained. It is sufficient at this time to mention that the break-up model does affect the results for the nominal break-up parameters used in the code. Parametrics are important in this case because it is known that the critical Weber number for break-up and the fragmentation factor do affect the lower speed flow in the nozzle. This would certainly be true in the even lower velocity region upstream of the submerged nozzle. The parameters may be very critical in this region. As would be expected, the particle mass mean diameter for particles trapped in the submerged nozzle cavity is reduced from case 5. The mass flow rate of slag trapped in the submerged cavity is about 73% greater than for the case without smoke agglomeration, yet the particulate mass mean diameter is smaller for case 6 with the break-up model and smoke agglomeration model active. This means that many of

the particle break-ups must have occurred after the particles were already trapped in the vortex in the submerged nozzle region or that the breakups occurred after the particles were already destined to be trapped. Comparing the results of the various runs seems to imply that most of the break-up occurred in the rear end of the motor since the amount of slag collected in the center slot was not affected. The parametric changes to the fragmentation factor and the critical break-up Weber number will therefore probably have a significant affect on the results. A more reasonable combination of these factors may be found.

**Table 19. Distributed Combustion Case 6 Solution Results**

<b>Motor Location</b>	<b>Particulate Mass flow rate (lbm/sec)</b>	<b>Particulate Arithmetic Mean Diameter (microns)</b>	<b>Particulate Mass Mean Diameter (microns)</b>
Nozzle Exit	2499.6	10.0	17.1
Submerged Nozzle Region	88.7	31.3	144.3
Head End Region	0.8	75.6	141.1
Forward Slot	0.09	64.8	113.5
Center Slot	27.1	72.9	108.7
Aft Slot	0.04	266.5	295.2
Total Motor	2616.3	10.0	22.4

\* Particulate Initial Mass Mean Diameter is 150  $\mu\text{m}$ .

\*\* Smoke agglomeration model active, smoke particle mass mean diameter, 1.5  $\mu\text{m}$ .

\*\*\* Particle break-up model active, fragmentation factor = 2.

\*\*\*\* Averaged over 1500 steps

Results for case 7, which are shown in Table 20, are similar to case 5. The smoke agglomeration model is run without the particle break-up model. The only difference in the two solutions is that the smoke size particle mass mean diameter of 1.0  $\mu\text{m}$  is used. A similar case with a smoke size particle mass mean diameter of 2.0  $\mu\text{m}$  is shown in Table 21. The variation of the size of the smoke particles from 1.0  $\mu\text{m}$  to 2.0  $\mu\text{m}$  diameter significantly affects the amount of slag collected in the motor. The amount of slag collected in the submerged nozzle cavity varies from 80.6 lbm/sec to 136.2 lbm/sec. The amount of slag collected in the center slot varies from 20.8 lbm/sec to 29.8 lbm/sec.

**Table 20. Distributed Combustion Case 7 Solution Results**

<b>Motor Location</b>	<b>Particulate Mass flow rate (lbm/sec)</b>	<b>Particulate Arithmetic Mean Diameter (microns)</b>	<b>Particulate Mass Mean Diameter (microns)</b>
Nozzle Exit	2389.0	100.1	147.7
Submerged Nozzle Region	80.6	90.1	164.1
Head End Region	0.72	70.7	149.1
Forward Slot	0.11	63.6	116.9
Center Slot	20.8	83.9	125.9
Aft Slot	0.04	250.8	299.0
Total Motor	2491.4	99.5	148.1

\* Particulate Initial Mass Mean Diameter is 150  $\mu\text{m}$ .

\*\* Smoke agglomeration model active, smoke particle mass mean diameter, 1.0  $\mu\text{m}$ .

\*\*\* 900 particle injection steps

**Table 21. Distributed Combustion, Case 8 Solution Results**

<b>Motor Location</b>	<b>Particulate Mass flow rate (lbm/sec)</b>	<b>Particulate Arithmetic Mean Diameter (microns)</b>	<b>Particulate Mass Mean Diameter (microns)</b>
Nozzle Exit	2501.0 $\pm$ 1.2	98.4 $\pm$ 0.1	159.5 $\pm$ 0.2
Submerged Nozzle Region	136.2 $\pm$ 0.1	103.4 $\pm$ 1.1	185.8 $\pm$ 0.5
Head End Region	0.58 $\pm$ 0.24	79.2 $\pm$ 1.7	155.7 $\pm$ 29.7
Forward Slot	0.115 $\pm$ 0.005	65.8 $\pm$ 2.7	116.8 $\pm$ 1.5
Center Slot	29.8 $\pm$ 0.1	92.75 $\pm$ 0.15	132.1 $\pm$ 0.5
Aft Slot	0.055 $\pm$ 0.005	252.5 $\pm$ 3.2	292.4 $\pm$ 2.3
Total Motor	2667.5 $\pm$ 1.5	98.45 $\pm$ 0.5	160.5 $\pm$ 0.1

\* Particulate Initial Mass Mean Diameter is 150  $\mu\text{m}$ .

\*\* Smoke agglomeration model active, smoke particle mass mean diameter, 2.0  $\mu\text{m}$ .

\*\*\* Averaged over the last 1000 particle injection steps

The last results presented for the two-phase RSRM 67 second motor analysis are for the same conditions used in case 5 except that an axial and lateral launch acceleration of 2.5 g's is applied at an 8° angle to the nozzle centerline. The angle of application of the g-force is in the direction of the case wall away from the centerline. Particles would tend to be accelerated toward the case wall. The results shown in Table 22 show that

the affect of the acceleration force is only significant in the regions of the motor where very little slag is accumulating such as the aft slot, forward slot and the head end of the motor. These regions do show significant increases in the amount of slag collected but the amount of slag, even with the acceleration force considered, is still very small.

**Table 22. Distributed Combustion, Case 6 Solution Results**

<b>Motor Location</b>	<b>Particulate Mass flow rate (lbm/sec)</b>	<b>Particulate Arithmetic Mean Diameter (microns)</b>	<b>Particulate Mass Mean Diameter (microns)</b>
Nozzle Exit	2496.9±1.6	100.0±0.4	154.4±0.2
Submerged Nozzle Region	108.1±0.3	98.85±0.05	175.4±1.0
Head End Region	0.9±0.5	65.5±2.7	142.6±0.1
Forward Slot	0.415±0.05	75.5±1.7	171.3±2.6
Center Slot	26.35±0.15	89.5±0.5	128.65±0.15
Aft Slot	0.305±0.005	258.6±2.5	282.8±2.4
Total Motor	2633.0±2.8	99.65±0.35	155.0±0.2

\* Particulate Initial Mass Mean Diameter is 150  $\mu\text{m}$ .

\*\* Smoke agglomeration model active, smoke particle mass mean diameter, 1.5  $\mu\text{m}$ .

\*\*\* Averaged over 1500 steps

\*\*\*\* Axial and Lateral Launch acceleration applied

### **CFD Methodology**

This section of the CFD report will provide information on the various CFD codes used by ERCI to perform analyses for NASA/MSFC. ERCI currently uses two Fluent Inc. CFD codes and CELMINT to perform analyses as directed by NASA/MSFC. The two Fluent Inc. codes are Fluent/BFC and Fluent version 4.22. ERCI is also using the CELMINT code which was developed by Scientific Research Associates Inc. (SRA).

### **Fluent/BFC**

Fluent/BFC is the oldest code of the Fluent family of codes and was used for several of the analyses presented in this report. The code has been validated against many different kinds of fluid dynamic problems including solid rocket motor internal flow problems by both Fluent Inc. and ERCI. Fluent /BFC has provided a rapid and accurate capability to perform CFD analysis for several years.

Fluent/BFC solves the steady 2-D or a 3-D Navier-Stokes and energy equations for laminar or turbulent, incompressible or compressible flows (subsonic, transonic and

supersonic) in general curvilinear geometries. The partial differential transport equations are discretized using a staggered-grid finite volume method with a power law differencing scheme that is stable and computationally efficient. The discretized equations are solved using the SIMPLER algorithm for pressure/velocity coupling in which the discretized equations are solved with line-iterative methods accelerated by block correction strategies. The code uses the standard  $\kappa$ - $\epsilon$  turbulence model to as a closure rule for the equations.

There are several fluid dynamic problems the Fluent/BFC code cannot solve. The code cannot solve fully coupled two-phase flow problems. The code does have the capability to consider finite-rate chemistry. The full system of the propellant reaction equations must be used because there is no equilibrium chemistry model such as available in CELMINT. Also, the code uses wall functions to bridge the viscous sub-layer and has no capability of solving for the boundary layer.

### **Fluent version 4.22**

Fluent version 4.22 was developed as a replacement for the Fluent/BFC code. Fluent 4.22 solves the steady or unsteady, 2-D or a 3-D Navier-Stokes and energy equations for laminar or turbulent, incompressible or compressible flows (subsonic, transonic and supersonic) in general curvilinear geometries.

The partial differential transport equations are discretized using a co-located grid finite volume method with a power law or higher order differencing scheme that is stable and computationally efficient. The discretized equations are solved using the SIMPLEC algorithm for pressure/velocity coupling in which the discretized equations are solved with line-iterative methods accelerated by block correction strategies. Multigrid techniques are also available for used which can provide an accelerated rate of convergence in many cases. The code uses the standard  $\kappa$ - $\epsilon$  turbulence model or a higher order RNG turbulence model as a closure rule for the equations. The code is able to resolve the flow down into the boundary layer but wall functions are also provided as an option.

Fluent 4.22 has many operational features which make it more attractive to use than Fluent/BFC. Fluent 4.22 also has a greatly expanded set of fluid dynamic capabilities. Some of the fluid dynamic improvements available in Fluent 4.22 that have not already been mentioned are:

1. The boundary condition capabilities have been expanded to handle cyclic and periodic boundary conditions. A propellant grain boundary condition based on the pressure coupled burn rate equations is also being developed.
2. The code can solve fully coupled two phase flow problems.



3. Several turbulence models have been added to the turbulence model portfolio including a Reynolds Stress Model.
4. Extended capabilities in the area of heat transfer prediction have been added.
5. More flexibility has been added to the code when patching primitive variable profiles at boundaries.

The code does not have an equilibrium thermochemistry option nor does it have the more sophisticated combustion models available in CELMINT.

### **CELMINT**

The CELMINT computer code solves the steady or time-dependent compressible non-reacting and reacting Navier-Stokes equations and the steady state incompressible Navier-Stokes equations. The code is a density-based finite difference code which uses a simultaneous solution technique instead of the point-wise solution technique employed by Fluent. This provides for a inherently more stable code when considering the transonic compressible problems usually associated with solid rocket motors. A linearized block implicit solution algorithm with Douglas-Gunn splitting is used to numerically solve these equations. Matrix conditioning techniques are used to accelerate convergence to steady solutions. Both  $\kappa$ - $\epsilon$  and algebraic mixing length turbulence models are available, with either resolution of the viscous sub-layer regions or the use of wall functions as option. Finite rate chemistry can be considered and there is also an equilibrium chemistry option available which allows a complete propellant system to be modeled in a very time-efficient manner within the motor chamber. In addition to the boundary condition options available in Fluent 4.22 or Fluent/BFC, CELMINT provides mass injection boundary conditions which are a very convenient boundary condition option with solid rocket motors. The code also allows the fully-coupled solution of two-phase flows and utilizes the industry standard Hermesen combustion model for aluminum combustion. In addition, the code also considers both particle agglomeration and break-up which can be very important in the solid rocket motor.

The CELMINT code is not a new code and has been tested for a number of years. It has been used at ERCI for more than a year. It has proven to be a well tested very stable code for modeling complex fluid dynamic problems.

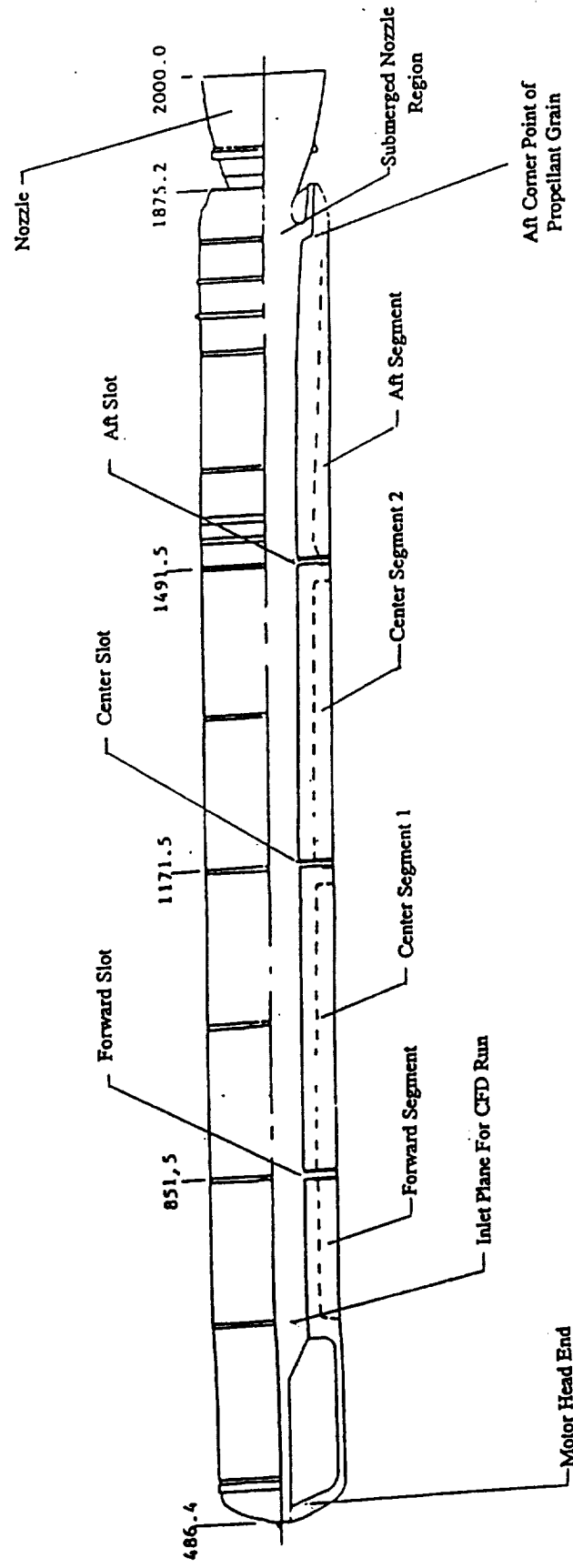
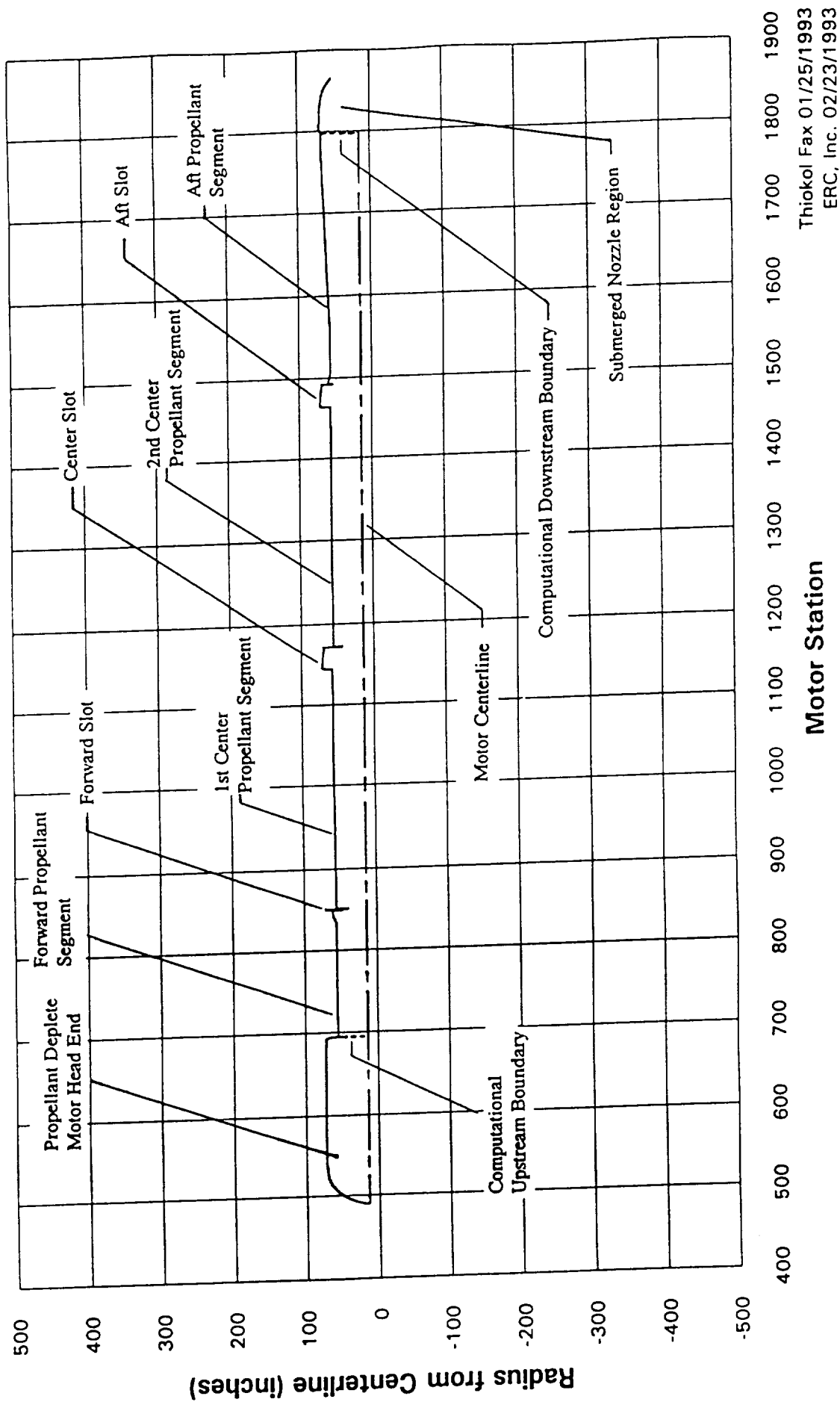
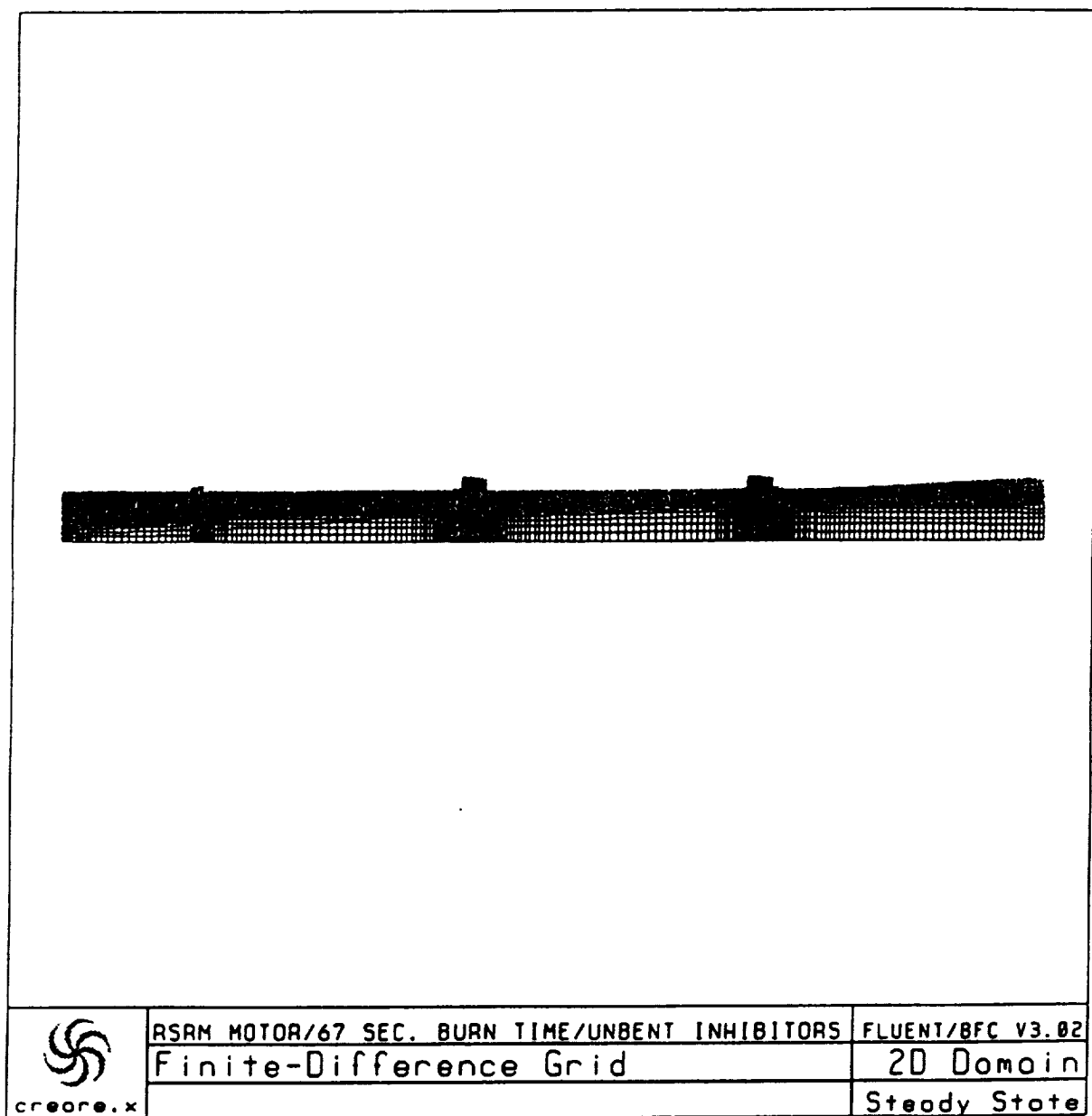


Figure 1. RSRM Motor Geometry



Thiokol Fax 01/25/1993  
ERC, Inc. 02/23/1993

Figure 2. Thokol 67 Second Burn Time RSRM Motor Geometry



**Figure 3. RSRM Excursion 1 Computational Grid, Full Motor**

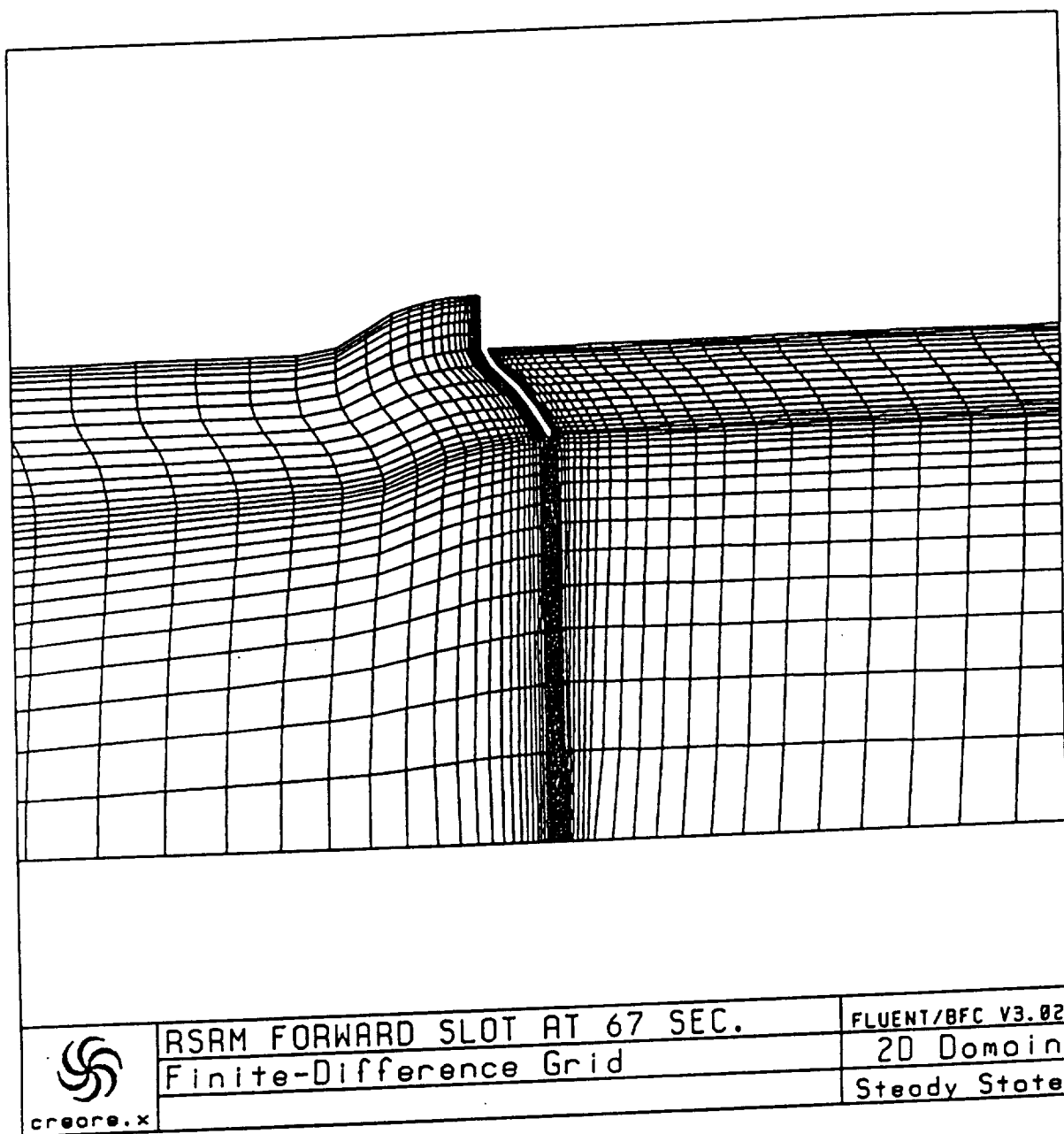


Figure 4. Computational Grid in the Forward Slot Region

SCHEMATIC OF FORWARD JOINT WITH DEFLECTED INHIBITORS

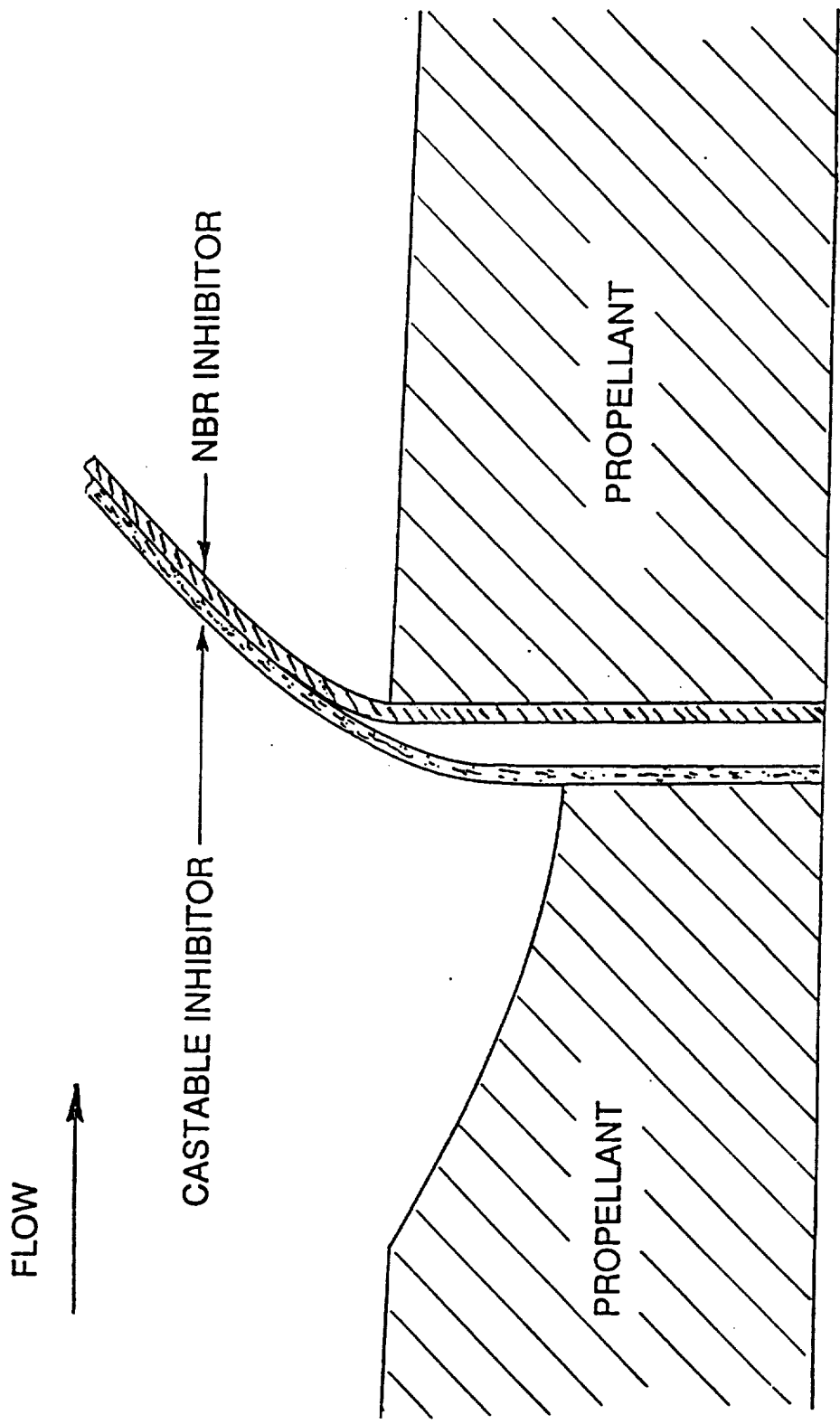


Figure 5. RSRM-29B Port Blockage Scenario

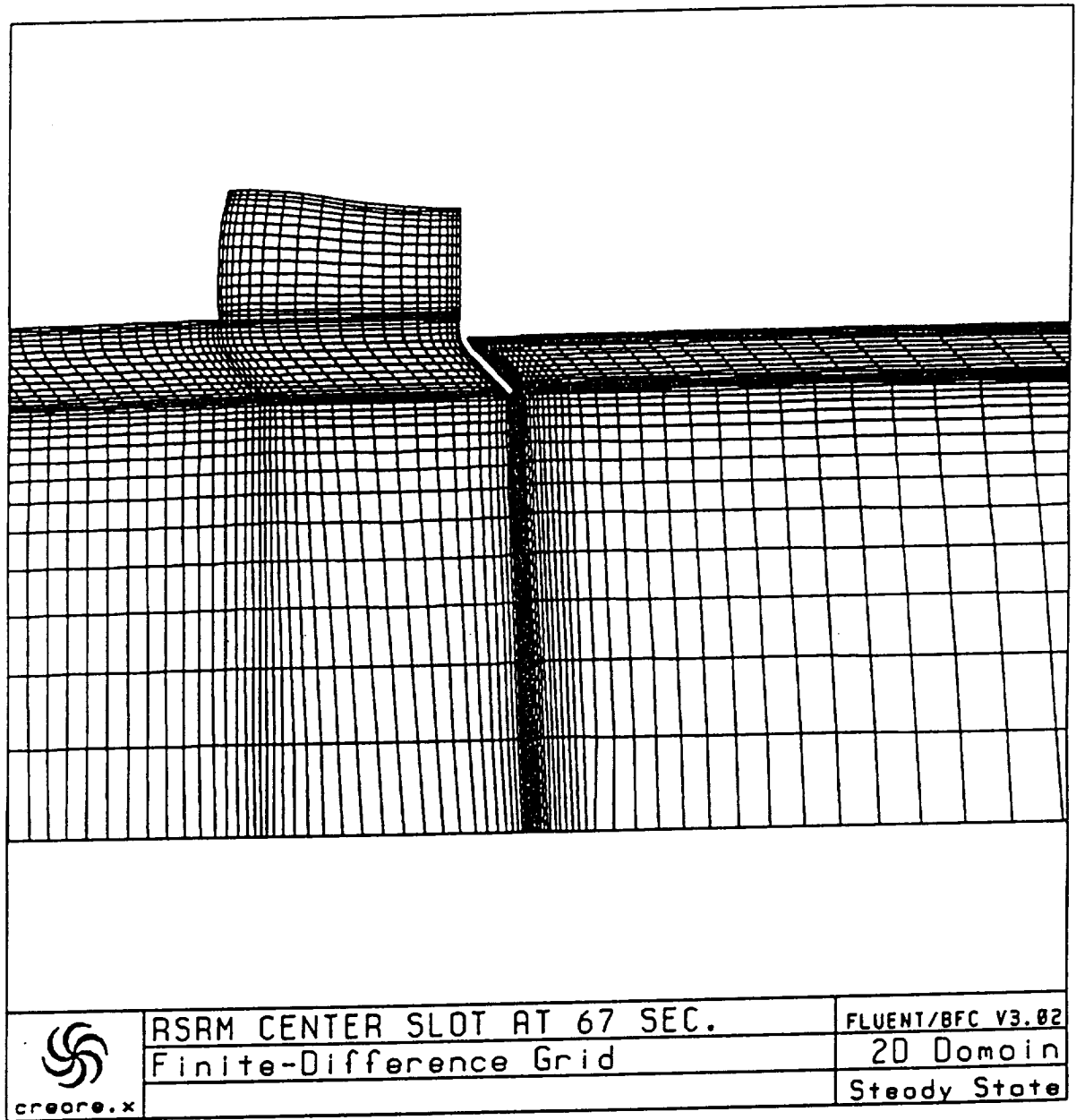
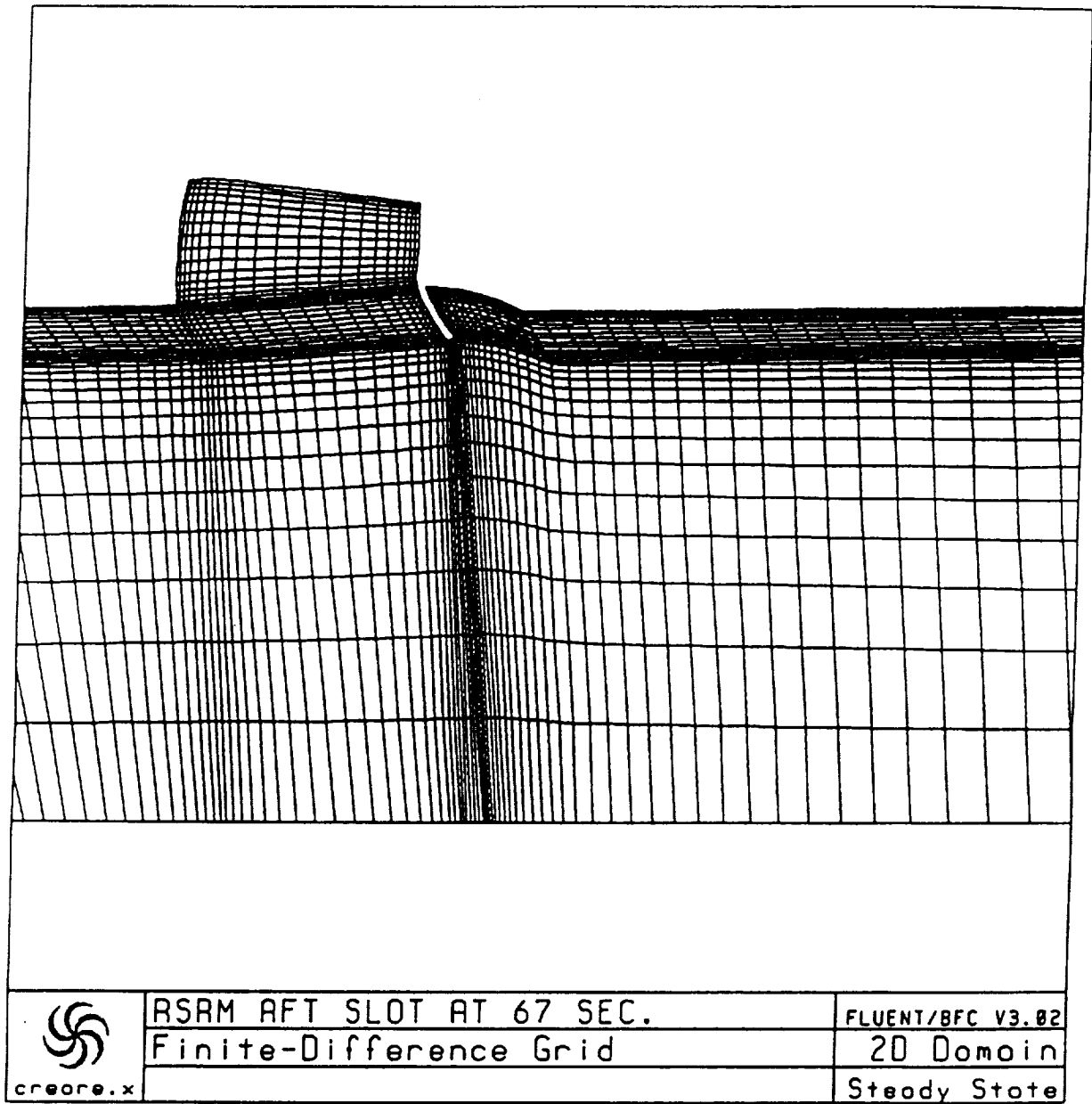


Figure 6. Computational Grid in the Center Slot Region



**Figure 7. Computational Grid in the Aft Slot Region**



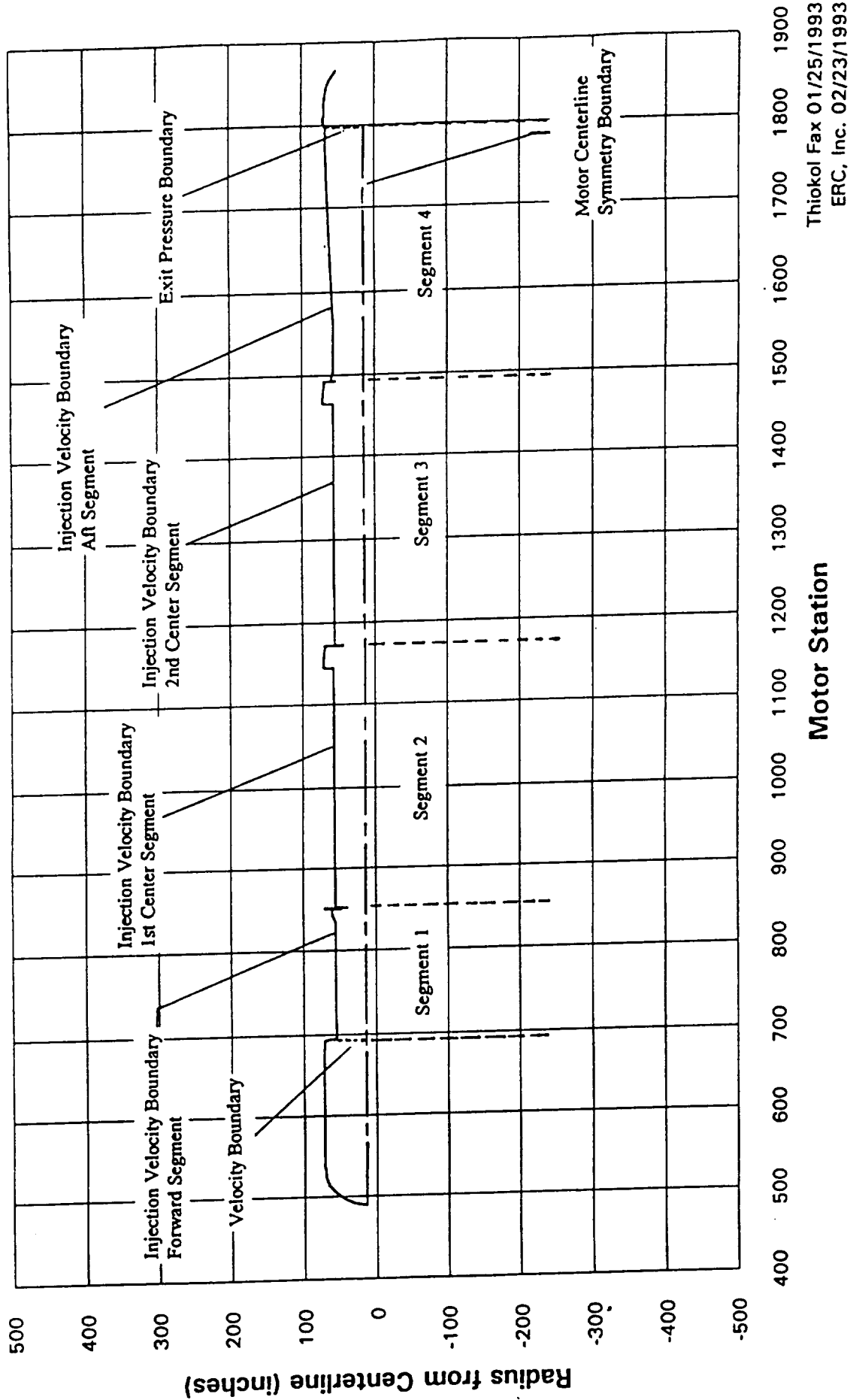


Figure 8. RSRM Excursion 1 Boundary Conditions

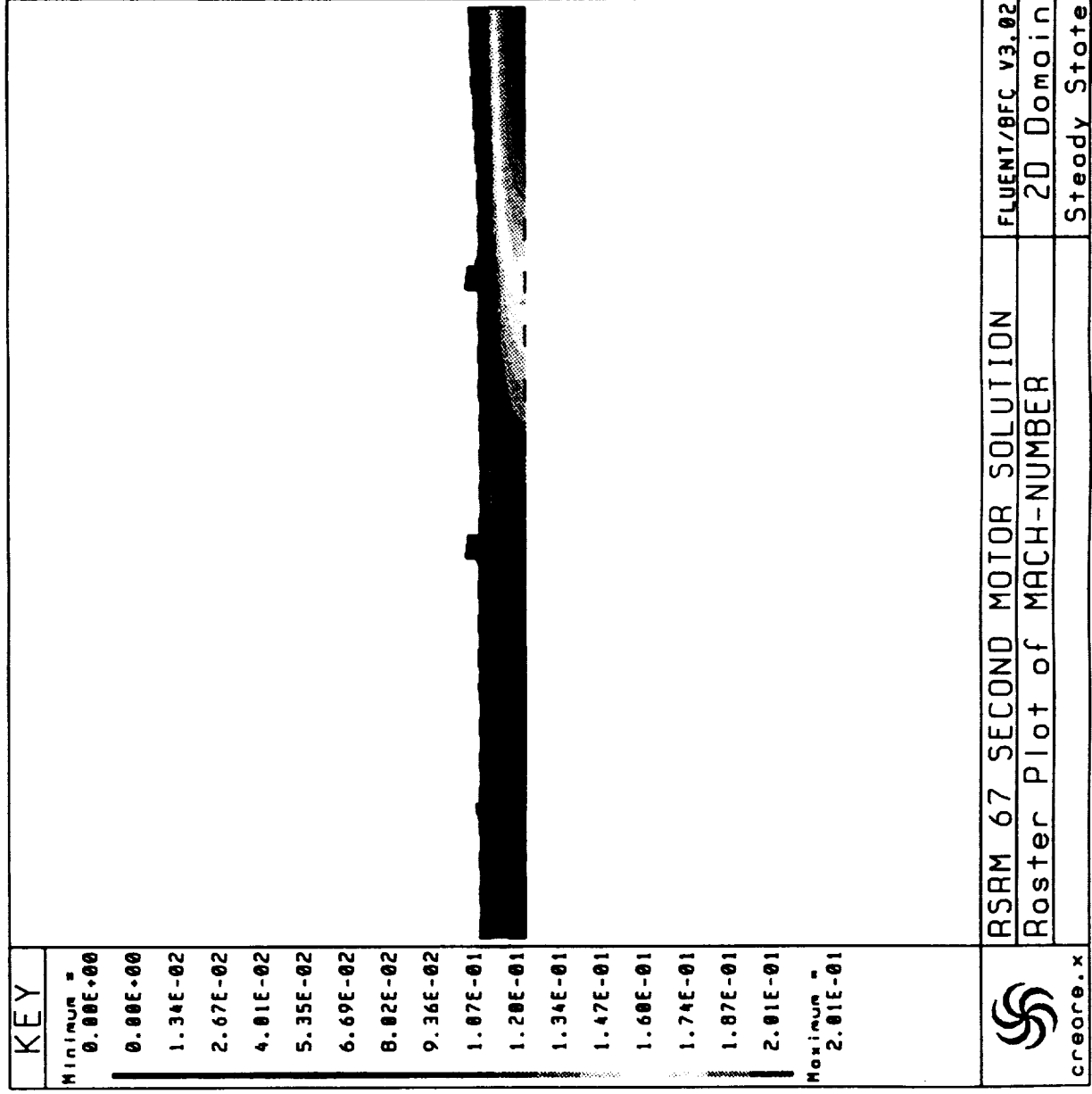


Figure 9. Mach Number Color Raster Plot Of The RSRM Motor At 67 Seconds.

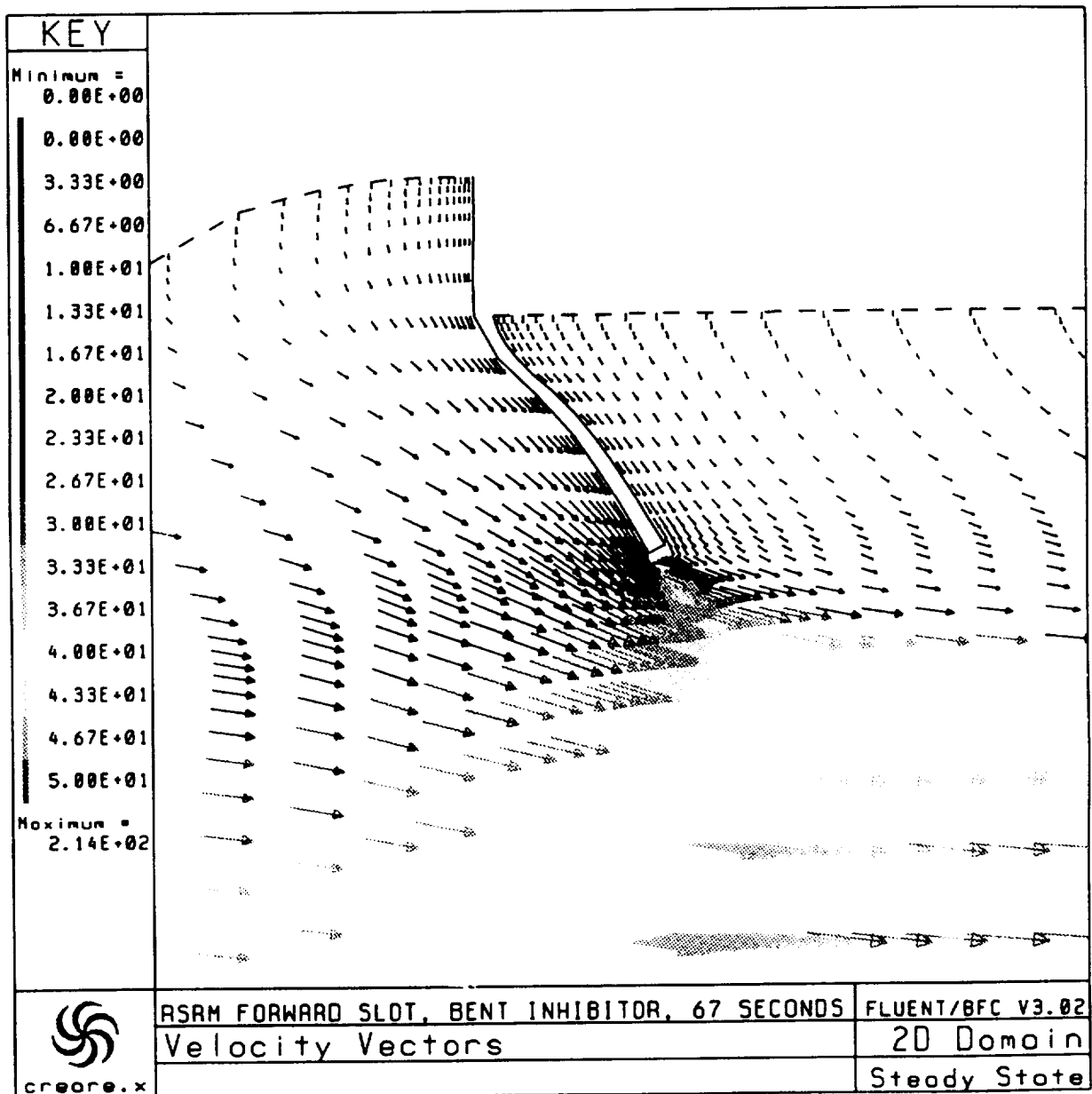


Figure 10. Flowfield Velocity Vectors In The Forward Slot Region.

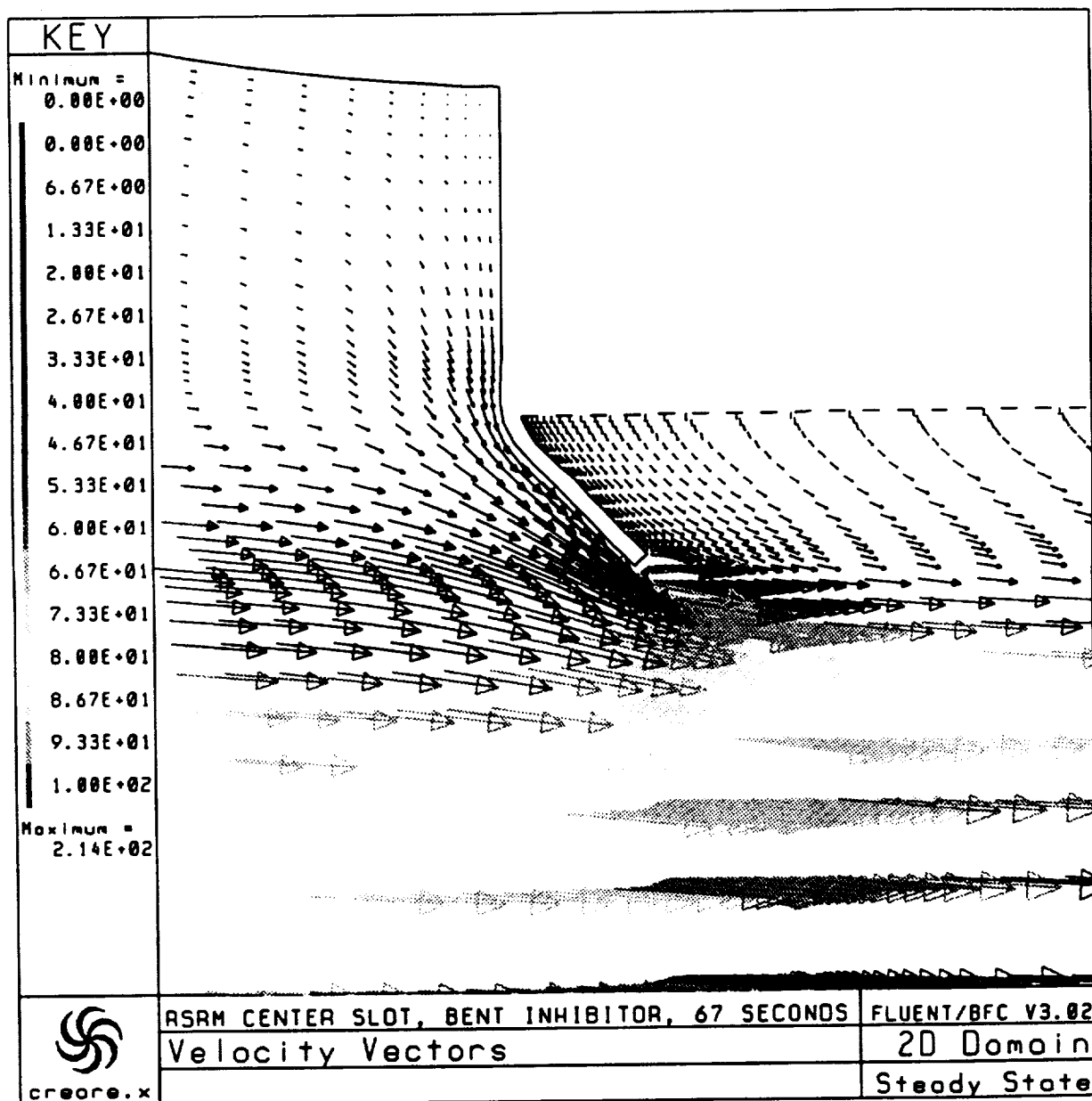


Figure 11. Flowfield Velocity Vectors In The Center Slot Region

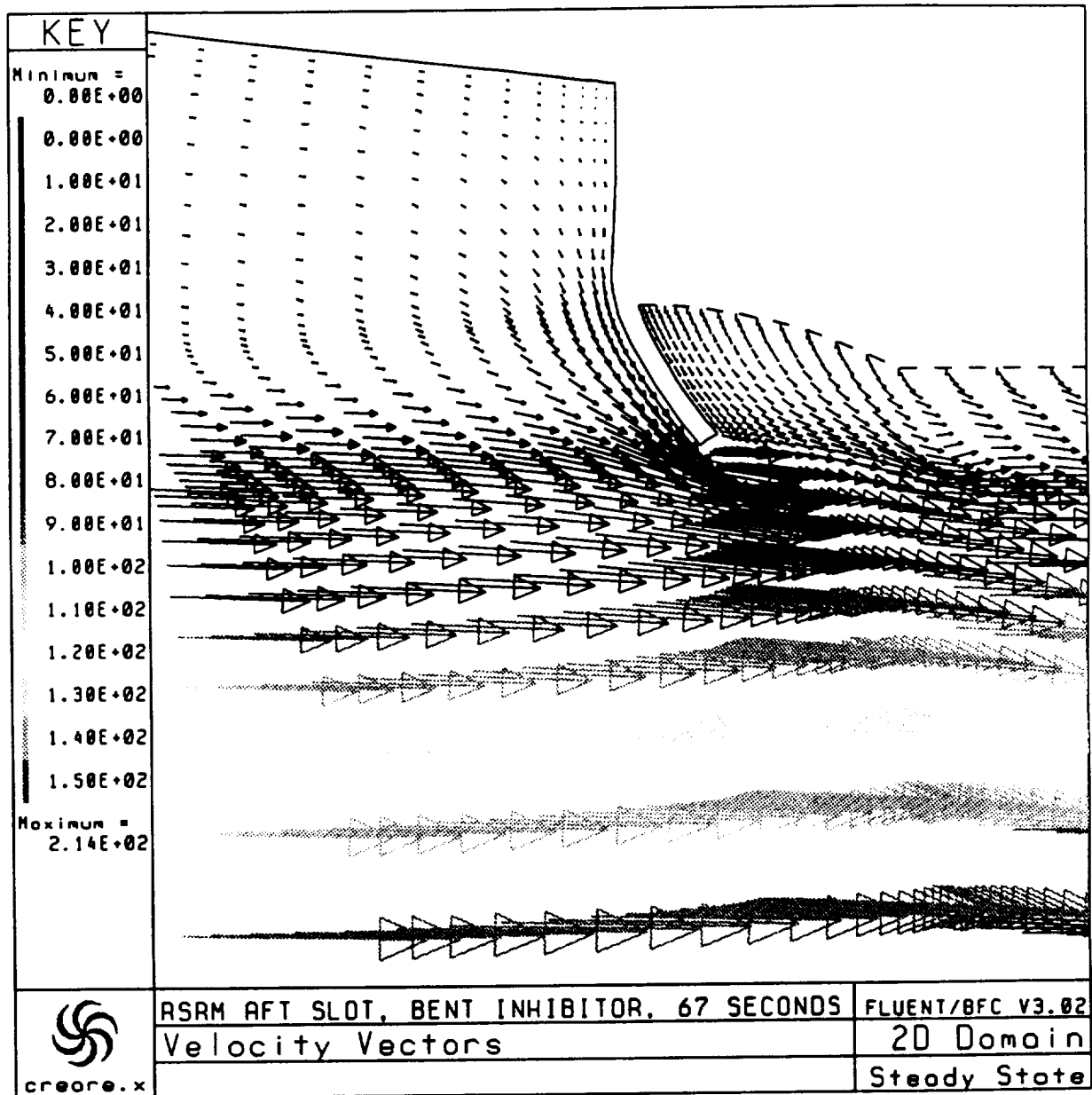


Figure 12. Flowfield Velocity Vectors In The Aft Slot Region.

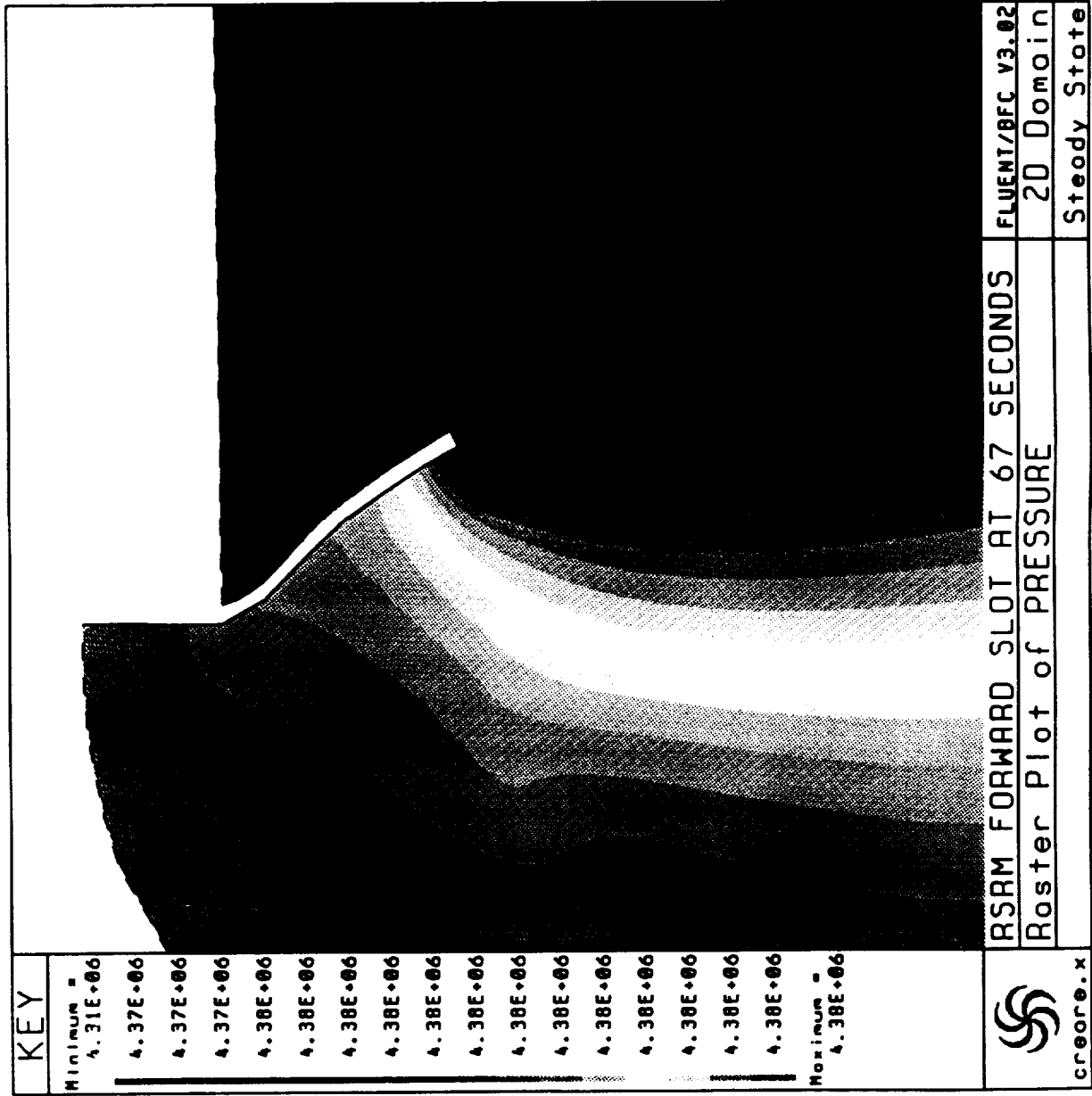


Figure 13. RSRM Forward Slot at 67 Seconds







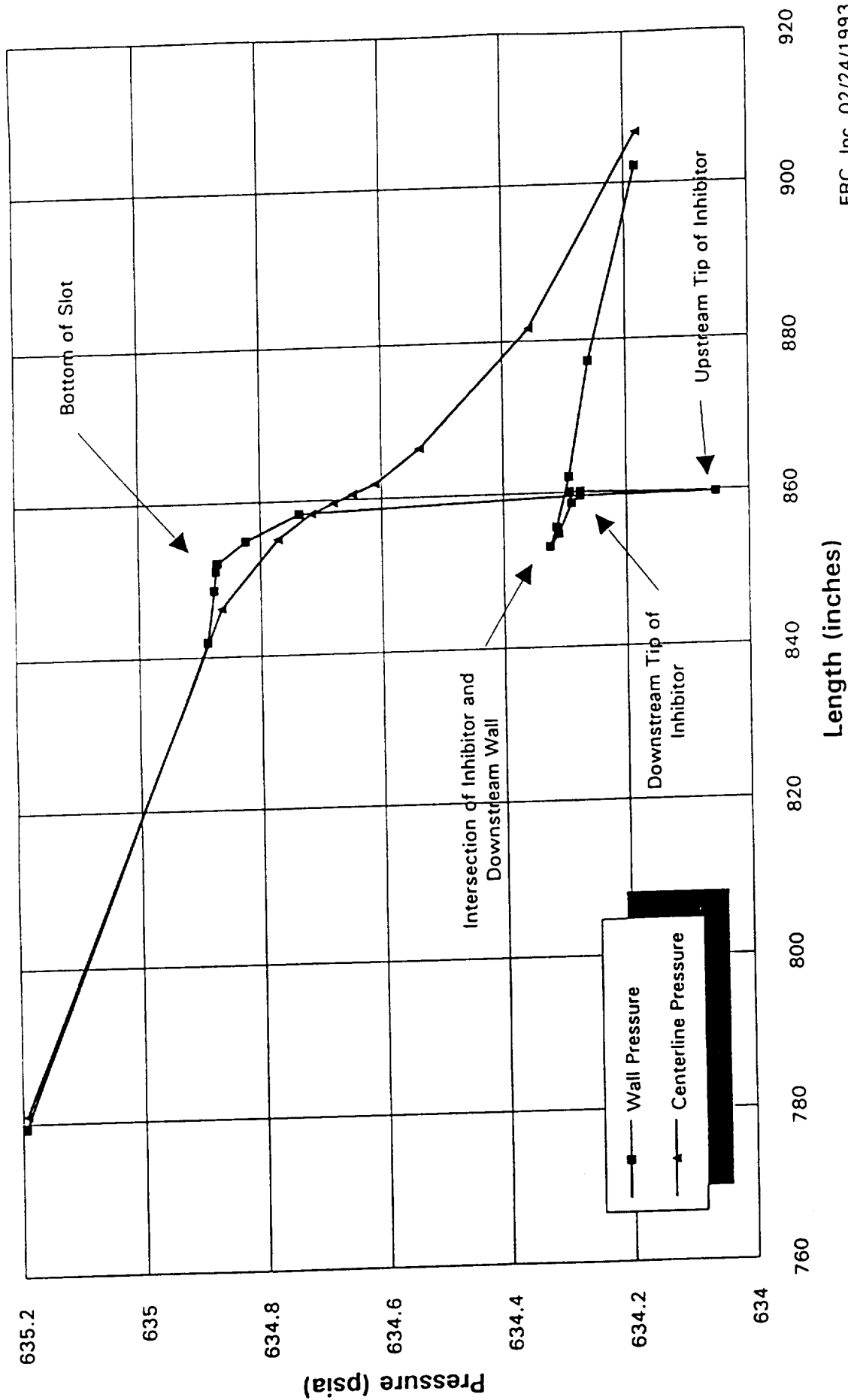
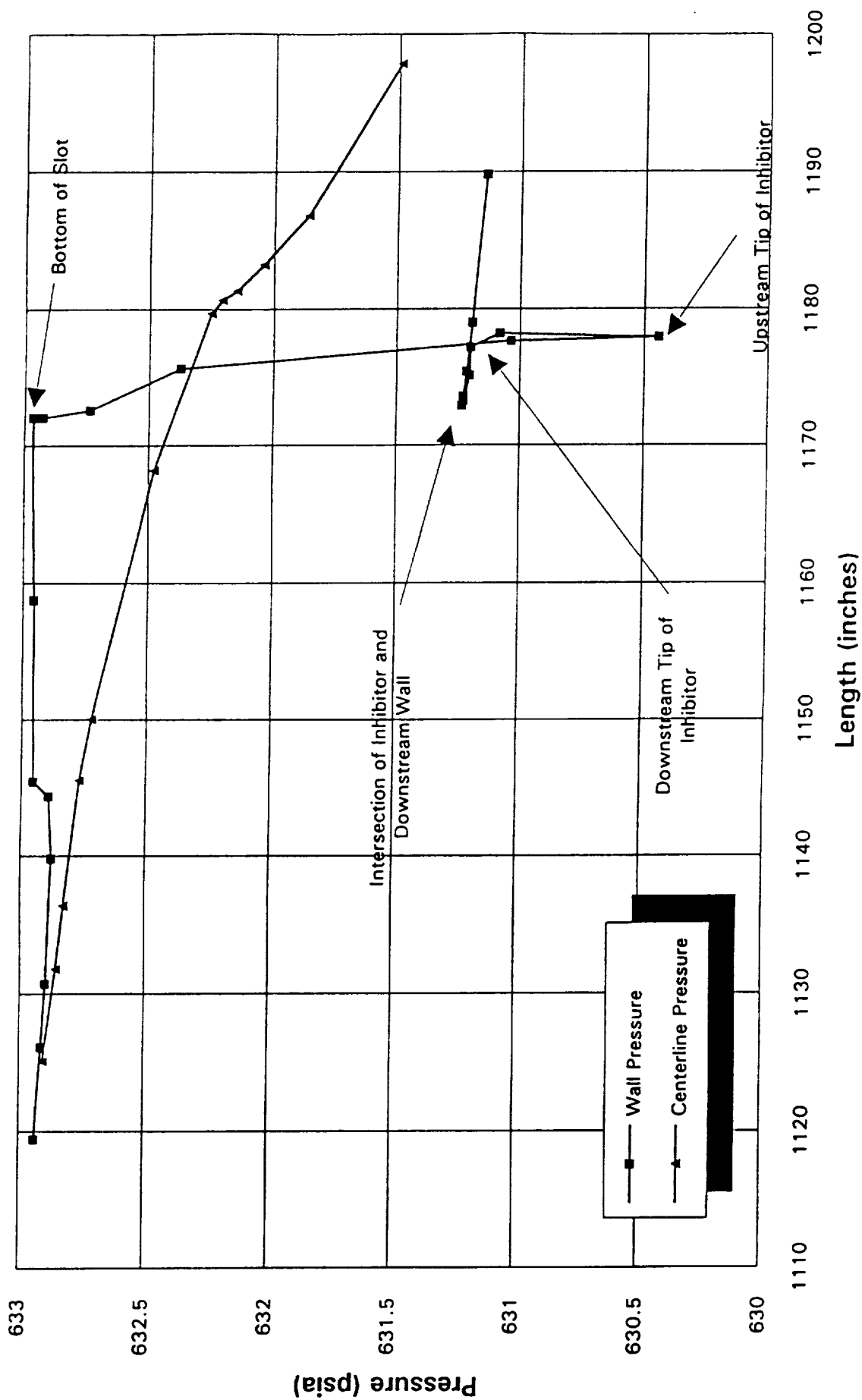


Figure 16. Forward Slot Pressure RSRM CFD Solution at 67 Seconds



ERC, Inc. 02/24/1993

Figure 17. Center Slot Pressure  
RSRM CRD Solution at 67 Seconds

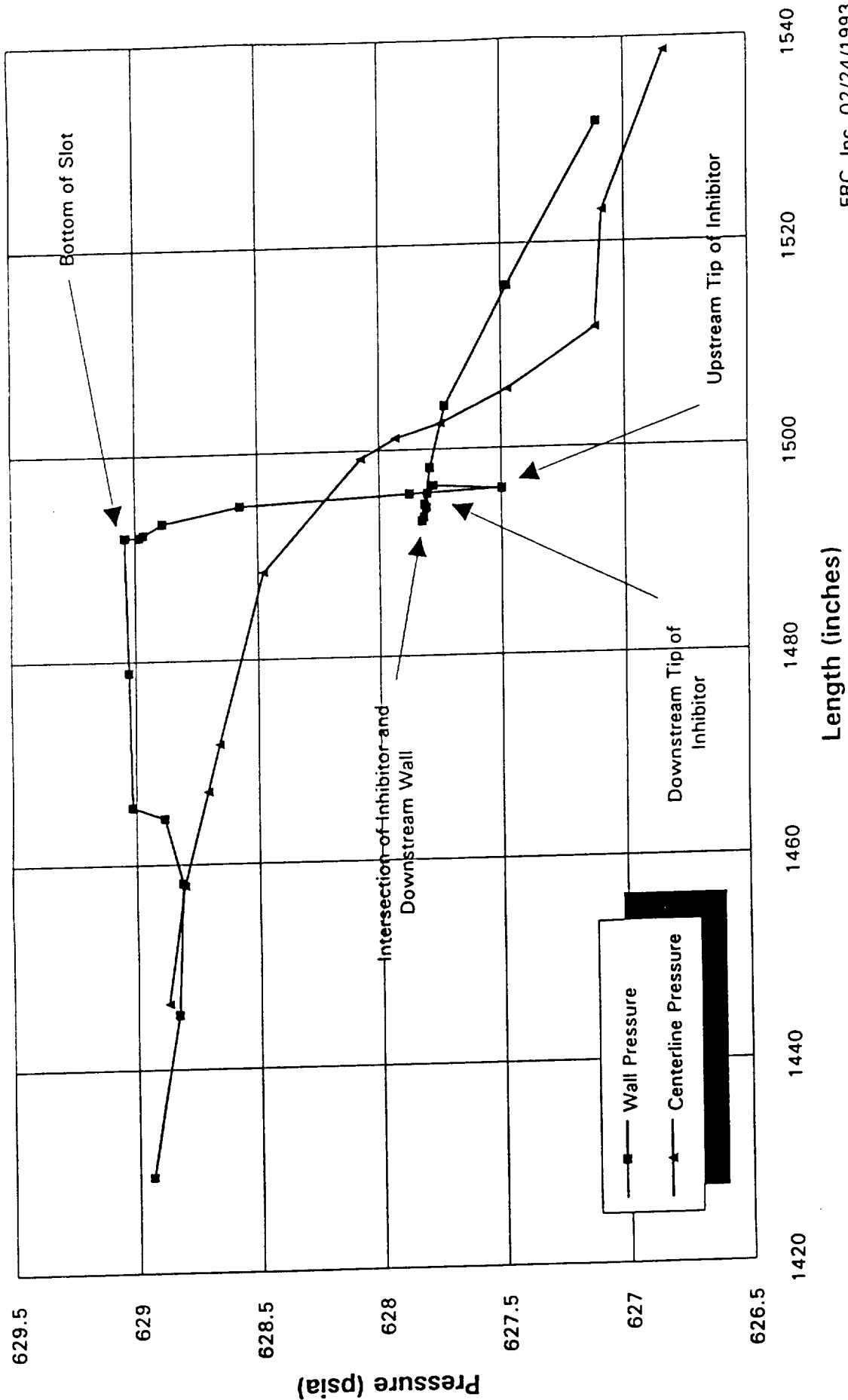


Figure 18. Aft Slot Pressure  
RSRM CFD Solution at 67 Seconds

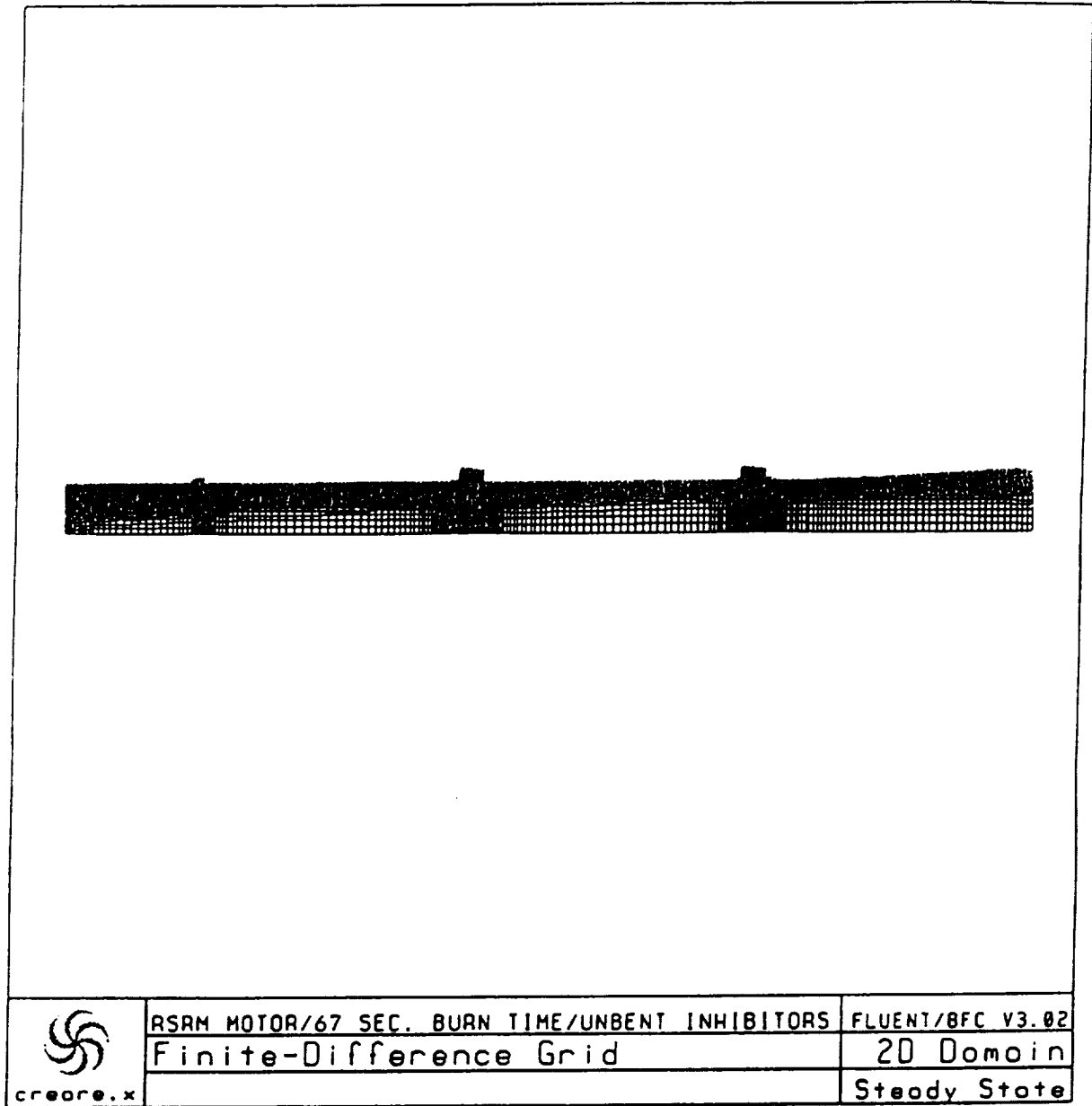


Figure 19. RSRM Excursion 1 Computational Grid, Full Motor

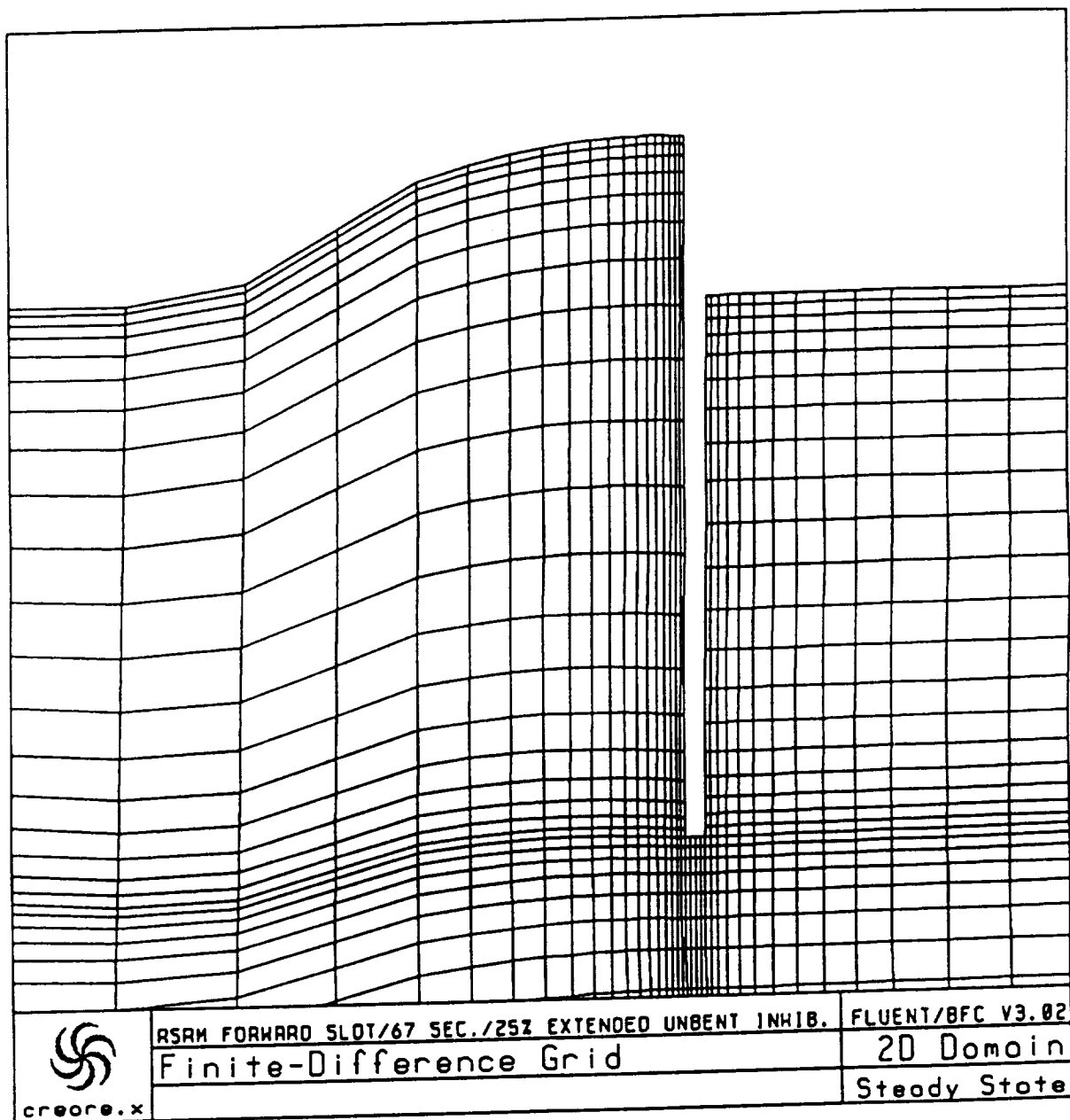


Figure 20. RSRM Excursion 2 Computational Grid, Forward Slot

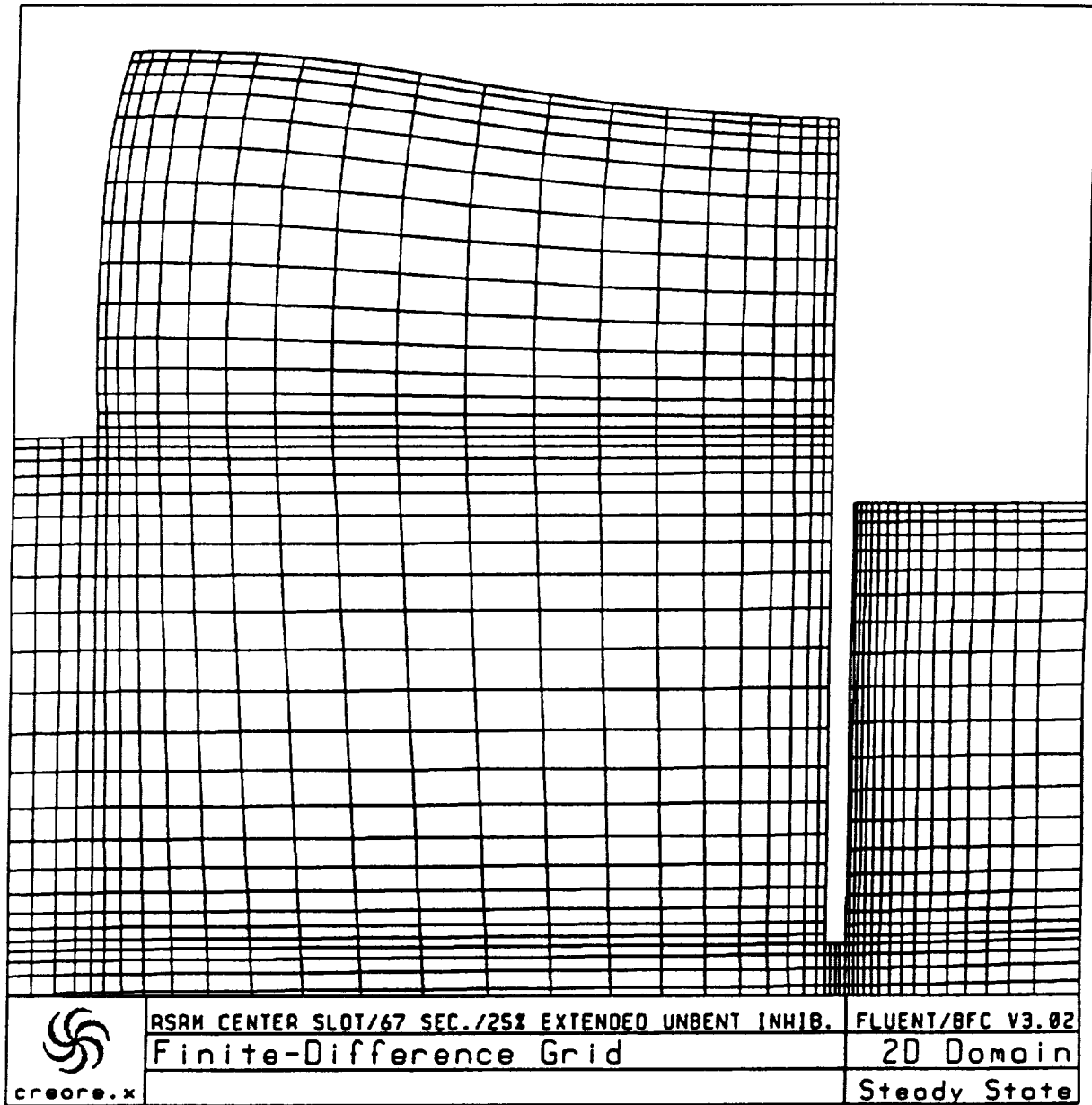


Figure 21. RSRM Excursion 2 Computational Grid, Center Slot

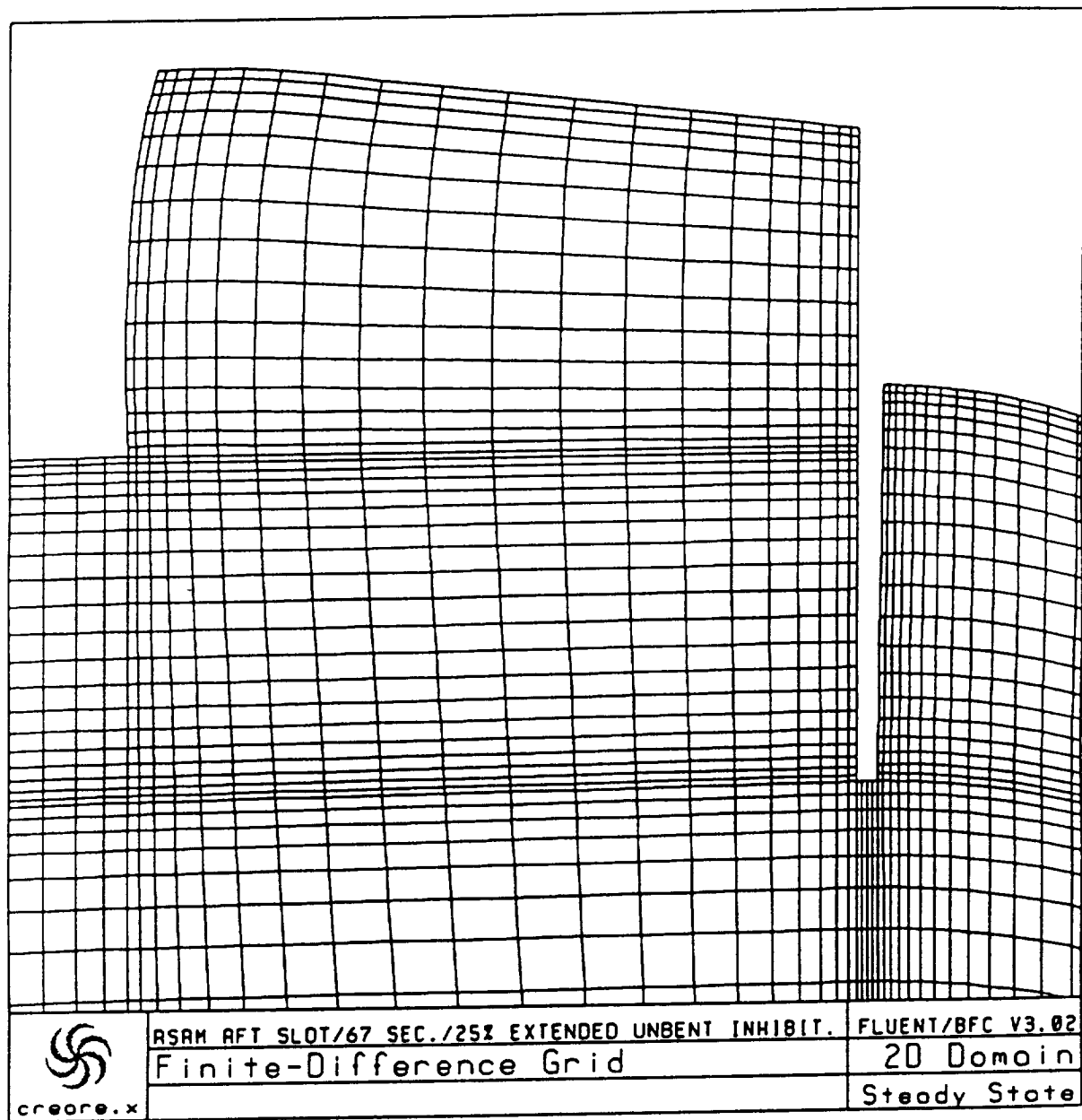


Figure 22. RSRM Excursion 2 Computational Grid, Aft Slot

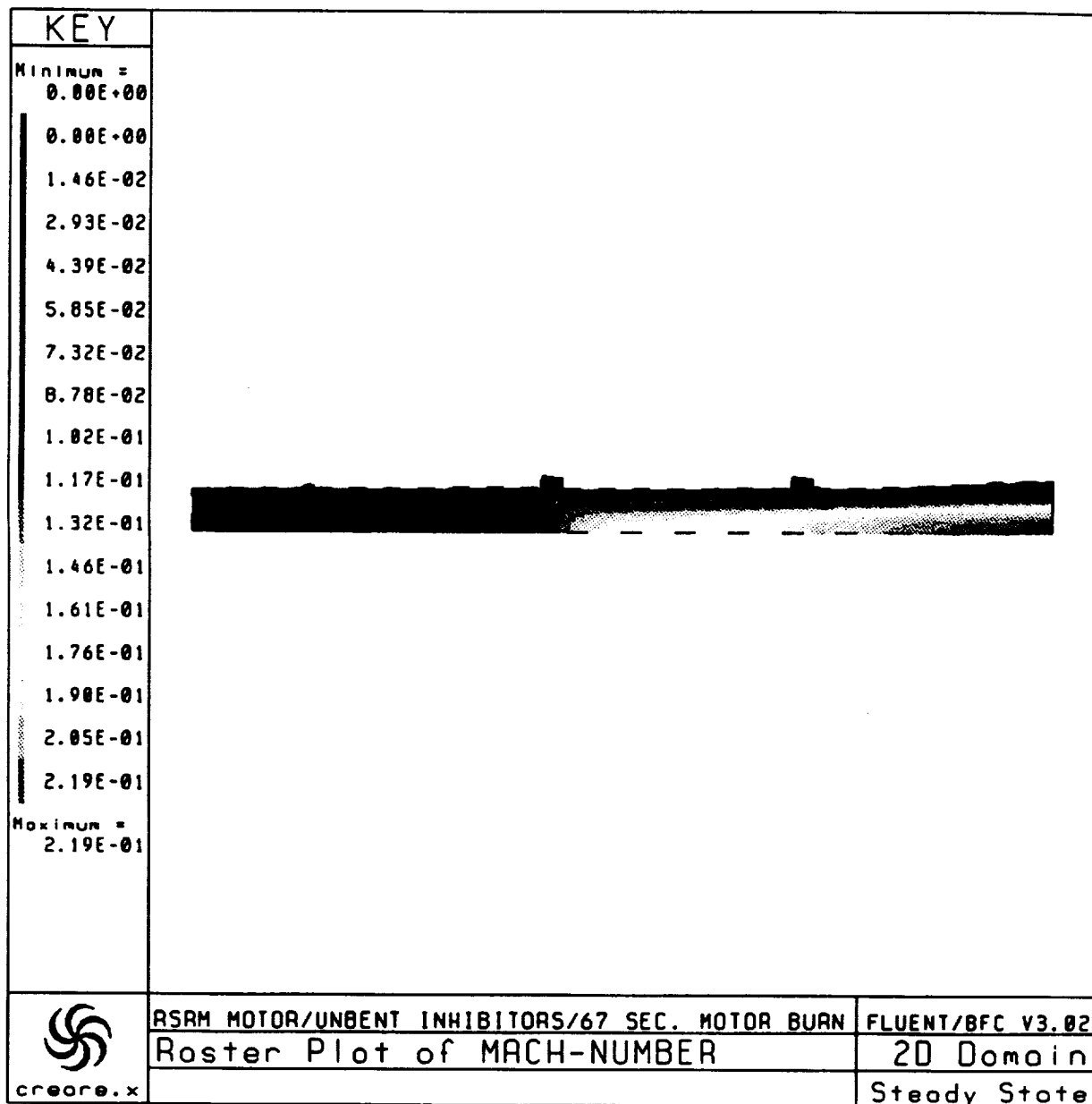


Figure 23. RSRM Excursion 1 Color Raster Mach Number Plot



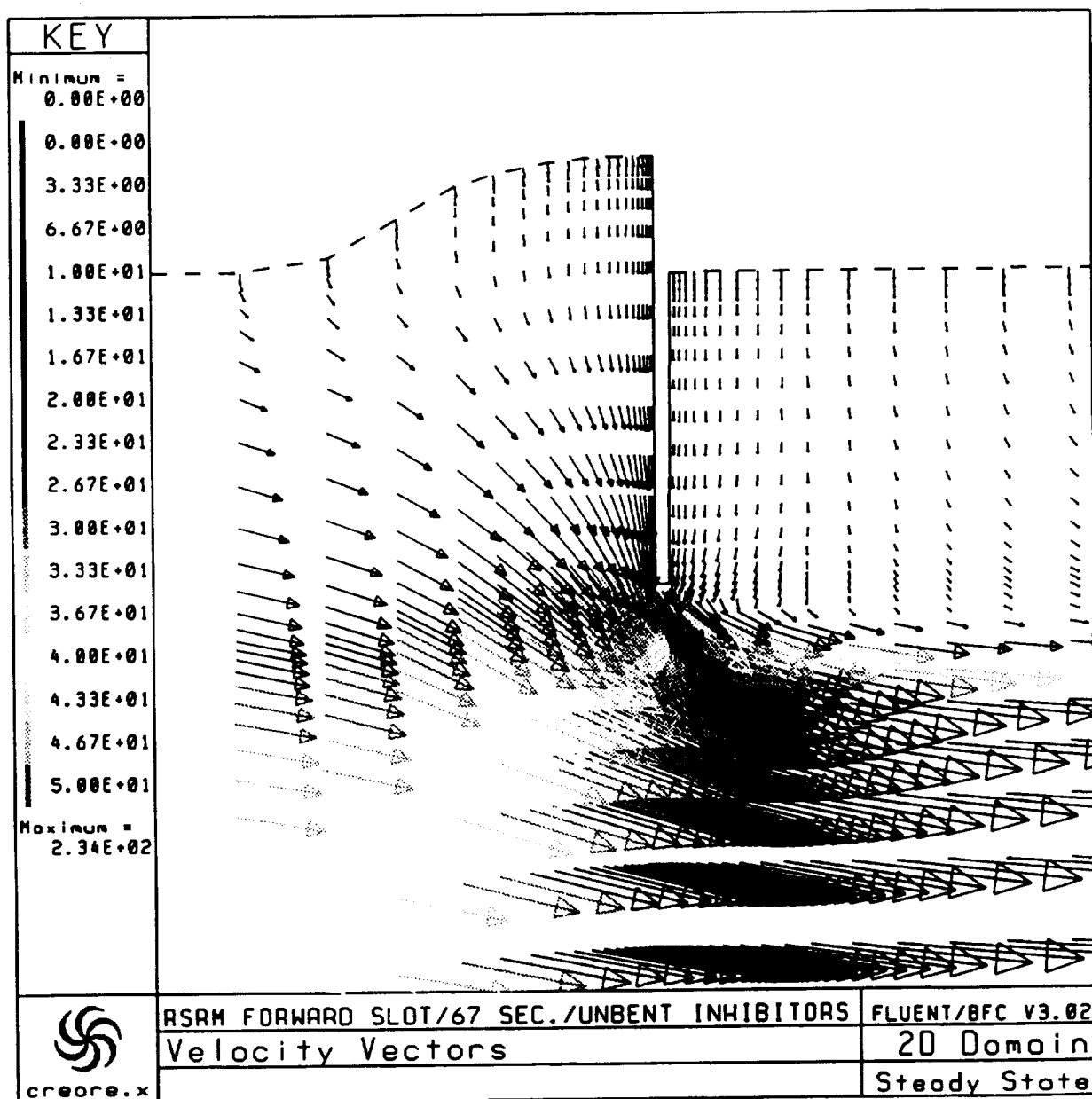


Figure 24. RSRM Excursion 1 Velocity Vector Field, Forward Slot

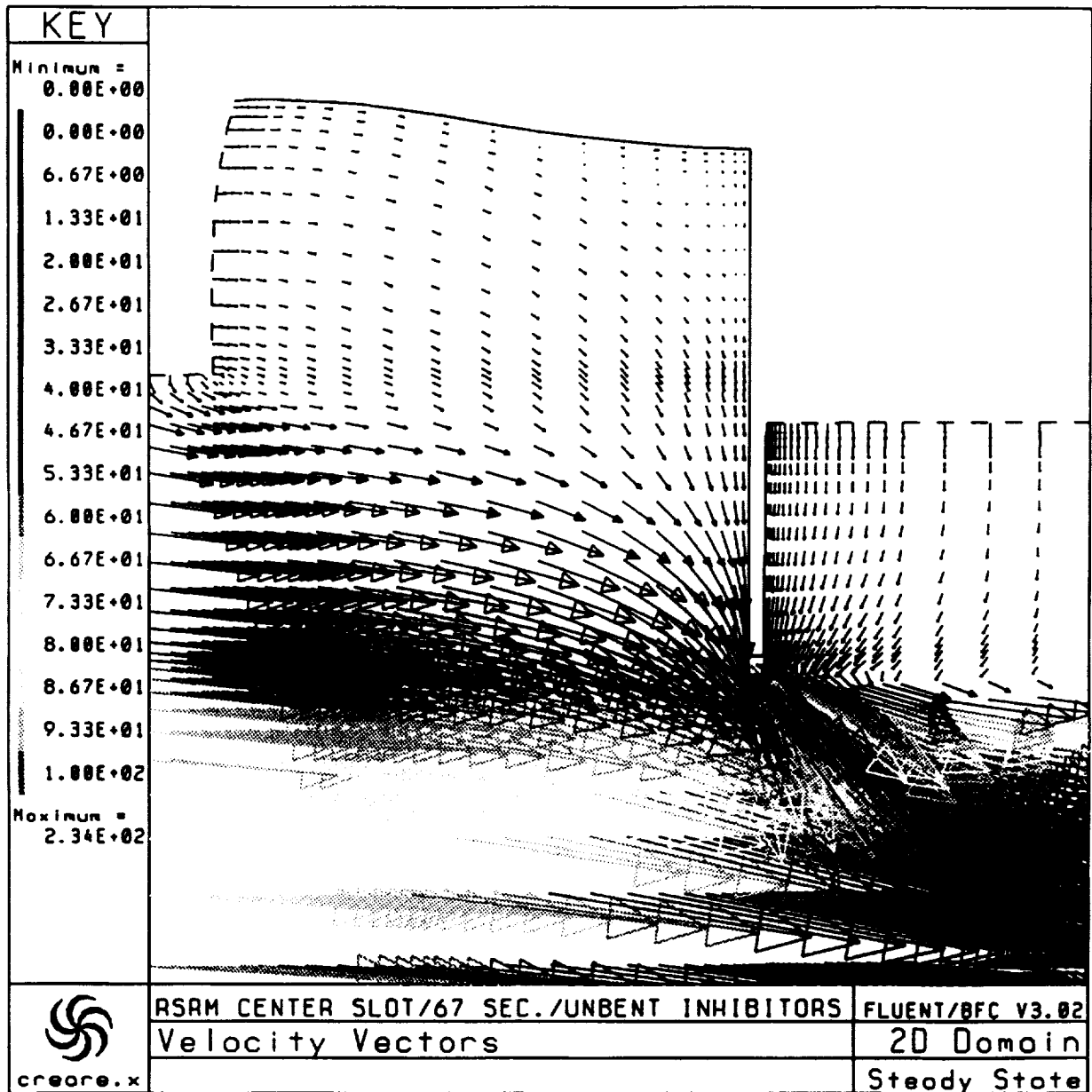


Figure 25. RSRM Excursion 1 Velocity Vector Field, Center Slot

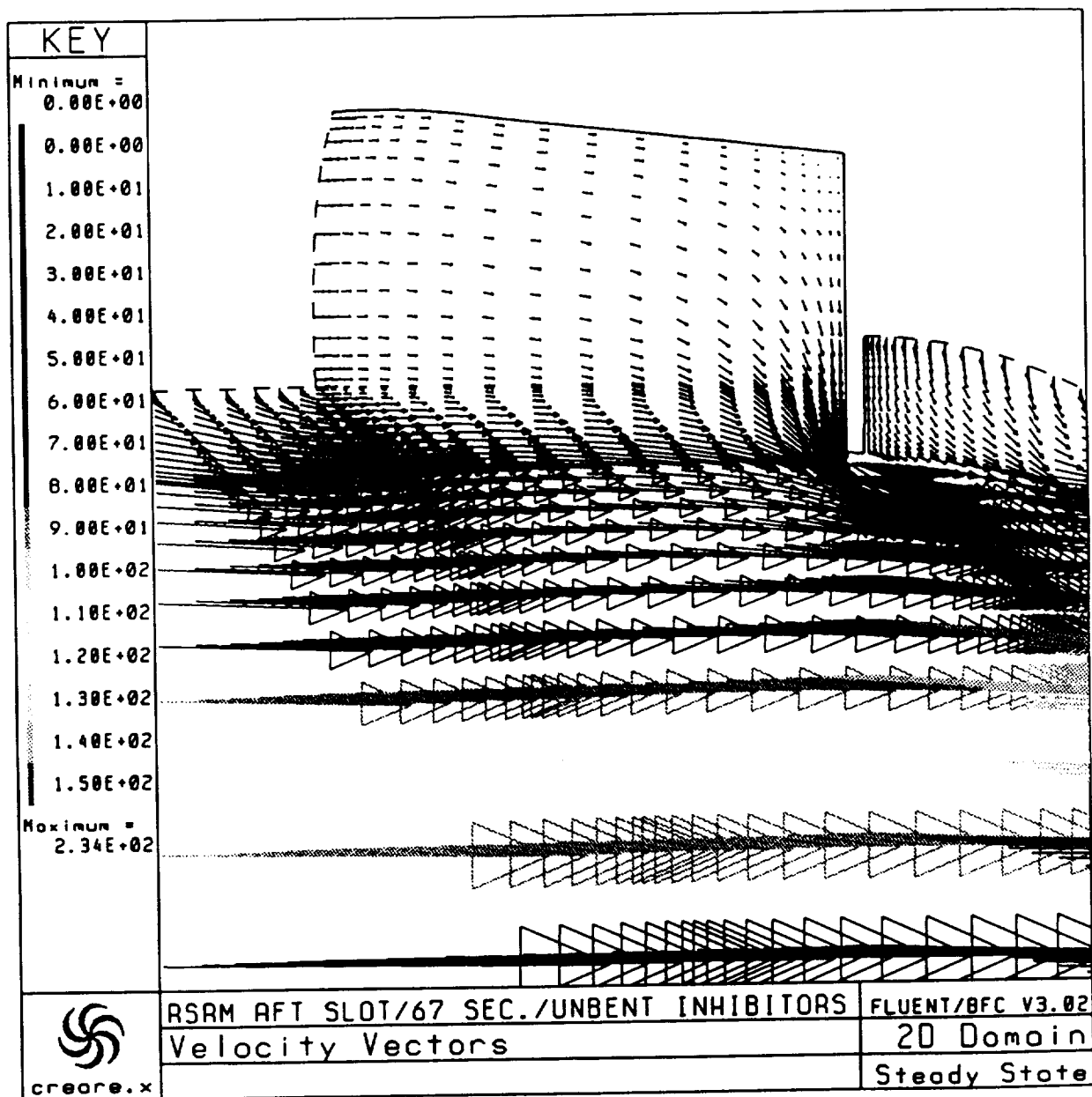
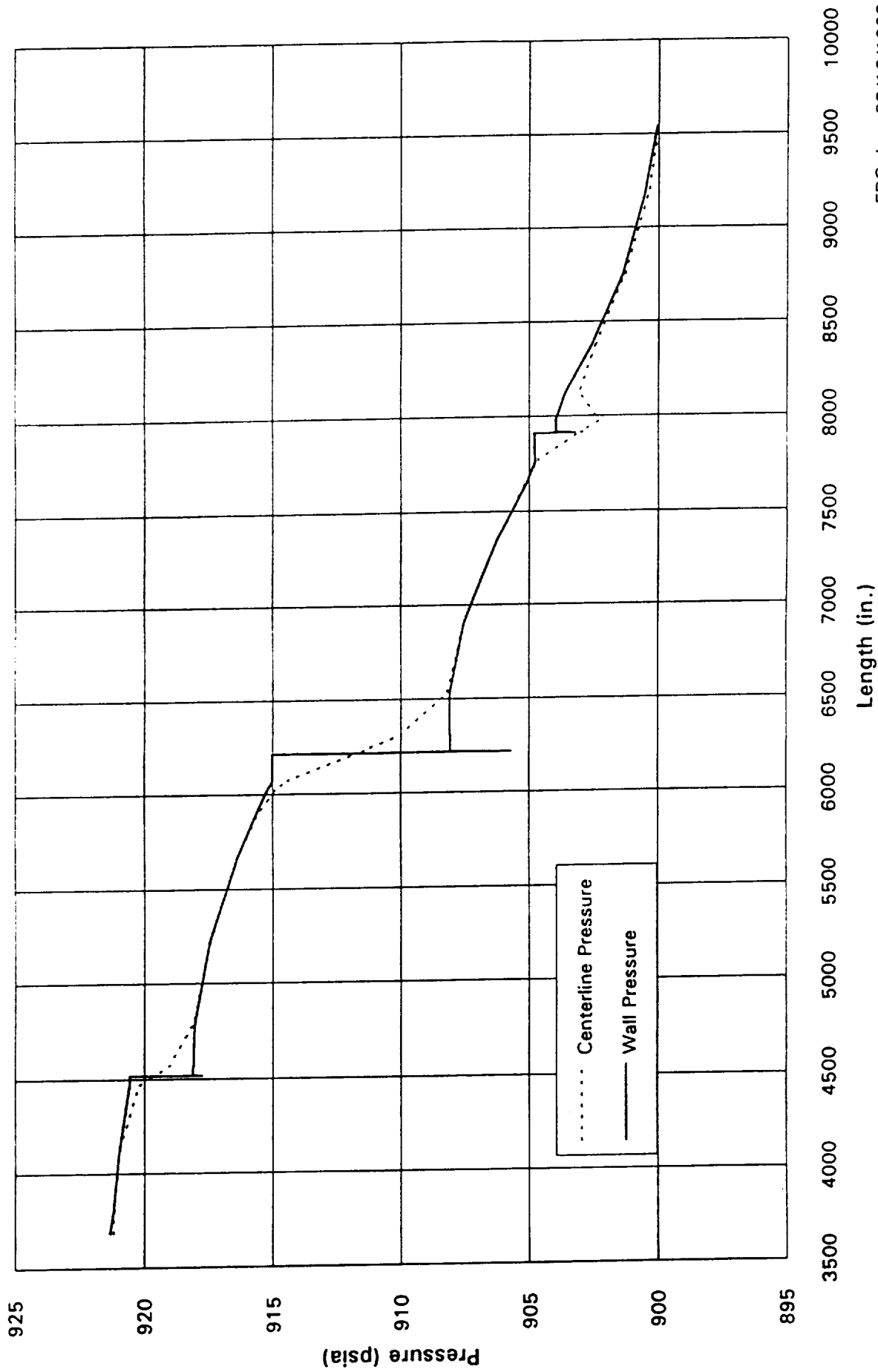


Figure 26. RSRM Excursion 1 Velocity Vector Field, Aft Slot



ERC, Inc. 03/18/1993

Figure 27. RSRM Motor Port Pressure Profile, Excursion 1

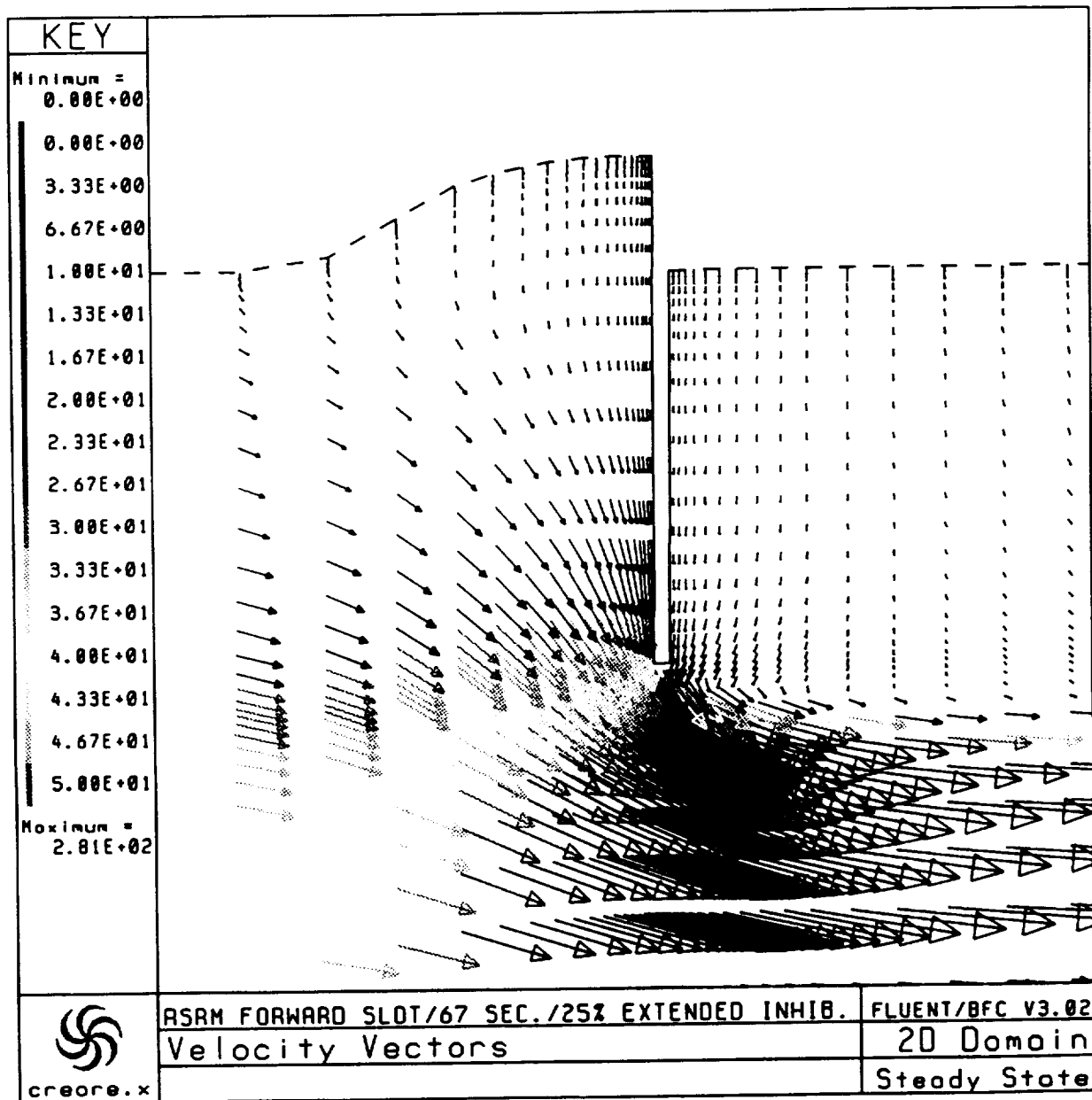


Figure 28. RSRM Excursion 2 Velocity Vector Field, Forward Slot

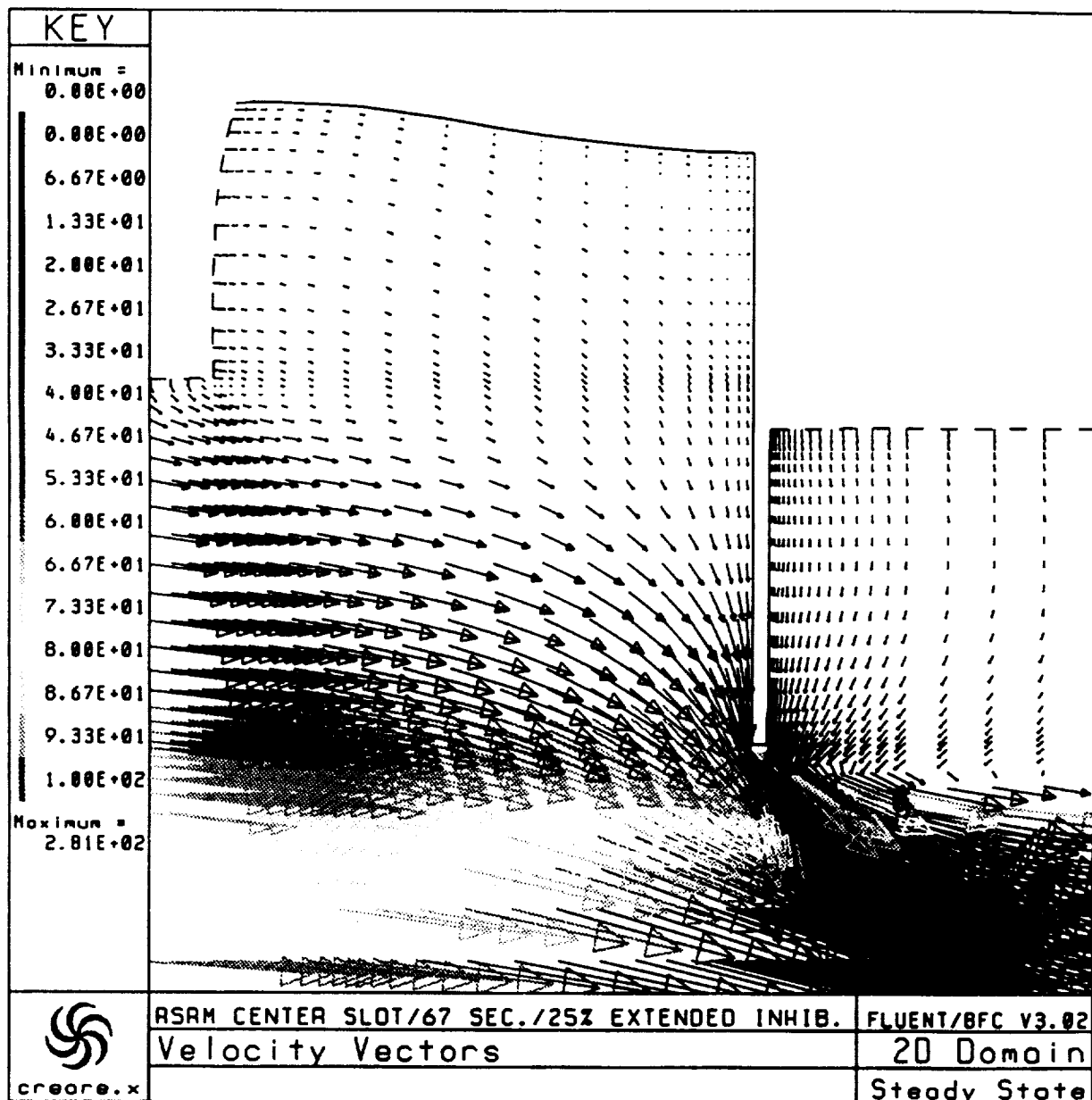


Figure 29. RSRM Excursion 2 Velocity Vector Field, Center Slot

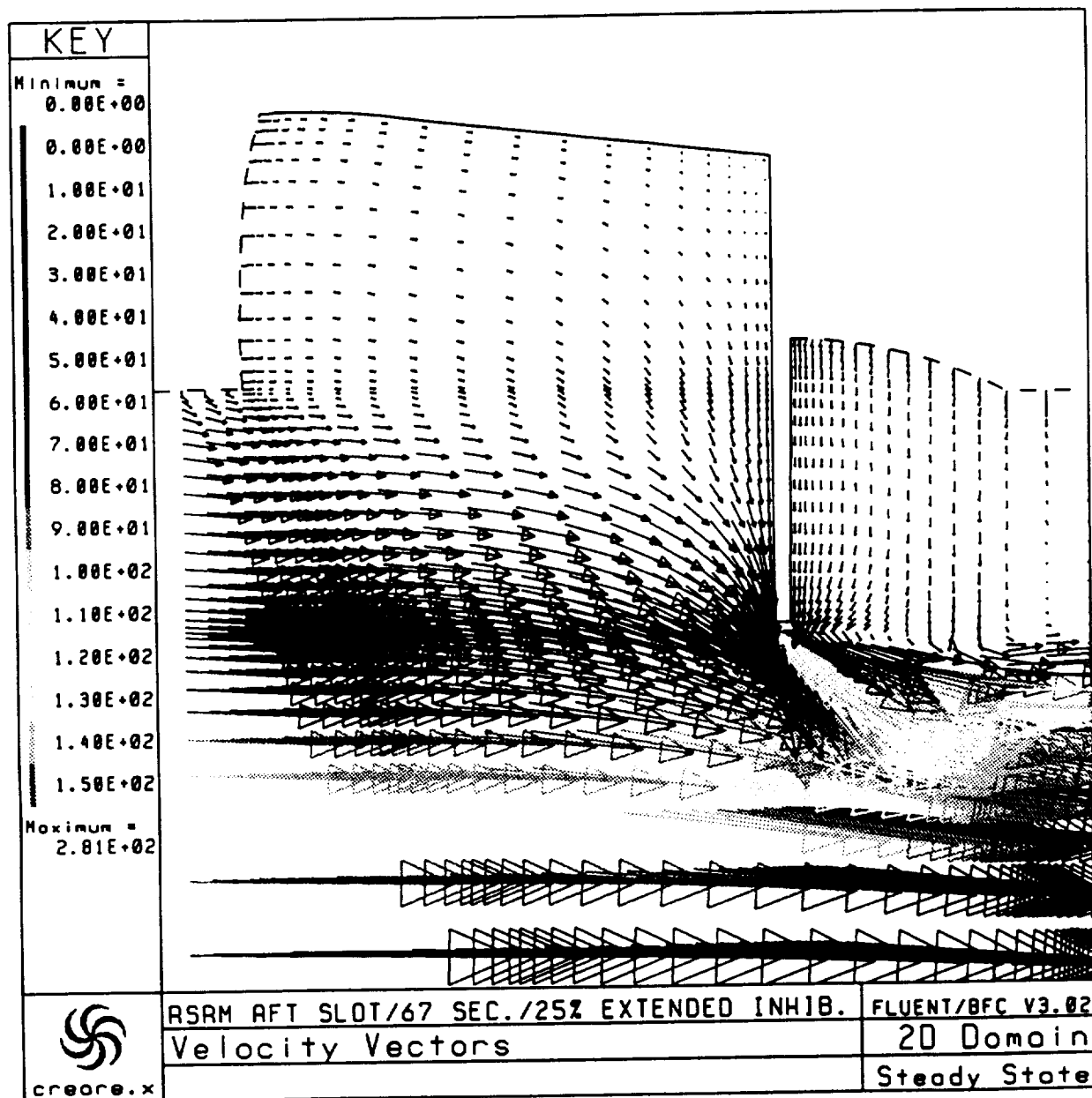
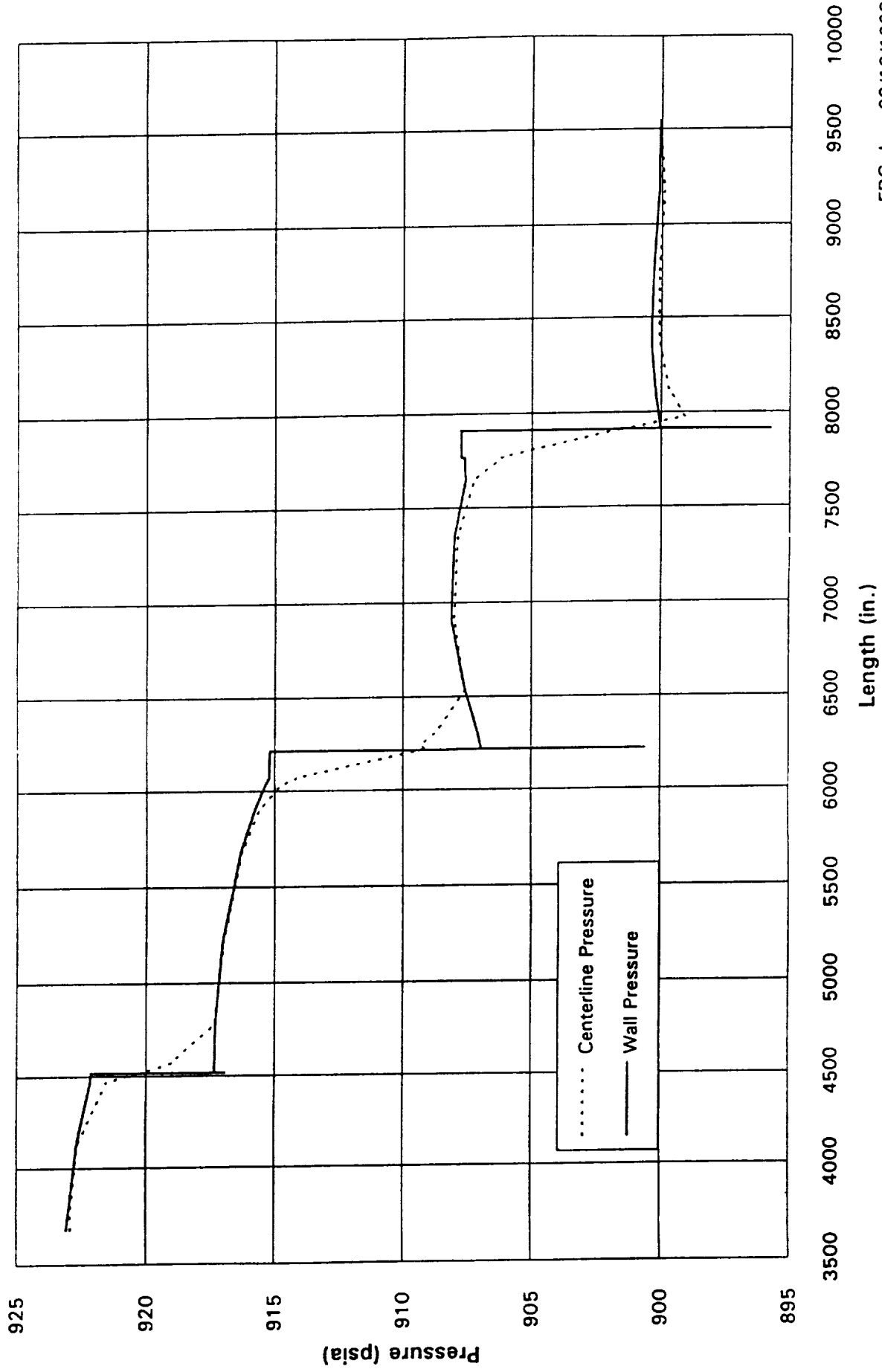


Figure 30. RSRM Excursion 2 Velocity Vector Field, Aft Slot



ERC, Inc. 03/18/1993

Figure 31. RSRM Motor Port Pressure Profile, Excursion 2



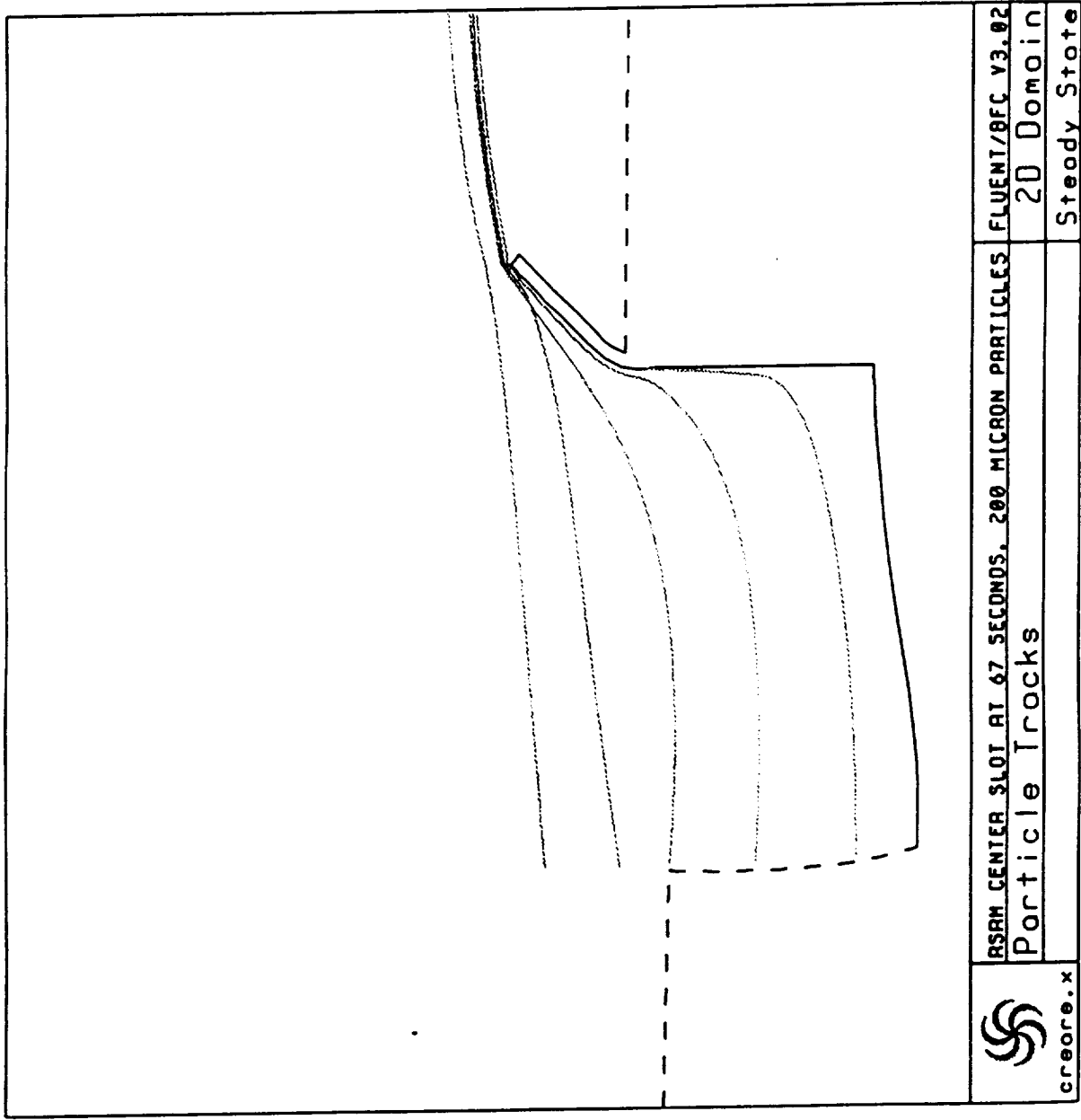


Figure 32. RSRM Center Slot at 67 Seconds, 200 Micron Particles

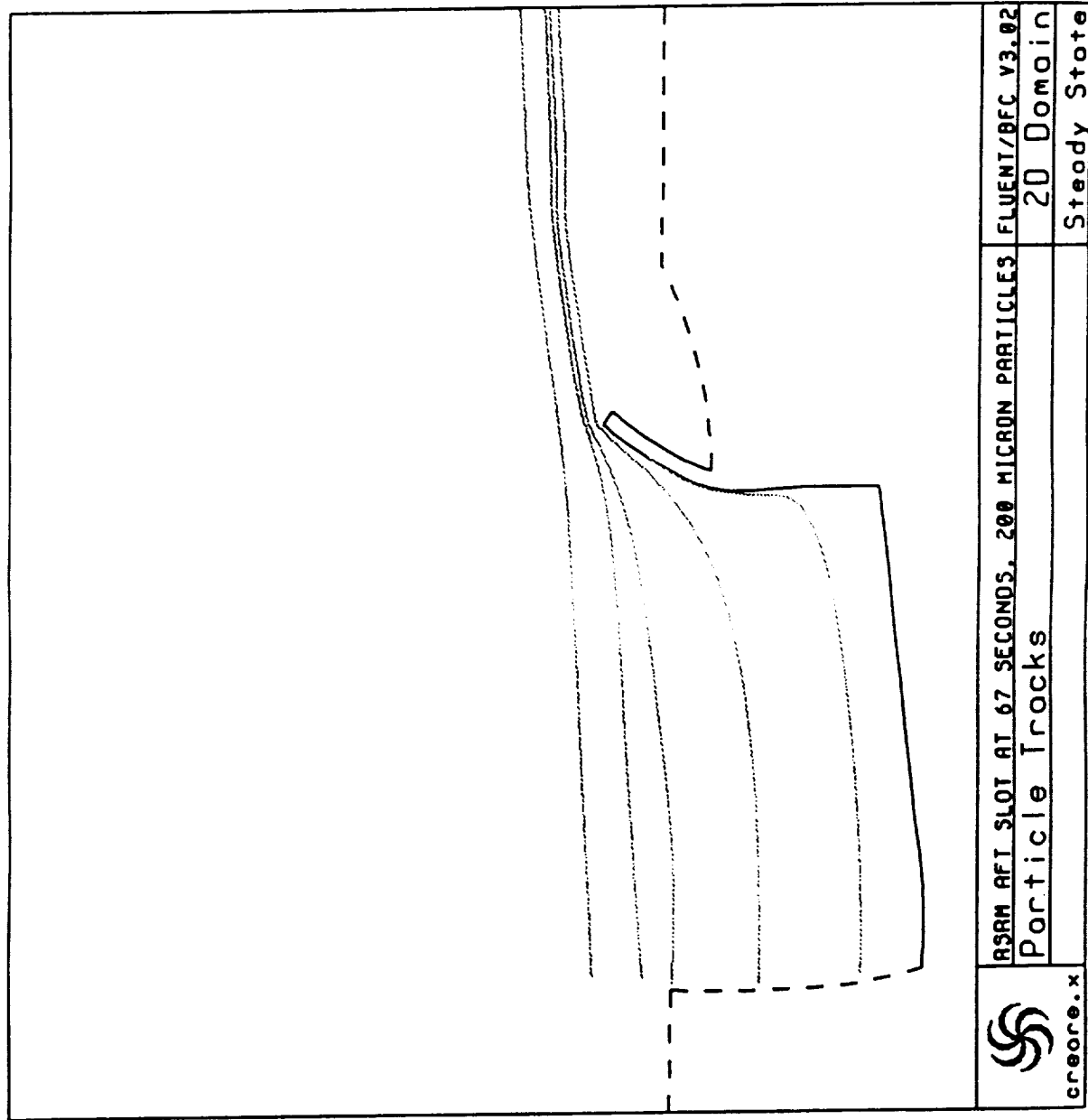


Figure 33. RSRM Aft Slot at 67 Seconds, 200 Micron Particles

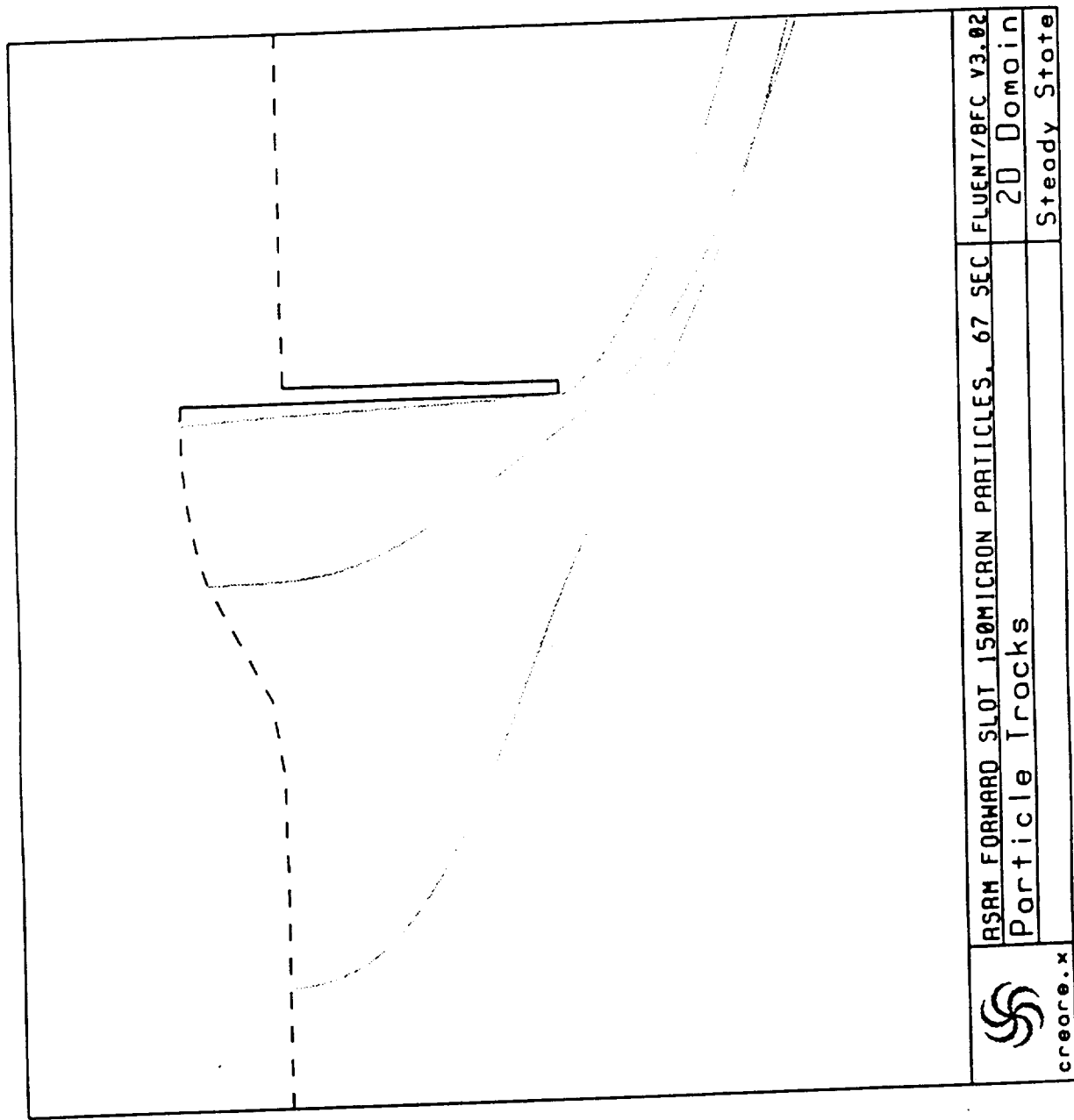


Figure 34. RSRM Forward Slot at 67 Seconds, 150 Micron Particles

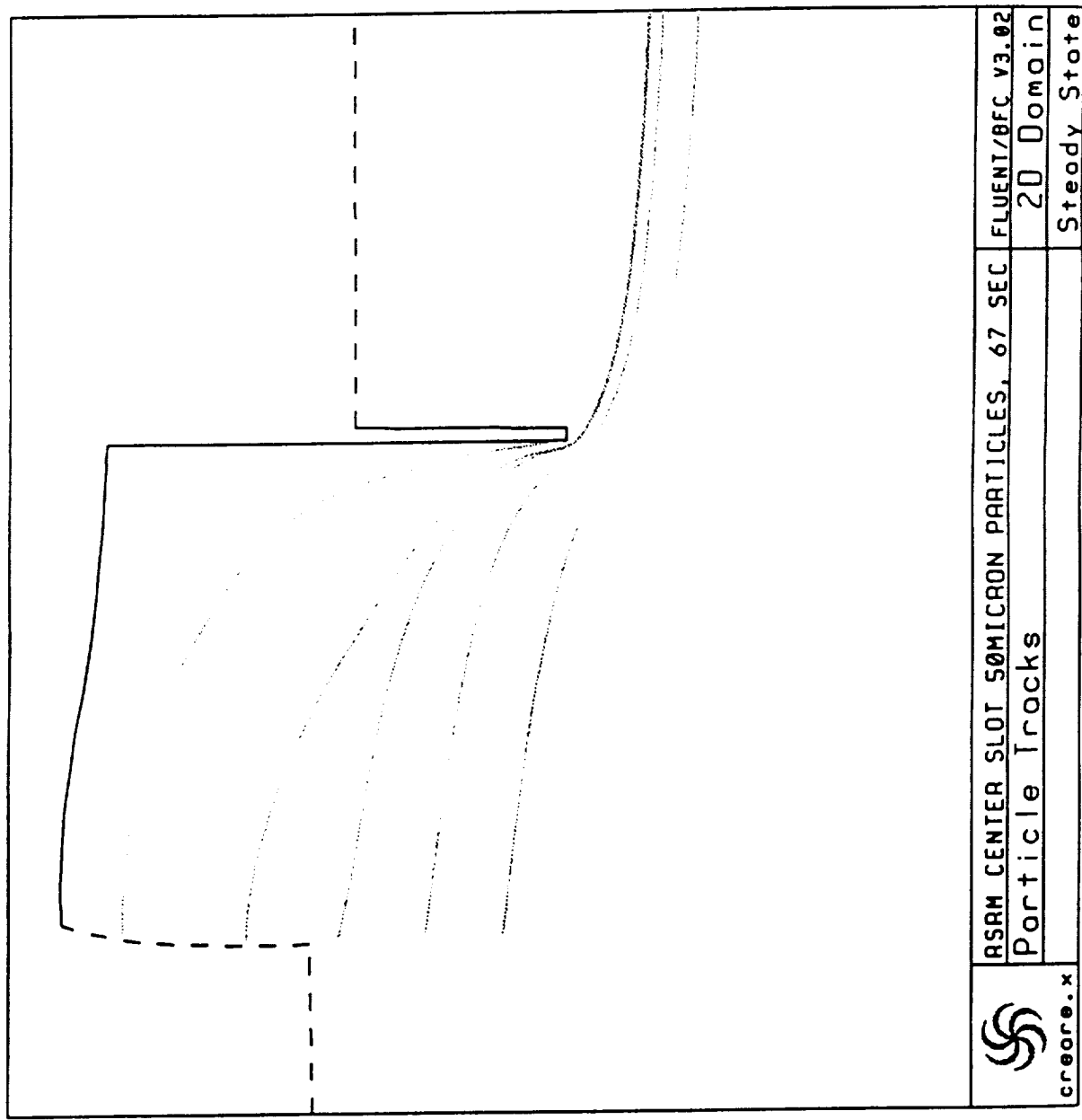


Figure 35. RSRM Center Slot at 67 Seconds, 50 Micron Particles

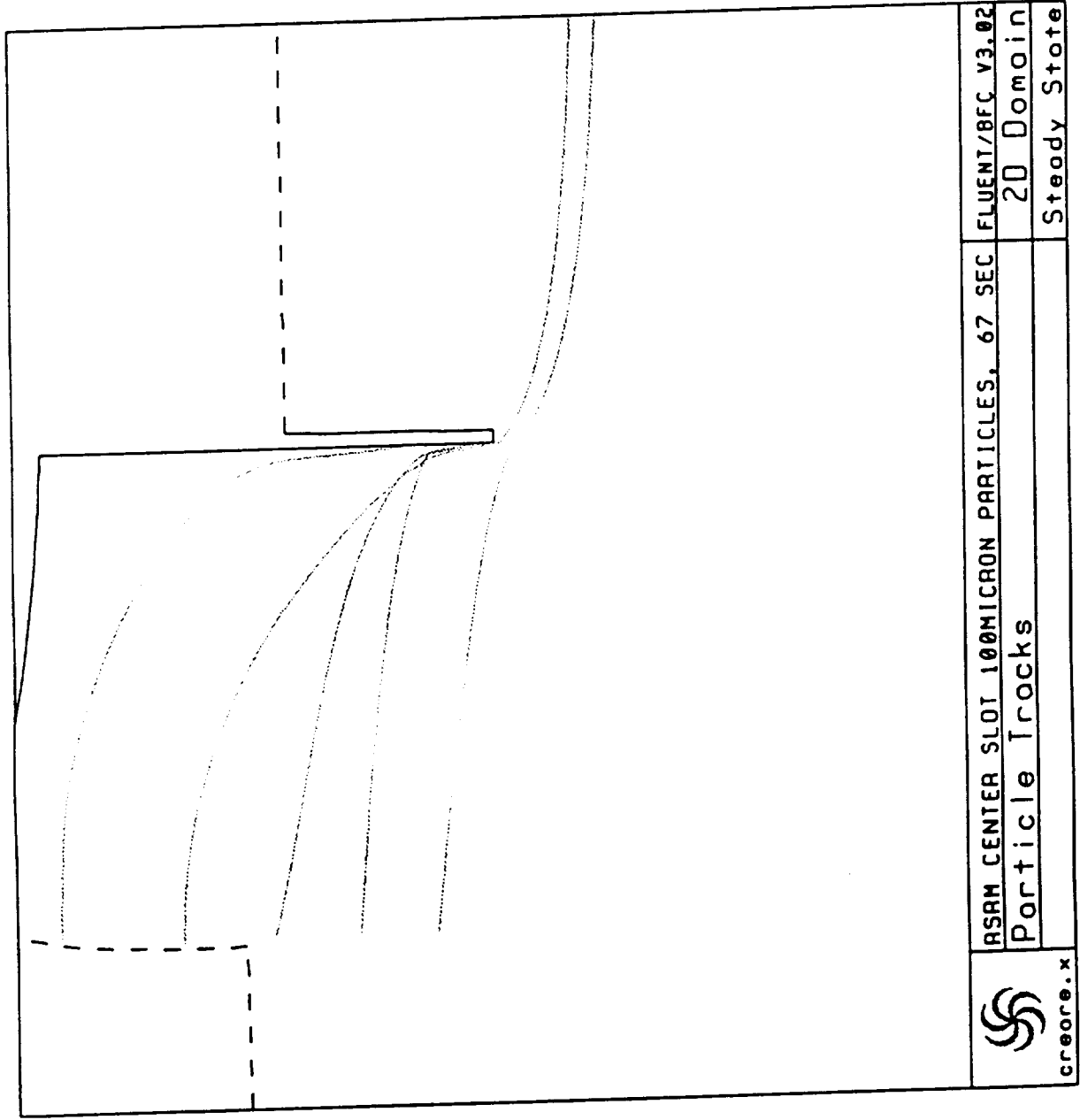


Figure 36. RSRM Center Slot at 67 Seconds, 100 Micron Particles

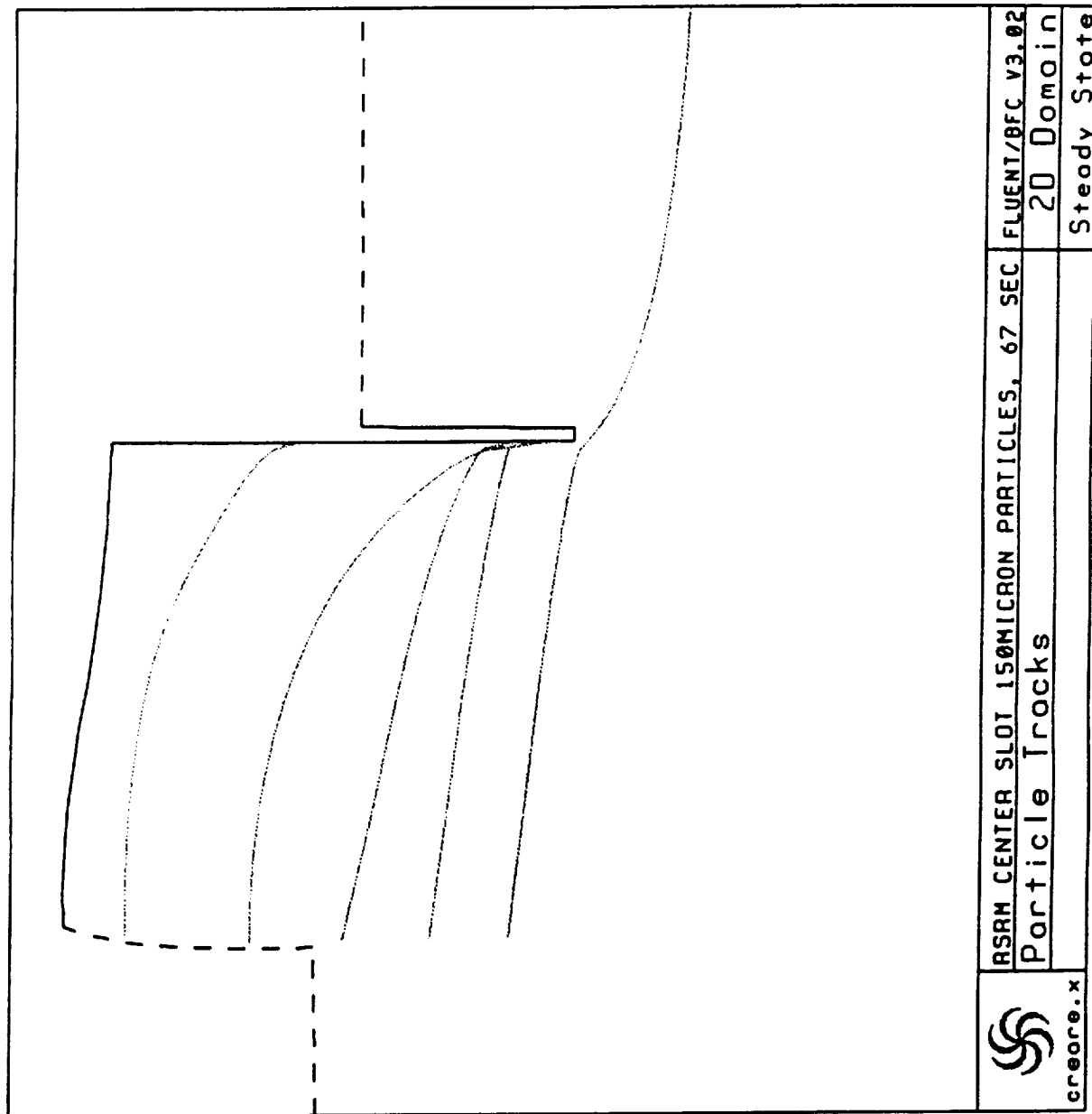


Figure 37. RSRM Center Slot at 67 Seconds, 150 Micron Particles

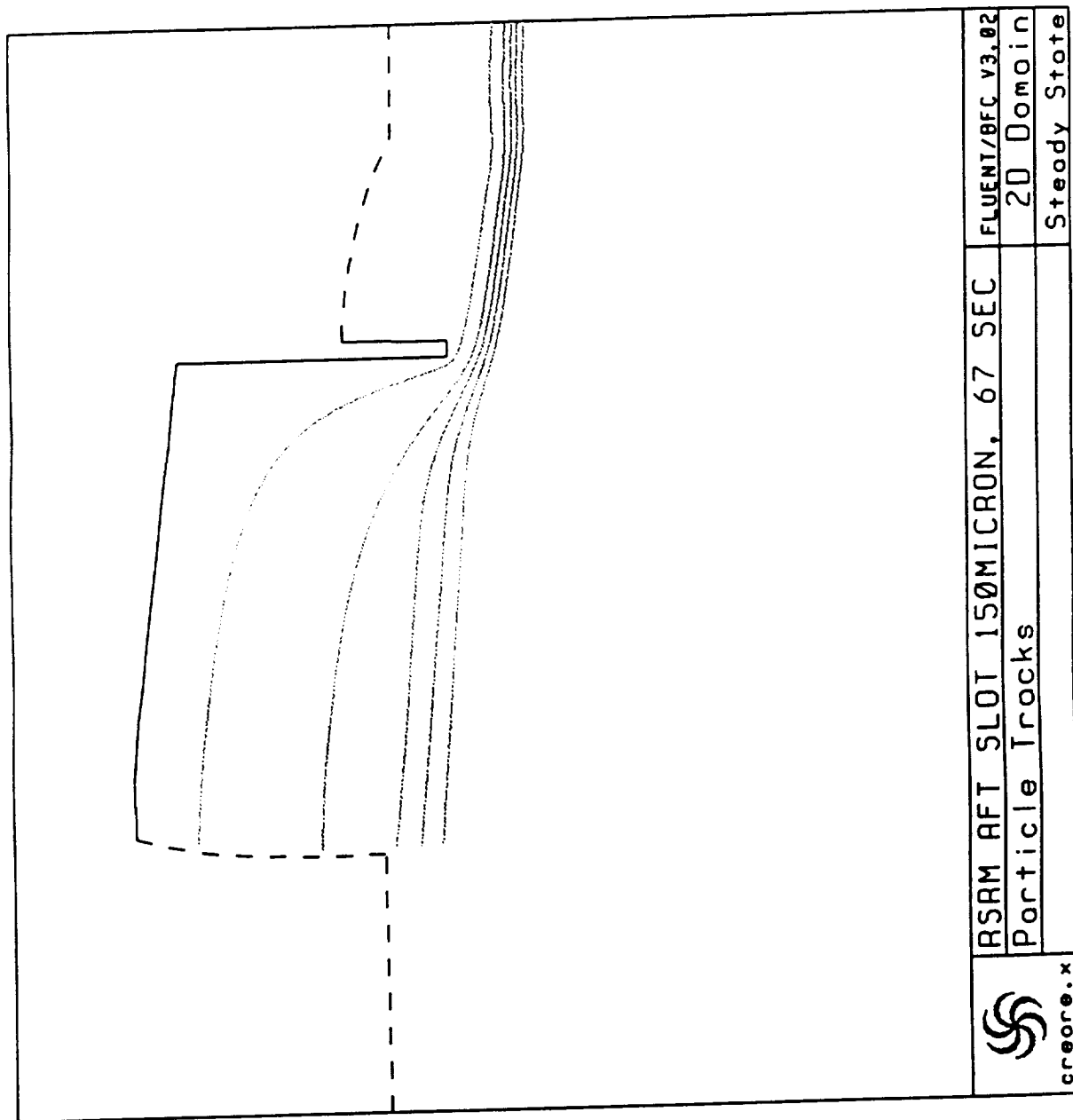


Figure 38. RSRM Aft Slot at 67 Seconds, 150 Micron Particles

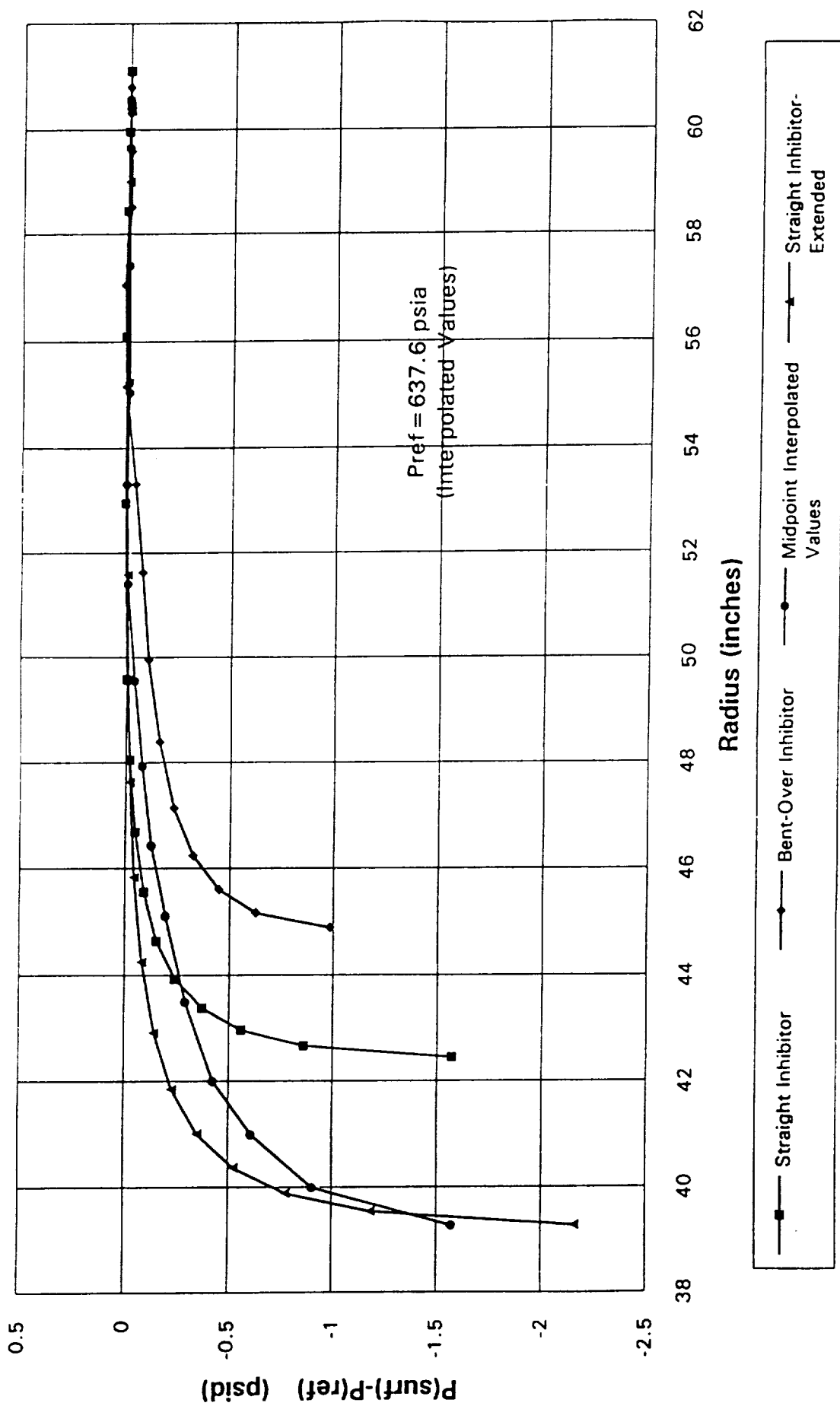
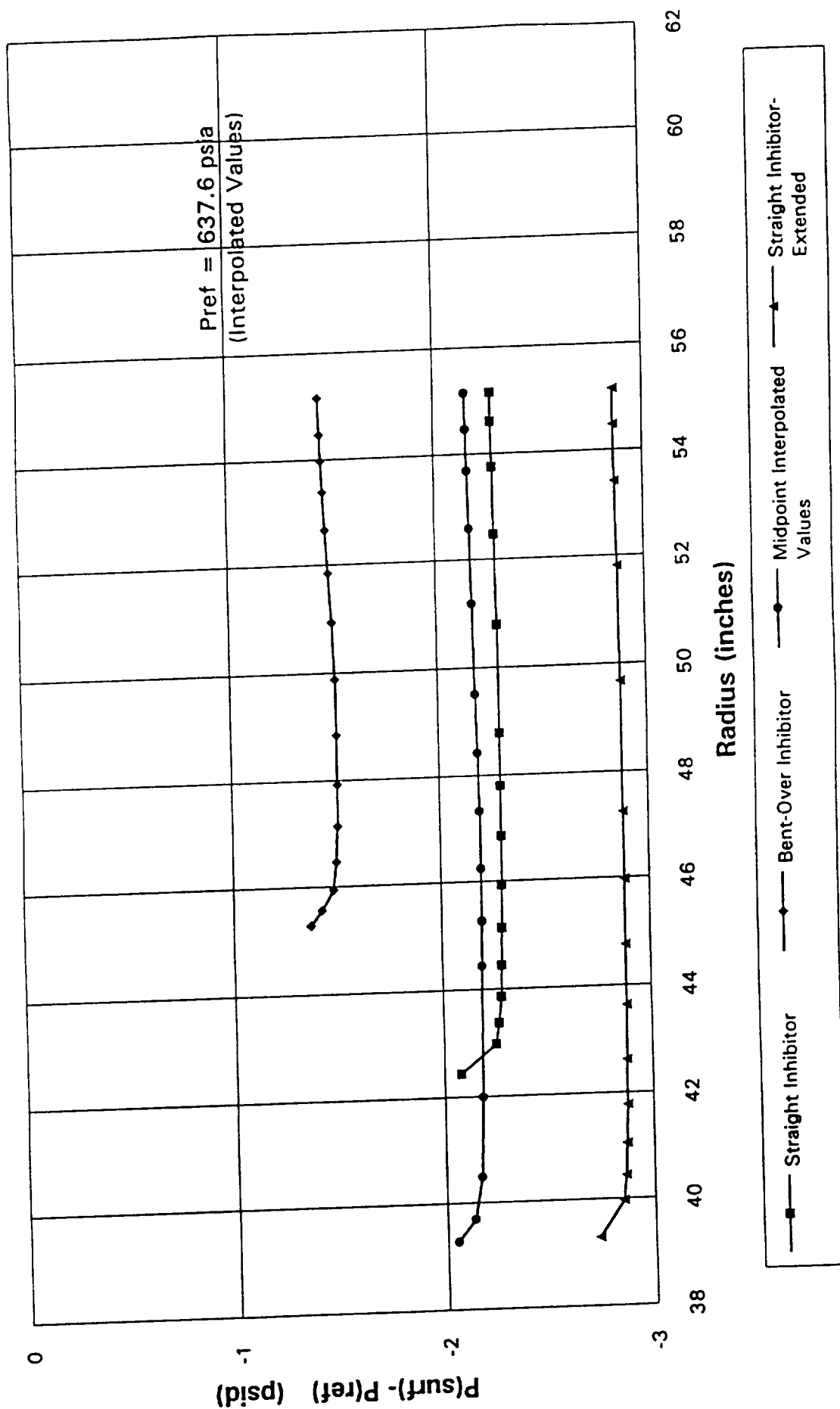


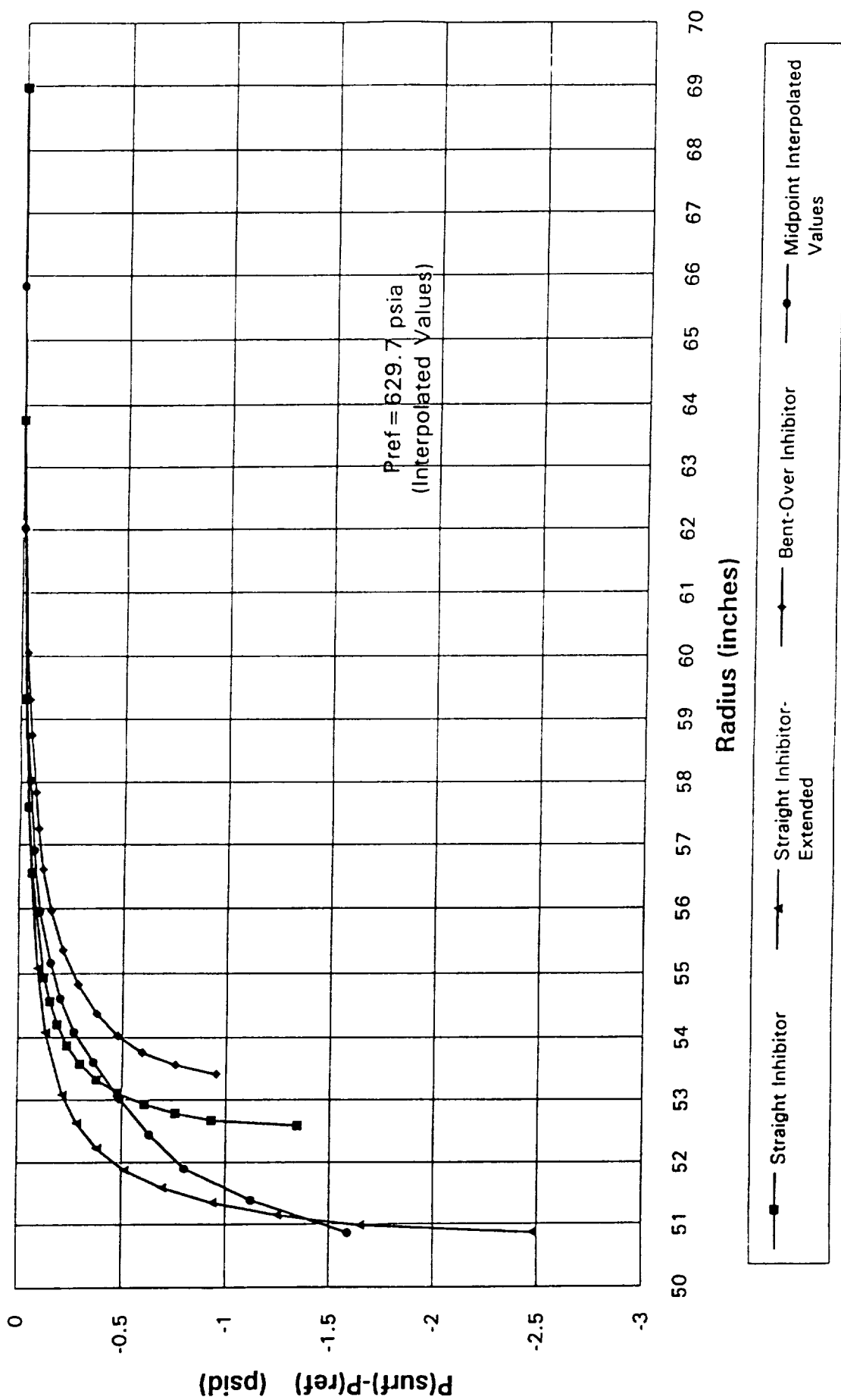
Figure 39. Forward Joint Inhibitor Upstream Face Pressure  
RSRM-29B, STS-54, 67 Seconds





ERC, Inc. 07/12/1993

Figure 40. Forward Joint Inhibitor Downstream Face Pressure  
RSRM-29B, STS-54, 67 Seconds



ERC, Inc. 07/12/1993

Figure 41. Aft Joint Inhibitor Upstream Face Pressure  
 RSRM-29B, STS-54, 67 Seconds

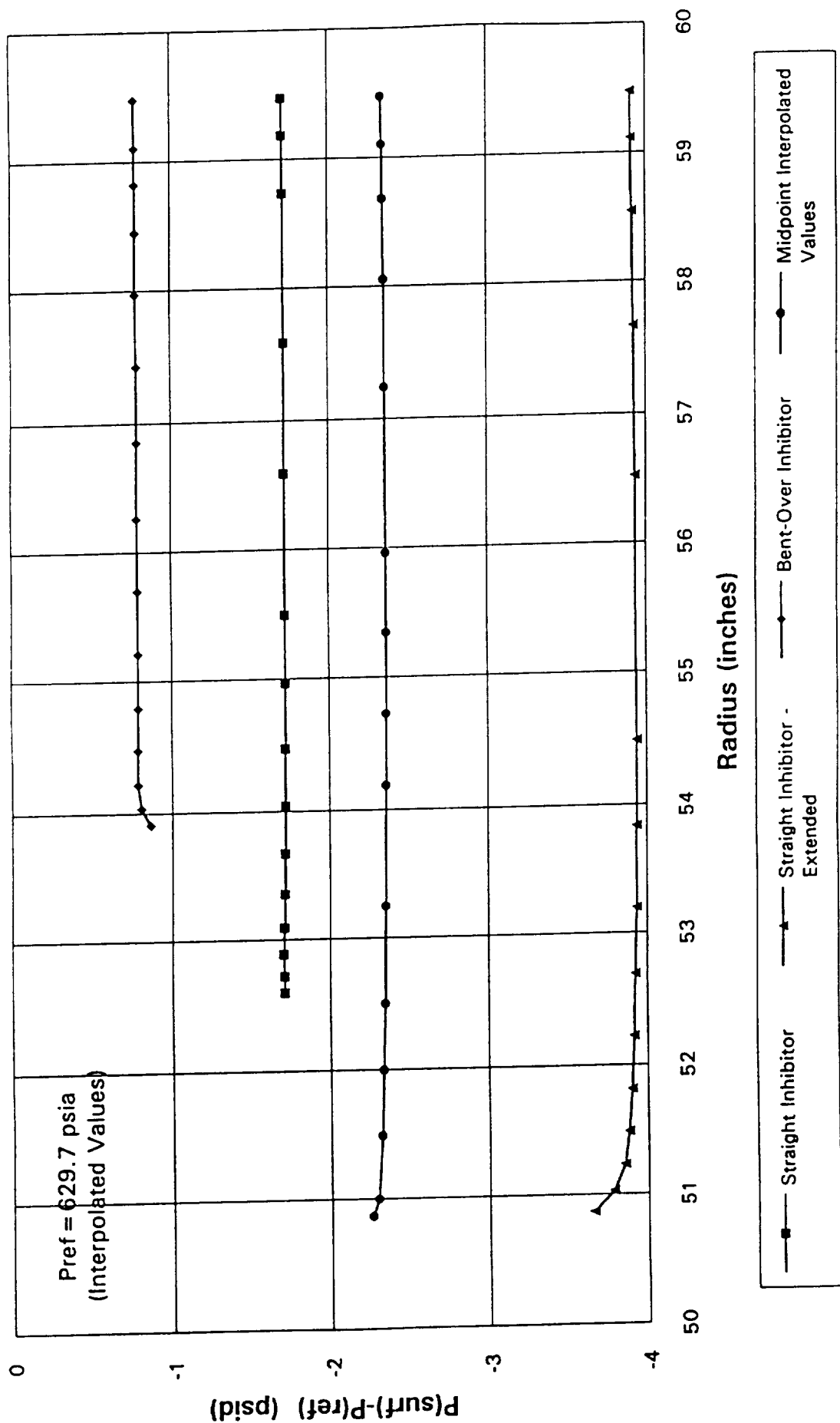
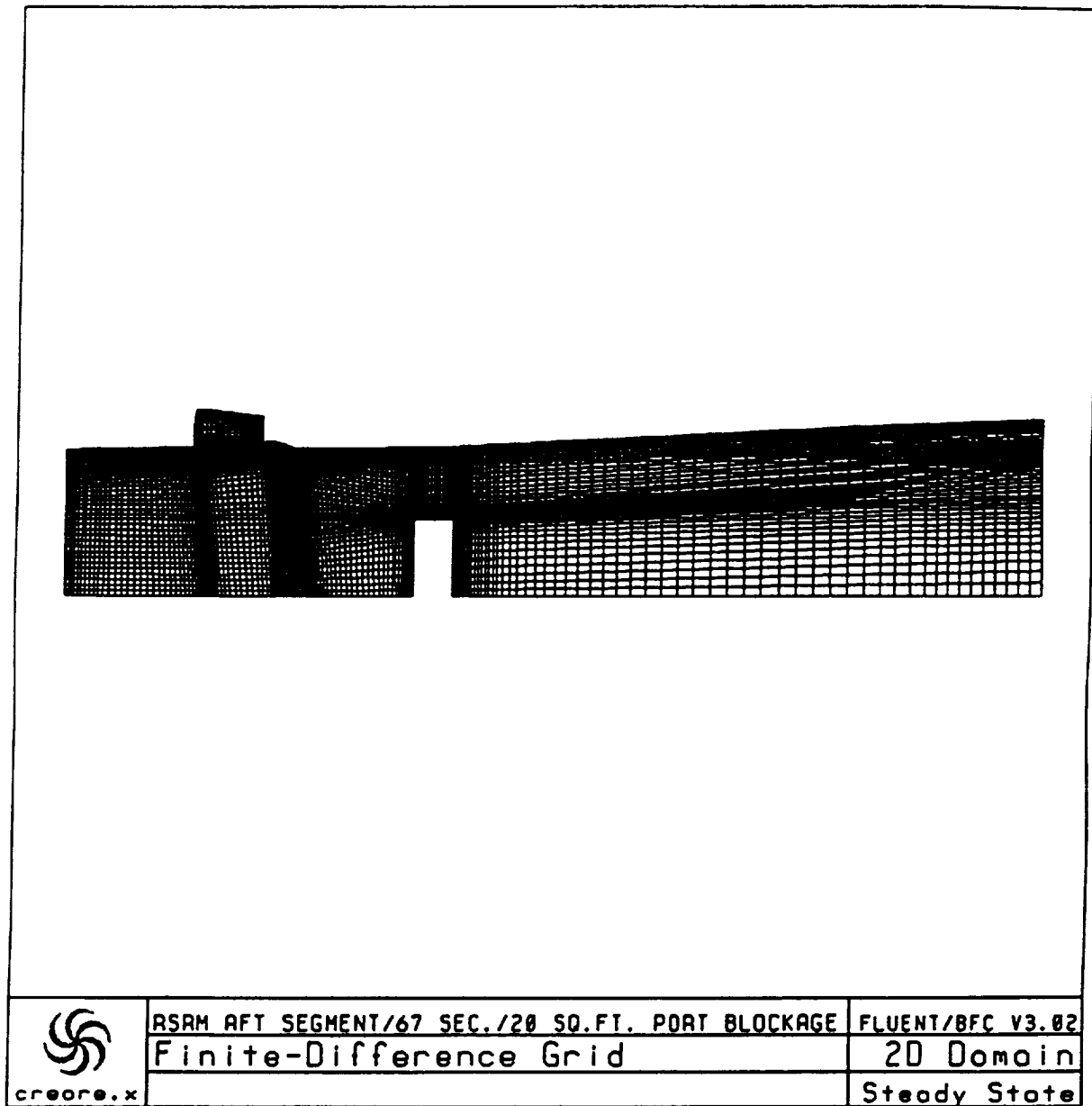
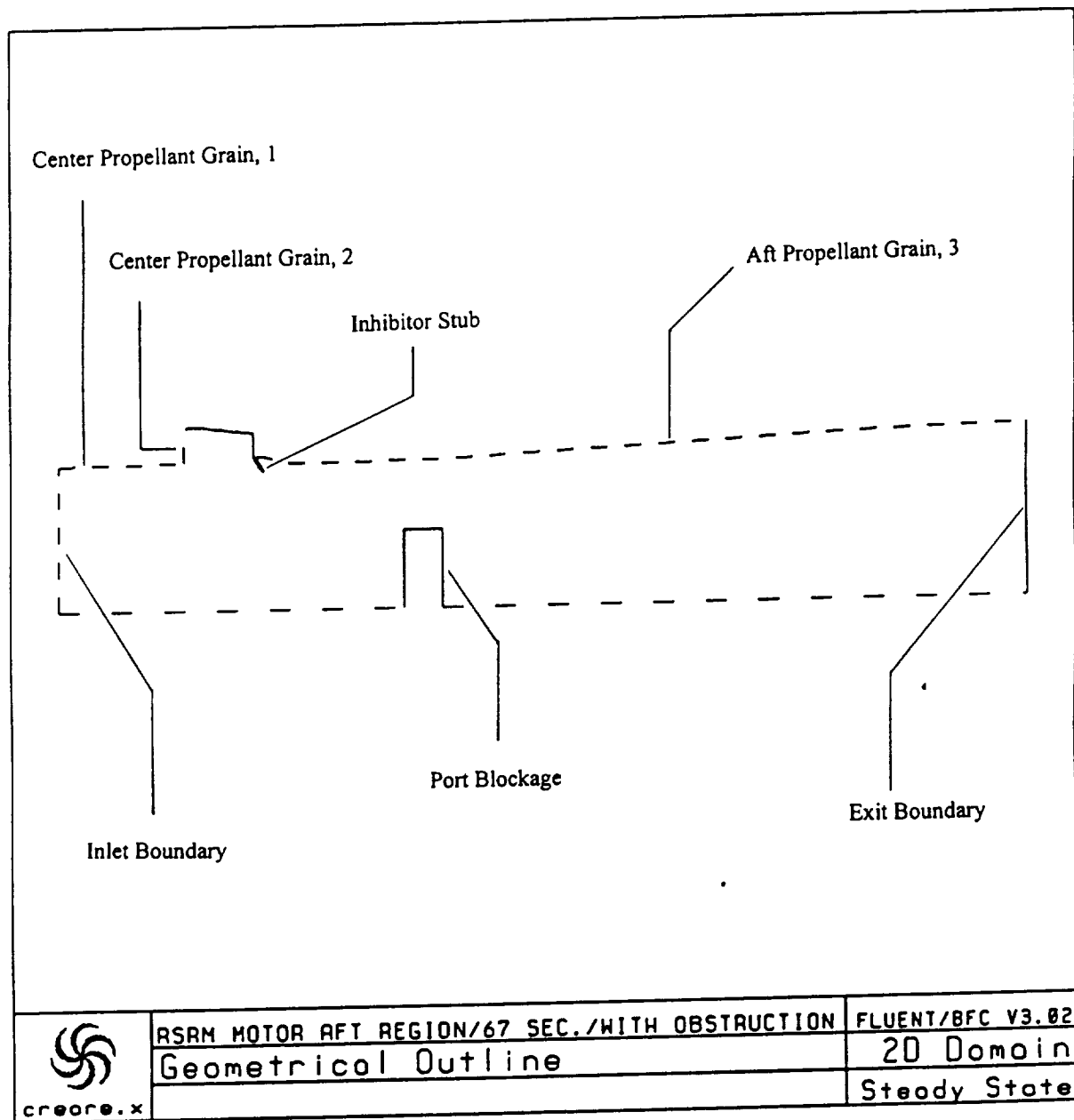


Figure 42. Aft Joint Inhibitor Downstream Face Pressure  
RSRM-29B, STS-54, 67 Seconds



**Figure 43. RSRM Aft Motor Region Port Blockage Case  
Computational Grid**



**Figure 44. RSRM Aft Motor Region Port Blockage Problem Geometry**

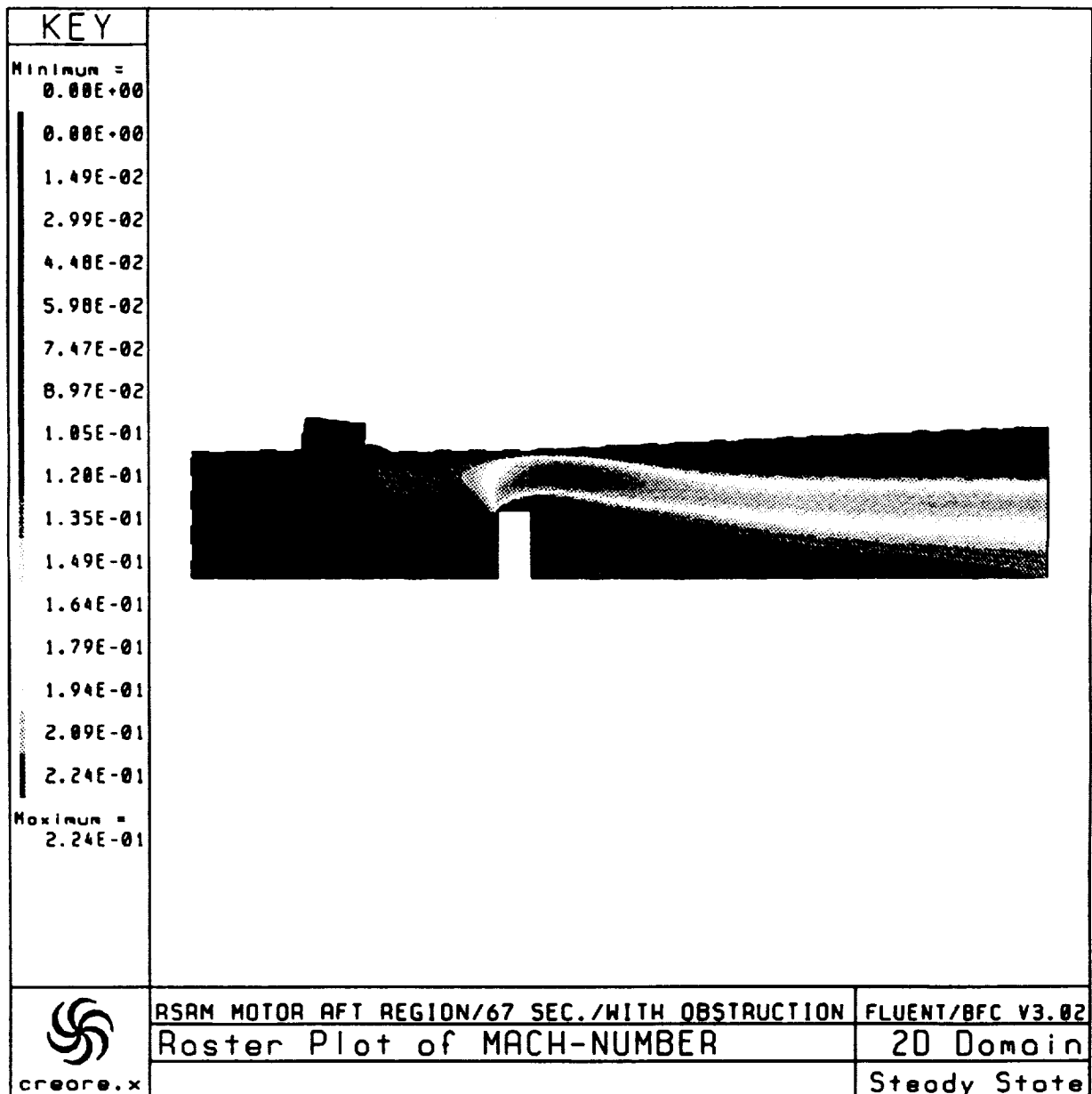


Figure 45. Color Raster Mach Number Plot for Port Blockage Problem

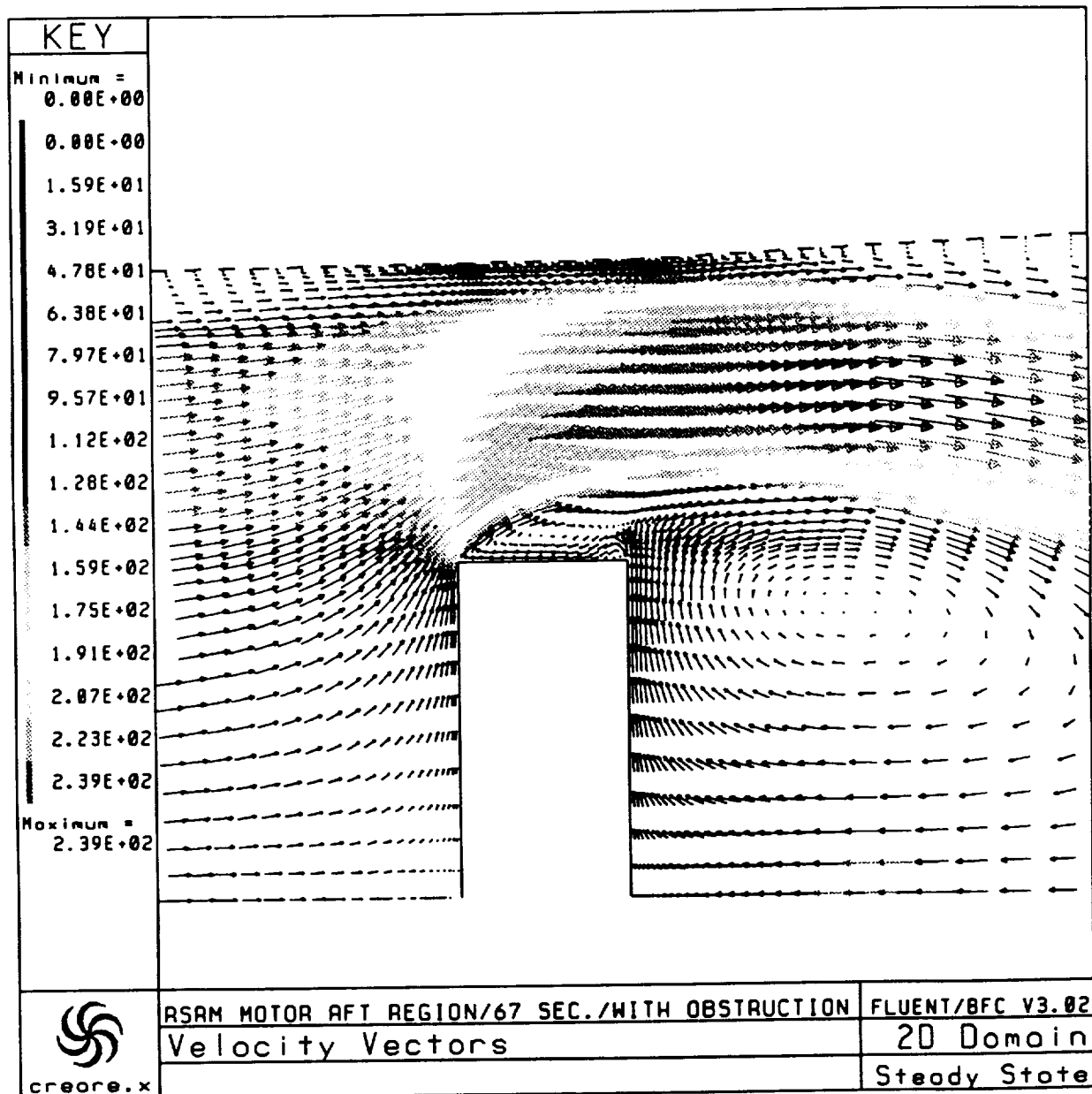
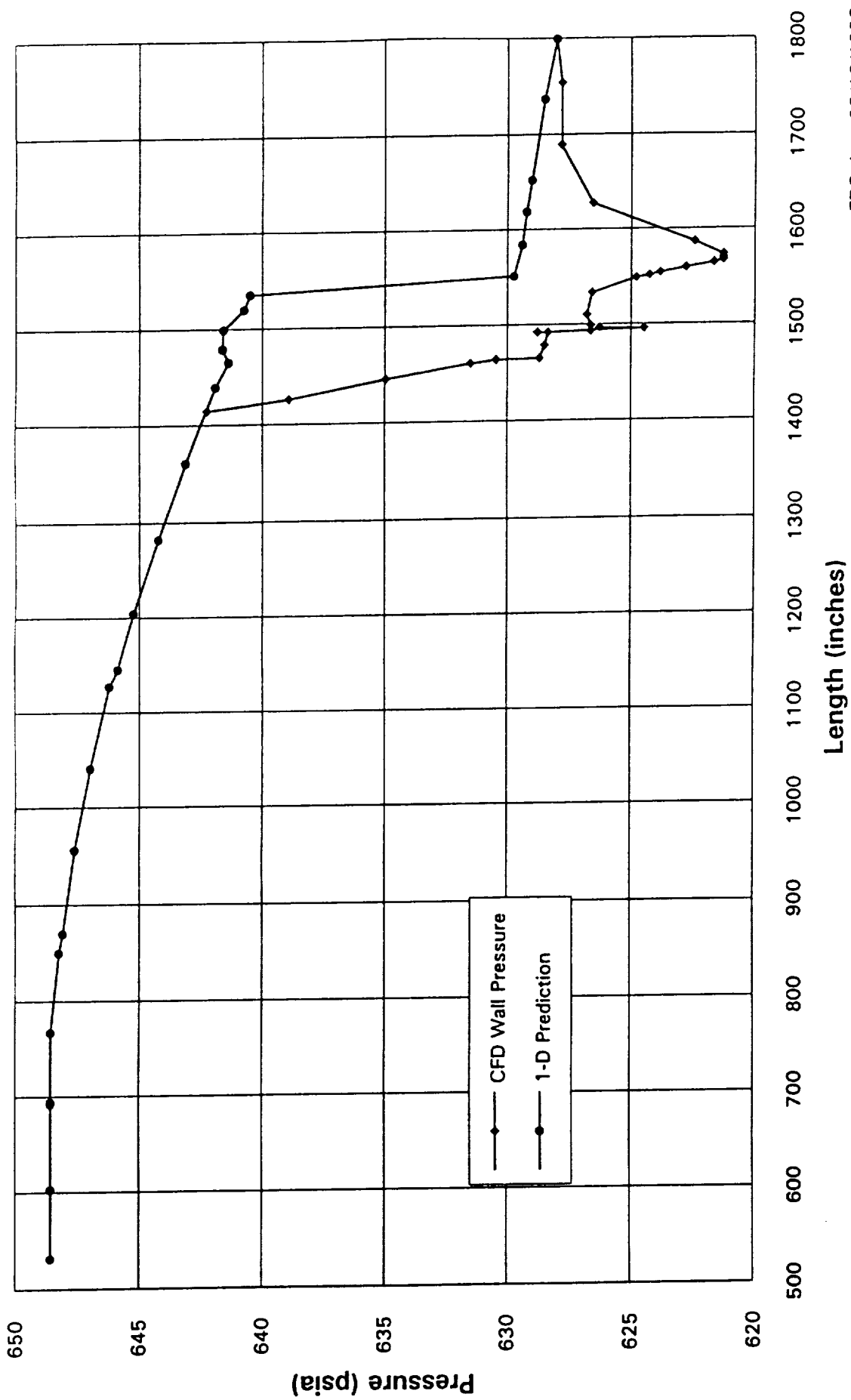


Figure 46. Velocity Vector Field for Port Blockage Problem



ERC, Inc. 03/18/1993

Figure 47. RSRM Aft Section Port Blockage  
RSRM-29B, STS-54



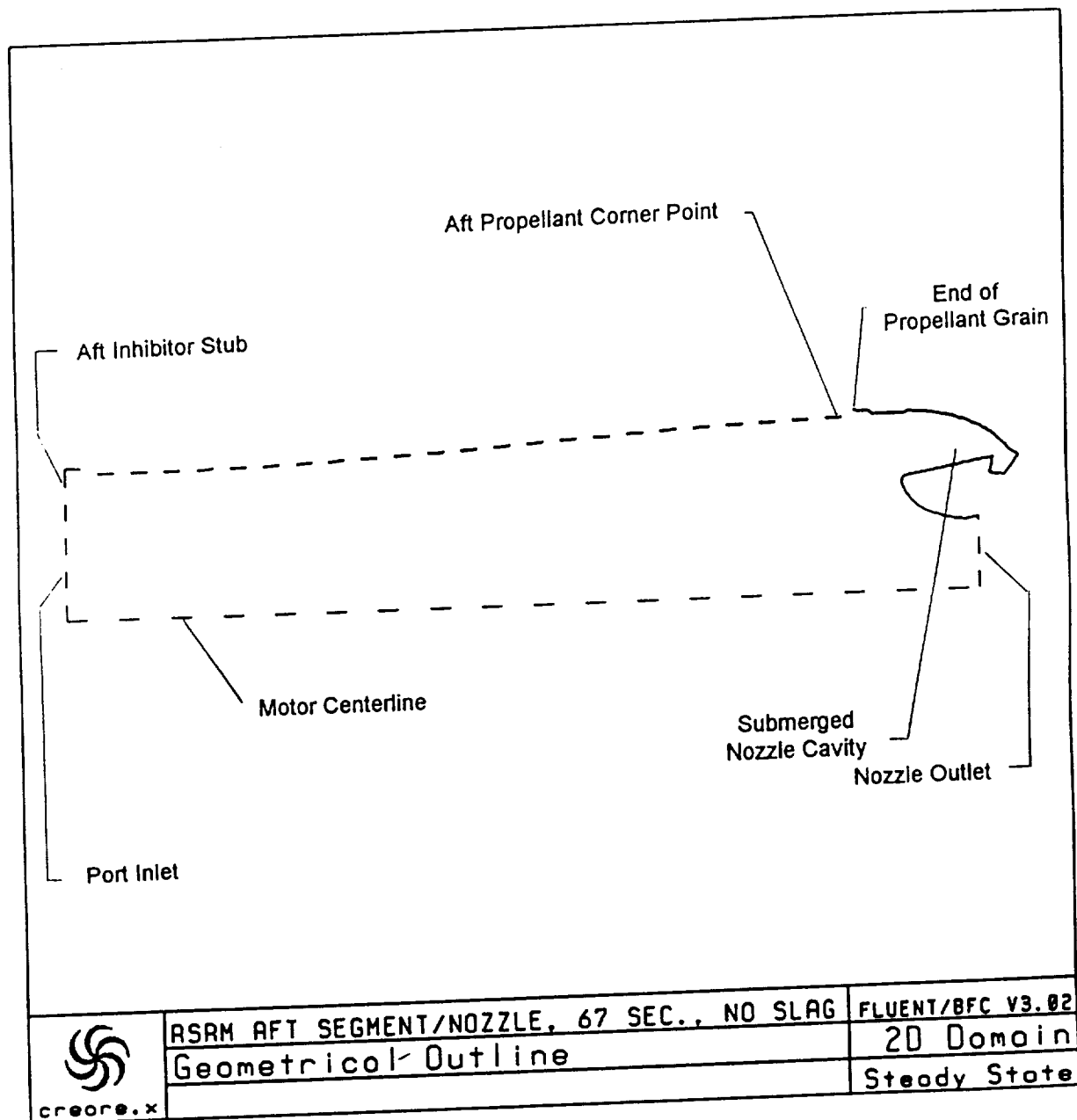
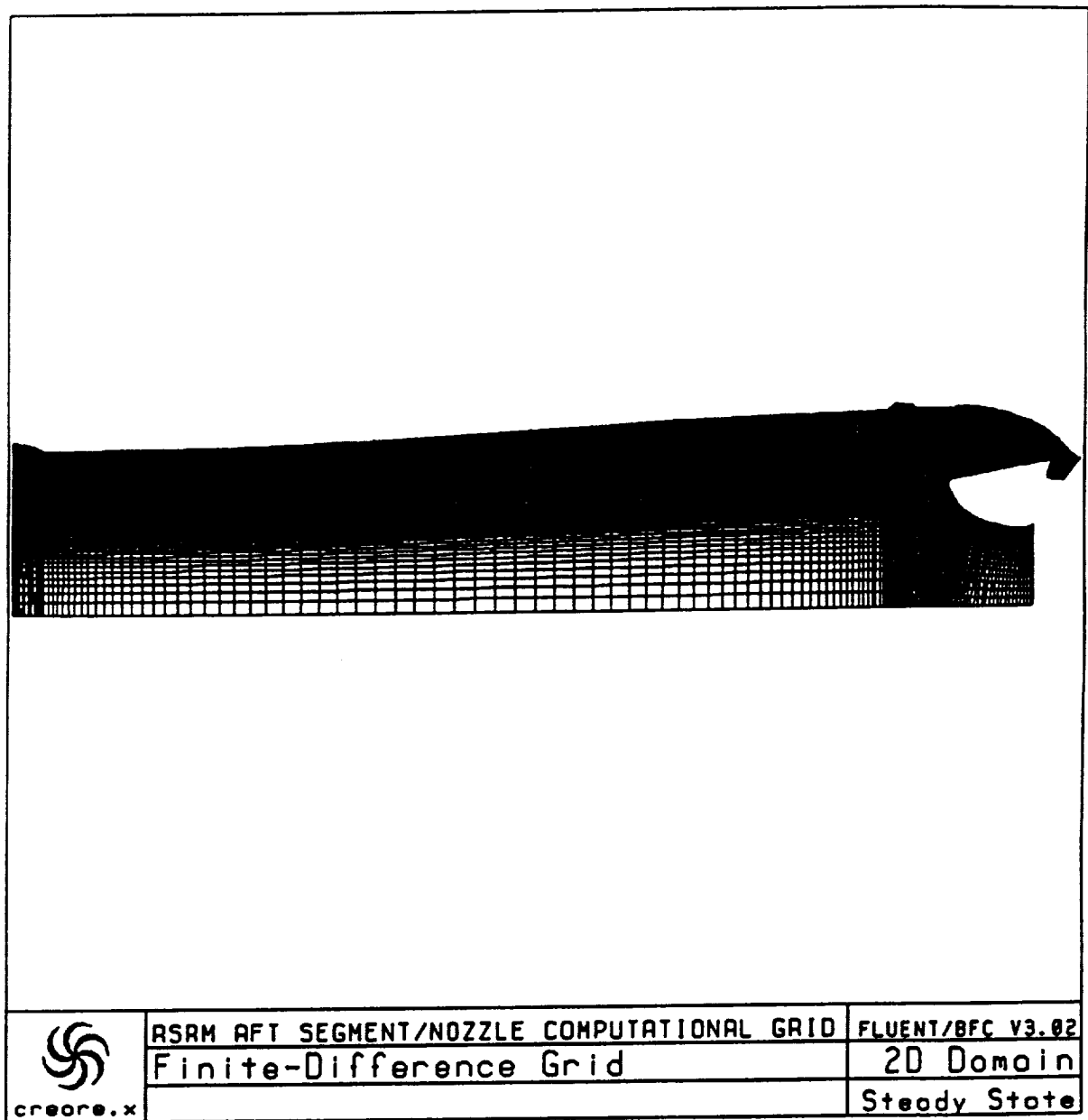


Figure 48. RSRM Aft Segment/Nozzle Geometry, No Slag



**Figure 49. RSRM Aft Segment/Nozzle Computational Grid**

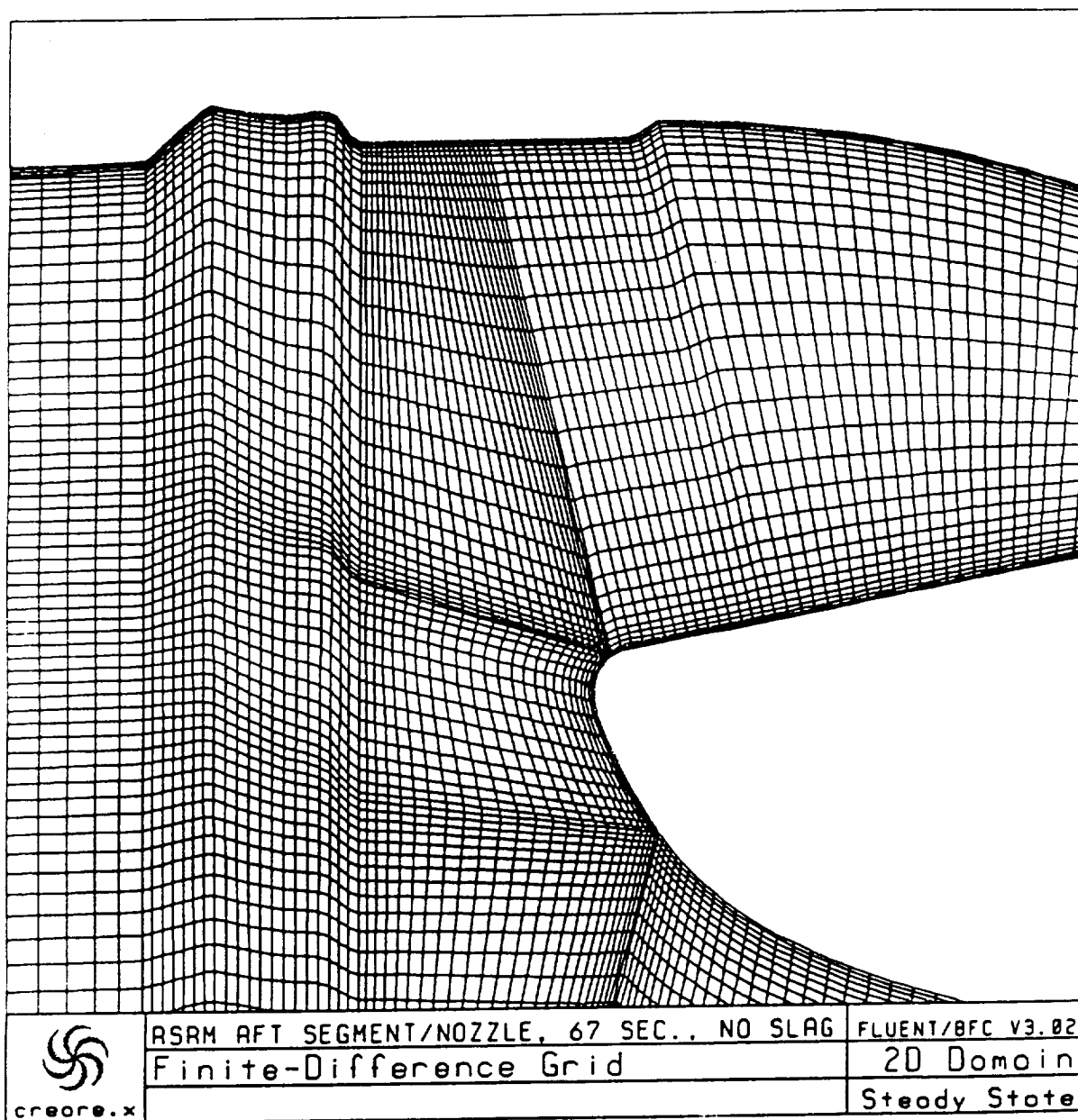


Figure 50. RSRM Aft Segment/Nozzle Region Grid, No Slag

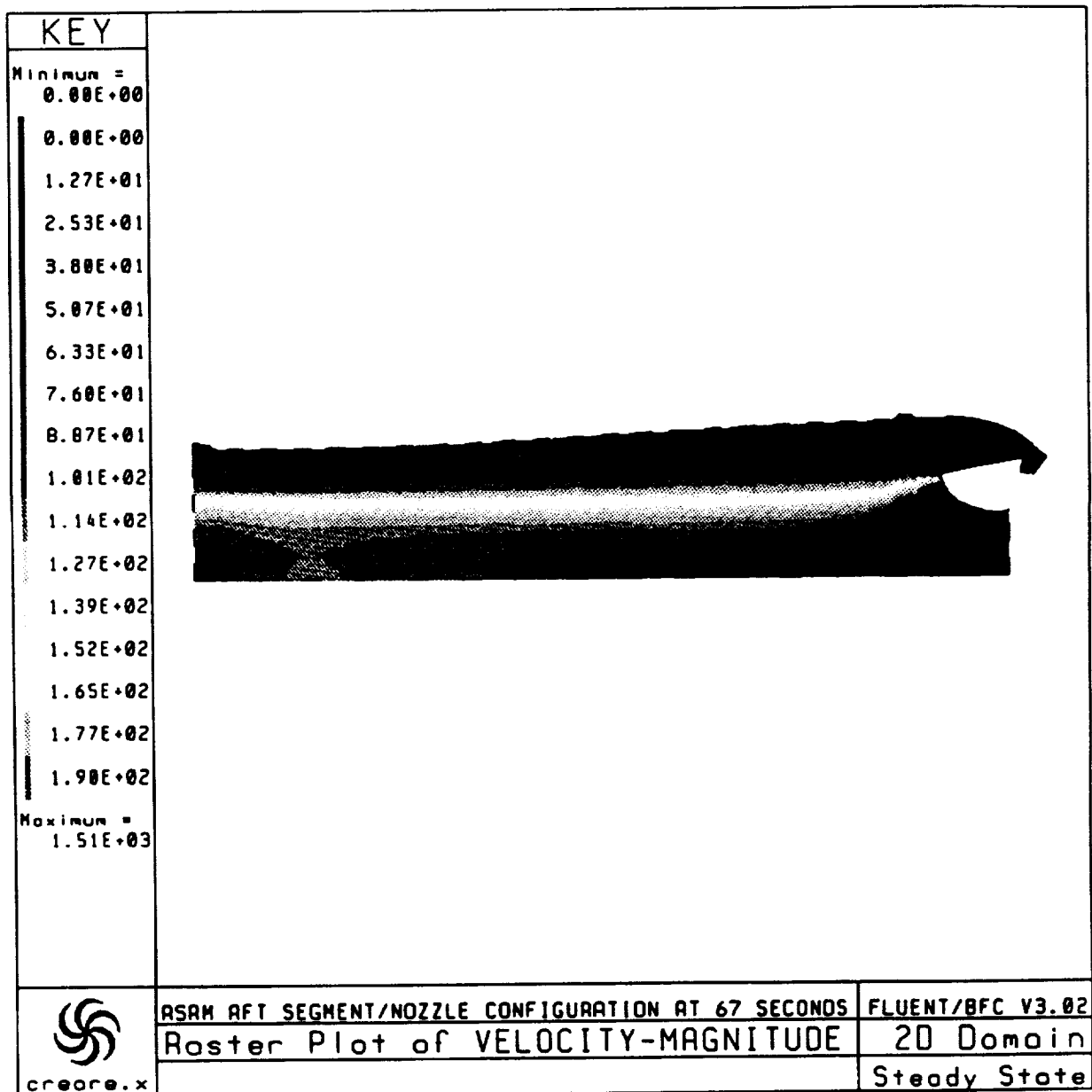


Figure 51. RSRM Aft Segment/Nozzle Velocity Magnitudes

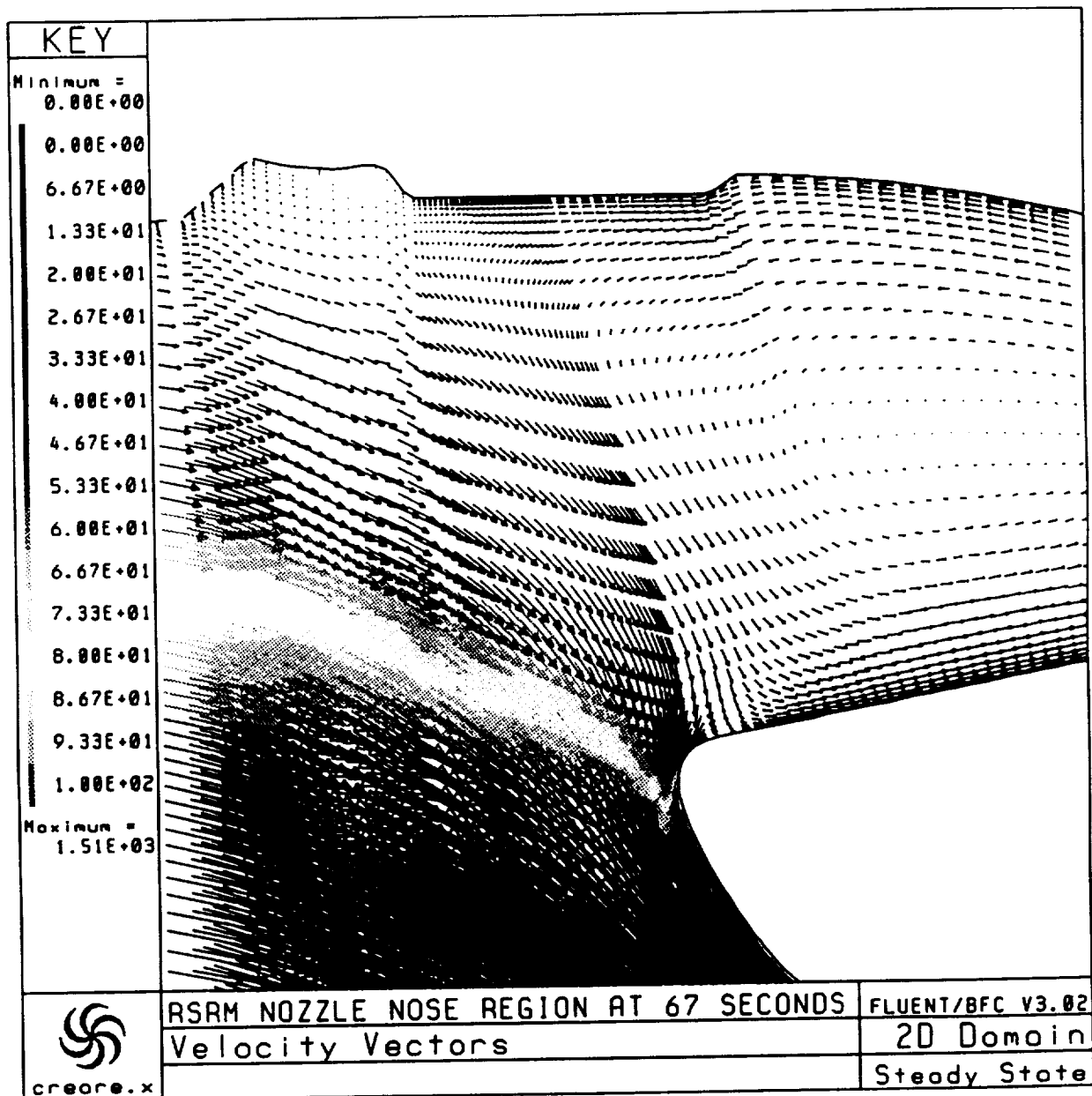
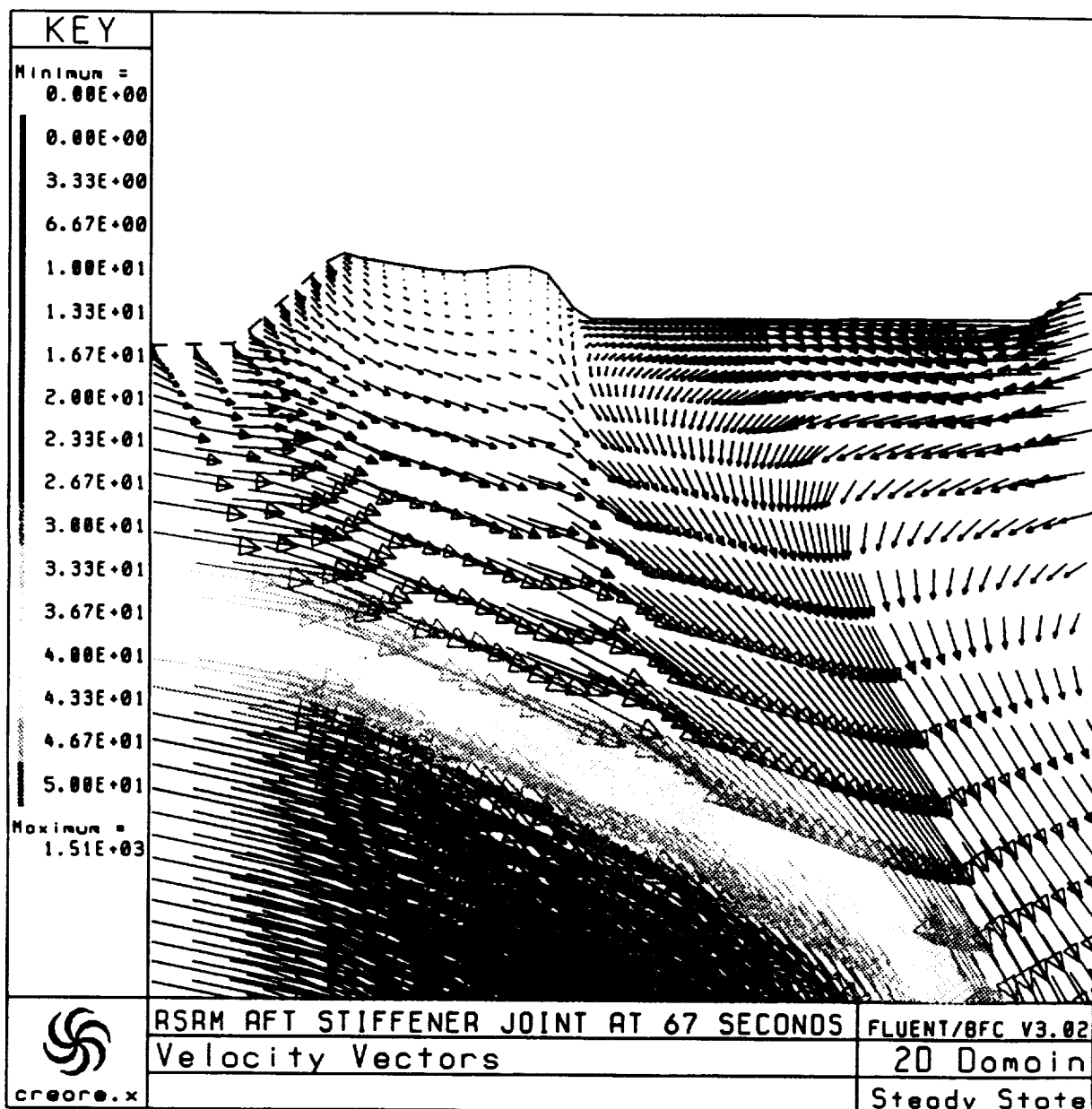


Figure 52. RSRM Flow Field Velocity Vectors in the Submerged Nozzle Region



**Figure 53. RSRM Flow Field Velocity vectors Around the Aft Dome-Stiffener Joint**

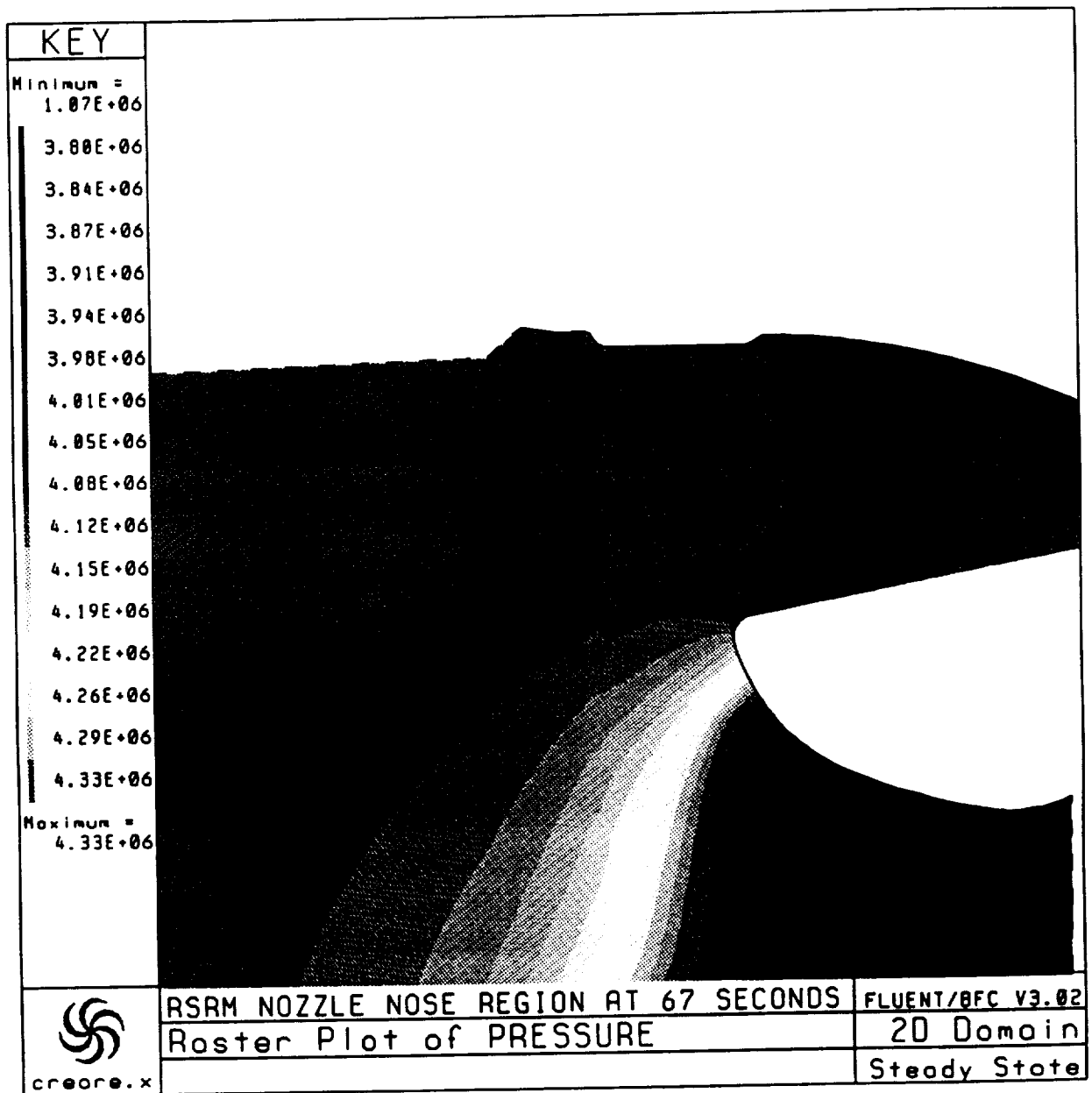
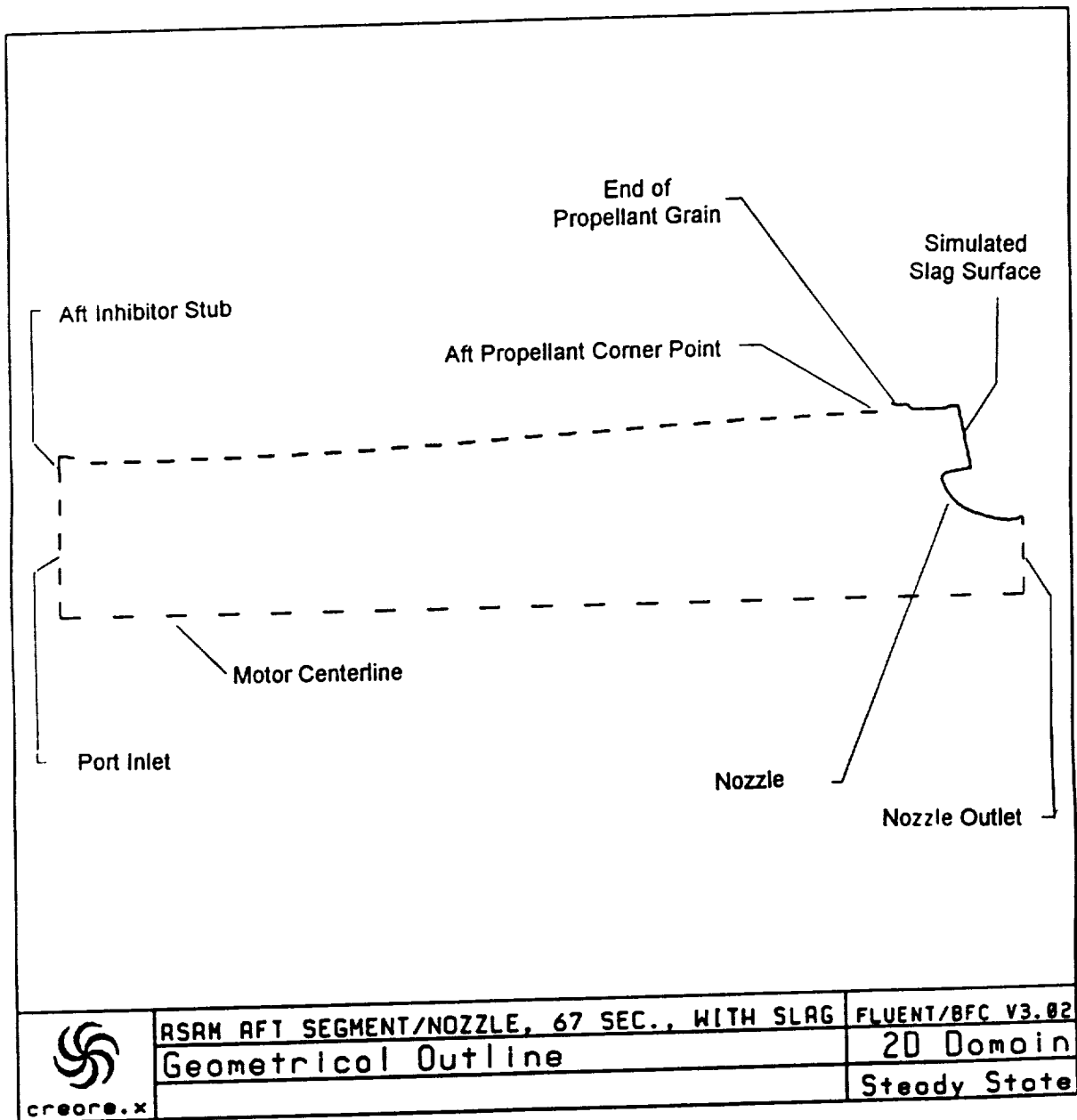
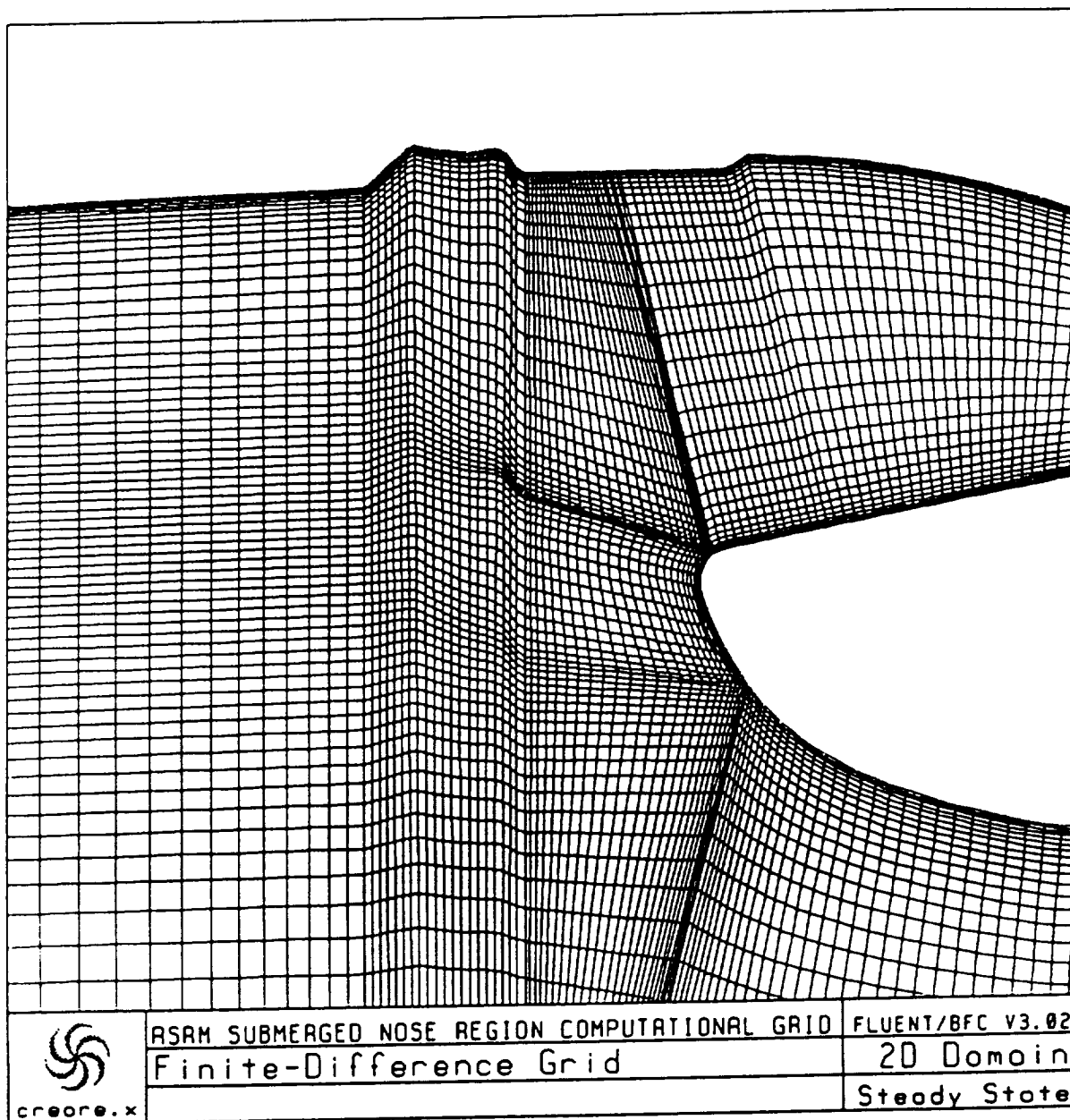


Figure 54. RSRM Pressure Field in the Submerged Nozzle Region



**Figure 55. RSRM Aft Segment/Nozzle Geometry, With Slag**





**Figure 56. RSRM Computational Grid Enlargement of the Submerged Nozzle Region**

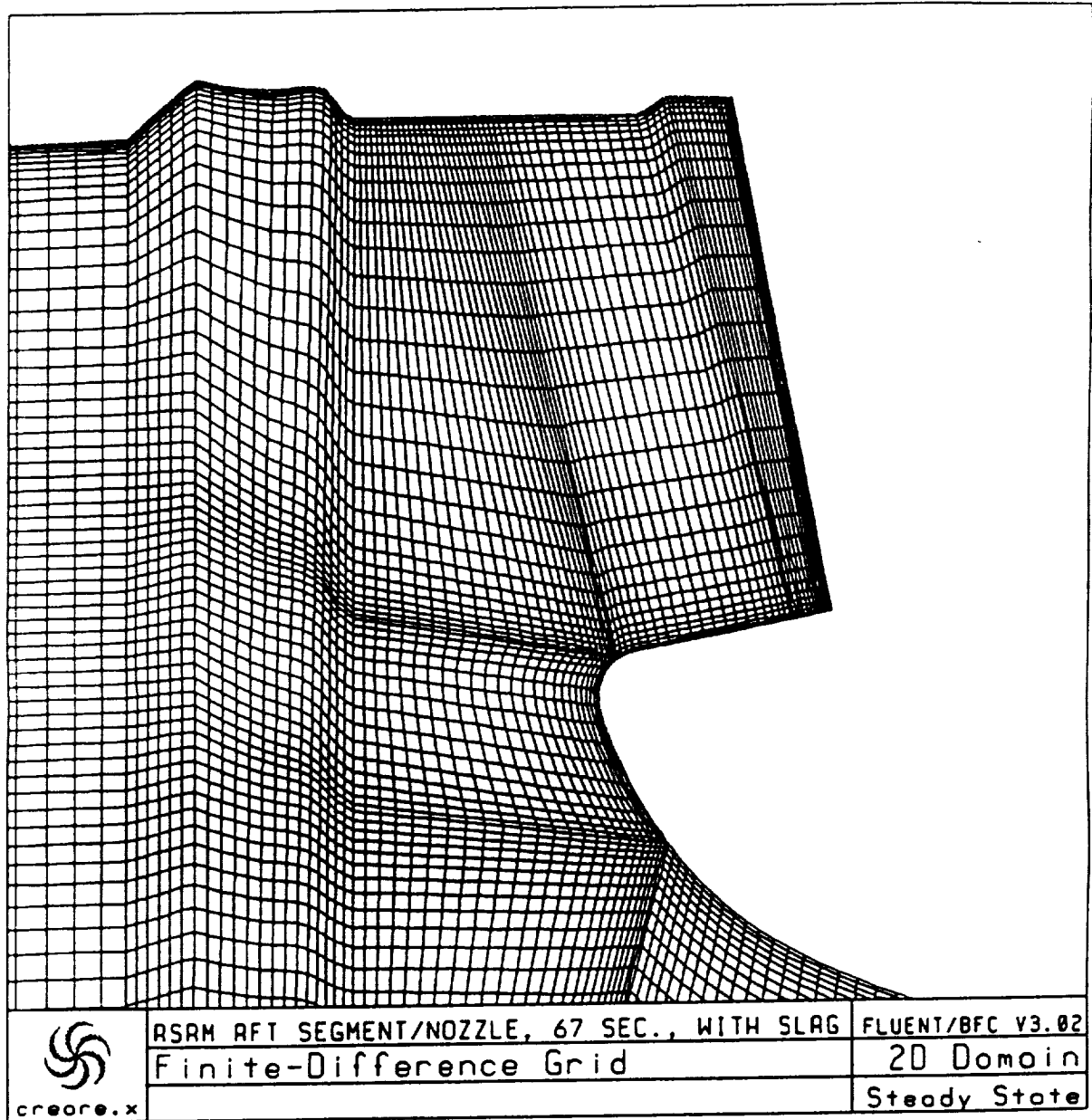


**Figure 57. RSRM Aft Segment/Nozzle Region Grid, With Slag**

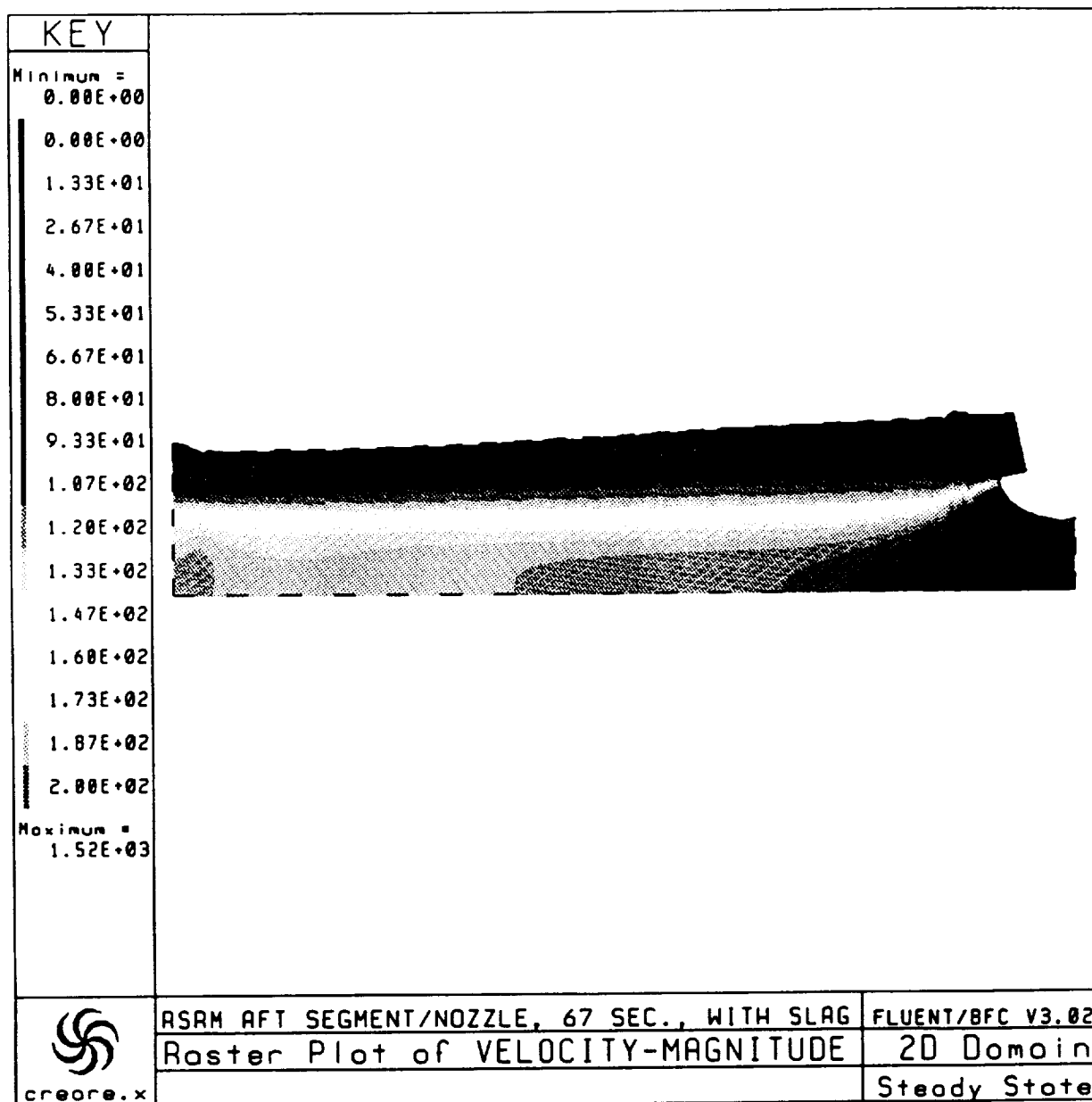


Figure 58. Color Raster Plot of Velocity Magnitude in the RSRM Aft Segment

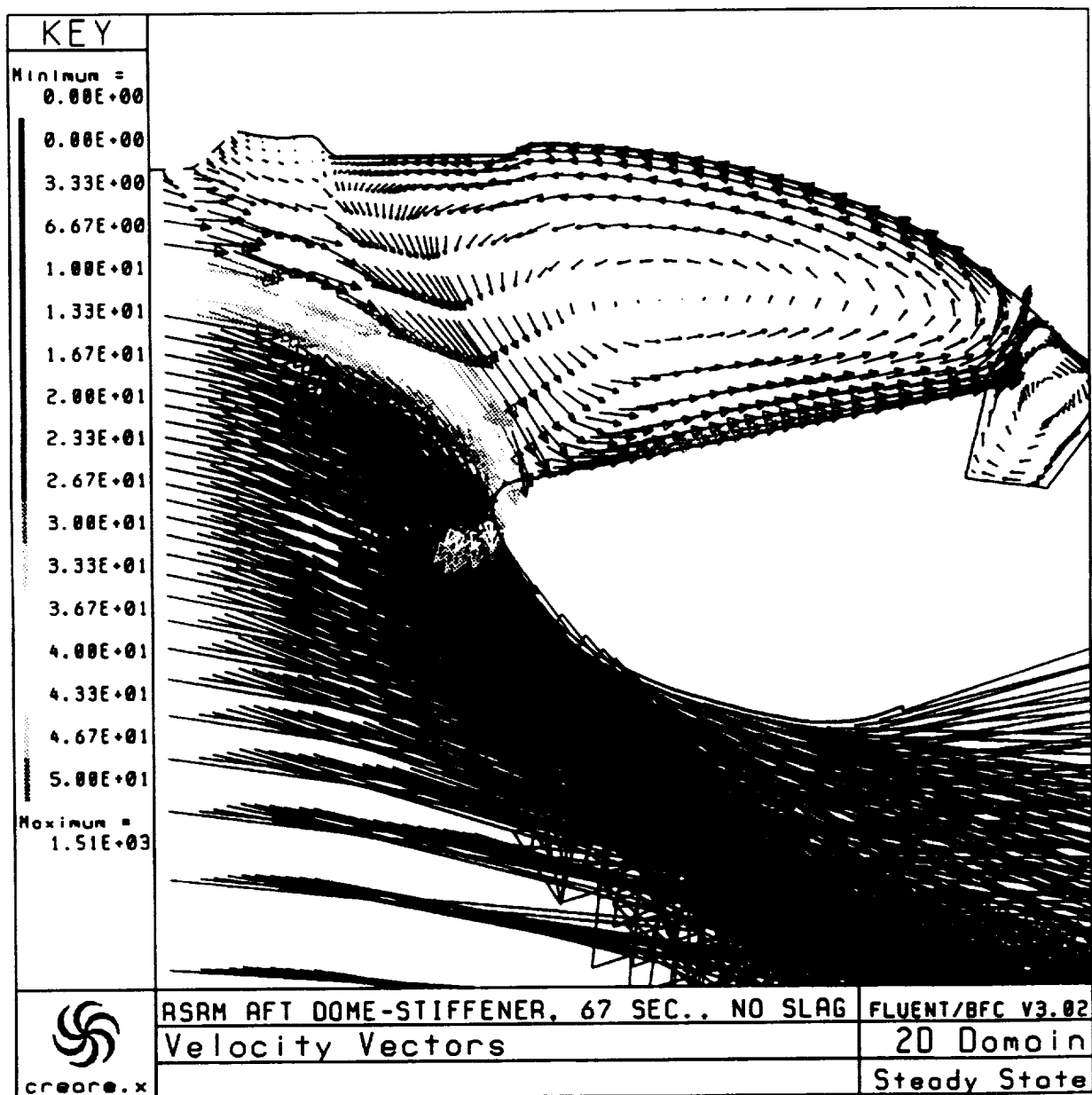


Figure 59. Velocity Field in the Nozzle Region, No Slag

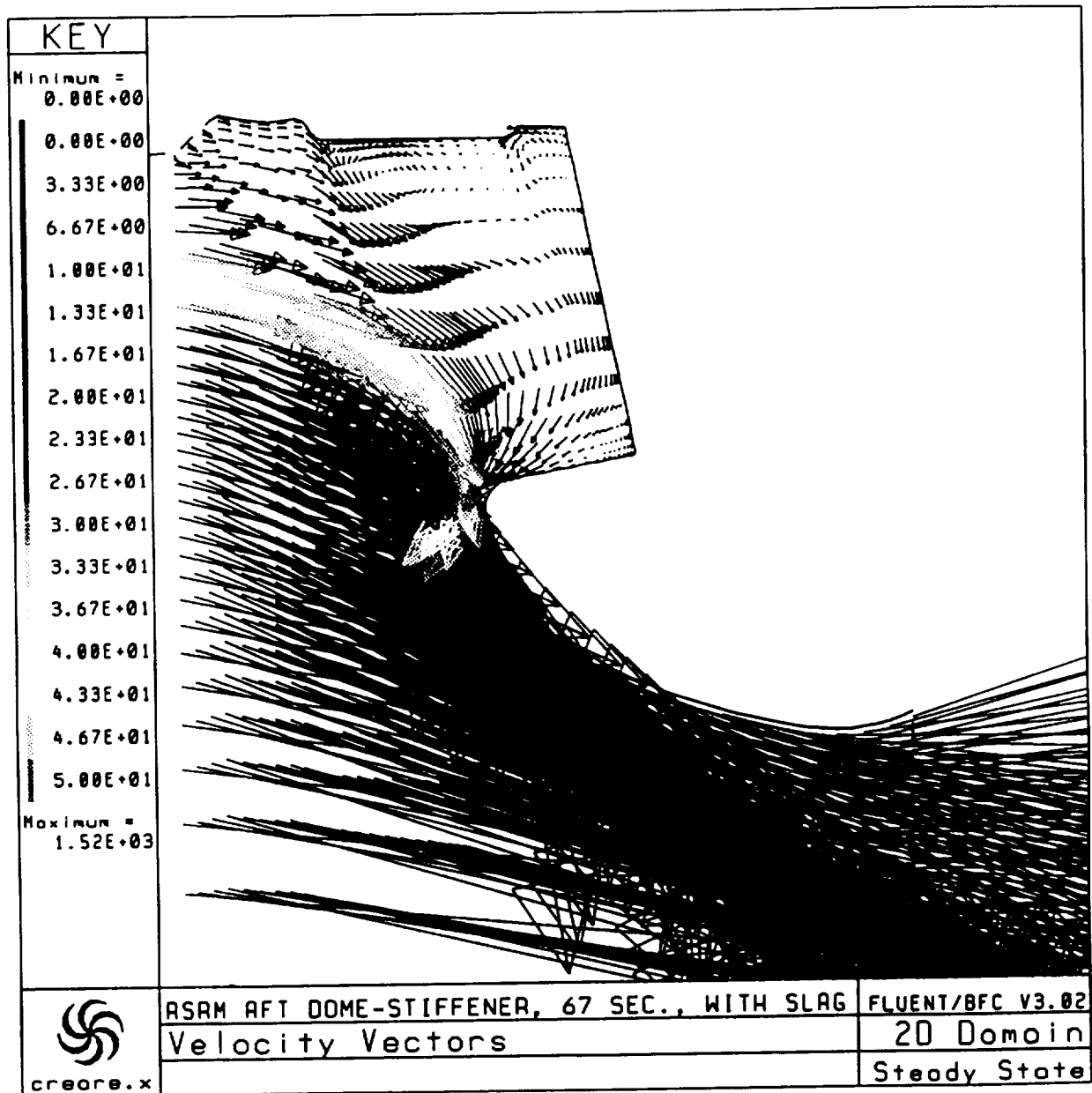


Figure 60. Velocity Field in the Nozzle Region, With Slag

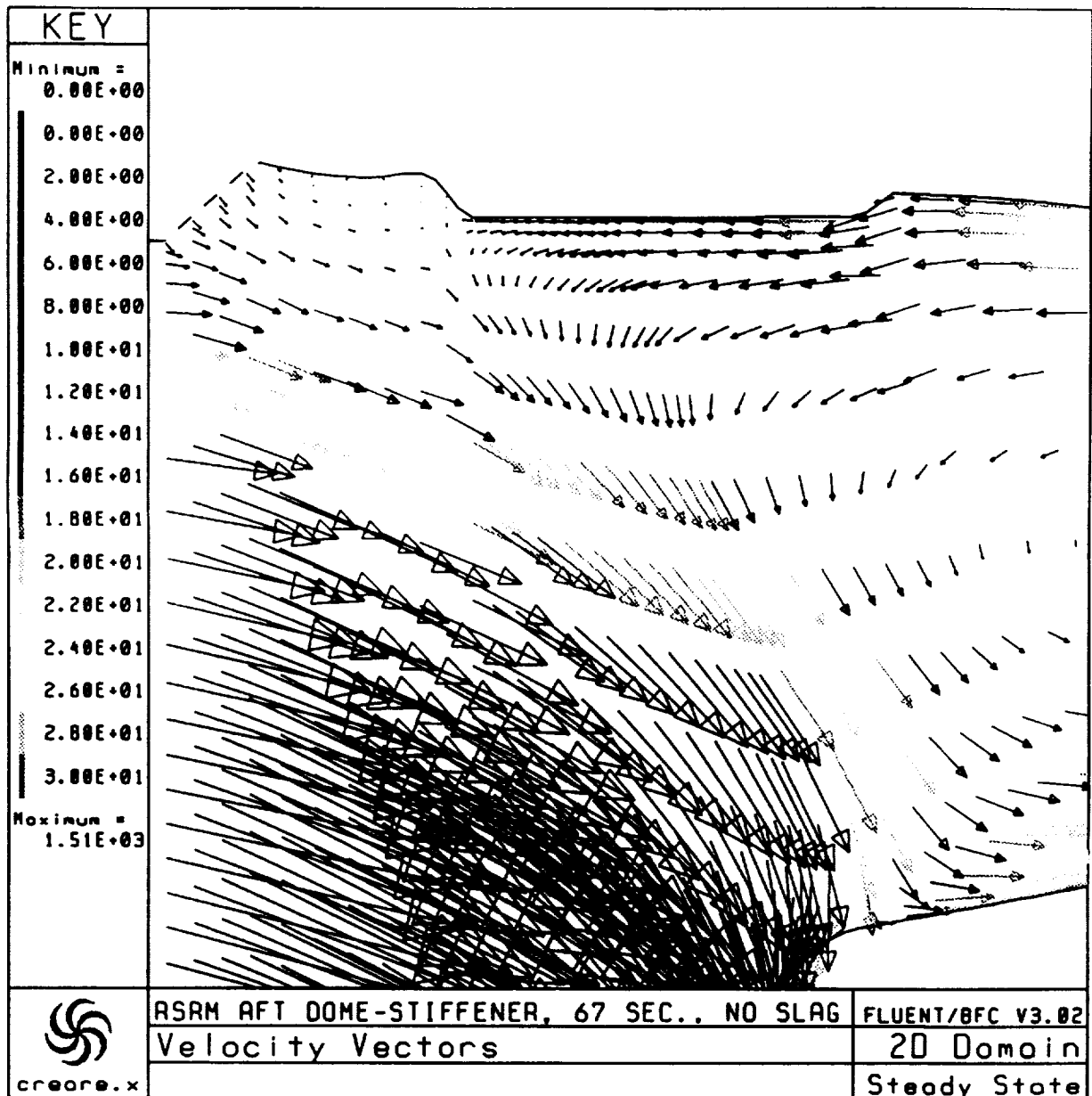


Figure 61. Velocity Field Near the Aft Dome-Stiffener, No Slag

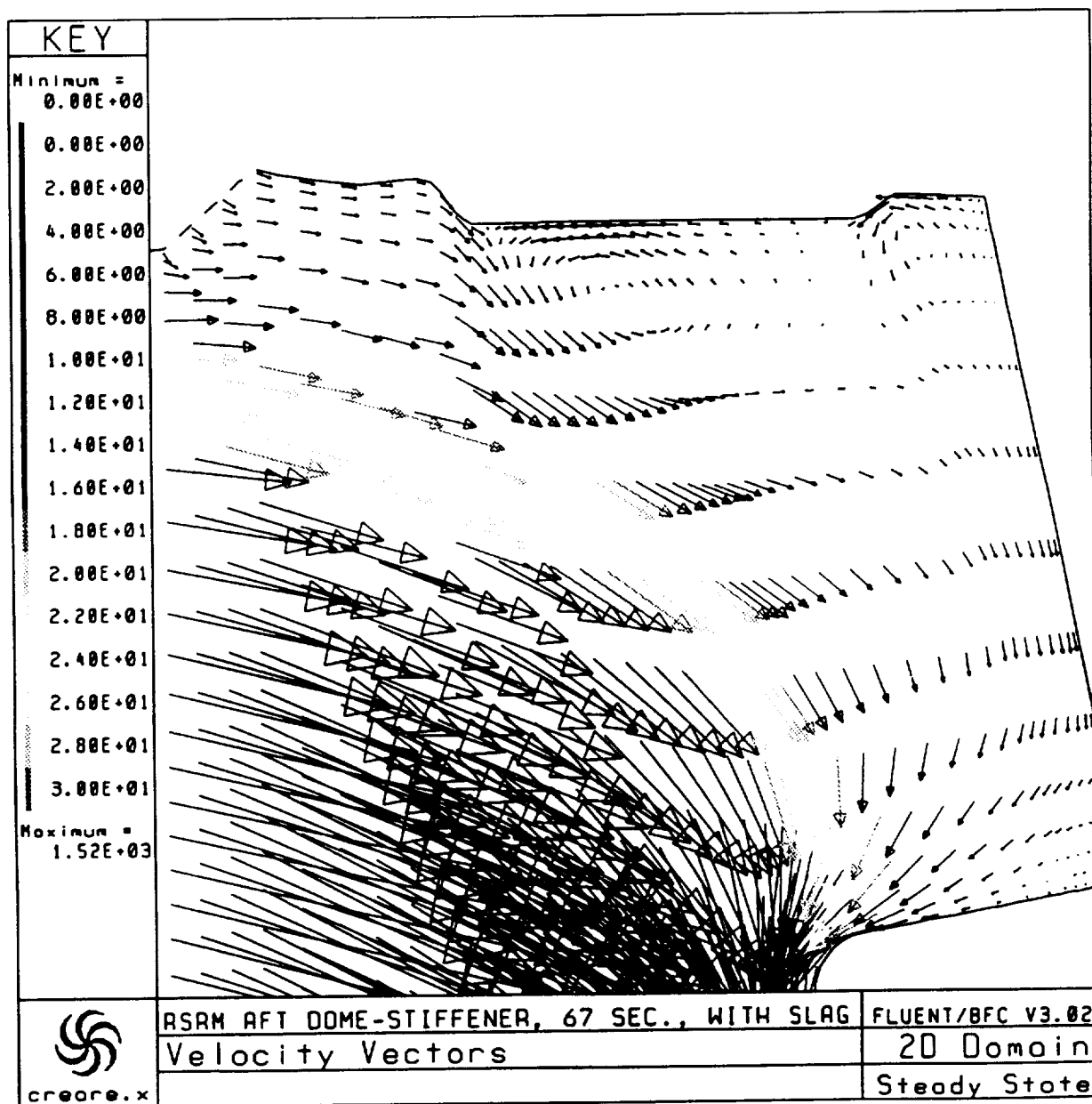
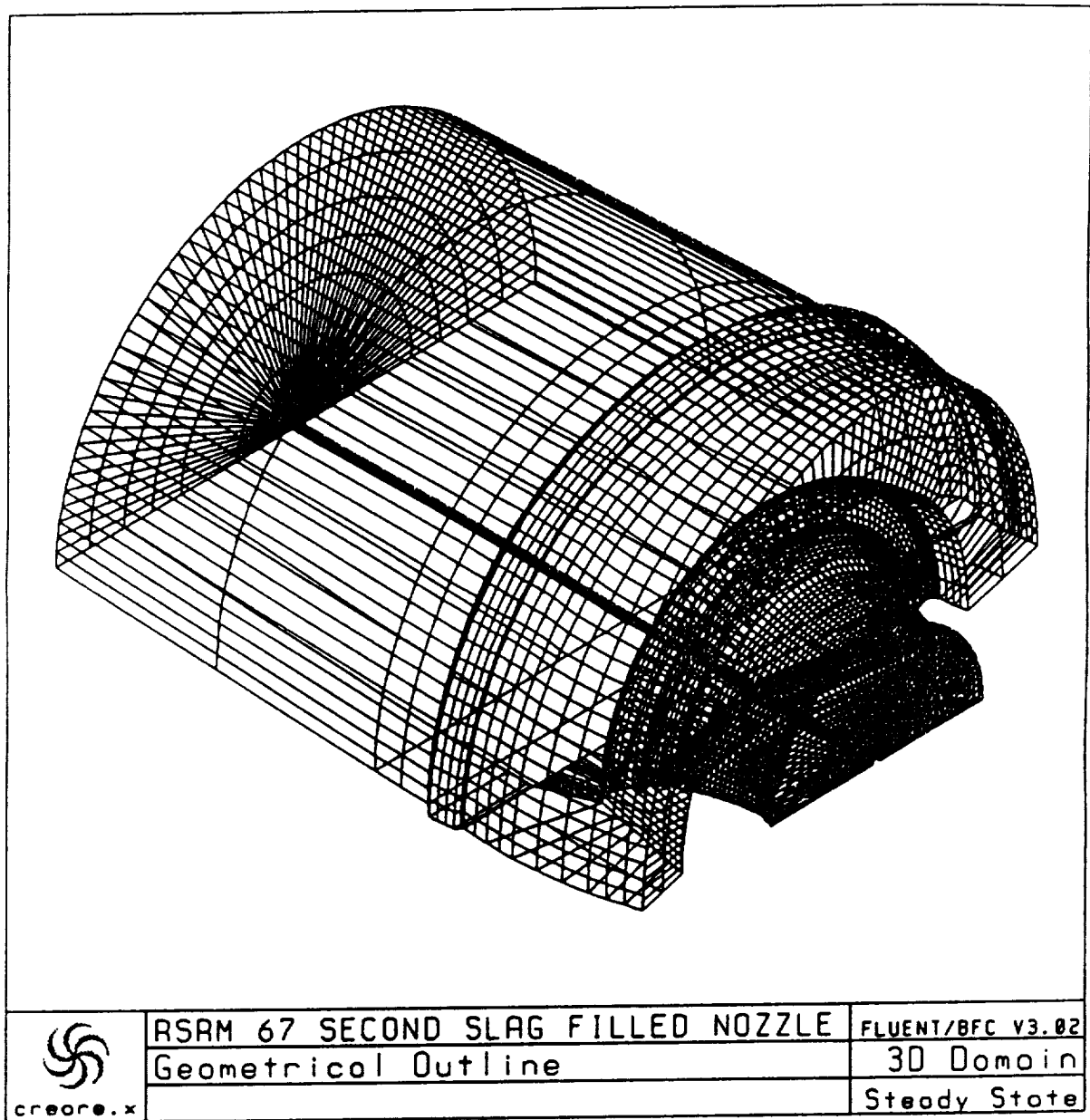


Figure 62. Velocity Field Near the Aft Dome-Stiffener, With Slag



**Figure 63. Wire-Frame Geometric View of RSRM  
Aft Segment/Nozzle Problem**



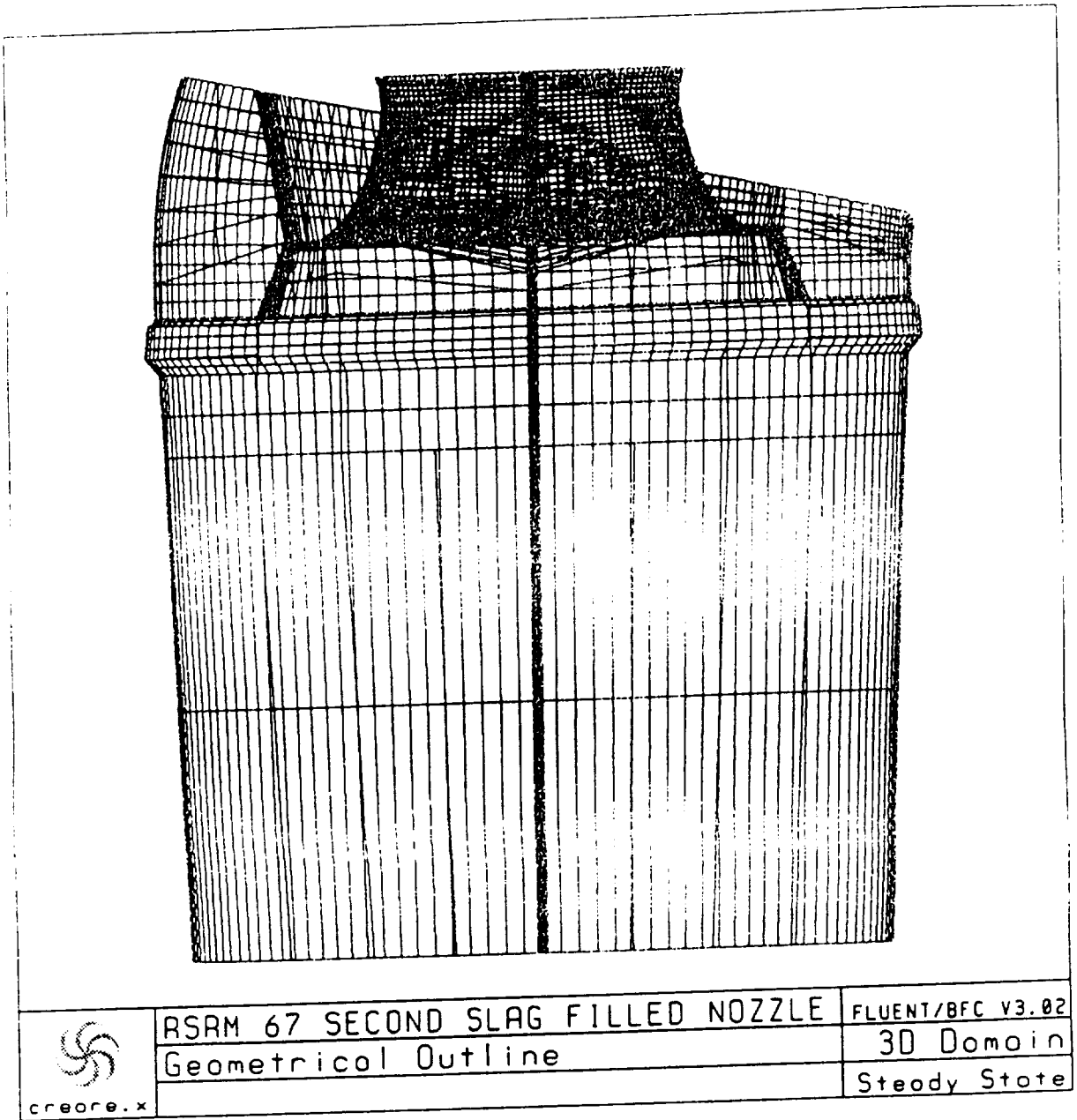


Figure 64. Top View of Wire-Frame Geometry of RSRM Aft Segment/Nozzle Problem

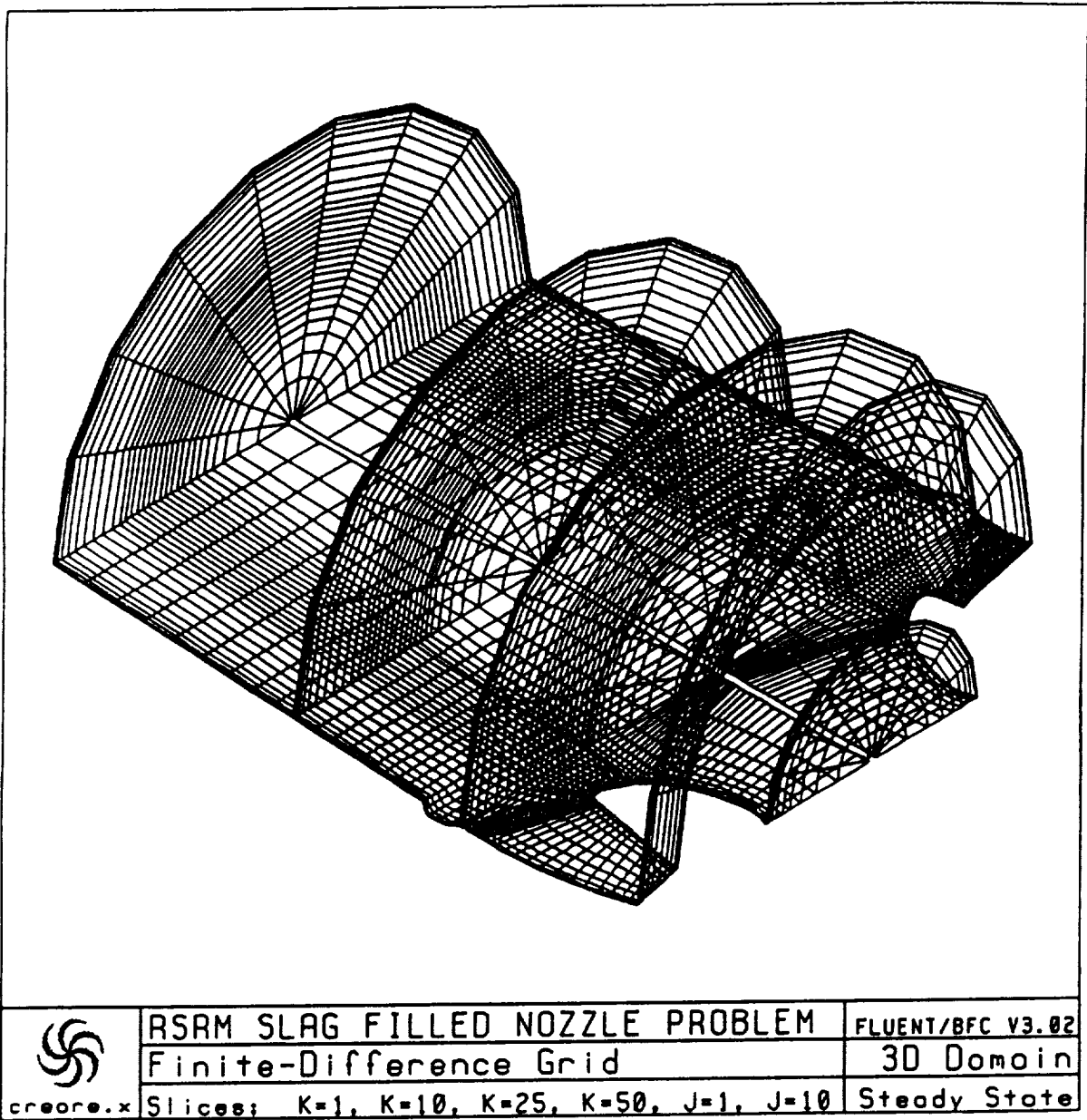
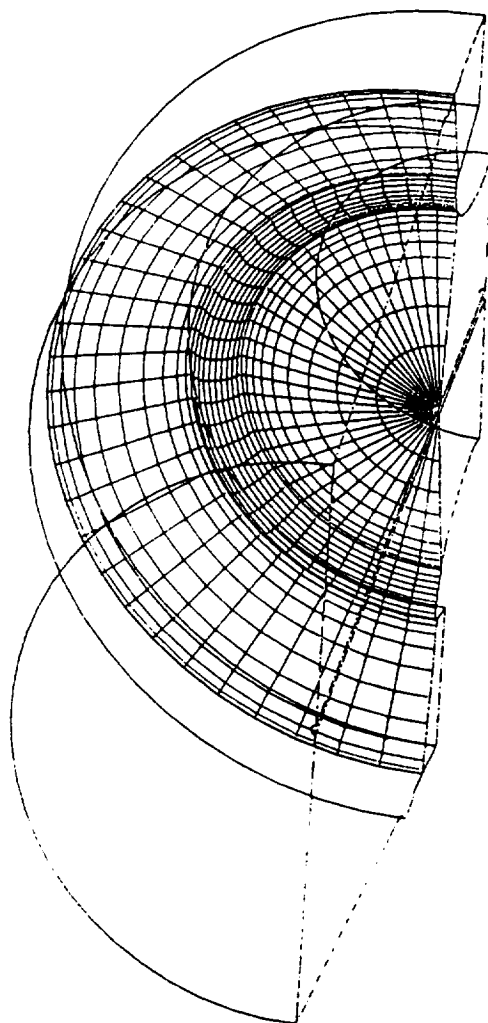


Figure 65. RSRM Aft Segment/Nozzle Coarse Grid



RSRM 67 SEC. 6 DEG SLAG INCLINATION  
Grid ( 31 X 30 X 50 )  
Slice: K=35

Sep 13 1993  
Fluent: 4.21  
Fluent Inc.

**Figure 66. RSRM 67 Seconds, 6° Slag Inclination Angle Radial  
Circumferential Grid**

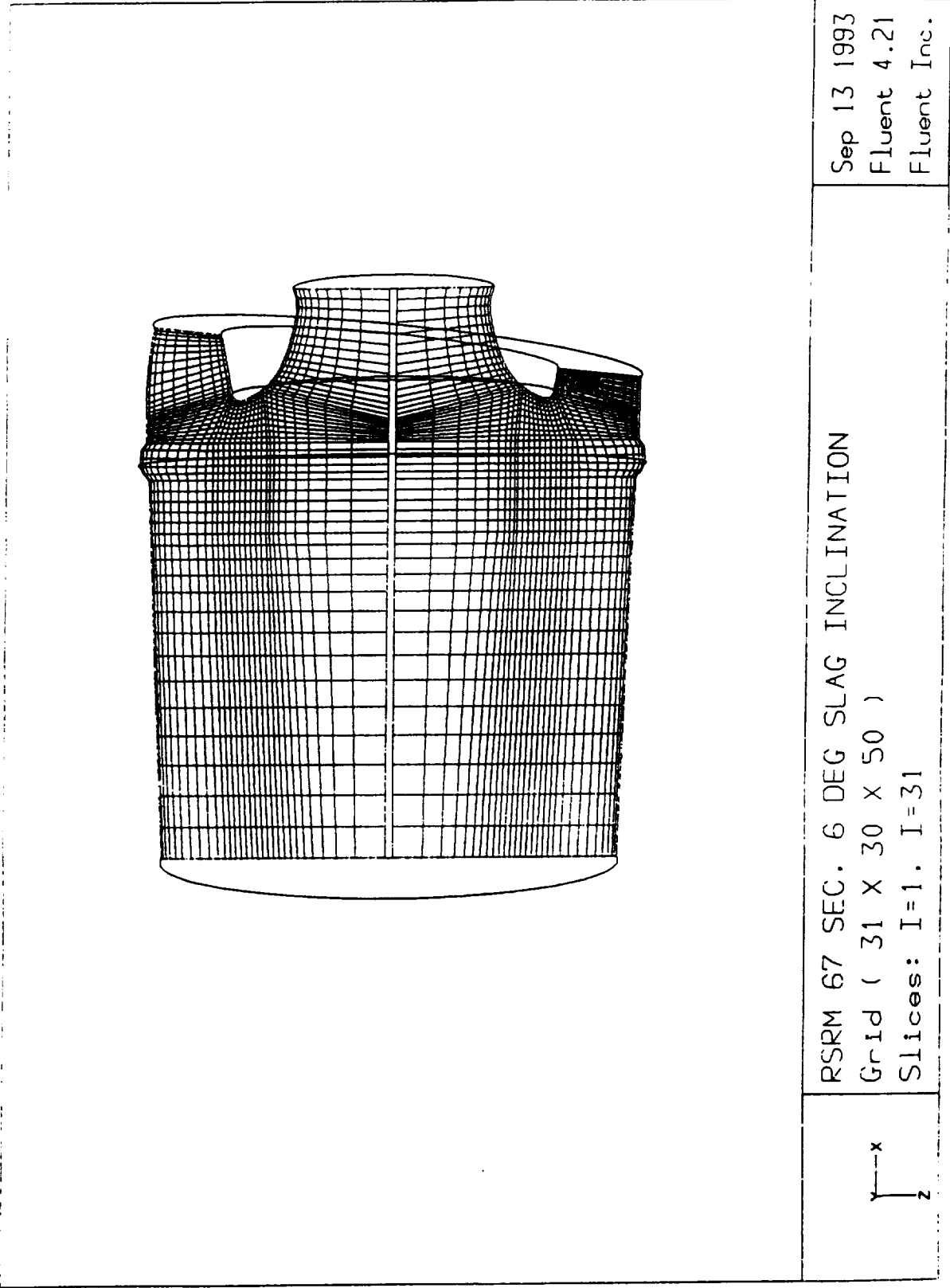


Figure 67. RSRM 67 Second, 6° Slag Inclination Angle Axial/Radial Grid

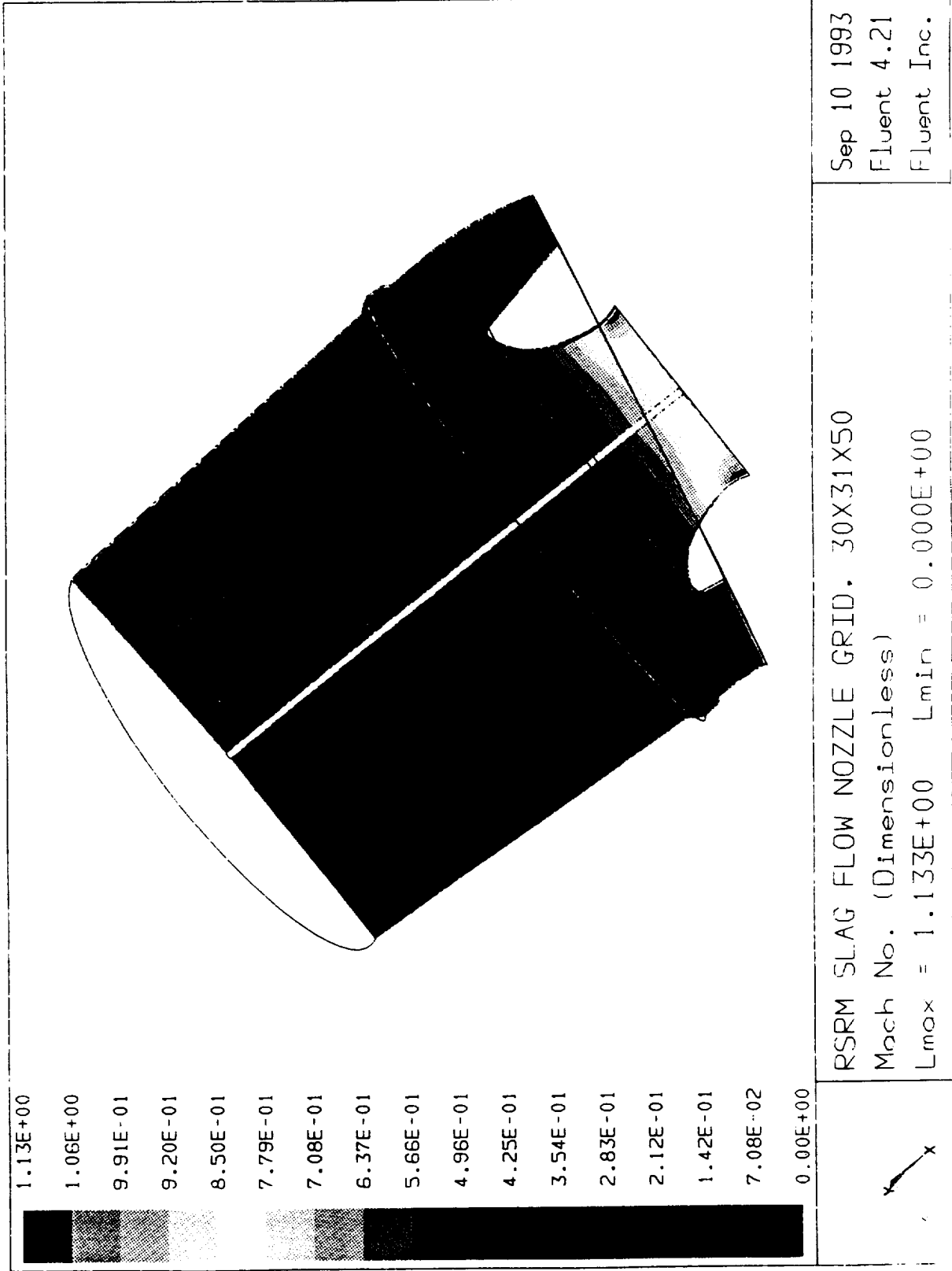
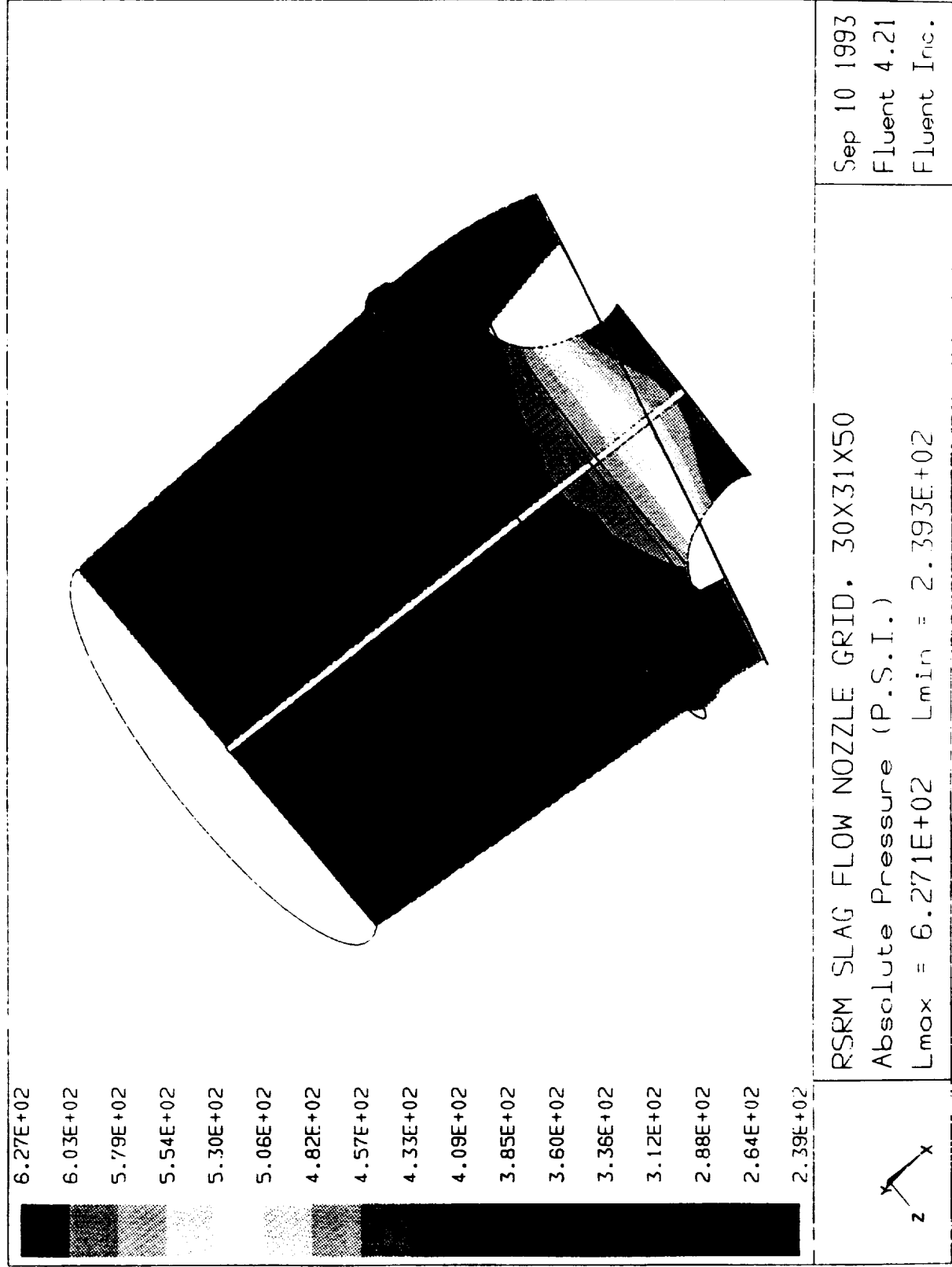


Figure 68. Mach Number Raster Plot Along the Symmetry Plane of the RSRM Aft Segment/Nozzle Configuration



**Figure 69. Pressure Field Raster Plot Along the Symmetry Plane of the RSRM Aft Segment/Nozzle Configuration**

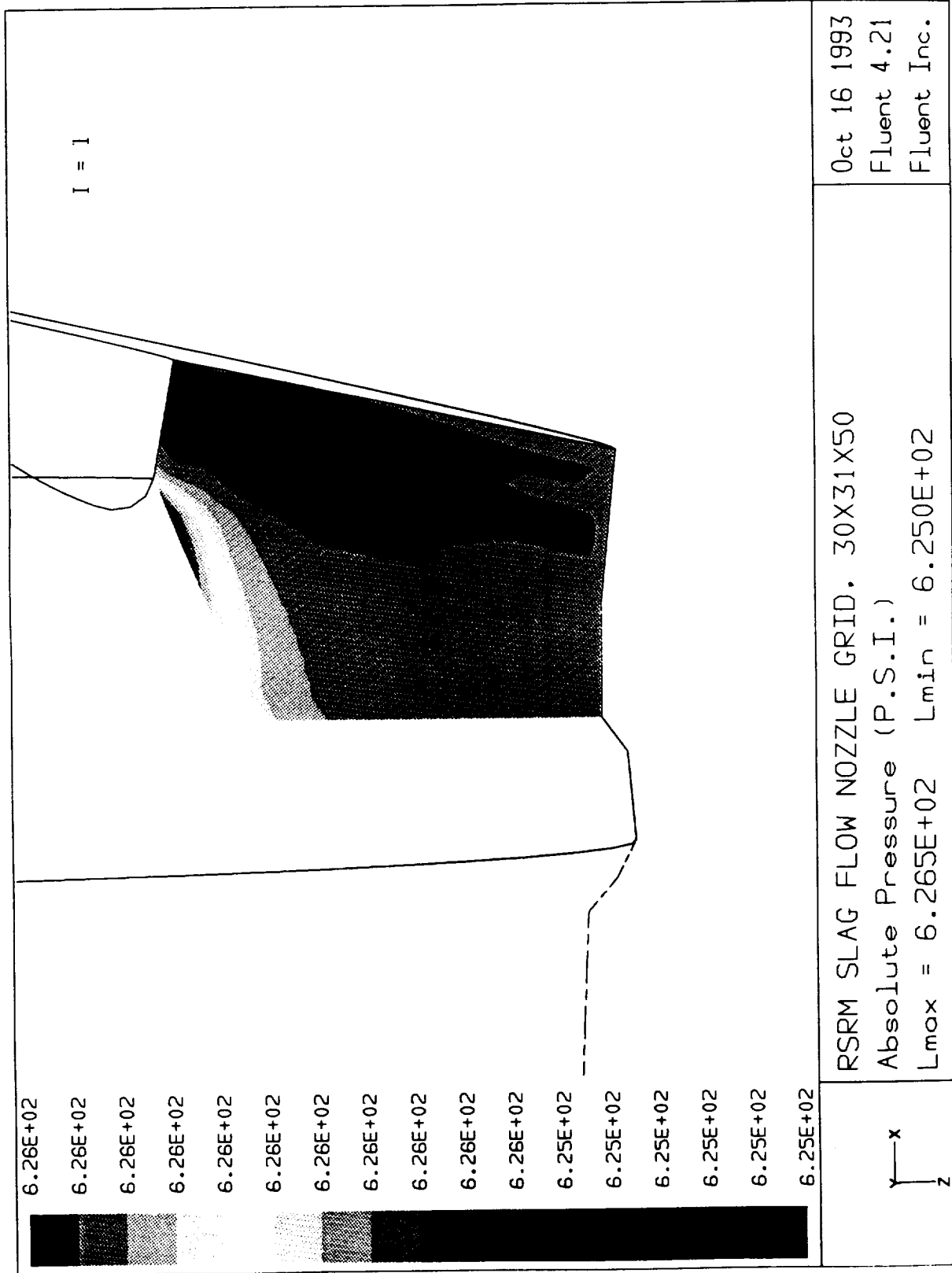


Figure 70. Filled Side Pressure Contours

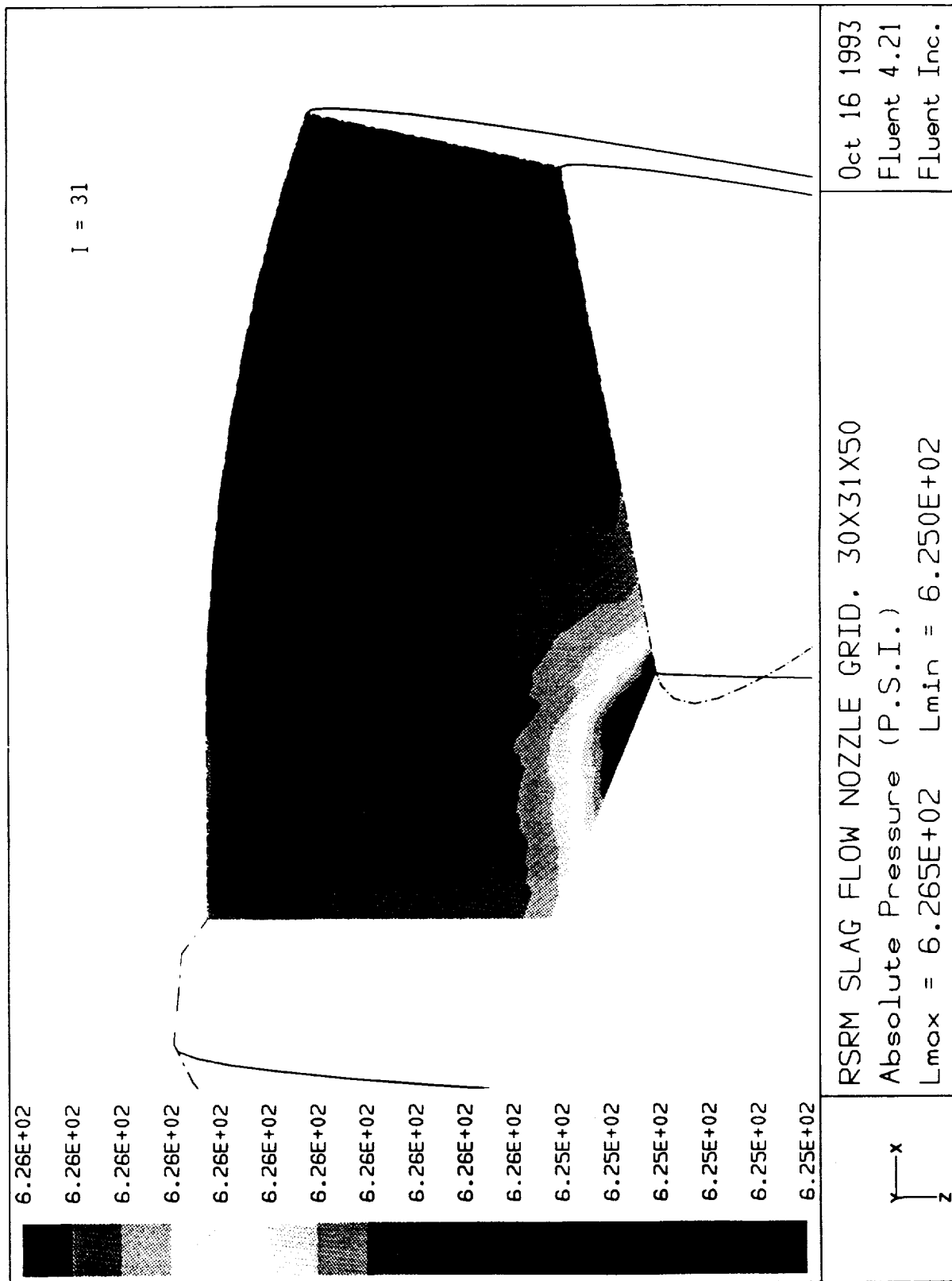


Figure 71. Recessed Side Pressure Contours



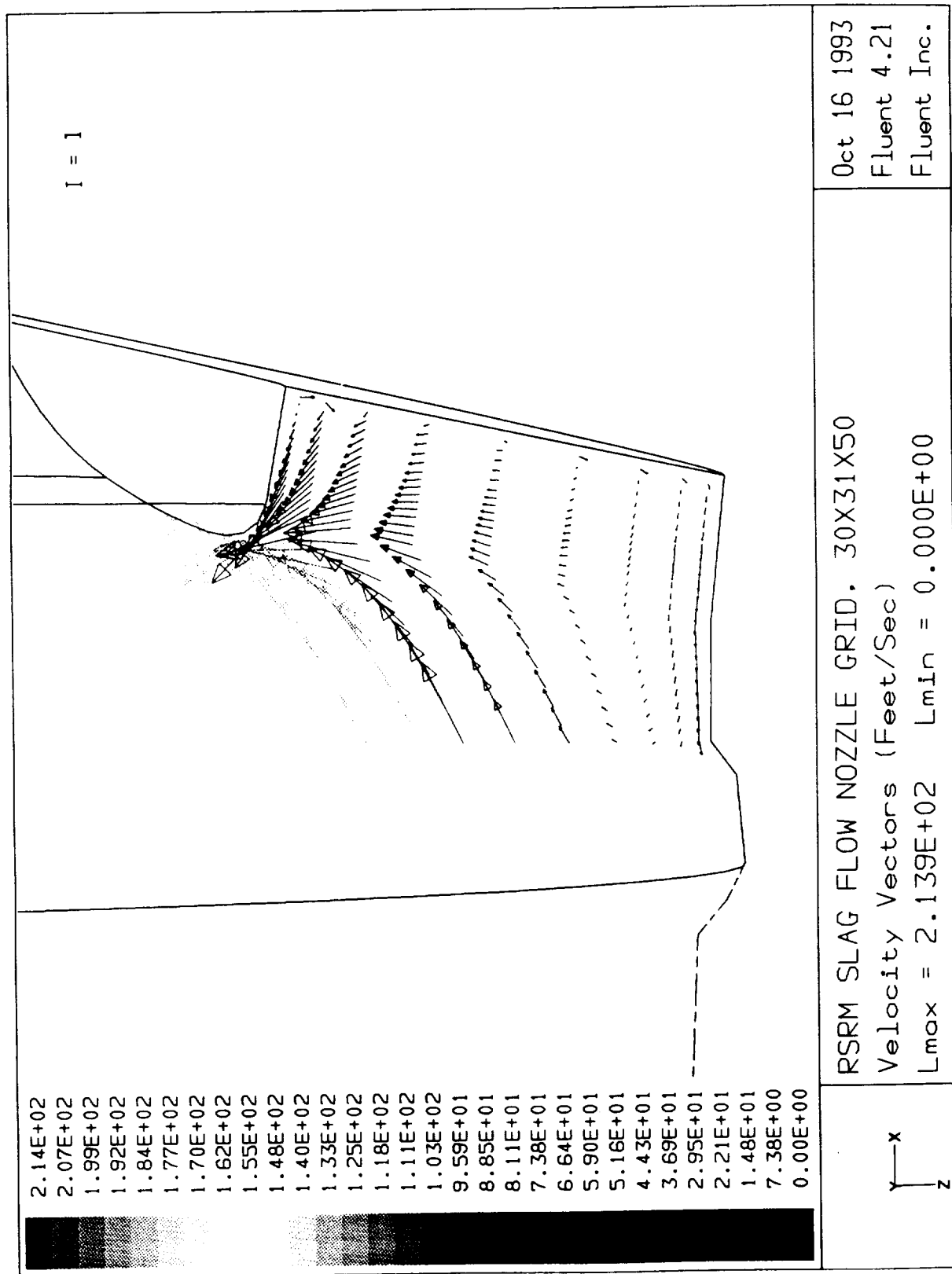


Figure 72. Filled Side Velocity Field

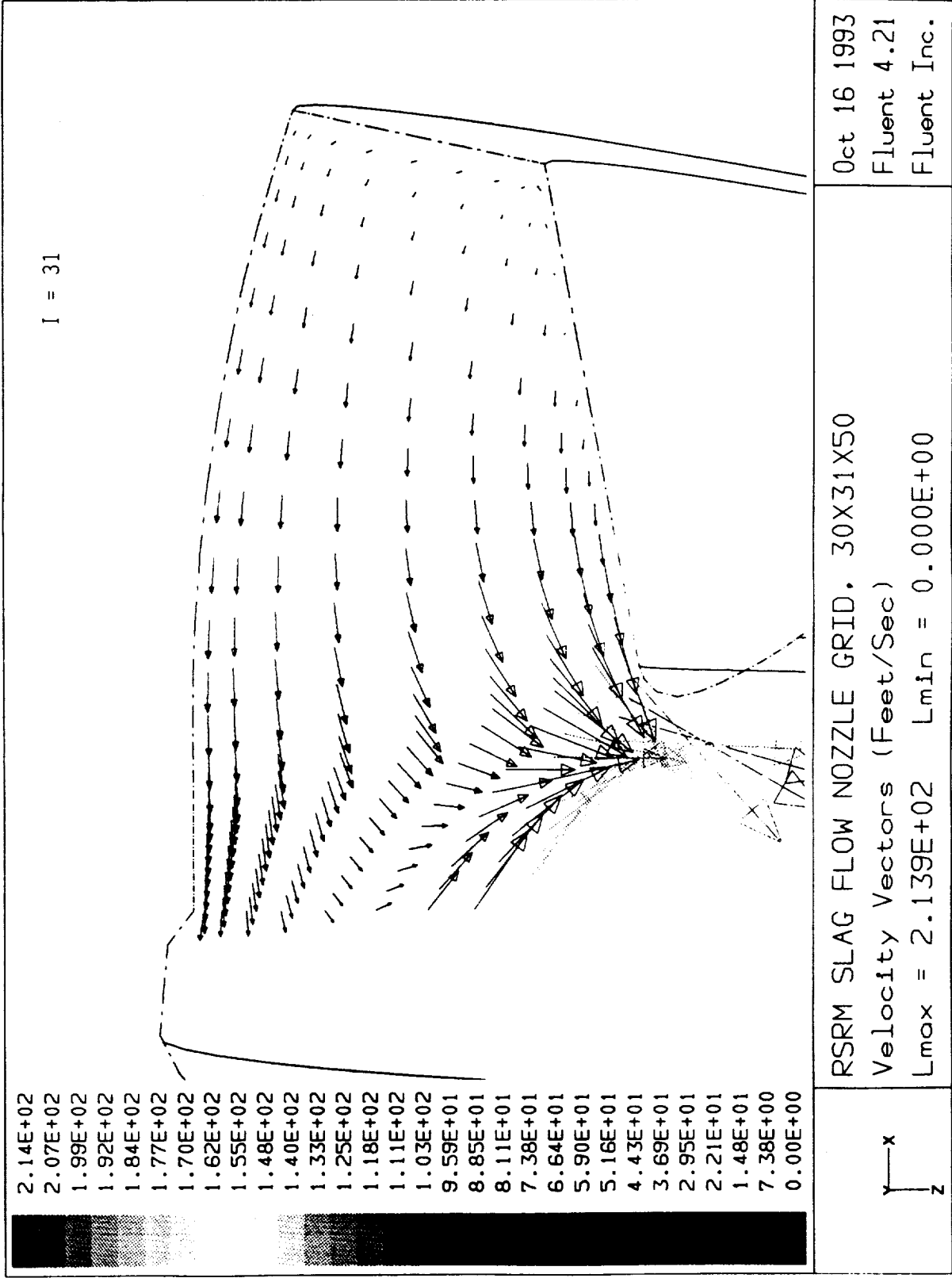


Figure 73. Recessed Side Velocity Field

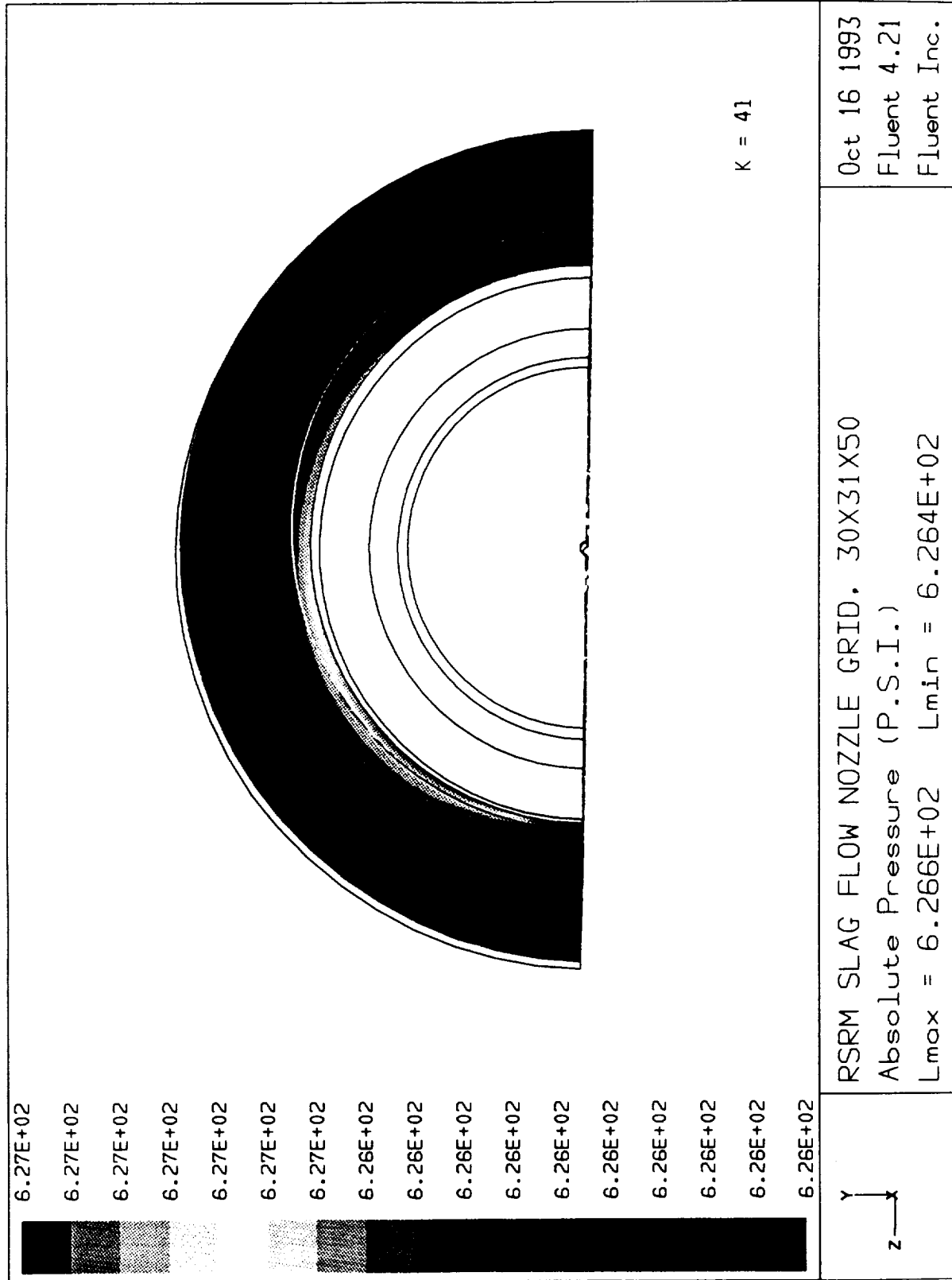


Figure 74. Circumferential Pressure Field

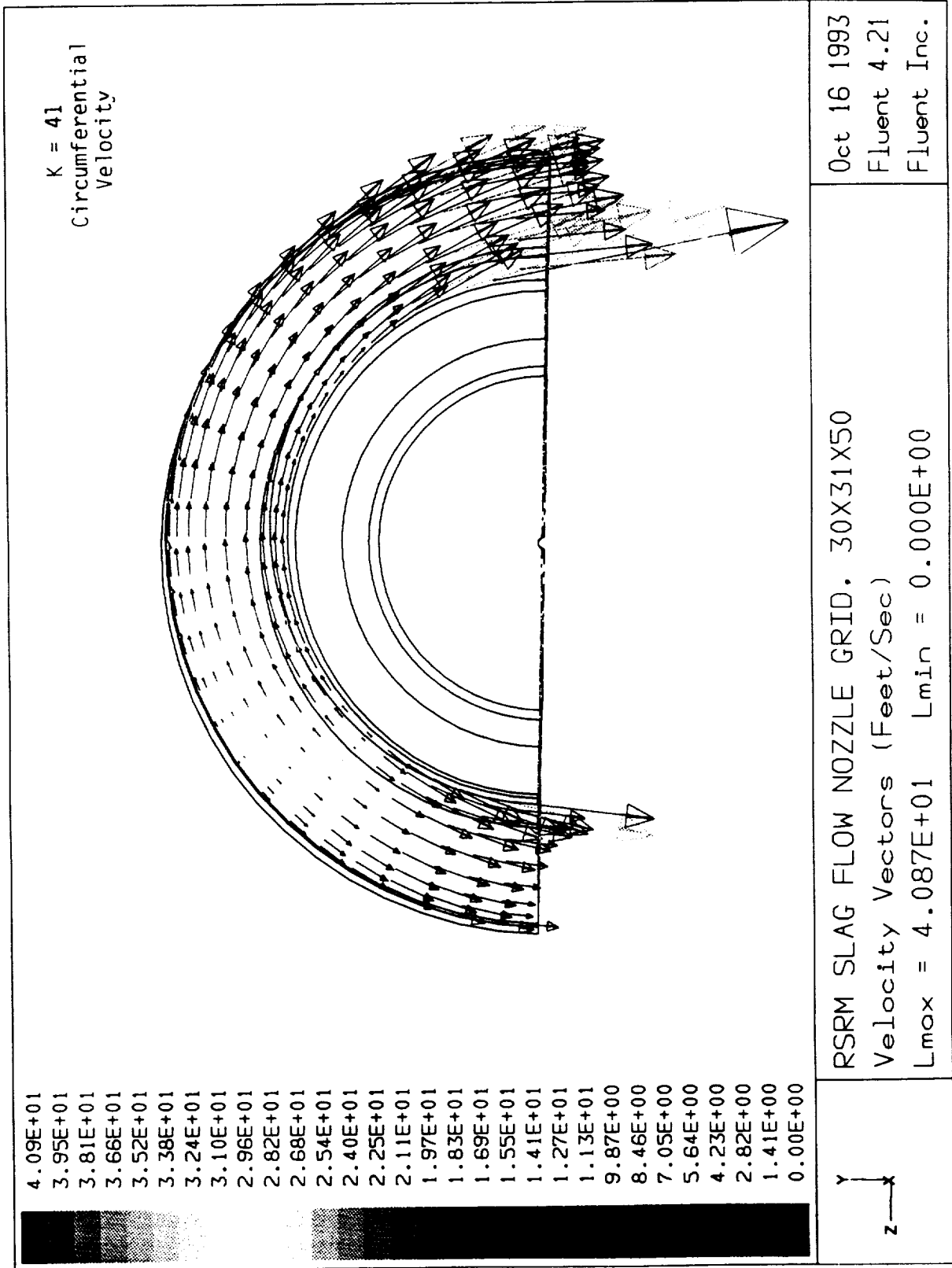
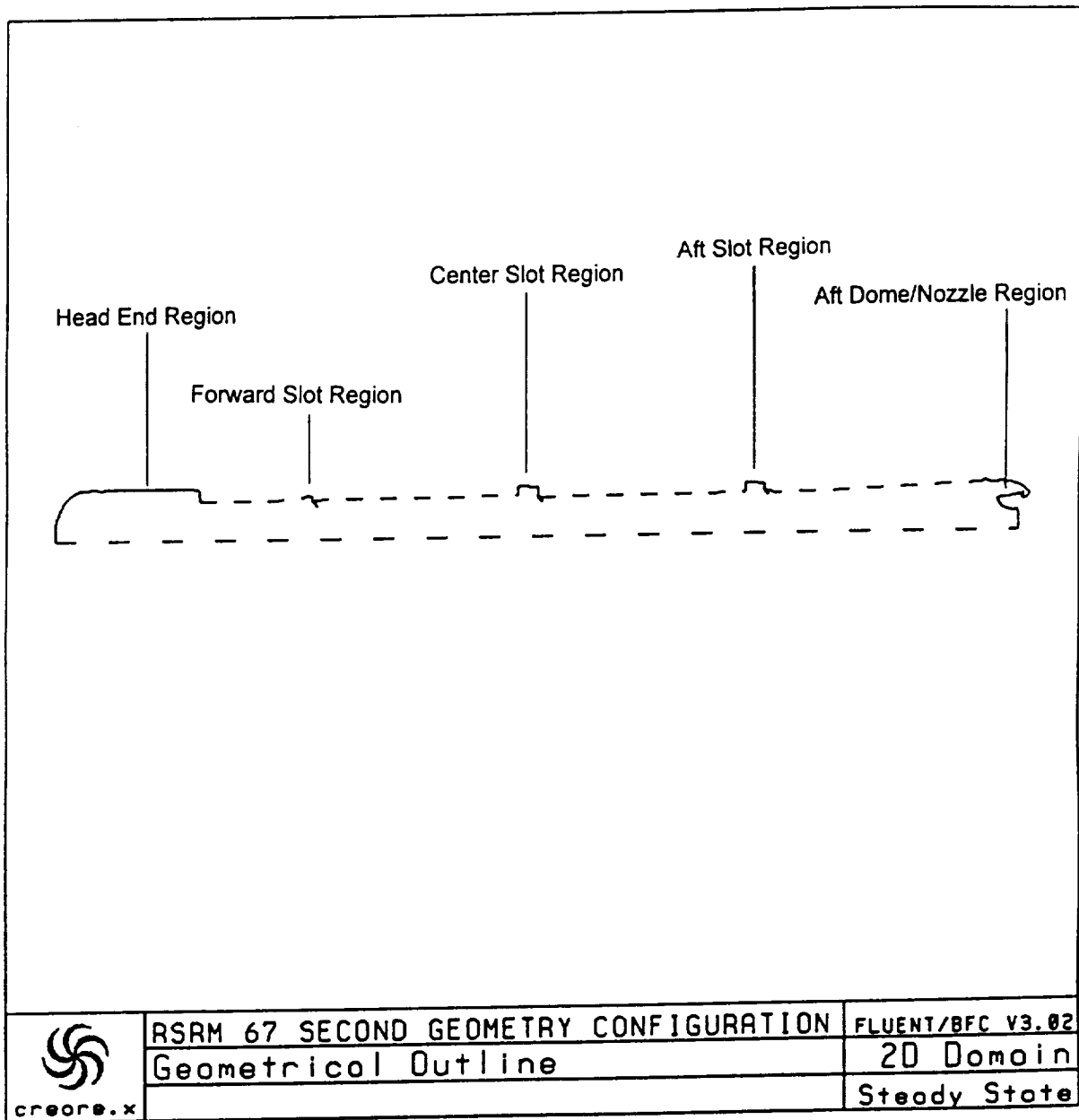
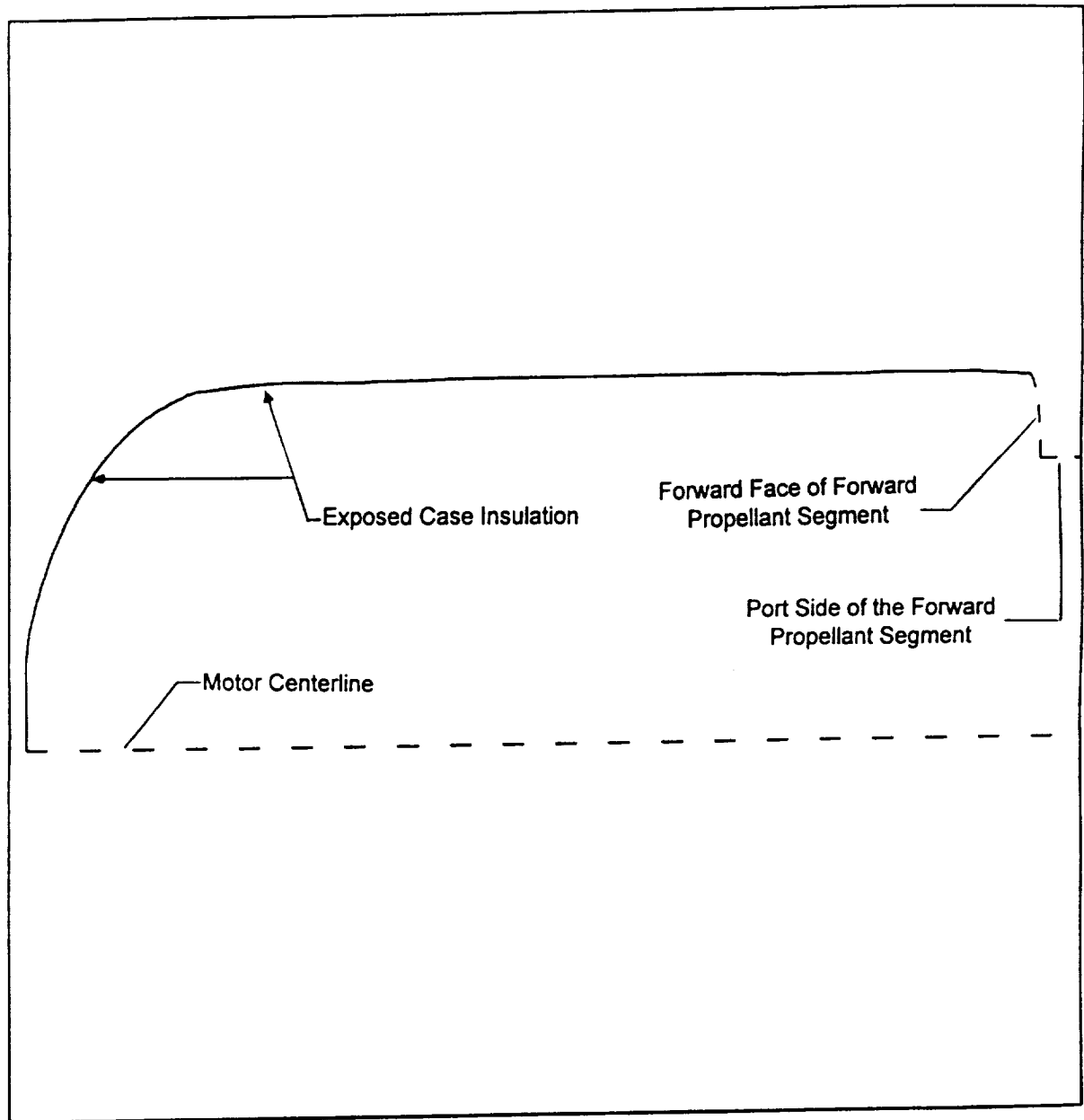


Figure 75. Circumferential Velocity Field



**Figure 76. RSRM 67 Second Motor Burntime Geometry**



**Figure 77. Head End Region of the RSRM 67 Second Burntime Motor**

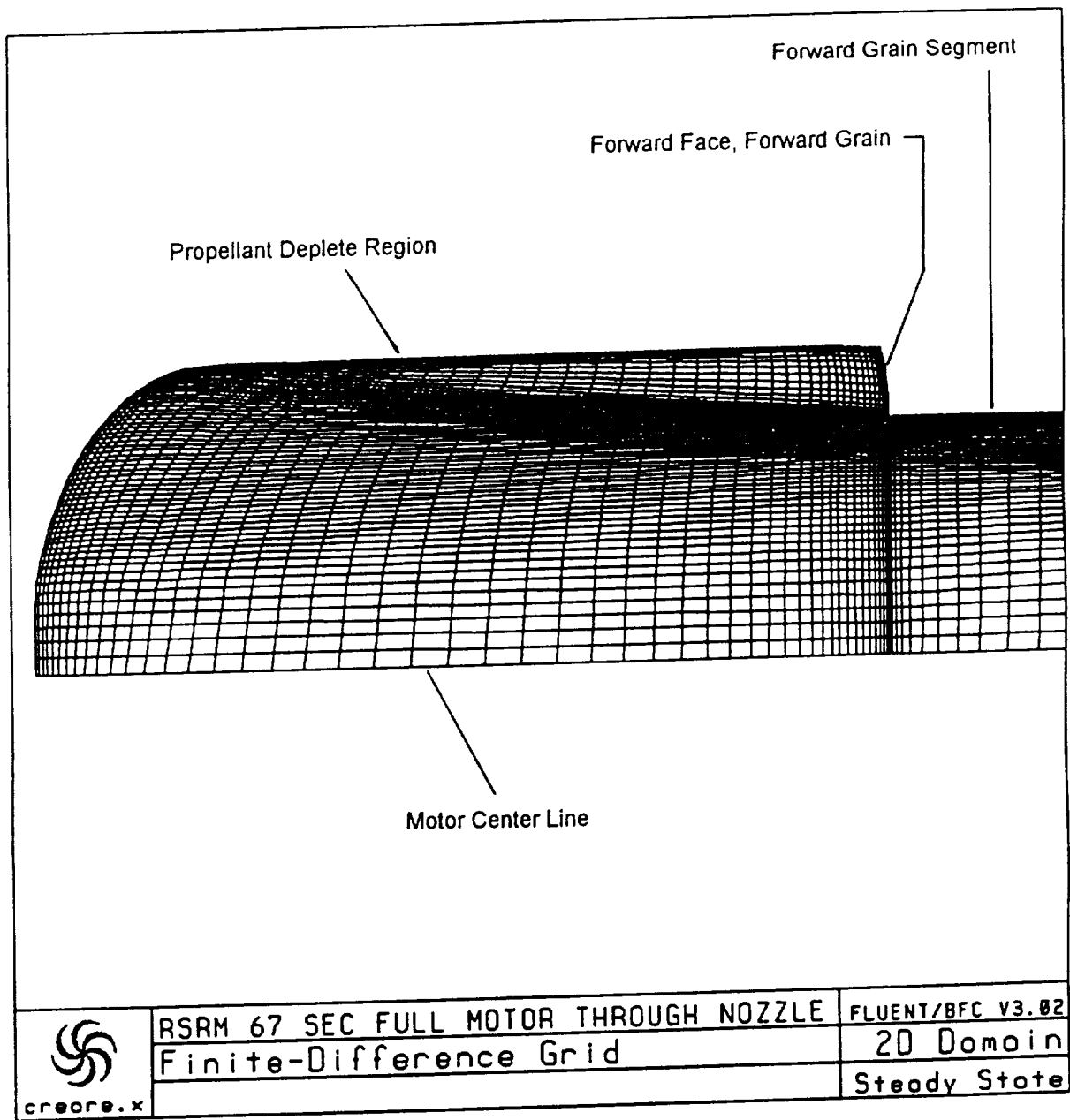


**Figure 78. Grid in the Head End Region of the Motor**

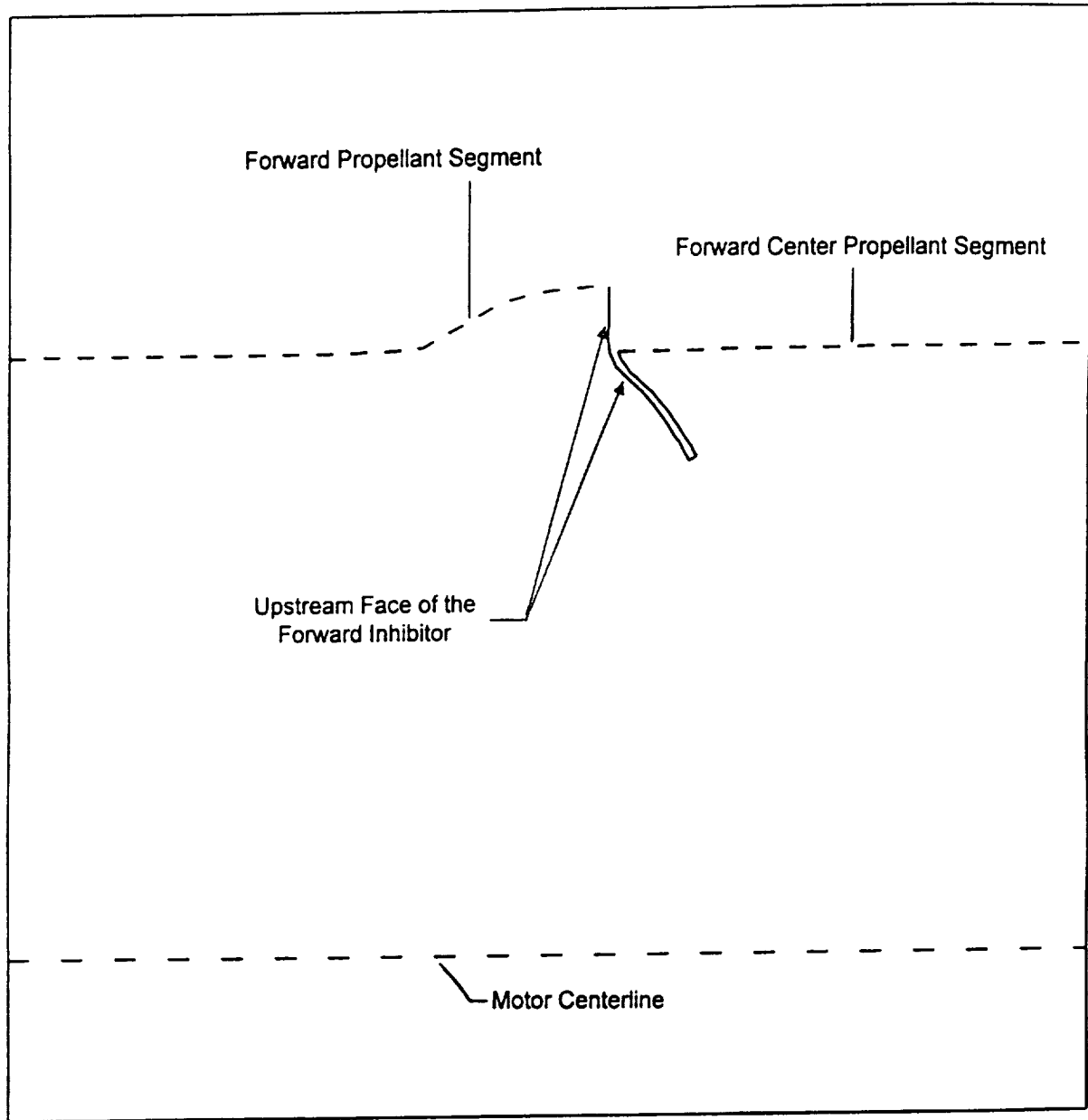


**Figure 79. Forward Slot Region of the 67 Second Burntime Motor**



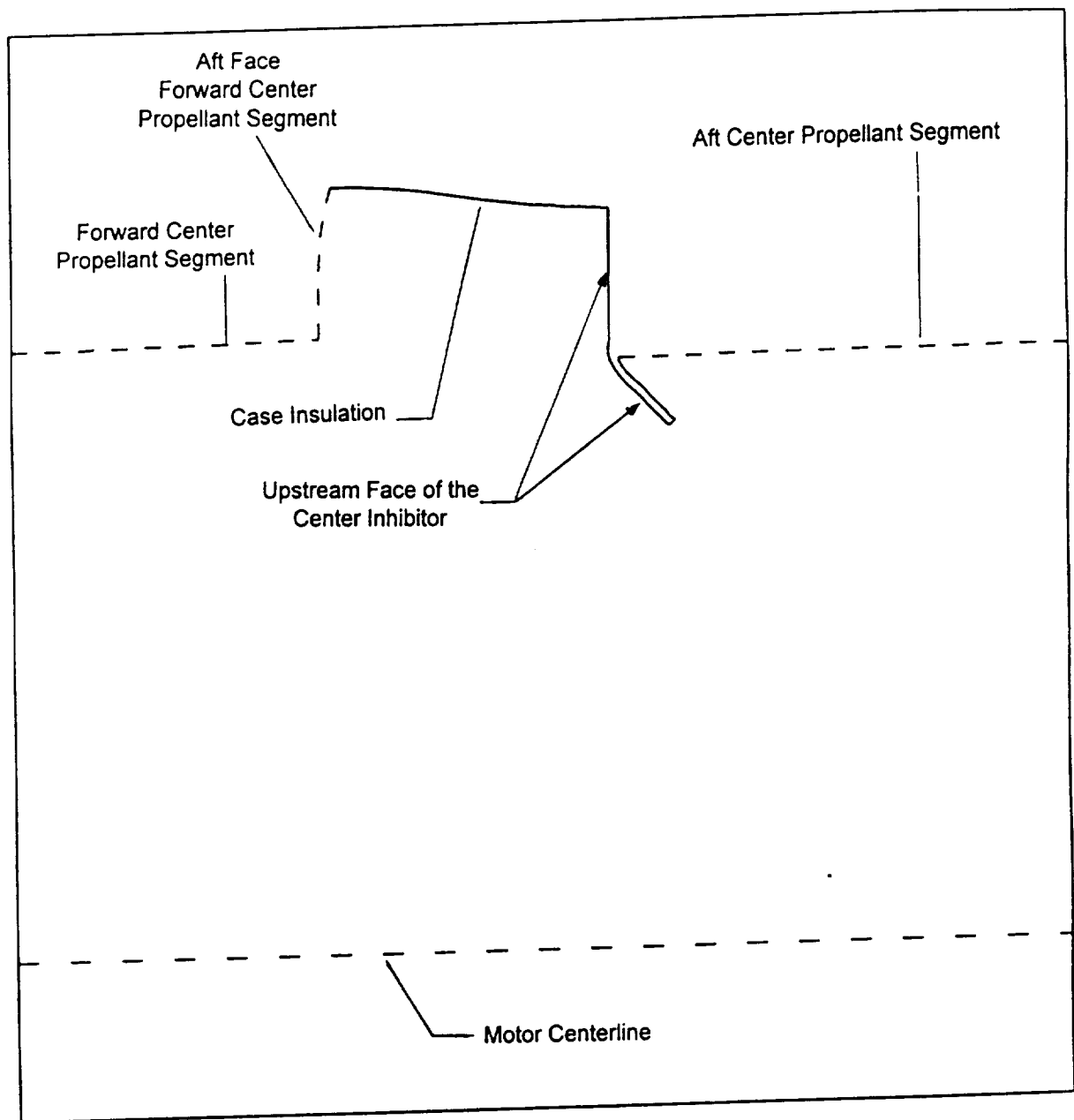


**Figure 80. Center Slot Region of the RSRM 67 Second Burntime Motor**

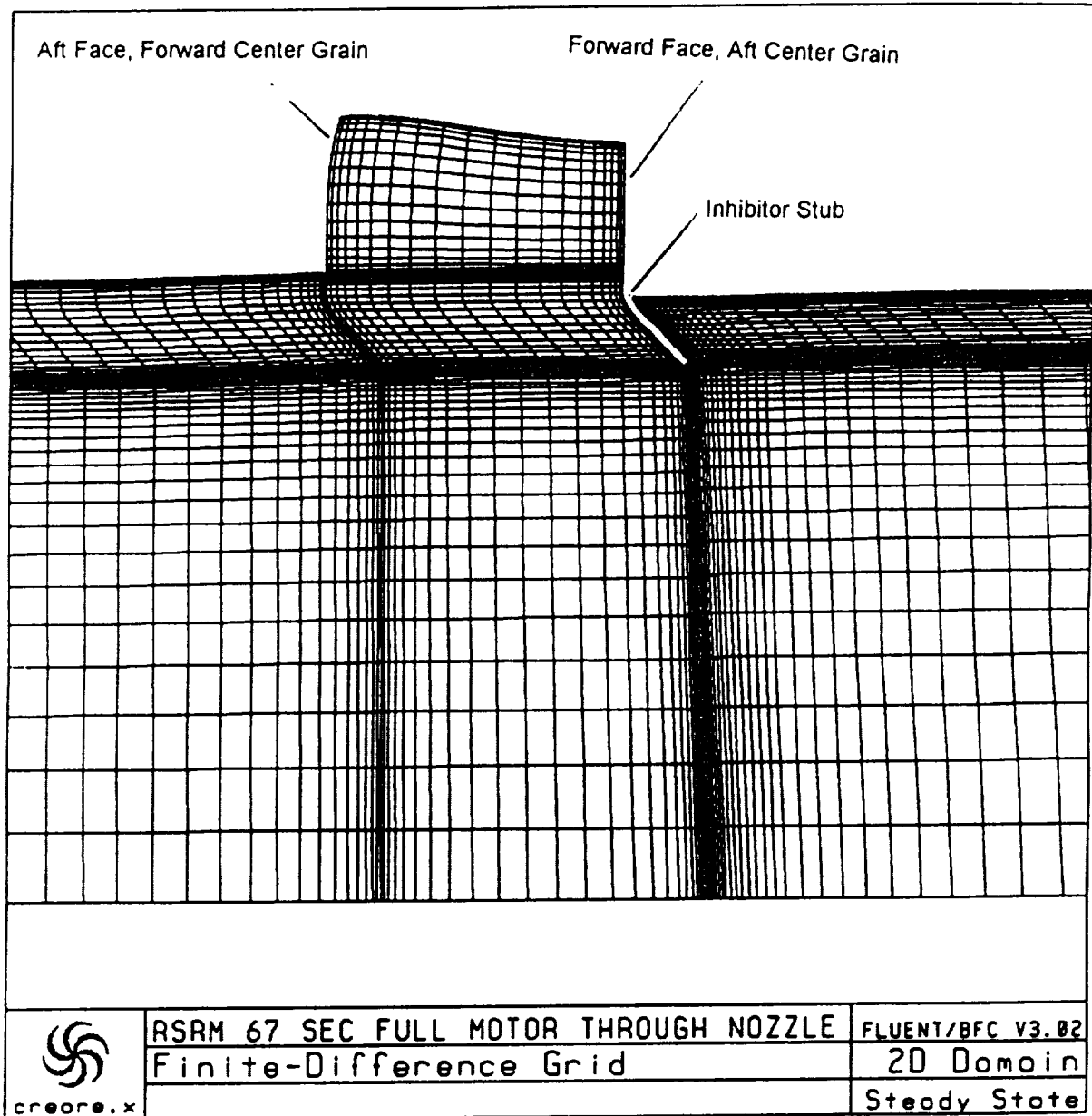


**Figure 81. Grid in the Center Slot Region of the Motor**

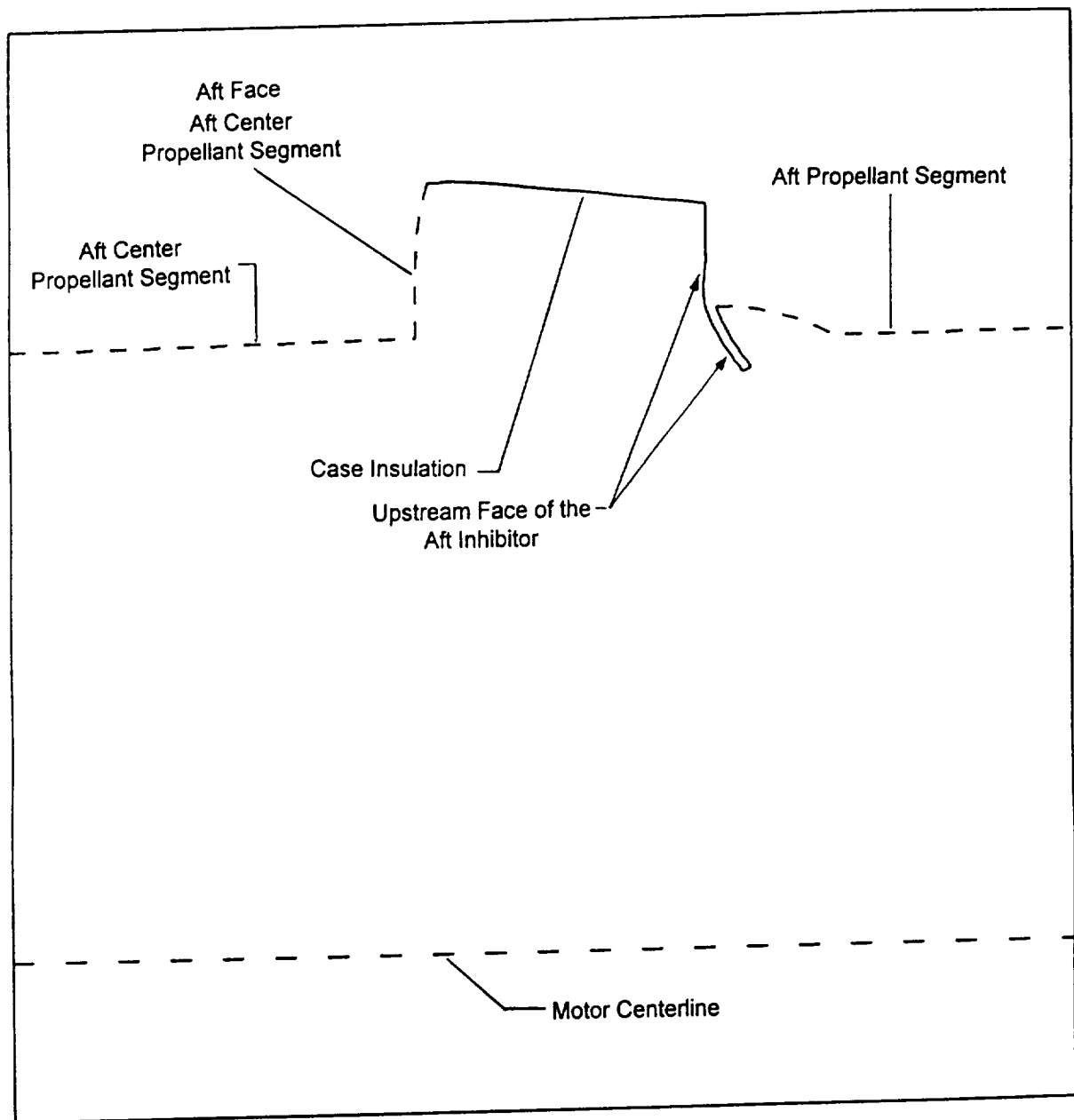


**Figure 82. Aft Slot Region of the RSRM 67 Second Burntime Motor**

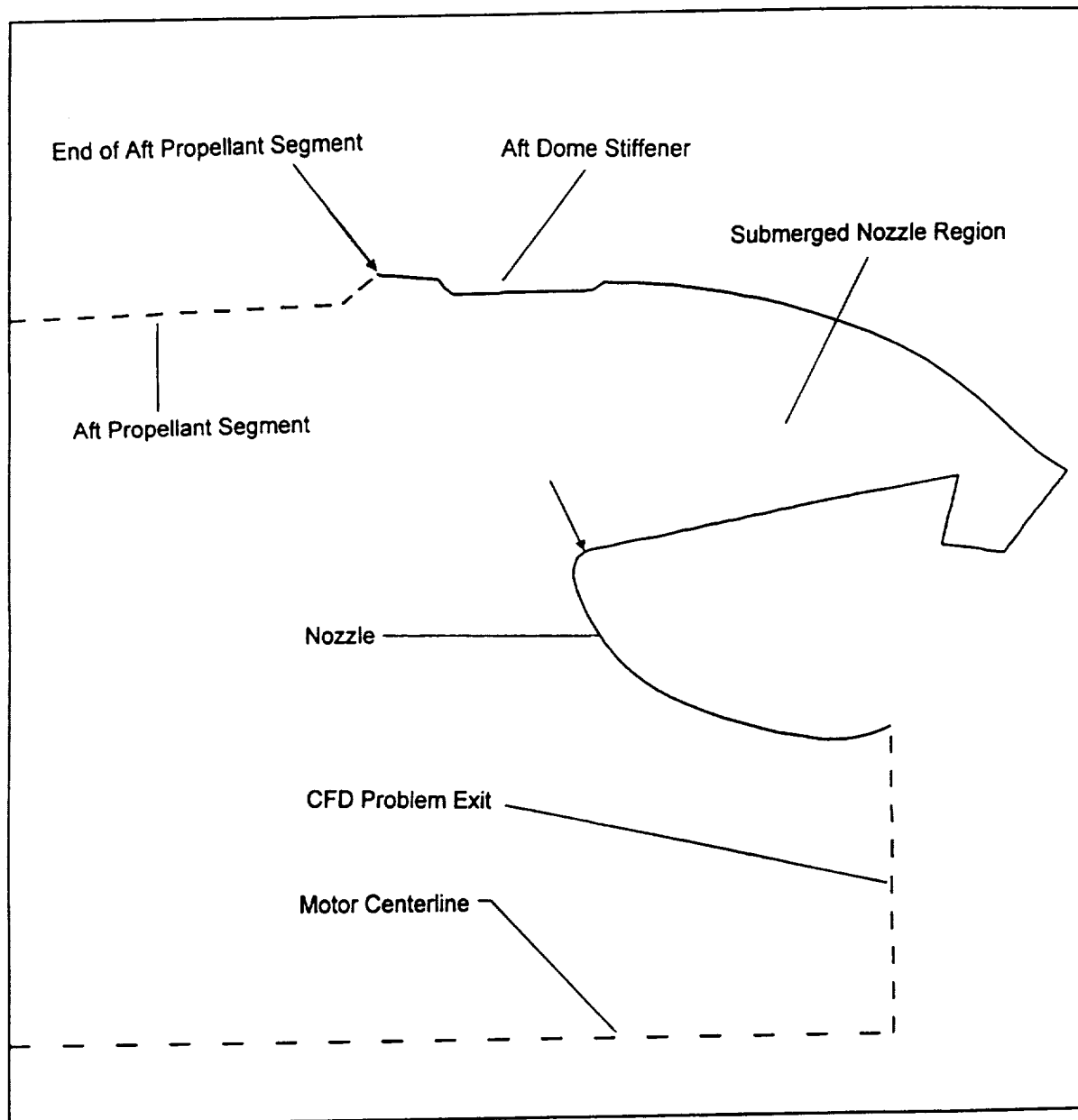


**Figure 83. Aft Dome/Nozzle Region of the RSRM  
67 Second Burntime Motor**

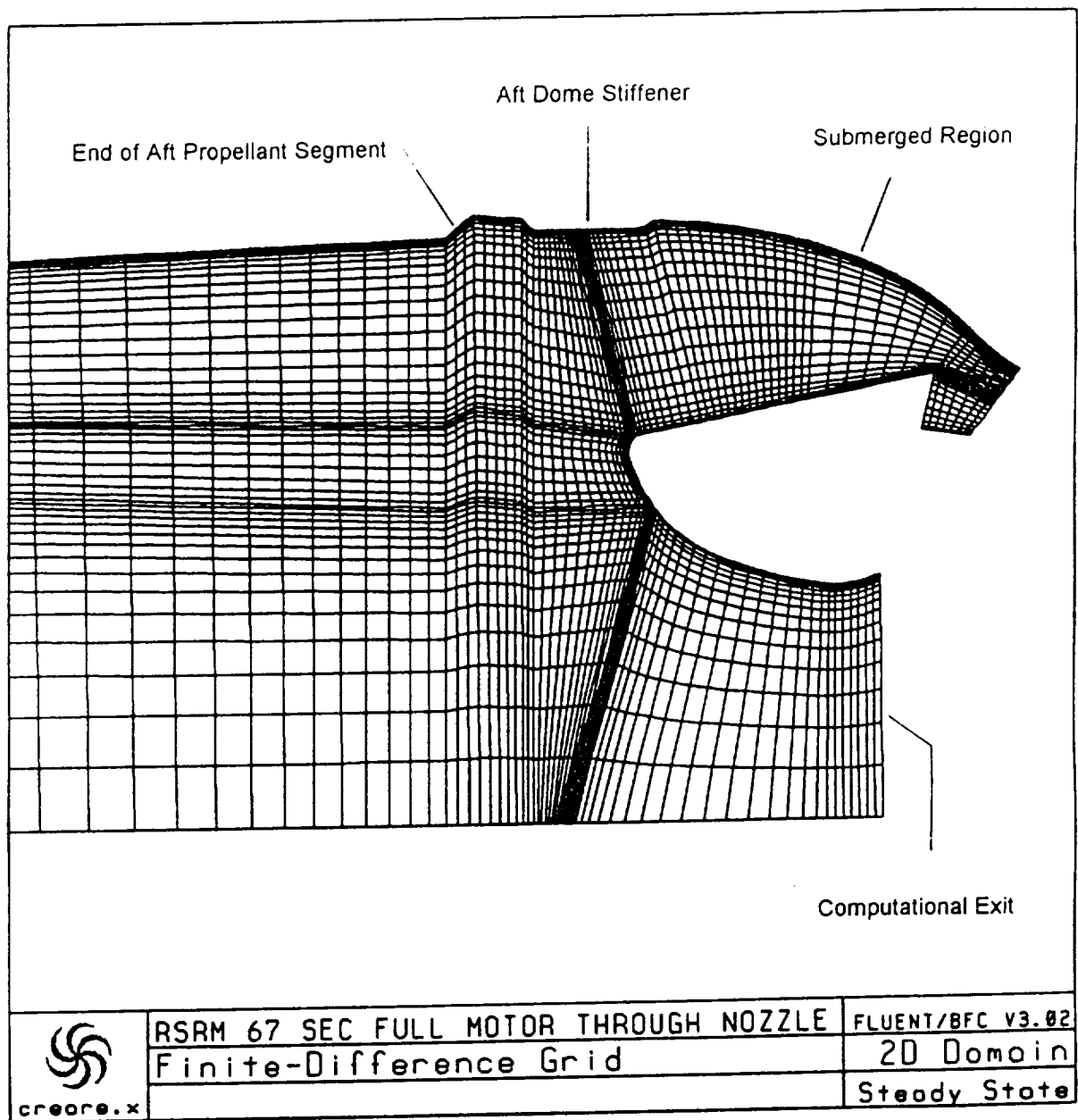


**Figure 84. Grid in the Nozzle Region of the Motor**

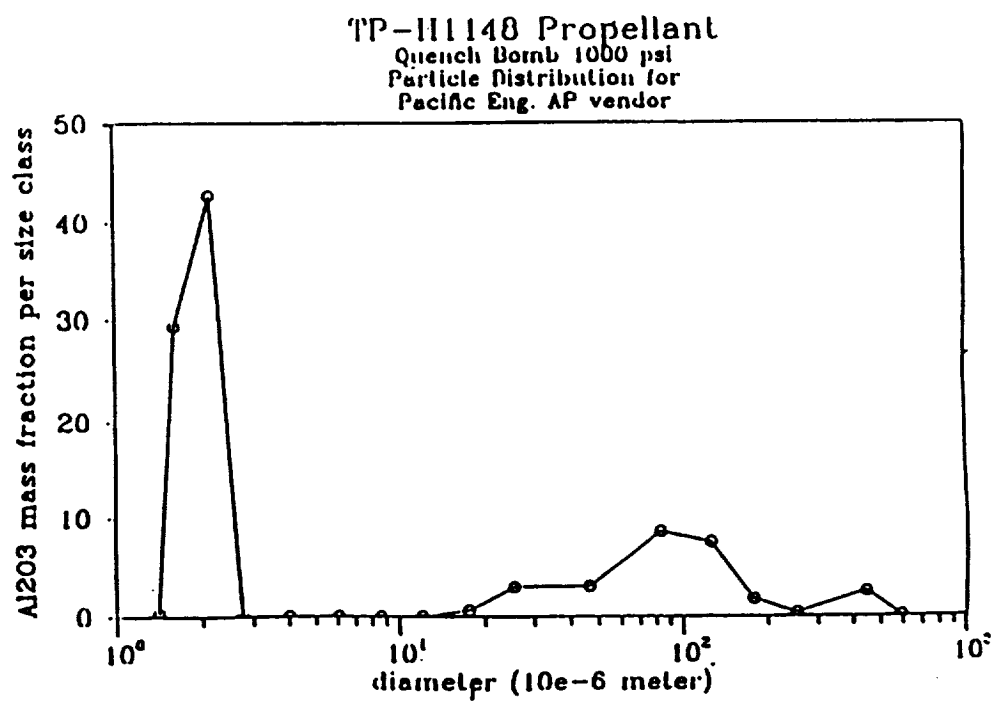
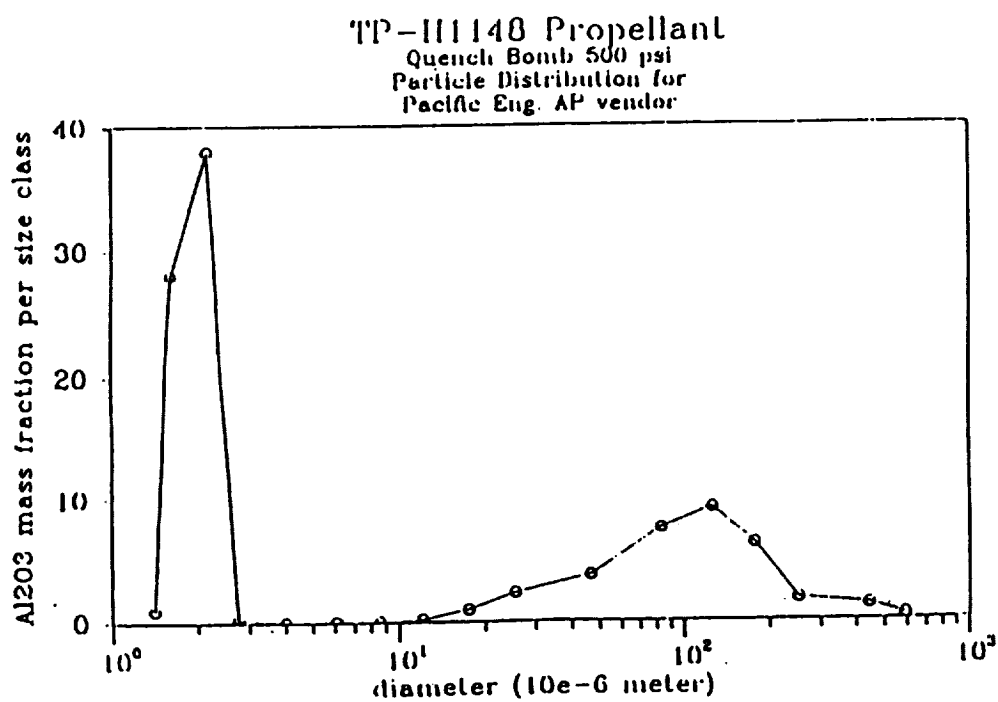


Figure 85. Bimodal Particle Size Distribution

# PARTICLE BOMB DATA COMPARISON

29A #8129, 29B #8081 & H650113 @ 500 PSI

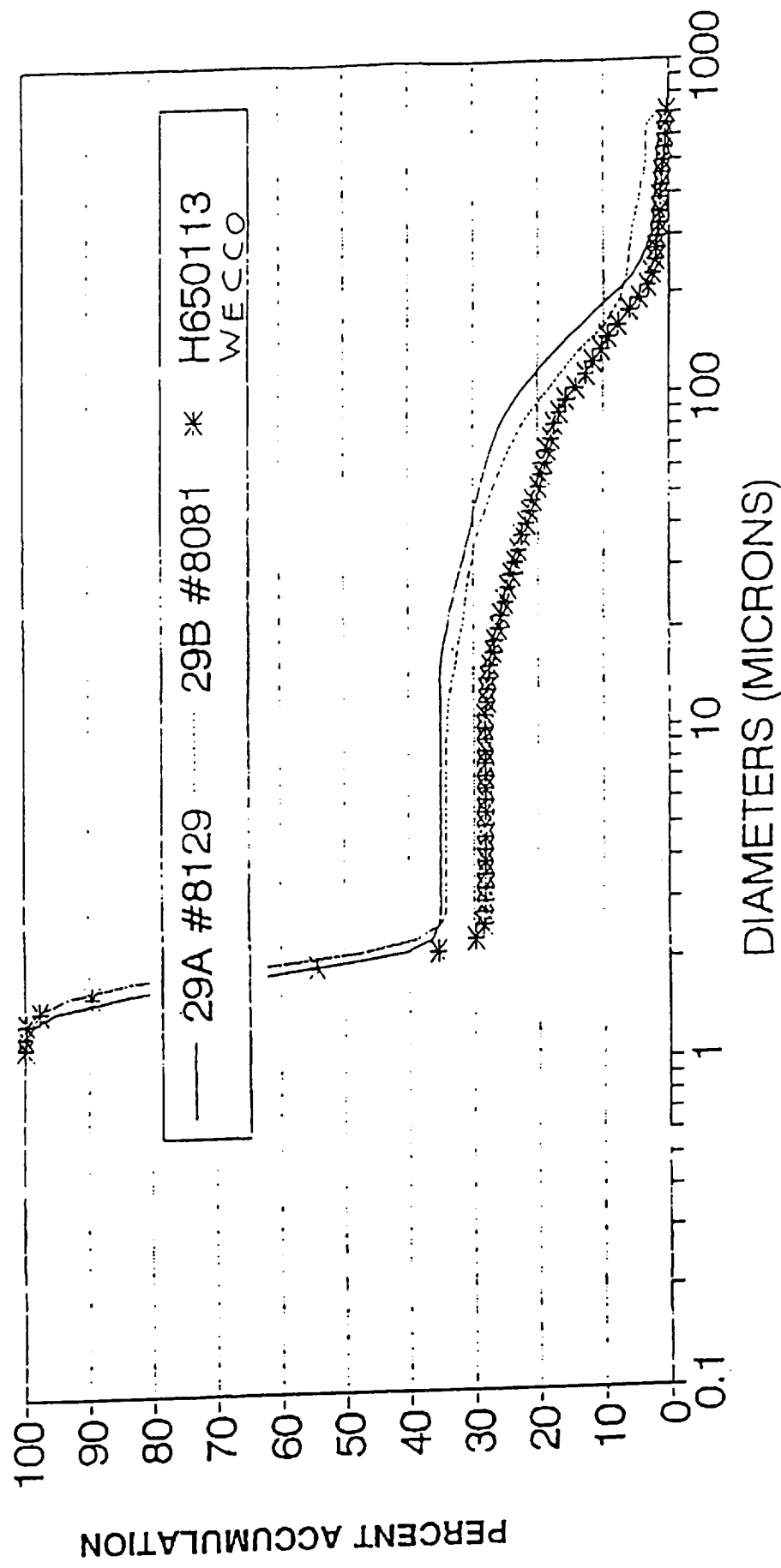


Figure 86. Particle Bomb Particle Size Data for 500 psia Chamber Pressure

# PARTICLE BOMB DATA COMPARISON

## 29A #8129, 29B #8081 & H650 @ 1000 PSI

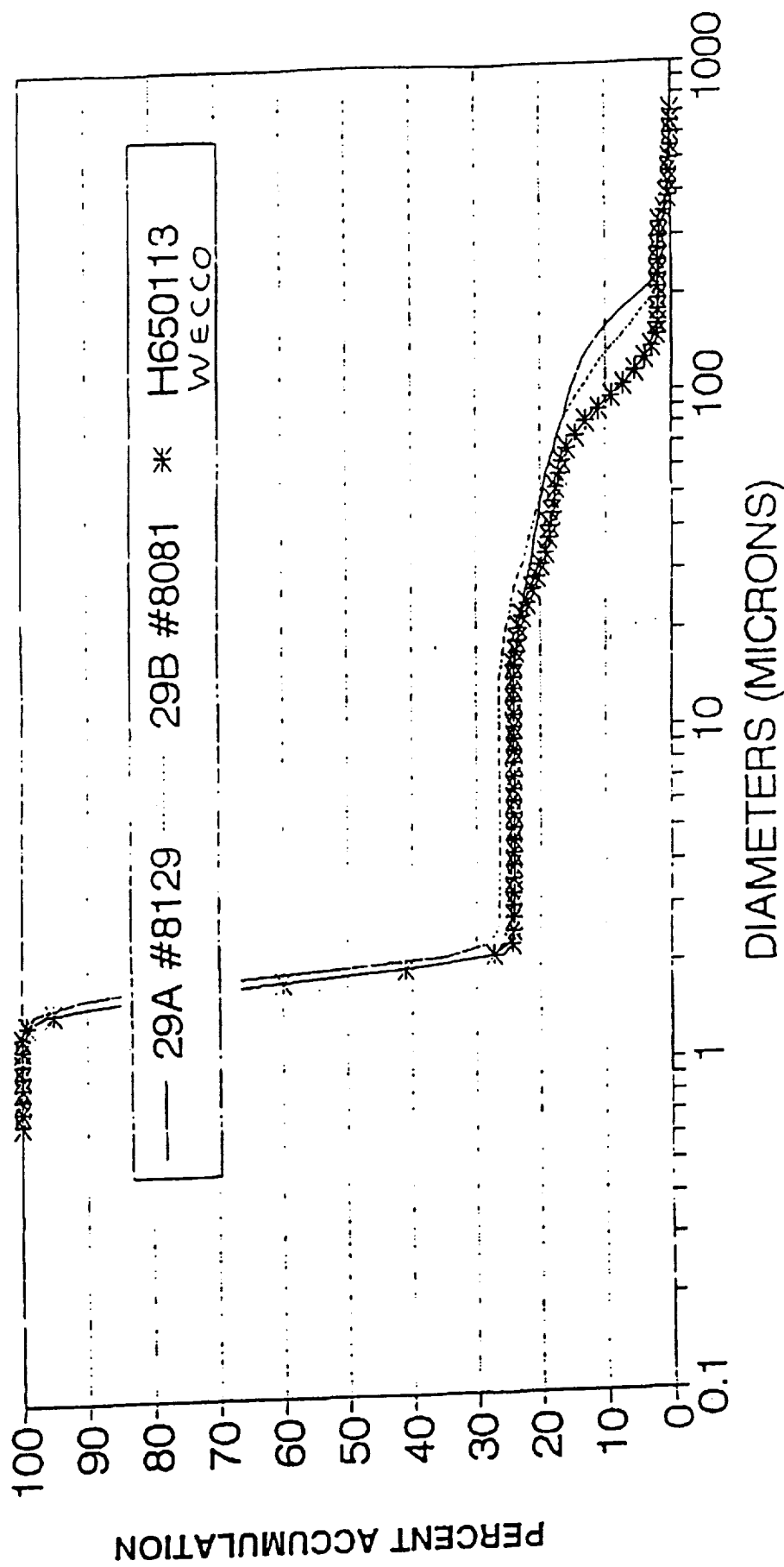


Figure 87. Particle Bomb Particle Size Data for 1000 psia Chamber Pressure



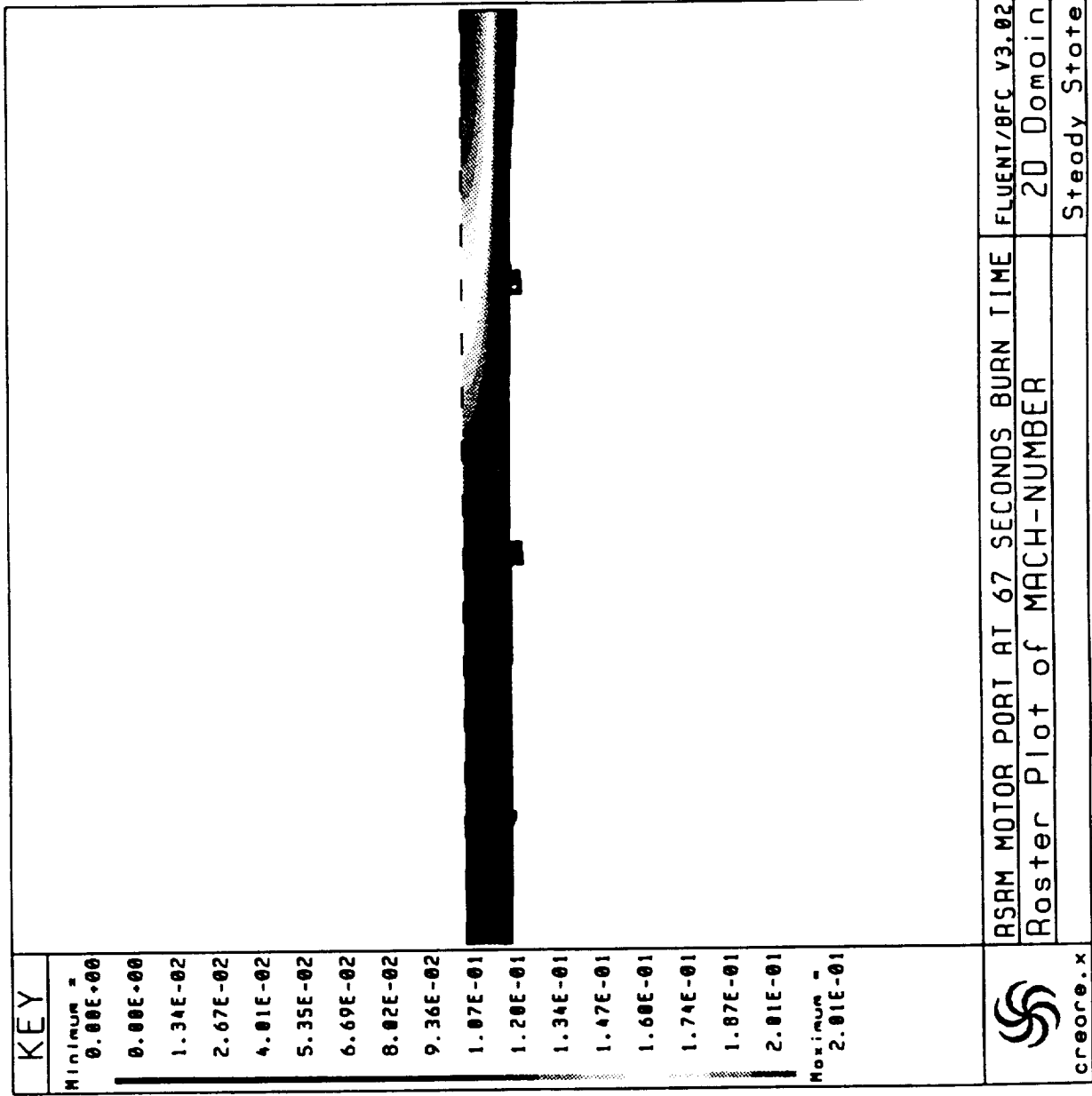


Figure 88. RSRM Motor Port Flow Mach Number

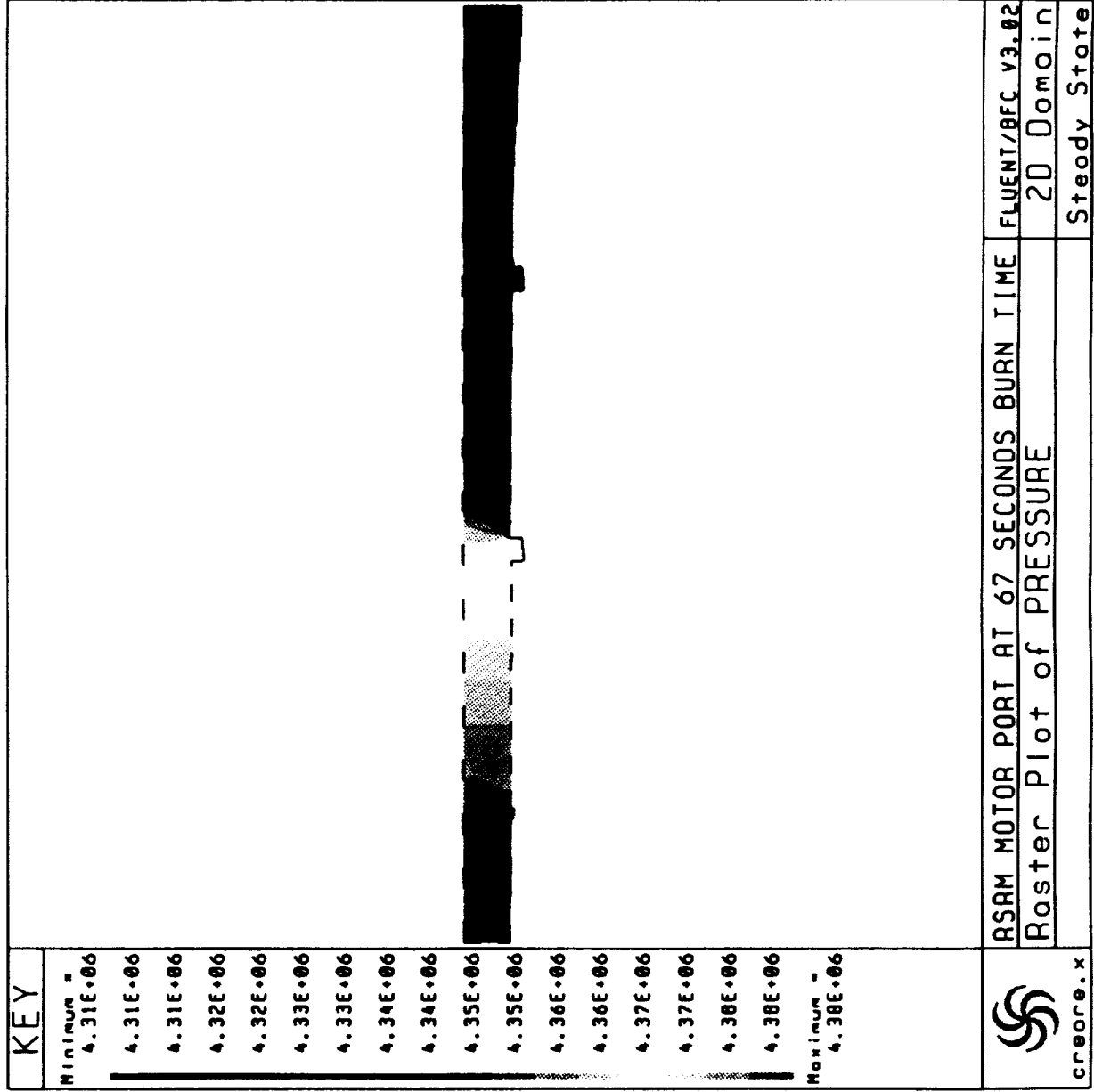


Figure 89. RSRM Motor Port Pressure Field

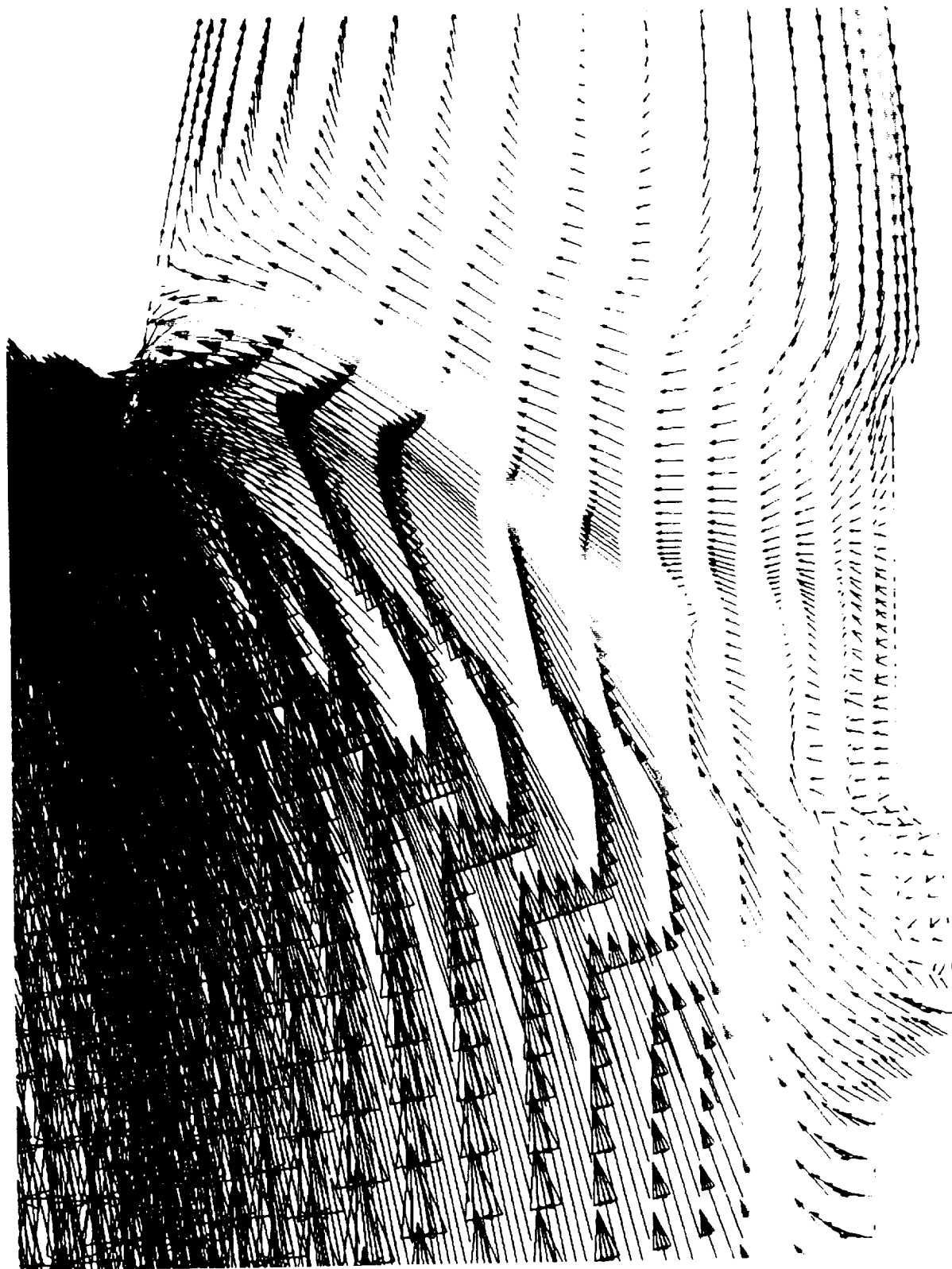


Figure 90. RSRM Submerged Nozzle Velocity Field



## **Full Scale Motor Slag Accumulation Analysis**

Two-phase flow analyses are being performed for several motor web times in order to generate a curve of slag accumulation rate versus motor web time. Once this curve is obtained, the area under the curve can be integrated to determine the total quantity of slag accumulating in the motor submerged nozzle region. The amount of slag collecting in the field joints and in the motor head end region is also being calculated. The analyses include the following set of burn times, (32.63, 49.57, 64.74, 79.75, and 110.83 seconds). Results for the 49.57, 79.75 and 110.83 second web times will be presented in this report. Figures 21, 22, and 23 show the internal flow field geometry used to model the three motor web times. Figure 24 shows an enlarged comparison of the five motor web time internal geometries. The scale in the radial direction is enlarged by twenty times in order to get a better idea of how the internal motor geometry changes with web time. In order to better match the one-dimensional motor ballistic flow rates, the motor nozzle and throat radius was changed for each web time. Figure 25 shows the variation of the nozzle contour used to model throat area erosion as a function of web time. Nozzle nose erosion was not considered in this analysis. The eroded nozzle geometry was obtained by taking the throat radius associated with each SPP ballistic run and fairing into the original geometry at the nozzle nose and at the down stream tangent point in the nozzle exit.

General information used to complete the analyses will now be presented before individual results are presented for each of the three web times. An equilibrium thermochemistry model developed by NASA/LEWIS was used to compute the motor chamber thermochemistry in the analyses. The motor mass flow rates were determined from SPP ballistic runs for each of the web times. All the solutions were obtained using the surface combustion model assuming all the aluminum is burned at the propellant surface. No smoke agglomeration model is used in the analyses. Results using the smoke agglomeration model will be generated after completion of the first set of results with no smoke agglomeration.

The discrete phase particle information necessary to perform the two-phase analyses was obtained from the same source as the data used to perform the spin motor analysis. The discrete phase particulate data was obtained from Jay Sambamurthi. The basic particulate data was obtained by Jay Sambamurthi from Thiokol and is documented in Thiokol document TWR-65162 in January of 1994. Jay took the raw experimental data and reformatted the data in a form which was useful for analytical purposes. He also computed the log-normal mathematical size distributions which were used in this analysis. The surface combustion analysis assumes that the motor particulates have a bi-modal particle size distribution. This bi-modal size distribution is created because aluminum combustion in the motor is completed by different modes. WECCO AP was considered in the as the propellant AP in the analyses. Figure 26 shows the mass fraction of particles as a function of diameter for the WECCO AP. The figure shows that the particle distribution for the WECCO AP tested is indeed bi-modal and that the largest mass fraction of particles is on the order of 1 micron diameter.

These small particles, or smoke, follow the flow field streamlines closely and are assumed in the analysis to be part of the continuous phase. The smoke is a large fraction of the total motor particulate. In this case, the smoke fraction for the WECCO AP is 71.67% of the total motor particulate. Figure 27 shows the cumulative mass fraction of smoke as a function of particle diameter for the WECCO AP. Notice the rapid rise in the mass fraction of particles at approximately the one micron size. The flat region from approximately 2 microns to 10 microns illustrates that there are no particles in this diameter range. Particles on the order of 10 microns begin to appear in the quench bomb collection data to form the lower end of the large particle side of the bi-modal distribution. These large particles are considered as the discrete phase in the two-phase flow field analysis. Figures 28 and 29 summarize the mass fraction as a function of particle diameter for the smoke and discrete phase particles as measured by the quench bomb instrumentation. The mass mean diameter of the smoke particles with size distribution as shown in Figure 28 was 1.7 microns and the mass mean diameter of the discrete phase particles was determined from Figure 29 to be 96 microns. The measured particle mass distribution and the mathematically modeled log-normal fit to the data which was used by CELMINT to generate particle sizes for the analyses is shown in Figure 29. The WECCO quench bomb data in Figure 29 is shown as the circles. The solid and dashed lines shown in the figure represent two different log-normal distribution estimates of the quench bomb data as reported by Jay Sambamurthi in an MSFC Pressure Perturbation Team Report. The dashed line estimation of the quench bomb data was used in the computational analysis because it fits the data slightly better than the solid line. The mass mean diameter corresponding to the dashed line is 96 microns with a distribution sigma of 0.3.

Results for the individual runs will be presented at this time beginning with the 49.57 second web time solution. Figures 30, 31 and 32 show the detailed internal motor geometries used to model the forward, center and aft field joints. Figure 33 shows the internal motor geometry in the submerged nozzle region. The computational grid for this run used 465 grid cells to span the axial dimension of the motor. The radial extent of the motor port was resolved by 45 computational cells. An additional 20 radial cells were used to resolve the motor head end and slots.

The total mass flow rate as computed by the SPP ballistic run was 8973 lbm/sec. The flow rates associated with the individual propellant segments is shown in Table 1.

At this time only the slag accumulation data will be presented. Table 2 shows the slag accumulation rates for the various sections of the motor labeled in Figure 34.

**Table 1. Mass Flow Rates For 49.57 Second Web Time**

Forward Segment	1548 lbm/sec.
Forward Center Segment	2345 lbm/sec.
Aft Center Segment	2373 lbm/sec.
Aft Segment	2707 lbm/sec.

**Table 2. Surface Combustion Slag Accumulation Rates For 49.57 Seconds.**

Motor Location	Particulate Mass flow rate (lbm/sec)
Nozzle Exit	688.14
Submerged Nozzle	6.22
Head End Region	3.00
Forward Slot	0.05
Center Slot	4.89
Aft Slot	5.40
Total Motor	734.40

Results for the 79.75 second web time solution are now discussed. Figures 35, 36 and 37 show the detailed internal motor geometries used to model the forward, center and aft field joints. Figure 38 shows the internal motor geometry in the submerged nozzle region. The computational grid for this run used 465 grid cells to span the axial dimension of the motor. The radial extent of the motor port was resolved by 50 computational cells. An additional 10 radial cells were used to resolve the motor head end and slots.

The total mass flow rate as computed by the SPP ballistic run was 9617 lbm/sec. The flow rates associated with the individual propellant segments is shown in Table 3.

**Table 3. Mass Flow Rates For 79.75 Second Web Time**

Forward Segment	1501 lbm/sec.
Forward Center Segment	2659 lbm/sec.
Aft Center Segment	2654 lbm/sec.
Aft Segment	2803 lbm/sec.

Table 4 shows the slag accumulation rates for the various sections of the motor labeled in Figure 39.

**Table 4. Surface Combustion Slag Accumulation Rates For 79.75 Seconds.**

Motor Location	Particulate Mass flow rate (lbm/sec)
Nozzle Exit	718.63
Submerged Nozzle	20.08
Head End Region	7.36
Forward Slot	1.72
Center Slot	1.23
Aft Slot	14.88
Total Motor	782.17

Results for the 79.75 second web time solution are now discussed. Figures 40, 41 and 42 show the detailed internal motor geometries used to model the forward, center and aft field joints. Figure 43 shows the internal motor geometry in the submerged nozzle region. The computational grid for this run used 465 grid cells to span the axial dimension of the motor. The radial extent of the motor port was resolved by 57 computational cells.

The total mass flow rate as computed by the SPP ballistic run was 6463 lbm/sec. The flow rates associated with the individual propellant segments is shown in Table 5.

**Table 5. Mass Flow Rates For 109.83 Second Web Time**

Forward Segment	1124 lbm/sec.
Forward Center Segment	2401 lbm/sec.
Aft Center Segment	2388 lbm/sec.
Aft Segment	550 lbm/sec.

Table 6 shows the slag accumulation rates for the various sections of the motor labeled in Figure 44.

The remaining solution web times of 32.63 and 64.74 seconds will be presented as completed along with relevant comparisons of the internal flow field solutions.



**Table 6. Surface Combustion Slag Accumulation Rates For 109.83 Seconds.**

<b>Motor Location</b>	<b>Particulate Mass flow rate (lbm/sec)</b>
<b>Nozzle Exit</b>	<b>477.08</b>
<b>Submerged Nozzle</b>	<b>3.51</b>
<b>Head End Region</b>	<b>0.86</b>
<b>Forward Slot</b>	<b>0.11</b>
<b>Center Slot</b>	<b>4.07</b>
<b>Aft Slot</b>	<b>33.95</b>
<b>Total Motor</b>	<b>524.50</b>

Figure 21. RSRM Full Motor Geometry, 49.57 Second Burn Time

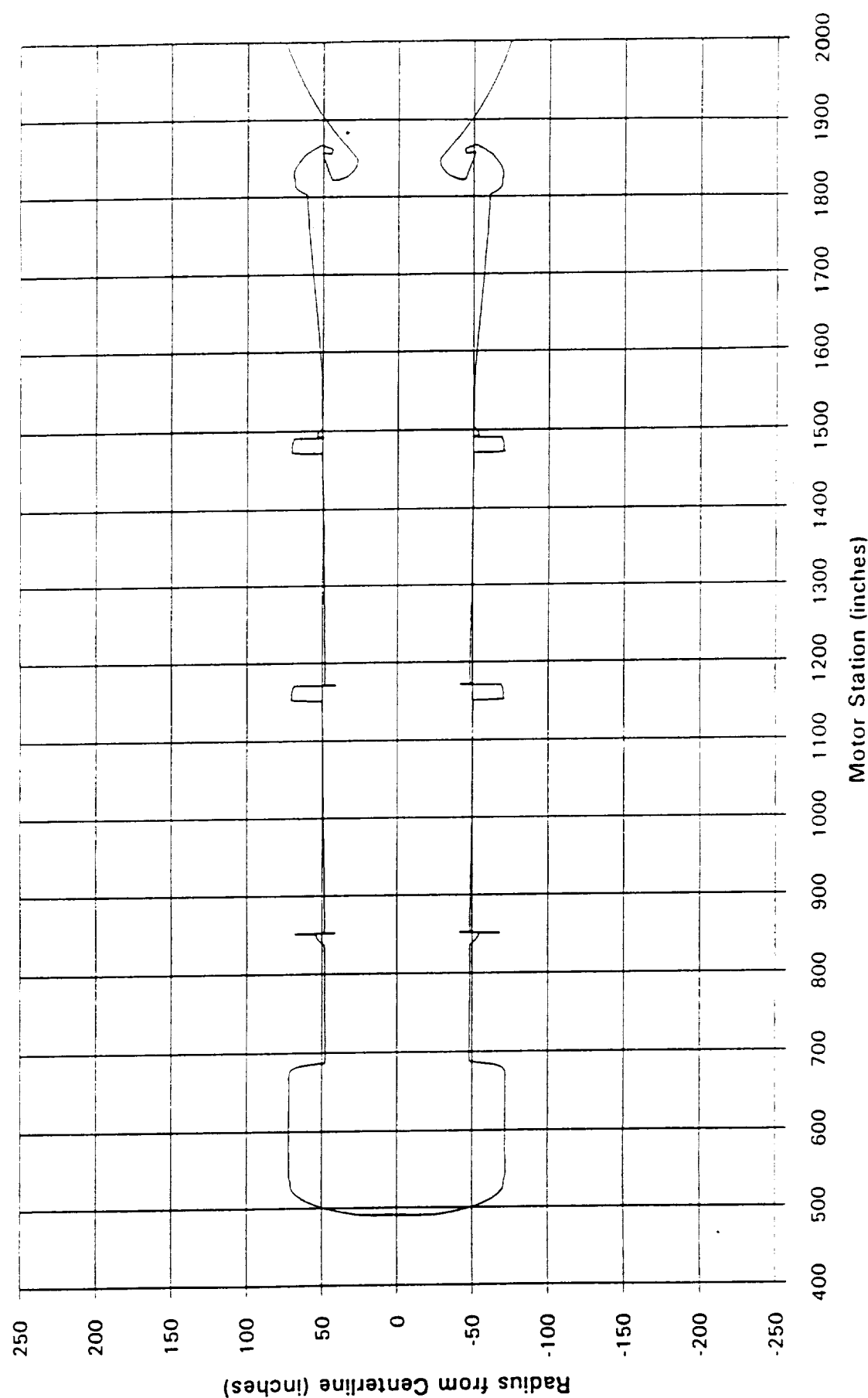


Figure 22. RSRM Full Motor Geometry, 79.75 Second Burn Time

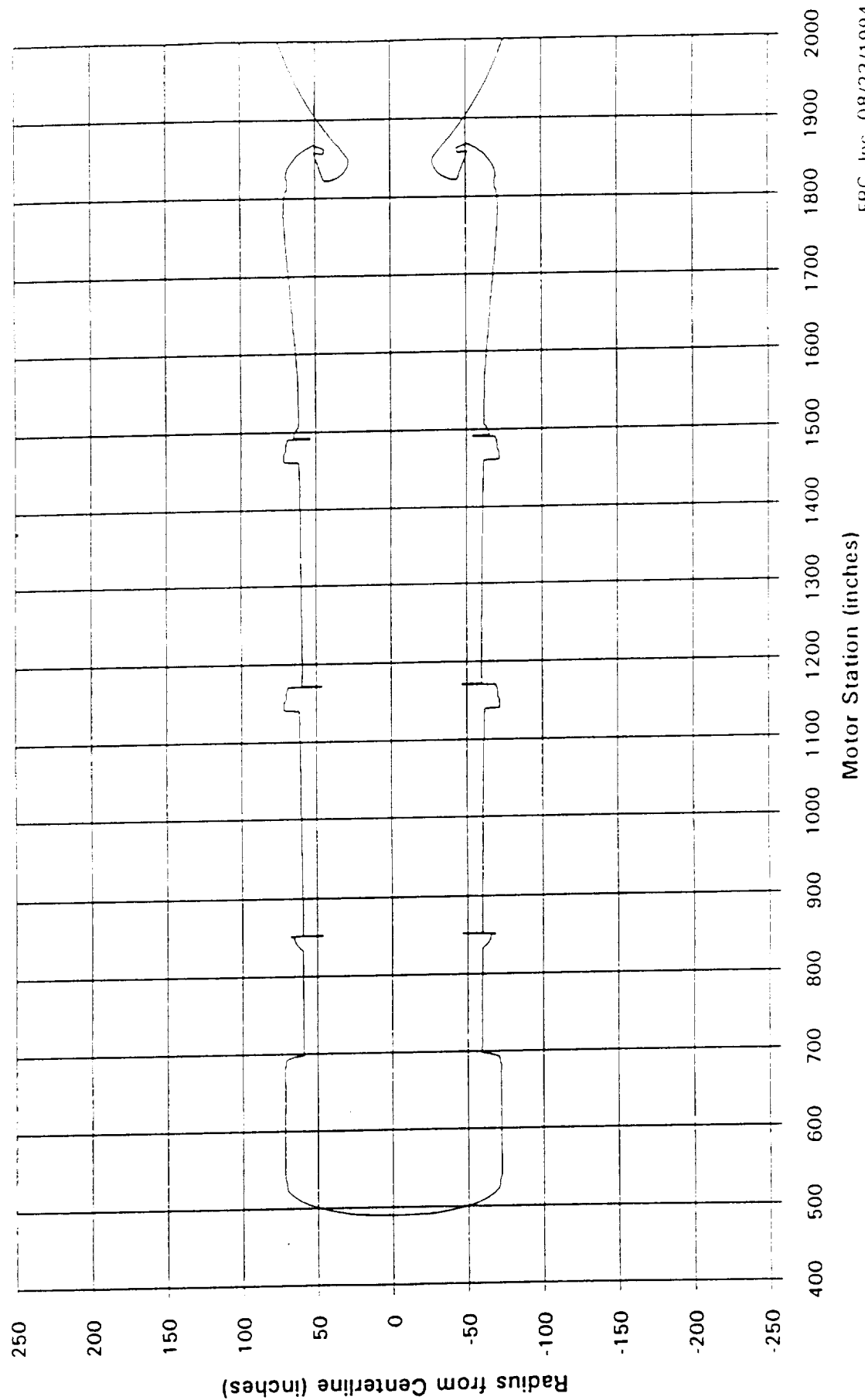
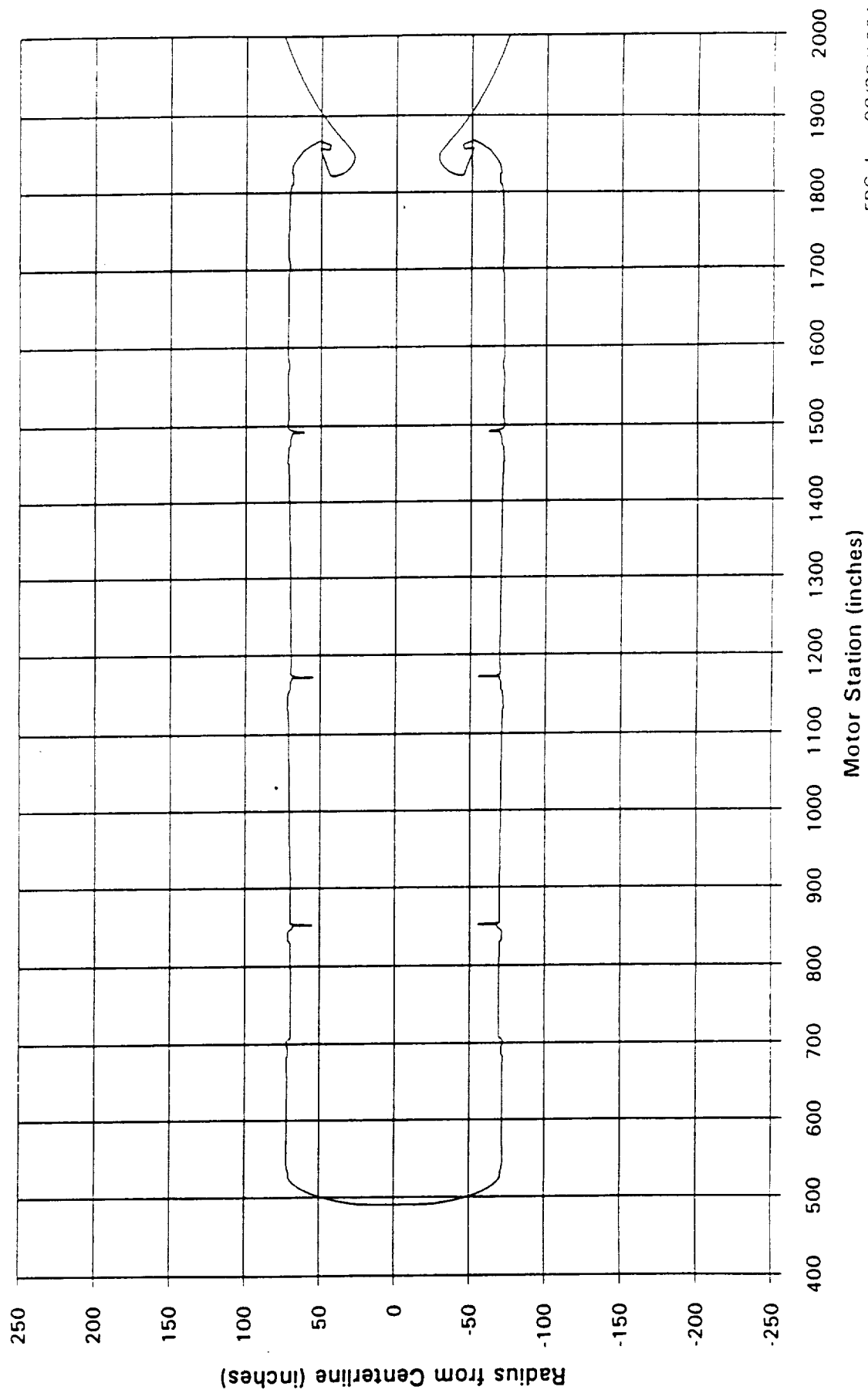


Figure 23. RSRM Full Motor Geometry, 109.83 Second Burn Time



**Figure 24. RSRM Geometry  
Burn Time Comparison**

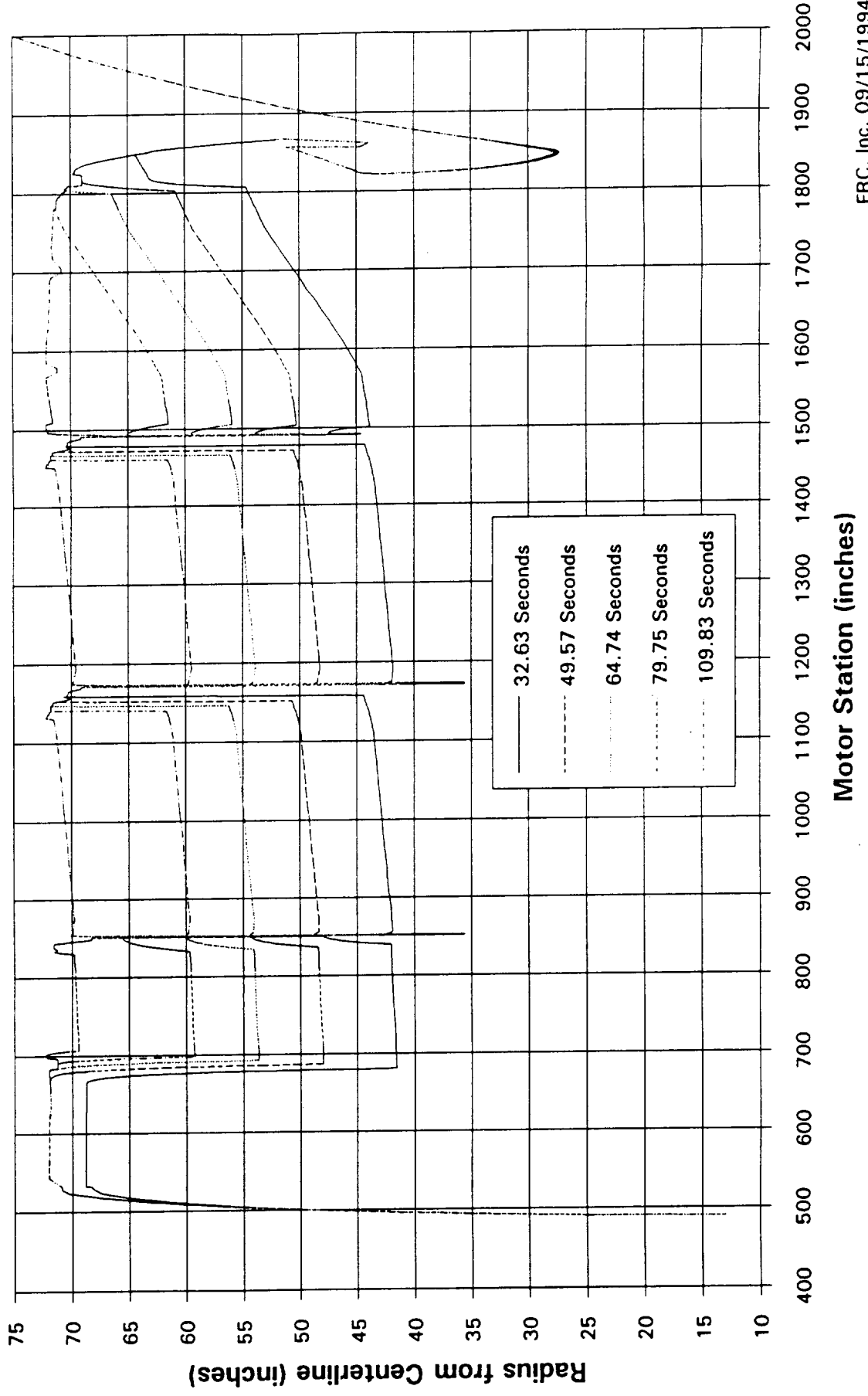


Figure 25. RSRM Geometry  
Nozzle Throat Comparison

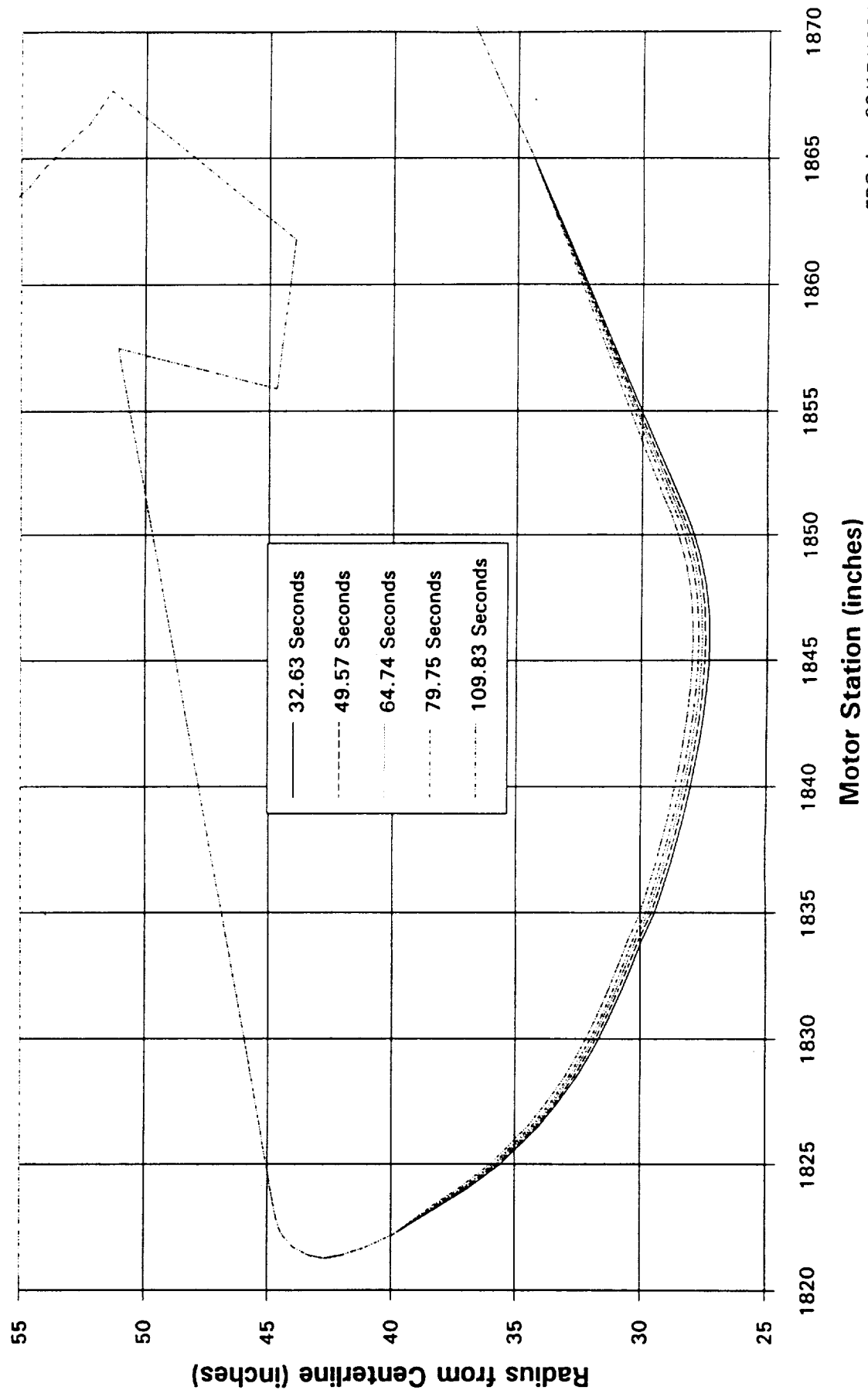


Figure 26. WECCO Bi-Modal Distribution, Mass Fraction of Each Particle Size Group  
for Quench Bomb Data- 500 psi WECCO at 3-inch

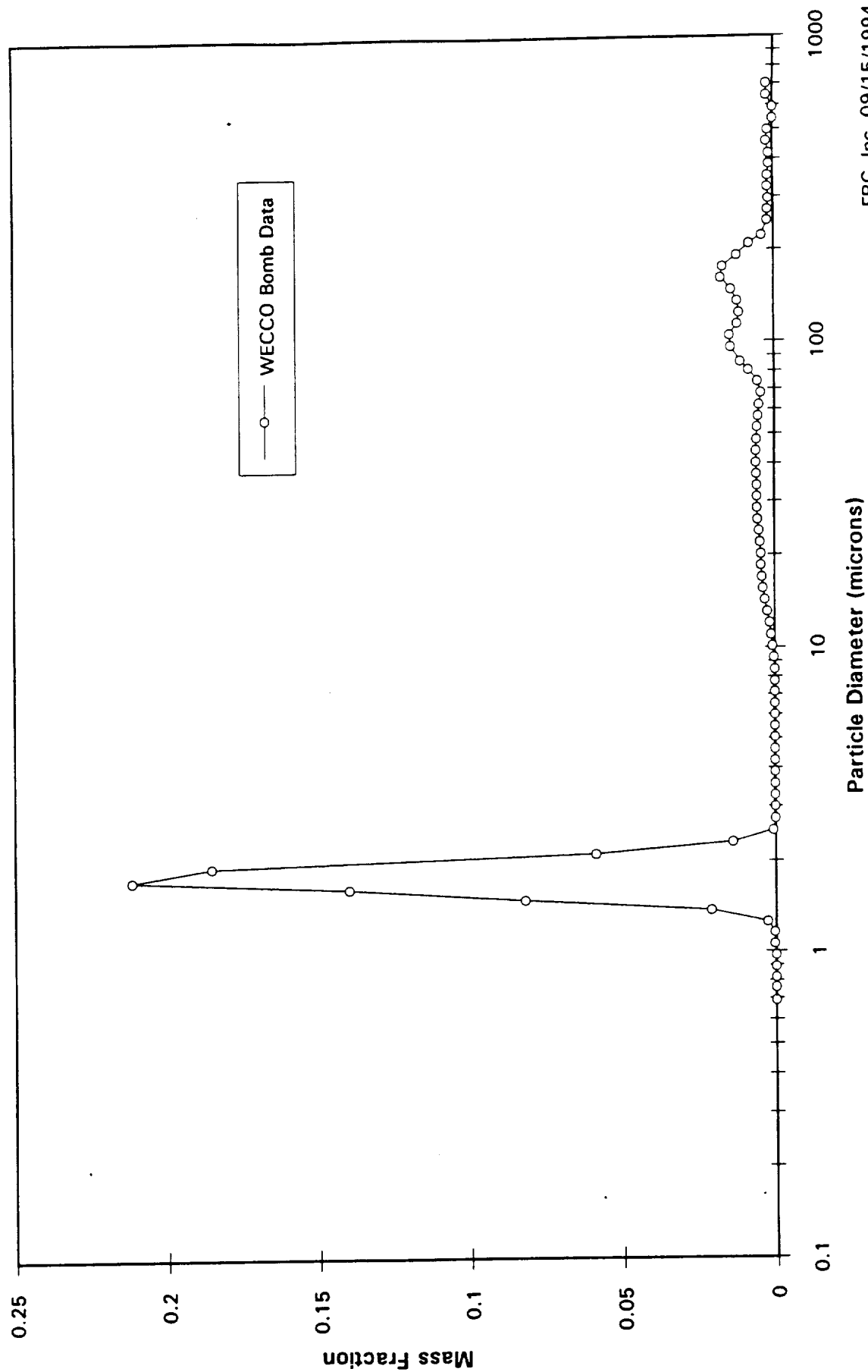


Figure 27. WECCO Bi-Modal Distribution, Cumulative Mass Fraction as a Function of Particle Size for Quench Bomb Data- 500 psi WECCO at 3-inch

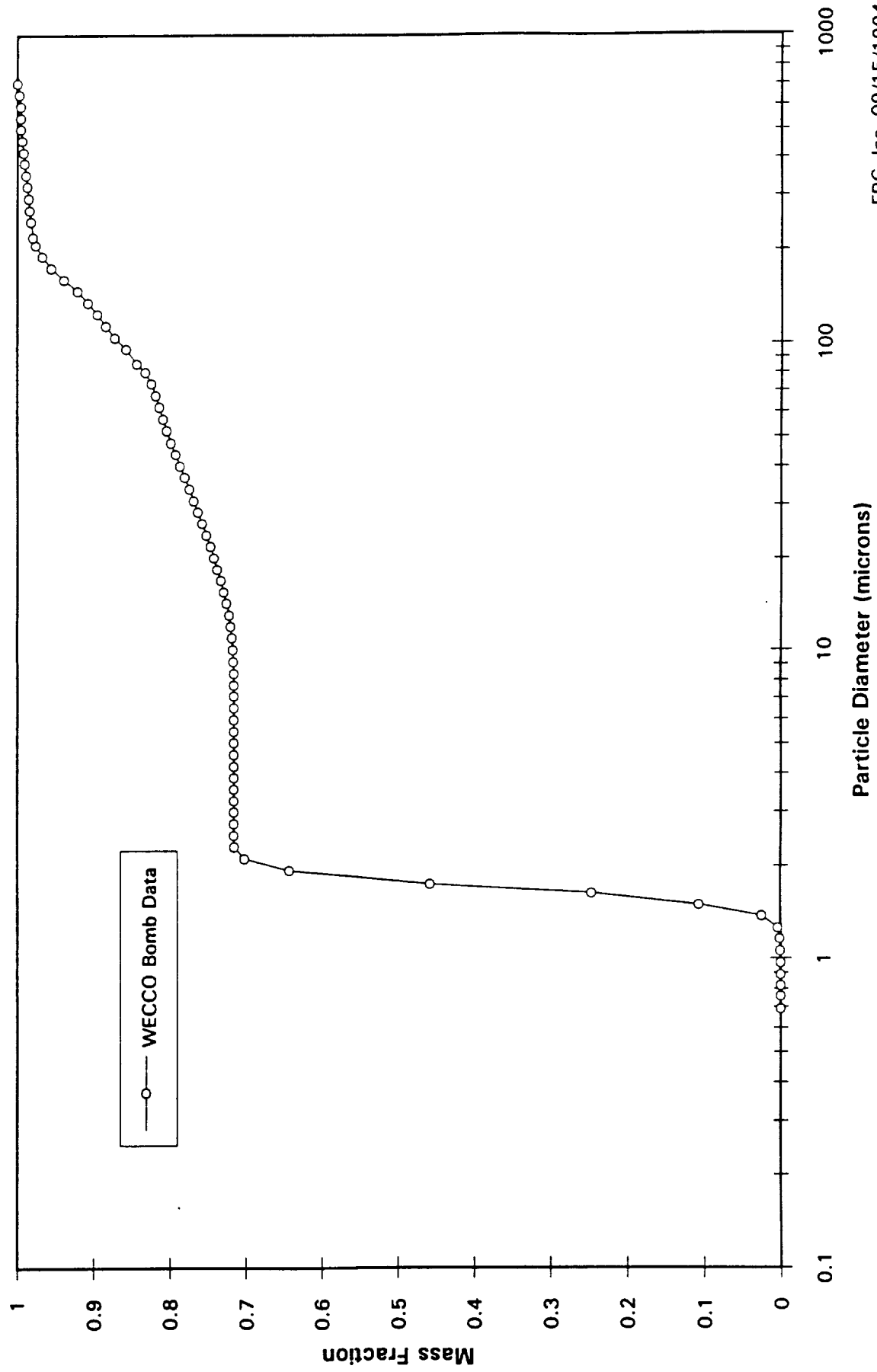




Figure 28. WECCO Smoke Size Particle Cumulative Mass Fraction Distribution for  
Quench Bomb Data- 500 psi WECCO at 3-inch

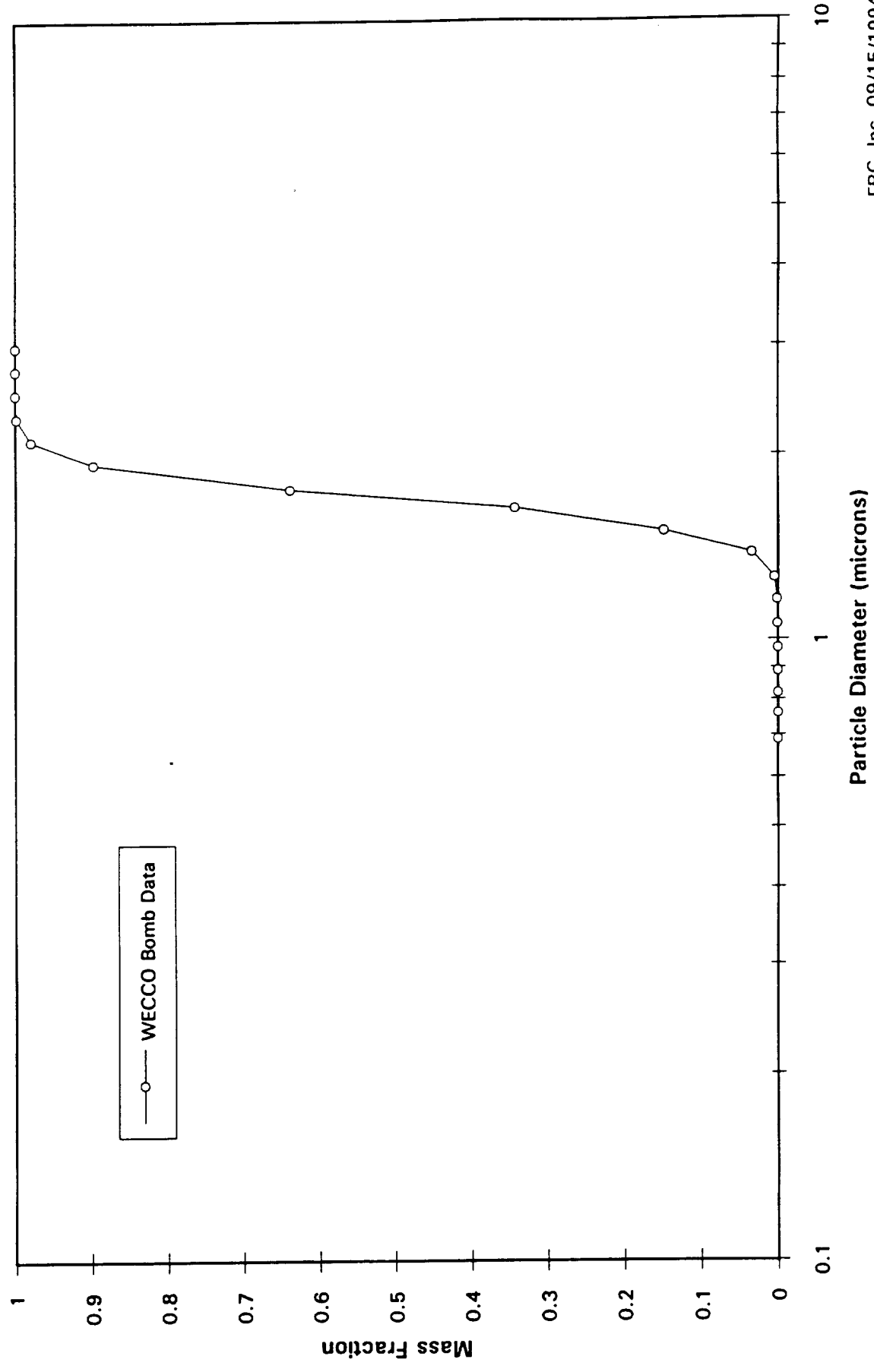
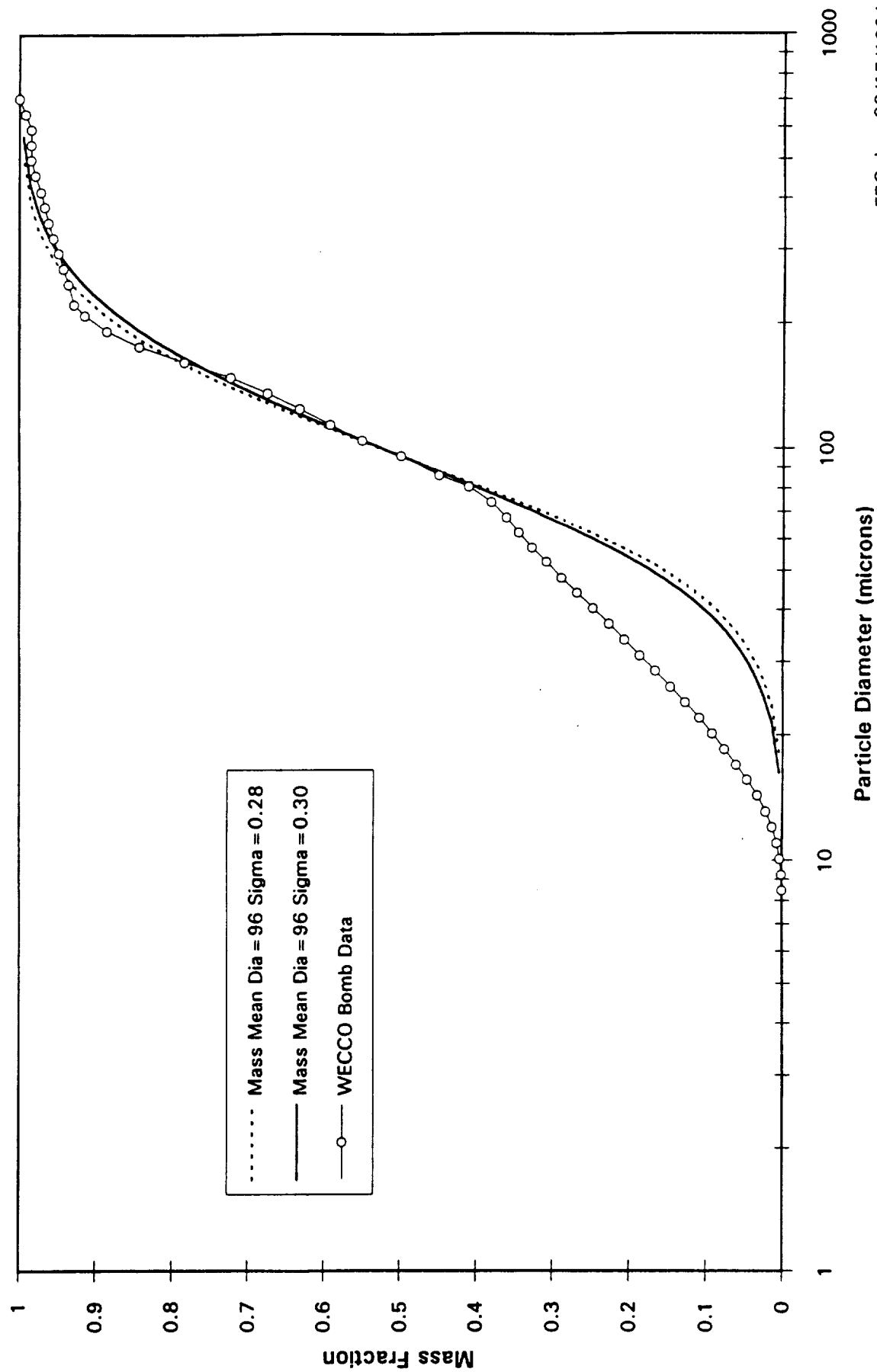
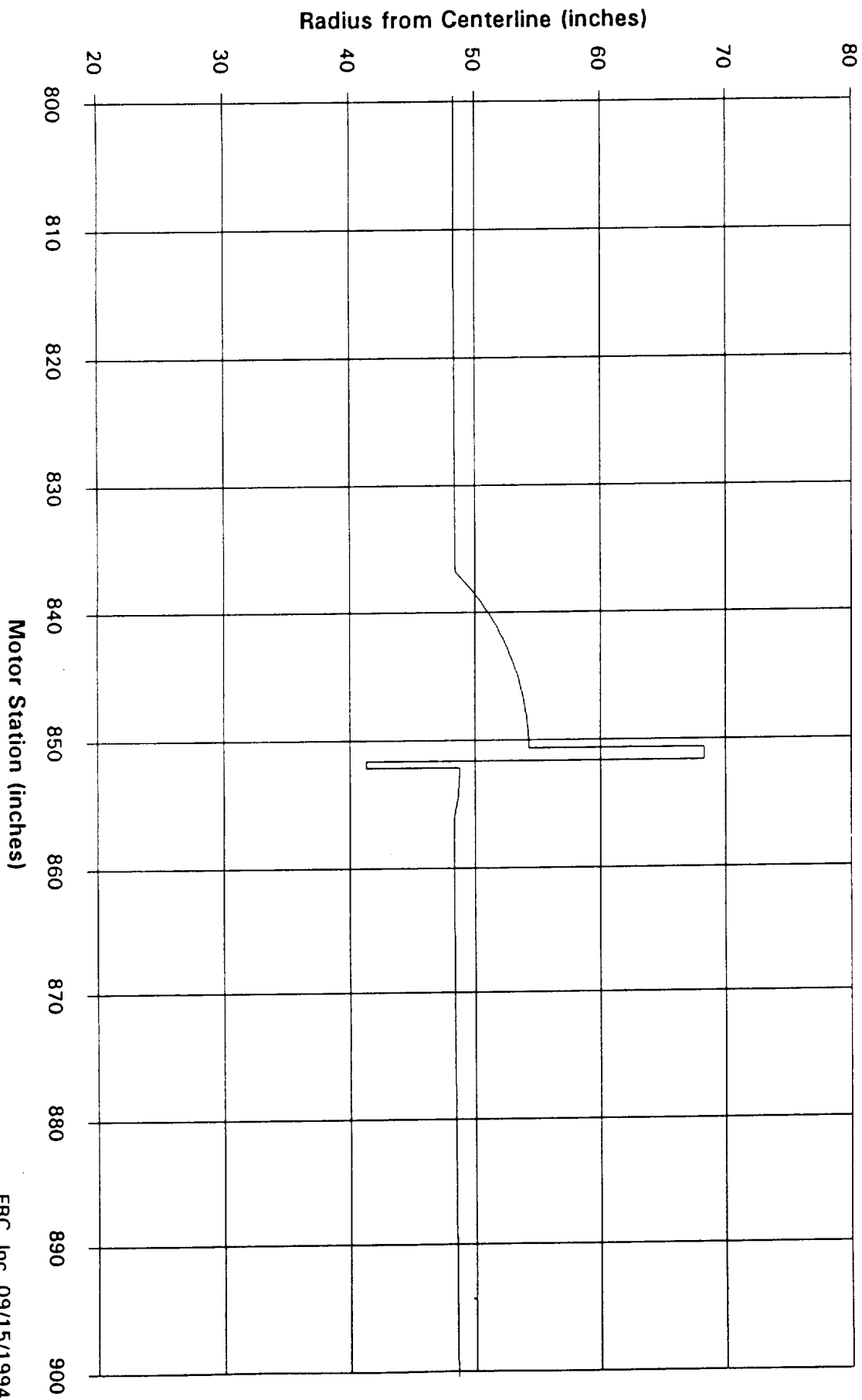


Figure 29. Discrete Particle Log-Normal Distribution Fit to the Quench Bomb Data-  
500 psi WECCO at 3-inch



**Figure 30. RSRM Geometry - Forward Joint  
49.57 Second Burn Time**



**Figure 31. RSRM Geometry - Center Joint  
49.57 Second Burn Time**

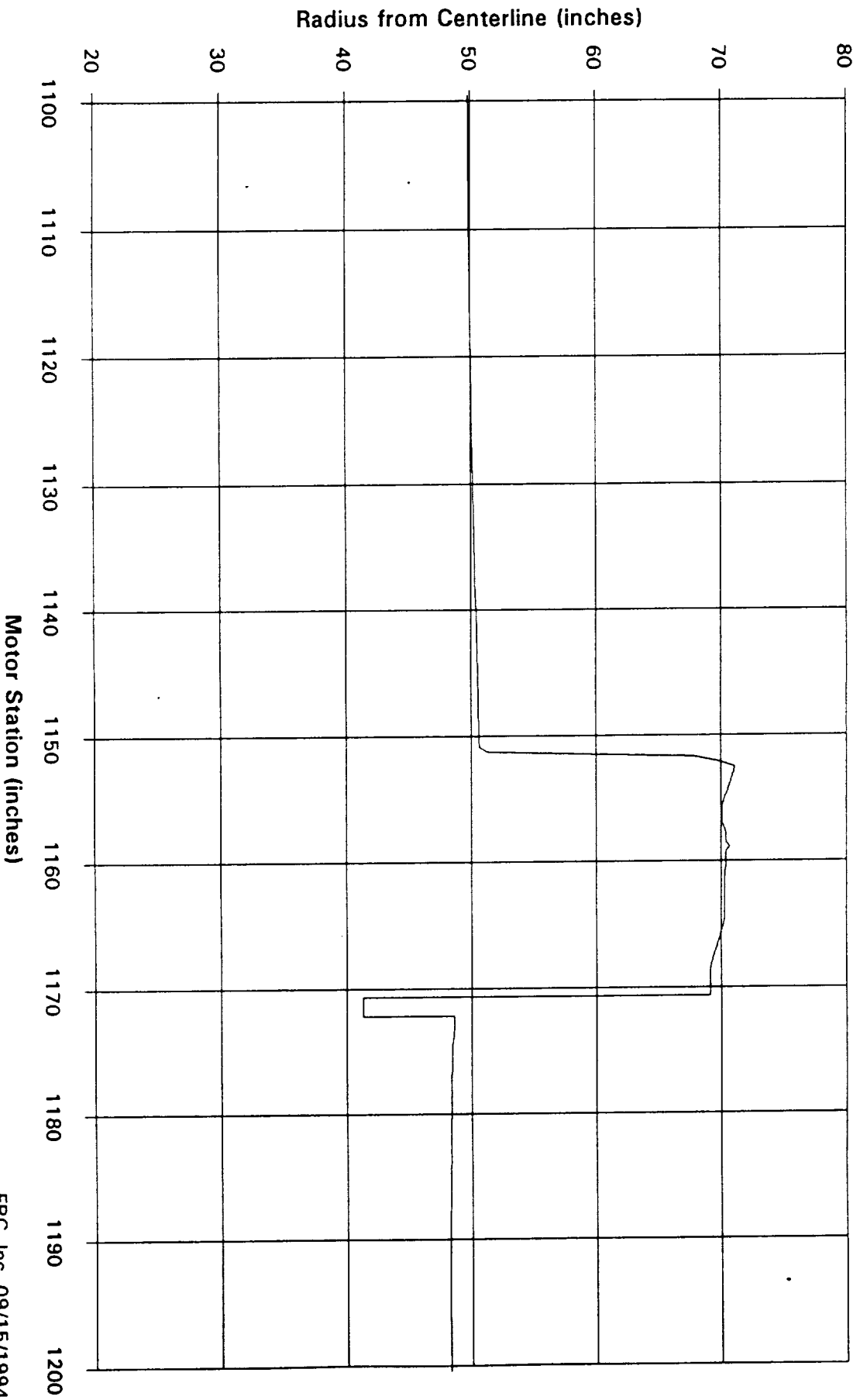


**Figure 32. RSRM Geometry - Aft Joint  
49.57 Second Burn Time**

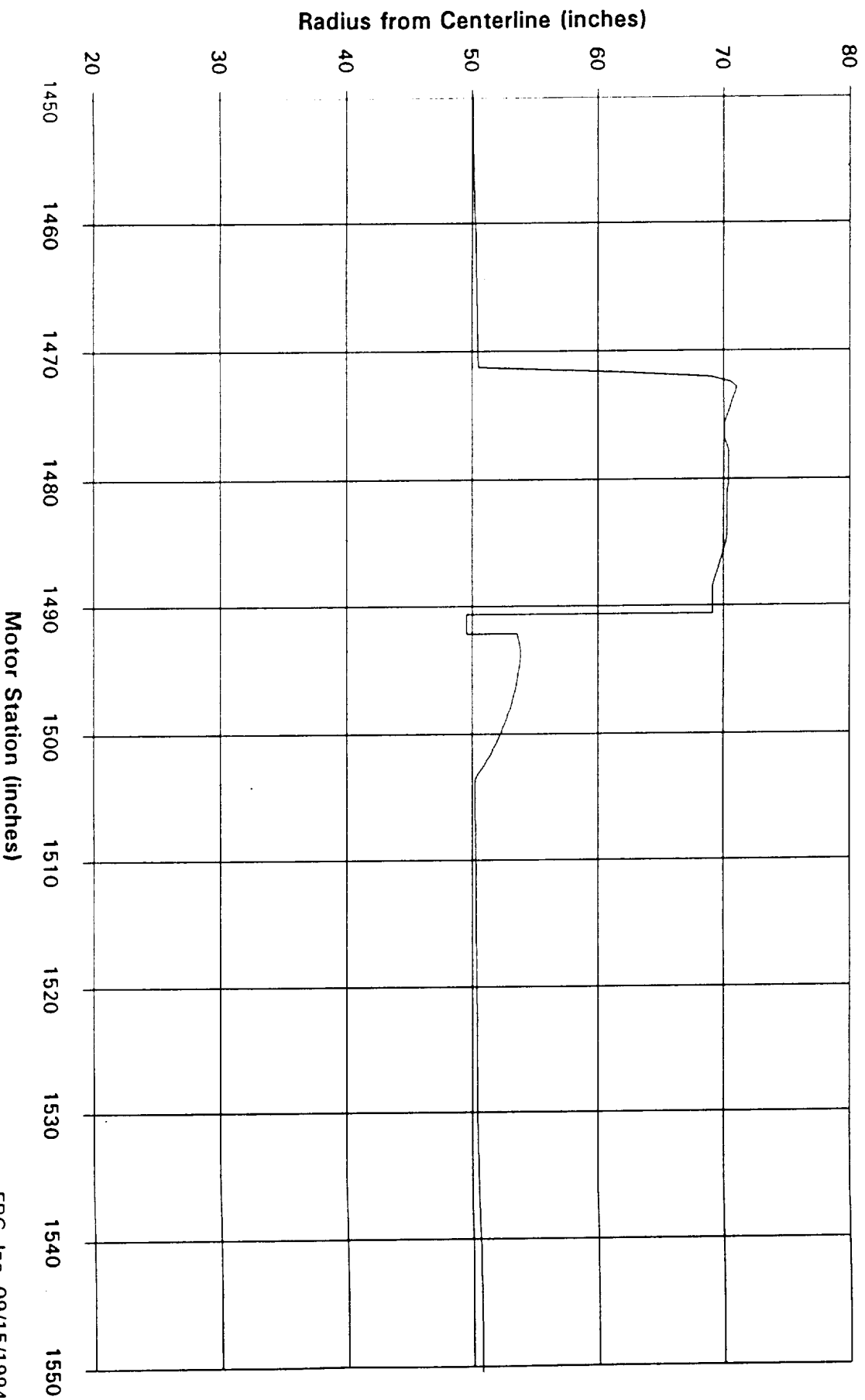


**Figure 33. RSRM Geometry - Nozzle Nose  
49.57 Second Burn Time**

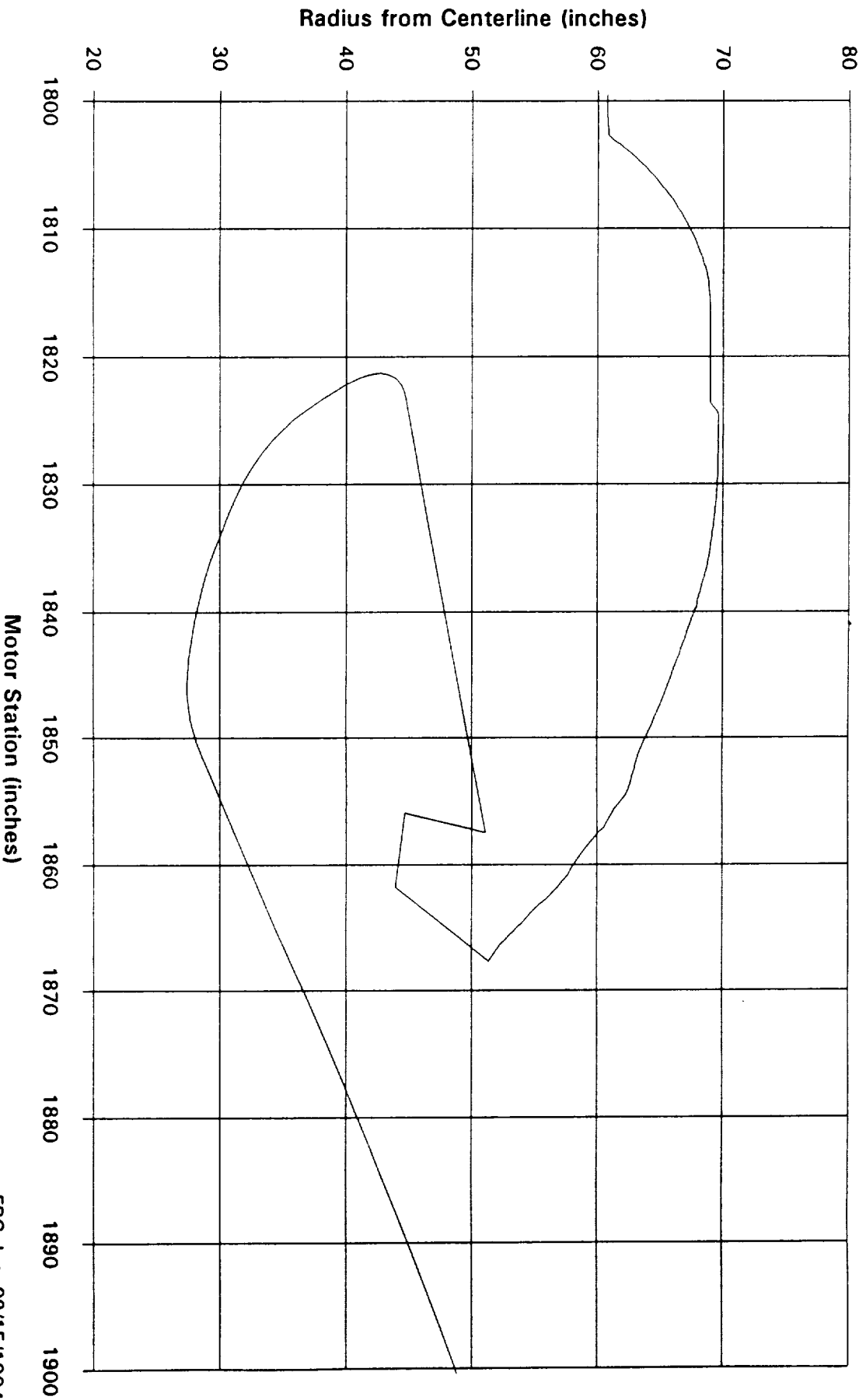
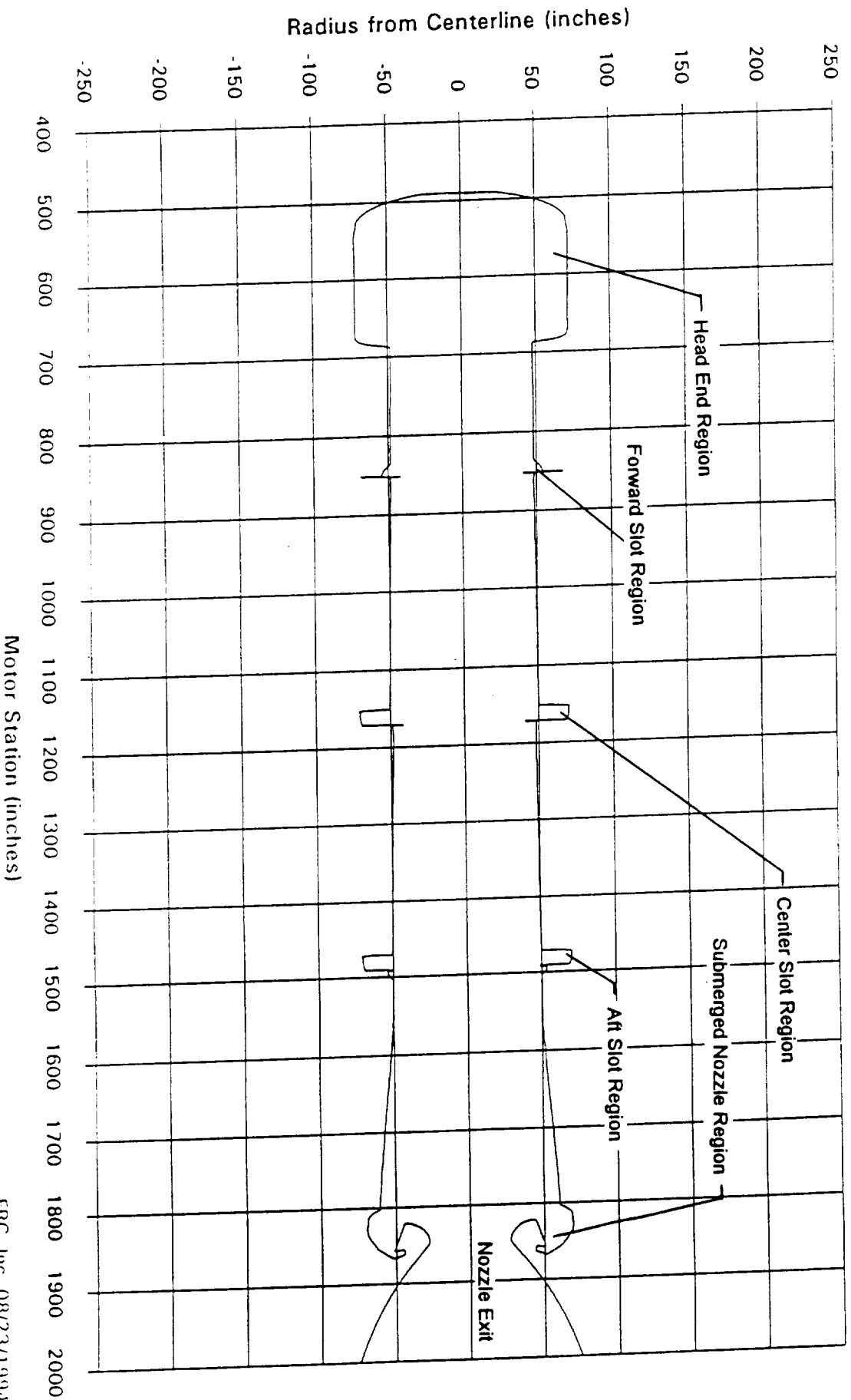


Figure 34. RSRM Full Motor Geometry, 49.57 Second Burn Time



**Figure 35. RSRM Full - Forward Joint  
79.75 Second Burn Time**

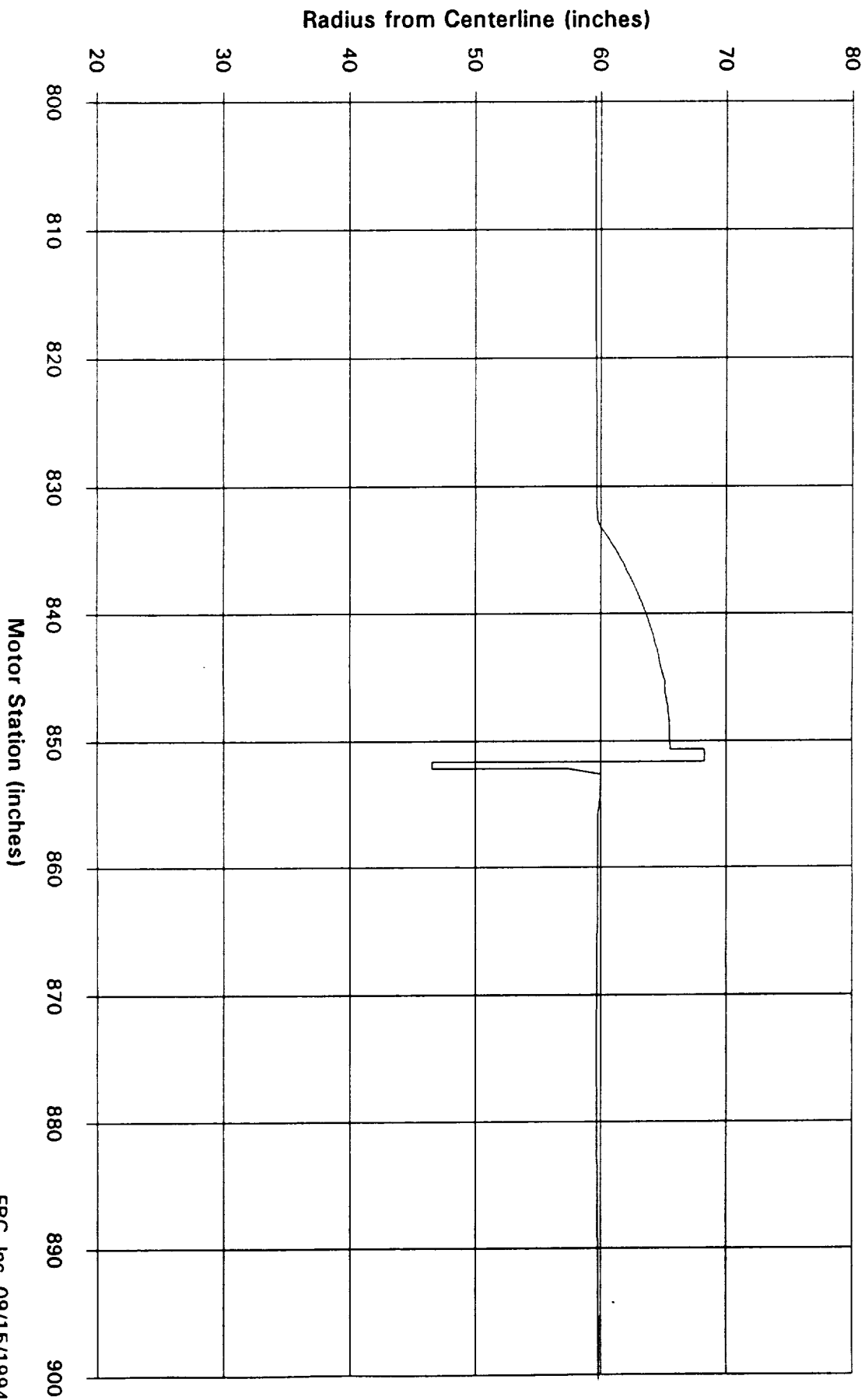
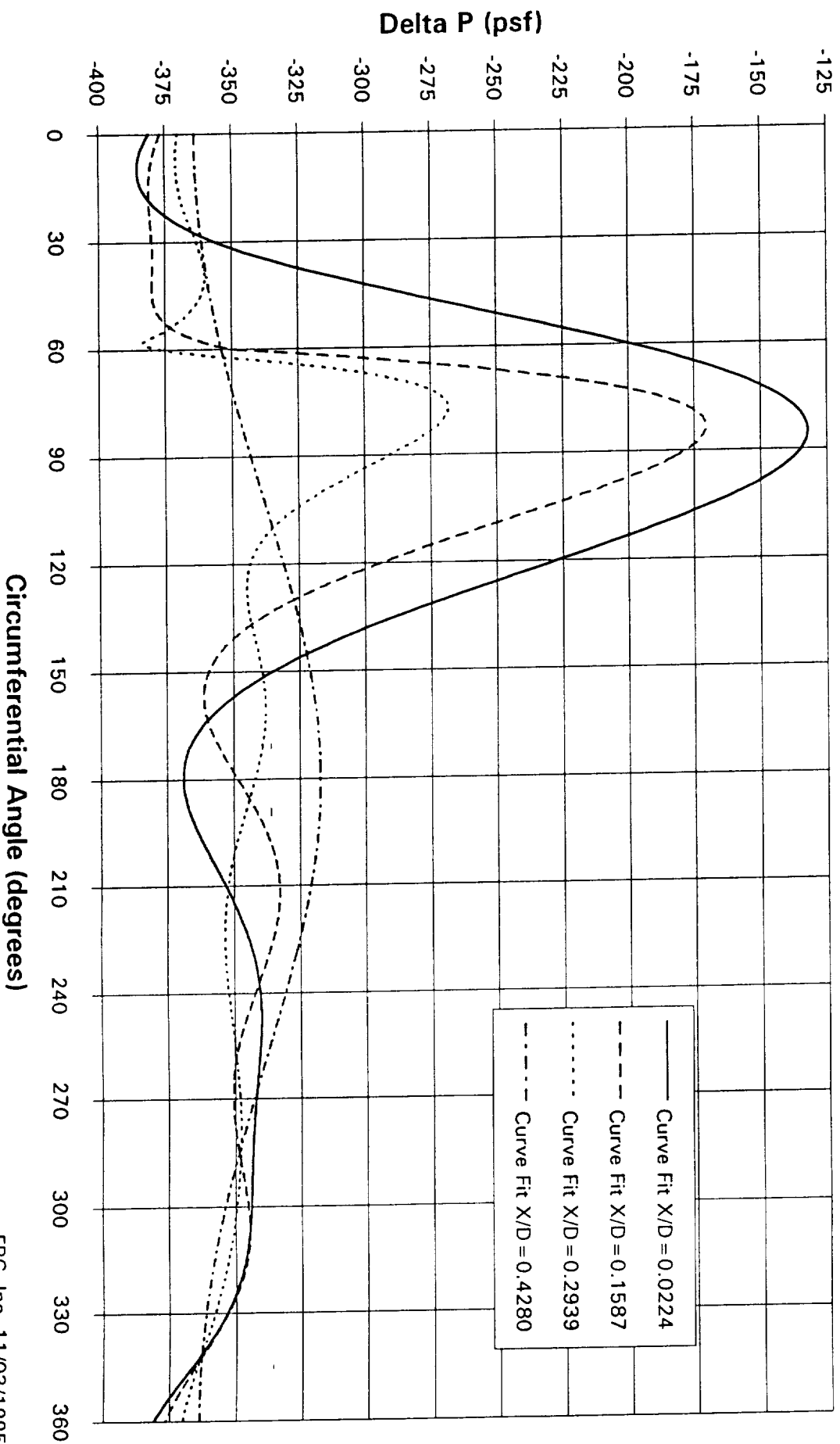




Figure 5. RSRM External Nozzle Pressures  
Mach No. = 0.95  $q = 696$  psf  
Pitch Angle = -2.9 Deg. Gimbal Angle = 2.26 Deg.



ERC, Inc. 11/03/1995



**Figure 36. RSRM Full - Center Joint**  
**79.75 Second Burn Time**

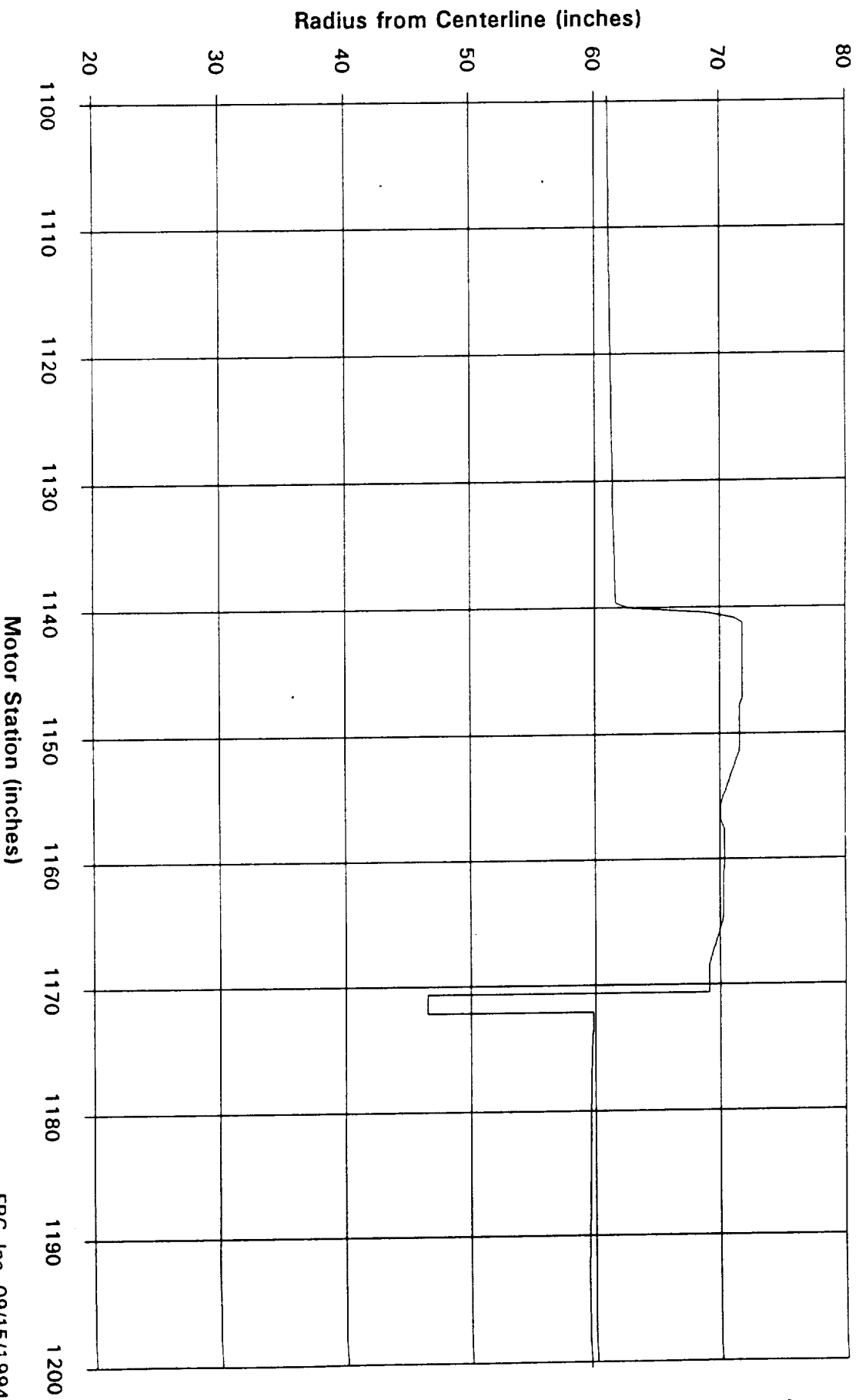


**Figure 37. RSRM Full - Aft Joint  
79.75 Second Burn Time**

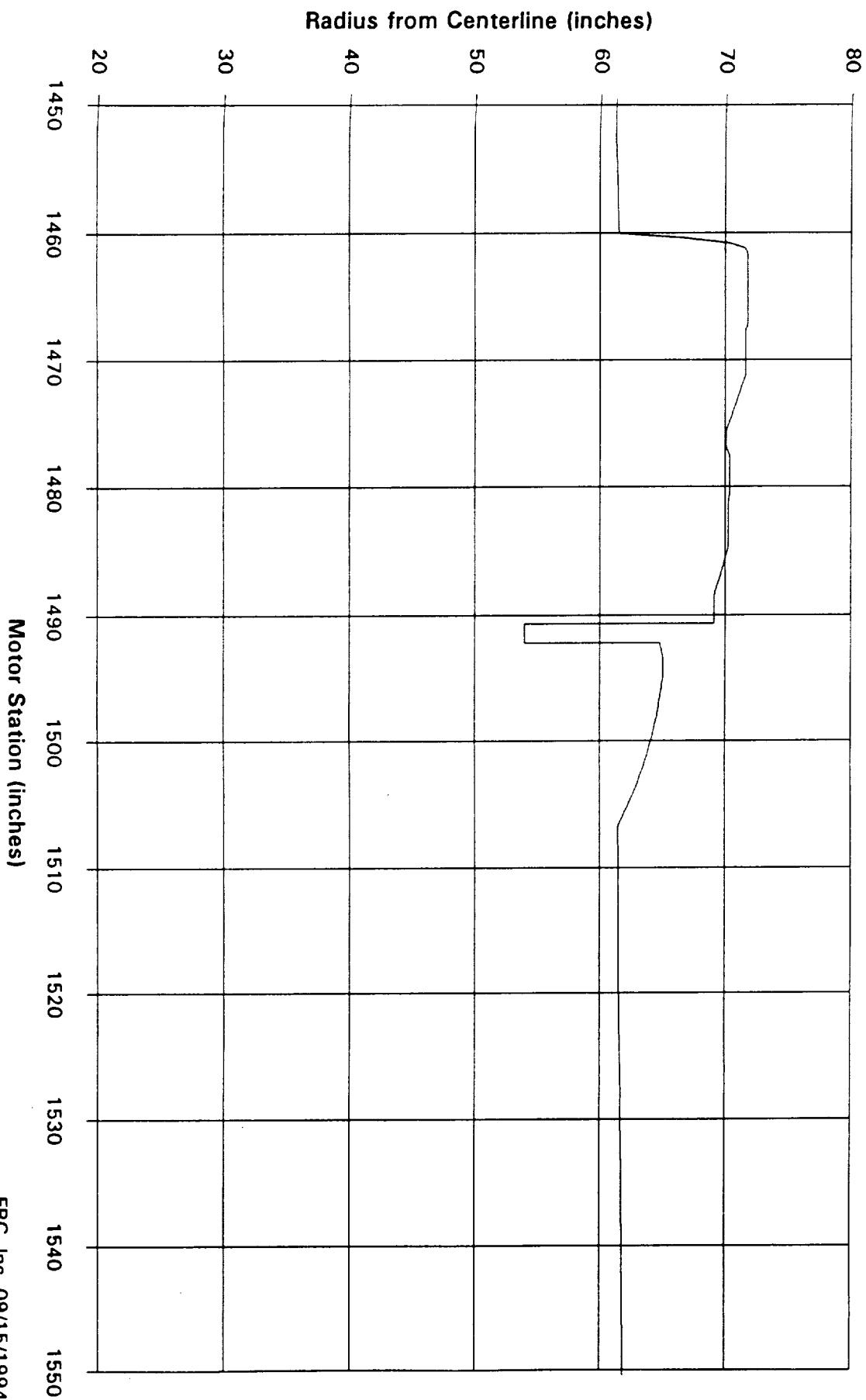


**Figure 38. RSRM Full - Nozzle Nose  
79.75 Second Burn Time**

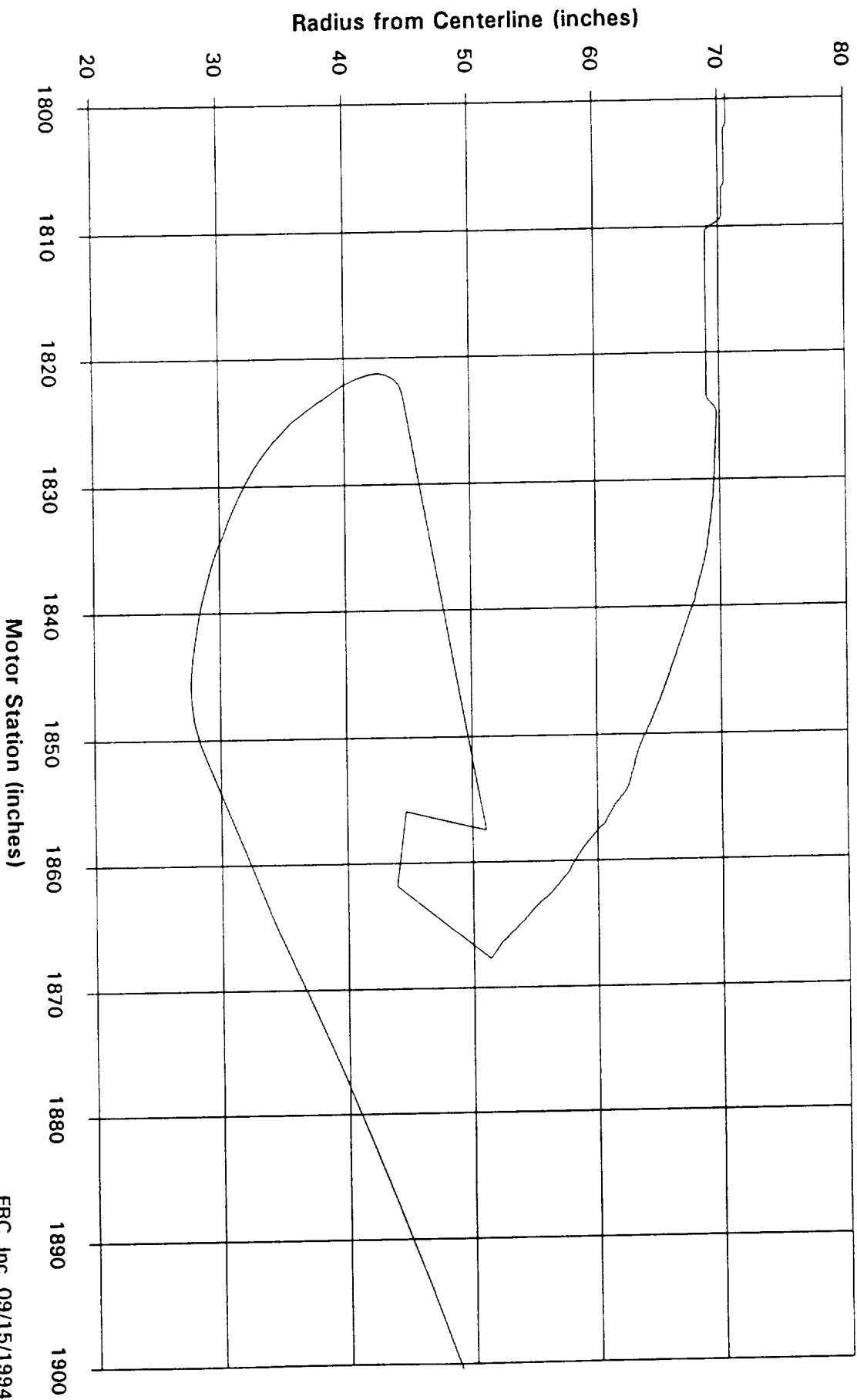
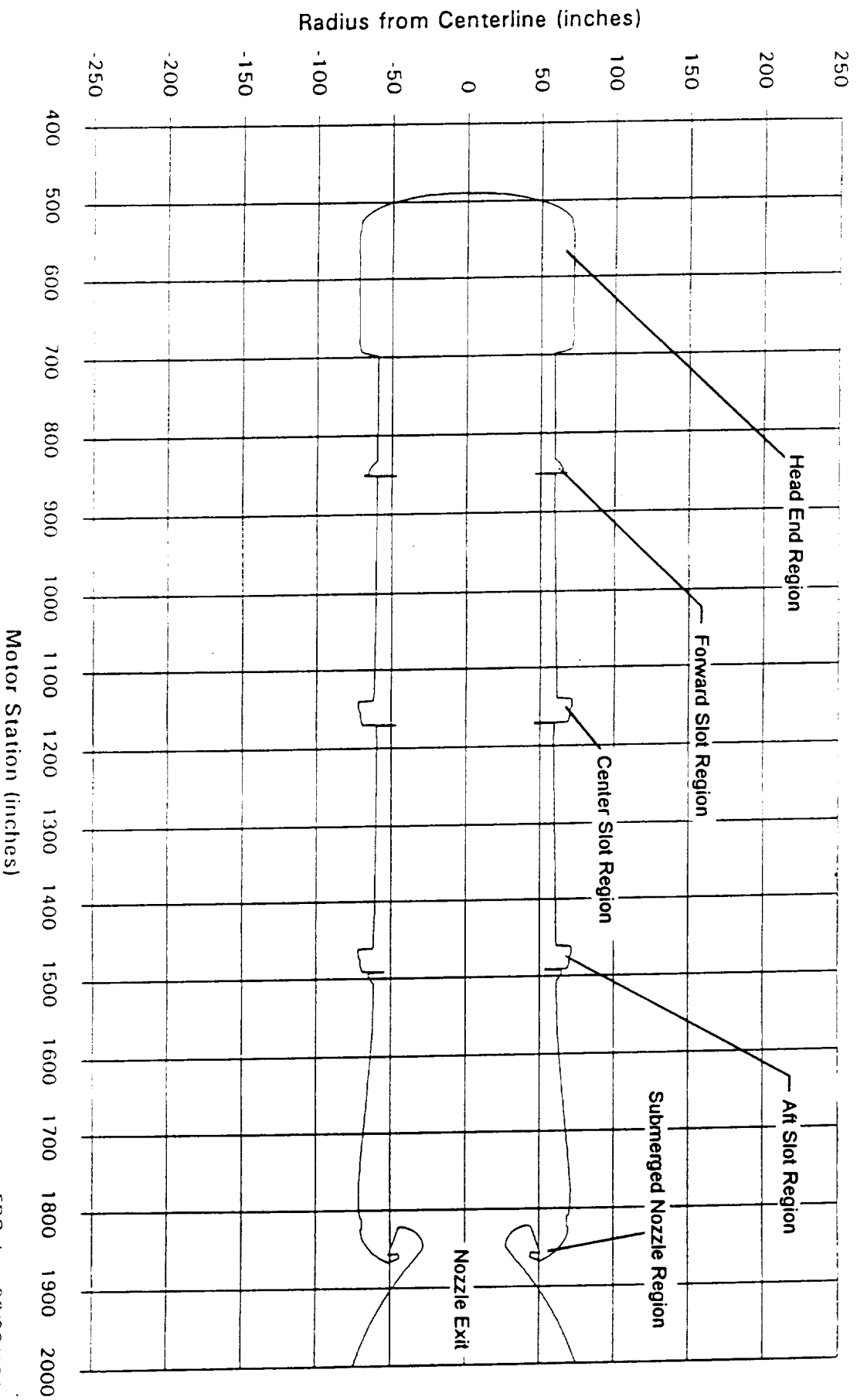
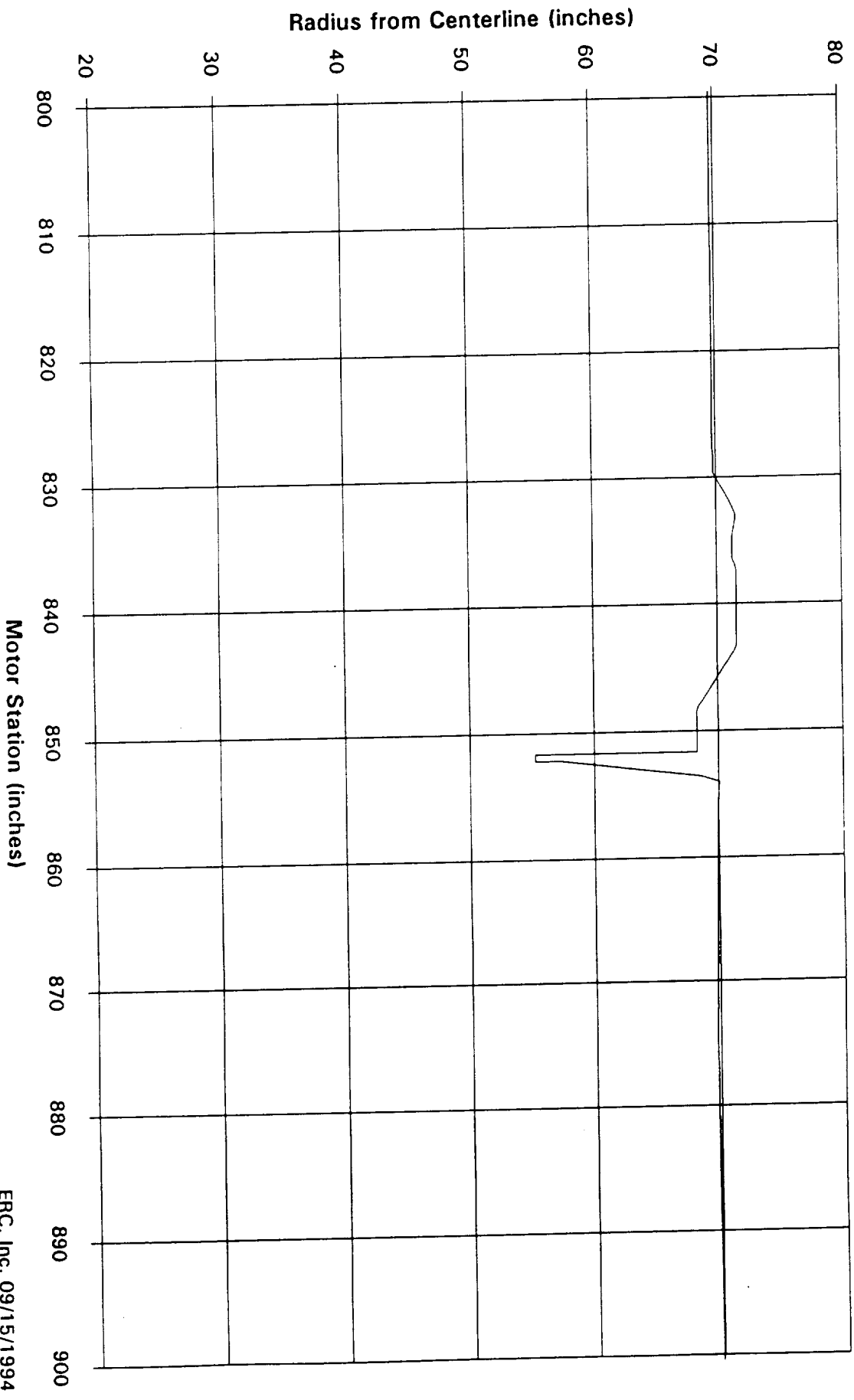


Figure 39. RSRM Full Motor Geometry, 79.75 Second Burn Time



**Figure 40. RSSRM Geometry - Forward Joint  
109.83 Second Burn Time**



**Figure 41. RSRM Geometry - Center Joint  
109.83 Second Burn Time**

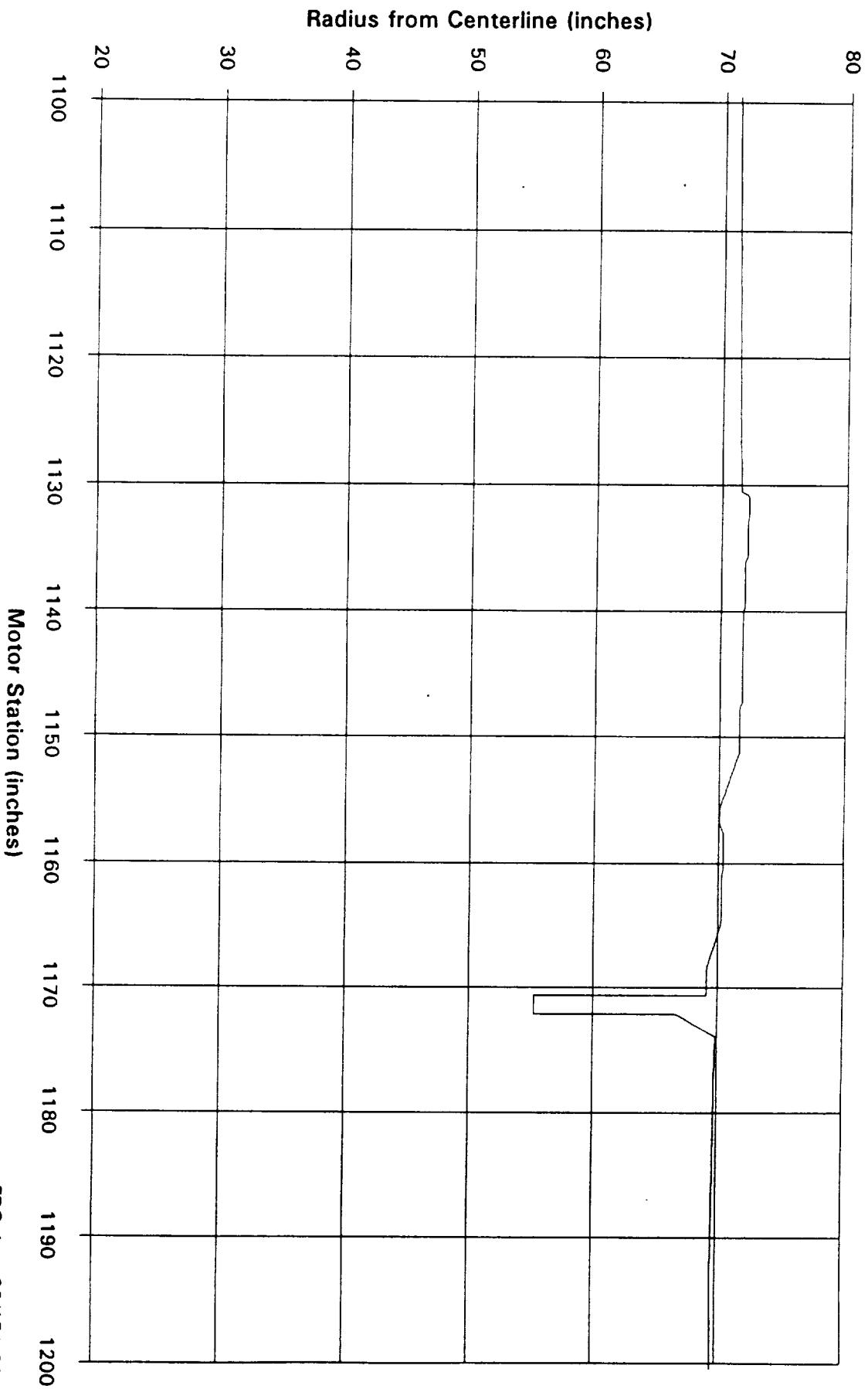
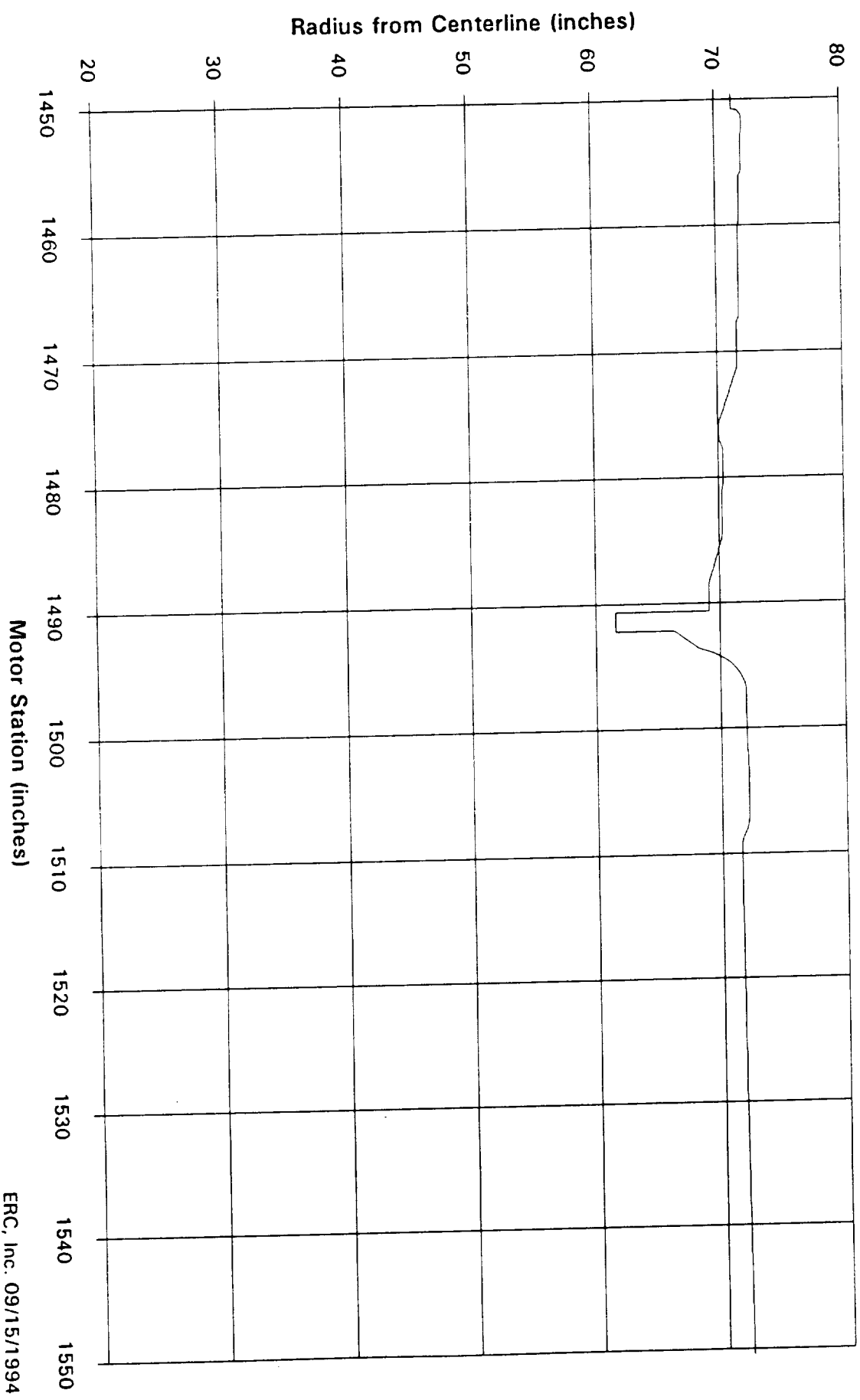




Figure 42. RSRM Geometry - Aft Joint  
109.83 Second Burn Time



**Figure 43. RSRM Geometry - Nozzle Nose  
109.83 Second Burn Time**

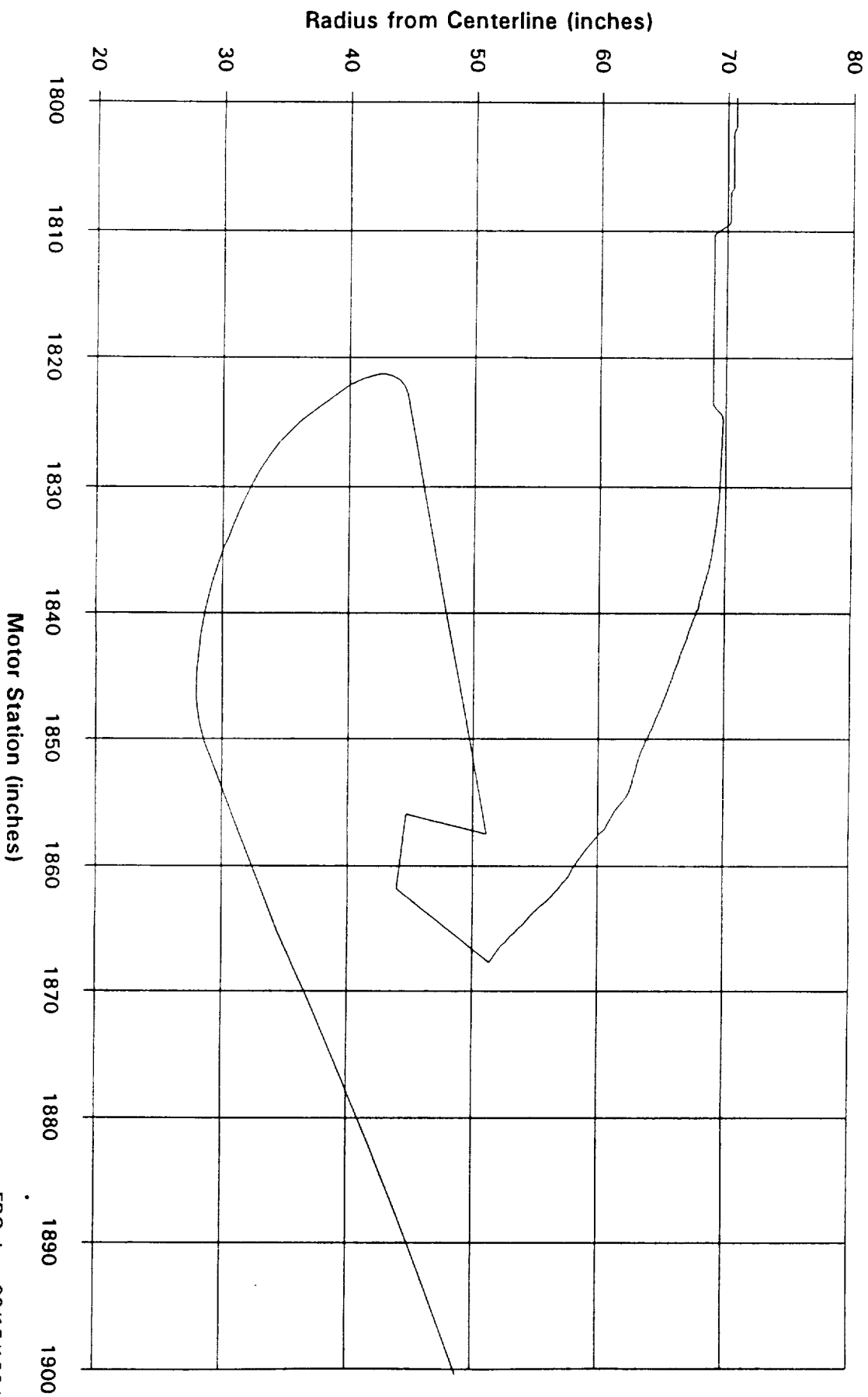
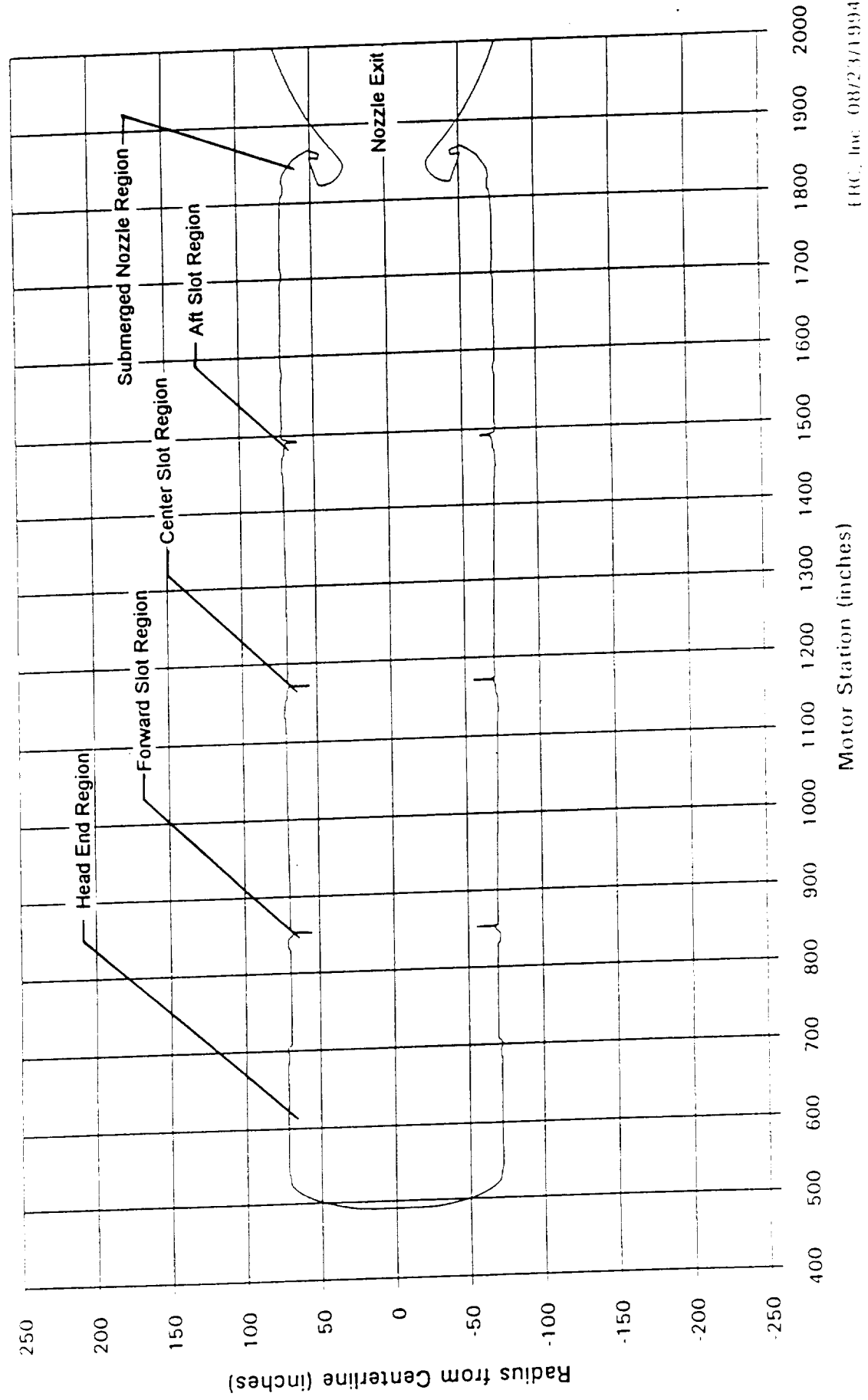


Figure 44. RSRM Full Motor Geometry, 109.83 Second Burn Time





## **NBR Stiffness Investigation Summary**

Trends towards a considerable increase in the stiffness of the NBR insulation material used in the bearing and boot of the flex nozzle caused concern about the torque margin of the TVC system. A review of all torque components and data was performed including aerodynamic torques, both internal and external. A inquiry was received from Thiokol inquiring about our cold flow test data for the ASRM model with nozzle gimbal angles of 0, 4, and 8 degrees. An AIAA paper was written on this work for the 1994 Joint Propulsion Meeting and can be found in section 3.3.3

A NASA/MSFC team was formed to address the short and long term issues associated with the increase in NBR stiffness as it relates to various aspects of motor operation. A cold flow model experiment was conceived and hardware and testing requirements were defined. This experiment evaluated the effect of stiff and nominal inhibitors on the amplitude of the oscillating pressure. Work was performed to scale the full scale RSRM inhibitors to a size which would be suitable for the RSRM 6.5% Scaled Nozzle Slag Model. The inhibitors were also scaled so that resonance would occur between the first longitudinal mode of the model and the hole tone frequency of the inhibitor. These calculations were performed for the center and aft inhibitors at 65 and 80 second burn times.

A large effort on this problem focused on completing the NBR Inhibitor Cold Flow Dynamics Model testing and CFD analyses to determine the effect of NBR stiffness on the deformed inhibitor geometry, the amplitude of pressure oscillations, and any possible effects on slag accumulation. These tasks are discussed elsewhere in this report. The cold flow data was not exhaustively analyzed due to a very tight time schedule, but preliminary assessment indicated lower oscillating pressure amplitudes with the stiffer inhibitors. However, stiffer inhibitors are less bent over in the flow and thus have higher velocities and edge tone frequencies at a given burn time. The associated dynamic pressure of the flow is thus higher which means that one would expect higher oscillating pressure amplitudes. However, the maximum pressure amplitudes occur during resonance between the edge tones and the motor longitudinal modes. This resonance would occur at a later burn time for stiffer inhibitors after they eroded down to the same inside diameter as the nominal inhibitors. At this later time near the end of motor operation the motor dynamic pressure is lower and therefore the time shift in the point of resonance would have the effect of reducing the oscillating pressure amplitudes. More detailed descriptions of the results are available in the final review package, "Inhibitor Stiffening Evaluation (NBR)", dated 22 December 1994.

Interest was expressed in continued cold flow testing of some other inhibitor material samples and in continuing to refine our ability to achieve tuning between the inhibitor edge tones and the model acoustic modes. An extended test plan for the NBR Inhibitor Dynamics Model was formulated and discussed at a planning meeting. Work on this model is covered in Section 3.3.10.

## **Nominal and Stiff NBR Inhibitor Materials Analysis**

The CFD task to analyze the deformation and flow field disturbance effects associated with the NBR inhibitor material used in the RSRM was completed during the month of December. This task has been a cooperative effort between ERC, Inc. and NASA/MSFC/ED28. All relevant material was submitted to NASA/MSFC on or before 23 December 1994. The CFD task included complete inhibitor deformation analyses of both the nominal NBR material, which has been used in past motor flights, and the new stiffer NBR material which will be used in future motor flights. When this task was initiated in November, several analysis goals were incorporated into the task schedule. Because of the limited analysis time schedule and the uncertain availability of timely information describing the various motor inhibitor properties, only the analyses of the forward and center inhibitors were included in the goals for this analysis. However, ERC, Inc. and NASA/MSFC/ED28 were able to perform enough analysis on the aft inhibitor to provide reasonable estimates of both the inhibitor deformations and associated flow field disturbances. All of the originally stated task goals were completed on schedule along with the previously mentioned inclusion of the effects due to the aft inhibitor deformations. The original goals of the CFD analysis included the following accomplishments. First, the coupled fluid dynamic/mechanical inhibitor deformation analysis was to show whether or not there was a difference in the deformations associated with the nominal and stiff NBR material. As expected, the stiffer NBR material deformed less than the nominal NBR material. The final deformed inhibitor geometries obtained from the fluid dynamic/mechanical iterative analysis were then used to perform a fully coupled two-phase flow slag accumulation analysis. This analysis was performed to determine the effect of the different inhibitor geometries on the accumulation of slag at the field joints and underneath the submerged nozzle. The final deformed geometry solutions were also used to compute the paths of large droplets of slag released from the motor inhibitor tips. This was to simulate the release of slag accumulating at the field joints and determine if there was a propensity for the released slag to collect underneath the submerged nozzle. The flow field solutions for the nominal and stiff inhibitor materials were then analyzed to determine if a difference between the flow fields existed downstream of the aft inhibitor near the nozzle nose. Finally, flow field solution information near the inhibitor tips was given to NASA/MSFC/ED33 so analyses to estimate vortex shedding and acoustic mode induced motor pressure fluctuations could be performed. The details of this analysis will be presented in the following paragraphs along with a short recap of the initial analysis details presented in the November 1994 monthly report.

Because of the time-critical nature of this task, only a single motor burn time could be analyzed. It was decided that since motor geometries at 33, 50, 65, 80, and 110 seconds were already available, one of these times would be used in order to save analysis time. The decision as to which burn time to use was made after discussions between NASA/MSFC, Thiokol and ERC, Inc. as to which burn time would provide the most information for the various tasks to be performed under the complete inhibitor stiffness analysis. The 80 second burn time geometry was chosen because the

pressure fluctuation amplitudes in the motor due to the internal flow induced phenomena were observed to be greater at this time than for the other available burn times.

The coupled fluid dynamic/mechanical deformation analysis of the inhibitors was performed as an iterative analysis. The fluid dynamic analysis of the inhibitors was performed by analyzing the full motor at the 80 second burn time from the head end to a point well within the supersonic region of the nozzle exit cone. This CFD solution of the full motor produced pressure distributions for all the inhibitors which were used by the mechanical analysis team of NASA/MSFC/ED28. The mechanical analysis was performed by analyzing each inhibitor/propellant segment separately. The pressure drop in the motor at the 80 second burn time was low enough so that a full mechanical analysis of the complete motor was not warranted. The initial configuration of the motor inhibitors was assumed as undeformed or straight. This analysis yielded an initial estimate of the pressure distribution on the front and back faces of the inhibitors as well as the pressure distribution on the propellant. The initial motor inhibitor geometry and CFD solutions were presented in the November monthly report and referred to as geometry 1 and flow field solution 1. This initial information was used by NASA/MSFC/ED28 to perform a mechanical deformation analysis on the motor inhibitors and propellant. The deformed inhibitor and propellant geometry predicted by the mechanical analysis, presented in the November monthly report and referred to as geometry 2, was then used to compute a new inhibitor and propellant pressure distribution, flow field solution 2. This solution was then used by the mechanical deformation analysis code of NASA/MSFC/ED28 to compute a new deformed geometry and so forth. Normally this iterative process would be continued until the changes in the deformed inhibitor geometries were within the tolerance of the solution accuracy. Since this analysis was very time critical, there was only enough estimated time to perform four iterations of the CFD and mechanical deformation codes. As the analysis progressed ahead of schedule, ERC, Inc. and NASA/MSFC/ED28 were able to add an additional iteration between the CFD and mechanical deformation codes. At the end of these five iterations, the solutions were examined and it was determined that the convergence of the deformed geometries for all the motor inhibitors was of sufficient accuracy to produce useful analytical results. The analysis determined the shape of both the nominal and stiff NBR motor inhibitors at the 80 second motor burn time.

The inhibitor lengths were obtained from Thiokol on 11 November 1994. Figures in the November monthly report show the data transmitted by Thiokol on 11 November 1994. The thicknesses of the inhibitors shown in these figures were modified by Ted Kovacevich, ED28, according to the inhibitor isotherm information sent to him at a latter date than the 11 November transmittal. The final thicknesses of the various inhibitors will be shown later in this section.

The analysis was performed as a two-phase analysis using the CELMINT surface combustion model and the equilibrium thermochemistry model to compute the composition and properties of the combusting gas flow. Table I shows the RSRM

propellant formulation used by the equilibrium code to compute the flow mixture properties. Table II shows the general thermochemical properties needed by CELMINT.

**Table I. RSRM Propellant Formulation used for the Thermochemistry Computations.**

Propellant Ingredient	Percent Weight
NH <sub>4</sub> ClO <sub>4</sub>	69.82%
Fe <sub>2</sub> O <sub>3</sub>	0.18%
C <sub>6.884</sub> H <sub>10.089</sub> O <sub>0.278</sub> N <sub>0.264</sub>	14.0%
Al	16.0%

**Table II. Thermochemical Properties Used For The RSRM Motor Analysis**

Viscosity, $\mu$	6.189x10 <sup>-5</sup> lbm/sec-ft
Prandtl Number, Pr	0.4777
Thermal Conductivity, k	6.222x10 <sup>-5</sup> Btu/sec-ft-°F

Mass flow rate boundary conditions were used at the propellant surfaces. These were obtained from SPP ballistic runs made by Sverdrup. Table III shows the mass flow rates from the various propellant surfaces used in this analysis. The total propellant surface area modeled by the computational grid for the 80 second burn time geometry was 411,361 square inches.

**Table III. Mass Flow Rates For 80 Second Web Time**

Forward Segment	1501 lbm/sec.
Forward Center Segment	2659 lbm/sec.
Aft Center Segment	2654 lbm/sec.
Aft Segment	2803 lbm/sec.
Total Mass Flow Rate	9617 lbm/sec.

Table IV shows the mass injection rates used by CELMINT in this analysis for the gas phase and the discrete particle phase analysis.



**Table IV. Conditions for the 80 Second Web Time Solution**

	<b>Mass Flow Rate (lbm/sec)</b>	<b>Mass Flow Rate (kg/sec)</b>	<b>Mass Flow Rate Per Unit Area (kg/m<sup>2</sup>-sec)</b>
<b>Total Mass</b>	9617	4362.2	16.44
<b>Injected Aluminum Oxide Surface Combustion</b>	783.8	355.5	1.34
<b>Injected Gas Phase Surface Combustion</b>	8833.2	4006.7	15.10

As mentioned in the November 1994 monthly report, the computational grid used to solve for the geometry 1 flow field was not resolved sufficiently in the slot regions. However, this existing grid mapping was chosen to provide for the rapid generation of an initial pressure distribution on the unbent inhibitors and it was deemed that the grid was sufficient to provide the initial pressure distribution on the inhibitors. The grid used to solve for flow field 2 was altered to alleviate this grid resolution problem. The grid used to solve for the geometry 2 flow field was altered in both the axial and radial directions. Twenty-three grid cells were added in the axial direction and the axial grid was redistributed as required based on the geometry 1 flow field gradients and the curvature of the geometry 2 inhibitors. Eight more radial grid cells were added to the head end, center slot, and aft slot cavities. Also, five more radial grid cells were added on the upstream side of the forward inhibitor. The overall grid for geometry 2 was 488 by 68. This was the grid resolution used on all the other CFD runs except for geometry 3, which because of excessive bending of the center inhibitor, required a special grid mapping.

Figures 2, 3, 4, and 5 show the computational grid in the forward, center, aft slot, and submerged nozzle regions which was used to obtain the CFD solution for the final nominal NBR deformed geometry iteration, (iteration 5). Figures 6, 7, 8, and 9 show the computational grid in the forward, center, aft slot, and submerged nozzle regions which was used to obtain the CFD solution for the final stiff NBR deformed geometry iteration, (iteration 5). The grids are very similar for the two configurations since the geometries themselves are very similar. The same grid resolution at the propellant and insulation surfaces was maintained for both configurations. The thickness of the inhibitors shown in the figures describing the computational grid accurately represent the final thicknesses used in the analyses. These thicknesses were obtained from Thiokol inhibitor isotherm plots analyzed by Ted Kovacevich of NASA/MSFC/ED28. The same grid was used to model both the nominal and stiff NBR inhibitor motor configurations in the far aft end of the motor. This allowed for a direct grid point to grid point comparison of the flow field solutions in the aft end of the motor near the nozzle nose.

Figure 10 shows all the deformed geometry iterations associated with the analysis of the nominal NBR forward inhibitor. It can be seen from the figure that the final two geometries, geometry 4 and geometry 5, converged to within a sufficient tolerance to fulfill the goals of this analysis. In the same way, Figure 11 shows all the deformed geometry iterations associated with the analysis of the stiff NBR forward inhibitor. A comparison of the nominal and stiff final deformed geometries is shown in Figure 12. The nominal NBR material deforms more in both the radial and axial directions than does the stiff NBR material. This was also true for all the motor inhibitors as expected. The shape difference between the nominal and stiff NBR forward inhibitors may have to do with how pressure is distributed along the length of the long, thin forward inhibitor.

The deformed geometry iterations associated with the analysis of the nominal NBR center inhibitor are shown in Figure 13. In the same way, Figure 14 shows all the deformed geometry iterations associated with the analysis of the stiff NBR center inhibitor. A comparison of the nominal and stiff final deformed geometries is shown in Figure 15.

Once property information was obtained for the aft inhibitor, there was only time to perform two deformation analysis iterations, but the final deformation solution was judged to be usable for this analysis for the following reasons. Several trial estimated geometries for the aft inhibitor were constructed and pressure distributions for these were determined. These pressure distributions provided estimates of the maximum and minimum deformation bounds of the inhibitor based on both positive (resultant force in the downstream direction) and negative (resultant force in the upstream direction) pressure differentials calculated between the front and back faces of the inhibitor. The greater thickness and much shorter height of the aft inhibitor compared to the forward and center inhibitors also means that only a small amount of deformation can occur for this inhibitor, thus acting as a further bound to the deformations. A comparison of the nominal and stiff final deformed geometries for the aft inhibitor are shown in Figure 16.

The internal flow field solution for the final deformed geometry, iteration 5, configuration of the propellant grain and inhibitors is described in the following paragraph. Figure 17 shows an overall view of the velocity magnitude in the nominal NBR inhibitor motor. This figure is sufficiently representative of the velocity magnitude for both the nominal and stiff NBR inhibitor motors such that no plot of the velocity magnitude in the stiff NBR inhibitor motor need be shown. Figures 18, 19, and 20 show the velocity field in the regions of the forward, center and aft slots for the nominal NBR inhibitors. The flow does not impinge extensively on the forward inhibitor due to both the low axial flow velocity in the forward region of the motor and the nature of the propellant geometry at the forward slot. The center and aft slots both form recirculation regions in the slot cavities due to the geometry formed by the burning propellant. There is a stagnation point on both the center and aft upstream inhibitor faces where the recirculation region in the slot is separated from the flow moving in the axial downstream direction. Figure 21 shows the velocity field in the region of the submerged nozzle. This type of recirculation region is similar to those shown before for this type of submerged cavity

problem. The recirculation region reattachment point is located on the outboard side of the nozzle downstream of the nozzle nose. Figures 22, 23, and 24 show the velocity field in the regions of the forward, center and aft slots for the stiff NBR inhibitors. The flow field associated with the stiff NBR inhibitors is very similar to that shown for the nominal NBR inhibitors. There are small differences in the location of the stagnation flow reattachment point on the center and aft inhibitors for the nominal and stiff NBR inhibitors but the nature of the flow in general is the same for both materials. Figure 25 shows the velocity field in the region of the submerged nozzle. Only extremely minor difference in the aft end flow field for the nominal and stiff NBR inhibitor motors exist as will be illustrated further when velocity profiles are shown for the aft end of the motor.

Figures 26, 27, and 28 show the final radial pressure distributions on the nominal NBR forward, center and aft inhibitors. Figures 29, 30, and 31 show the final radial pressure distributions on the stiff NBR forward, center and aft inhibitors. The pressure distributions for the nominal/stiff pair of forward, center, and aft inhibitors are similar. The amplitude and location of the pressure changes are the only difference. Figures 26 and 29 show that there is no recirculation region in front of or behind the inhibitors and the pressure distribution curves are smooth, monotonically decreasing curves. There is more acceleration of the flow on the front face of the forward inhibitor than on the back face due to the confluence of both the upstream axial flow and the radial flow from the propellant just in front of the inhibitor. This causes the larger pressure drop on the front face of the forward inhibitor. The same is true for the front faces of the center and aft inhibitors. The pressure distributions for the front faces of the center and aft inhibitors illustrate the recirculation region within the center and aft slot cavity. This is illustrated by the inflection in the curve rather than the smooth monotonically decreasing curve for the front face of the forward inhibitor. There is no corresponding recirculation on the back side of the inhibitors and thus the pressure distribution for the back side curves are smooth.

Velocity profiles showing the axial velocity as a function of radial distance from the motor centerline are shown in Figures 32, 33, and 34 at the forward, center and aft nominal NBR inhibitors, respectively. Figures 35, 36, and 37 show the same plots for the stiff NBR inhibitors. All plots show the velocity profile constructed from the aft tip of the inhibitors to the motor centerline. Also shown in the figures are the average motor pressure, mass flow rate and velocity at the appropriate motor station associated with the aft tip of the inhibitors. This information was given to NASA/MSFC/ED33 and this information was used to perform analyses to estimate the amplitude of vortex shedding and acoustic mode induced motor pressure fluctuations.

Figure 38 shows the summary results for the two-phase flow slag accumulation analysis. The percent of the total slag captured in the motor is shown for the nominal and stiff forward, center, and aft inhibitors. Only a small amount of slag collects at the forward and center slots at this burn time. There is also a small difference in the amount of slag collecting at the aft slot. The slag collecting underneath the submerged nozzle is almost identical for the two inhibitor materials. There was also a desire to

know whether the extra slag which might collect on the stiff NBR inhibitors would spill into the region underneath the submerged nozzle or out the nozzle exit. An analysis was performed to analyze this by releasing large particles (ranging in size from 0.2 inches to 1.6 inches diameter) from the tips of the inhibitors. Figures 39, 40, 41, and 42 show the paths of these large particles of diameter 0.2, 0.4, 0.8, and 1.6 inches. These figures are for the nominal NBR inhibitor motor and all the particles pass out the motor nozzle. Figures 43, 44, 45 and 46 show the paths of the large particles previously specified diameter for the stiff NBR inhibitor motor. These figures show all the particles regardless of diameter pass out the nozzle exit except for those released from the aft inhibitor tip. The particles of all diameters released from the aft inhibitor tip impact the nozzle throat ramp on the outboard side of the nozzle. Table VII shows a summary of this information for all the particles.

One final bit of information was delivered to NASA/MSFC. This is shown in Figure 47. This is the axial velocity profile from the motor case insulation to the motor centerline just upstream of the nozzle nose. This illustrates that the inhibitor deformation effects caused by inhibitors of different stiffness have dissipated in the aft end of the motor. The velocity profiles are almost identical for the nominal and stiff NBR inhibitor motor configurations at this motor location.

The ERC, Inc. analyses results may be summarized by the following findings. The stiff NBR material caused the inhibitors to deform less in the axial and radial directions than the nominal NBR material. There is a larger amount of slag accumulated at the center slot in the stiff NBR inhibitor motor than in the nominal NBR inhibitor motor but the amount of slag collected is still very small for both the stiff or nominal NBR inhibitor motors. There is also a slightly larger amount of slag which collects in the aft slot for the stiff NBR inhibitor motor. However, this does not appear to be important since analysis shows that the slag released from the slot does not collect underneath the nozzle. Overall, the amount of slag collecting underneath the nozzle for the stiff or nominal NBR inhibitor motors is almost the same. Analysis of the flow field in the aft end of the motor also shows that the effects of deformation differences upstream of the nozzle have dissipated by the time the flow reaches the far aft end of the motor.

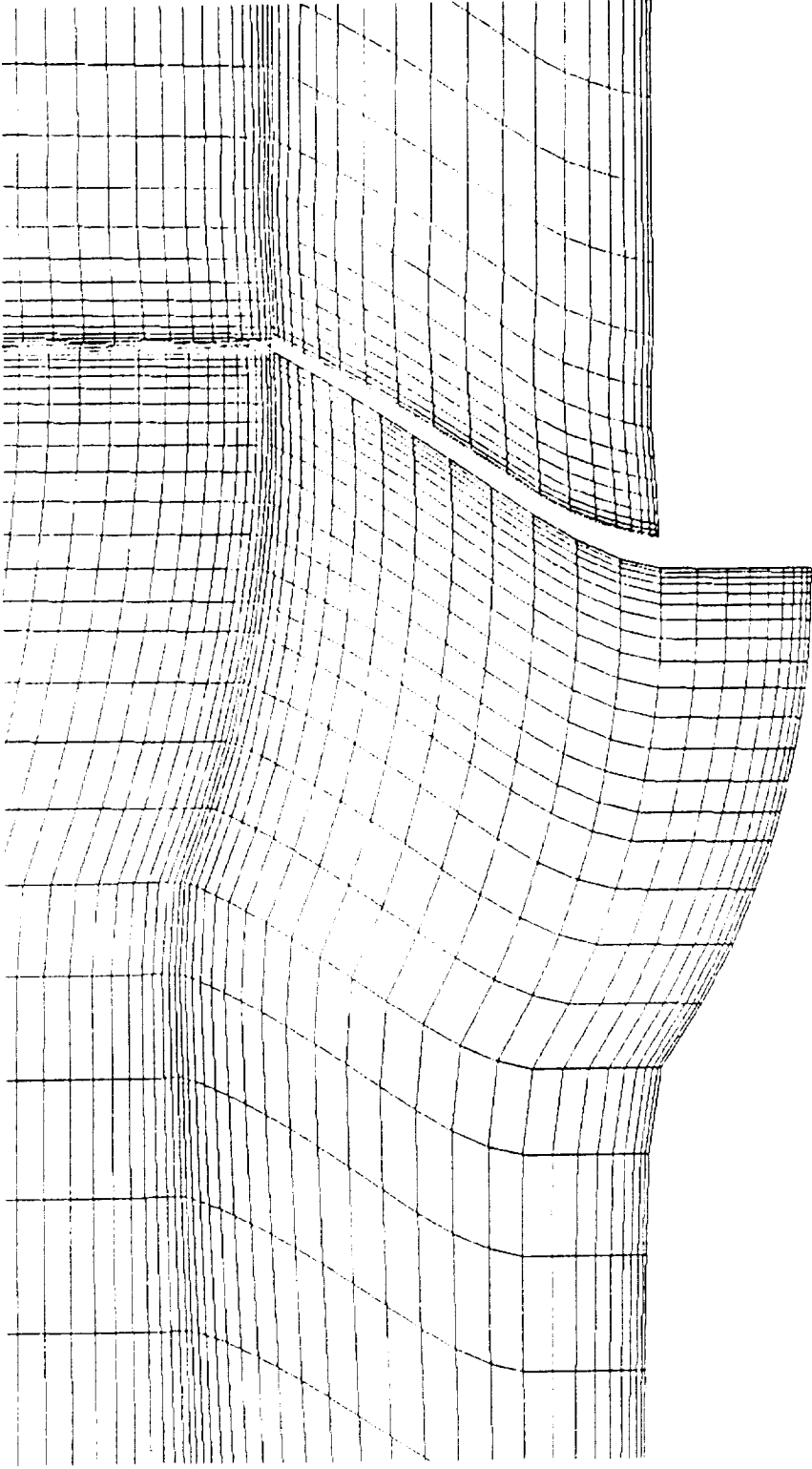


Figure 2. Computational Grid in the Forward Slot Region, Nominal NBR Inhibitor Motor

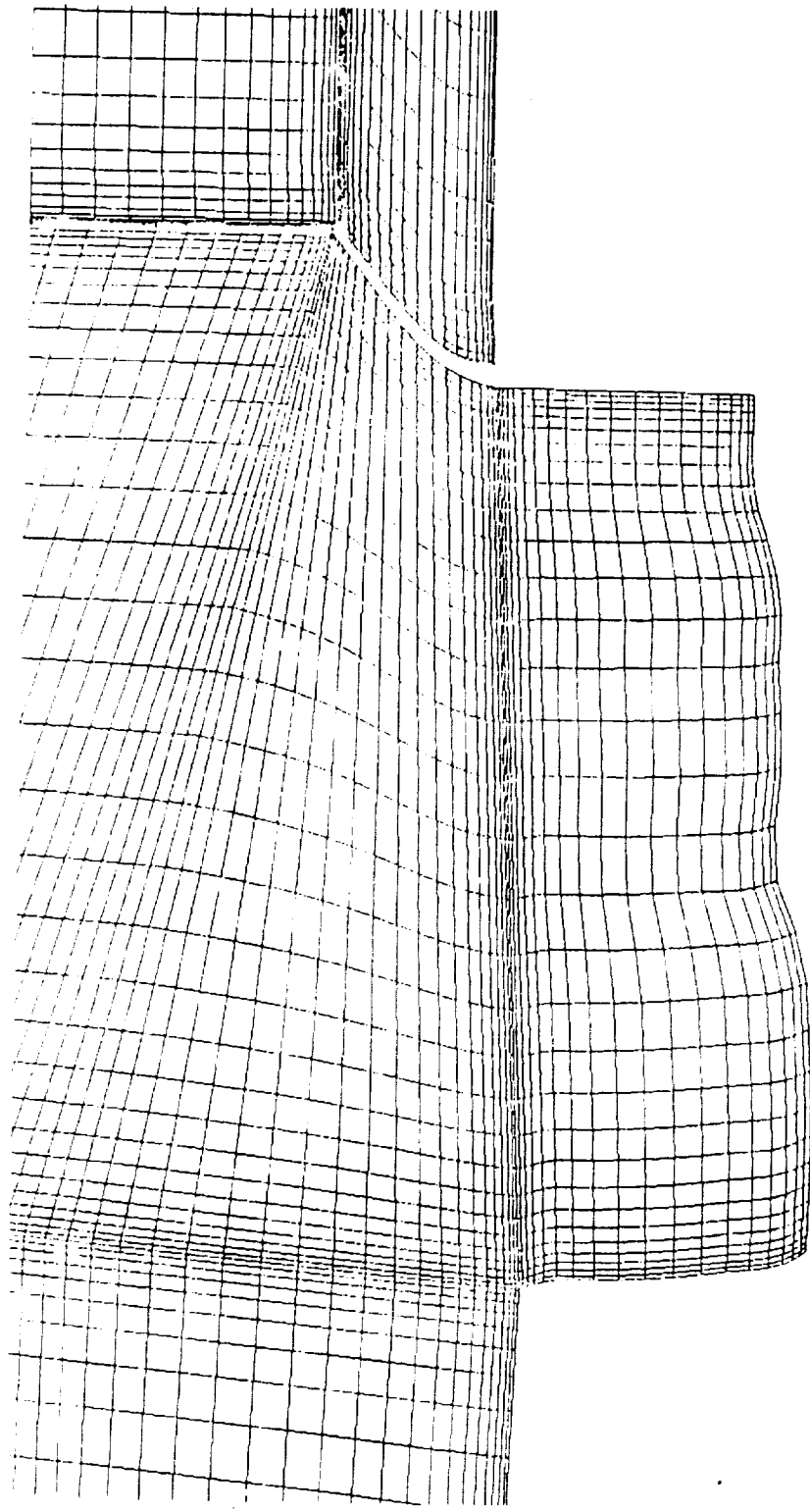


Figure 3. Computational Grid in the Center Slot Region, Nominal NBR Inhibitor Motor

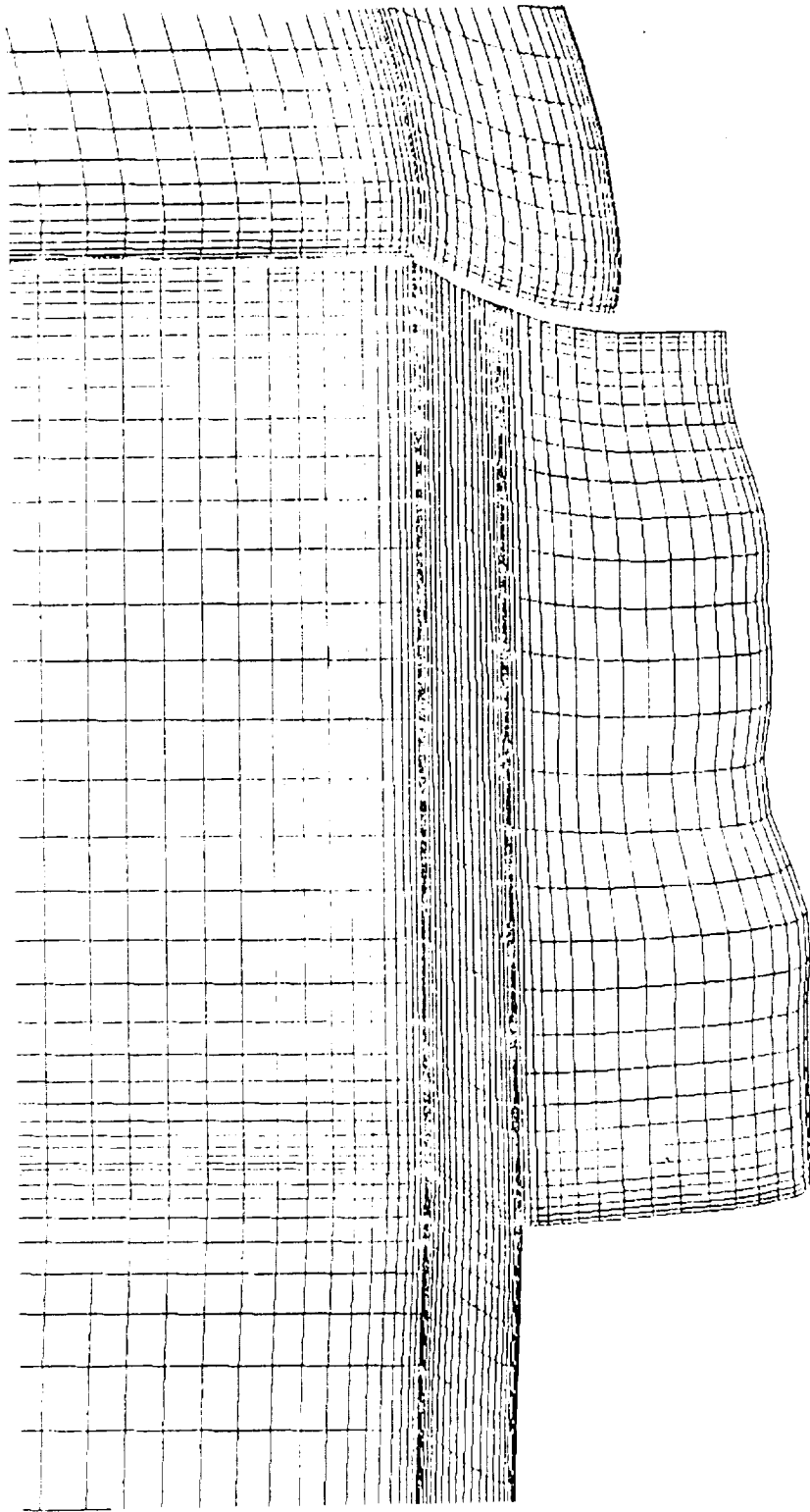


Figure 4. Computational Grid in the Aft Slot Region, Nominal NBR Inhibitor Motor

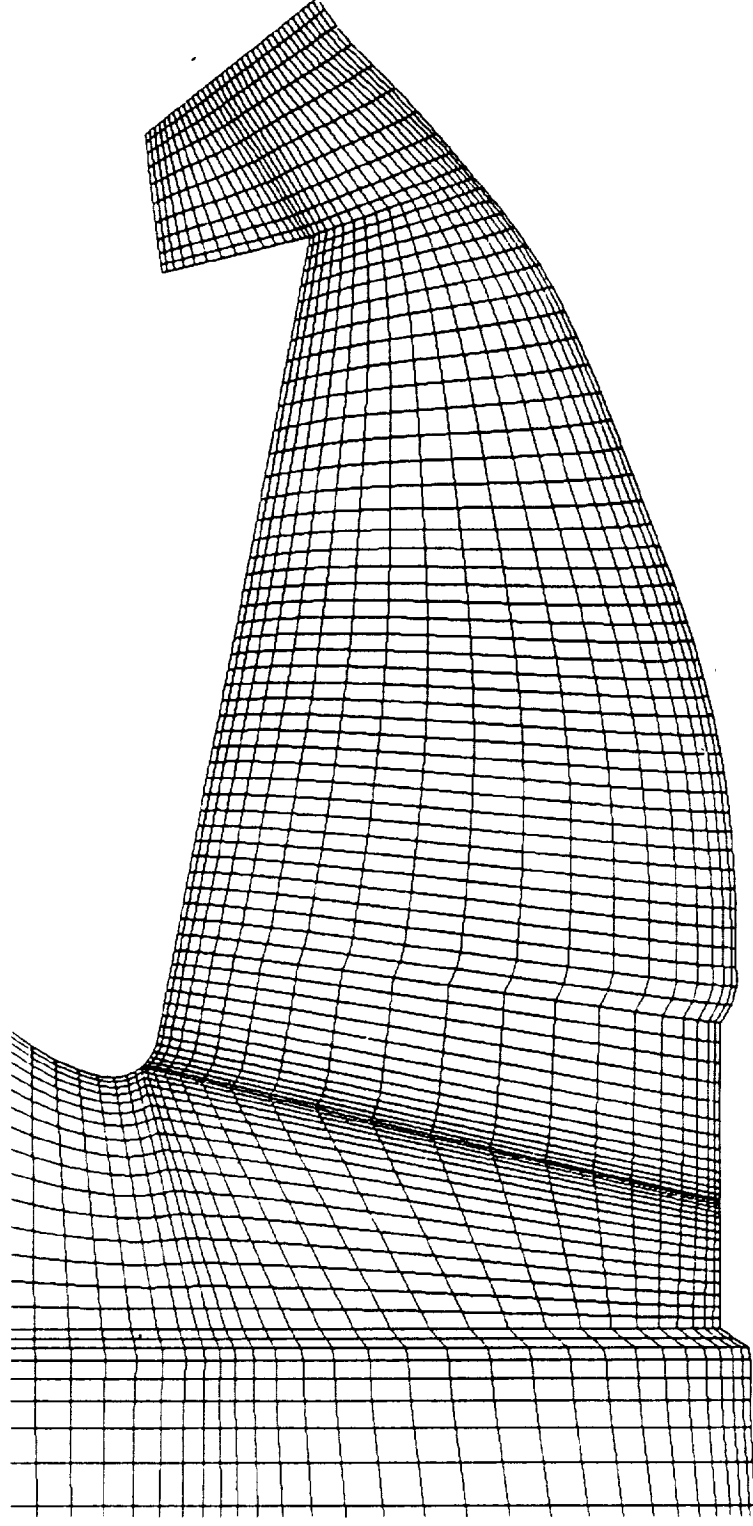


Figure 5. Computational Grid in the Submerged Nozzle Region, Nominal NBR Inhibitor Motor



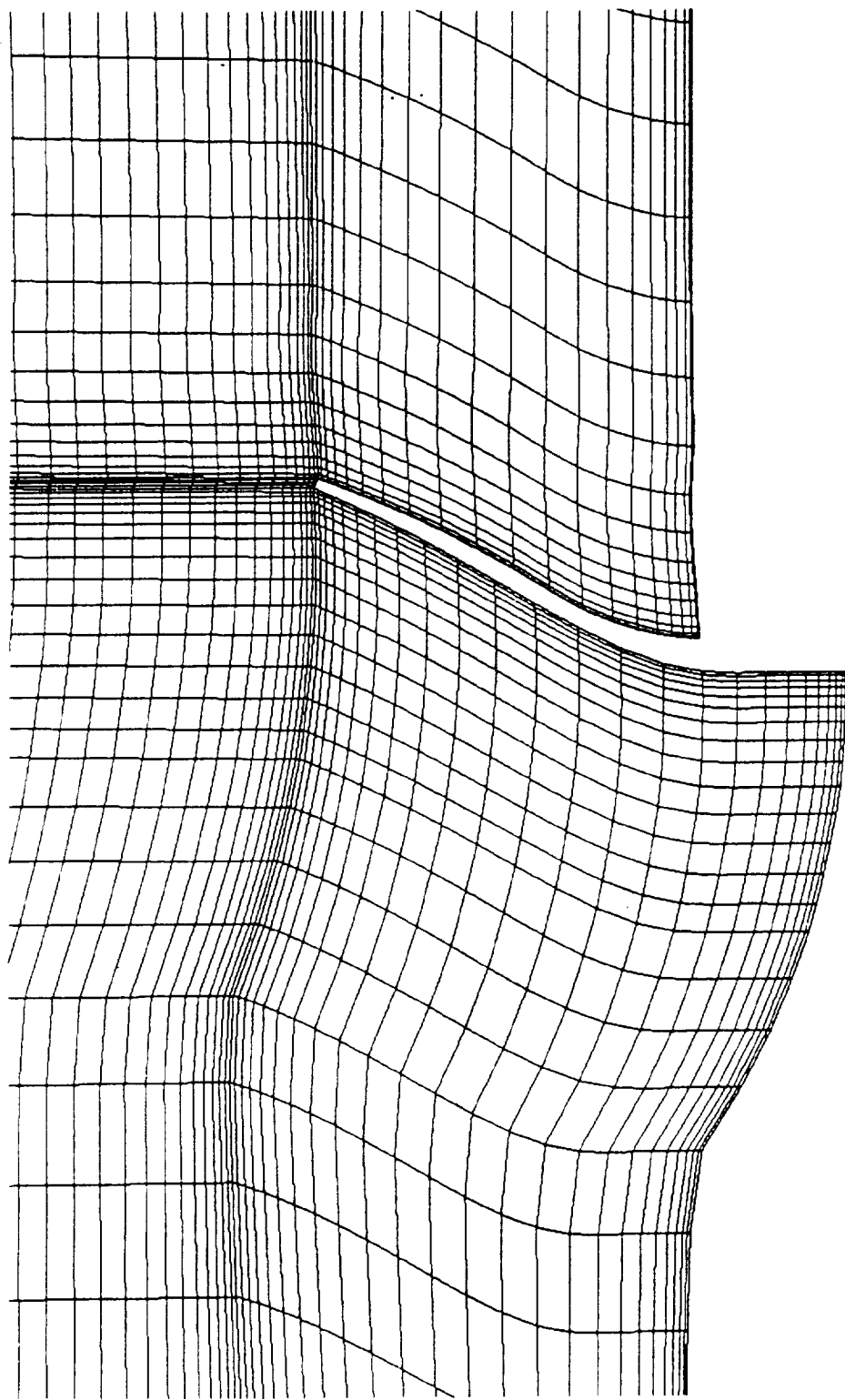


Figure 6. Computational Grid in the Forward Slot Region, Stiff NBR Inhibitor Motor

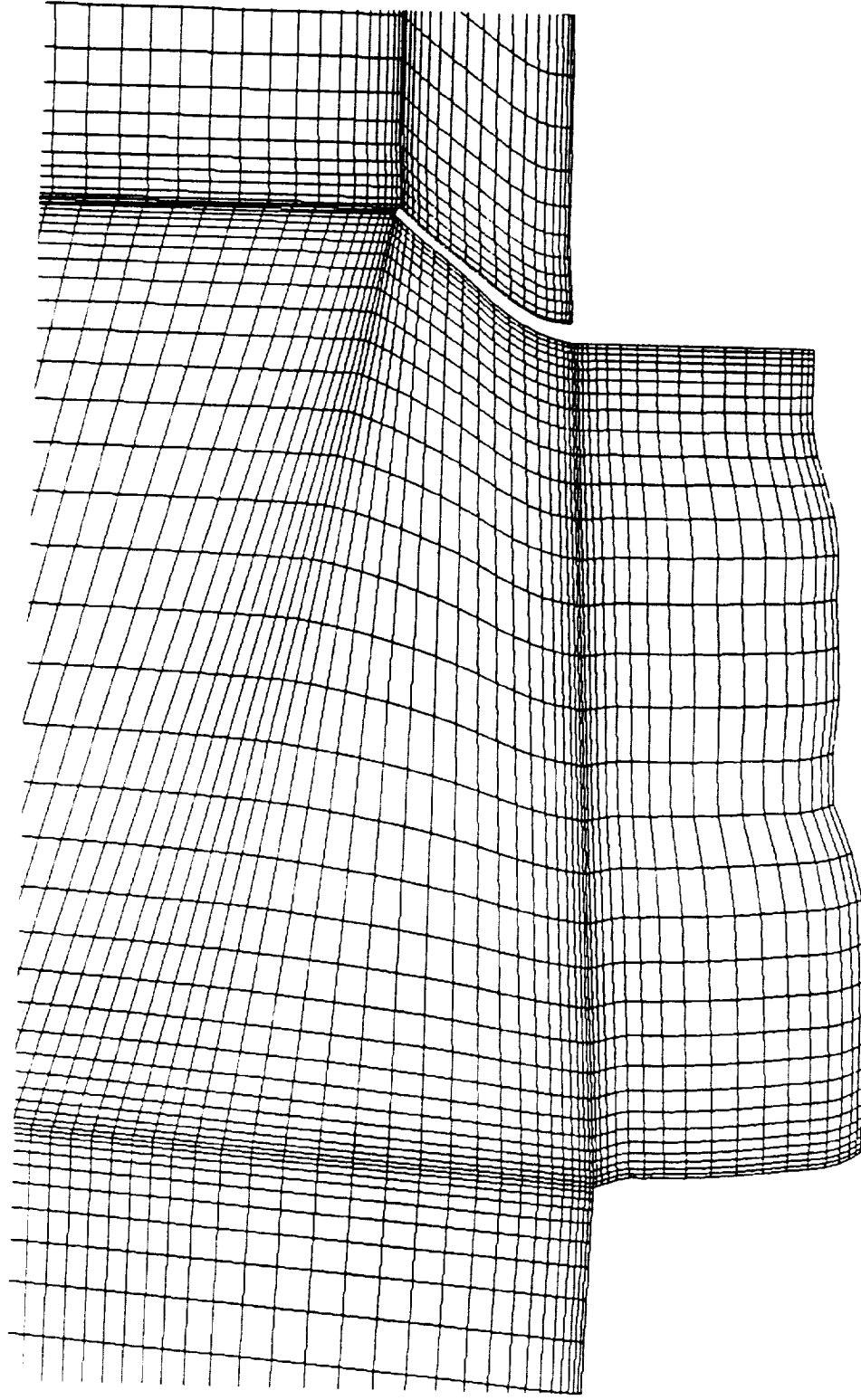


Figure 7. Computational Grid in the Center Slot Region, Stiff NBR Inhibitor Motor

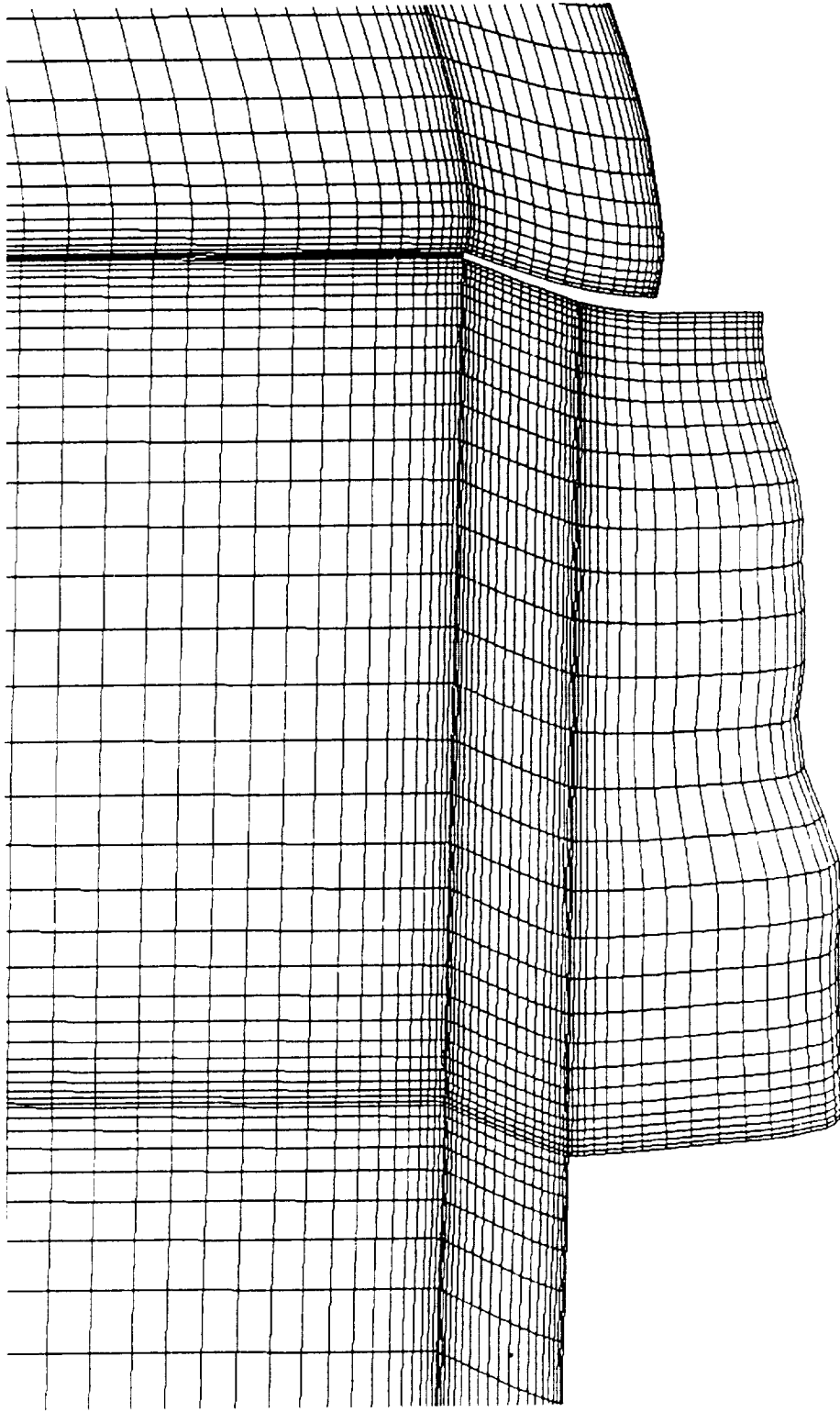


Figure 8. Computational Grid in the Aft Slot Region, Stiff NBR Inhibitor Motor

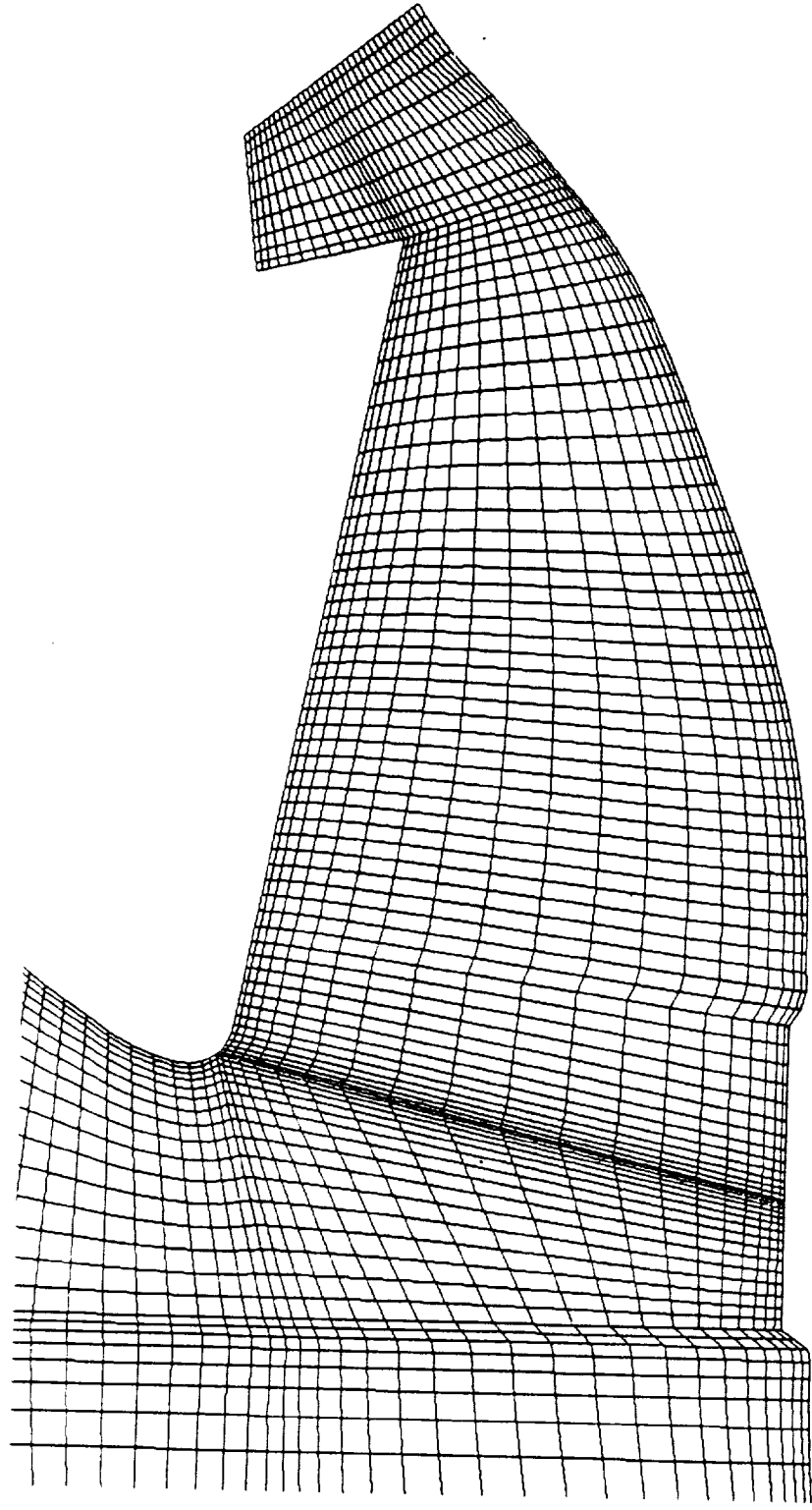


Figure 9. Computational Grid in the Submerged Nozzle Region, Stiff NBR Inhibitor Motor

Figure 10. Nominal Forward Inhibitor Deformations for Iterative Analysis  
 RSRM 79.75 Seconds Burn Time

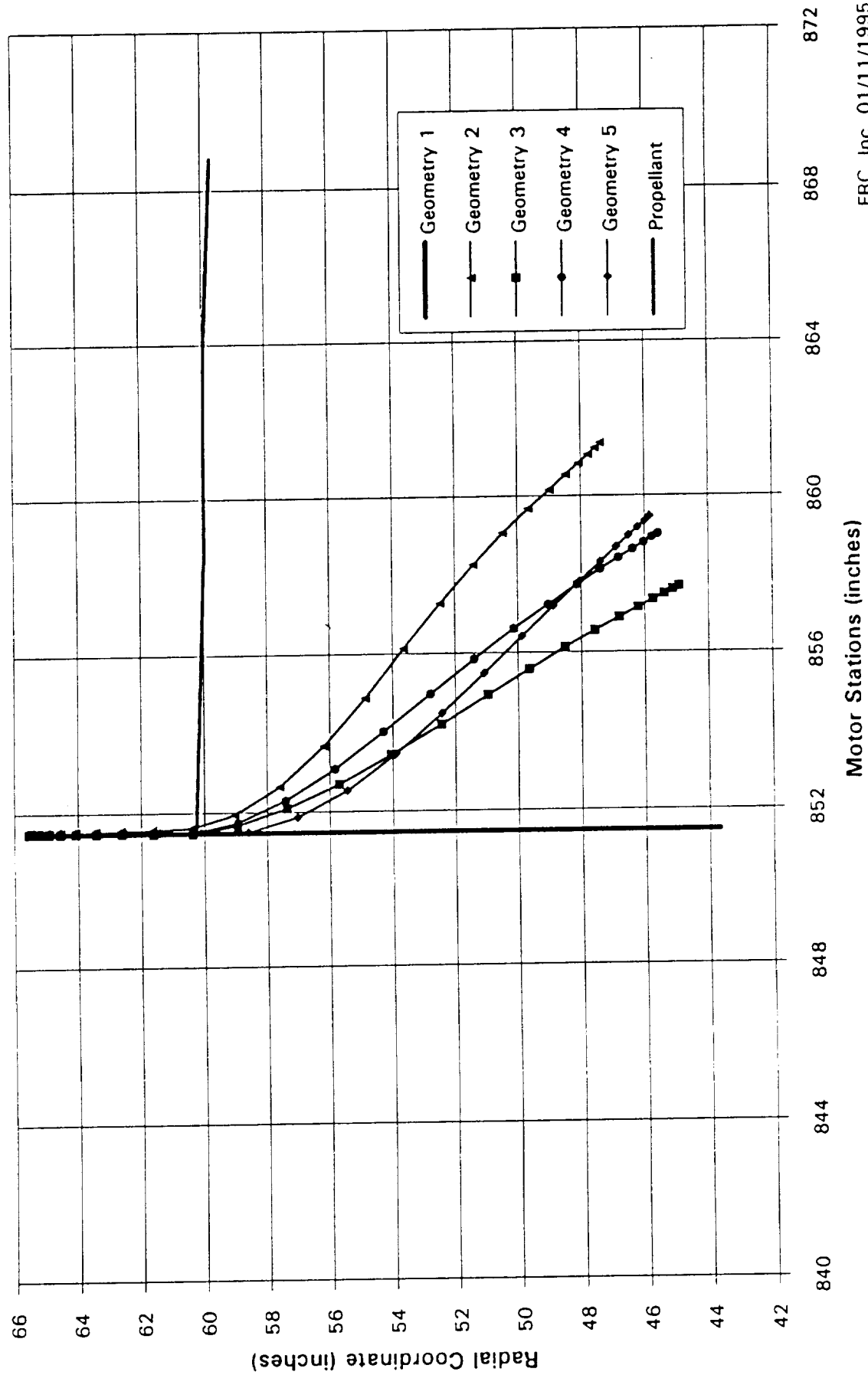


Figure 11. Stiff Forward Inhibitor Deformations for Iterative Analysis  
RSRM 79.75 Seconds Burn Time

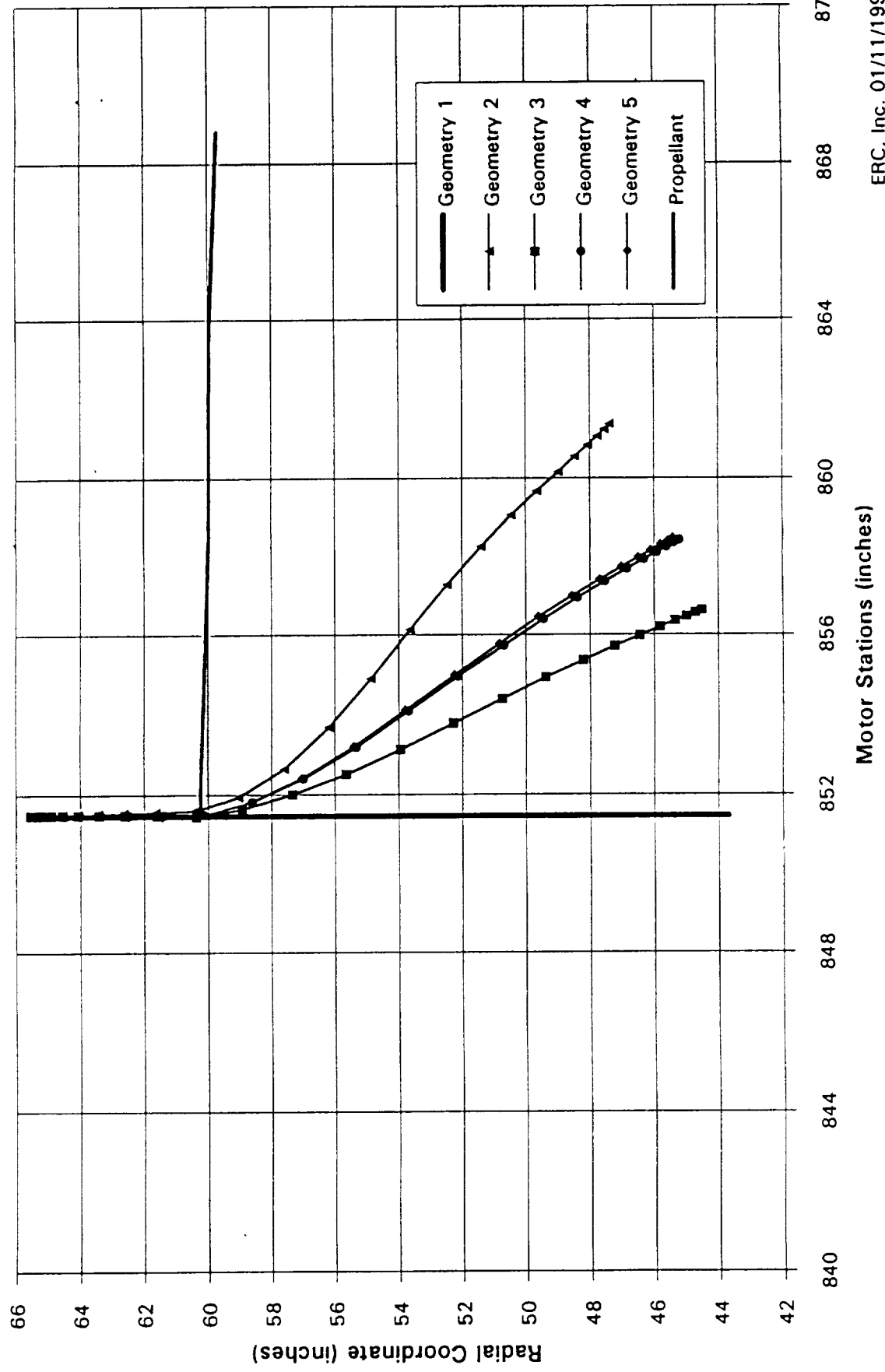


Figure 12. Forward Inhibitor Deformations for Nominal and Stiff NBR

NBR  
RSRM 80 Seconds Burn Time

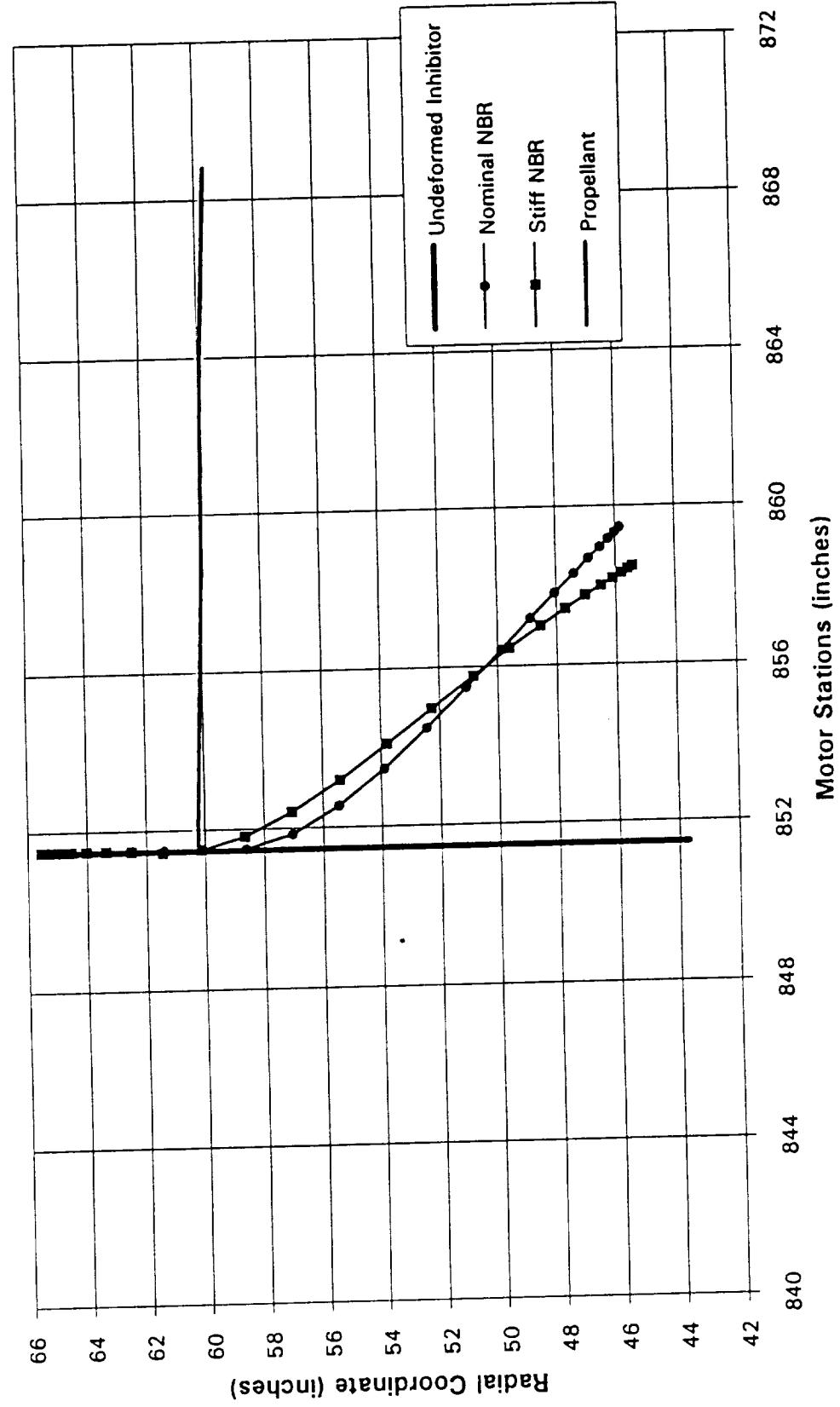


Figure 13. Nominal Center Inhibitor Deformations for Iterative Analysis  
 RSRM 79.75 Seconds Burn Time

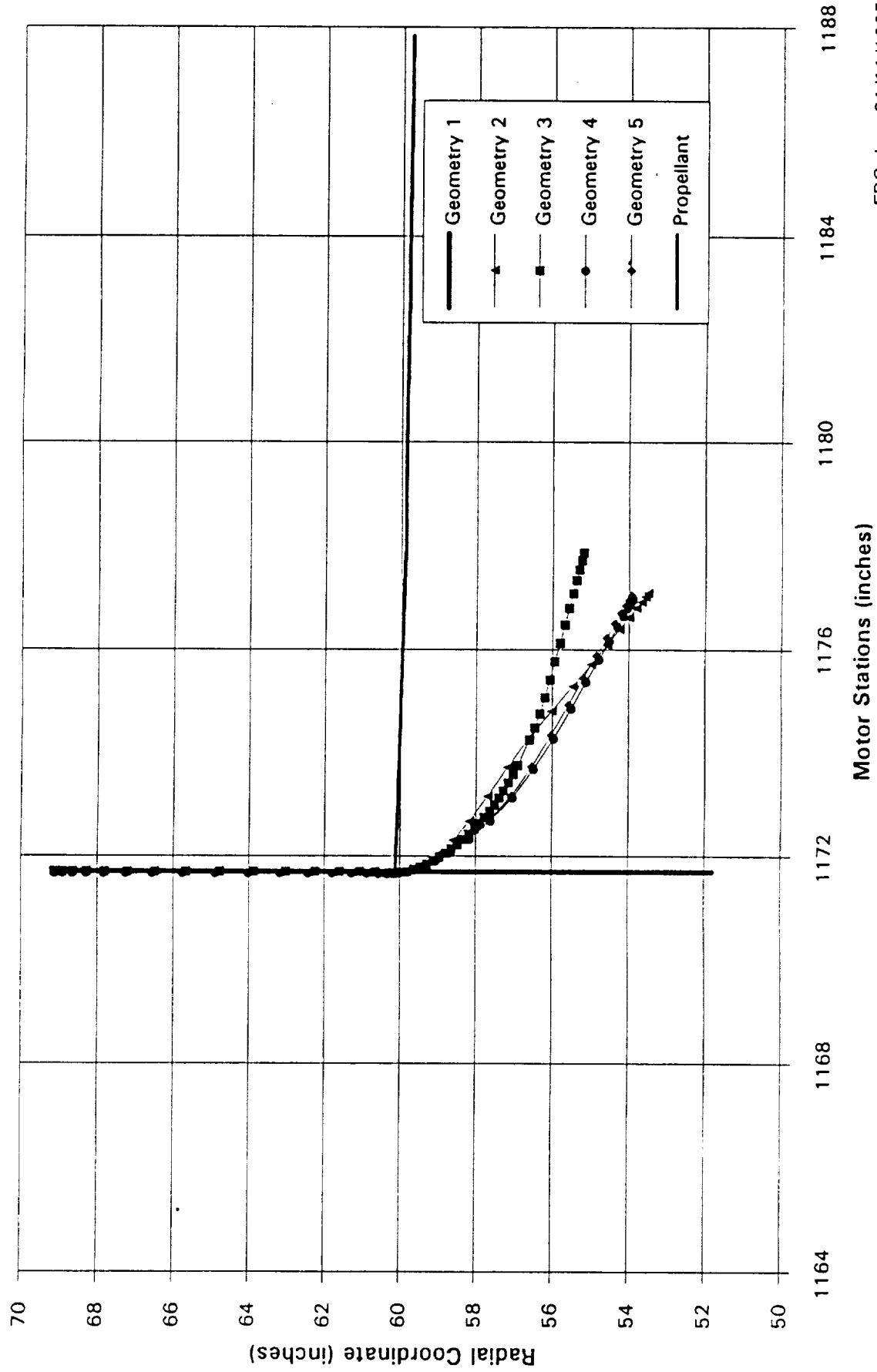




Figure 14. Stiff Center Inhibitor Deformations for Iterative Analysis  
RSRM 79.75 Seconds Burn Time

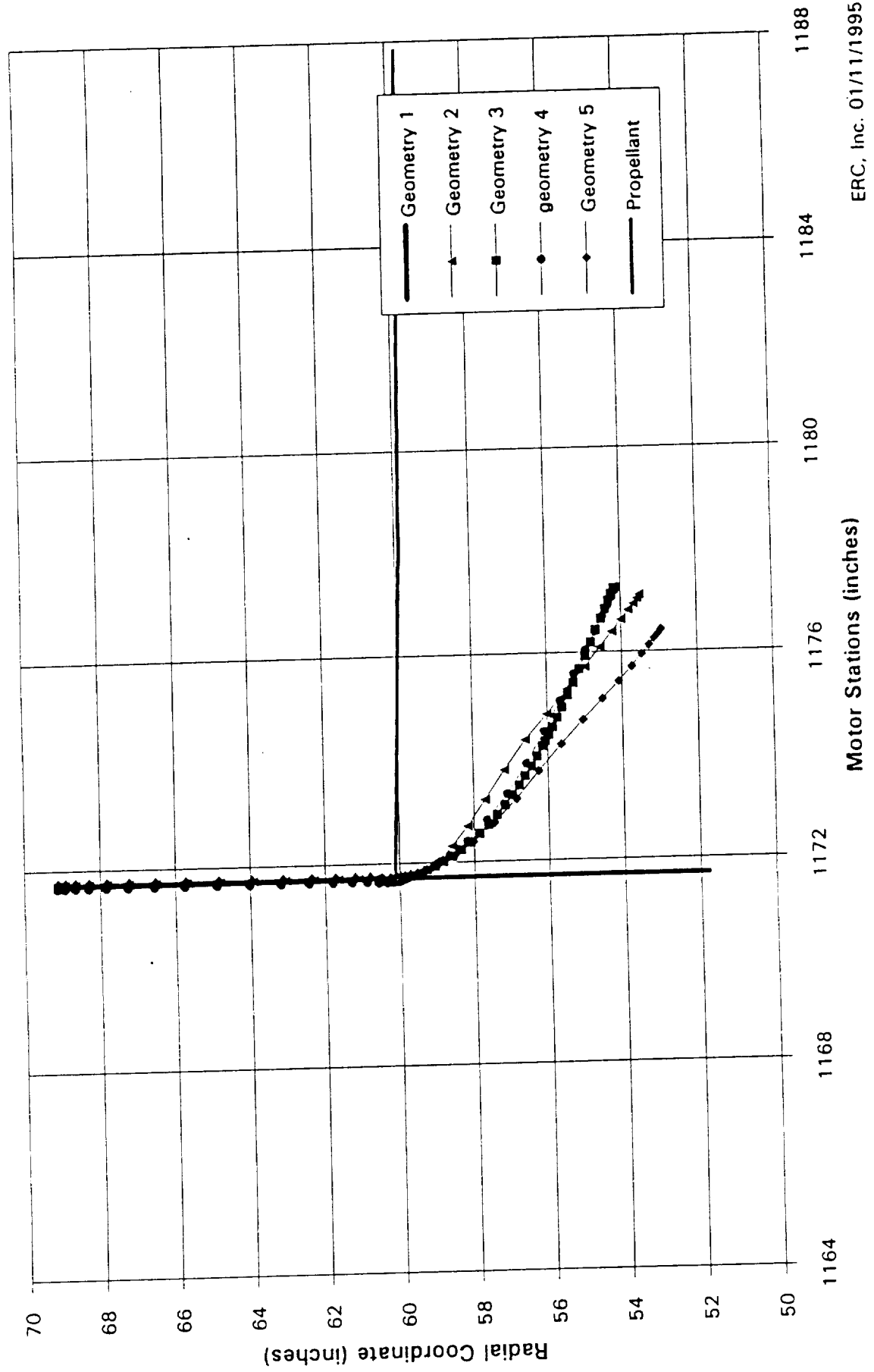


Figure 15. Center Inhibitor Deformations for Iterative Analysis  
RSRM 79.75 Seconds Burn Time

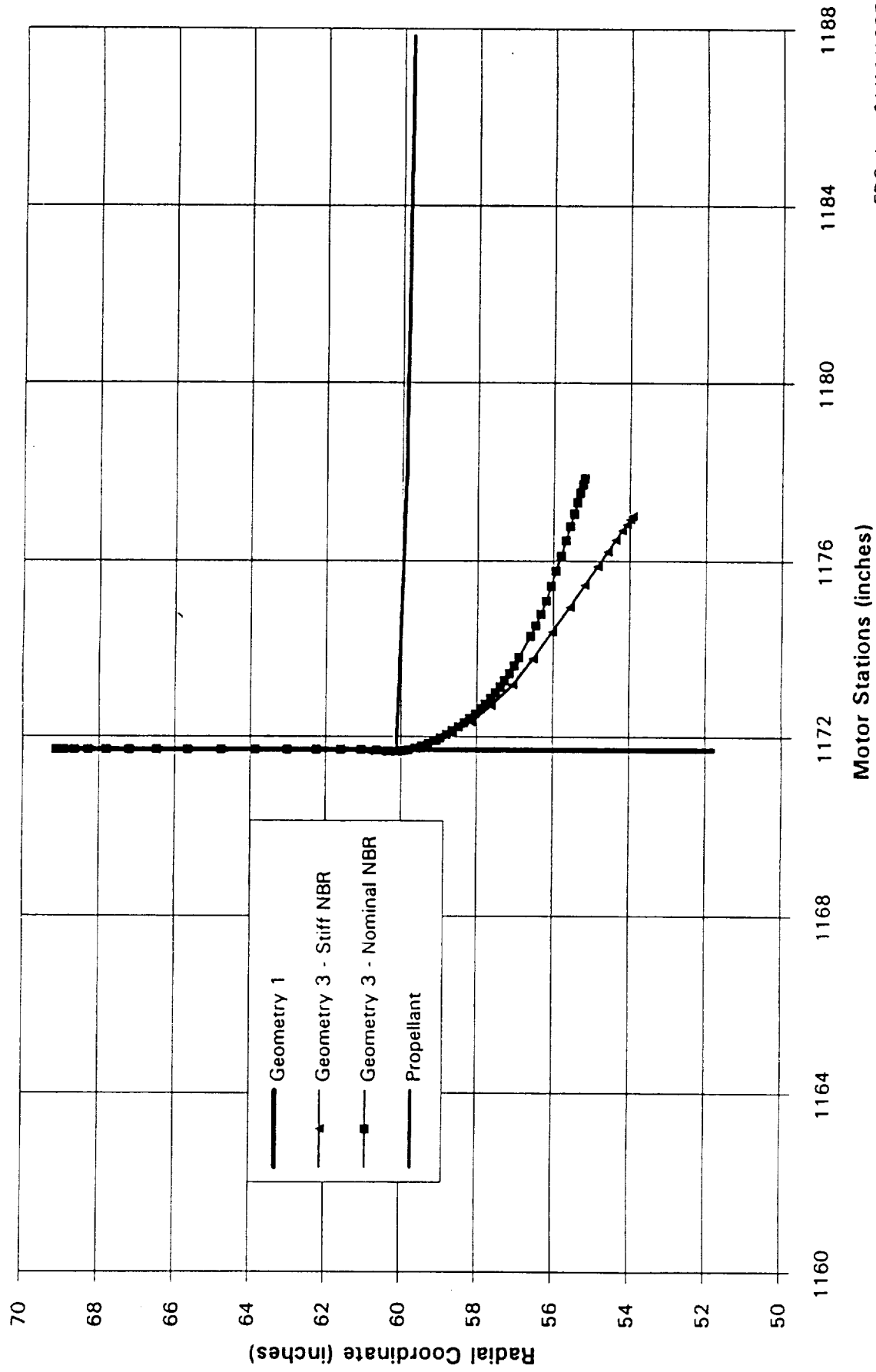
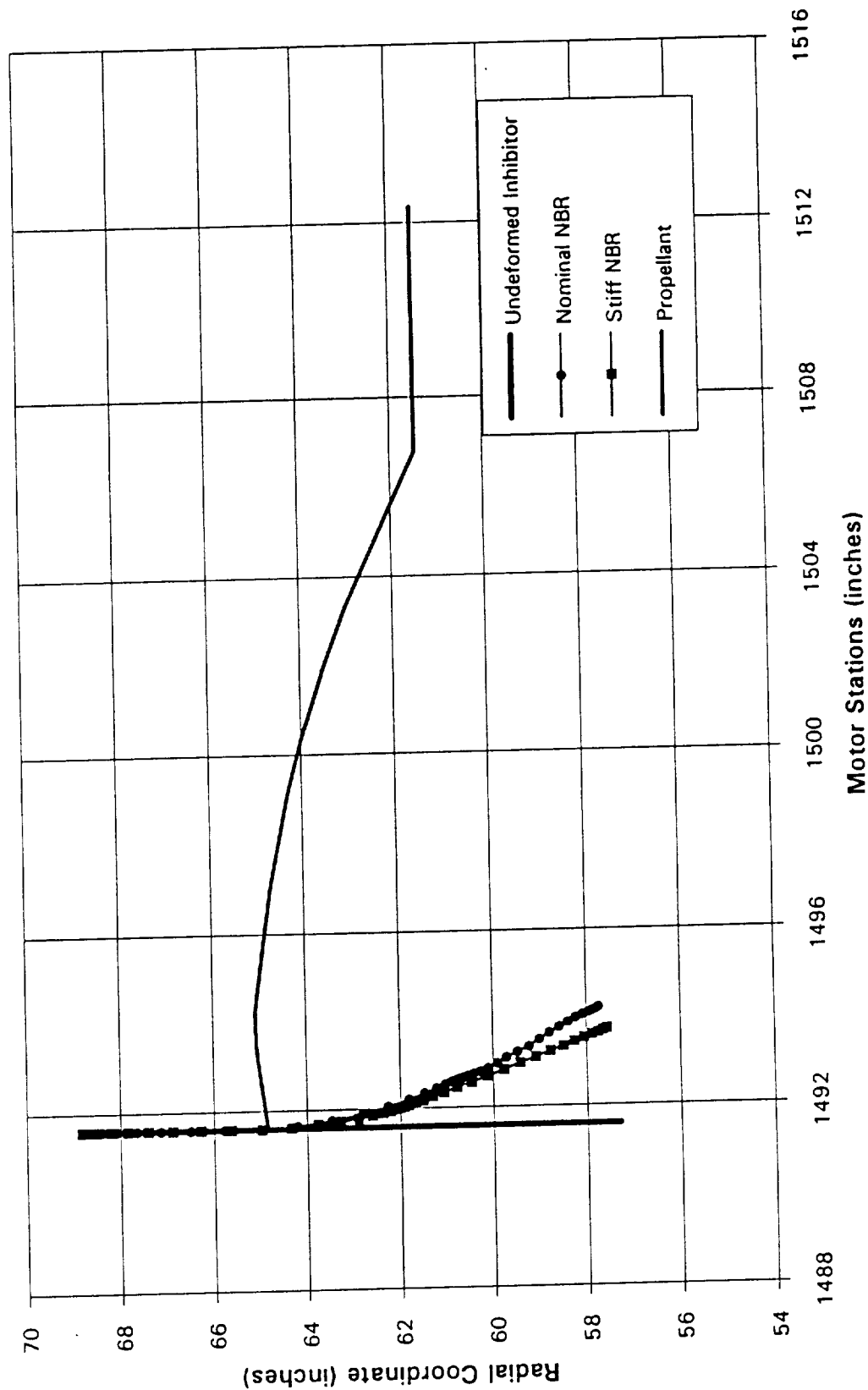


Figure 16. Aft Inhibitor Deformations for Nominal and Stiff NBR  
RSRM 80 Seconds Burn Time



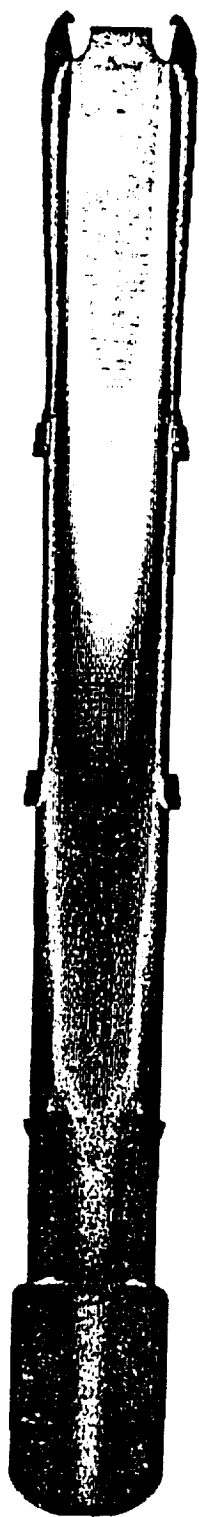


Figure 17. RSRM 80 Second Burn Time Internal Flow field Velocity Magnitude



Figure 18. Velocity Field in the Forward Slot Region, Nominal NBR  
Inhibitor Motor

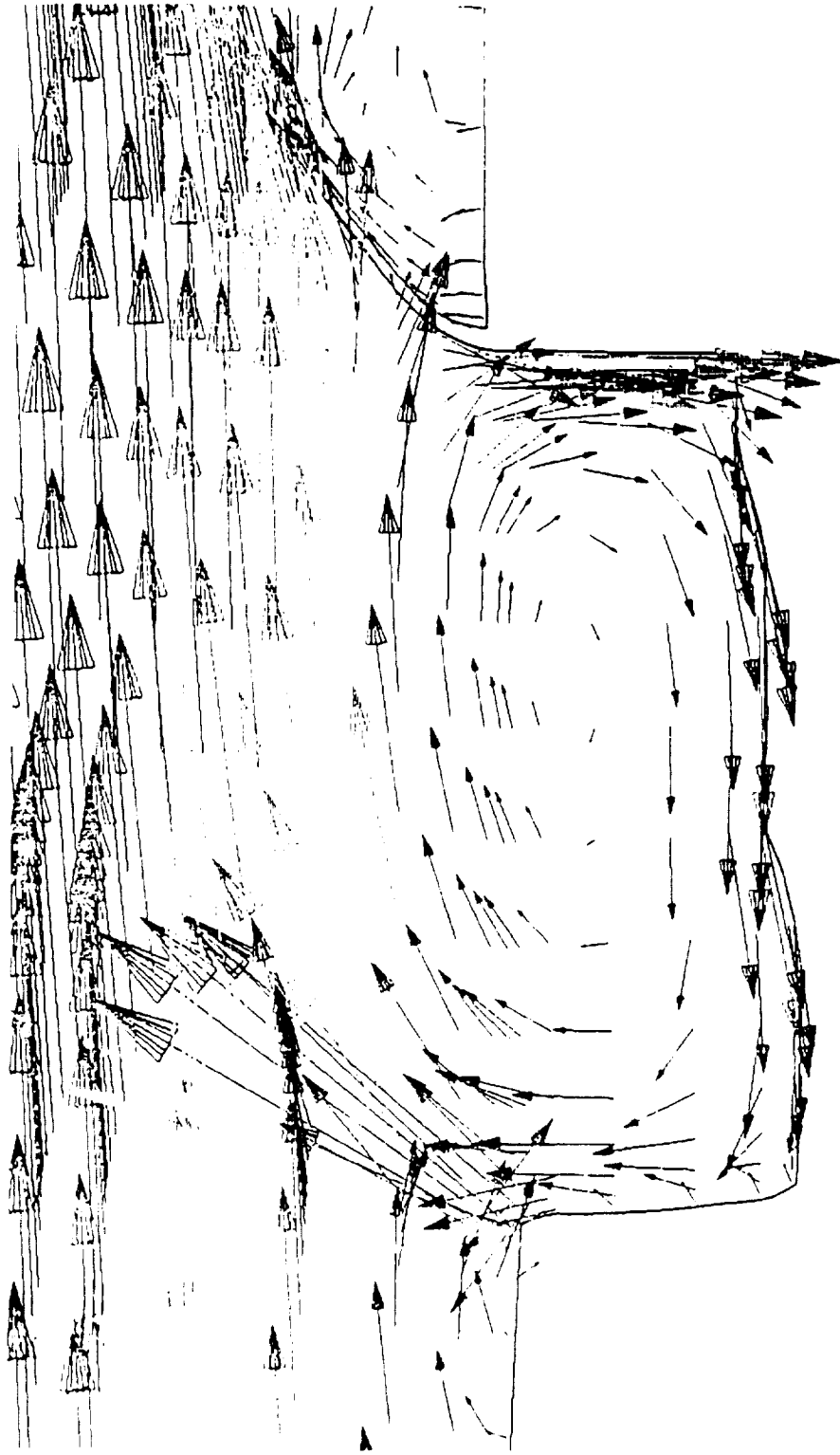


Figure 19. Velocity Field in the Center Slot Region, Nominal NBR Inhibitor Motor

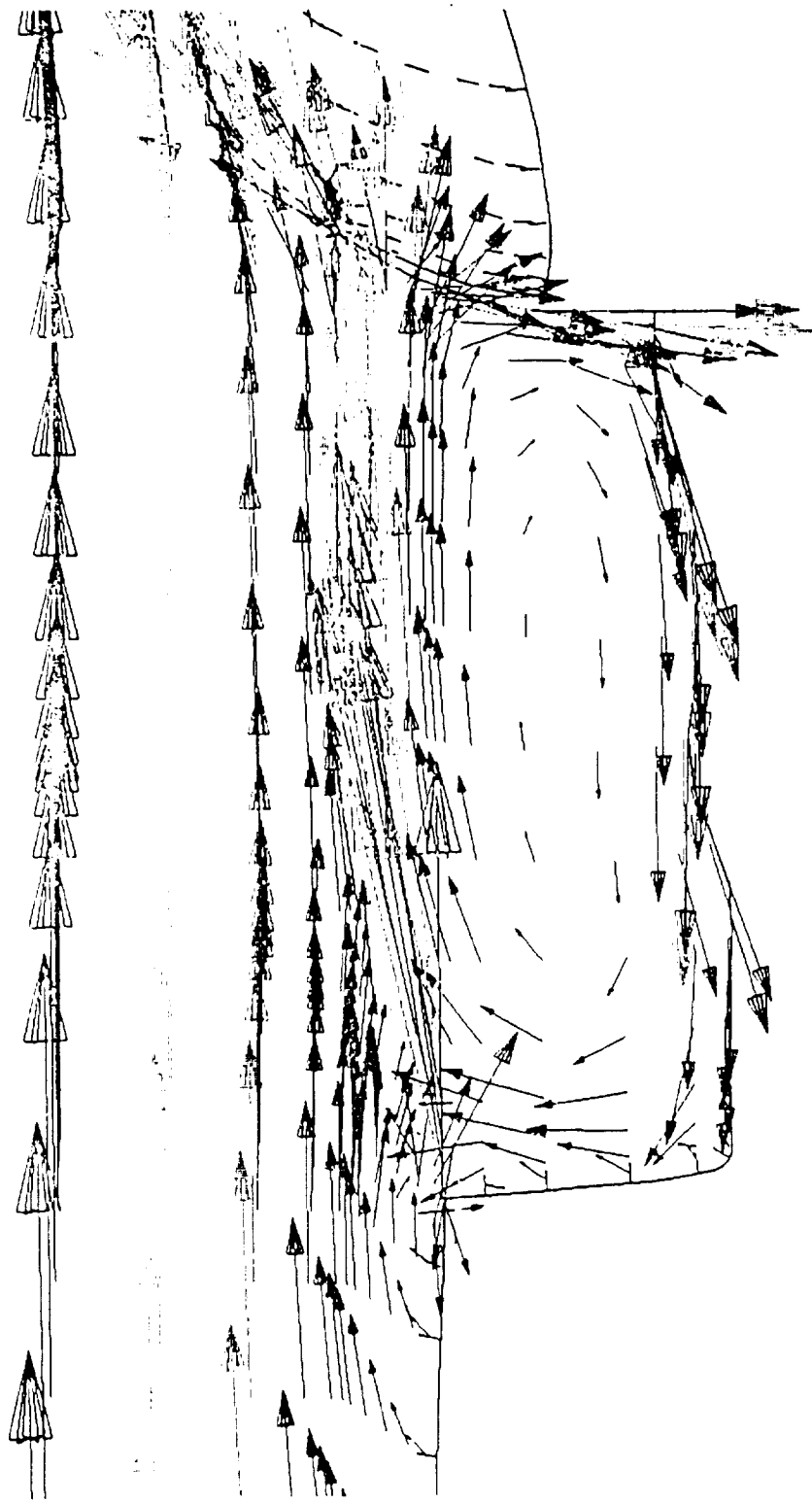
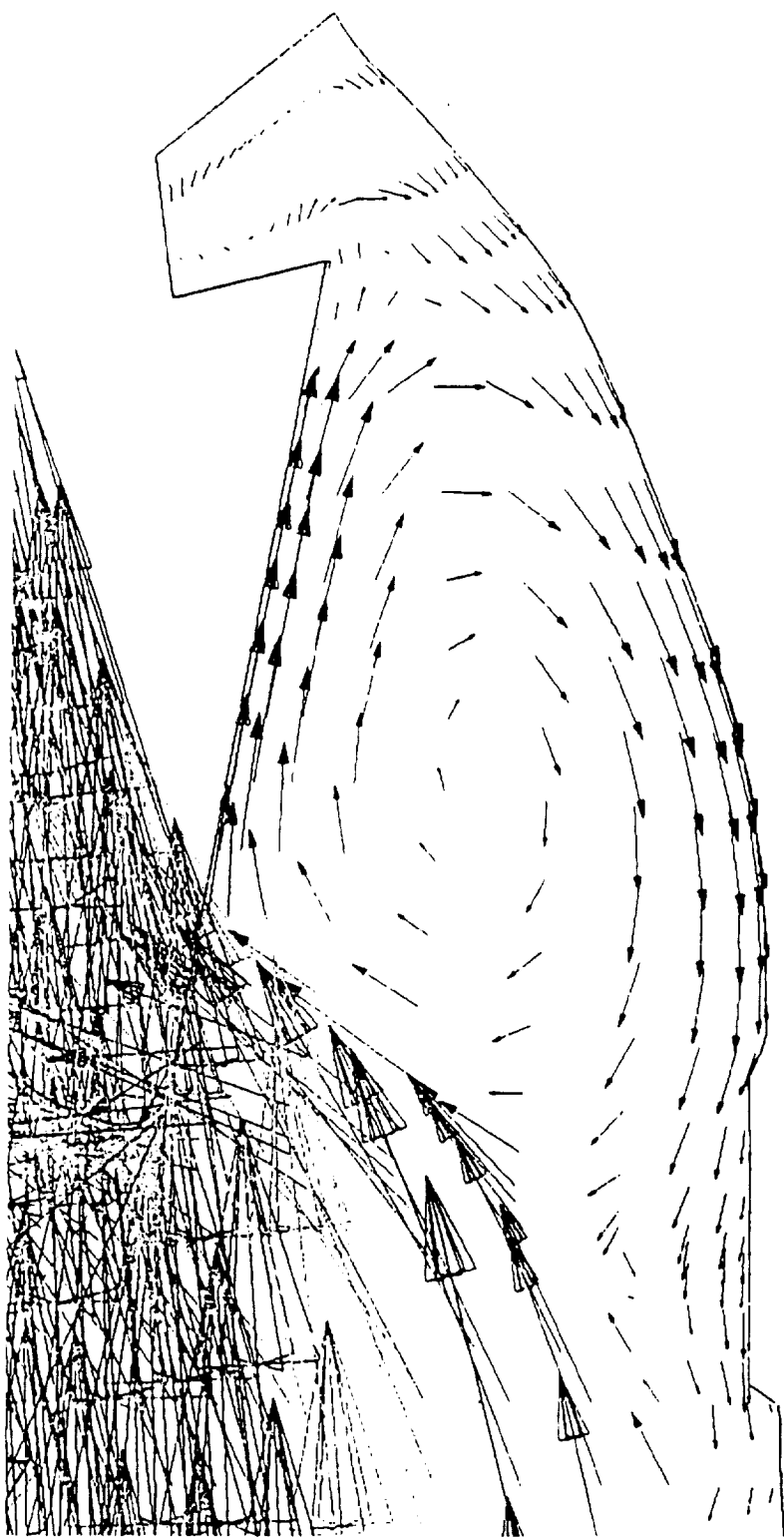


Figure 20. Velocity Field in the Aft Slot Region, Nominal NBR Inhibitor Motor







**Figure 21. Velocity Field in the Submerged Nozzle Region, Nominal NBR  
Inhibitor Motor**



**Figure 22. Velocity Field in the Forward Slot Region, Nominal NBR  
Inhibitor Motor**

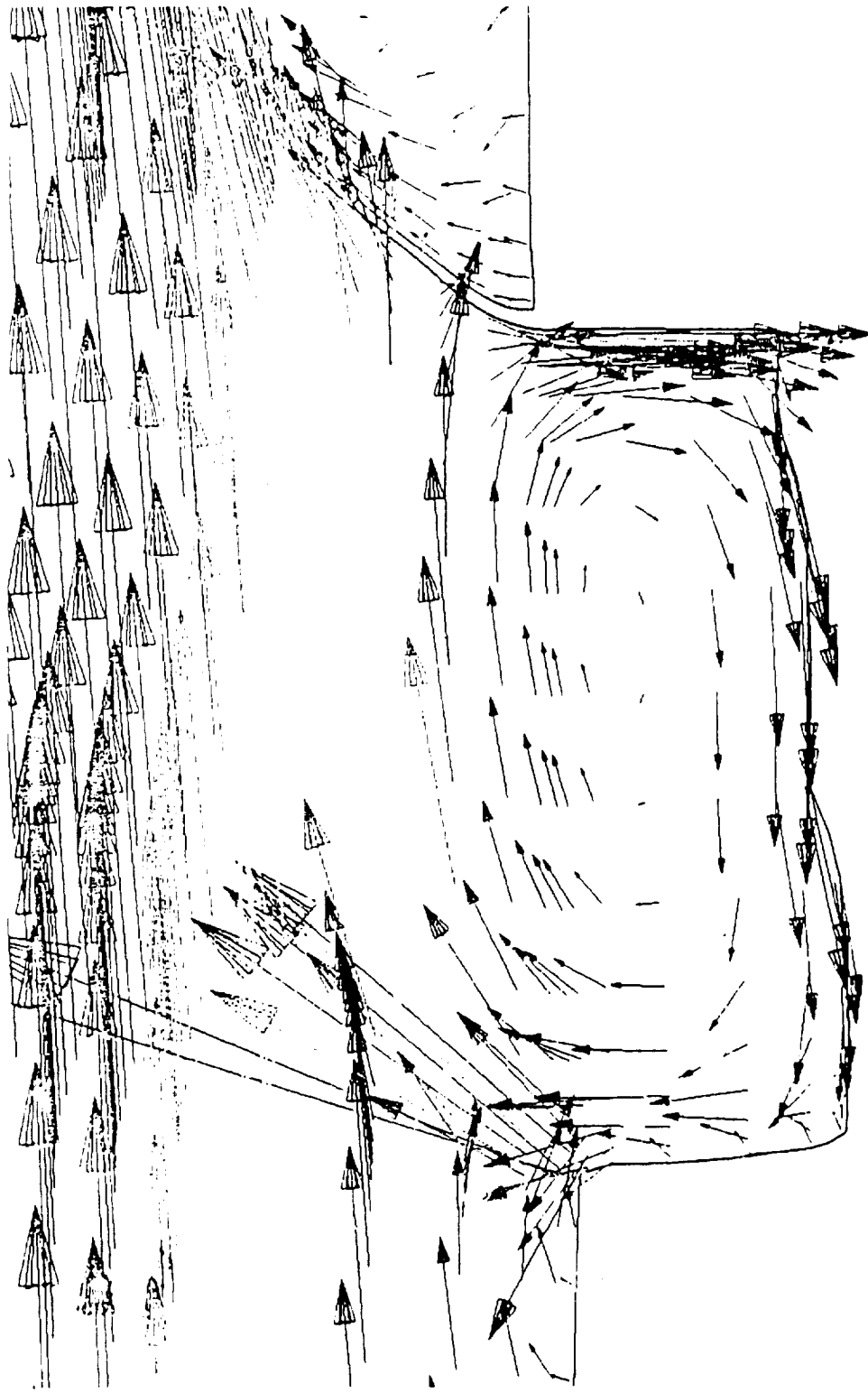


Figure 23. Velocity Field in the Center Slot Region, Nominal NBR Inhibitor Motor

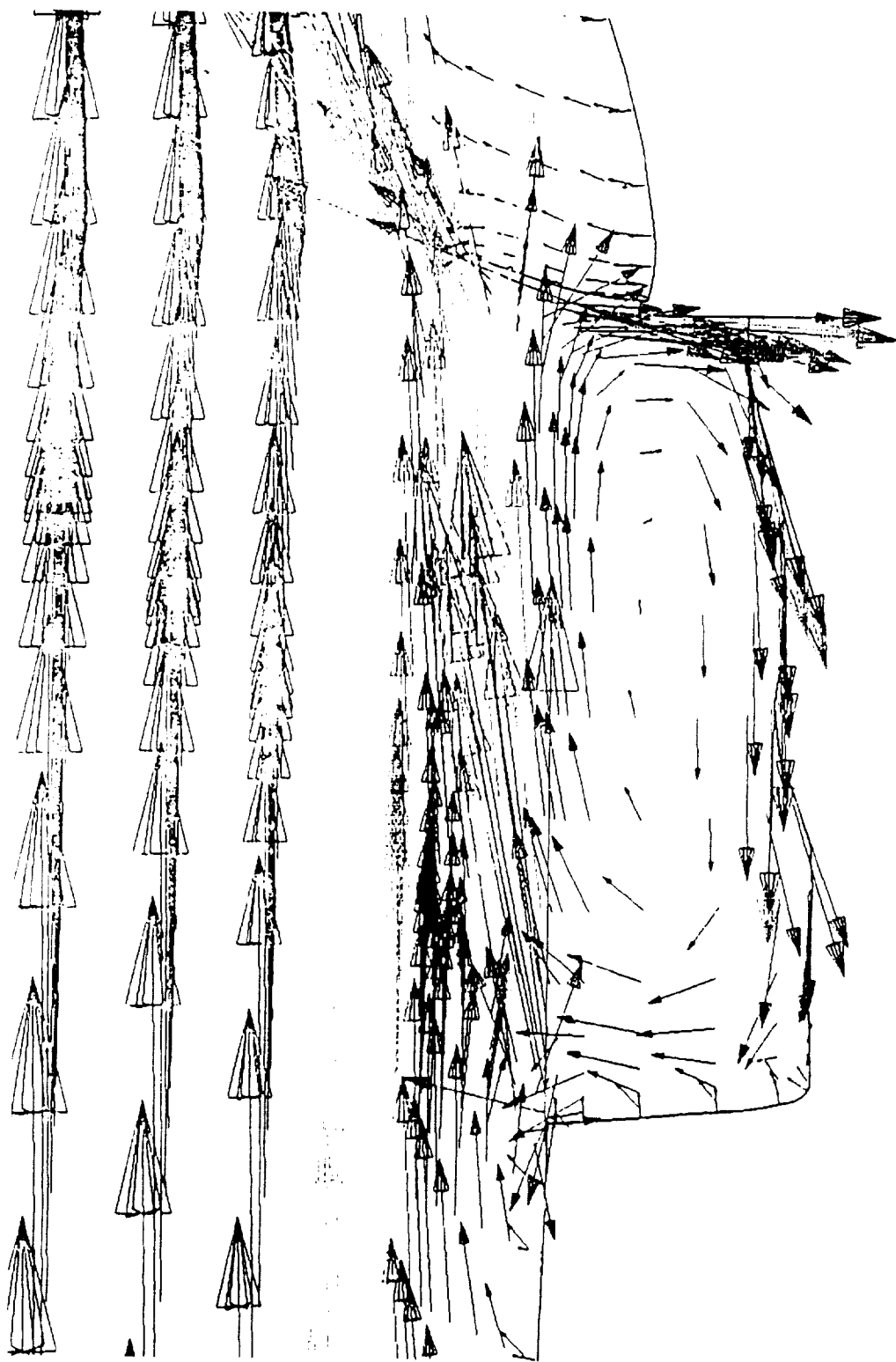
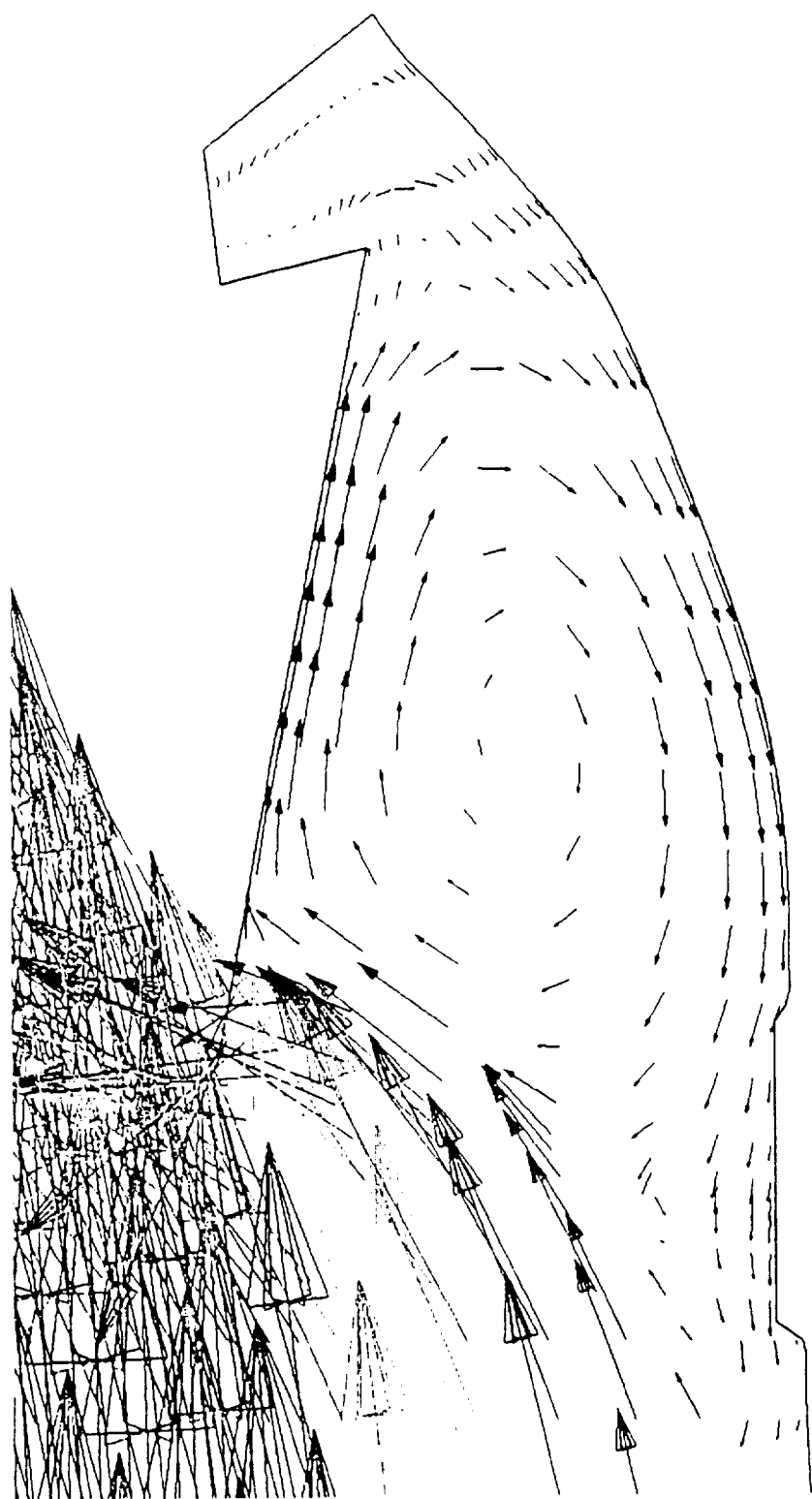


Figure 24. Velocity Field in the Aft Slot Region, Nominal NBR Inhibitor Motor



**Figure 25. Velocity Field in the Submerged Nozzle Region, Nominal NBR  
Inhibitor Motor**

Figure 26. Forward Inhibitor Radial Pressure Distribution  
 RSRM 80 Seconds Burn Time  
 Nominal NBR

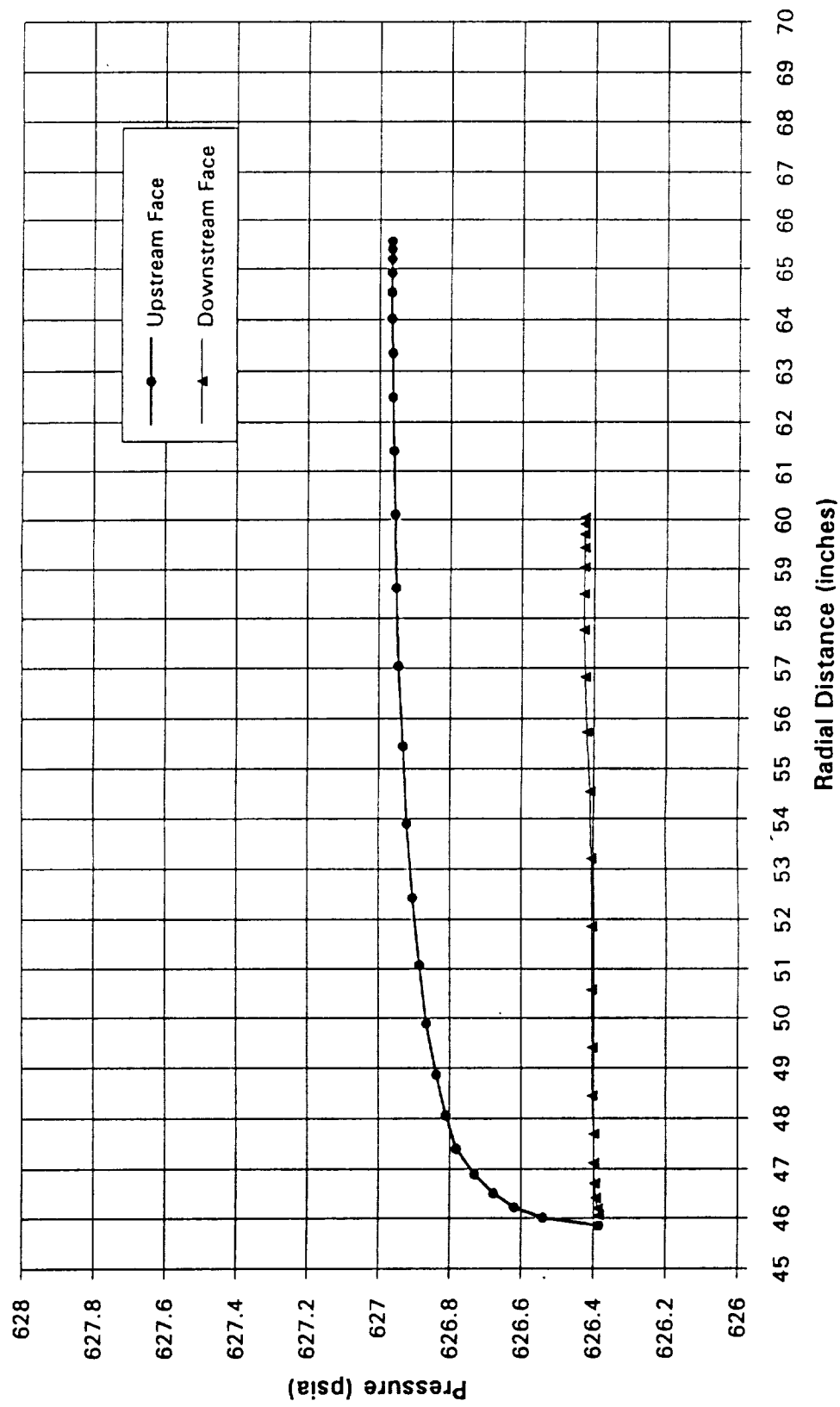


Figure 27. Center Inhibitor Radial Pressure Distribution  
 RSRM 80 Seconds Burn Time  
 Nominal NBR

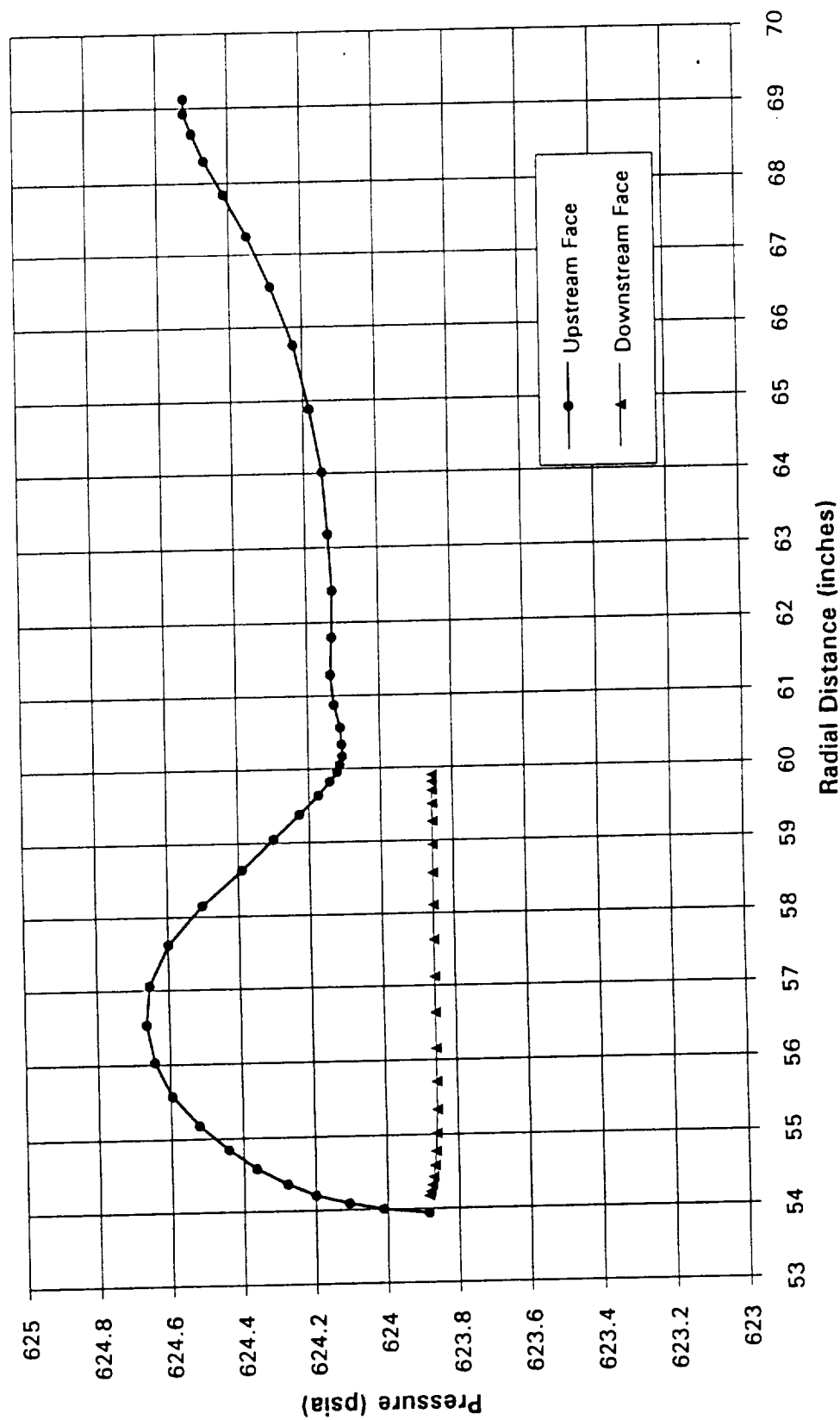


Figure 28. Aft Inhibitor Radial Pressure Distribution  
 RSRM 80 Seconds Burn Time  
 Nominal NBR

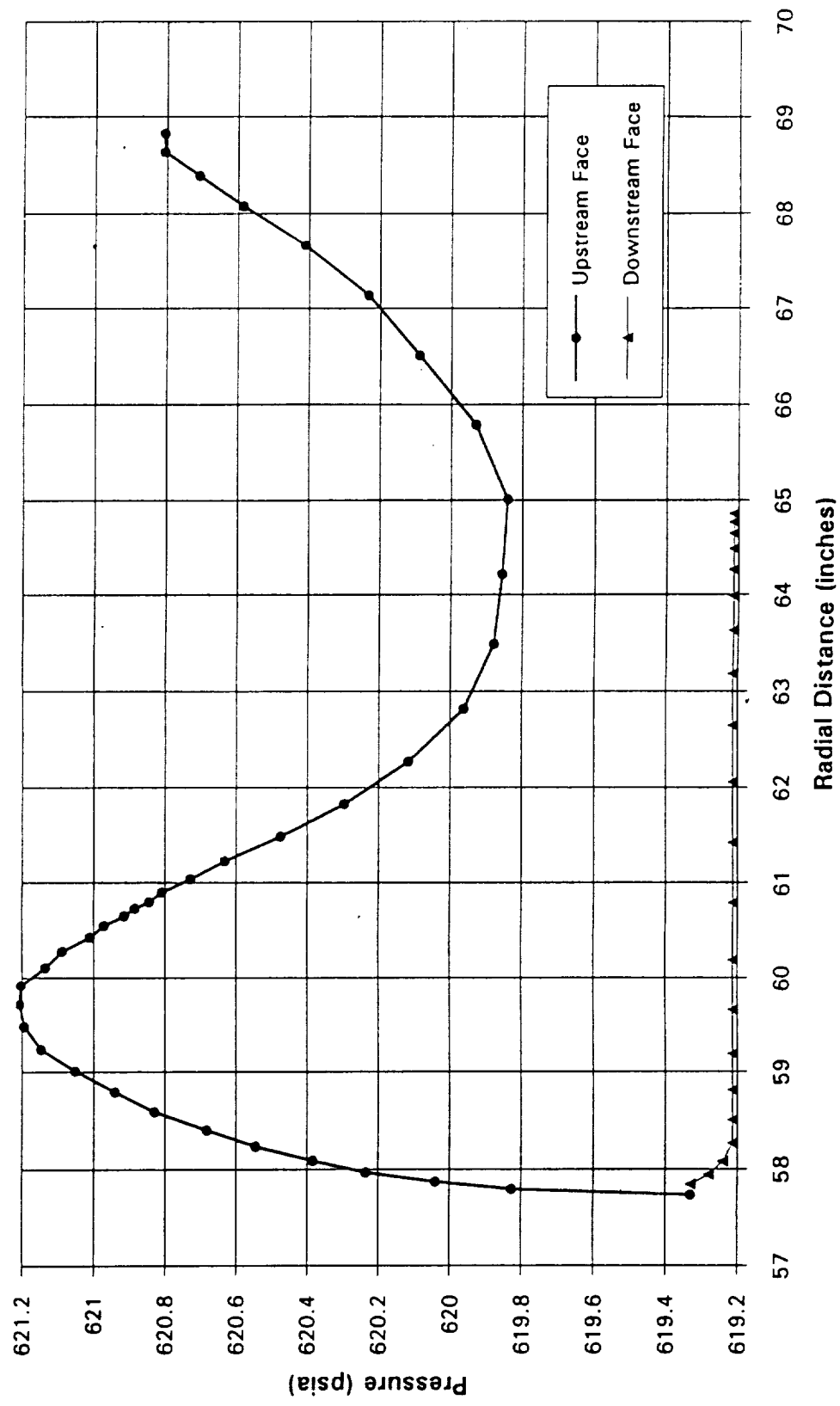




Figure 29. Forward Inhibitor Radial Pressure Distribution  
 RSRM 80 Seconds Burn Time  
 Stiff NBR

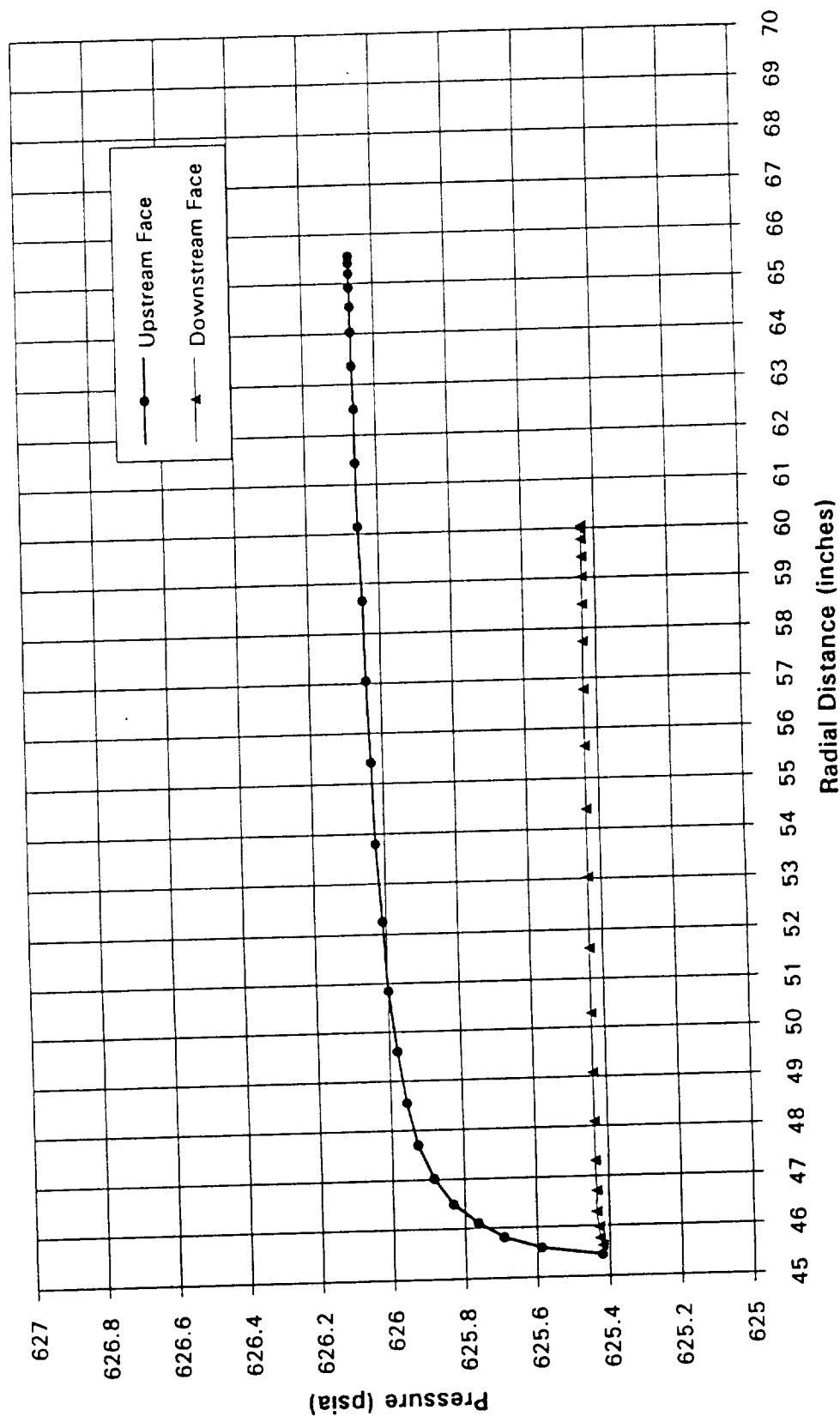


Figure 30. Center Inhibitor Radial Pressure Distribution  
 RSRM 80 Seconds Burn Time  
 Stiff NBR

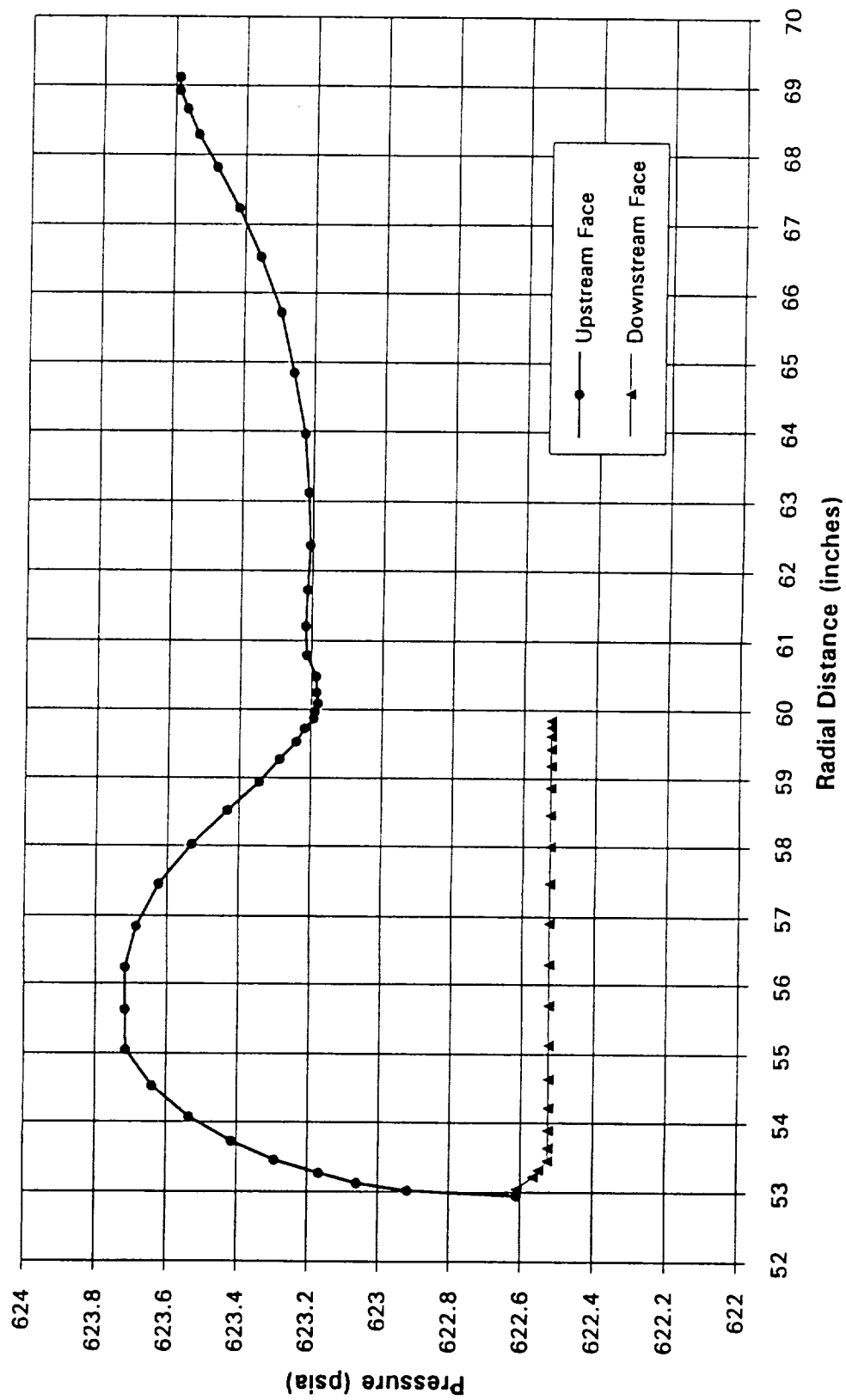


Figure 31. Aft Inhibitor Radial Pressure Distribution  
 RSRM 80 Seconds Burn Time  
 Stiff NBR

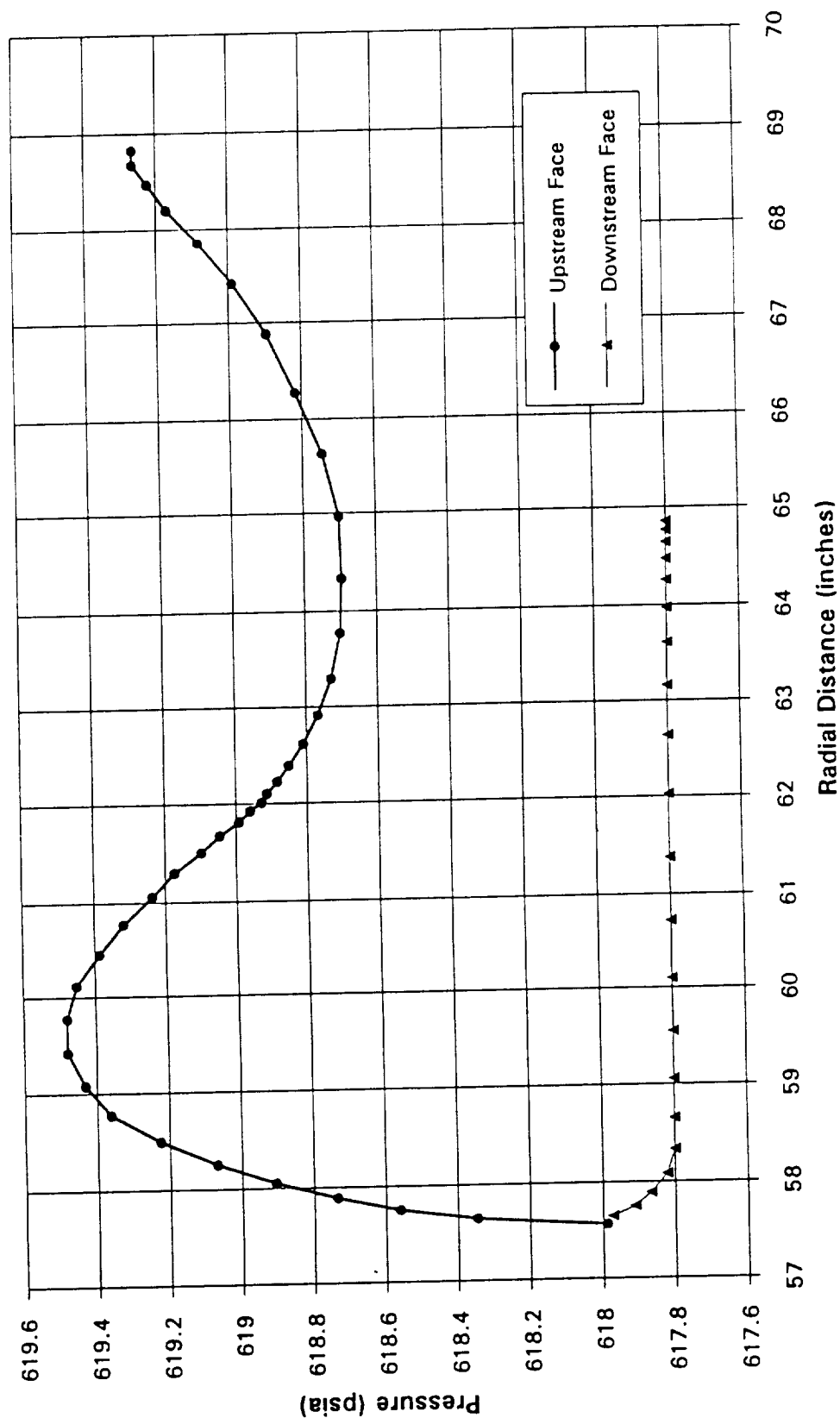


Figure 32. Velocity Profile for Nominal NBR Forward Inhibitor  
Deformed Inhibitor Geometry  
RSRM 80 Seconds Burn Time

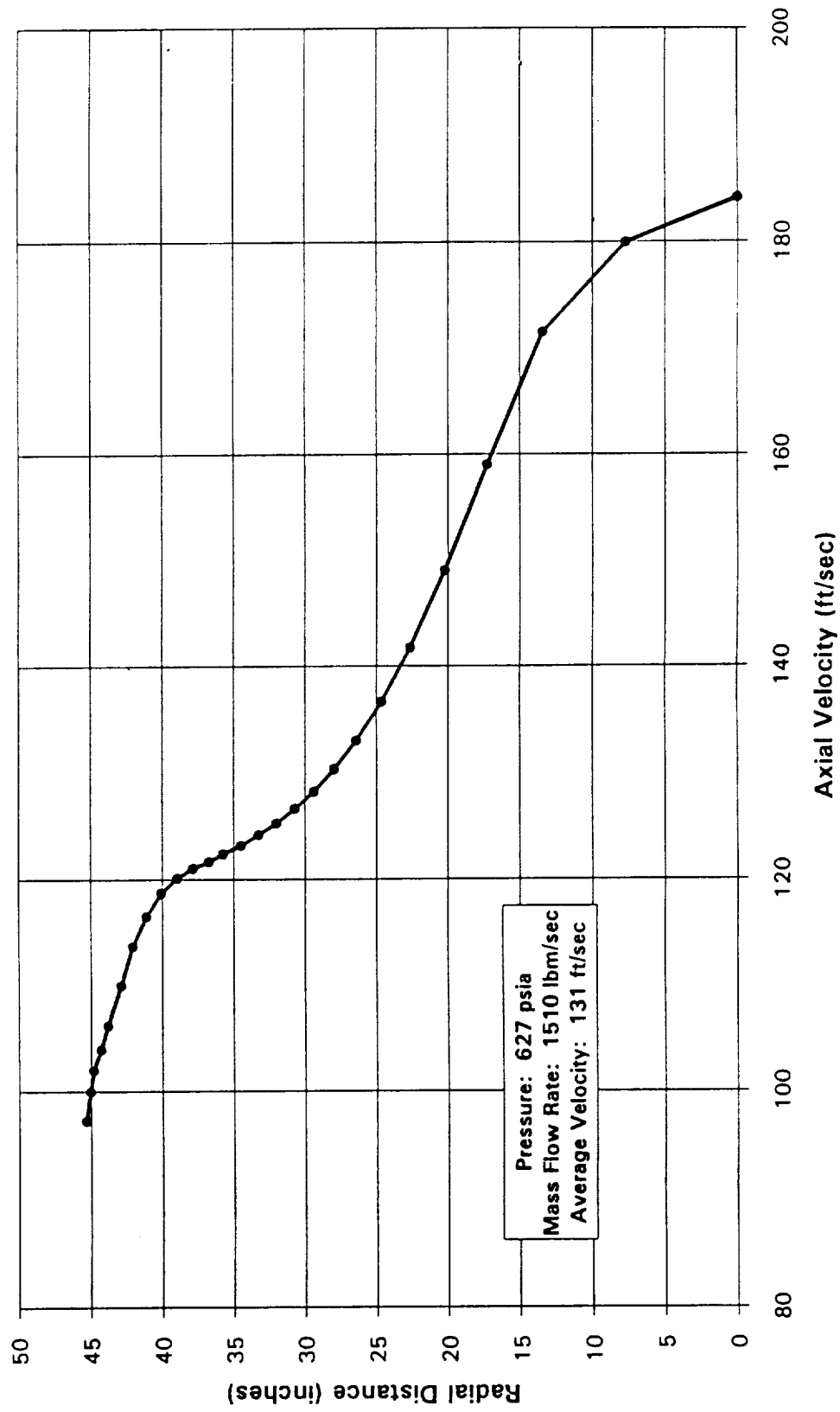


Figure 33. Velocity Profile for Nominal NBR Center Inhibitor  
Deformed Inhibitor Geometry  
RSRM 80 Seconds Burn Time

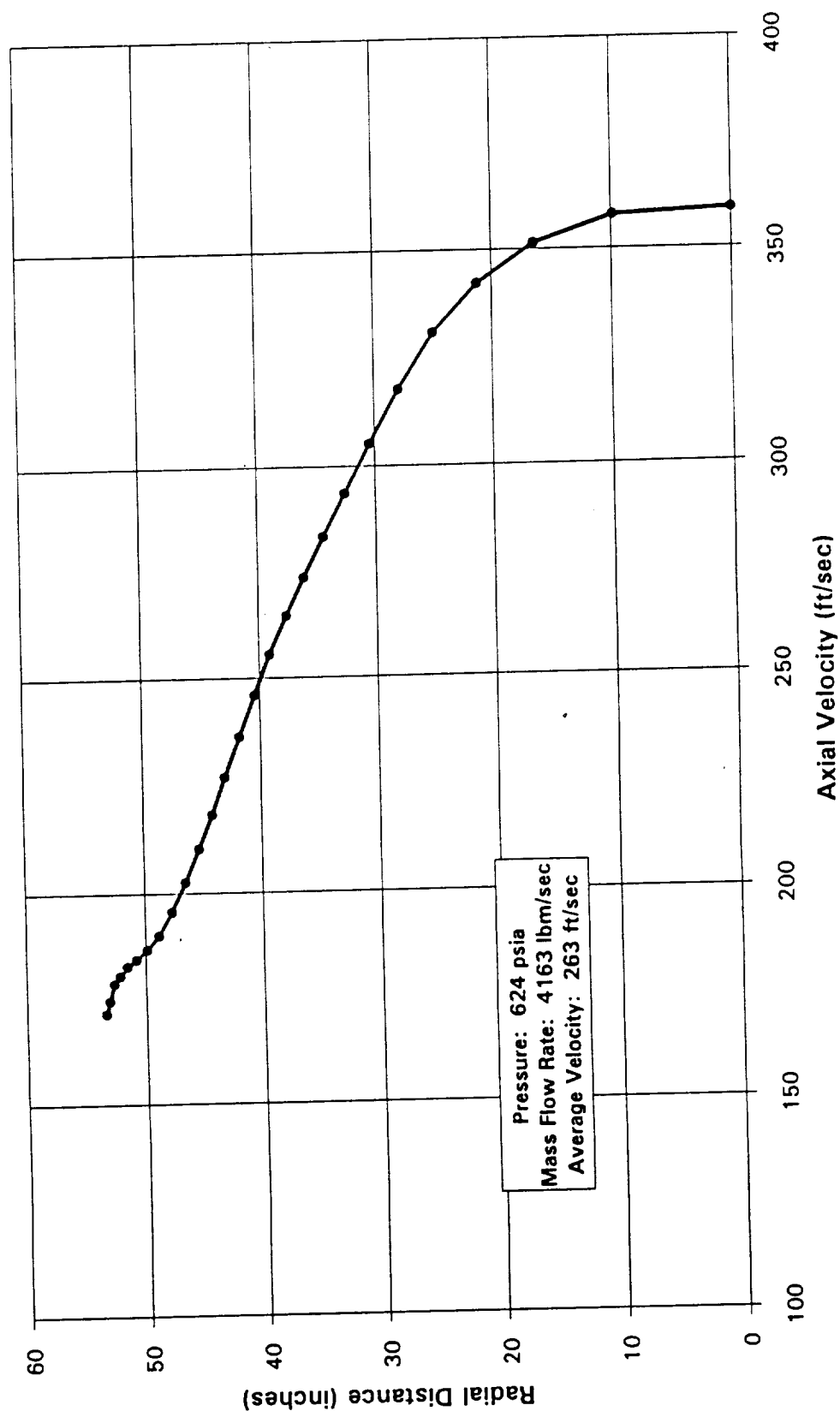


Figure 34. Velocity Profile for Nominal NBR Aft Inhibitor  
Deformed Inhibitor Geometry  
RSRM 80 Seconds Burn Time

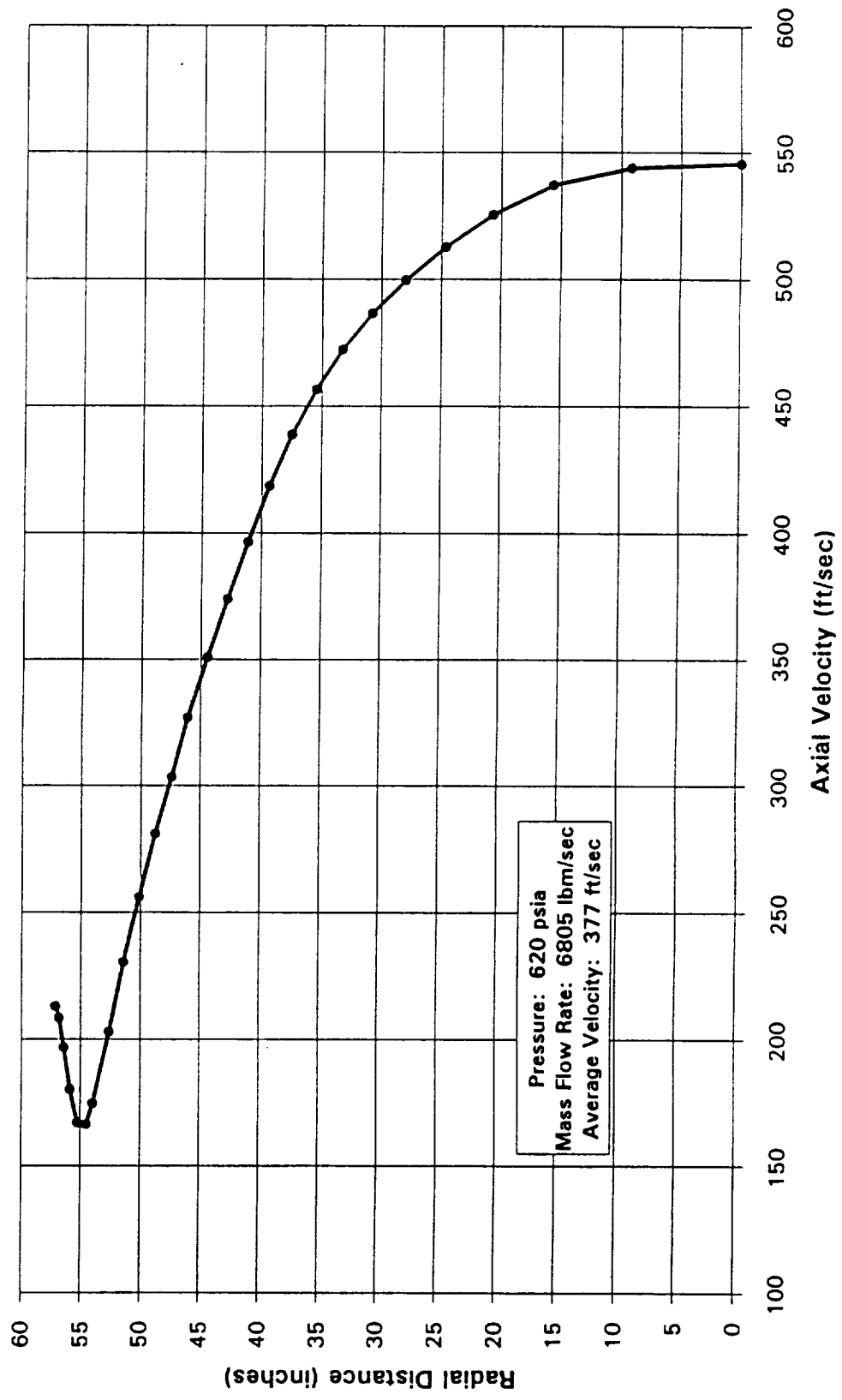


Figure 35. Velocity Profile for Stiff NBR Forward Inhibitor  
Deformed Inhibitor Geometry  
RSRM 80 Seconds Burn Time

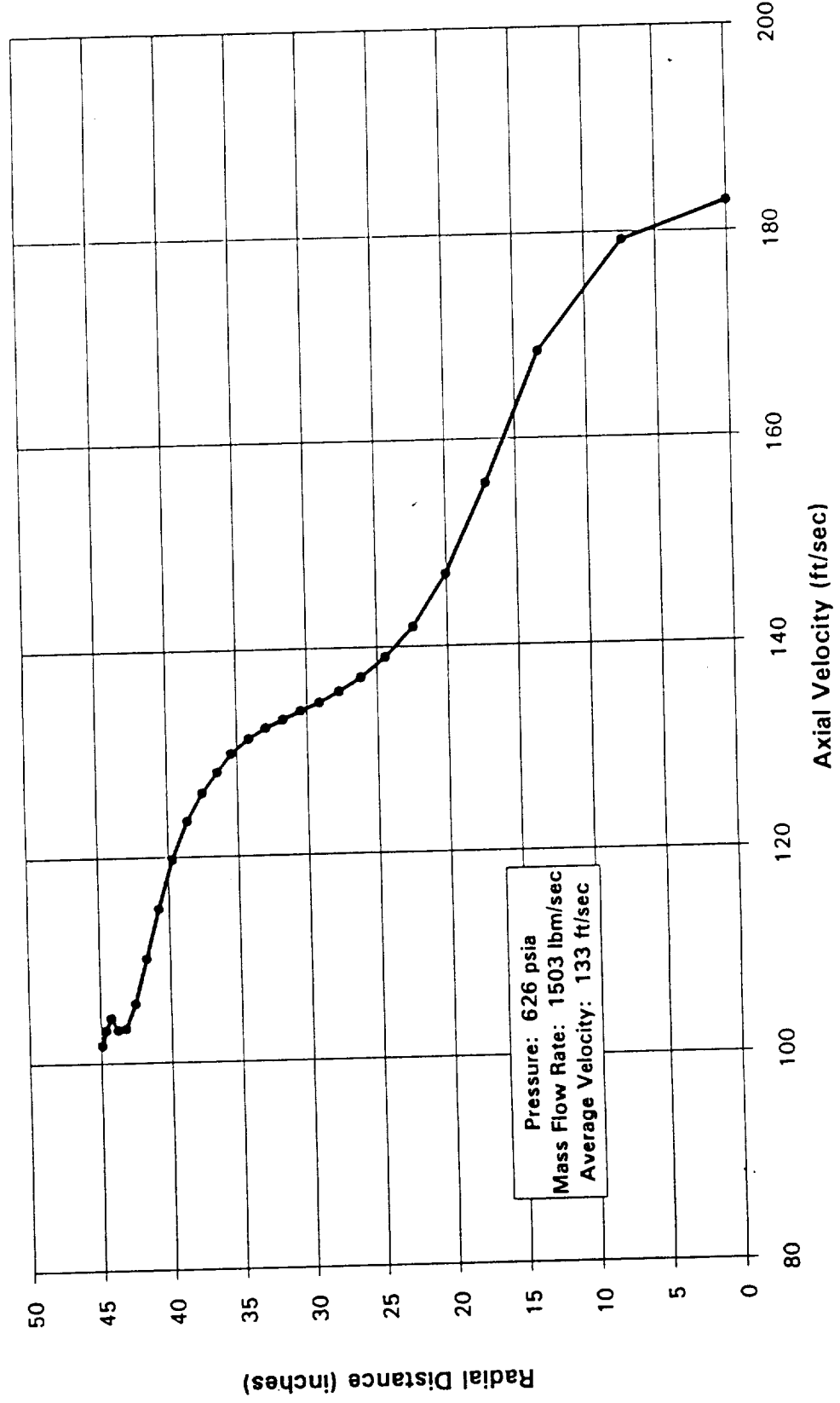


Figure 36. Velocity Profile for Stiff NBR Center Inhibitor  
Deformed Inhibitor Geometry  
RSRM 80 Seconds Burn Time

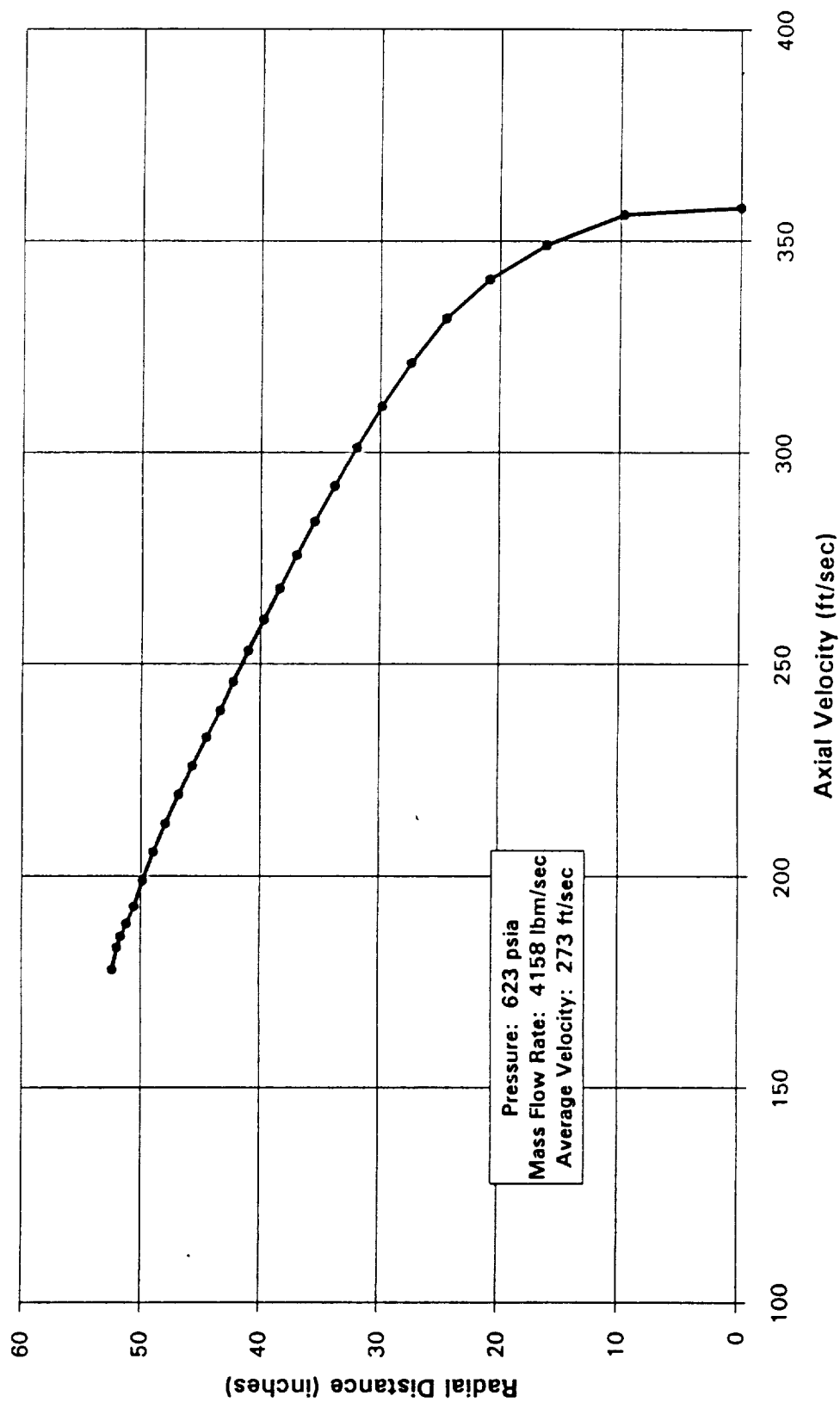




Figure 37. Velocity Profile for Stiff NBR Aft Inhibitor  
Deformed Inhibitor Geometry  
RSRM 80 Seconds Burn Time

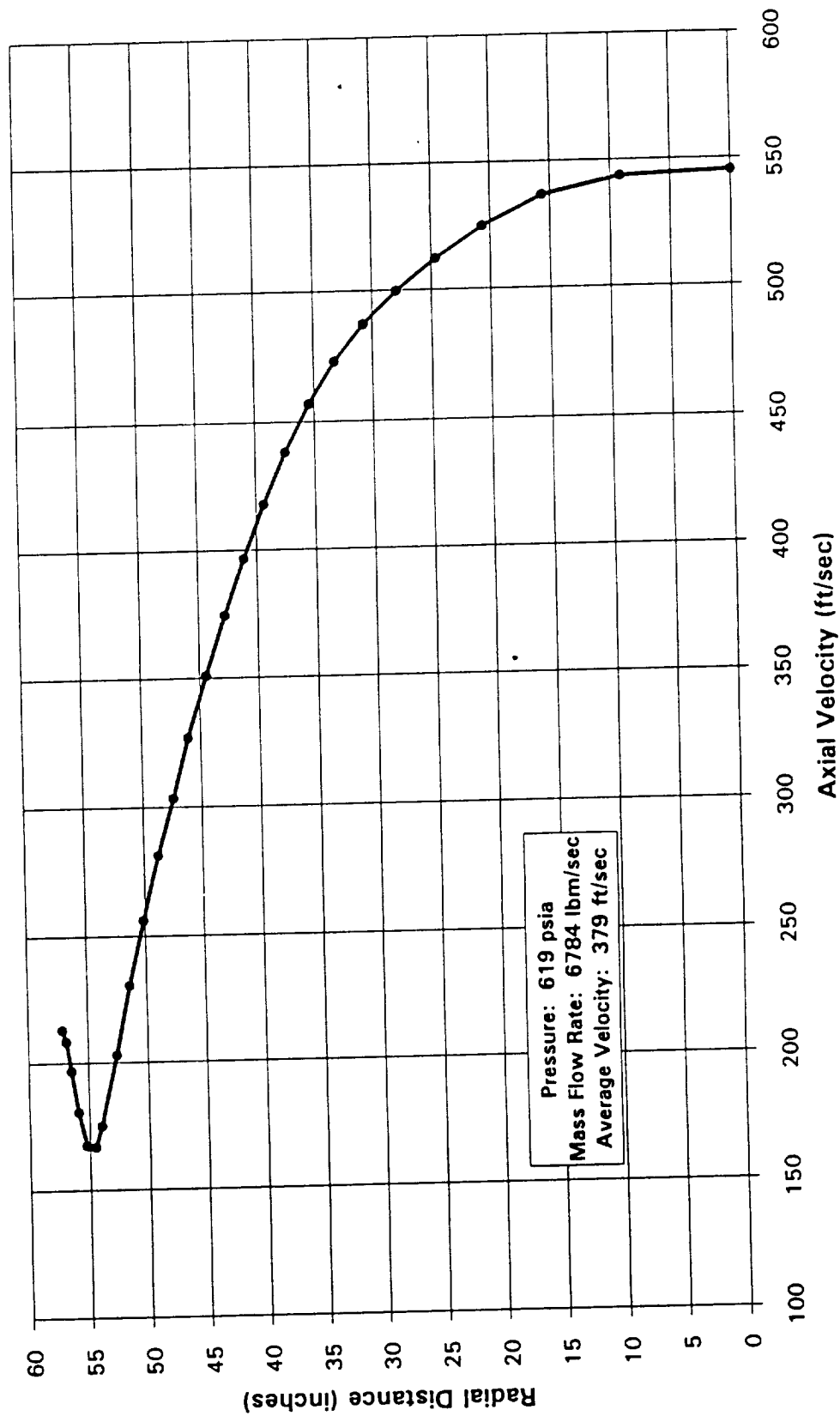
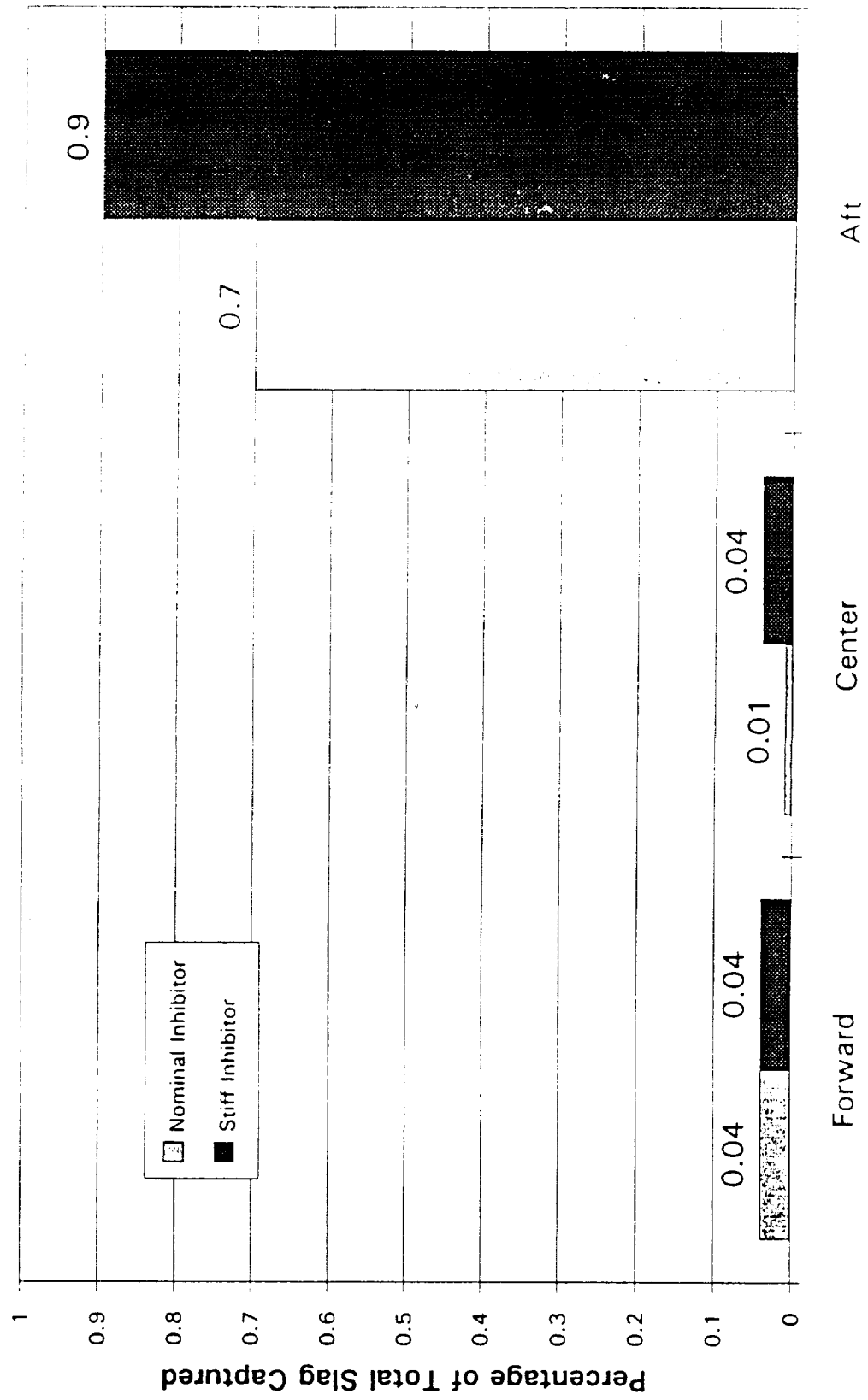
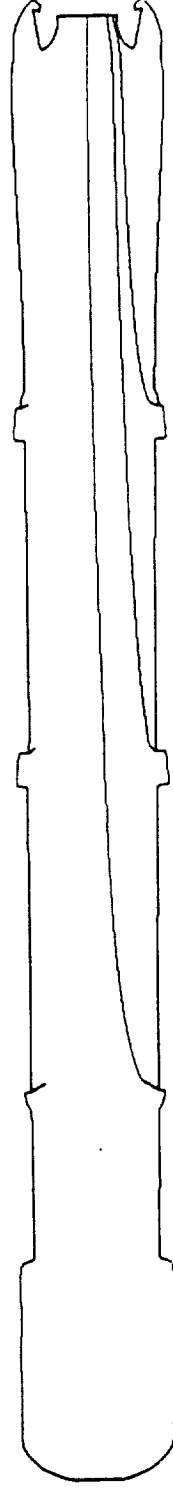
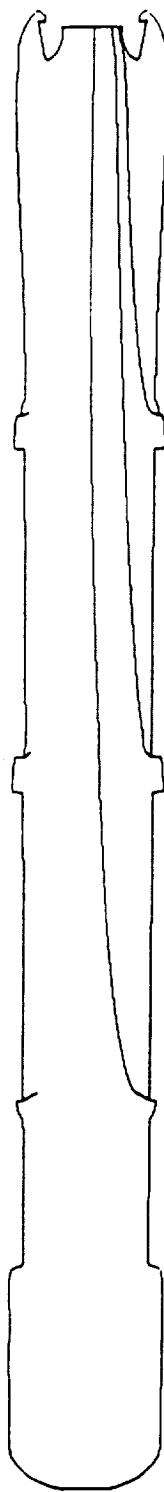


Figure 38. RSRM Two-Phase Flow Analysis  
Nominal and Stiff NBR Inhibitors





**Figure 39. Large Particle Trajectories, Nominal NBR Inhibitor Motor,  
Particle Radius: 0.2 Inches**



**Figure 40. Large Particle Trajectories, Nominal NBR Inhibitor Motor,  
Particle Radius: 0.4 Inches**

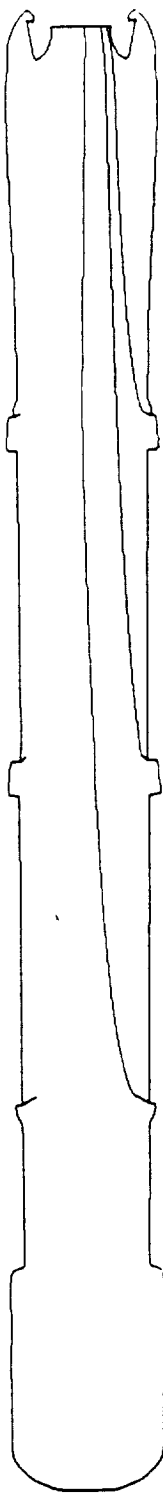


**Figure 41. Large Particle Trajectories, Nominal NBR Inhibitor Motor,  
Particle Radius: 0.8 Inches**

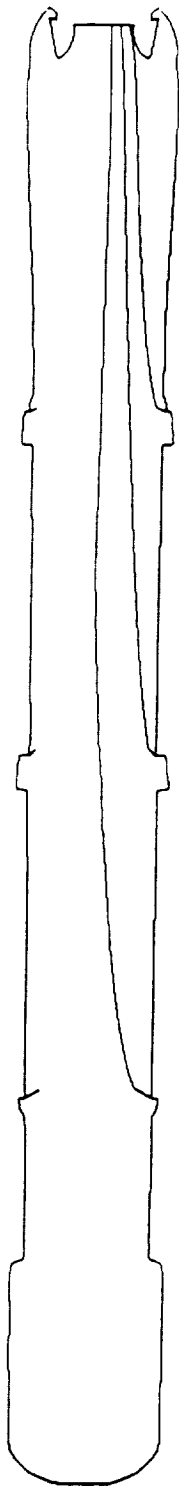


**Figure 42. Large Particle Trajectories, Nominal NBR Inhibitor Motor, Particle Radius: 1.6 Inches**

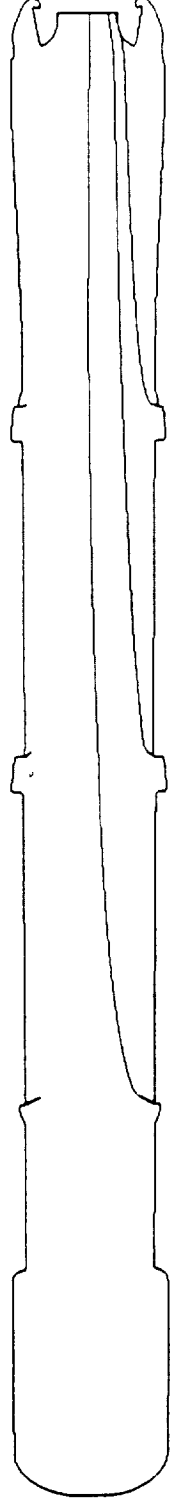


**Figure 43. Large Particle Trajectories, Stiff NBR Inhibitor Motor, Particle Radius: 0.2 Inches**

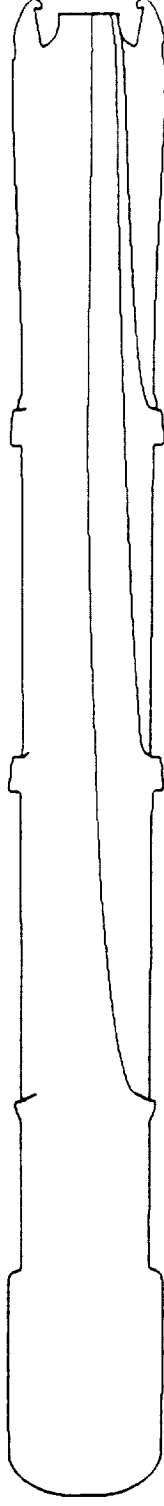


**Figure 44. Large Particle Trajectories, Stiff NBR Inhibitor Motor, Particle Radius: 0.4 Inches**



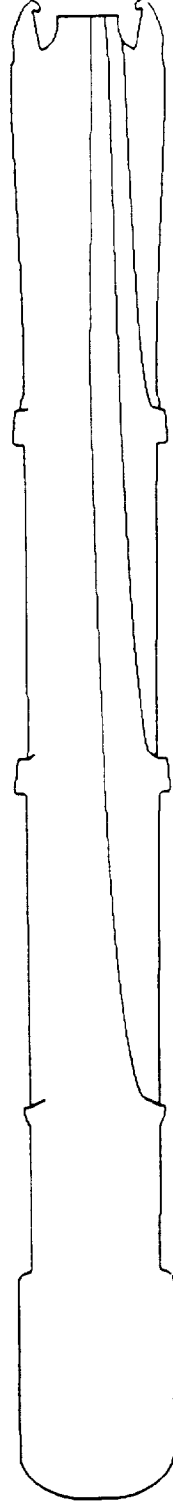


**Figure 45. Large Particle Trajectories, Stiff NBR Inhibitor Motor, Particle  
Radius: 0.8 Inches**

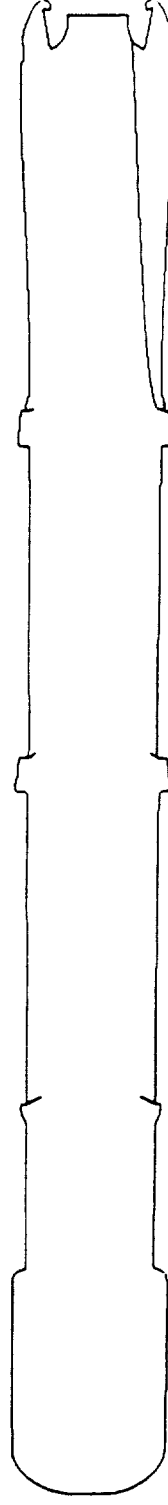


**Figure 46. Large Particle Trajectories, Stiff NBR Inhibitor Motor, Particle Radius: 1.6 Inches**

**Figure 47. Large Particle Slag Analysis**

<b>Nominal NBR Inhibitors</b>	<b>Particle Radius</b>			
	<b>0.2 Inches</b>	<b>0.4 Inches</b>	<b>0.8 Inches</b>	<b>1.6 Inches</b>
Forward Inhibitor Center Inhibitor Aft Inhibitor	Exits Motor	Exits Motor	Exits Motor	Exits Motor
	Exits Motor	Exits Motor	Exits Motor	Exits Motor
	Exits Motor	Exits Motor	Exits Motor	Exits Motor
<b>Stiff NBR Inhibitors</b>				
Forward Inhibitor Center Inhibitor Aft Inhibitor	Exits Motor	Exits Motor	Exits Motor	Exits Motor
	Exits Motor	Exits Motor	Exits Motor	Exits Motor
	Impacts Nozzle	Impacts Nozzle	Impacts Nozzle	Impacts Nozzle

**Large Particles were released from the downstream tips of the inhibitors noted above with no axial or radial velocity**

## Large Particle Trajectory Study for the Stiff Inhibitor Analysis

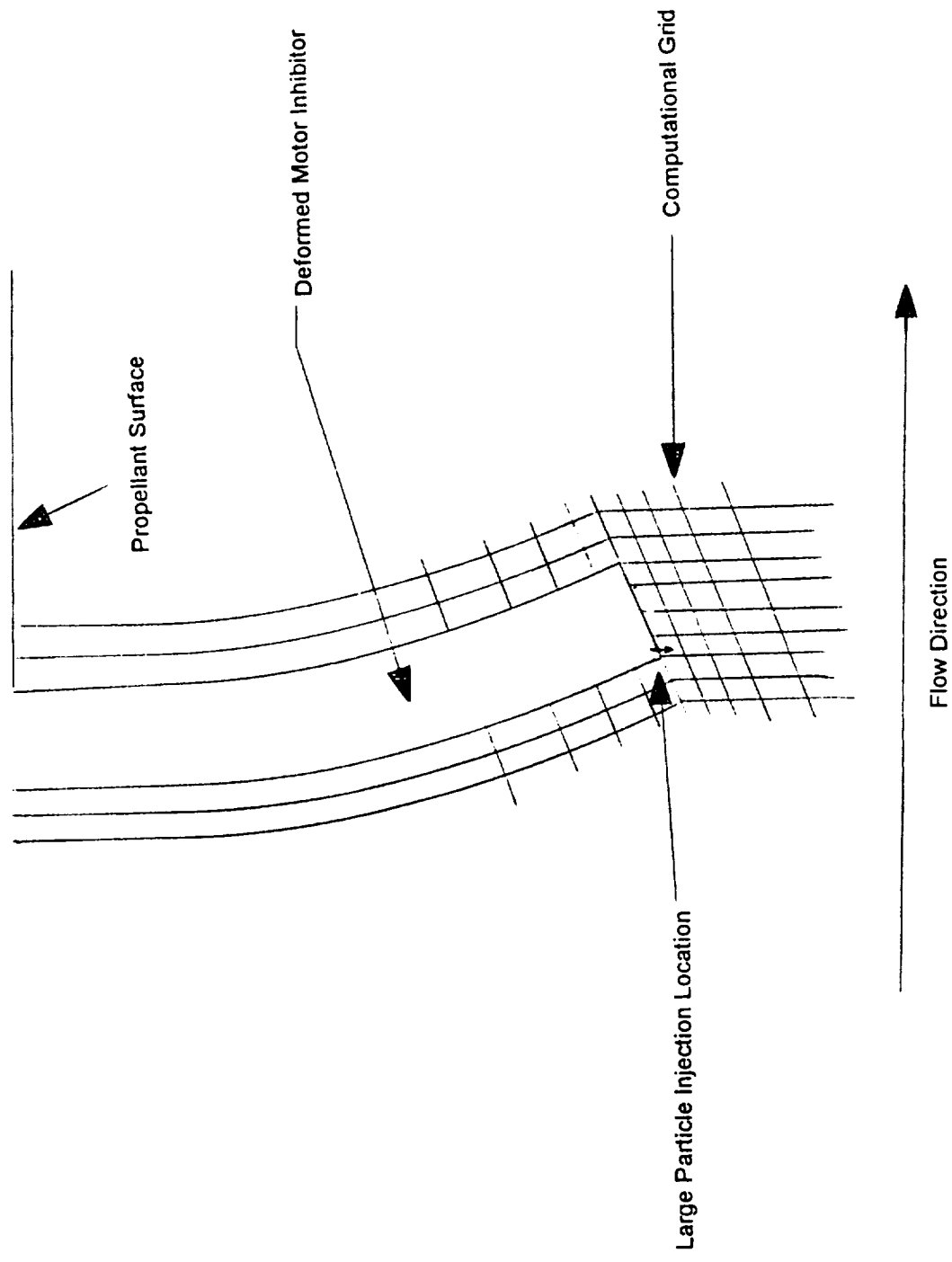
As part of this nominal/stiff material inhibitor analysis completed in December of 1995, a large particle trajectory analysis was also performed to determine the disposition of large globules of slag which might be released from the inhibitor tips. The trajectory analysis was performed to determine if particles of different diameters become trapped in the submerged nozzle region, strike the motor nozzle throat entrance ramp, or pass out the motor exit without striking a solid surface. Large particles of diameters ranging from 0.2 inches to 1.6 inches were analyzed with an aluminum oxide particle density of 110 lbm/sec. A 2.5g's vehicle acceleration was also added to the forces acting on the large particles. The particles were all released with an initial axial and radial velocity of zero in order to delete the additional effect of initial velocity on particle trajectories.

Table I shows the disposition of the large particles released from the upstream tip of the aft inhibitor. See Figure 3A for a pictorial description of the large particle release point from the inhibitor. Figure 4A shows a plot of the large particle trajectories traced from their release from stiff aft motor inhibitor to their impact location on the motor nozzle. The radial coordinate is stretched in the plot shown in Figure 4A so that the radial separation of the particles can be shown. Figure 5A shows an enlarged view of the nozzle nose region for this same set of large particle trajectories. In this figure the axial and radial coordinates are scaled to the same physical dimension so that the figure does give a physical perspective of the particle impacts on the nozzle surface. The nozzle contour is also drawn into the figure to give a better perspective of the location along the nozzle where the particle impacts the nozzle surface. It might seem that the particles would impact the nozzle surface in such a way that the largest particle would impact closest to the nozzle nose and the smallest particle farthest away from the nozzle nose. As can be observed in Figure 5A, this is not the case. The actual trajectories and impact locations of the various particles are a complex function of the particle axial and radial velocities, particle motor residence time which is also related to the axial velocity, particle diameter and mass, and vehicle accelerations. These quantities, integrated from the particle release point to the particle impact point define the individual trajectory for each particle size. This can be further illustrated by the following two figures of the particles axial and radial velocities. Figure 6A shows the development of the particle radial velocity as the particle moves from the aft inhibitor tip to the nozzle. Figure 7A shows the development of the particle axial velocity as the particle moves from the aft inhibitor tip to the nozzle. Figure 6A shows a rapid rise in the radial component of the particle velocity tending to move the particle inboard. The particles radial velocities are ordered such that the largest particle has the least radial velocity at any axial station and the smallest particle has the most radial velocity at any axial station. The same trend hold true for the particles' axial velocities shown in Figure 7A. This is as expected since the larger particle has more mass to be accelerated, proportional to the cube of the particle diameter. Without considering the axial velocity and particle residence time in the motor it would seem that the smallest particle would move further inboard but the axial velocity is also a very important factor. The much larger axial velocity of the smallest particles translates into less motor

residence time and less time for the radial inboard accelerations to act on the particle. In order to be sure that the complex interaction of forces acting on the large particles were being applied correctly, analyses were performed in which various forces were held constant while analyzing only one variable. These analyses showed that the complex interaction of forces acting on the particles was correct and that the particle trajectories for various particle diameters are indeed correct as shown in Table I.

**Table I. Impact Locations of Large Particles Released from the Aft Inhibitor**

<b>Particle Diameter (inches)</b>	<b>Nominal Inhibitor Motor Axial Disposition of the Large Particle</b>	<b>Stiff Inhibitor Motor Axial Disposition of the Large Particle</b>
0.2	Exits the motor without impacting the nozzle	Impacts nozzle at the axial motor station 1828.4
0.4	Exits the motor without impacting the nozzle	Impacts nozzle at the axial motor station 1831.3
0.8	Exits the motor without impacting the nozzle	Impacts nozzle at the axial motor station 1834.3
1.6	Impacts nozzle at the axial motor station 1835.1	Impacts nozzle at the axial motor station 1827.8



**Figure 3A. Schematic of the Location of Large Particle Release from the Aft Motor Inhibitor**

Figure 4A. Large Particle Trajectories

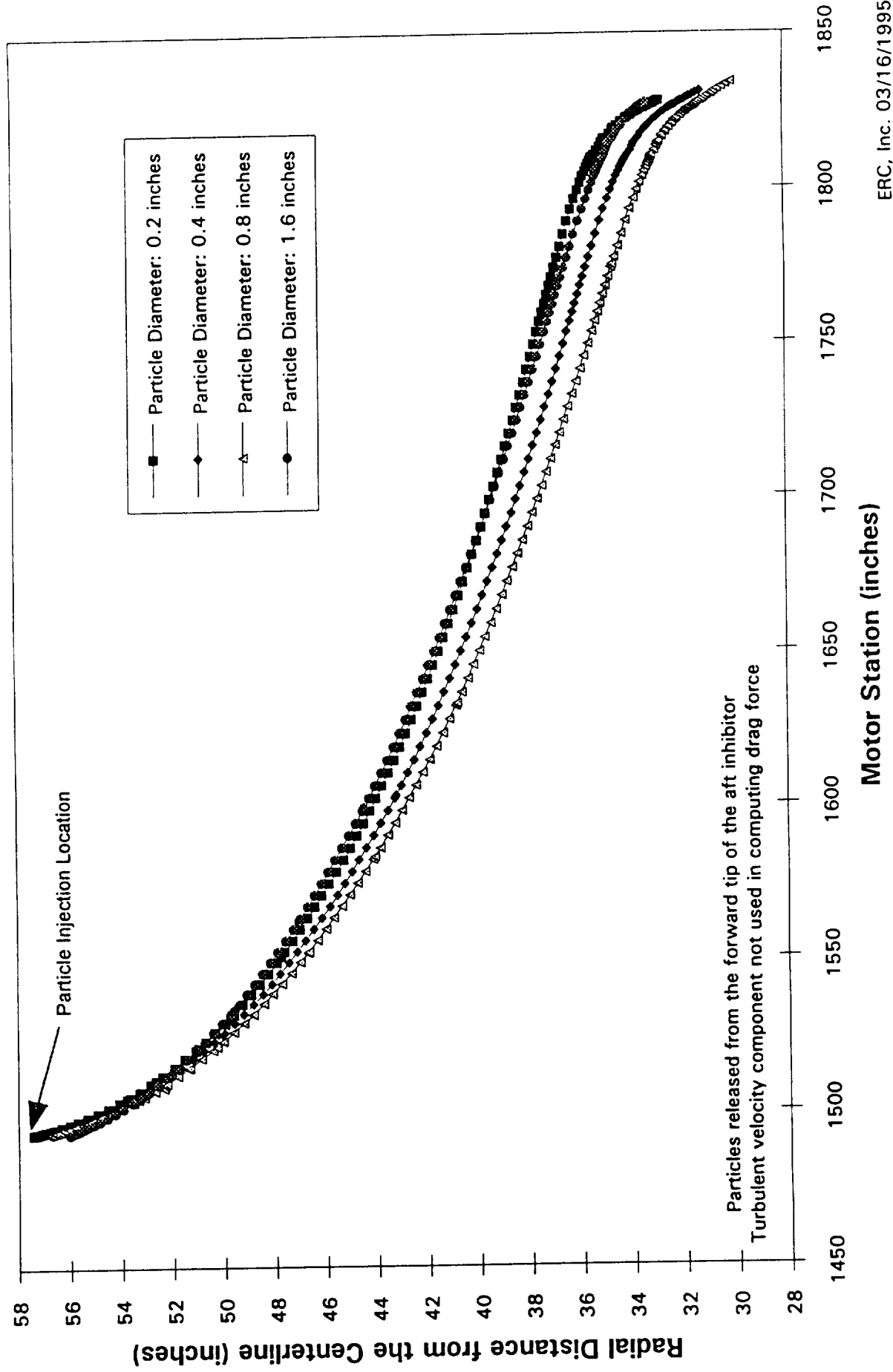


Figure 5A. Large Particle Trajectory Impacts On The Nozzle

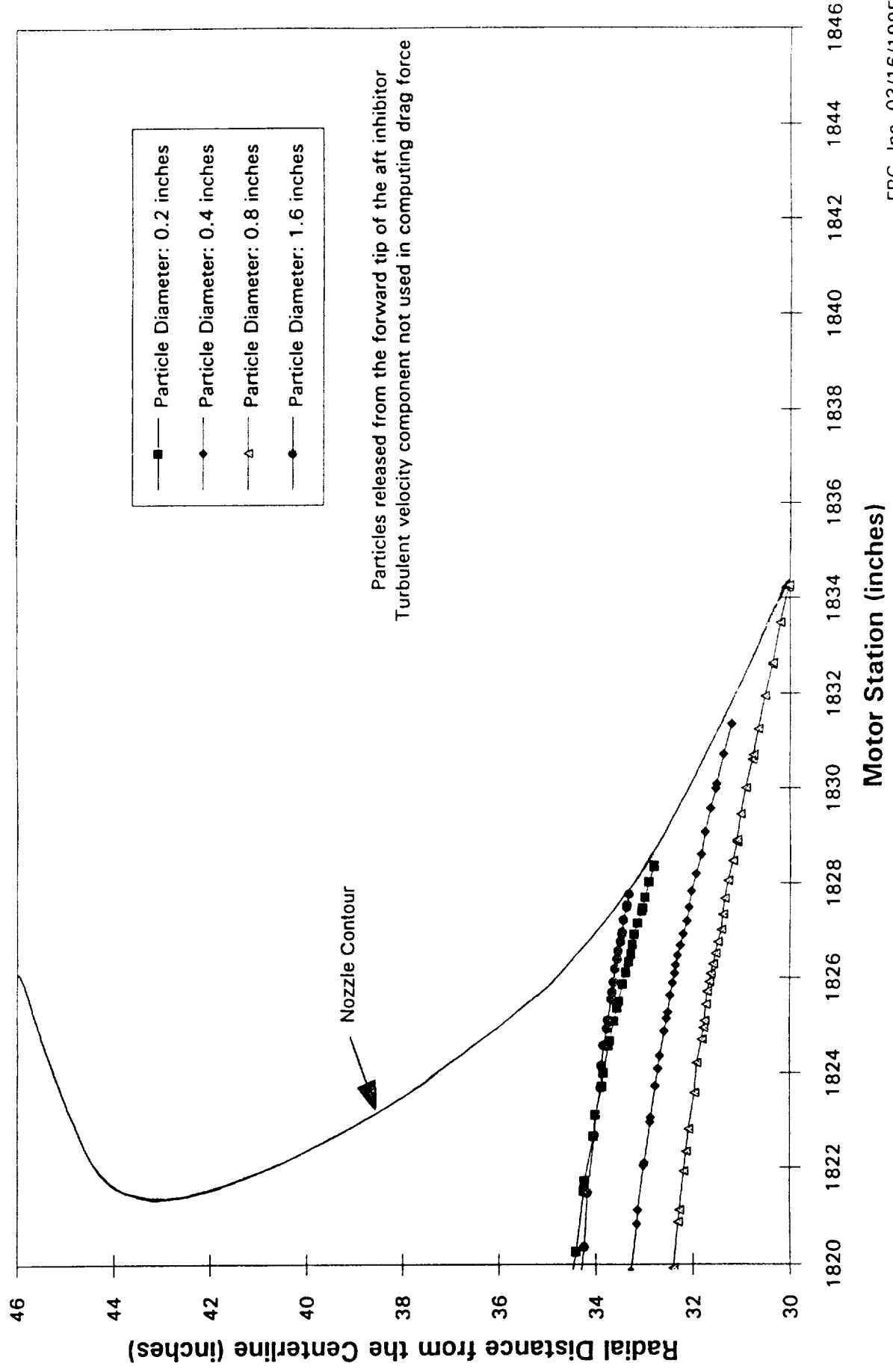




Figure 6A. Large Particle Radial Velocity

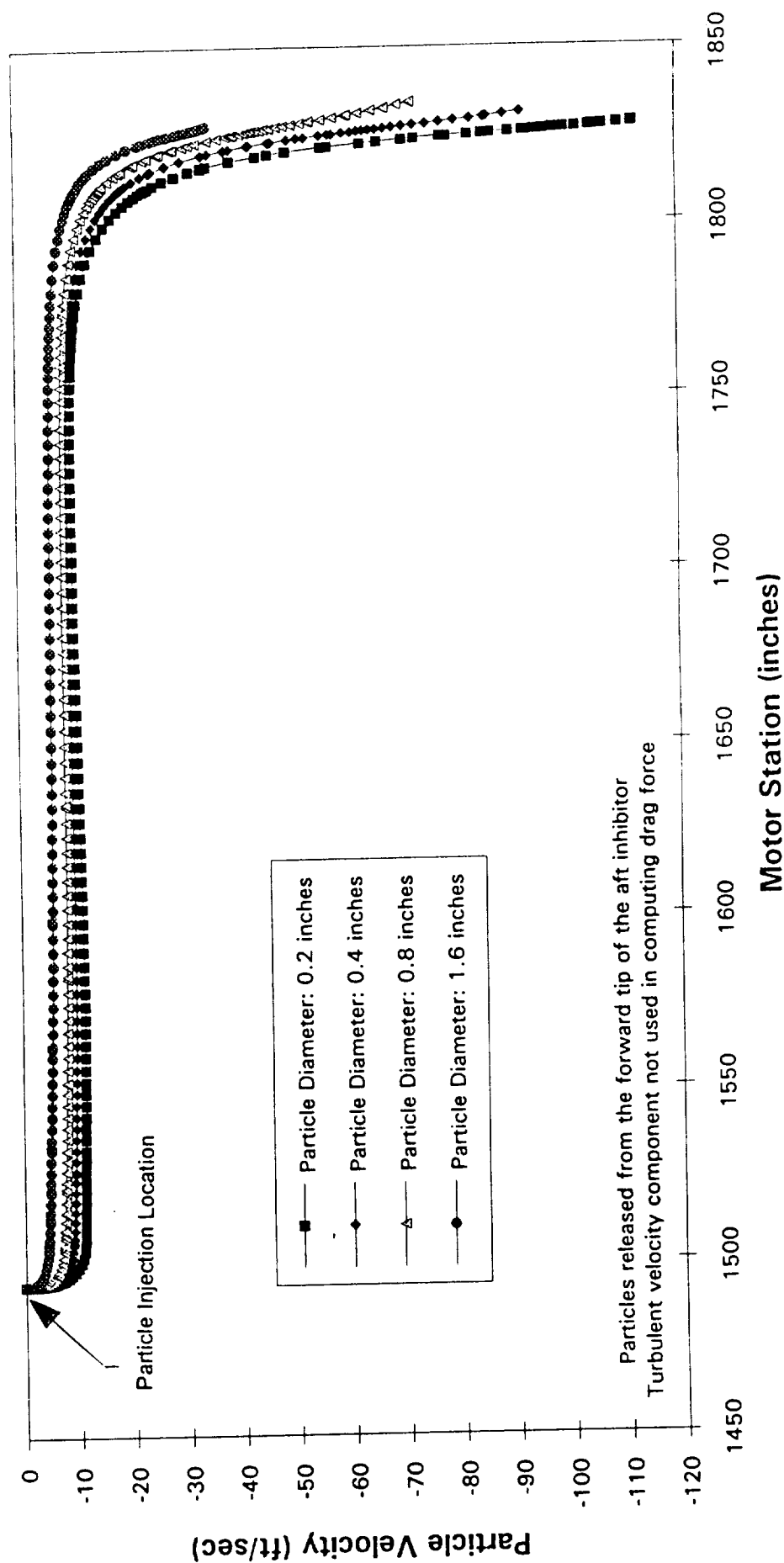
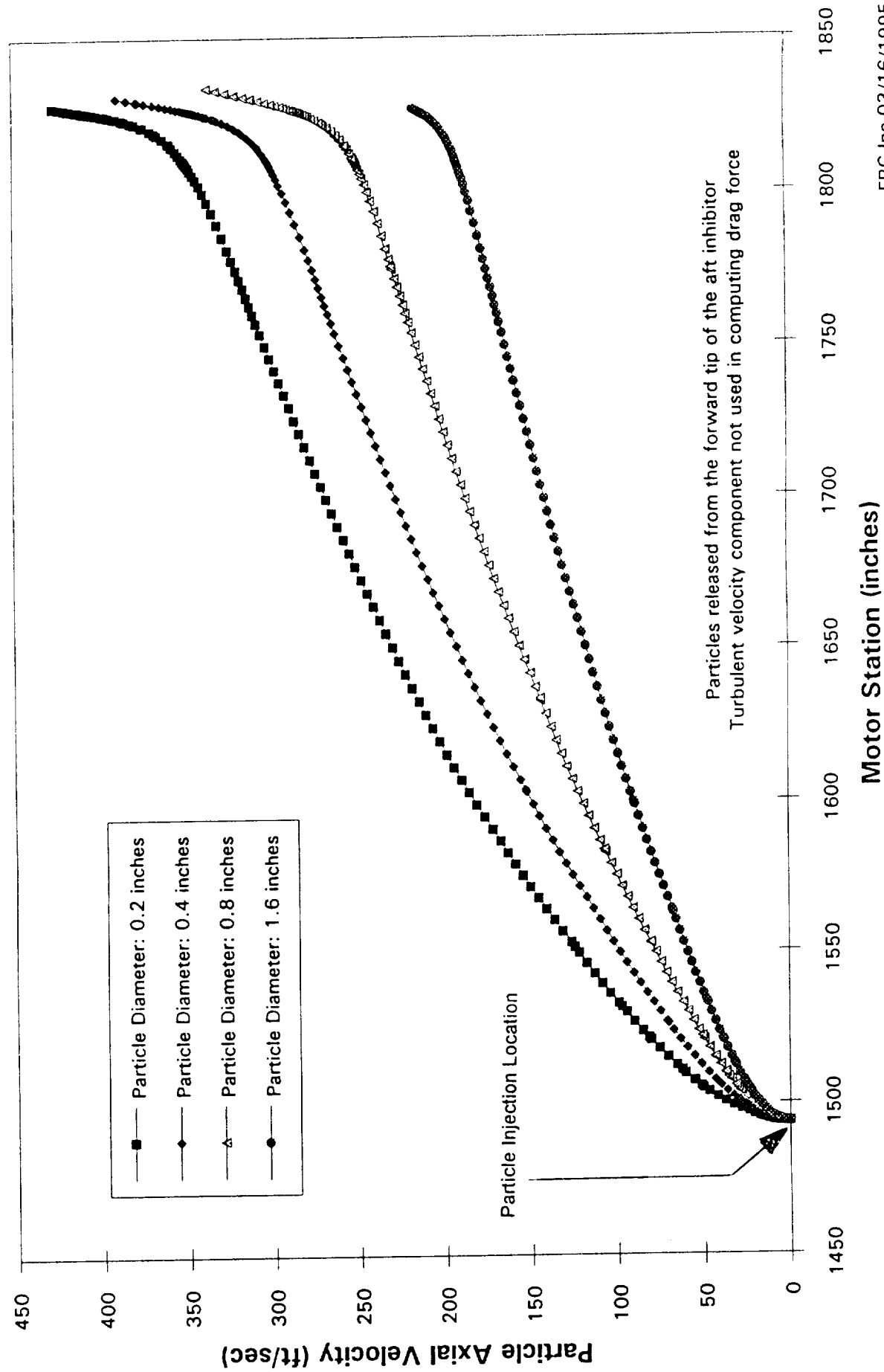




Figure 7A. Large Particle Axial Velocity





## **Effect of Inhibitor Height Variation on Slag Accumulation**

During the month of May 1995, an analysis was performed on the RSRM 80 second burn time full scale motor geometry. The purpose of the analysis was to determine the sensitivity of slag accumulation in the submerged nozzle region of the motor to inhibitor geometry variations. The analysis made use of the inhibitor lengths for the RSRM 80 second burn time as prescribed by Thiokol and as detailed in the 1994 December monthly report. Internal motor geometries were analyzed for five inhibitor configurations. Two of the inhibitor configurations involved deformed inhibitor configurations which were obtained from an iterative deformed inhibitor analysis reported in the 1994 December monthly. These two inhibitor configurations used the mechanical properties of the nominal and stiff NBR inhibitor materials to obtain the amount of deformation associated with the forward, center and aft inhibitors. The remaining three inhibitor configurations analyze different combinations of straight inhibitors. The inhibitor lengths used in this portion of the analysis are the same as those used for the deformed inhibitor configurations. In one of these three straight inhibitor configurations the forward, center and aft inhibitors are included in the analysis. In another of the configurations the center inhibitor stub is missing so that the inhibitor is flush with the port edge of the aft center propellant grain. This reduces the disruption of the port flow downstream of the center joint. In the last configuration, both the center and aft inhibitor stubs are missing. The center inhibitor is flush with the port edge of the aft center propellant grain and the aft inhibitor is flush with the port edge of the aft propellant grain. This configuration yields the minimum disturbance to the downstream port flow along the aft propellant grain from which slag accumulating in the submerged nozzle region originates.

This analysis addresses concerns as to how inhibitor variations in the motor affect slag accumulation in the submerged nozzle region as well as at the field joints. The five configurations considered yield a wide variety of inhibitor conditions so that this question can be confidently answered. The straight inhibitor stub (the inhibitor stub is the portion of the inhibitor which protrudes into the port flow) represents a maximum disturbance to the port flow downstream of the inhibitor, while the configurations without inhibitor stubs represent the minimum disturbance to the port flow. The inhibitor configurations considered in this analysis do not include inhibitor lengths that are greater than the Thiokol lengths presented in the 1994 December monthly report. The effect of reduced inhibitor erosion and therefore longer inhibitor lengths is not considered in this analysis. The conclusions made are for maximum inhibitor lengths as specified by Thiokol.

Figure 1A shows a summary of the results from this analysis. The figure shows that the slag accumulation rate is small at all the field joints, although there is some variation in the slag accumulation rate as a function of the internal motor inhibitor configuration. Slag accumulation rates below 0.01 lbm/second are considered to be zero for this analysis. The discussion will begin with slag accumulation at the forward joint motor inhibitor. The forward inhibitor is the same on all three inhibitor geometry

configurations which analyzed the straight inhibitors. The variation in the slag accumulation rate from 2.0 to 2.2 lbm/second is within the statistical variation of the CFD analysis and therefore does not reflect any inherent difference in the flow field or inhibitor at the forward joint. The slag accumulation for the two deformed inhibitor geometries does show that as the inhibitors are bent over slag accumulation in the joint is reduced. The slag accumulation rate at the center joint is very small at this motor burn time. No slag accumulates for the configurations in which there is no center inhibitor stub. A small amount of slag accumulates for the straight center inhibitor stub. The CFD analysis of the deformed inhibitor configurations predicts an order of magnitude lower slag accumulation rate than for the straight inhibitor configuration. The difference between the slag accumulation rate for the stiff and nominal NBR deformed inhibitors is statistically small and the slag accumulation rates are shown as the same rate, 0.01 lbm/second. The slag accumulation rate at the aft joint is greatest for the straight inhibitor and smallest for the configuration with no aft inhibitor. Although the slag accumulation rate is small at the aft joint, the analysis does show that for the straight inhibitor configurations the center inhibitor has the effect of slightly increasing the slag accumulation rate at the aft joint. The deformed inhibitor geometries yield about the same slag accumulation rate as when the center and aft inhibitors are missing. For all the motor joints, the greatest slag accumulation rate occurs for the straight inhibitor stubs and the smallest slag accumulation rate occurs for the configurations where the inhibitor stubs protrude a minimum distance into the port. This is according to intuition since the longer inhibitor stubs create a longer path over which the discrete aluminum oxide particles must turn in order to escape the joint region.

Figure 2A shows the velocity profiles in the port just downstream of the center joint. These curves illustrate the disruption of the flow field caused by the center inhibitor stub. Notice that the straight inhibitor stub causes the largest disruption of the flow field, as expected. There is a recirculation region near the propellant surface created by the straight inhibitor stub. The two configurations with no center inhibitor stub show the minimum disturbance to the port flow. There is still a small disturbance to the port flow near the propellant surface in these two configurations caused by the jet of flow emanating from the center slot. This jet is created by the burning propellant on the upstream face of the joint. Figure 3A shows that the disturbances to the port flow shown in Figure 2A have been significantly dissipated at a position a few inches upstream of the aft joint. Figure 4A shows the port flow velocity profiles just downstream of the aft joint. The disturbance to the port flow is much smaller at the aft joint because the inhibitor stub is much shorter at the aft joint. A significant difference can be noted between the four configurations with some kind of aft inhibitor stub and the one configuration with no aft inhibitor stub. As in the case of the center joint, the only disturbance to the port flow for the case with no aft inhibitor stub is caused by the jet emanating from the aft joint. It is expected that, since there is a significant difference in the velocity profiles comparatively for the configurations having inhibitor stubs and the configuration without an inhibitor stub, the discrete particles in the flow field will be redistributed to some extent. The quantitative amount of this redistribution

will be assessed and reported in a latter monthly report along with an assessment of other variables that might affect the particle distribution in the motor port.

Figure 5A shows the port velocity profiles for the five inhibitor configurations just upstream of the nozzle nose. The port velocity profiles are very similar at this point in the motor. Most of the upstream flow disturbances have died out. This means that the velocity profile in front of the nozzle nose and near the aft propellant grain surface is similar for the various inhibitor configurations. Obviously, the disturbances caused by the aft inhibitor stub wash out as the flow moves down the motor port toward the submerged nozzle. The speed with which the disturbances die out also has a bearing on perturbations to the distribution of discrete particles in the motor port. As already mentioned, the direct effect of the aft inhibitor stub on the particle distribution will be further investigated but for the configurations considered in this report the distribution of particles in the motor port does not seem to have been affected enough to cause a large variation in slag accumulation in the submerged region. Figure 1A illustrates this is the case. The two deformed inhibitor configurations show statistically the same slag accumulation rate. The configuration with straight center and aft inhibitors does show a statistically significant smaller slag accumulation rate than the other configurations but the slag accumulation rate variation is small over all of the configurations.

Figure 1A. RSRM Inhibitor Slag Accumulation Rate  
Deformed and Straight Inhibitors  
80 Second Burn Time

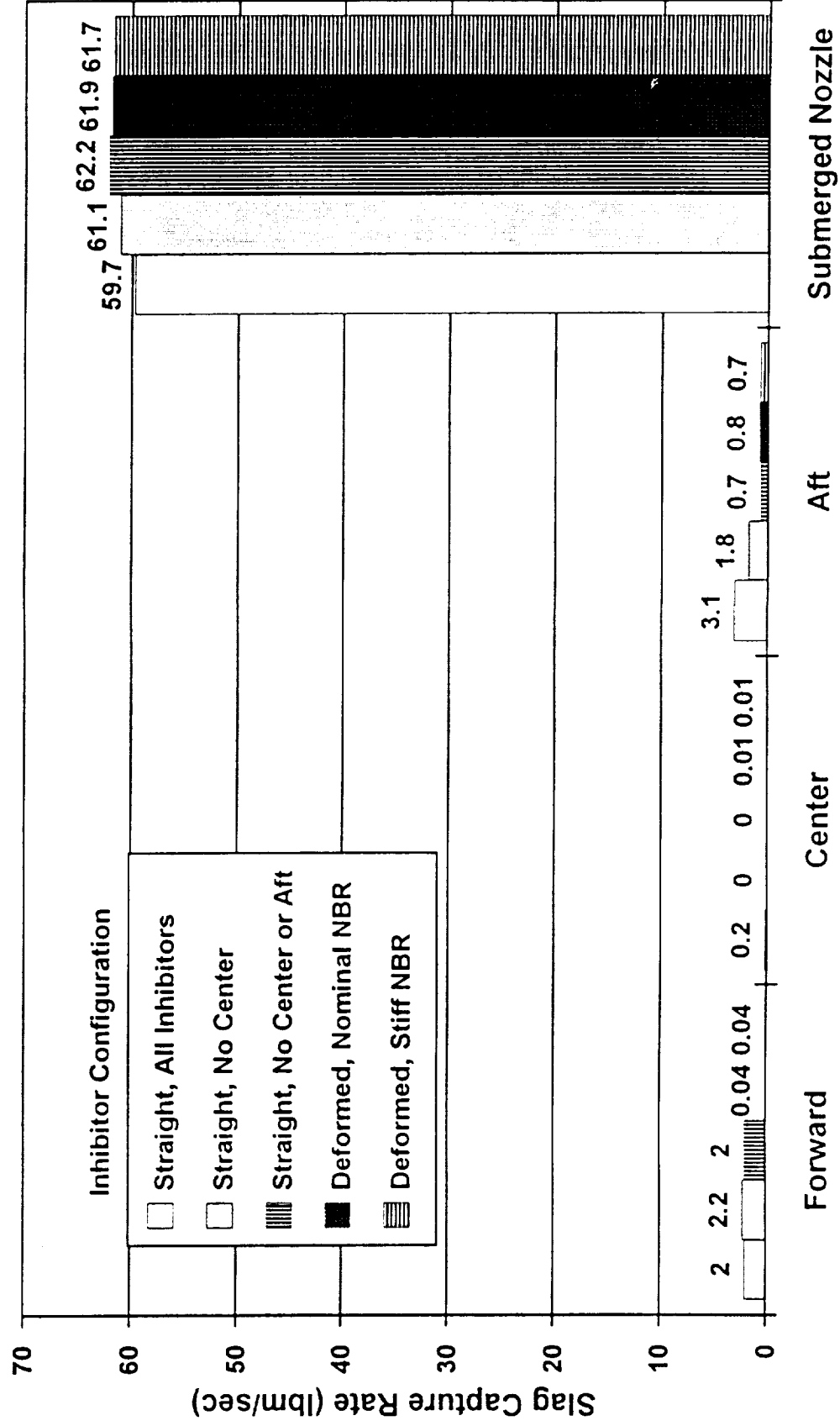




Figure 2A. Port Velocity Profiles aft of the Center Joint  
RSRM 80 Second Burn Time Geometry

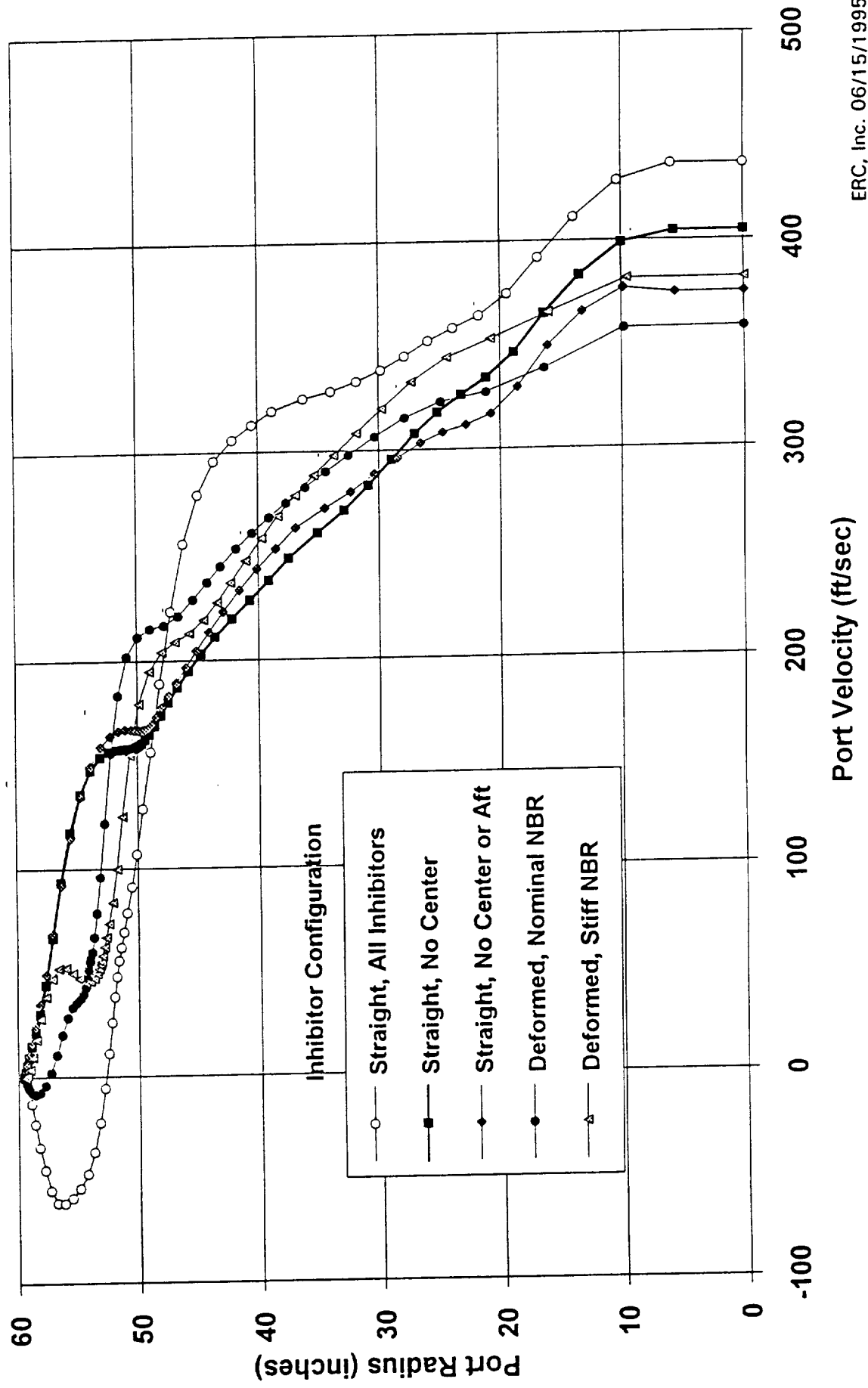


Figure 3A. Port Velocity Profiles Forward of the Aft Joint  
RSRM 80 Second Burn Time Geometry

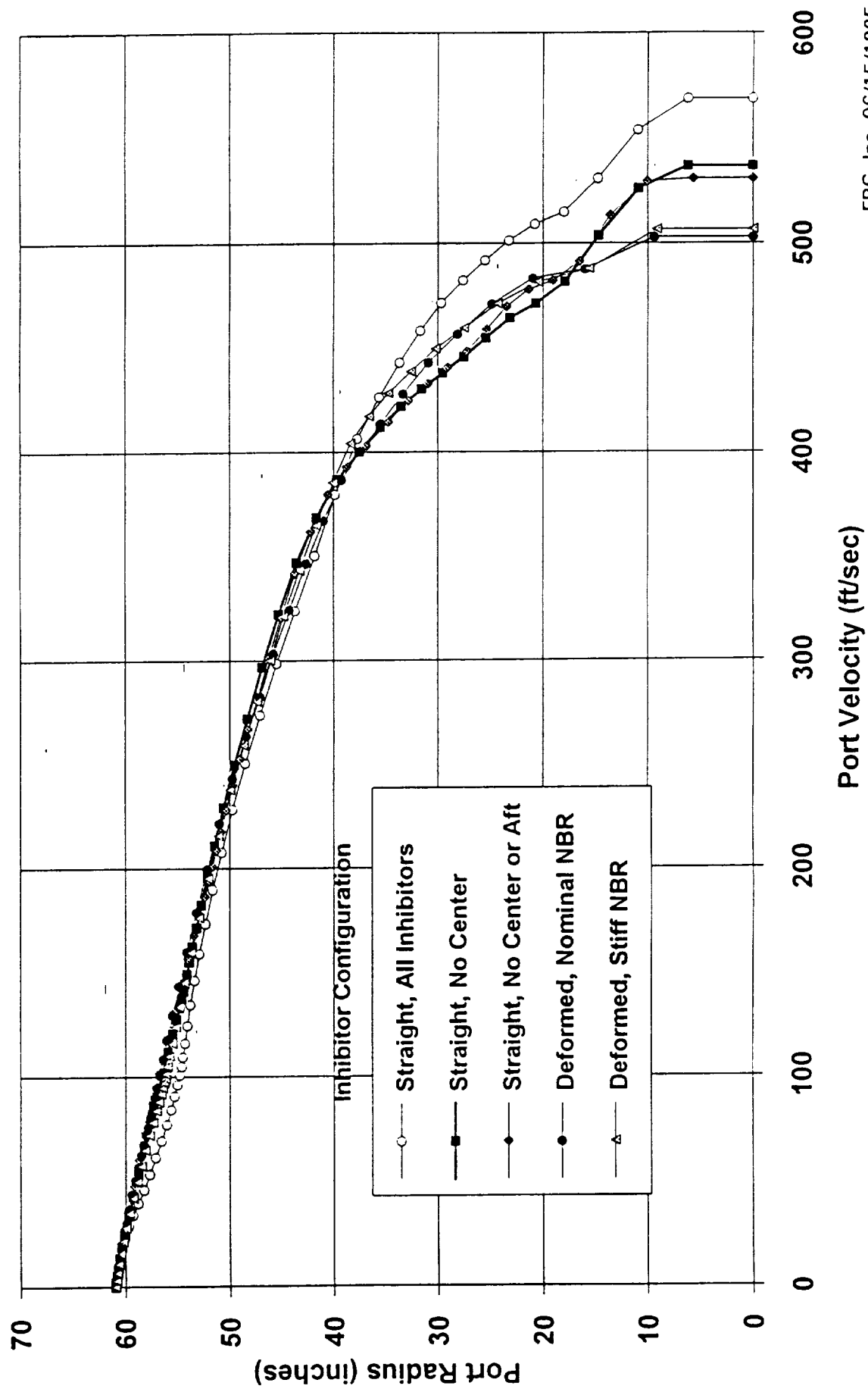


Figure 4A. Port Velocity Profiles Aft of the Aft Joint  
RSRM 80 Second Burn Time Geometry

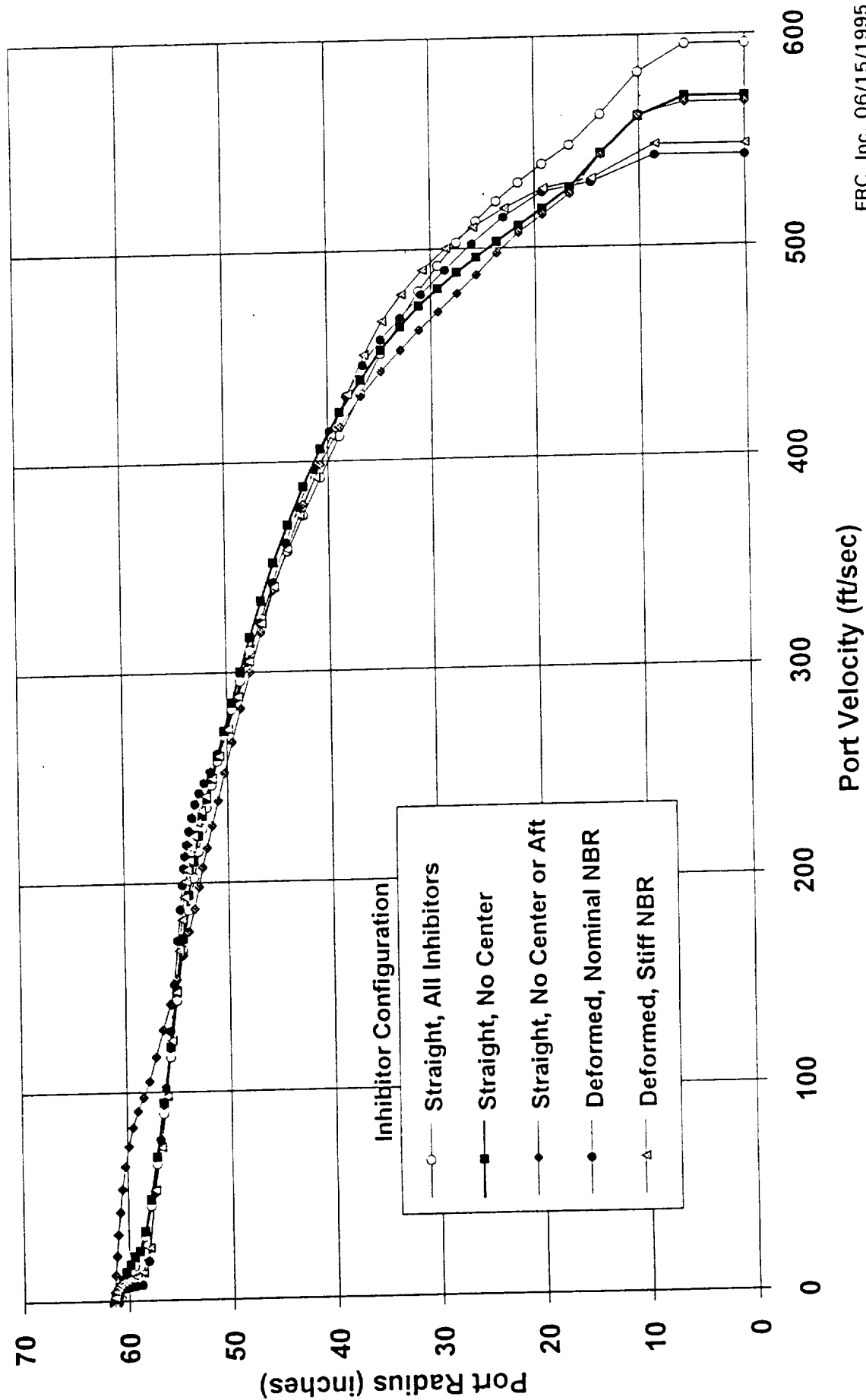
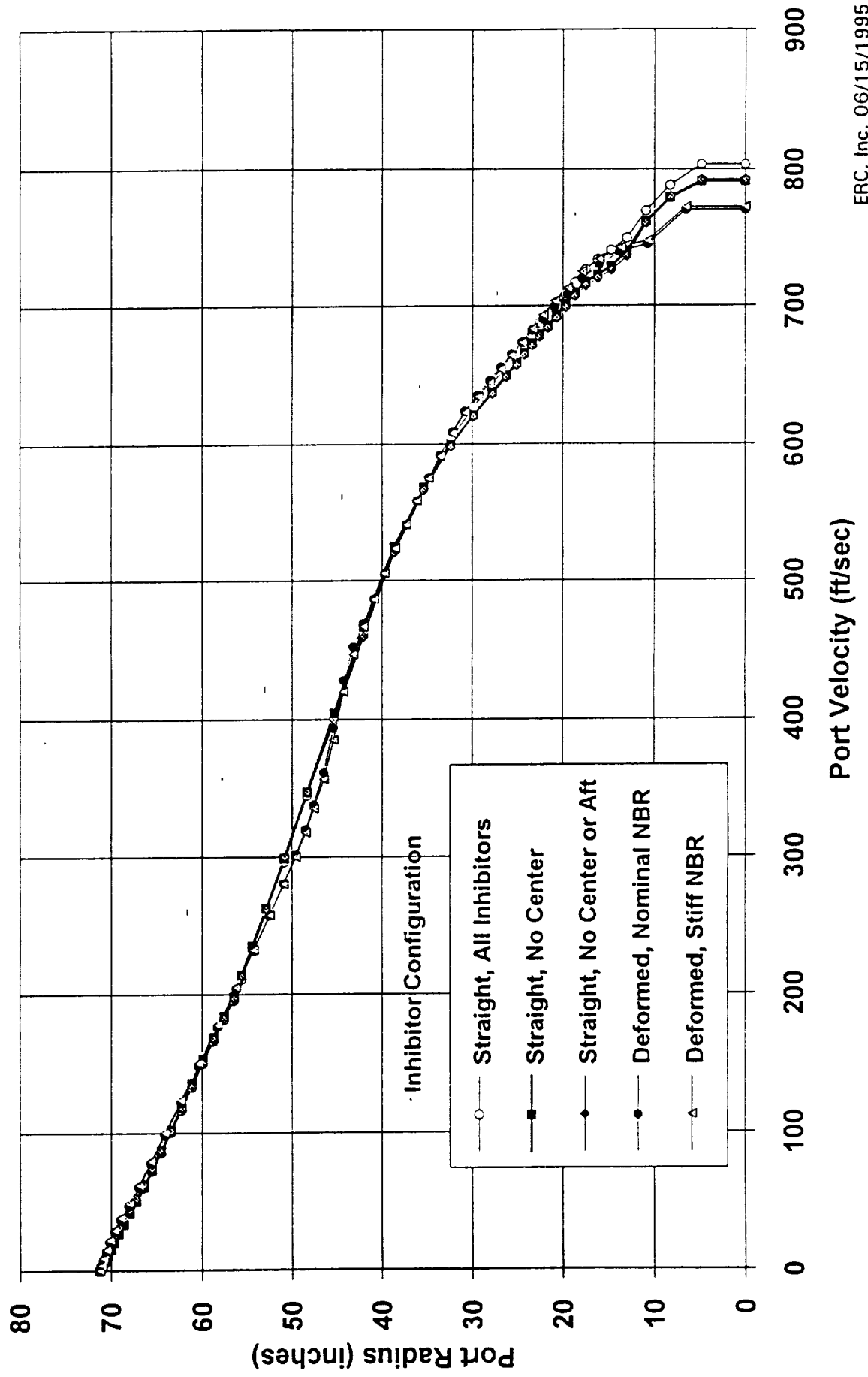


Figure 5A. Port Velocity Profiles Near of Nozzle Nose  
RSRM 80 Second Burn Time Geometry



## **Extended Inhibitor Height Variation Analysis**

In the May 1995, monthly report, results were presented which demonstrated the effects of inhibitor height variation on the aft segment flow field and the amount of slag accumulating in the submerged nozzle region. The 80 second burn time RSRM motor geometry was used to perform this analysis and the motor configurations considered were as follows:

1. Nominal height, straight inhibitors used at each field joint.
2. Nominal height, Nominal NBR deformed inhibitors used at all the joints.
3. Nominal height, Stiff NBR deformed inhibitors used at all the joints.
4. Nominal height, straight inhibitors used at the forward and aft joints. No inhibitor was located at the center joint.
5. Nominal height, straight inhibitor used at the forward joint. No inhibitors were located at either the center or aft joint.

The results of the slag accumulation analysis showed that there was only a small difference in the amount of slag collected in the submerged nozzle cavity for the five configurations considered. Slag accumulation varied from 59.7 to 62.2 lbm/second. Further analysis was performed during the month of July, 1995, because of an interest in the effect of longer inhibitors on the flow field and slag accumulation in the submerged cavity.

This analysis considers the effect of extending the length of only the aft inhibitor stub. This is a reasonable approach for two reasons. Changing only one inhibitor permits an observation of difference in the flow field and slag accumulation affected by only the aft inhibitor and not possible effects caused by other inhibitors. Also, the slag which accumulates in the submerged cavity emanates from the aft propellant grain. The aft inhibitor is closest to the aft propellant grain and has the greatest affect on the flow field and thus the slag accumulation in the submerged cavity. The stub height was increased by a factor of two. Figure 1A shows a schematic of the nominal height and extended height aft joint inhibitors. The nominal aft inhibitor stub height was 7.54 inches and the extended length was 15.09 inches. The RSRM 80 second burn time motor geometry was used to perform this analysis in order to compare the results with the previously reported results. The CFD parameters used to obtain the solution reported in this monthly can be found in the December 1994 monthly report.

Three solutions are compared in this analysis. The solutions include the solutions for the extended length aft inhibitor configuration, the nominal length aft inhibitor configuration, and the configuration with no center or aft inhibitors. Plots of the port axial and radial velocity profiles are shown for the motor stations shown in Figure 2A. Figure 3A shows the axial velocity profile just downstream of the aft inhibitor. Comparing the profile for the extended length inhibitor to the other two configurations shows that the extended aft inhibitor causes a significant disturbance to the flow downstream of the inhibitor. The flow fields for the nominal length inhibitor stub and

the configuration without an inhibitor stub are similar because the nominal length inhibitor stub does not protrude far enough radially inward from the propellant surface to significantly obstruct the upstream flow. Figure 4A shows this pictorially. The upstream flow which is parallel to the aft center propellant grain is not greatly disrupted because the aft propellant is recessed below the aft center grain propellant segment due to the way the propellant near the aft inhibitor stub burns back. The figure also shows that the extended length inhibitor stub is long enough to have a significant effect on the upstream flow field. Figures 5A and 6A show the axial velocity profiles for the three solutions at approximately the mid-point of the aft propellant grain and near the nozzle nose, respectively. These profiles show that the disturbance to the extended length inhibitor port flow is still evident even near the nozzle nose. The other two flow field solutions show a similar port axial velocity profile near the nozzle nose. The radial velocity profiles at the same motor stations for which the axial velocity profiles were shown, Figure 2A, will now be shown to further illustrate why the axial velocity profiles remain disturbed for such a prolonged distance. Figure 7A shows the radial velocity profiles for the solutions just downstream of the aft inhibitor. The profile shows that there is a region of recirculation behind the extended inhibitor and a strong radially inward movement of the flow caused by the extended inhibitor stub which obstructs the port flow at the aft joint. Figure 8A shows the flow field is re-expanding radially toward the propellant surface near the mid-point of the aft propellant grain because of the strong radial inward movement of the flow field at the aft inhibitor stub and because of the expanding diameter of the motor port. Figure 9A shows the radial velocity profile near the nozzle nose. The port radial flow has readjusted itself so that the profiles are similar in the direction of radial flow but the radial profile for the extended inhibitor has a significantly larger magnitude.

Since the velocity profiles for the extended inhibitor stub configuration are so different, it would be expected that the slag accumulation in the submerged cavity would be significantly affected. Table I shows that this is true. There is a 20% reduction in the amount of slag which accumulates in the submerged nozzle cavity caused by the extension of the aft inhibitor stub from nominal length.

**Table I. Slag Accumulation in the Submerged Cavity for the Three Configurations Considered in this Analysis.**

<b>Inhibitor Configuration</b>	<b>Slag Trapped in the Submerged Cavity</b>
Extended Length Inhibitor Stub	47.7 lbm/second
Nominal Length Inhibitor Stub	59.7 lbm/second
No Center or Aft Inhibitor Stub	62.2 lbm/second

Also as expected, the slag accumulating in the aft field joint significantly increases. Table II shows this effect. The amount of slag accumulating in the aft field joint increases as a function of the inhibitor height.

**Table II. Slag Accumulation at the Aft Field Joint for the Three Configurations Considered in this Analysis.**

<b>Inhibitor Configuration</b>	<b>Slag Trapped in the Aft Field Joint</b>
Extended Length Inhibitor Stub	23.9 lbm/second
Nominal Length Inhibitor Stub	3.1 lbm/second
No Center or Aft Inhibitor Stub	0.7 lbm/second

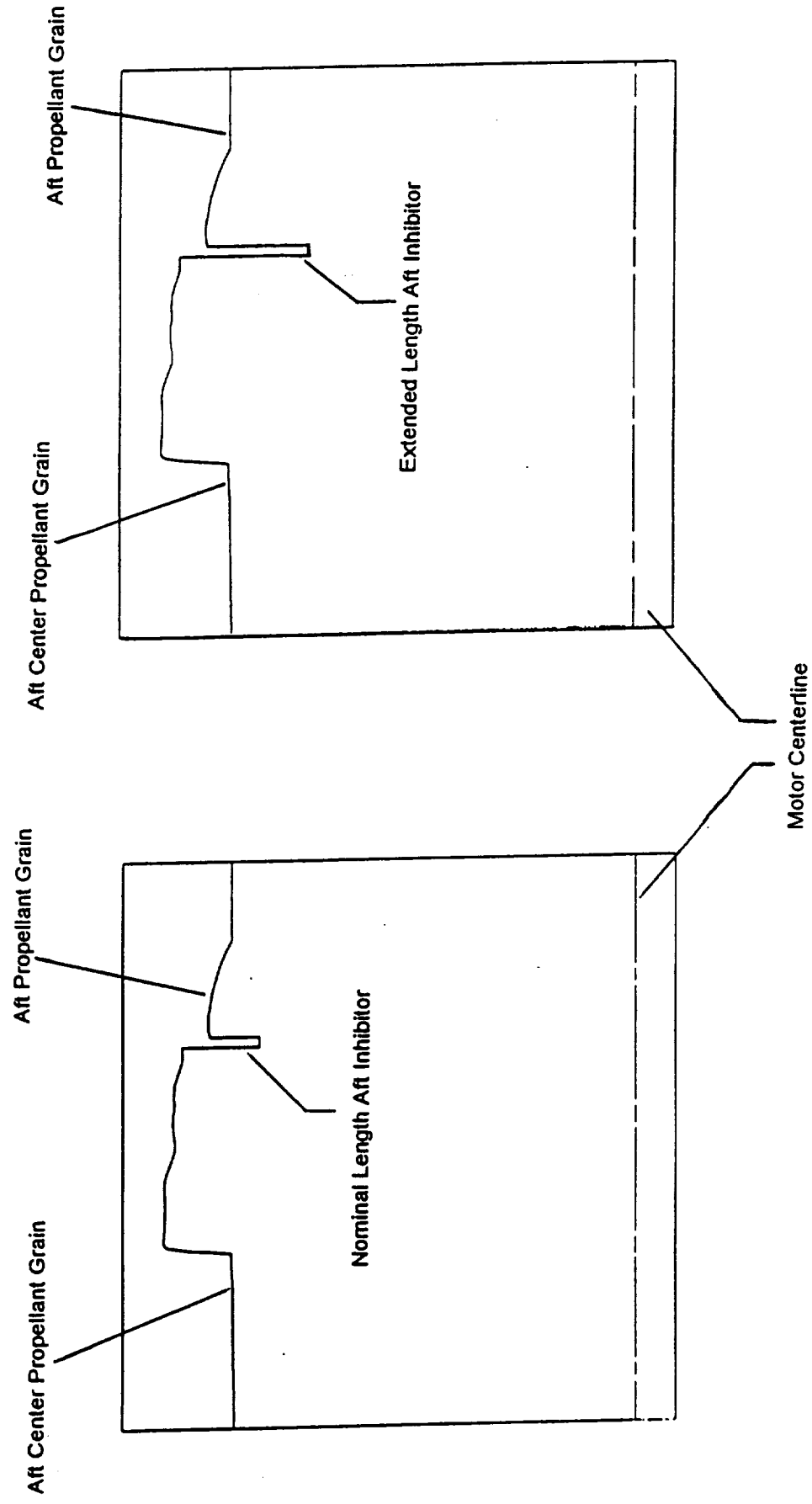


Figure 1A. Schematic of the Nominal and Extended Length Aft Inhibitor Stubs.



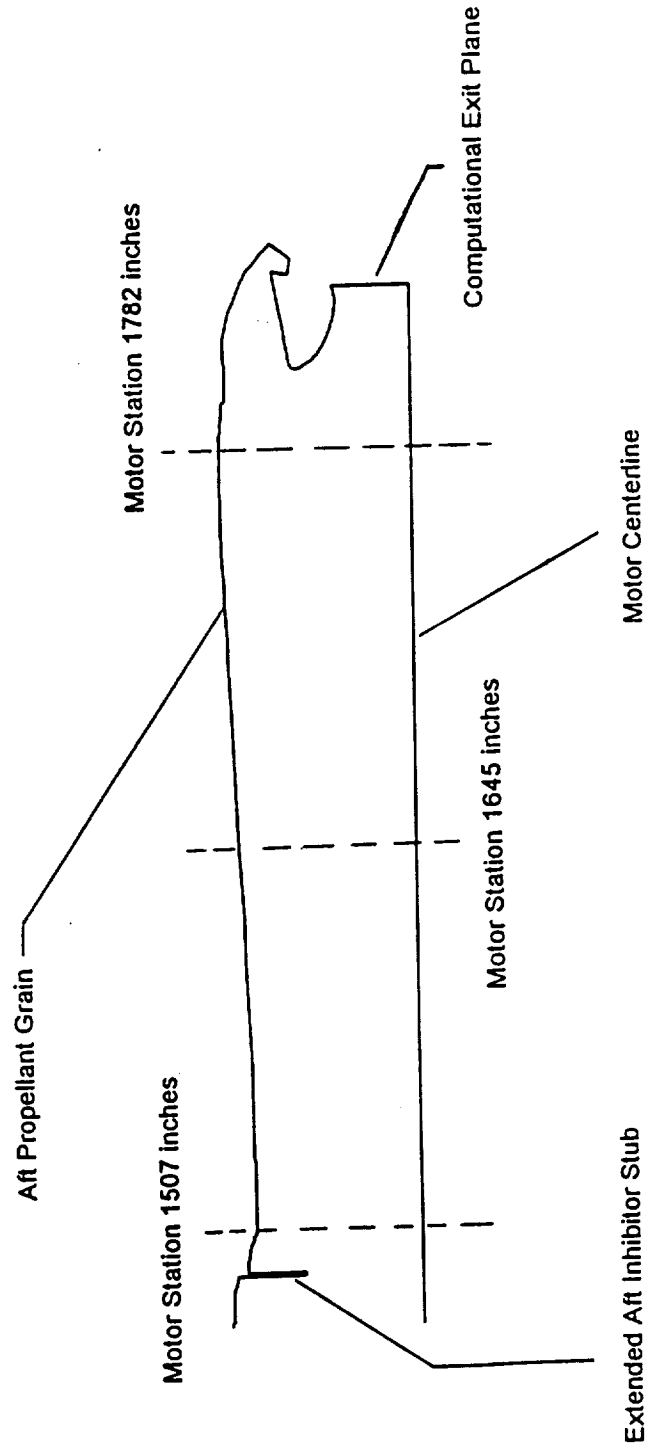
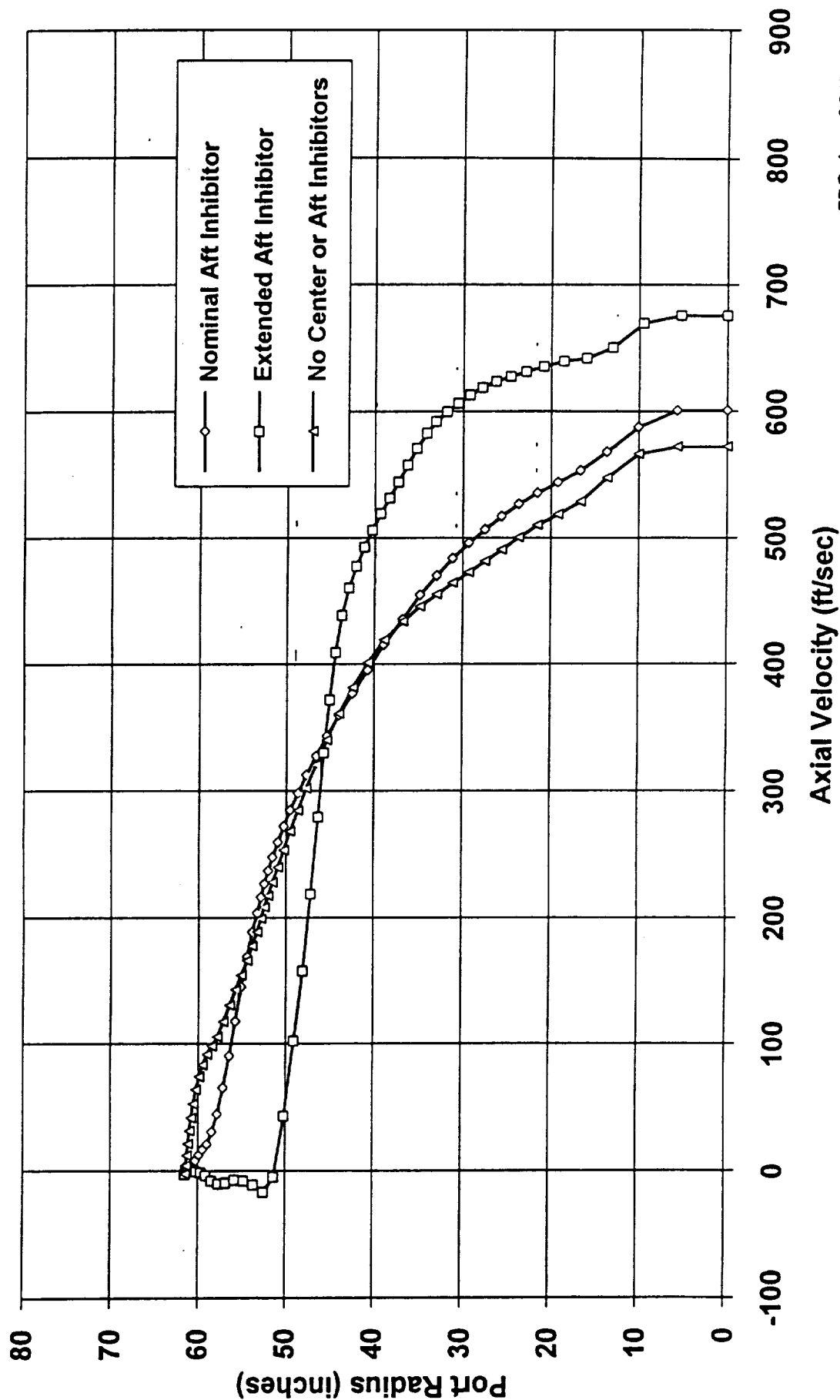


Figure 2A. Schematic of the Aft Segment Velocity Profile Port Motor Stations.

Figure 3A. Port Axial Velocity Profiles  
 Motor Station 1507  
 RSRM 80 Second Burn Time Geometry



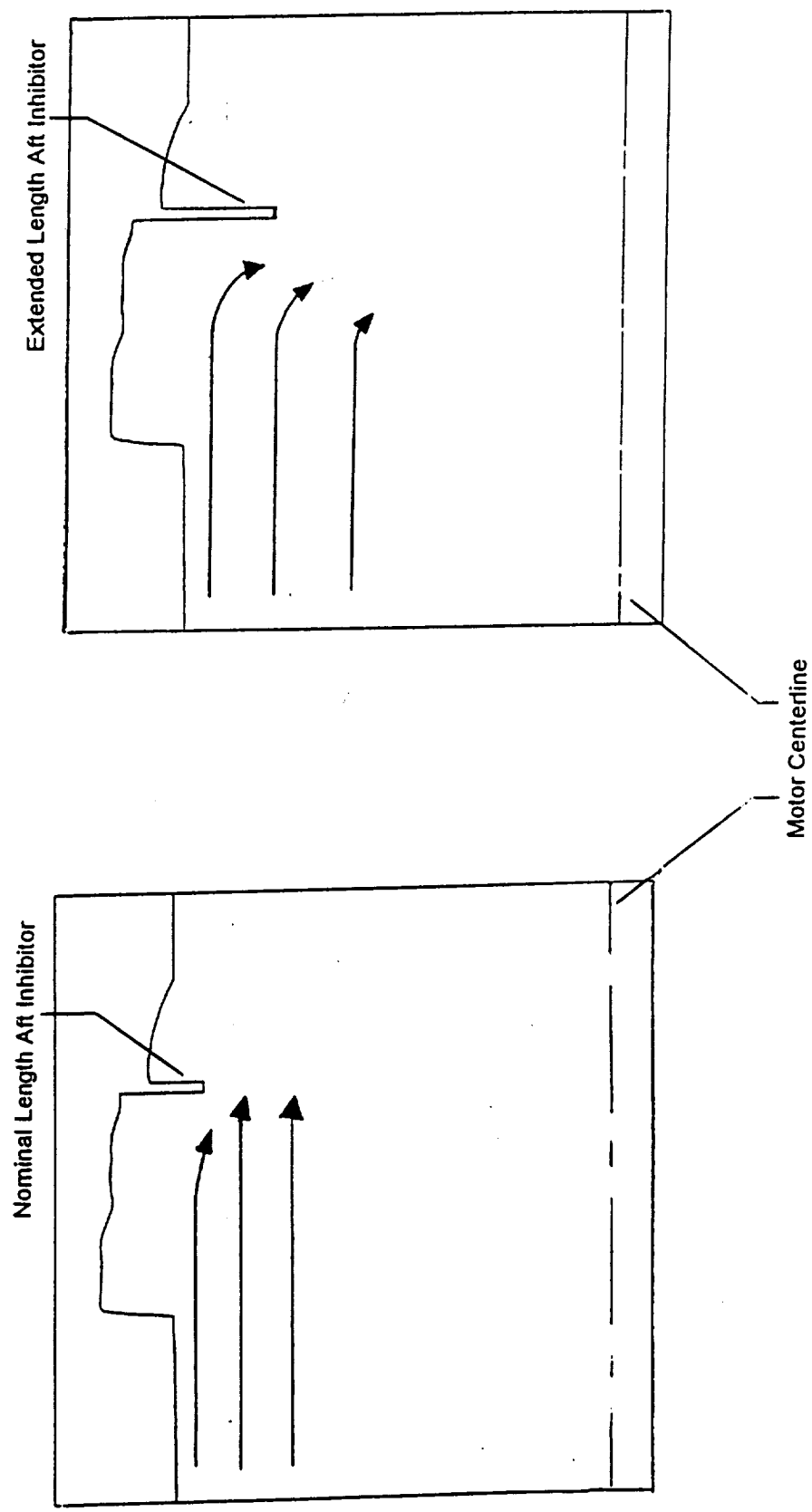


Figure 4A. Schematic Showing How the Port Flow is Disrupted by the Aft Inhibitor Stub

Figure 5A. Port Axial Velocity Profiles  
Motor Station 1645  
RSRM 80 Second Burn Time Geometry

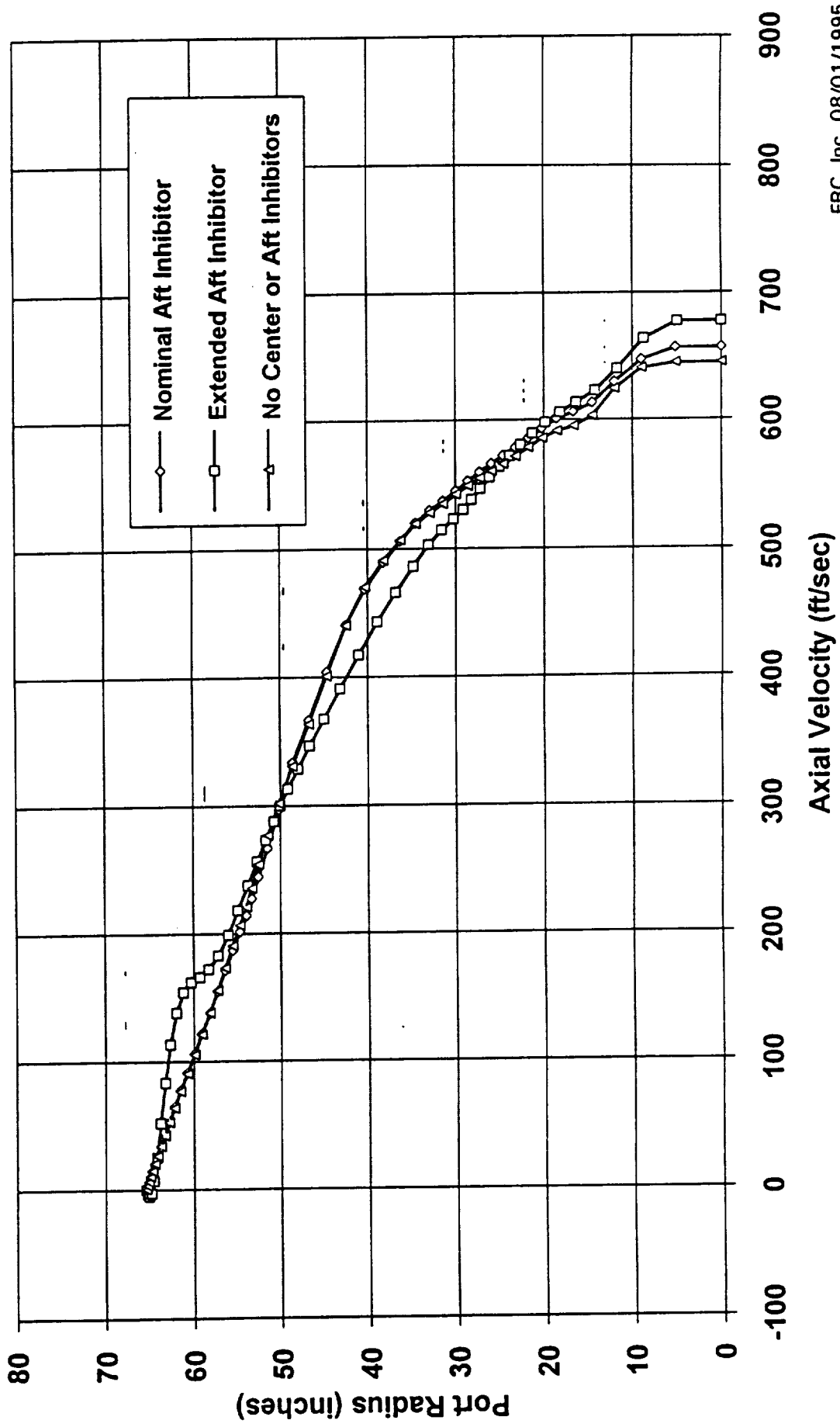


Figure 6A. Port Axial Velocity Profiles  
 Motor Station 1782  
 RSRM 80 Second Burn Time Geometry

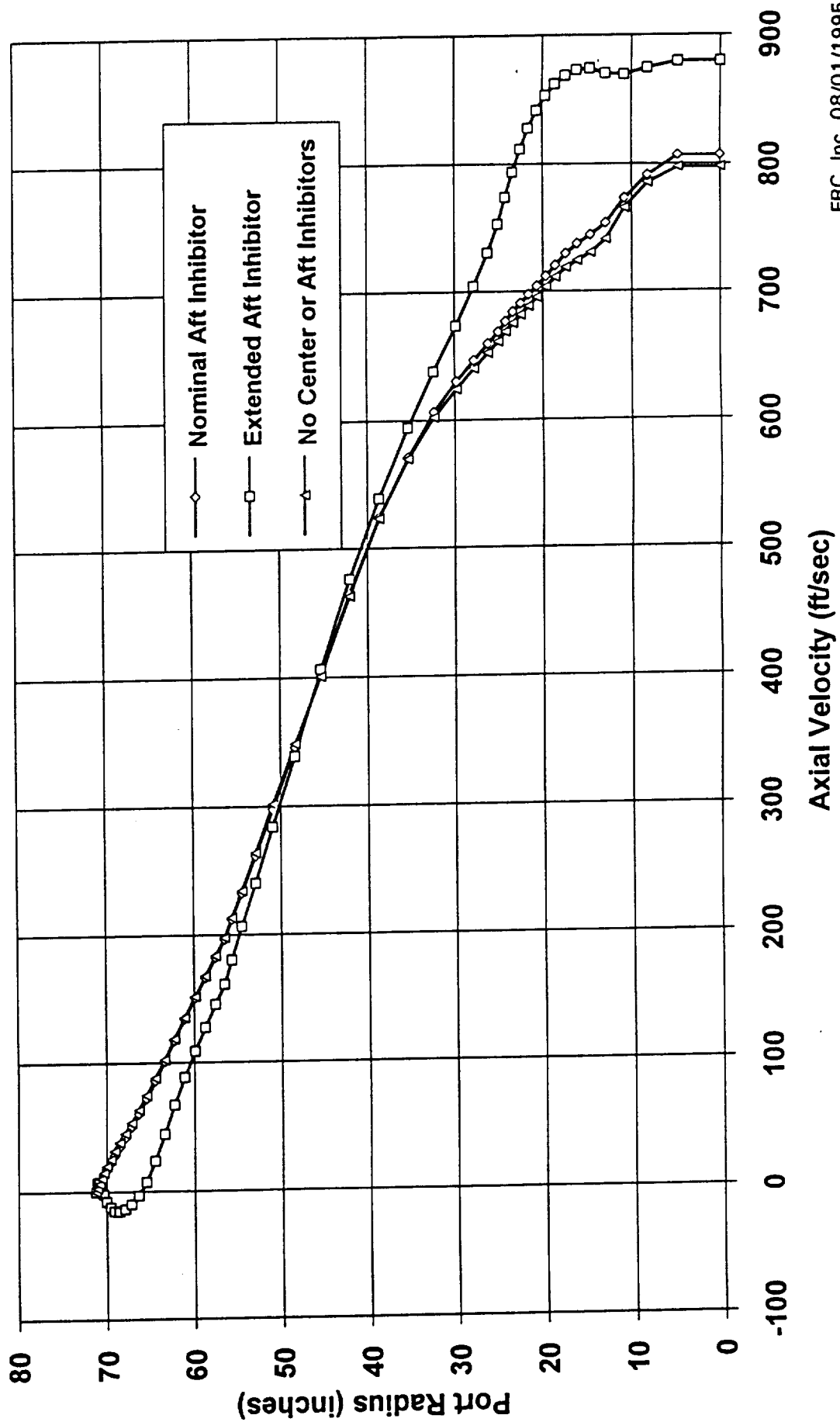
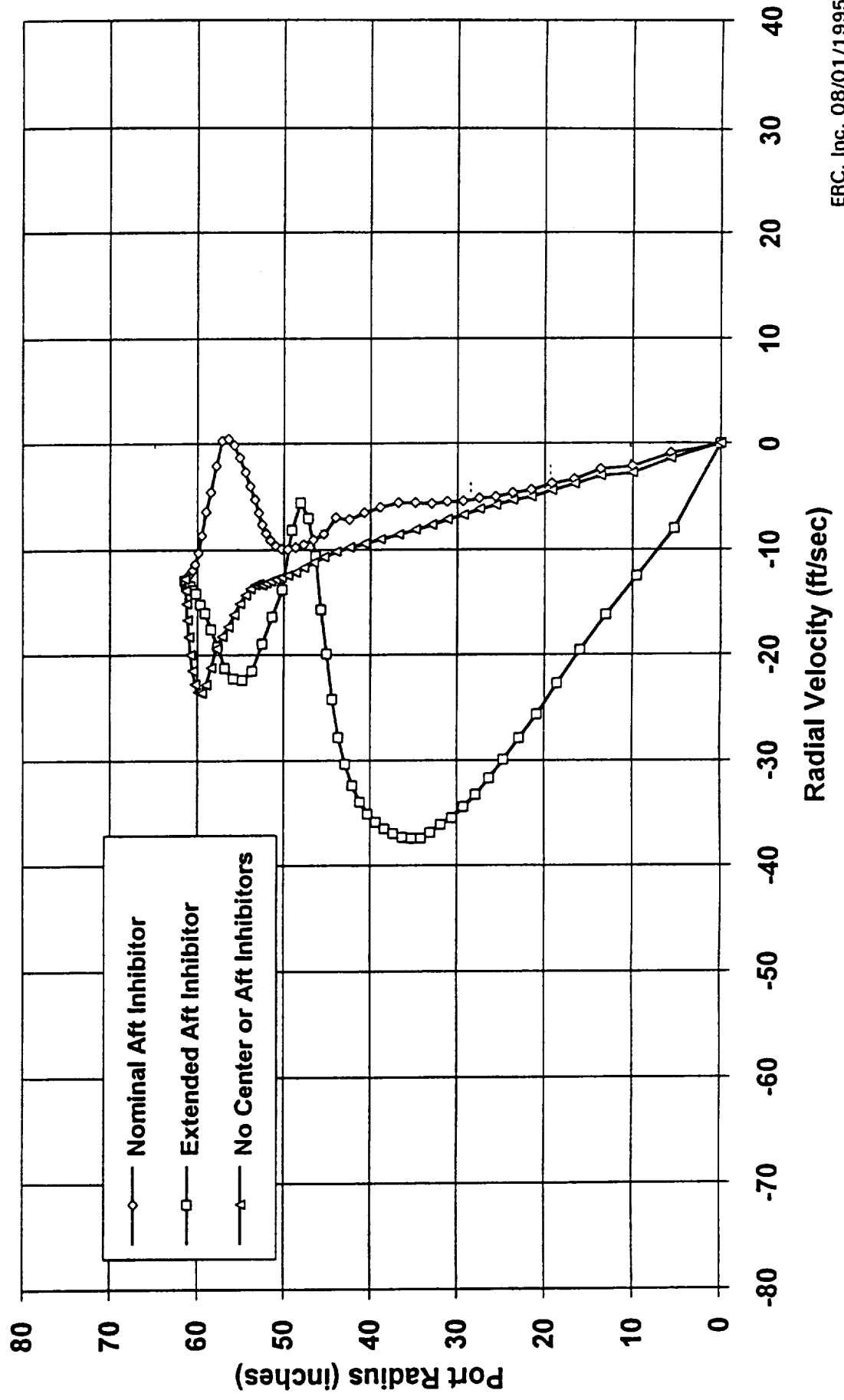


Figure7A. Port Radial Velocity Profiles  
 Motor Station 1507  
 RSRM 80 Second Burn Time Geometry



**Figure 8A. Port Radial Velocity Profiles**  
**Motor Station 1645**  
**RSRM 80 Second Burn Time Geometry**

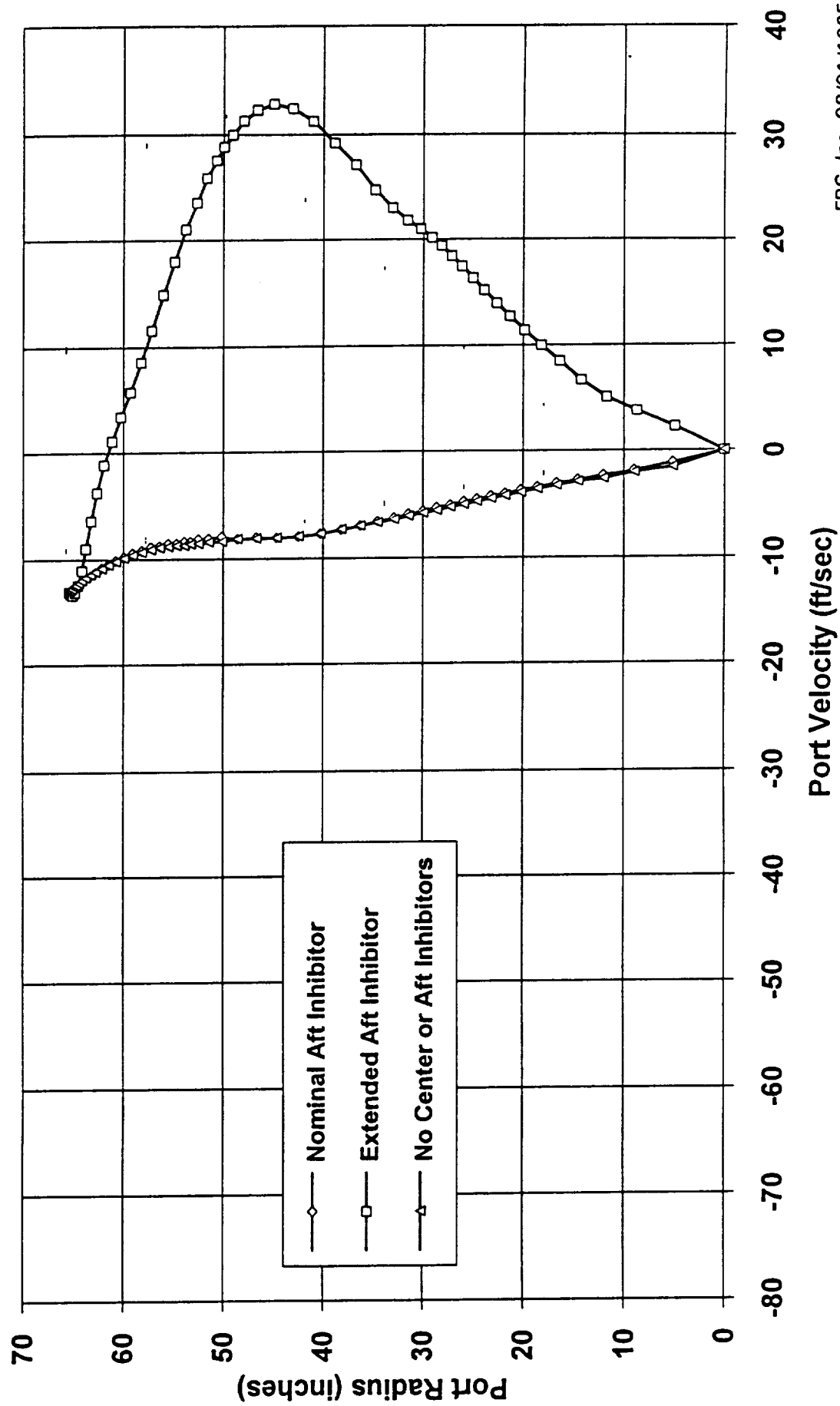
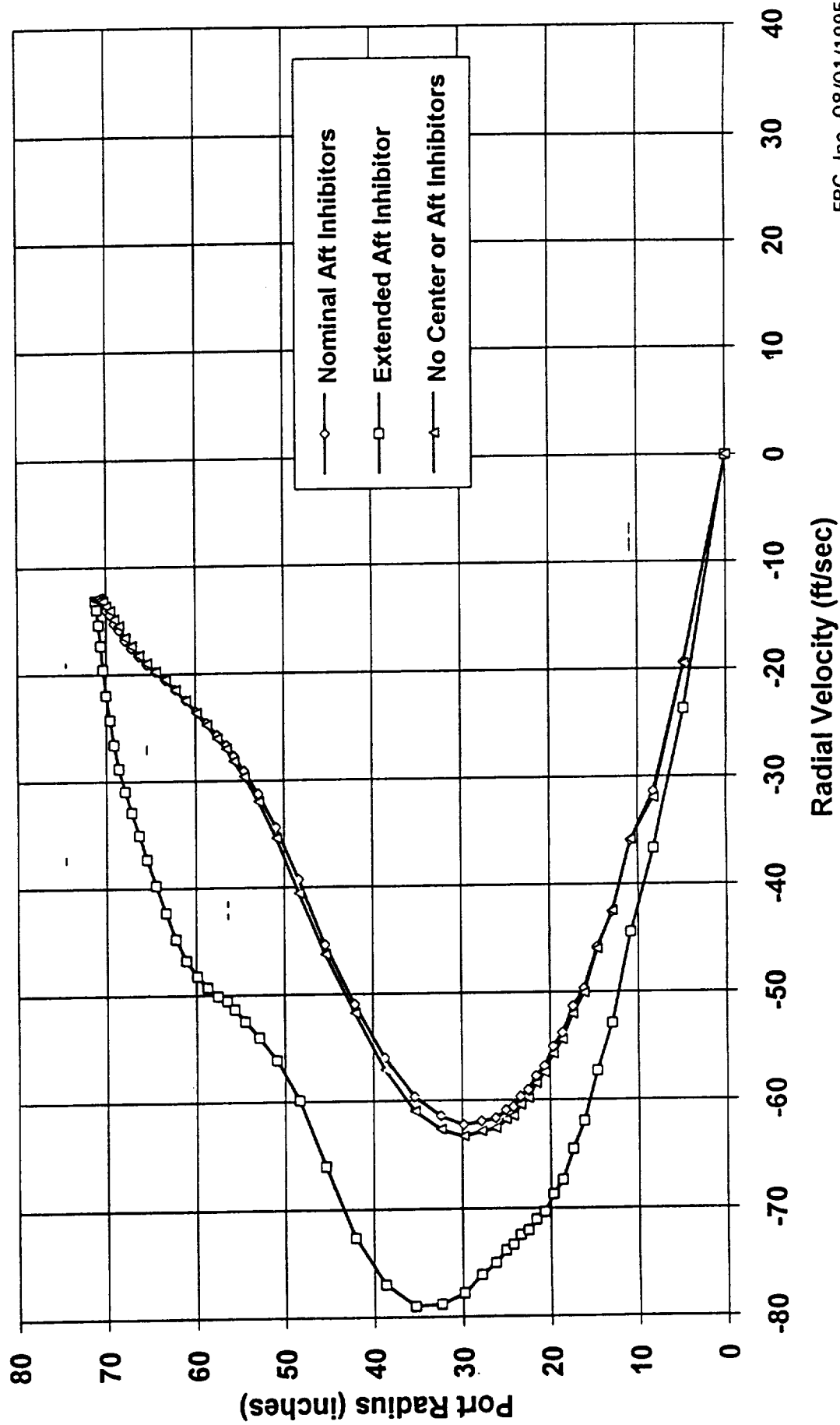


Figure 9A. Port Radial Velocity Profiles  
 Motor Station 1782  
 RSRM 80 Second Burn Time Geometry





## Nozzle O-Ring Investigation Analysis

ERC was asked to review the technical data and analysis results generated by Thiokol to support their conclusions regarding the origins and timing of events which resulted in smoke stain paths in the radial and axial bondlines of the nozzle nose inlet assembly. A Flight Readiness Review meeting was stalled due to the extensive time spent dealing with a minority opinion which differed with Thiokol's conclusions. The basic difference centered on whether the nozzle bondline observations were caused by hot gas leaks which occurred during motor burn or whether the observations were the result of post burn bond nozzle separations and pyrolysis gas contamination. A decision was made to fly at the Delta FRR after an S & E Team concurred with the Thiokol findings. A decision was also made to continue investigation of this nozzle phenomena and ERC became involved in the design of a subscale nozzle joint model and selection of a subscale motor to drive it. A test plan was developed to generate data for analytical flow/thermal models and also data which could be applied directly to the RSRM since current plans call for using full scale joint dimensions for gap widths, lengths, and material thickness.

Further investigations showed the cause could be traced to "close-out" voids through the RTV backfill down to the metal to metal gap in front of the o-ring. Dr. Jim Blair headed a MSFC team to provide an independent assessment and analysis of the problem. Flow and thermal analyses were performed to define the aerothermal environment and predict the thermal response of the hardware. ERC participated in the calculation of the pressure and recovery temperature of the combustion gases entering the various nozzle joints. All joints came under renewed scrutiny. The issue of circumferential flow in the o-ring groove due to two communicating void paths prompted the need for definition of circumferential pressure gradients as a function of gimbal angle. ERC used the cold flow data from the 8 percent ASRM gimbaled nozzle model for this task. The data was transferred to RSRM geometry using equivalent area ratios. It was then scaled to the full scale RSRM using pressure ratios with a slight correction for specific heat ratio. Scaling of the data to RSRM nozzle locations required knowledge of the nozzle end stagnation pressure which was taken from Thiokol ballistic analyses for a maximum pressure trace motor. (Maximum PMBT and three-sigma burn rate) Figure 1 shows a plot of both the motor head end stagnation pressure as well as calculated nozzle end stagnation pressure. Initially, the nozzle end pressure is significantly lower than head end pressure due to the relatively high port Mach number and effects of wall mass addition. Also shown is the pressure at various joint locations calculated with local pressure ratios at specific joint location area ratios as determined from a one-dimensional, shifting equilibrium thermochemistry calculation. Figure 2 shows the effect of gimbal angle on the pressure ratio at joint #3 as determined by interpolation of the cold flow model data. Figure 3 shows the circumferential pressure distribution induced by a 4 degree gimbal angle at joint #3. Similar results for joints #4 and #1 are shown in Figures 4 through 7. The results shown in these figures were used together with a gimbal angle duty cycle from a worst case flight profile to calculate the circumferential pressure gradients as a function of motor burn time. ED33 took the

scaled circumferential pressure gradient data as a function of gimbal angle and combined it with trajectory gimbal angle duty cycle data to produce the circumferential pressure gradient as a function of flight time. The aerodynamic flow conditions at the joint locations varied during motor burn and with nozzle gimbal angle. The axisymmetric flow conditions varied due to motor pressure variation and nozzle throat erosion during the burn. Additionally, three-dimensional flow effects are introduced by gimbaling of the nozzle. At nozzle gimbal angles, other than null, circumferential pressure gradients are introduced at the joint locations.

The above environments were used as driving boundary conditions for transient thermal analyses of the various joints including o-ring erosion. ERC also calculated local aerothermal recovery temperatures at the joint locations to use as gas temperature boundary conditions for the thermal analyses performed by ED64.

Figure 1. RSRM Nozzle Joint Pressure Versus Time  
Maximum Predicted Pressures (TWR=16592)

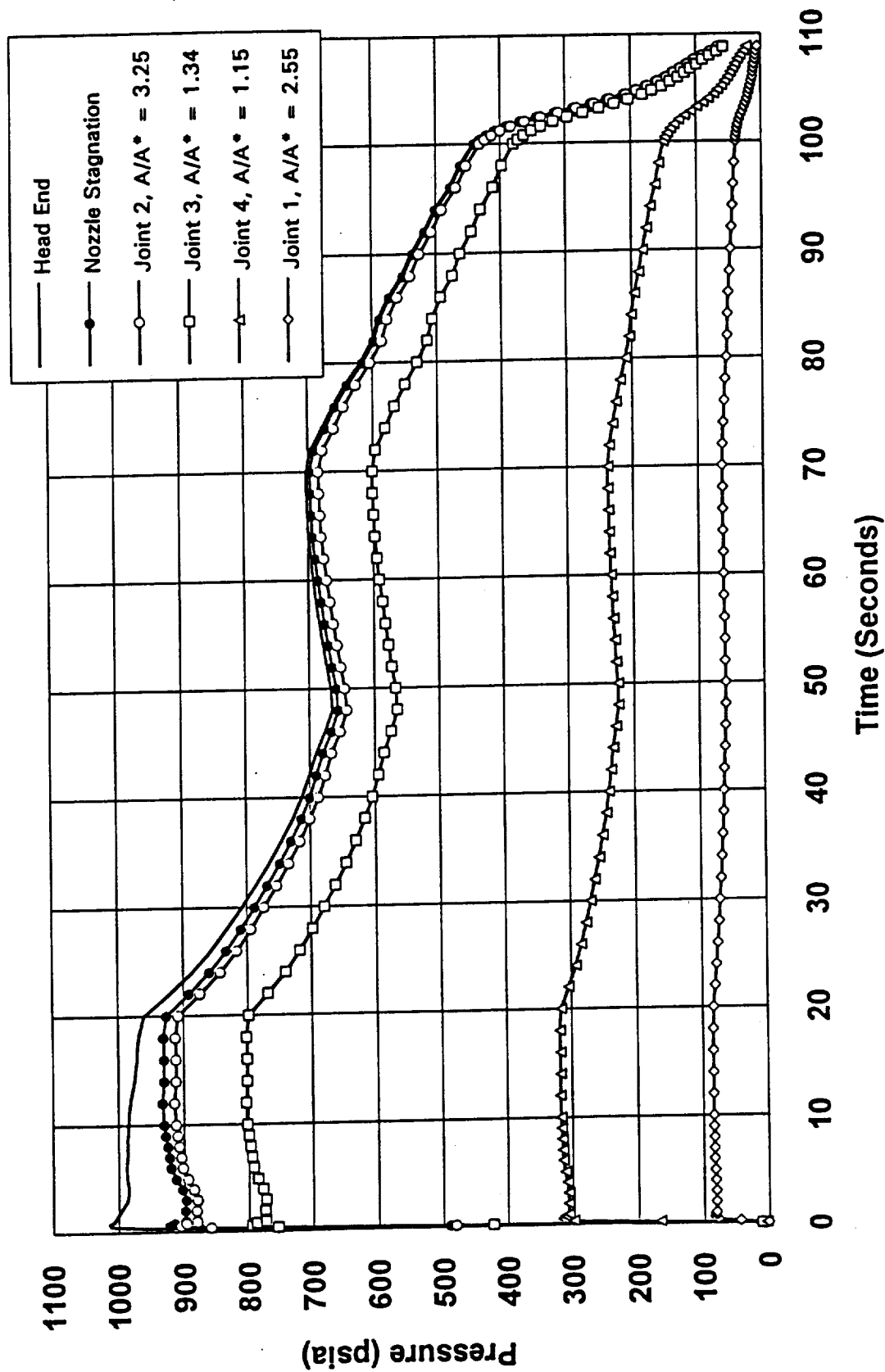


Figure 2. 8% Scale Cold Flow Model Data  
 RSRM Nozzle Joint #3 Location  
 4 Degree Gimbal Angle

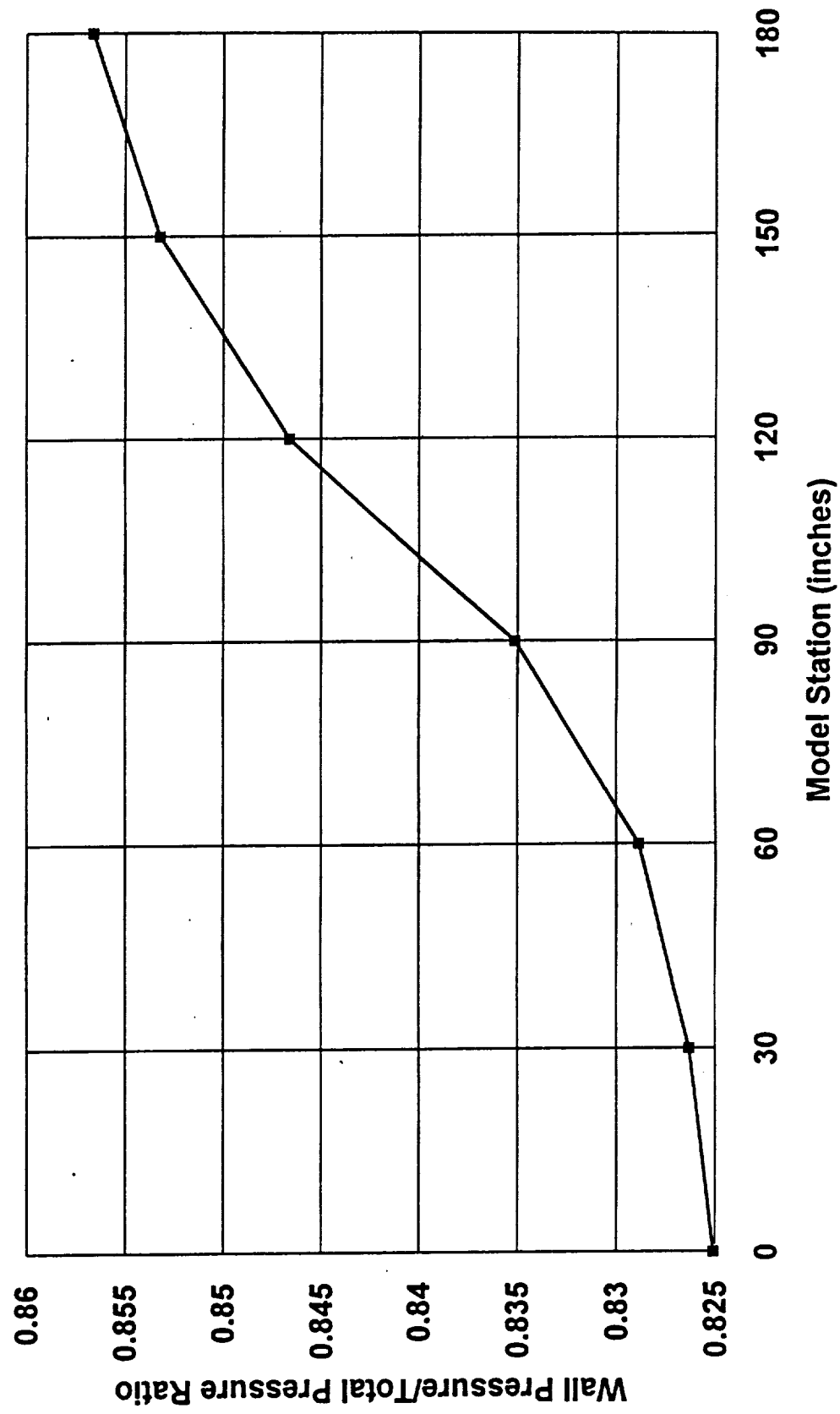
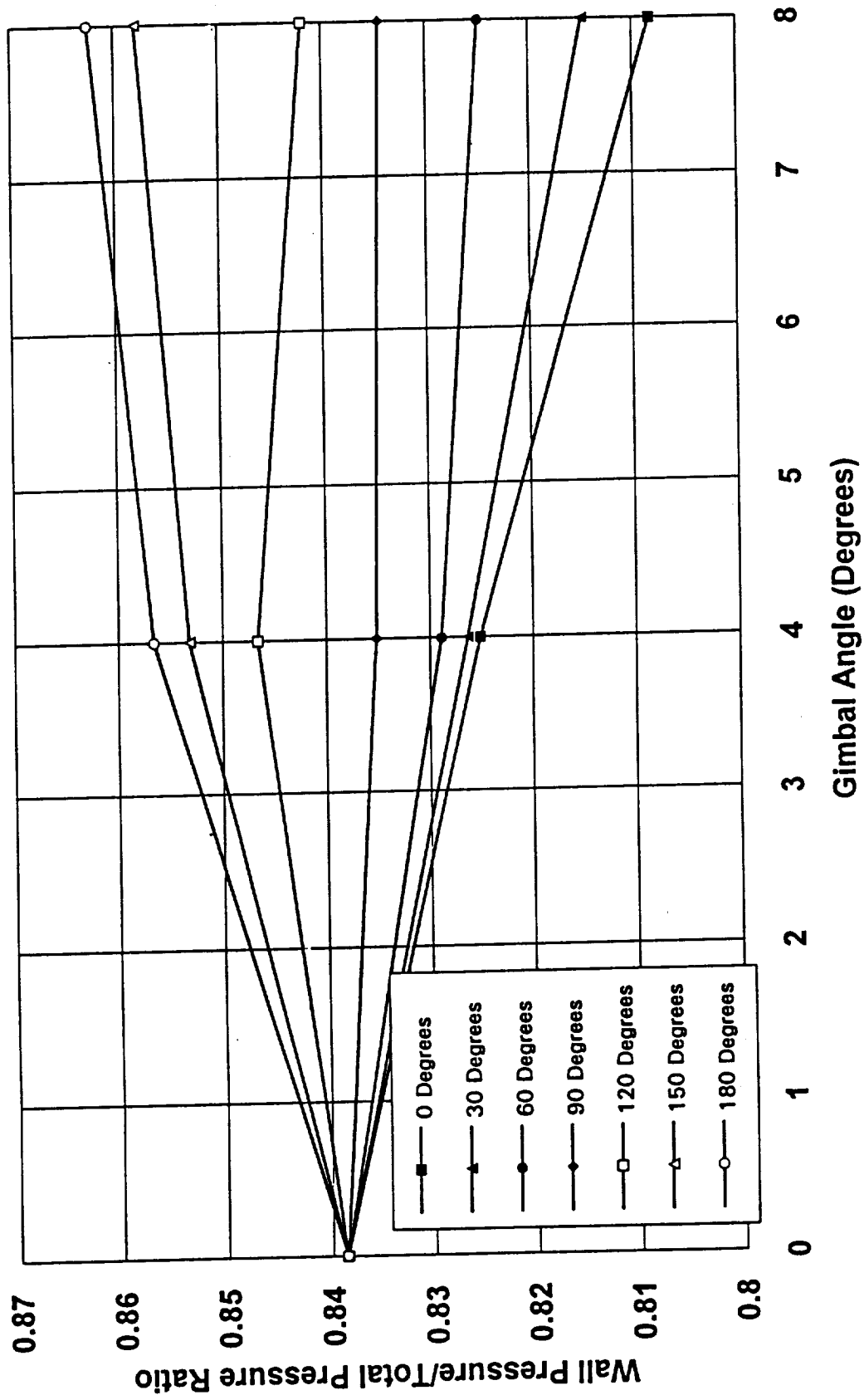


Figure 3. 8% Scale Cold Flow Model Data  
RSRM Nozzle Joint #3 Location



**Figure 4. 8% Scale Cold Flow Model Data**  
**RSRM Nozzle Joint #4 Location**  
**4 Degree Gimbal Angle**

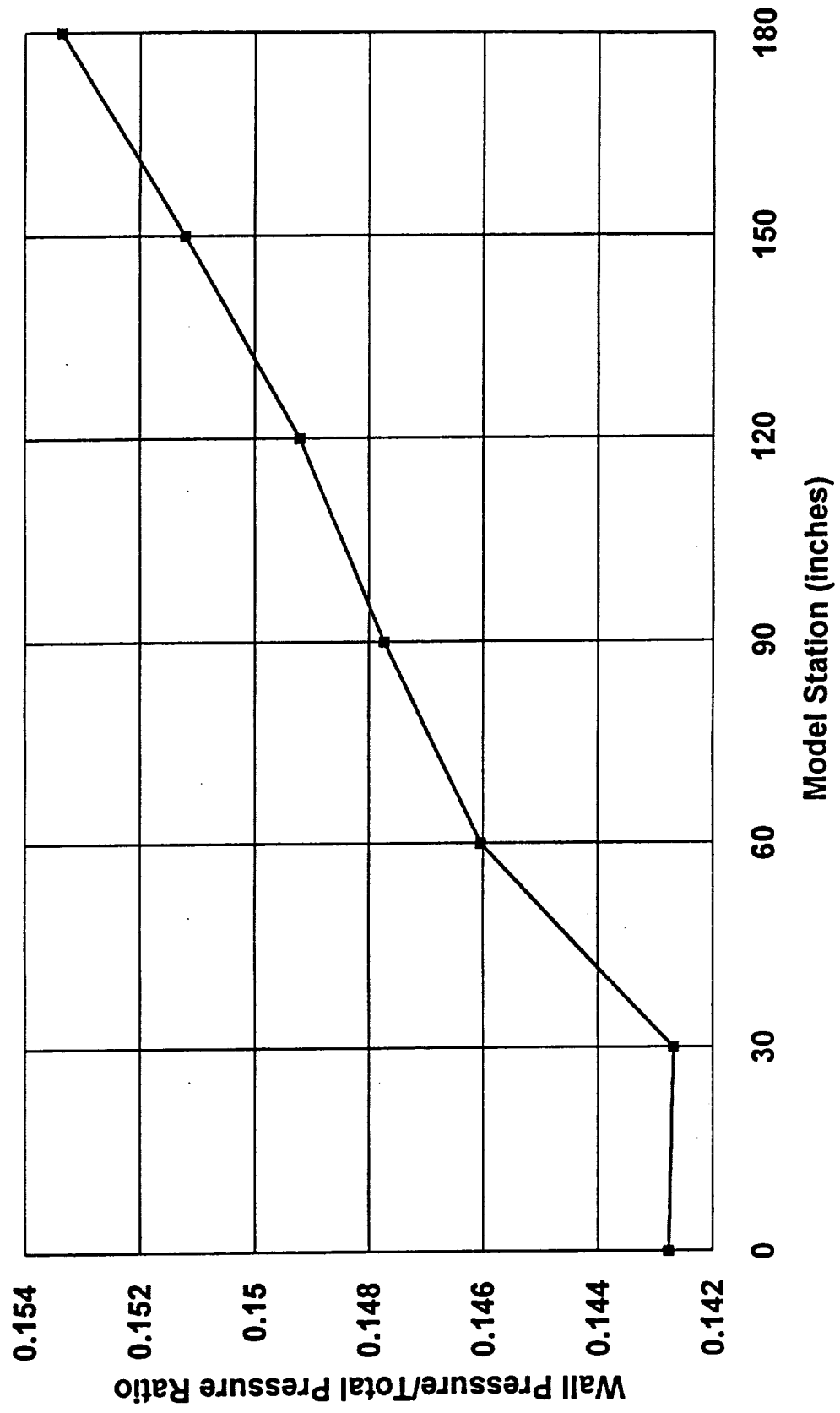


Figure 5. 8% Scale Cold Flow Model Data  
RSRM Nozzle Joint #4 Location

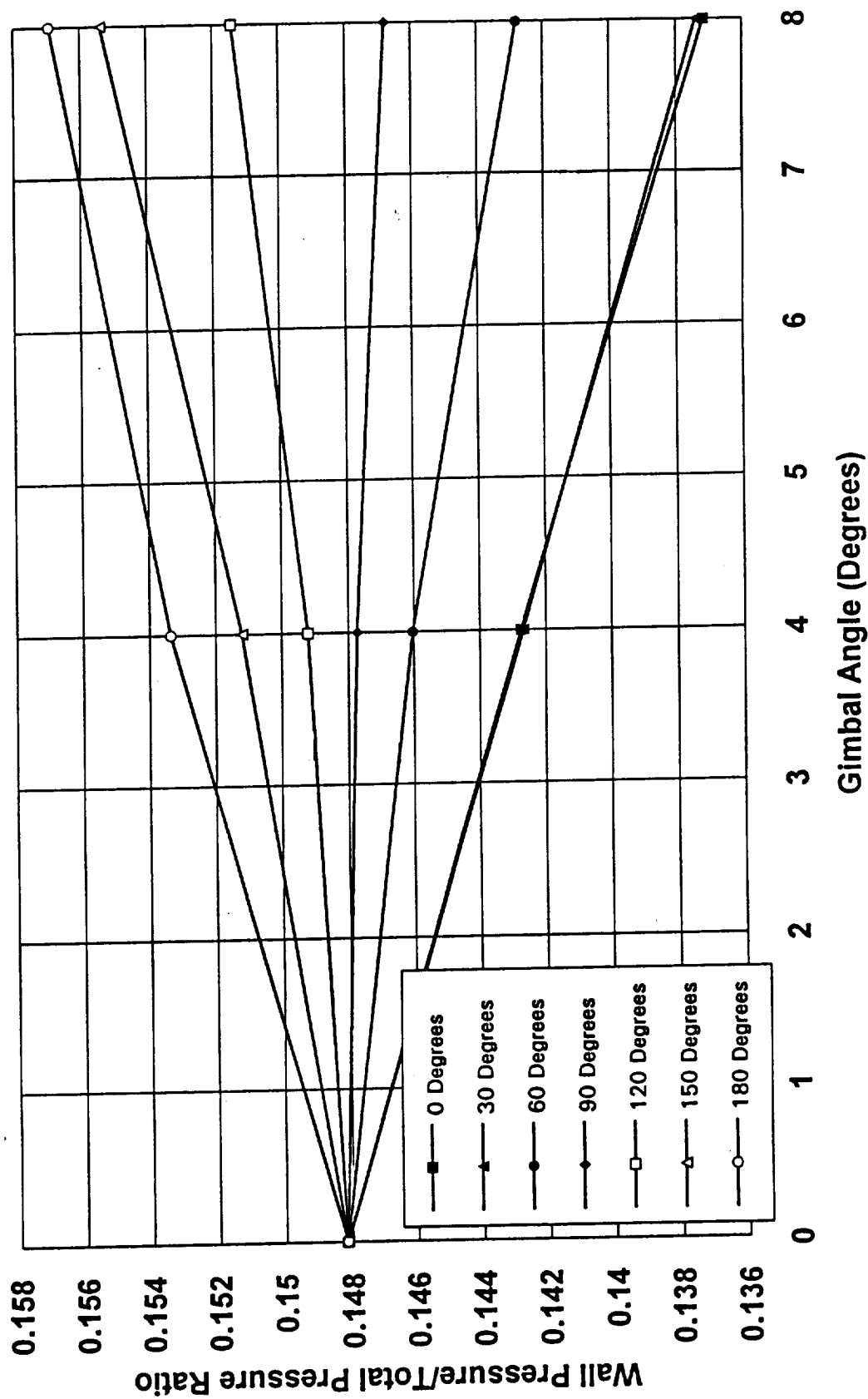


Figure 6. 8% Scale Cold Flow Model Data  
 RSRM Nozzle Joint #1 Location  
 4 Degree Gimbal Angle

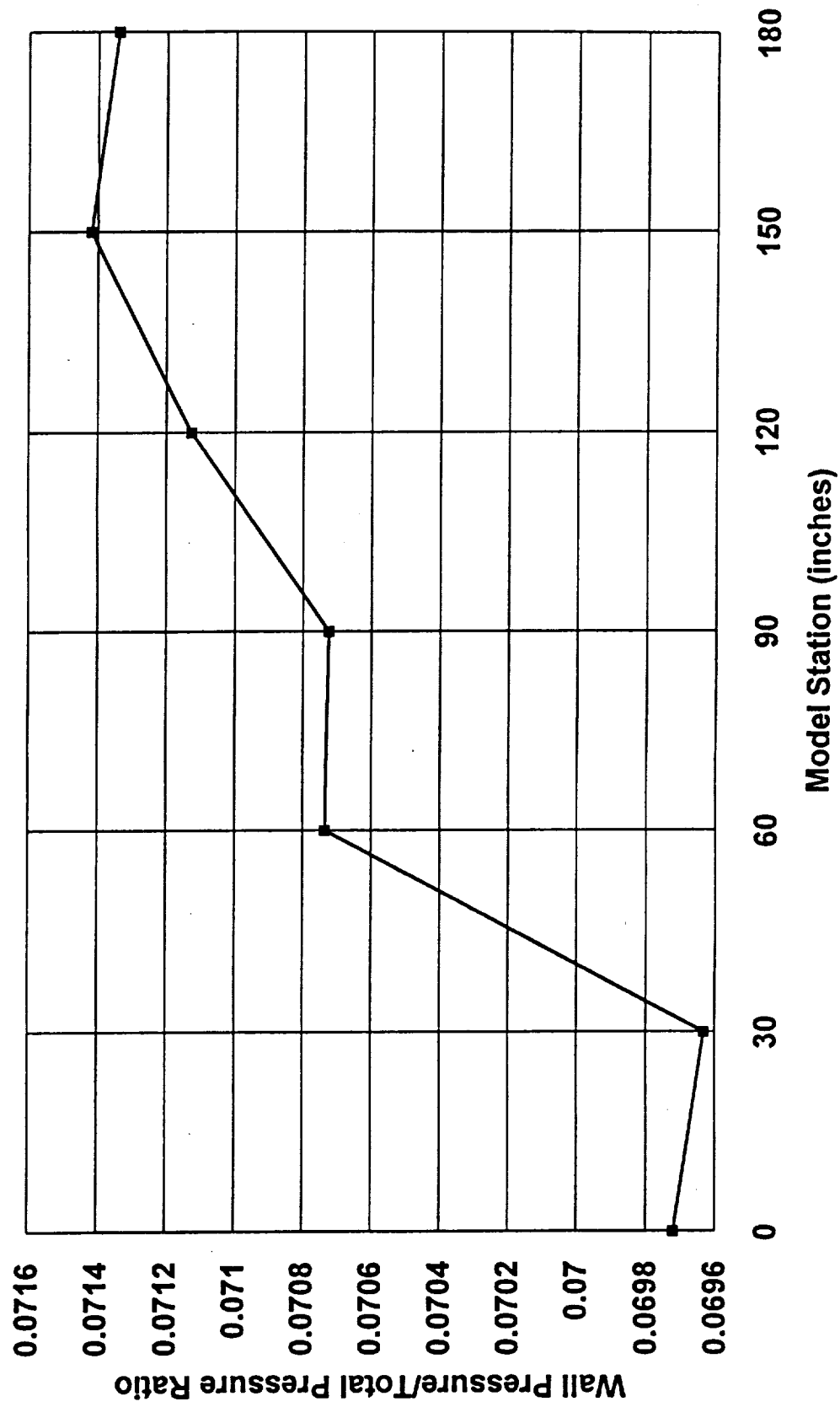
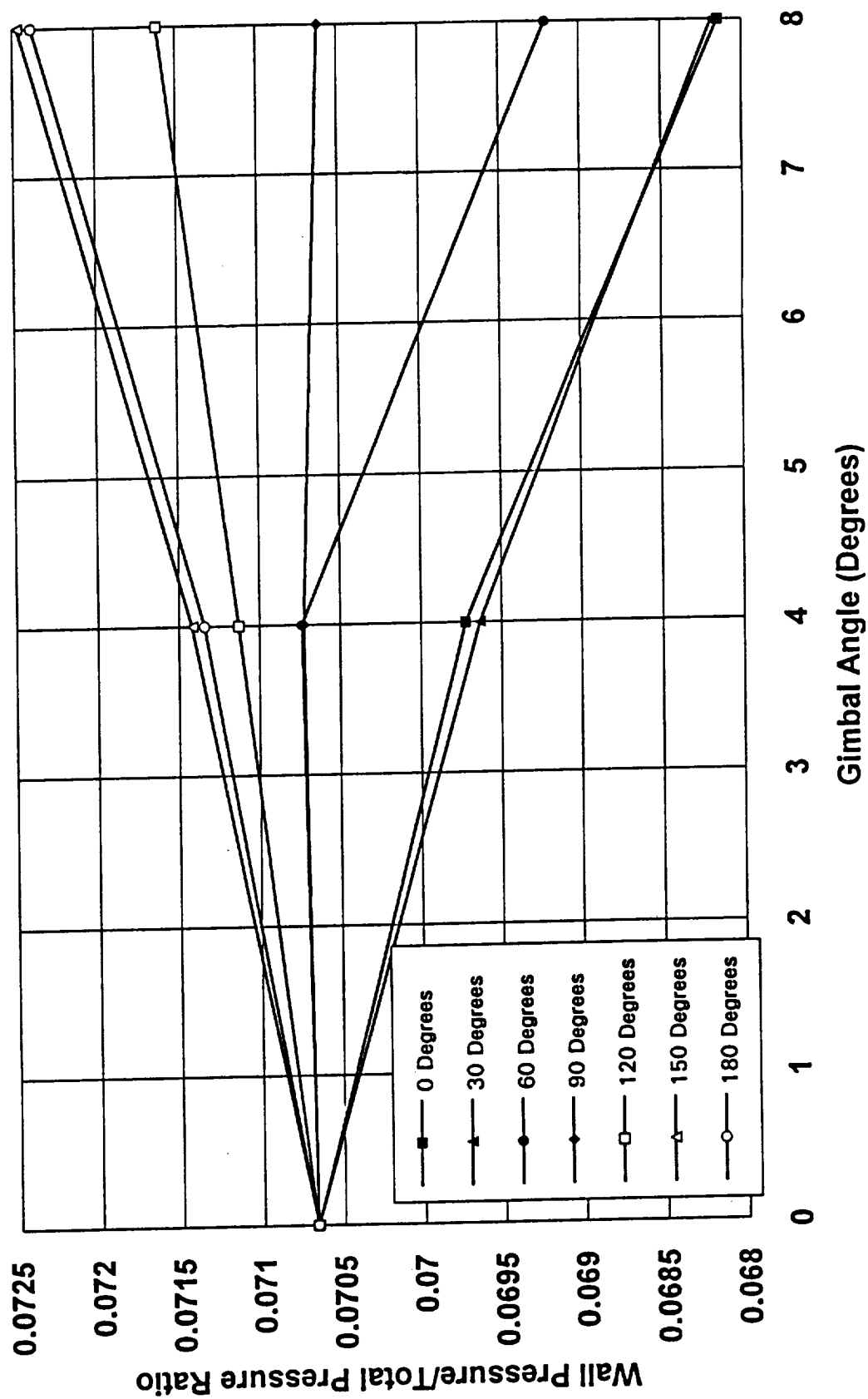




Figure 7. 8% Scale Cold Flow Model Data  
RSRM Nozzle Joint #1 Location





## **RSRM Analysis Drawings**

<b>Drawing Number</b>	<b>Drawing Title</b>
H6100	Motor Assembly
H6101	Aft Segment Loaded with Nozzle Assembly
H6102	Nozzle Assembly
H6103	Forward Segment Loaded
H6104	Case Loaded Center Segments



## Internal Aerodynamic Torque Analysis

A file of three-dimensional pressure data for the RSRM nozzle was received from NASA/MSFC ED32. This data was generated by a CFD code being run by ED32. The data was run through the ERC nozzle pressure integration program which calculates the internal aerodynamic forces and moments on nozzle. The pressure data received was only for the nozzle exit cone, i.e., from the nozzle throat plane to the nozzle exit plane. The results from the program were transmitted back to ED32 to help with CFD code validation. This program was written to calculate the forces and moments on the 8% ASRM Aft Section/Nozzle Model using pressures measured experimentally with the model. In addition, a second, similar program was used to calculate results for the same case so that a comparison could be made and validation of the two codes reached. This second program was written to solve for the forces and moments on a more general problem than the one written for the 8% ASRM Aft Section/Nozzle Model. Both programs used an input geometry file as well as input pressure data to solve for the forces and moments.

ED32 supplied two sets of pressure data. One set was for the exit cone of the ASRM nozzle scaled to 8% and set at a gimbal angle of 8 degrees. The other data was for a cone at zero degree gimbal angle. This second case was used a validation case as an analytical solution was available for comparison. The results from the two cases run with two different FORTRAN programs are summarized in Table I. The experimental program was written to calculate the forces and moments on the 8% ASRM Aft Section/Nozzle Model using pressures measured experimentally with the model. The second program, NOZINT, was written to solve for the forces and moments on a more general problem than the one written for the 8% ASRM Aft Section/Nozzle Model. Both programs use an input geometry file as well as input pressure data to solve for the forces and moments.

**Table I. Pressure Integration Program Results**

<b>ASRM Nozzle Exit Cone Problem - 8 Degree Gimbal Angle</b>		
	<b>NOZINT Program</b>	<b>Experimental Program</b>
<b>Fx (lbf)</b>	2992.11	-
<b>Fy (lbf)</b>	-307.01	-725.12
<b>Fz (lbf)</b>	-1603.67	-2953.38
<b>Mx (lbf-in)</b>	938.89	938.91
<b>My (lbf-in)</b>	6239.82	-
<b>Mz (lbf-in)</b>	0.00	-

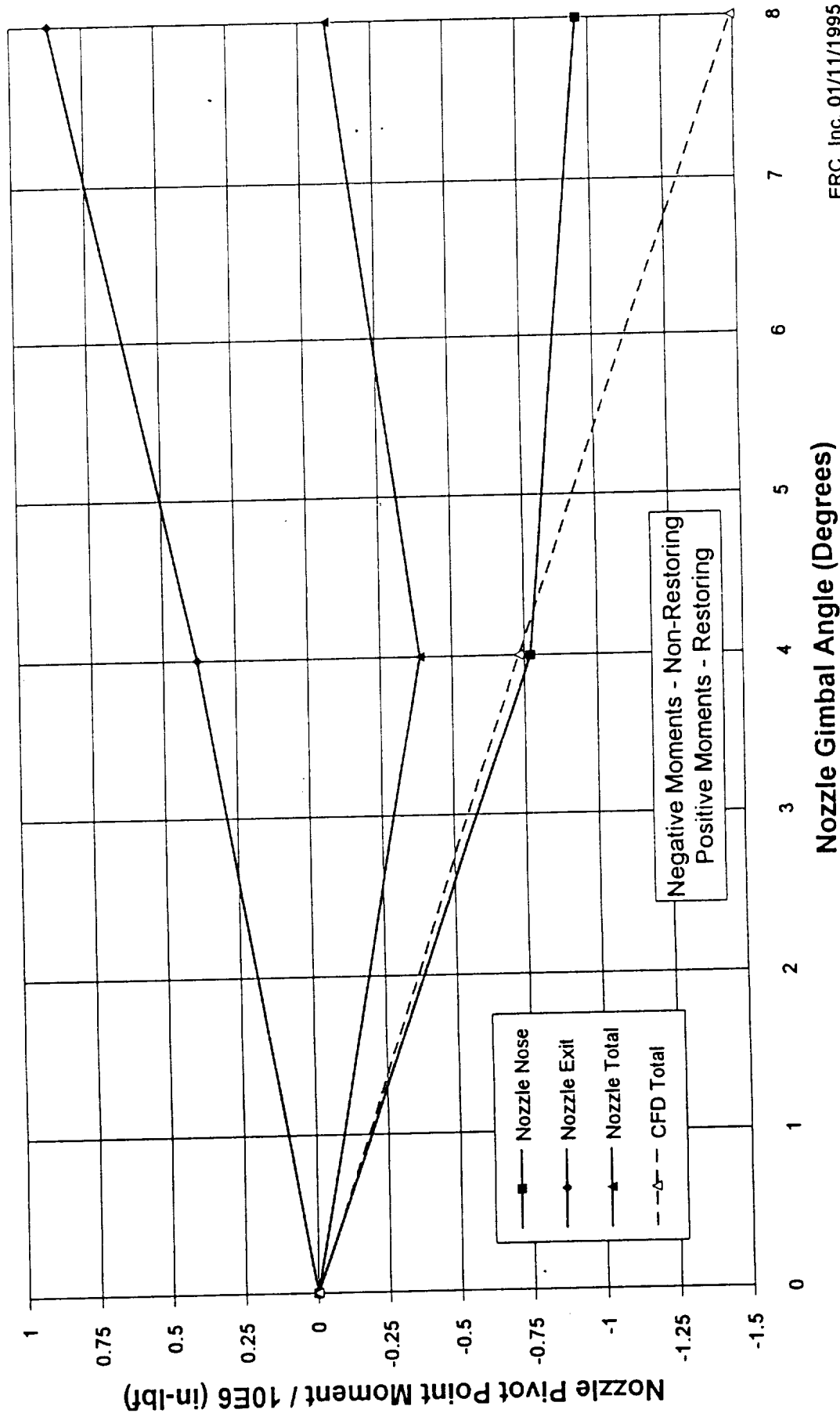
<b>Cone Problem - 0 Degree Gimbal Angle</b>		
<b>NOZINT Program</b>	<b>Experimental Program</b>	<b>Analytical Solution</b>

<b>Fx (lbf)</b>	13966.63	1624.92	19614.00
<b>Fy (lbf)</b>	791.86	-1187.16	791.20
<b>Fz (lbf)</b>	-6706.94	-712.79	-8124.00
<b>Mx (lbf-in)</b>	-10377.53	10271.74	-10412.00
<b>My (lbf-in)</b>	181387.68	14059.26	22820.00
<b>Mz (lbf-in)</b>	0.00	0.00	0.00

It can be seen from the results in Table I that there is generally good agreement between the NOZINT and experimental programs for the value of Mx. There is also good agreement for the value of Fy between the analytical results and the NOZINT program. There is not a good comparison between the other values computed by the two programs or with the analytical results. The reason for these discrepancies has not been determined as yet. This problem will continue to be worked to try and discover the reason for the discrepancies.

The results of this testing were used to calculate the internal aerodynamic torque on the full scale RSRM. This was done in the following manner. First, the 8% model data for gimbal angles of 0, 4, and 8 degrees had the 0 degree gimbal angle bias subtracted out. Next, the values were multiplied by 1/0.08 to scale the data to the full scale ASRM. Finally, to scale the data to the full scale RSRM the full scale ASRM numbers were multiplied by the ratio of the RSRM throat diameter to the ASRM throat diameter raised to the third power. The results of these calculations are presented in Figure 1.

Figure 1. RSRM Internal Aerodynamic Pivot Point Moment  
(Scaled from Cold Flow Model Data @ 19 Seconds)  
Preliminary







## External Aerodynamic Torque Analysis

Information from the ERC archives on the external aerodynamic torque was gathered and reviewed. This was in preparation to make new calculations of the aerodynamic forces and torques on the exterior surface of the RSRM nozzle including a proposed nozzle extension.

A meeting was held at NASA/MSFC with J. Hengel, ED34, to discuss the work which would be done for the RSRM external aerodynamic torque calculation for the extended aft exit cone nozzle. The initial efforts mainly consisted of program checkout. A number of previously calculated cases were rerun to check out the program and to refresh the user with its operation. All of the cases run checked out and matched the previously calculated numbers. In addition to the program checkout, the inputs for the new calculations were reviewed and set up. The main change to the program inputs from the previous cases is the new RSRM nozzle geometry with the nozzle exit cone extension. This new geometry was determined and a new geometry input file was created for the program.

A number of runs were made to determine how the test data from NASA test IA119 would be used for this particular nozzle. Two different methods were compared. The first consisted of reapportioning the pressure taps from test IA119 over the extended aft exit cone at the same ratio of axial distance to local radius which they were measured in the test. The second kept the pressure measurements at the same absolute axial position as in the IA119 test and extrapolated values to the end of the extended aft exit cone. The second method produced higher moments and this method was chosen to perform the calculations for the extended aft exit cone. It was decided that this method would produce numbers which were more conservative. A baseline of runs were made at conditions which produced the highest moments for the current nozzle configuration. A number of runs were made with these conditions over a range number of Mach numbers from 0.6 to 0.95. A plot comparing these numbers for the two methods of using data with the extended aft exit cone as well as the current RSRM nozzle configuration were generated. It was then decided to extend the Mach number range to cover from 0.6 to 1.4. The work to make these calculations was carried out and a plot made. In addition, it was decided that other runs should be made to enable calculation for the conditions which are in the Design Loads Handbook.

Two simple test cases were run to check the accuracy of the computations made in the program which calculates the forces and moments on the external surface of the nozzle. The test cases were a right circular cone and a right circular cylinder. Each test case involved placing a uniform pressure on half of the surface of the body and using the program to calculate the forces and moments. In addition, the forces and moments were also calculated analytically in order to produce a verification of the results. The outcome of the test cases are shown in Table I below. The errors in  $F_y$  and  $M_x$  are assumed to be due to the interpolation done in the program. The pressure applied to half of the body in the input file to the program is interpolated to produce

more computation points and this produces a slightly non-uniform pressure distribution over the surface of the body. When the integration is done in the program this slight non-uniformity produces the non-zero results shown in Table I.

**Table I. Test Cases of External Forces and Moments**

<b>Test Case</b>	<b>Force/Moment</b>	<b>Program Result</b>	<b>Calculated Result</b>
Cone	Fx	1599.87 lbf	1599.88 lbf
Cone	Fy	-17.57 lbf	0 lbf
Cone	Fz	-1261.89 lbf	-1263.62 lbf
Cylinder	Fx	3199.76 lbf	3202.2 lbf
Cylinder	Fy	-35.17 lbf	0 lbf
Cylinder	Fz	0 lbf	0 lbf
Cylinder	Mx	1387.18 lbf-in	0 lbf-in
Cylinder	My	126314.3 lbf-in	127990.3 lbf-in
Cylinder	Mz	0 lbf-in	0 lbf-in

Different interpolation methods were investigated because the conditions at which the forces and moments were desired were not represented in the IA119 test data which was being used for this analysis. The condition being matched was condition 1 from the Design Loads Data Handbook. In the first method a number of runs were made using the External Moment Program which bracketed the desired conditions. After the forces and moments were calculated an interpolation was done with the forces and moments in order to arrive at the values of the forces and moments for the desired conditions.

In the second method, the raw data was interpolated to obtain pressure coefficient data which was then analyzed by the External Moment Program to determine the forces and moments at the desired test conditions. The differences between the two methods were negligible.

A write-up for this effort was completed and review comments were incorporated. Additional work concentrated on generating smooth curve fits for the experimental data from test IA119. These curve fits accompany the memo describing the work, methodology, and results of the RSRM external aerodynamic torque analysis and included in this appendix. The curve fits were changed for the final version of the memorandum to reflect the reference axes which are used in the RSRM Design Loads Data Handbook. The curve fitting was an extensive effort due to the very limited data being fit.

This effort also included the generation of a hinge moment versus Mach number plot. This plot was generated using data available at two angles of attack and a single gimbale angle. The plot was done for the hinge moments in the plane of the actuators and included data for both the rock and tilt moments. This work had been previously completed in a memo written by D. Bacchus, ED34. This work was repeated and a new

plot produced. This plot was given to J. Hengel, ED34, early in the month accompanied by a short memo explaining the work done to produce the plot.

Finally, a reworking of the memo on this effort to delete references to the extended aft exit cone work was performed. Since the extended aft exit cone was canceled it was desired to remove reference to it from the memo. Two versions of the memo were created and both distributed together. One version of the memo covered both the current and the extended aft exit cone hinge moment calculations. The second memo covered only the current RSRM nozzle exit cone hinge moment calculations.



7 November 1995

TO: John E. Hengel, ED34

FROM: R. Harold Whitesides, ERC, Incorporated *RHW*  
David C. Purinton, ERC, Incorporated *DCP*

SUBJECT: RSRM Extended Nozzle External Aerodynamic Torque Analysis

REFERENCES: (1) Chrysler Rpt. DMS-DR-2404 (NASA-CR-160,510), "Results of Tests using a 0.020 Scale Model (88-OTS) of the Space Shuttle Integrated Vehicle Jet-Plume in the NASA/ARC UPWT 11 x 11 Foot Leg," August 1990.

(2) Thiokol Rpt. TWR-16801, "RSRM Design Loads Data Book."

(3) Rockwell Letter SAS/MR&I-77-056, "Mission 3A High and Low Dynamic Pressure Ascent Trajectories for Compartment Venting Analyses (EMS Milestone 390-700-055) and Structural Loads Verification (EMS Milestone 390-700-035)," April 19, 1977.

This memo summarizes completed work on the RSRM Extended Nozzle External Aerodynamic Torque Analysis. The purpose of the analysis was to determine the external aerodynamic moments on the exit cone of the RSRM nozzle with the extended aft exit cone. This nozzle has an additional length of 8.697 inches compared to the nozzle currently flying on the RSRM. The exit diameter of the extended nozzle is 156.098 inches. The geometry of both nozzles is shown in Figure 1. The zero location in this figure is in the plane of the aft skirt. The throat plane is located at an axial plane of -84.74 in this reference frame. The pivot point of the nozzle is located at an axial station of -67.117 inches in the coordinate system of the geometry figure. The moments calculated are done so about this point.

The forces and moments on the exterior surface of the nozzle exit cone were calculated by integrating the pressures on the surface. The pressures were taken from existing test data from Test IA119 which was performed at NASA/Ames in 1977 (Ref. 1). The model used in Test IA119 was a 2 percent model of the space shuttle integrated vehicle. This model had the capability of simulating the jet plumes from both the shuttle main engines as well as the solid rocket boosters by flowing high pressure air through the nozzles of those components. The data obtained from this test was tabulated pressure coefficients at 40 locations on the nozzle exit cone exterior surface. These locations were every 30 degrees circumferentially around the nozzle and at 4 different axial locations. The axial stations were denoted by the ratio of their axial distance from the exit plane divided by the exit plane diameter of the nozzle. The  $x/D_{ref}$  values for test IA119 were 0.015, 0.135, 0.256, and 0.378. It should be noted that at the  $x/D_{ref}$  station of 0.378 there were only 4 circumferential stations every 90 degrees. This

explains why there were 40 pressure measurements as opposed to 48. The program which actually calculates the forces and moments produces many more computational points than are present in the raw data. The program interpolates points at 89 axial locations and 360 circumferential locations. Figure 2 shows this additional data along with the raw data for the zero degree circumferential location for the current aft exit cone as well as the extended aft exit cone. It should be noted that the values plotted in Figure 2 are pressure coefficients.

In order to calculate the forces and moments on the nozzle exit cone a FORTRAN program was developed. However, before the integration program could be run, the raw data was processed through an adapter program. This was done for two reasons. The first reason was to fill in the missing circumferential pressure measurements at the  $x/D_{ref}$  station of 0.378. The second function of the adapter program was to fill in two erroneous pressure measurements in the data. These erroneous pressure measurements were signified by values of 0.000 in the data and were located at  $x/D_{ref}$  equal to 0.015 and a circumferential location of 270 degrees, and  $x/D_{ref}$  equal to 0.135 and a circumferential station of 60 degrees. The adapter program uses a second order fit to fill in the missing and erroneous data. The adapter program also changes the  $x/D_{ref}$  coordinates to actual coordinates on the nozzle exit cone. This is accomplished by employing a scale factor to move from the model to the full scale geometry. The user inputs the reference length, in this case the distance from the aft skirt to the nozzle exit, and an effective nozzle exit diameter. This effective diameter is not the physical exit diameter of the full scale nozzle. Instead, it is a computed number such that the length to diameter ratio of the model and the full scale motor are equal. The following is the equation for the effective exit diameter.

$$D_{eff_{Full\ Scale}} = \frac{D_{model}}{L_{model}} \cdot L_{Full\ Scale}$$

This effective diameter is used instead of the actual exit diameter of the nozzle because the geometry of the model and the full scale RSRM nozzle were slightly different. The model nozzle was slightly shorter and had a slightly larger diameter than a two percent scaled RSRM nozzle.

For the extended aft exit cone calculations, the pressure measurements were left at the same physical locations as they were when scaled to the full scale RSRM motor from the IA119 test. The pressures acting over the nozzle extension were extrapolated from the pressures further forward on the nozzle. It was found that this method of distributing the pressure coefficients yielded the most conservative calculations of the force and moment loads.

After the use of the adapter program, the FORTRAN program was used to actually calculate the forces and moments on the nozzle exit cone. The lateral forces and pitch

and yaw moments were calculated by the program. The following equations show the formulae used to make the calculations.

$$F_x = \int P_s(\theta, z) \cdot \cos(\theta) \cdot \cos(\psi) \cdot [r_s(z) + \frac{1}{2} \cdot \Delta r_s(z)] \cdot d\theta \cdot \frac{dz}{\cos(\psi)}$$

$$F_y = \int P_s(\theta, z) \cdot \sin(\theta) \cdot \cos(\psi) \cdot [r_s(z) + \frac{1}{2} \cdot \Delta r_s(z)] \cdot d\theta \cdot \frac{dz}{\cos(\psi)}$$

$$M_x = \int r_s(z) \cdot \sin(\theta) \cdot P_s(\theta, z) \cdot \sin(\psi) \cdot [r_s(z) + \frac{1}{2} \cdot \Delta r_s(z)] \cdot d\theta \cdot \frac{dz}{\cos(\psi)} \\ - \int z \cdot \sin(\theta) \cdot P_s(\theta, z) \cdot \cos(\psi) \cdot [r_s(z) + \frac{1}{2} \cdot \Delta r_s(z)] \cdot d\theta \cdot \frac{dz}{\cos(\psi)}$$

$$M_y = \int z \cdot \cos(\theta) \cdot P_s(\theta, z) \cdot \cos(\psi) \cdot [r_s(z) + \frac{1}{2} \cdot \Delta r_s(z)] \cdot d\theta \cdot \frac{dz}{\cos(\psi)} \\ - \int r_s(z) \cdot \cos(\theta) \cdot P_s(\theta, z) \cdot \sin(\psi) \cdot [r_s(z) + \frac{1}{2} \cdot \Delta r_s(z)] \cdot d\theta \cdot \frac{dz}{\cos(\psi)}$$

where

$P_s$  = Surface Pressure

$r_s$  = Radius of Nozzle from Centerline

$\theta$  = Circumferential Angle around Nozzle

$\psi$  = Angle between Nozzle Surface and Nozzle Centerline

The forces  $F_y$  and  $F_x$  represent the pitch force and the yaw force, respectively, in Table I. The moments  $M_y$  and  $M_x$  represent the yaw moment and pitch moment, respectively, in Table I.

The data from the IA119 test was generated with a number of parametric variables. These included Mach number, angle of attack, and gimbal angle. For this analysis calculations were made at specific values of these parametric variables. First, a series of calculations was done over a Mach number range of 0.60 to 1.40 at an angle of attack of -8.0 degrees and a gimbal angle of 2.64 degrees. The actual Mach numbers run were 0.6, 0.8, 0.9, 0.95, 1.05, 1.1, 1.15, 1.25, and 1.4. The results of this Mach number scan are shown in Figure 3. From these calculations it was determined that the external aerodynamic moment on the nozzle exit cone increased with Mach number up to a maximum at 0.95 and then decreased with any further increase in Mach

number. It was also seen that the yaw moment on the nozzle was larger in magnitude than the pitch moment.

Specific calculations for forces and moments were made for condition 1 in the RSRM Design Loads Data Handbook since these flight conditions resulted in the maximum moment (Ref. 2). The case that was chosen had the following conditions:

Mach number	0.90
Angle of Attack	-2.9 Degrees
Gimbal Angle	2.26 Degrees up
Yaw Angle	0 Degrees
Dynamic Pressure	663 psf

The dynamic pressure was taken from the maximum dynamic pressure composite trajectory conditions for the compartment venting analysis (Ref. 3). This is also referred to as the "819" trajectory because of its maximum value of dynamic pressure of 819 psf. In addition, it was decided to run the same RSRM Design Loads Data Handbook condition at a Mach number of 0.95 with a corresponding dynamic pressure of 696 psf because the results of Figure 3 show a higher moment at Mach 0.95. The conditions in the table above are denoted as condition 1 in the RSRM Design Loads Data Handbook. The second case at Mach 0.95 will be denoted as condition 1a. Figure 4 shows curve fits of interpolated pressure data as a function of circumferential position for flight condition 1a for the standard RSRM nozzle. This plot includes data for four axial locations and is plotted versus circumferential angle. Figure 5 is a similar plot which shows the curve fits for condition 1a for the extended RSRM nozzle.

A number of computational runs had to be made to calculate the forces and moments at this condition because the data from test IA119 was not available at the Condition "1" angle of attack or gimbal angle. It was necessary to make a number of calculations which bounded the given conditions and then interpolate within these runs to arrive at values for the desired cases. The method used in these calculations was to calculate the forces and moments at conditions available from test IA119 and then linearly interpolate the forces and moments to arrive at results for the desired conditions. Runs were made at Mach numbers of 0.90 and 0.95, at angles of attack of 0, -4, and -8 degrees, and at gimbal angles of 0, 2.64, and 5.656 degrees. After the calculations were made the results were plotted and it was determined to use a linear interpolation scheme to arrive at the conditions in the RSRM Design Loads Data Handbook. An additional condition was created at a Mach number of 0.95 as this produced a higher moment than the condition at a Mach number of 0.90. The results from these calculations are presented in Table I.

After this was done it was decided to determine the effect of first interpolating the pressures to the conditions in the RSRM Design Loads Data Handbook and then calculating the forces and moments with the interpolated pressure data. For this method the raw pressure data from test IA119 was linearly interpolated to arrive at the



Table I. Forces and Moments

RSRM Aerodynamic Design Hinge Moments (Left SRM)

Extended Aft Exit Cone,  $Ae/At = 8.04$

Condition	Mach #	q psf	Gimbal Angle			Moment/(1*10E6)			Moment/(1*10E6)			Forces		
			Alpha deg	Beta deg	Pitch deg	Yaw deg	Pitch in-lbf	Yaw in-lbf	Rock in-lbf	Tilt in-lbf	Pitch lbf	Yaw lbf		
1	0.90	663	-2.9	0	2.26 UP	0	0.097221	0.334051	0.304955	0.167464	872	2232		
1a	0.95	696	-2.9	0	2.26 UP	0	0.140818	0.494026	0.448903	0.249756	1326	3533		
1b	0.95	696	-8.0	0	2.64 UP	0	0.030571	0.629639	0.466839	0.423605	498	4549		

RSRM Aerodynamic Design Hinge Moments (Left SRM)

Current Aft Exit Cone,  $Ae/At = 7.72$

Condition	Mach #	q psf	Gimbal Angle			Moment/(1*10E6)			Moment/(1*10E6)			Forces		
			Alpha deg	Beta deg	Pitch deg	Yaw deg	Pitch in-lbf	Yaw in-lbf	Rock in-lbf	Tilt in-lbf	Pitch lbf	Yaw lbf		
1	0.90	663	-2.9	0	2.26 UP	0	0.087162	0.181417	0.189914	0.066648	799	1242		
1a	0.95	696	-2.9	0	2.26 UP	0	0.152731	0.325300	0.338019	0.122024	1406	2446		
1b	0.95	696	-8.0	0	2.64 UP	0	0.058293	0.441043	0.353084	0.270645	679	3335		

Note: Forces and moments interpolated directly for specific listed values of alpha and gimbal angle for Case 1 and Case 1a.

conditions in the RSRM Design Loads Data Handbook. Then the interpolated pressure data was used to calculate forces and moments. It was found that this made very little difference in the values calculated for the forces and moments. The final calculated values from the direct interpolation of the pitch and yaw moments for the extended aft exit cone are 140,818 lbf-in and 494,026 lbf-in, respectively. The corresponding forces are 1326 lbf and 3533 lbf. These values are for a Mach number of 0.95. The corresponding numbers for a Mach number of 0.95 for the current aft exit cone are 152,731 lbf-in, 325,300 lbf-in, 1406 lbf, and 2446 lbf.

Also given in Table I are the values for the rock and tilt moments. The values represent the moment which must be generated by the nozzle actuators. The relevant equations are presented below.

$$M_{\text{Rock}} = M_x \cdot \cos(\beta) + M_y \cdot \sin(\beta)$$

$$M_{\text{Tilt}} = -M_x \cdot \sin(\beta) + M_y \cdot \cos(\beta)$$

where  $\beta=45^\circ$

Figure 1. RSRM External Nozzle Geometry

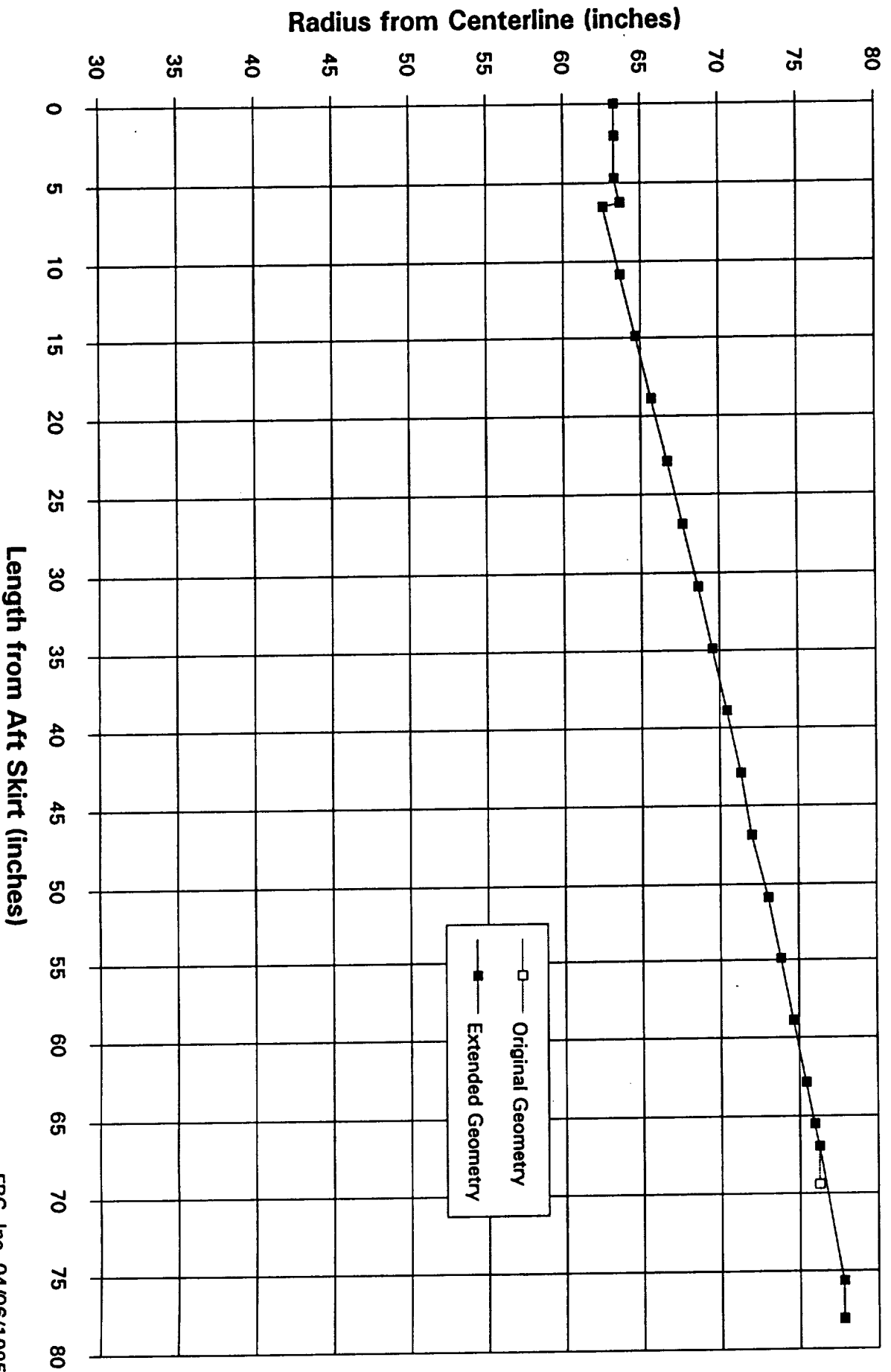


**Figure 2. RSRM External Nozzle Pressures  
Interpolated Pressure Data - Model Test IA119  
0 Deg. Circumferential Station**

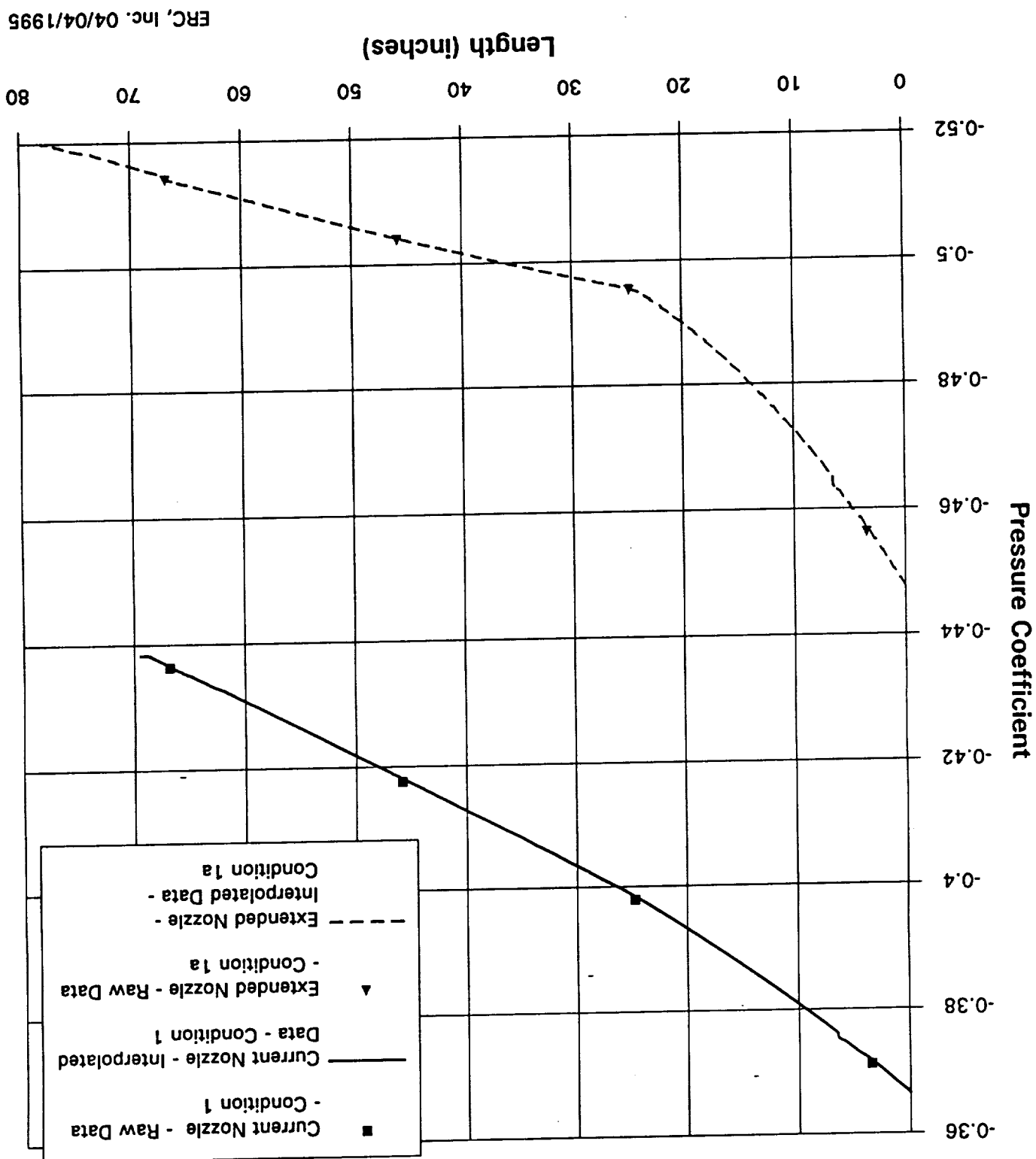


**Figure 3. RSRM Nozzle Moments**  
**RSRM Maximum Dynamic Pressure Trajectory**  
**Gimbal Angle = 2.64 Degrees**

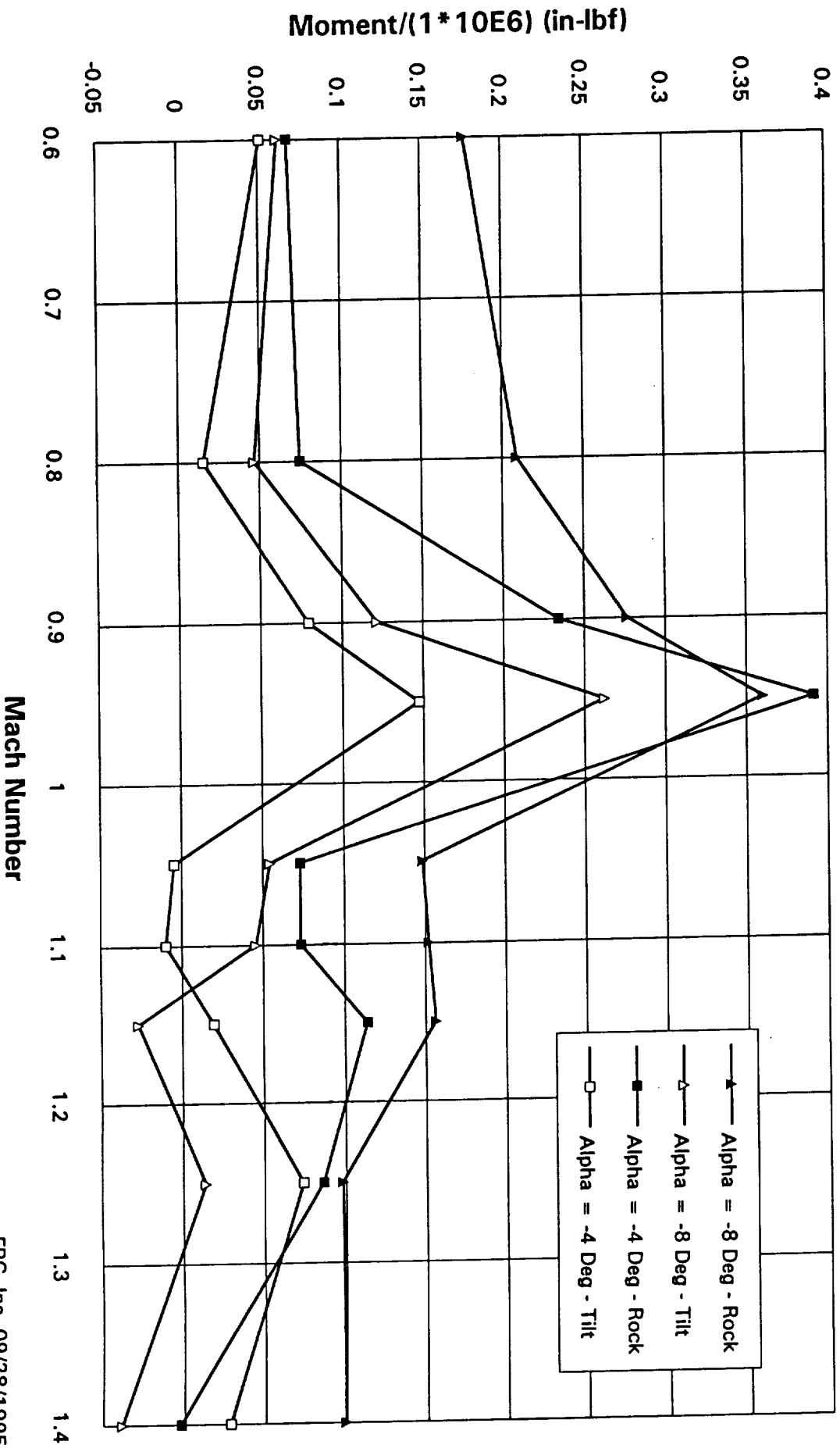


Figure 4. RSRM External Nozzle Pressures  
Mach No. = 0.95  $q = 696$  psf  
Pitch Angle = -2.9 Deg. Gimbal Angle = 2.26 Deg.

